DOE/ER-0045/8

Alloy Development for Irradiation Performance

Semiannual Progress Report
For Period Ending March 31, 1982

U.S. Department of Energy
Office of Fusion Energy

Printed in the United States of America. Available from
National Technical information Service
U.S. Department of Commerce
5285 Port Royal Road, Springfield, Virginia 22161
NTIS price codes—Printed Copy: A23 Microfiche A01

This report was prepared as an account of work sponsored by an agency of the United States Government Neither the United States Government nor any agency thereof. nor any of their employees, makes any warranty, express or implied, or assumes any legal liability or responsibility for the accuracy, completeness, or usefulness of any information, apparatus. product, or process disclosed, or represents that its use would not infringe privately owned rights Reference herein to any specific commercial product, process. or service by trade name, trademark, manufacturer. or otherwise, does not necessarily constitute or imply its endorsement, recommendation. or favoring by the United Stales Government or any agency thereof. The views and opinions of authors expressed herein do not necessarily stale or reflect those of the United States Government or any agency thereof.

DOE/ER-0045/8
Distribution
Category
uc-20. 20c

ALLOY DEVELOPMENT FOR IRRADIATION PERFORMANCE SEMIANNUAL PROGRESS REPORT FOR PERIOD ENDING MARCH 31, 1982

ARGONNE NATIONAL LABORATORY

GENERAL ATOMIC COMPANY

McDONNELL DOUGLAS ASTRONAUTICS COMPANY

MASSACHUSETTS INSTITUTE OF TECHNOLOGY

NAVAL RESEARCH LABORATORY

OAK RIDGE NATIONAL LABORATORY

SANDIA NATIONAL LABORATORIES

WESTINGHOUSE FUSION POWER SYSTEMS

WESTINGHOUSE HANFORD COMPANY

Date Published - September 1982

CAUTION

This document has not been given final patent clearance and the dissemination of its information is only for official use. No release to the public shall be made without the approval of the Law Department of Union Carbide Corporation. Nuclear Division.

Prepared by
OAK RIDGE NATIONAL LABORATORY
Oak Ridge, Tennessee 37830
operated by
UNION CARBIDE CORPORATION
for the
DEPARTMENT OF ENERGY
Under Contract No. W-7405-eng-26

Reports previously issued in this series are as follows:

DOE/ET-0058/1	Period Ending March 31, 1978
DOE/ET-0058/2	Period Ending June 30, 1978
DOE/ET-0058/3	Period Ending September 30, 1978
DOE/ET-0058/4	Period Ending December 31, 1978
DOE/ET-0058/5	Period Ending March 31, 1979
DOE/ET-0058/6	Period Ending June 30, 1979
DOE/ET-0058/7	Period Ending September 30, 1979
DOE/ER-0045/1	Period Ending December 31, 1979
DOE/ER-0045/2	Period Ending March 31, 1980
DOE/ER-0045/3	Period Ending June 30, 1980
DOE/ER-0045/4	Period Ending September 30, 1980
DOE/ER-0045/5	Period Ending December 31, 1980
DOE/ER-0045/6	Period Ending March 31, 1981
DOE/ER-0045/7	Period Ending September 30, 1981

FOREWORD

This report is the fourteenth in a series of Technical Progress Reports on *"Alloy Development for Irradiation Performance"* (ADIP), which is one element of the Fusion Reactor Materials Program, conducted in support of the Magnetic Fusion Energy Program of the U.S. Department of Energy. Other elements of the Materials Program are

- *Damage Analysis and Fundamental Studies (DAFS)*
- *Plasma-Materials Interaction (PMI)*
- *Special-Purpose Materials (SPM)*

The first seven reports in this series are numbered DOE/ET-0058/1 through 7. This report is the eighth in a new numbering sequence that begins with DOE/ER-0045/1.

The ADIP program element is a national effort composed of contributions from a number of National Laboratories and other government laboratories, universities, and industrial laboratories. It was organized by the Materials and Radiation Effects Branch, Office of Fusion Energy, DOE, and a Task Group on Alloy *Development for Irradiation Performance,* which operates under the auspices of that Branch. The purpose of this series of reports is to provide a working technical record of that effort for the use of the program participants, for the fusion energy program in general, and for the Department of Energy.

This report is organized along topical lines in parallel to a Program Plan of the same title so that activities and accomplishments may be followed readily relative to that Program Plan. Thus, the work of a given laboratory may appear throughout the report. Chapters 1, 2, 8, and 9 review activities on analysis and evaluation, test methods development, status of irradiation experiments, and corrosion testing and hydrogen permeation studies, respectively. These activities relate to each of the alloy development paths. Chapters 3, 4, 5, 6, and 7 present the ongoing work on each alloy development path. The Table of Contents is annotated for the convenience of the reader.

This report has been compiled and edited under the guidance of the Chairman of the Task Group on *Alloy Development for Irradiation Performance.* E. E. Bloom, Oak Ridge National Laboratory, and his efforts and those of the supporting staff of ORNL and the many persons who made technical contributions are gratefully acknowledged. T. C. Reuther, Materials and Radiation Effects Branch, is the Department of Energy Counterpart to the Task Group Chairman and has responsibility for the ADIP Program within DOE.

D. L. Vieth, Chief
Materials and Radiation Effects Branch
Office of Fusion Energy

CONTENTS

FOREWORD.. iii

1. ANALYSIS AND EVALUATION STUDIES 1

1.1 Materials Handbook for Fusion Energy Systems (McDonnell Douglas Astronautics Company and Westinghouse Hanford Company) 2

Data sheets covering both the unirradiated and irradiated properties of the glass-epoxy laminate G-10 CR have been distributed to holders of the MHFES. This material is used as an insulator in superconducting magnets and these data sheets represent the first step in fulfilling a commitment for the handbook to provide data on all materials, metallic and non-metallic, used in designing fusion systems. Other data sheets that should be released in the near future cover carbon, lithium compounds, and structural materials (316 SS and HT-9).

2. TEST MATRICES AND METHODS DEVELOPMENT 5

2.1 Neutronic Calculations in Support of the ORR-MFE-4 Spectral Tailoring Experiments (Oak Ridge National Laboratory) . . . 6

The geometric model of the ORR-MFE-4 experimental capsules has been modified, and calculated fluences are being scaled to agree with the experimental data. As of March 8, 1982, this treatment yields 36.30 at. ppm He (not including 2.0 at. ppm He from ^{10}B) and 4.35 dpa for type 316 stainless steel in ORR-MFE-4A, and 17.52 at. ppm He and 2.87 dpa in ORR-MFE-4B.

2.2 Operation of the ORR Spectral Tailoring Experiments ORR-MFE-4A and ORR-MFE-4B (Oak Ridge National Laboratory) 10

The ORR-MFE-4A experiment has operated for an equivalent of 391 d at 30-MW reactor power, with maximum specimen temperatures in the upper and lower regions of 400 and 330°C, respectively. A problem caused by a leak in the capsule primary system has been resolved, and the capsule is again in operation. The ORR-MFE-4B experiment, with specimen temperatures of 500 and 600°C, has operated for 283 d at 30-MW reactor power.

2.3 TEM Specimen Matrix for the AD-2 Reconstitution (Westinghouse Hanford Company) 13

TEM specimens have been prepared for inclusion in the reconstitution of the AD-2 test. The matrix includes specimens of HT-9 weld fusion zones and simulated heat-affected zones, undoped and nickel doped 12Cr-1Mo and 9Cr-1Mo alloys, and rapidly solidified Path A alloys.

2.4 HFIR/FFTF Irradiation Experiment — Conceptual Plan (Westinghouse Hanford Company and Oak Ridge National Laboratory) 17

Plans for a combined HFIR/FFTF irradiation experiment on Path A PCA and long-range ordered alloys are described. Irradiation will be up to ~160 dpa with the appropriate helium levels expected for fusion environments. Irradiation temperatures will be from 400 to 600°C. A tentative matrix of swelling disks, creep tubes, and tensile, crack growth and fracture toughness specimens has been identified.

2.5 Specimen Size Effects and Fusion Materials Research (Westinghouse Hanford Company) 25

Available data from specimens compatible with the Fusion Materials Irradiation Test (FMIT) facility have been compared with large specimen data to determine and quantify specimen size effects. For most of the properties examined, including properties where size effects are welt documented, it was determined that the data obtained from small specimens are in good agreement with, and in some cases indistinguishable from, large specimen data. Small specimens however, require careful attention to the details of design, testing and analysis. Nevertheless, a good approximation of engineering or design quality data can be obtained despite the comparatively limited irradiation volume of fusion spectrum neutron mdiation sources such as FMIT.

2.6 Neutron Source Characterization €or Materials Experiments (Argonne National Laboratory) 66

Data are presented from HFIR-CTR32, EBRII-X287, and the Omega West Reactor. An important new source of damage in nickel arises from the 340 keV ^{56}Fe recoil from the $^{59}Ni(n,\alpha)$ reaction used to produce high helium levels in materials irradiations in a thermal spectrum. The status of all other experiments is summarized in Table 2.6.1.

2.7 Elevated Temperature Irradiation of Ferritic Steel Charpy Specimens: Experiments HFIR-CTR-34 and -35 (Oak Ridge National Laboratory) 87

The HFIR-CTR-34 and -35 experiments contain miniature Charpy V-notch specimens of nickel-doped 12 Cr-1 MoVW and 9 Cr-1 MoVNb alloys. Different nickel contents result in different helium levels generated during irradiation in HFIR, to allow for an assessment of the effect of helium on impact properties. Irradiations at 300 and 400°C, to a midplane damage level of 10 dpa, have been completed.

2.8 Elevated-Temperature Irradiation of Ferritic Steel Tensile Specimens: Experiments HFIR-CTR-39, -40, and -41 (Oak Ridge National Laboratory) 91

The HFIR-CTR-39, -40, and -41 experiments contain rod tensile specimens of the nickel-doped 9 Cr-1 MoVNb and 12 Cr-1 MoVW alloys and the 2 1/4 Cr-1 Mo alloy. Different nickel levels result in different helium levels generated during irradiation. Testing of these alloys will provide data on the effect of helium on tensile properties. Irradiations will be at 300, 400, and 500°C to a midplane fluence equivalent to 12 dpa.

3. PATH A ALLOY DEVELOPMENT – AUSTENITIC STAINLESS STEELS 97

3.1 Swelling of Path A PCA Irradiated to 10 dpa in HFIR (Oak Ridge National Laboratory) 98

The Path A PCA with various pretreatments and 20%-cold-worked type 316 stainless steel (CW 316) were irradiated in HFIR at 300 to 600°C to fluences producing up to 9.7 dpa and 620 at. ppm He. Very tittle melting was observed at 500°C and below, but swelling at 600°C ranged from 0.2 to 1.26. Swelling appears coupled to precipitate phase and dislocation microstructural development.

3.2 Grain Boundary Microstructure in Path A PCA Irradiated to 10 dpa in HFLR (Oak Ridge National Laboratory) 118

Path A PCA in several preirradiation grain boundary microstructural conditions was irradiated in HFIR at 300 to 600°C to 10 dpa, together with 20%-cold-worked (N lot) type 316 stainless steel (CW 316). None of the samples show significant grain boundary bubble formation at 300 to 500°C. At 600°C, PCA-B1 and -B2, with stable, moderately sized grain boundary MC, have the finest dispersions of grain boundary bubbles.

3.3 Fatigue Life at 650°C of 20%-Cold-Worked Type 316 Stainless Steel Irradiated in the HFIR at 550°C (Oak Ridge National Laboratory) 136

Strain controlled fatigue tests were performed in vacuum at 650°C on 20%-cold-worked type 316 stainless steel irradiated in the HFIR at 550°C. Fluences ranged from 0.85 to 1.4 x 10^{26} neutrons/m^2. Little effect of irradiation was observed, but testing at 650°C failed to show the 10^7-cycle endurance limit observed at 550°C.

3.4 Irradiation Response of Rapidly Solidified Path A Type Prime Candidate Alloys (Massachusetts Institute of Technology) 141

The microstructural irmdiation response of the Path A prime candidate alloy and two similar alloys with increased titanium and carbon content prepared by mpid solidification processing, has been investigated by neutron irradiation to 8.5 dpa (360 appm He) in the HFIR, and by dual ion irmdiation to much higher dose (>100 dpa). The results show minor differences between conventionally prepared E A and E A prepared by mpid solidification techniques. However, these differences and the characteristic features of the response, the formation of very high densities of small cavities or bubbles and changes in the composition of initially existing TiC particles, are explained by a hypothesis of much importance to the mpid solidification approach. Our results suggest that increasing concentrations of titanium and carbon are beneficial, but only if the elements are initially in solution or present as very small (~2 nm) particles of TiC. The only way to practically achieve this for higher TiC contents than in PCA, is by using mpid solidification processing.

3.5 Some Effects of Increased Helium Content on Void Formation and Solute Segregation in Neutron-Irradiated Type 316 Stainless Steel (Oak Ridge National Laboratory) 169

During EBR-11 irmdiation of solution-annealed (SA) and 20%-cold-worked type 316 stainless steel (CW), void formation and melting are often coupled to radiation-induced solute segregation (RISS). A refined sink structure, including high cavity concentration, results if helium is preinjected before EBR-11 irradiation or produced during HFIR irmdiation. This can suppress both the void swelling and the RISS.

3.6 Application of Quantitative Electron Energy Loss Spectroscopy to Analysis of the Titanium Carbide Phase in Austenitic Stainless Steels (Oak Ridge National Laboratory and Argonne National Laboratory) 217

Quantitative analytical electron microscopy employing both x-ray energy dispersive spectroscopy (XEDS) and electron energy loss spectroscopy (EELS) was used to determine the carbon content of carbide particles in the Path A PCA. These results show that the experimental techniques must be adequate to resolve the Mo M and C K shell edges before quantitative measurement of carbon content is possible. Precipitate particles of different sizes had different metal-to-carbon ratios, which could be related to their titanium and molybdenum contents.

3.7 Dynamic Powder Compaction of Rapidly Solidified Path A Alloy with Increased Carbon and Titanium Content (Massachusetts Institute of Technology) 223

Different techniques for consolidation of rapidly solidified alloys which are available or are under study at the present time include conventional consolidation techniques 1hot extrusion, HIP,. ..), high velocity consolidation of atomized partially solidified particulates and dynamic powder compaction (DPC). This report describes the results of dynamic compaction of Path A alloy with increased carbon and titaniwn content. The microstructure of the as-compacted alloy is highly complex, evidencing an extreme degree of deformation. TEM revealed very high dislocation and twin density reflecting high hardness of the as-compacted alloy. Annealing studies revealed that recovery and recrystallization processes in dynamically compacted alloy are slower than in conventionally treated materials. High dislocation density appears to be an intrinsic property of the dynamic compaction process and it may be potentially useful in developing materials for irradiation performance. Other potential applications of dynamic compaction include preparation of graded materials and ceramic materials.

3.8 Mechanical Properties and Structure of Y_2O_3 Dispersion Stabilized, Rapidly Solidified 316 Type Stainless Steel (Massachusetts Institute of Technology) 239

An oxide dispersion stabilized 316 stainless steel has been prepared by mechanical alloying of a few 100 A size yttria powders with attrited flakes of 316 staintess steet prealloyed with 1 wt% aluminum. Alloys with 4 vol% and 5 vol% yttria additions have been prepared and they show significant improvements in microstructural stabitity. Austenitic stainless steel containing 4 vol% yttria showed very high room temperature YS and UTS, with sufficient ductility. Stress rupture testing at 650°C as a function of different thewnomechanicat treatments is currently in progress.

3.9 Microstructures Developed in Austenitic Stainless Steels Irradiated in HFIR at 55°C (Oak Ridge National Laboratory) . . . . . , ... 250

Samples of solution annealed types 316 and 347 stainless steel (SA 316 and SA 347) and 20%-cold-worked type 316 stainless steel (CW 316) have been irradiated in the High Flux Isotope Reactor (HFIR) at 55°C. No voids or bubbles were detected. All samples contained a fine "black spot" component of the dislocation structure. Both SA 316 and SA 347 contained a high concentration of Frank interstitial loops (14–30 nm diam) but no dislocation networks, whereas CW 316 shows network recovery with few Frank loops.

3.10 Statistical Analysis of the MFE-5 In-Reactor Fatigue Crack Growth Experiment Results (Westinghouse Hanford Company) 256

Results from the in-reactor fatigue crack propagation experiment and thermal control test have been quantitatively analyzed using statistical comparisons of the data. The analysis showed that at the 95% confidence limits, the in-reactor growth rates exceeds the thermal control by at most a factor of about two. However, the average growth rates in-reactor were less than that for the thermal controls, but statistically there were no significant differences between the crack growth rates from the two tests.

3.11 Tensile Properties of U.S.S.R. Austenitic Stainless Steel After Low-Temperature High FLux Isotope Reactor Irradiation (Oak Ridge National Laboratory) 266

Two tensile specimens of the U.S.S.R. low-nickel, high-manganese stainless steel EP-838 were irradiated in the High Flux Isotope Reactor (HFIR) at about 55°C to produce about 5.2 dpa and 63 at. ppm He. The tensile properties at room temperature and 300°C of the irradiated and ***unirradiated*** *20%-cold-worked steel were quite similar to the properties of 20%-cold-worked type 316 stainless steel (CW 316) that was similarly irradiated.*

4. PATH B ALLOY DEVELOPMENT – HIGHER STRENGTH Fe-Nf-Cr ALLOYS . . . 277

No contributions.

5. PATH C ALLOY DEVELOPMENT — REACTIVE *AND* REFRACTORY ALLOYS . . . 279

5.1 Mechanical Property Evaluations of Path C Vanadium Scoping Alloys (Westinghouse Electric Corporation) 281

Nominal oxygen impurity levels of 600 and 1200 wppm, above the residual content of the alloys, have been introduced by gas-metal reaction into 0.76 mm sheet specimens of vadium-base alloys. Tensile tests have been performed on each alloy at RT, 500, and 700°C and the results compared to previous tests on noncontaminated specimens. The oxygen contamination affected both strength and fracture behavior; these effects varied for the three alloys.

5.2 Swelling in Neutron Irradiated Titanium Alloys (Westinghouse Hanford Company) 304

Immersion density measurements have been performed on a series of titanium alloys irradiated in EBR-II to a fluence of 5×10^{22} n/cm^2 (E >0.1 MeV) at 450 and 550°C. The materials irradiated were the near-alpha alloys Ti-6242s and Ti-56215, the alpha-beta alloy Ti-64 and the beta alloy Ti-38644. Swelling was observed in all alloys

with generally the greater swelling being observed at 550°C. Preliminary microstructural examinations revealed the presence of voids in all alloys. Ti-38644 was found to be the most radiation resistant. Ti-6242s and Ti-5621S also displayed good radiation resistance, whereas considerable swelling was observed in Ti-64 at 550°C.

6. INNOVATIVE MATERIAL CONCEPTS 313

6.1 Microstructures of Iron-Base Long-Range-Ordered Alloys Bombarded to 70 dpa with Nickel Ions (Oak Ridge National Laboratory) 314

Disks of LRO-37-5 in the as-ordered and 20%-cold-worked conditions were bombarded with 4-MeV nickel wns to 70 dpa at temperature8 from 570 to 680°C. Both conditions retained order for bombardment below the critical ordering temperature of about 650°C, and cold work improved the swelling resistance, especially above T_c. Both conditions showed better resistance to swelling than 20%-cold-worked type 316 stainless steel.

6.2 Status of Scale-Up of an Iron-Base Long-Range-Ordered Alloy (Oak Ridge National Laboratory) 321

The semiproduction scale-up of an iron-base LRO alloy is under way by a commercial source. Three 18-kg ingots have been produced by two different melt practices. Chemical analyses indicate that the compositions of the ingots are near the alloy specifications. Specimens from the ingots were successfully cold rolled at room temperature and hot rolled at 1100°C. Further evaluation of alloy homogeneity and distribution of second phases is in progress.

6.3 Microstructures of Iron-Base Long-Range-Ordered Alloys Irradiated to 10 dpa in HFIR (Oak Ridge National Laboratory) 327

The LRO-16, -20, and -37 alloys were irradiated in HFIR at 300 to 600°C to nominally 8.3 dpa and 1000 at. ppm He. All three remained ordered, and interstitial loops, dislocation segments, and cavities formed in the microstructure. cavities grew preferentially on {111} loops, and helium bubbles formed on grain boundaries at the higher temperatures. Swelling in LRO-20 and -37 was low; LRO-16 swelled more than annealed EA.

7. PATH E ALLOY DEVELOPMENT – FERRITIC STEELS 335

7.1 Postirradiation Notch Ductility and Fracture Toughness Behavior of AOD Heat of Alloy HT-9 (Naval Research Laboratory) 336

Alloy HT-9 is being euatuated for potential application as a first wall material in magnetic fusion reactors. One objective of the current studies is the assessment of material notch ductility and fracture toughness in the pre- and postirradiation conditions.

Charpy-V (C_v) and fatigue precracked Charpy-V (PCC_v) specimens of a 1.7 cm thick plate from the HT-9 reference melt (AOD process) were irradiated at 93° and at 288°C to ~8 × 10^{19} n/m^2, E> 0.1 MeV, in a water-cooled test reactor. The C_v transition temperature elevation produced by the 93°C irradiation was more than three times that produced by the 288°C irradiation. The 93°C irradiation data showed the alloy to be unacceptable for 93°C service unless (only) elastic fracture resistance is acceptable. Good agreement was observed between C_v and PCC_v determinations of radiation-induced embrittlement.

7.2 Impact Test Results for Irradiated Ferritic Alloys (Westinghouse Hanford Company) 342

To be reported in the next semiannual report.

7.3 Microstructural Examination of HT-9 and 9Cr-1Mo Contained in the AD-2 Experiment (Westinghouse Hanford Company) . . . 343

The microstructures of HT-9 and modified 9Cr-1Mo have been examined before and after irradiation in EBR-II in the AD-2 experiment to a fluence of 2.5 x 10^{22}n/cm^2 (E>0.1 MeV) at temperatures from 400 to 550°C. The precipitate structure of unirradiated HT-9 consists of $M_{23}C_6$ which forms at martensite lath and prior austenite grain boundaries. 9Cr-1Mo shows much less $M_{23}C_6$ at grain boundaries, but contains finely-dispersed (Nb,V,Cr)C within grains. Irradiation of both alloys at 400°C causes extensive additional precipitation, formation of a dislocation substructure, and, in 9Cr-1Mo, void formation. The irradiation-induced precipitate in HT-9 was identified as G-phase, a nickel silicide with fcc crystal structure and lattice parameter of 1.12 nm. Only very small additions of nickel are required in ferritics to promote the formation of G-phase. 9Cr-1Mo irradiated at 400°C formed rod-shaped Cr_2C. Above 450°C, the HT-9 formed additional $M_{23}C_6$, whereas the 9Cr-1Mo formed additional MC and a phosphide with Fe, Cr, and Mo. No voids were observed above 450°C in the 9Cr-1Mo alloy. The formation of finely-dispersed G phase in HT-9 and Cr_2C in 9Cr-1Mo during irradiation below 450°C is believed to contribute to observed irradiation hardening and increased DBTT.

7.4 The Procurement and Characterization of the Electroslag Remelted National Fusion Program Heat of 12Cr-1Mo Steel (General Atomic Company) 363

Previously it was reported that a 30,000 lb heat of a 12Cr-1Mo steel melted to the specification of Sandvik HT-9 was procured by General Atomic Company from Electralloy Corporation for the Ferritic Steel Program. This heat of argon-oxygen decarburization (AOD) 12Cr-1Mo steel has, since, been electroslag remelted (ESR) by Universal Cyclops Corporation in Pittsburg, and converted to plate and bar stock. This remelted heat (No.9607R2) was within the chemical specification requirement of HT-9. The remelted ingot was homogenized at 1100C for 16 hrs prior to conversion to the product forms. After conversion to plate and bar stock, each form was given a stress relief at 700C for 6 hrs. Subsequent mechanical property analysis on the 0.625 in (1.58 cm) plate has shown that it meets the strength and tensile elongation specifications. The UTS was 121 ksi (835 MPa), the yield stress was 87.5 ksi (604 MPa), and the elongation was 21%. The upper shelf energy determined on standard Charpy impact specimens was 85 ft-lbs (115J) as compared to the upper shelf of the AOD heat of 66 ft-lbs (89J). Microstructural examination showed a uniform tempered martensitic structure with a delta ferrite content less than 1%.

7.5 The Weldability of HT-9: Preheat and Position Effects (General Atomic Company) 370

To be reported in the next semiannual report.

7.6 The Toughness of Simulated Heat-Affected Zone Microstructures in a 12Cr-1Mo-0.3V Martensitic Stainless Steel (Sandia National Laboratories) 371

The four distinct HAZ microstructures which were identified in HT9 GTA welds were simulated in the Gleeble in order to produce bulk microstructural Charpy V-notch samples suitable for evaluation of notch toughness. Samples both transverse and longitudinal to the rolling direction (R.D.) of AOD melt plate stock were evaluated. Following the Gleeble thermal treatment the samples were given a postweld heat treatment (PWHT) for 1 hour at 760°C. Charpy tests of the individual microstructures were performed over the temperature range from -60 to 200°C. The toughness values of samples oriented transverse to the rolling direction (notch aligned parallel to R.D.) fell in a wide scatterband which enclosed the base metal toughness at low temperatures and was slightly less than the base metal value on the upper shelf. When samples oriented parallel to the R.D. Inotch transverse to R.D.) were evaluated the toughness of three of the microstructural regions was again equivalent to that of the base metal.

The fourth region, which contained a fine prior austenite grain size exhibited superior toughness properties with respect to both the ductile-to-brittle transition temperature (DBTT) and the upper shelf energy.

7.7 The Effect of Postweld Heat Treatment on the Toughness of the Heat-Affected Zone in a 12Cr-1Mo-0.3V Steel (HT9) (Sandia National Laboratories) 388

Samples both transverse and longitudinal to the rolling direction (R.D.) of the plate were subjected to thermal cycles in the Gleeble which simulated four distinct microstructures in the HAZ. Following the Gleeble heat treatment, the samples were tempered at either 760°C or 600°C for one hour and subsequently tested over a range of temperatures in the Charpy apparatus. Charpy test results revealed that the higher PWHT decreased the ductile-to-brittle transition temperature (DBTT) and increased the upper shelf energy of three of the microstructures. A fourth microstructure was relatively unaffected by the PWHT since the peak temperature experienced by this HAZ region is not sufficient to reaustenitize the structure during welding. The region of the microstructure heated just slightly above the austenitization temperature during welding exhibits the best toughness properties due to the refinement of the austenite grain size.

The Charpy results indicate that a 600°C postweld heat treatment is not sufficient to increase the toughness of the weld region to a level which would guarantee the structural integrity of a large component. It is imperative that the ambient temperature toughness should be sufficient to ensure extended life during cyclic loading and periodic shutdown of the reactor.

7.8 Interpretive Report on the Weldability of 12Cr-1Mo-0.3V (HT9) Martensitic Stainless Steel, Part 2: Suitability for Fusion Reactor First Walls and Blanket Structures (Sandia National Laboratories) 399

A previous report summarized the results of both commercial experience and ADP-sponsored research concerned with the weldability of the HT9 candidate alloy. The general conclusion of this report was that HT9 exhibits adequate weldability and is suitable from a fabrication standpoint; however, the question of in-service behavior and survivability in an operating reactor have not been addressed. To date, the data to make such judgments are not available. Continuing research in the areas of irradiation damage, fatigue behavior, hydrogen embritttement, and the synergism among these issues and others must be pursued before the suitability of HT9 weld microstructures in fusion reactor environments can be property assessed.

7.9 Hydrogen Embrittlement of ESR Processed 12Cr-1Mo Steel (Sandia National Laboratories) 401

Tensile tests were performed to determine the effect of hydrogen on the ductility of a quenched-and-tempered 12Cr-1Mo alloy from the National Fusion Heat-ESR processed. specimens were cathodically charged with hydrogen at 0.003 A/cm^2 and 0.006 A/cm^2 for 15 to 150 minutes. In the uncharged condition, the ESR specimens failed by intergranular rupture with prominent secondary cracking along prior austenite grain boundaries. For the least severe cathodic charge (0.003 A/cm^2 – 15 minutes), the tensile ductility (R_A) decreased 33% and the degree of secondary cracking increased. At 0.003 A/cm^2 for 150 minutes, the ductility decreased further and the fracture mode changed to classical intergranular fracture. These results generally mztched those for the AOD processed 12Cr-1Mo alloy that had been tested previously.

Auger analysis indicates that there is segregation of phosphorous and the carbide-forming elements Cr, Mo, W to the prior austenite grain boundaries. In the literature, phosphorous has been shown to embrittle these boundaries, especially in the presence of hydrogen.

The combination of tensile data on hydrogen charged ESR and AOD 12Cr-1Mo steet present several reasons for concern regarding the susceptibility of this alloy to hydrogen embrittlement. Earlier results of hydrogen charged Sandvik HT-9 are addressed in terms of these more recent findings.

7.10 Tensile Properties of Ferritic (Martensitic) Steels After Low-Temperature HFIR Irradiation (Oak Ridge National Laboratory) 414

In addition to the ferritic steels previously tested, experiment HFIR-CTR-33 also contained tensile specimens of 20%-cold-worked type 316 stainless steel for irmdiation at about 55°C. The tensile behavior of the type 316 stainless steel was determined at room temperature and 300°C, and the results showed the irmdiated properties of the two classes of steels to be quite similar.

7.11 Helium Embrittlement Tests on Ferritic Steels (Oak Ridge National Laboratory) 424

Tensile tests at 700°C a nickel-doped 9 Cr-1 MoVNb and 12 Cr-1 MoVW steels that were irmdiated at 55°C in HFIR to produce up to about 50 at. ppm He indicated that there was no helium embritttement. These results contrast with literature data showing that very small amounts of helium can cause a large decrease in ductility for many alloys when tested under equivalent conditions.

7.12 Reconstitution of the AD-2 Ferritics Experiment (Westinghouse Hanford Company) 431

Six uninstrumented B-7c capsules were removed from the EBR-II after undergoing irradiation during Cycles 109-113. Several specimens were removed and distributed for interim examination, white the remaining specimens were re-encapsulated into four new B-7c capsules. In addition, some irradiated specimens were included in the new capsules. Irradiation continued with Cycle 118 and will end after Cycle 123.

7.13 Fractographic Examination of Compact Tension Specimens of Unirradiated HT-9 and Modified 9Cr-1Mo Welds (Westinghouse Hanford Company) 442

Miniature compact tension specimens of HT-9 and modified 9Cr-1Mo weld metal and HT-9 HAZ material have been tested and examined by scanning electron microscopy in order to provide baseline data for comparison with irradiated specimens, to provide understanding of the fracture process in these mzteriats, and to assess the usefulness of crack opening displacement measurements based on fractographic analysis. For specimens tested at 205°C, crack propagation is found to be due to microvoid coalescence.

7.14 Postirradiation Notch Ductility of the Weld Heat Affected Zone (HAZ) of Alloy HT-9 Plate (AOD Heat) (Naval Research Laboratory and Sandia National Laboratories) 460

Alloy HT-9 is being evaluated for potential application as a first wall material in magnetic fusion reactors. The size and complexity of projected components may necessitate the use of welding for component fabrication; according1y, studies of Alloy HT-9 mdiation resistance capabilities are including assessments of weld deposits and weld HAZ materials. The present investigation represents a joint effort by the Naval Research Laboratory (NRL) and the Sandia National Laboratories at Livermore (SNLL).

Charpy-V (C_v) specimens simulating four positions across a weld HAZ and specimens of the parent plate material were irradiated at 288°C to 8 x 10^{19} n/cm^2, E> 0.1 MeV. The HAZ specimens were thermally cycled on a Gleeble apparatus; individual thermal cycles provided peak temperatures of 1380, 1152, 974 or 828°C. Postirradiation notch ductility determinations revealed the HAZ to have essentially uniform mdiation embrittlement sensitivity across its width. In addition, the data showed the mdiation resistance level of the HAZ to be comparable to that of the parent plate. The results in turn suggest that, for the 288°C service condition, the fracture resistance of irradiated HT-9 weldments will not be governed primarily by the weld HAZ.

8. **STATUS OF IRRADIATION EXPERIMENTS AND MATERIALS INVENTORY** . . . 467

8.1 **Irradiation Experiment Status and Schedule (Oak Ridge National Laboratory)** 46%

principal features of mny ADIP irradiation experiments are tabulated. Bar charts show the schedule for recent, current, and planned experiments. Experiments are presently under way in the Oak Ridge Research Reactor (ORR) and the High Flux Isotope Reator (HFIR), which are mixed spectrum reactors, and in the Experimental Breeder Reactor (EBR-II), which is a fast reactor.

8.2 **ETM Research Materials Inventory (Oak Ridge National Laboratory)** 476

The office of Fusion Energy has assigned program responsibility to ORNL for the establishment and operation of a central inventory of research materials to be used in the Fusion Reactor Materials research and development programs. The objective is to provide a common supply of material for the Fusion Reactor Materials Program. This will minimize unintended materials variables and provide for economy in procurement and for centralized record-keeping. Initially this inventory will focus on materials related to first-wall and structural applications and related research, but various special purpose mteriats m y be added in the future.

9. **MATERIALS COMPATIBILITY AND HYDROGEN PERMEATION STUDIES** 481

9.1 **Corrosion of Austenitic, Ferritic, and Long-Range-Ordered Alloys in Flowing Lithium (Oak Ridge National Laboratory)** 482

Results from lithium thermal-convection loop (TCL) tests of type 316 stainless steel, Sandvik HT9, and a long-range-ordered (LRO) alloy composed of Fe-31.8 Ni-22.5 V-0.4 Ti (ut %) are reported. Type 316 stainless steel and HT9 had similar steady-state dissolution rates at 500°C. The LRO alloy was rapidly corroded in type 316 stainless steel TCLs. However, results from isothermal tests in lithium showed that dissimilar-metal transfer probably mde a very significant contribution to the overall LRO alloy corrosion rate measured in the above experiments.

9.2 **Environmental Effects on Properties of Structural Alloys (Argonne National Laboratory)** 491

Compatibility tests were conducted with several candidate structural mteriats to study the corrosion behavior in flowing lithium, and fatigue tests were performed with HT-9 alloy specimens that were preexposed to lithium. The results indicate that the corrosion rate of ferritic steels

is an order of magnitude lower than for the austenitic stainless steel. The corrosion rate for cold-worked Type 316 stainless steel is a factor of 3 greater than that for the annealed steel. Preexposure (1000 h) of the HT-9 alloy to tow-nitrogen lithium has no effect a fatigue life. Preliminary scoping studies indicate that V-15Cr and V-15Cr-5Ti alloys are highly corrosion resistant in 523 K (250°C) deoxygenated water.

9.3 Corrosion of Austenitic and Ferritic Steels in Static Pb-17 at. % Li (Oak Ridge National Laboratory) . . . . . , 500

Specimens of type 316 stainless steel and Sandvik HT9 were exposed to static, molten Pb-17 at. % Li. Weight losses of these alloys exposed to Pb-17 at. % Li were much greater than those measured in static, pure lithium. Decreased weight losses at longer exposure times were thought to be a result of possible corrosion product formation a the specimen surfaces due to impurities in the melt.

9.4 Compatibility Studies of Structural Alloys with Solid Breeder Materials (Argonne National Laboratory) 507

The compatibility of solid Li_2O, $LiAlO_2$, and Li_2SiO_3 breeder materials with Type 316 stainless steel and ET-9 alloy has been investigated at 773 K (500°C). The results show that for Li_2O, the alloy-ceramic interactions at 773 K are similar to that observed at 973 K (700°C). Both steels show a uniform layer of internal penetration and a thick outer scale that consists of the ceramic rmteriat embedded with iron-rich corrosion products. Specimens exposed with $LiAlO_2$ or Li_2SiO_3 show no measurable interaction. A compatibility test with Li_2O has been initiated at 823 K (550°C) in a flowing helium environment containing controlled mounts of moisture and hydrogen.

1. **ANALYSIS AND EVALUATION** STUDIES

1.1 MATERIALS HANDBOOK FOK FUSION ENERGY SYSTEMS – J. W. Davis (McDonnell Douglas Astronautics Company – St. Louis) and T. K. Bierlein (Hanford Engineering Development Laboratory)

1.1.1 ADIP Task

Task Number 1.A.1 – Define material property requirements and make structural life predictions.

1.1.2 Objective

To provide a consistent and authoritative source of material property data for use by the fusion community in concept evaluation, design, safety analysis, and performance/verification studies of various fusion energy systems. A secondary objective is the early identification of areas in the materials data base where insufficient information or voids exist.

1.1.3 Summary

The third publication package of data sheets for the MHFES has been released. This publication package contains seven new tab dividers, revisions to the table of contents, a new revision control page, and 21 pages on properties of a glass epoxy laminate called G-10 CR which is used in superconducting magnets. These pages describe the ultimate tensile strength, interlaminar shear strength, ultimate tensile strain, Poisson's ratio, static Young's modulus in tension, dynamic Young's modulus, ultimate compressive strength, compressive strength under gamma irradiation, flexural strength under gamma irradiation, thermal conductivity, thermal expansion, electrical resistivity, resistivity under irradiation, electric strength, density, composition of gases generated by irradiation, radioactivity after irradiation, and weight loss due to irradiation. Data pages covering the electrical resistivity and tritium permeability of 20% cold worked type 316 stainless steel, the thermal expansion of lithium oxide, and the mechanical properties of graphite have been received and are currently being reviewed by the Analysis and Evaluation task group prior to release to the handbook. In addition, page preparation of data sheets on lithium compounds, alumina, and ferritic steels are in progress.

1.1.4 Progress and Status

Superconducting magnets are currently planned for use on near term machines such as EBT-P and MFTF-B and longer term devices such as FED/ETR and DEMO along with the commercial designs. In order to support the near term design projects and the longer range conceptual designs, requests were made to various organizations active in the field of superconducting magnets to provide data sheets on G-10CR (glass epoxy laminate) which is used as an insulator in superconducting magnets. In response to these requests, data sheets were prepared by G. P. Lang of MDAC and R. R. Coltman of ORNL. These data sheets, which cover a wide range of physical and mechanical properties, were prepared in support of the EBT-P project and were distributed to holders of the handbook in the third publication package. The 24-page G-10CR data package consists of the ultimate tensile strength, interlaminar shear strength, ultimate tensile strain, Poisson's ratio, static Young's modulus in tension, dynamic Young's modulus, ultimate compressive strength, compressive strength under gamma irradiation, flexural strength under gamma irradiation, thermal conductivity, thermal expansion, electrical resistivity, resistivity under irradiation, electric strength, density, composition of gases generated by irradiation, radioactivity after irradiation, and weight loss due to irradiation.

Data sheets relating to the electrical resistivity and the tritium permeability of 20% cold worked 316 stainless steel have been prepared by R. F. Mattas of ANL as part of their Starfire Studies. These data sheets have been submitted for review and approval to the Analysis and Evaluation task group and shouid be available to the handbook holders in early fall. In addition to data sheets on 316 stainless steel, there are a number of other data sheets currently nearing completion which should be available for review and approval this summer and will likely be part of the fourth publication package. These data pages cover the thermal expansion of lithium oxide (submitted by G. W. Hollenberg, HEDL), properties of graphite (submitted jointly by G. P. Lang, MDAC, and W. Eatherly, ORNL) and the properties of lithium (submitted by W. Brehm, HEDL).

One of the primary difficulties the handbook has encountered over the past year has been to maintain a constant supply of data sheets to

the handbook holders. In an effort to remedy this situation, the Materials and Radiation Effects branch of O.F.E. sent a programmatic letter to all principal investigators, involved in materials research, soliciting their support in preparing data sheets and setting a goal of incorporrting into the handbook 24 additional data pages for this year. A number of the researchers have responded with commitments to prepare data sheet?, on a variety of materials ranging from Alumina to ferritic steels. The support of these researchers should help to alleviate this problem.

1.1.5 Future Work

The effort for the handbook over the next six months will be directed towards the preparation of data sheets for a wide range of materials. Currently planned data sheets will cover ferritic steels, alumina, solid lithium compounds, and graphite. The longer range effort will be directed towards developing correlations on swelling and irradiation creep along with preparing data sheets showing the irradiated mechanical properties of 316 stainless steel.

2. TEST MATRICES AND **METHODS** DEVELOPMENT

2.1 NEUTRONIC CALCULATIONS IN SUPPORT OF THE ORR-MFE-4 SPECTRAL TAILORING EXPERIMENTS — R. A. Lillie, R. L. Childs, and T. A. Gabriel (Oak Ridge National Laboratory)

2.1.1 ADIP Task

ADIP Task I.A.2, Define Test Matrices and Test Procedures.

2.1.2 Objective

The objective of this work is to provide the neutronic design for materials irradiation experiments in the Oak Ridge Research Reactor (ORR). Spectral tailoring to control the fast and thermal fluxes is required to provide the desired displacement and helium production rates in alloys containing nickel.

2.1.3 Summary

The geometric model of the ORR-MFE-4 experimental capsules **has** been modified, and calculated fluences are being scaled to agree with the experimental data. As of March 8, 1982, this treatment yields 36.30 at. ppm He (not including 2.0 at. ppm He from ^{10}B) and 4.35 dpa for type 316 stainless steel in ORR-MFE-4A, and 17.52 at. ppm He and 2.87 dpa in ORR-MFE-4B.

2.1.4 Progress and Status

The geometric model of the ORR-MFE-4 experimental capsules employed in the three-dimensional neutronics calculations[1,2] has been modified. The new model includes more detail and lowers the calculated-to-experimental fluence ratios[3-5] from 1.46 to 1.32. All calculated fluences are presently being scaled to force agreement with the experimental data. The operating and current calculated data (fluences scaled by 0.76 to agree with the experimentally measured fluences[4] and helium production[5]) for the ORR-MFE-4A and -4B experiments are summarized in Table 2.1.1.

The real-time projections of the at. ppm He to dpa levels based on current calculated data (fluences scaled by 0.76) as of March 8, 1982 are given in Figs. 2.1.1 and 2.1.2 for the ORR-MFE-4A and -4B experiments,

Table 2.1.1. Operating and Calculated Data for Experiments ORR–MFE–4A and –4B as of March 8, 1982

	ORR-MFE-4A	ORR-MFE-4B
ORR cycles	34	21
Power (MWh)	266,186	188,769
Thermal fluence (neutrons/m^2)	5.47×10^{25} (7.20×10^{25})[a]	3.65×10^{25} (4.80×10^{25})
Total fluence (neutrons/m^2)	1.72×10^{26} (2.26×10^{26})	1.14×10^{26} (1.50×10^{26})
Helium (at. ppm)[b]	36.30 (59.43)	17.52 (28.83)
dpa[b]	4.35 (5.72)	2.87 (3.78)

[a]Values in parentheses represent unscaled calculated data.

[b]helium and dpa values are for type 316 stainless steel.

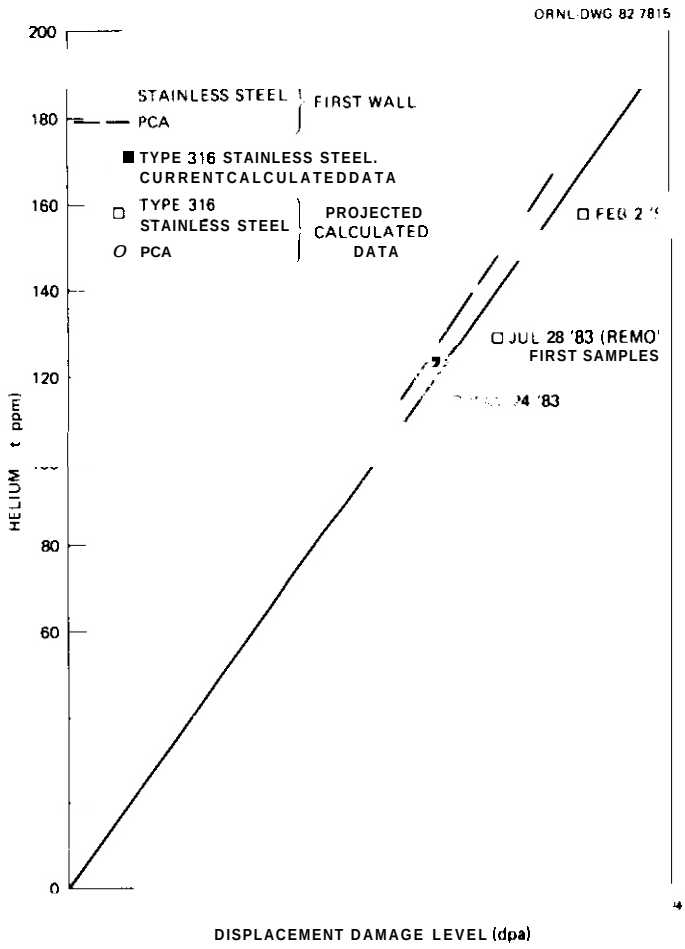

Fig. 2.1.1. Current and Projected Helium and Displacement Damage Levels Expected in the ORR-MFE-4A Experiment.

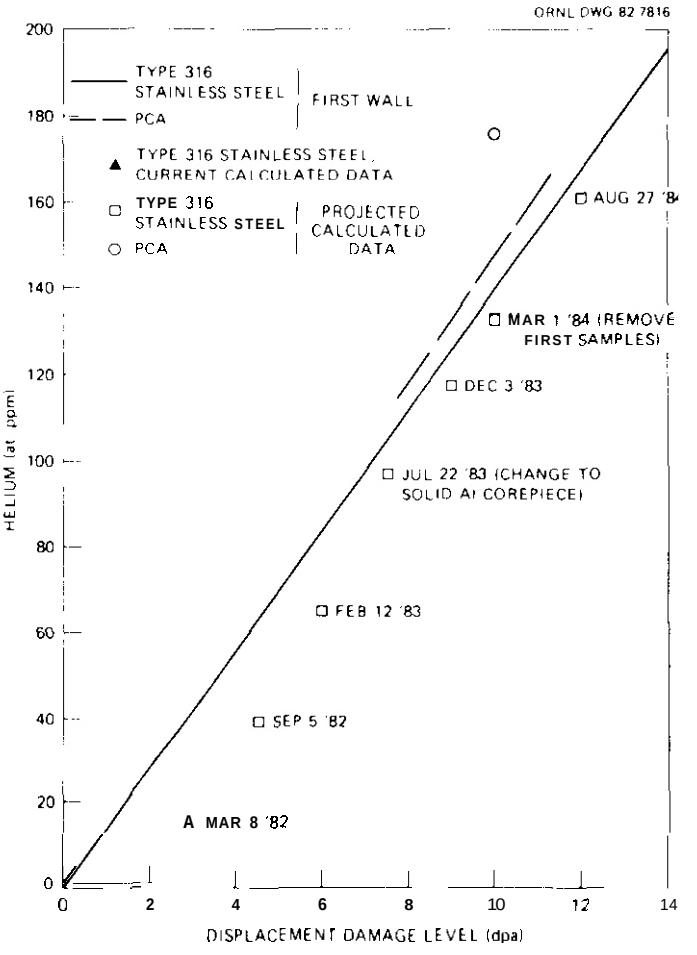

Fig. 2.1.2. Current and Projected Helium and Displacement Damage Levels Expected in the ORR-MFE-4B Experiment.

respectively. The projected dates were obtained by assuming an ORR duty factor of 0.86. The projected dates in both figures have changed from those previously given[3] because of the 24% reduction in calculated fluences imposed because of the experimental data. Also, because of the reduction in thermal fluence, the dpa level at which the solid aluminum core piece is required has increased from 6 to 7.5 dpa.

2.1.5 Future Work

The investigation to determine the reason for the relatively large calculated-to-experimental fluence ratio of 1.32 will be continued. Until this discrepancy is resolved, the calculated fluences from the ongoing three-dimensional neutronics calculations for each ORR reactor cycle will continue to be revised.

2.1.6 References

1. D. R. Vondy, T. B. Fowler, and G. W. Cunningham, *VENTURE, A Code Block for Solving Multigroup Neutron Problems Applying Fine-Diffusion-Theory Approximations to Neutron Transport*, ORNL-5062 (October 1975).
2. T. A. Gabriel, R. A. Lillie, B. L. Bishop, and R. L. Childs, "Neutronics Calculations in Support of the ORR-MFE-4A Spectral Tailoring Experiment," *ADIP Quart. Prog. Rep. June 30, 1980*, DOE/ER-0045/3, pp. 7–9.
3. R. A. Lillie, R. L. Childs, and T. A. Gabriel, "Neutronics Calculations in Support of the ORR-MFE-4 Spectral Tailoring Experiments," *ADIP Semiannu. Prog. Rep. Sept. 30, 1981*, DOE/ER-0045/7, pp. 20–23.
4. L. R. Greenwood, "Neutron Source Characterization for Materials Experiments," *ADIP Semiannu. Prog. Rep. Sept. 30, 1981*, DOE/ER-0045/7, pp. 8–19.
5. J. G. Bradley, *Helium in Nickel and Stainless Steel Irradiated in the ORR-MFE-4A Experimental Assembly*, 82ESG-211, Rockwell International, Canoga Park, Calif. (Jan. 19, 1982).

2.2 OPERATION OF THE ORR SPECTRAL TAILORING EXPERIMENTS ORR-MFE-4A AND ORR-MFE-4B — I. T. Dudley and J. A. Conlin (Oak Ridge National Laboratory)

2.2.1 ADIP Task

ADIP Task I.A.2, Define Test Matrices and Test Procedures.

2.2.2 Objective

Experiments ORR-MFE-4A and -4B, which irradiate austenitic stainless steel, use neutron spectrum tailoring to achieve the same helium-to-displacement-per-atom (He/dpa) ratio as predicted for fusion reactor first-wall service. Experiment ORR-MFE-4A contains mainly type 316 stainless steel and Path A Prime Candidate Alloy (PCA) at irradiation temperatures of 300 and 400°C. Experiment ORR-MFE-4B contains similar materials at irradiation temperatures of 500 and 600°C.

2.2.3 Summary

The ORR-MFE-4A experiment has operated for an equivalent of 391 d at 30-MW reactor power, with maximum specimen temperatures in the upper and lower regions of *400* and 330°C, respectively. A problem caused by a leak in the capsule primary system has been resolved, and the capsule is again in operation. The ORR-MFE-4B experiment, with specimen temperatures of 500 and 600°C, has operated for 283 d at 30-MW reactor power.

2.2.4 Progress and Status

On September 8, 1981, two of the multijunction thermocouples located in the lower region of the ORR-MFE-4A capsule, as previously described,[1-3] indicated sharp drops in temperatures of about 90°C on each. The capsule was removed from the reactor on September 10, 1981, for an investigation into the cause of the temperature drop. It was suspected that a leak had developed in the inner cylindrical primary boundary and allowed some NaK to enter the annulus. A series of leak tests were made on the capsule systems. The tests did reveal that, indeed, a leak had developed in the primary system. It was also found that the leak was between the primary system and region "A" of the capsule. The leakage amounted to approximately 1 std cm^3/min of helium with a differential pressure of 3.45×10^5 Pa (50 psi).

Region "A" is defined as the volume inside the capsule lead tube, which is made of 51-mm (2-in.), sched-40 pipe and extends from the top of the capsule bulkhead to the next bulkhead located about 0.3 m (12 in.) above the reactor tank top.

The series of pressure tests indicated that there were no other leaks in the primary system or region "A" and that there were no leaks in either the thermocouple well or the secondary system. After a review of the capsule design and the location of the leak, it was concluded that operation could be safely resumed by rearranging the primary and secondary system boundaries, changing system operating pressures, and adding a thermocouple well pressurization system.

Region "A" is now designated as a part of the primary system boundary. This region is pressurized to 50 psig and maintained at the same pressure as the volume immediately above the NaK, which was originally designated as the primary system. The two volumes, now communicating through the small leak, are positively joined externally by tying their gas lines together. After pressurization, the primary gas system is sealed by closing the inlet and oulet valves and is continuously monitored for inward or outward leakage. The pressure is greater than reactor cooling water pressure, so that any leakage would be outward.

The multijunction thermocouple well is kept pressurized with helium to 4.5×10^5 Pa (65 psig). This pressure is greater than the pressure of the primary system, so that if a leak should develop between it and the primary system, it would result in a helium flow into the primary system. The control gas system pressure was increased to 4.5×10^5 Pa (65 psig) also. Leakage of the control gas into the primary system would be indicated by a rise in the primary system pressure. It should be noted that this arrangement constitutes single containment of the NaK.

The leak in the primary system may allow NaK to continue seeping into the annulus around the central thermocouple well and cause uncertainties in the temperature measurement correlations. For that reason another means of temperature control was needed. A study of historical capsule operating data indicated that the temperatures could be held within 10°C of the desired value over an ORR fuel cycle by maintaining predetermined

fixed ratio argon-helium gas mixtures for the control gases to each capsule region. This method of temperature control is now being used for ORR-MFE-4A capsule operation, and through March 31, 1982, the capsule has accumulated an equivalent of 391 d at 30-MW reactor power operation.

The ORR-MFE-4B capsule continues to operate as planned since it was installed in the reactor on April 23, 1981. Through March 31, 1982, it has accumulated an equivalent 283 d at 30-MW reactor power operation with maximum specimen temperature of 600°C in the upper region and 500°C in the lower region. Thermocouple TE-1 located in the upper region[3] failed on February 12, 1982.

2.2.5 References

1. K. R. Thoms and M. L. Grossbeck, "Operation of the ORR Spectral Tailoring Experiment ORR-MFE-4A," *ADIP Quart. Prog. Rep. Sept. 30, 1980*, DOE/ER-0045/4, pp. 20–24.
2. K. R. Thoms, "Operation of the ORR Spectral Tailoring Experiment ORR-MFE-4A," *ADIP Quart. Prog. Rep. March 31, 1981*, DOE/ER-0045/6, pp. 18-21.
3. I. T. Dudley, "Operation of the ORR Spectral Tailoring Experiments ORR-MFE-4A and ORR-MFE-4B," *ADIP Semiannu. Prog. Rev. Sept. 30, 1981*, DOE/ER-0045/7, pp. 24–29.

2.3 TEM SPECIMEN MATRIX FOR THE AD-2 RECONSTITUTION - D. T. Peterson (Westinghouse Hanford Company)

2.3.1 ADIP Task

The Department of Energy (DOE) Office of Fusion Energy (OFE) has cited the need for these data under the ALIP Program Task, Ferritic Material Development (Path E).

2.3.2 Objective

The objective of this work is to study the microstructural response of a variety of ferritic and austenitic alloys to fast neutron irradiation.

2.3.3 Summary

TEM specimens have been prepared for inclusion in the reconstitution of the AD-2 test. The matrix includes specimens of HT-9 weld fusion zones and simulated heat-affected zones, undoped and nickel doped 12Cr-1Mo and 9Cr-1Mo alloys, and rapidly solidified Path A alloys.

2.3.4 Progress and Status

The AD-2 experiment was recently discharged from EBR-II for interim examination and reconstitution. One set of TEM specimens, as described in reference 1, was removed for examination. A duplicate set of specimens will continue irradiation in the reconstituted experiment. A set of cold specimens was included in the reconstitution to replace the discharged specimens.

Table 2.3.1 lists the specimens prepared by the Hanford Engineering Development Laboratory (HEDL). Specimens K7 through KR are being irradiated in the HFIR-MFE-RB1 test but were not included in the original AD-2 matrix. These specimens are discussed in reference 2. The Path B alloys have been irradiated in a series of HFIR experiments.[3,4] These specimens are presently being examined to assess the effect of irradiation in a high helium environment upon their ductility. A limited set of these specimens was included in the AD-2 reconstitution to provide a low helium baseline.

Table 2.3.1 Specimens Prepared by HEDL

Alloy[1]	Code	TMT
HT-9 (91353)	K7	Mill annealed round bar
9Cr-1Mo (30176)	KA	1038°C/5min/AC+760°C/1hr/AC
2¼Cr-1Mo (56447)	KB	900°C/0.5hr/AC+700°C/1hr/AC
HT-9 (91353)	KE	Weld fusion zone + 760°C/2hr/AC
HT-9 (91353)	KF, KH	HAZ #1 + 760°C/2hr/AC
HT-9 (91353)	KJ, KK	HAZ #2 + 760°C/2hr/AC
HT-9 (91353)	KL, KN	HAZ 113 + 760°C/2hr/AC
HT-9 (91353)	KP, KR	HAZ 114 + 760°C/2hr/AC
B1 (5-271-1)	KT	30%CW
B2 (J-268-2)	KU	30%CW
B3 (J-267-1)	KV	30%CW
B4 (3-264-1)	KX	30%CW
B6 (5-262-1)	NI	40%CW

[1]The heat numbers are listed in parenthesis.

Table 2.3.2 lists the specimens prepared by the Oak Ridge National Laboratory (ORNL). These specimens consist of a series of nickel doped 12Cr-1Mo and 9Cr-1Mo alloys and their undoped counterparts. These nickel doped alloys were developed by ORNL to enhance the production of helium during irradiation in mixed spectrum reactors such as HFIR.(5) These specimens are being irradiated in EBR-II where negligible helium will be produced to provide a comparison with specimens irradiated in HFIR.

Table 2.3.3 lists the specimens prepared by the Massachusetts Institute of Technology (MIT). These specimens are all rapidly solidified austenitic alloys. The PA-1 alloy is the Path A PCA alloy; PA-2 is the Path A PCA modified to obtain 0.081%C and 0.60%Ti; PA-3 is the Path A PCA modified to obtain 0.17%C and 0.90% Ti; and 316 + 1%Al is a ultra low carbon and nitrogen content 316 stainless steel remelted with the addition of 1%Al to form dispersed aluminum oxide precipitates.

Table 2.3.2 Specimens Prepared by ORNL

Alloy[1]	TMT[2]
12Cr-1Mo (3587)	N;NT;NFT
12Cr-1Mo-1Ni (3588)	N;NT;NFT
12Cr-1Mo-2Ni (3589)	N;NT;NFT
9Cr-1Mo (3590)	N;NT;NFT
9Cr-1Mo-2Ni (3591)	N;NT;NFT
12Cr-1Mo-2Ni Adj. (3592)	N;NT;NFT
9Cr-1Mo-2Ni Adj. (3593)	N;NT;NFT

[1]The heat numbers are listed in parenthesis.
[2]N = Normalized; NT = Normalized + Tempered 700°C/1hr; NFT = Normalized + Fully Tempered.

Table 2.3.3 Specimens Prepared by MIT

Alloy	Code	TMT
PA-1	N7	20%CW
PA-1	NA	40%CW
PA-2	NB	20%CW
PA-2	NE	40%CW
PA-3	NF	850°C/1½hr
PA-3	NH	40%CW
PA-3	NJ	As consolidated
316+1%Al	NK	1100°C/1hr
316+1%Al	NL	25%CW

2.3.5 Future Work

Microstructural examinations will be performed on selected specimens after the final discharge of the AD-2 test.

2.3.6 References

1. R. J. Puigh and N. F. Panayotou, "Specimen Preparation and Loading for the AD-2 Ferritics Experiment," ADIP *Quarterly* Progress *Report, April-June, 1980,* DOE/ER-0045/3, 260.

2. D. T. Peterson, "TEM Specimen Preparation for the HFIR-MFE-RB1 Experiment," ADIP *Semiannual Progress Report, April-September 1981*, DOE/ER-0045/7, 230.

3. D. T. Peterson, "Specimen Matrix for the HFIR Irradiation of the Path B Alloys," *ADIP* Quarterly *Progress Report, July-September 1939*, DOE/ER-0045/4, 54.

4. M. L. Grossbeck, J. W. Woods and G. A. Potter, "Experiments HFIR-CTR-30, -31, and -32 for Irradiation of Transmission Electron Microscopy Disk Specimens," Ibid., 36.

5. R. L. Klueh and J. M. Vitek, "Characterization of Ferritic Steels for HFIR Irradiation," *ADIP Quarterly Progress Report, April-June 1980*, DOE/ER-0045/3, 294.

2.4 HFIR/FFTF IRRADIATION EXPERIMENT — CONCEPTUAL PLAN — A. M. Ermi (Hanford Engineering Development Laboratory) and J. M. Vitek (Oak Ridge National Laboratory)

2.4.1 ADIP Task

ADIP Task I.A.2, Define Test Matrices and Test Procedures.

2.4.2 Objective

A combined HFIR/FFTF irradiation experiment is being planned to obtain mechanical properties data and microstructural information on nickel-bearing first-wall candidate alloys at very high displacement damage levels (100-200 dpa) while maintaining helium concentration levels appropriate for a fusion reactor. By utilizing the HFIR for high helium production rates and the FFTF for high displacement damage rates, the high displacement damage at the appropriate He/dpa (10-15 appm/dpa) can be achieved more rapidly than by utilizing existing single irradiation facilities.

2.4.3 Summary

Plans for a combined HFIR/FFTF irradiation experiment on Path A PCA and long-range ordered alloys are described. Irradiation will be up to ~180 dpa with the appropriate helim levels expected for fusion environments. Irradiation temperatures will be from 400 to 600°C. A tentative matrix of swelling disks, creep tubes, and tensile, crack growth and fracture toughness specimens has been identified.

2.4.4 Progress and Status

2.4.4.1 Introduction

Development of materials for fusion reactor first wall application requires that the material properties be characterized as a function of the hostile first-wall irradiation environment. Since no high fluence fusion test facility is currently available for the fusion alloy development program, simulated studies must be undertaken in existing irradiation facilities. A review of the problems associated with the simulations and

of the facilities available for fusion first wall materials development has been detailed by Klueh and Bloom.[1] One experiment which HEDL and ORNL are jointly planning is a combined HFIR/FFTF irradiation test which would achieve high displacement damage levels with the appropriate average He/dpa ratio more rapidly than in other existing facilities. Using the HFIR for high helium production rates in nickel-bearing alloys (PCA and the long-range ordered alloys), and the FFTF for high displacement damage rates, it will be possible to achieve the desired displacement damage at the appropriate average He/dpa ratio in a relatively short period of time (100 dpa by 1989).

2.4.4.2 Irradiation Plan and Test Matrix

The general HFIR/FFTF experiment test plan calls for a series of irradiations alternating between the HFIR and the FFTF. The loading, irradiation, and unloading cycle in each facility is to be approximately one year. For the majority of the specimens, irradiation would begin in the HFIR, following what is designated as Path 1. At the end of each reactor irradiation, a number of specimens would be discharged for interim examination or testing. The Path 1 test plan is illustrated in Fig. 2.4.1. Specimens not located in the peak flux position will have a slightly lower helium content.

After the first FFTF discharge, a number of specimens of all types are removed (except creep tubes which are measured and replaced). This provides space for the addition of swelling and tensile specimens to the second HFIR irradiation. These specimens will be included in the first FFTF irradiation and will therefore follow a slightly different sequence of irradiations. This sequence, designated as Path 2, is illustrated in Fig. 2.4.2 along with Path 1. Swelling and tensile specimens would be discharged along Path 2 only at the four times which coincide with the Path 1 irradiations (after the 3rd, 5th, 7th, and 9th year).

The test plan described above pertains only to irradiation of the austenitic stainless steel Prime Candidate Alloy (PCA). Details of the tentative Path A PCA test matrix are given in Table 2.4.1. The specific alloy variants have not been identified at this time.

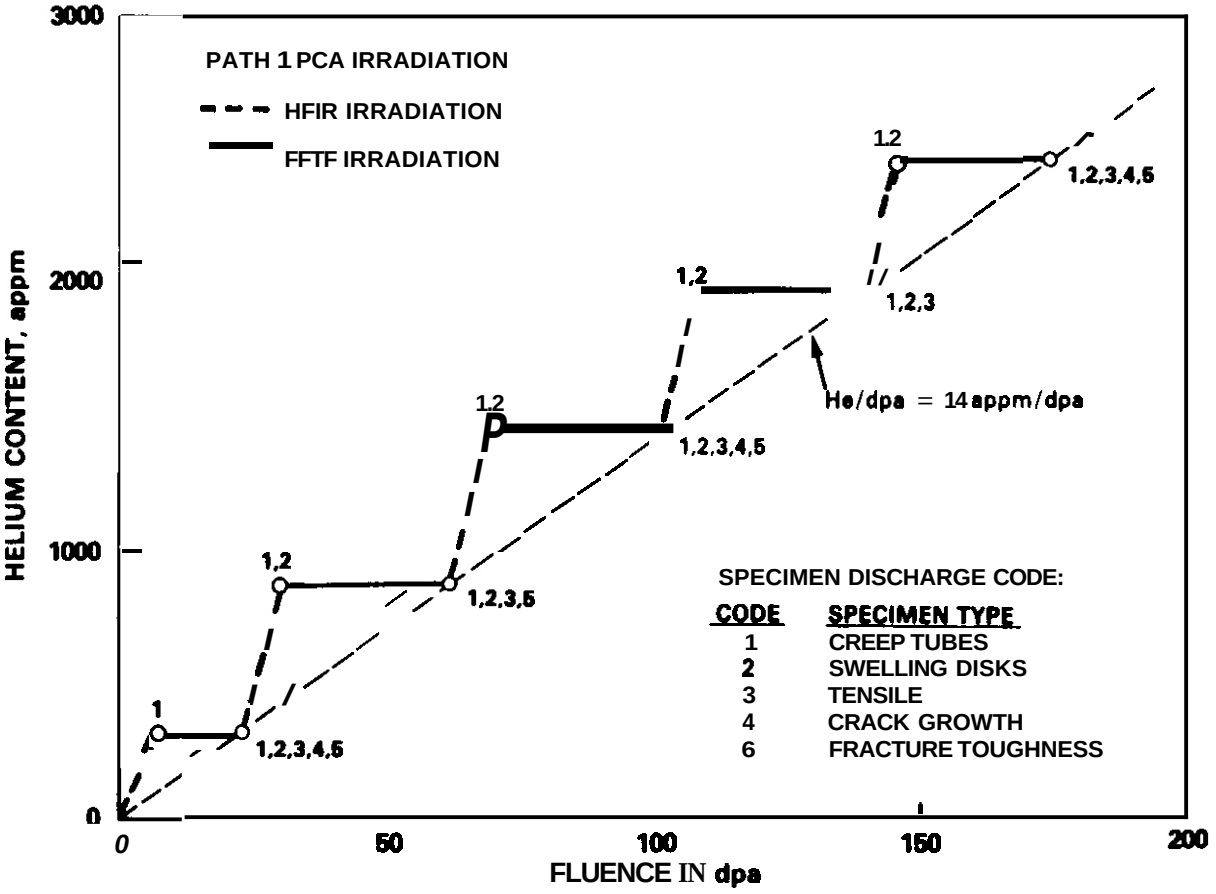

Fig. 2.4.1 Proposed Irradiation Test Plan for PCA Using the HFIR and FFTF (Path 1).

In addition to Path A PCA, it is of interest to include the long-ranged ordered (LRO) alloys. Once a space analysis at the extremities of the HFIR capsule has been completed the addition of the LRO to the test program will be evaluated. The lower flux and concurrent lower helium production rates at the HFIR capsule extremities will be compensated by the higher nickel content of these alloys so the appropriate He/dpa ratio may be achieved. At this time, it is likely that some space for swelling and tensile specimens at two temperatures will be available.

2.4.4.3 Description of Test Hardware

The major factor dictating the course which the HFIR capsule design has taken is temperature control. Since it is important to maintain the same temperatures, within limits, in HFIR as in FFTF, it was determined that sodium filled capsules with controllable gas blends through a gas gap were necessary. This limited the experiment to the instrumented removable

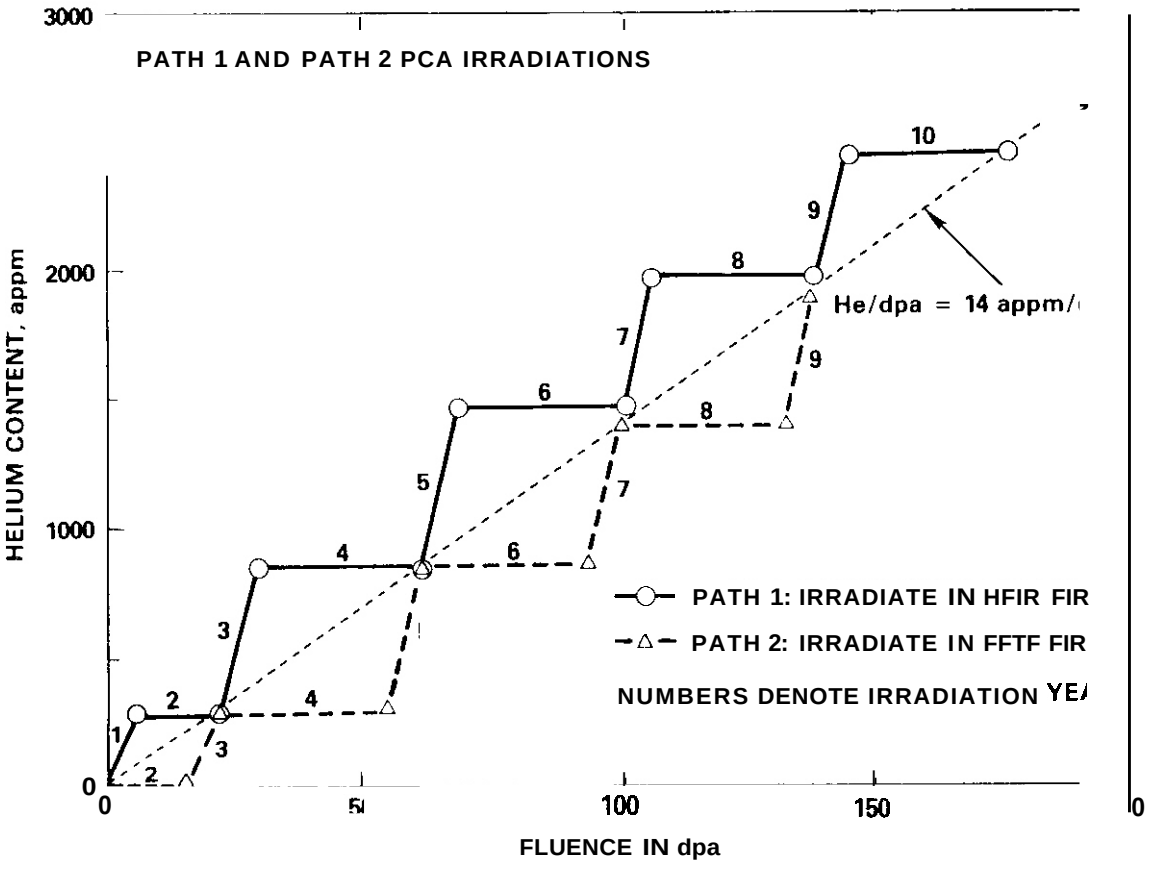

Fig. 2.4.2 Proposed Irradiation Test Plan for PCA Using the FFTF and HFIR, Illustrating Two Irradiation Paths.

beryllium (RB) positions in HFIR.[2] The diametral requirement for the specimen irradiation volume was dictated by the 1.27 cm wide fatigue crack growth tabs. Since specimens and instrumentation must be doubly encapsulated, the large RB facility (3.56 cm ID) was selected for the irradiations.

A schematic of a section of a proposed RB subassembly is illustrated in Fig. 2.4.3. In this particular design, specimen packets are inserted into baskets (~2.3 cm diameter) which are loaded into a primary containment tube. Insulators separate the baskets which will be operated at different temperatures. The primary containment is filled with sodium and slipped inside a secondary containment tube. The secondary tube provides both the gap needed to accommodate the variable helium/argon gas mixture for temperature control, and the double containment necessary to separate the coolant water from the sodim.

Table 2.4.1 Proposed PCA Test Matrix for the HFIR/FFTF Irradiation Experiment.[a]

MATERIAL: PRIME CANDIDATE ALLOY (PCA)

SPECIMEN TYPE	IRRAD. PATH[b]	# OF ALLOY VARIANTS	DUPLI-CATIONS	# OF EXAMS	# OF SPECIMENS AT EACH TEMPERATURE (°C) 400	500	550	600	TOTAL # OF SPEC,
SWELLING	1	5 PRIM.	3	9	135	135	135	135	960
	1	5 2ND	3	3	45	45	45	45	
	2	5 PRIM.	3	4	60	60	60	60	
CREEP	1	1	4 STRESSES	10	4	4	4	4	16
TENSILE	1	4	2	5	40	40		40	168
	2	2	2	4	16	16	0	16	
FATIGUE CRACK GROWTH	1	1	3	3	9	9	0	9	27
FRACTURE TOUGHNESS	1	1	1	4	4	0	0	0	4

[a] NOTE: DOES NOT INCLUDE LRO MATERIALS PORTION.

[b] PATH 1: IRRADIATE IN HFIR FIRST.
PATH 2: SKIP FIRST HFIR IRRADIATION: IRRADIATE IN FFTF FIRST

An instrument tube runs down the center of the assembly, containing up to ten thermocouples and two preheaters. The preheaters are used initially to melt sodim in the instrument tube, thus providing a path to the free surfaces for the expanding sodim which melts first at the center of the specimen region during reactor startup.

During operation, a flowing blend of helium and argon will pass within the secondary tubes, entering at the bottom and exiting at the top. The secondary will be operated at ~50 psig back pressure. The primary containment will contain a helium cover gas at ~10 psig. The primary and secondary pressures, the secondary inlet and outlet flow rates, and the capsule temperatures will be monitored during the experiment. In addition, moisture detectors will be located at the secondary gas outlet as part of the safety system.

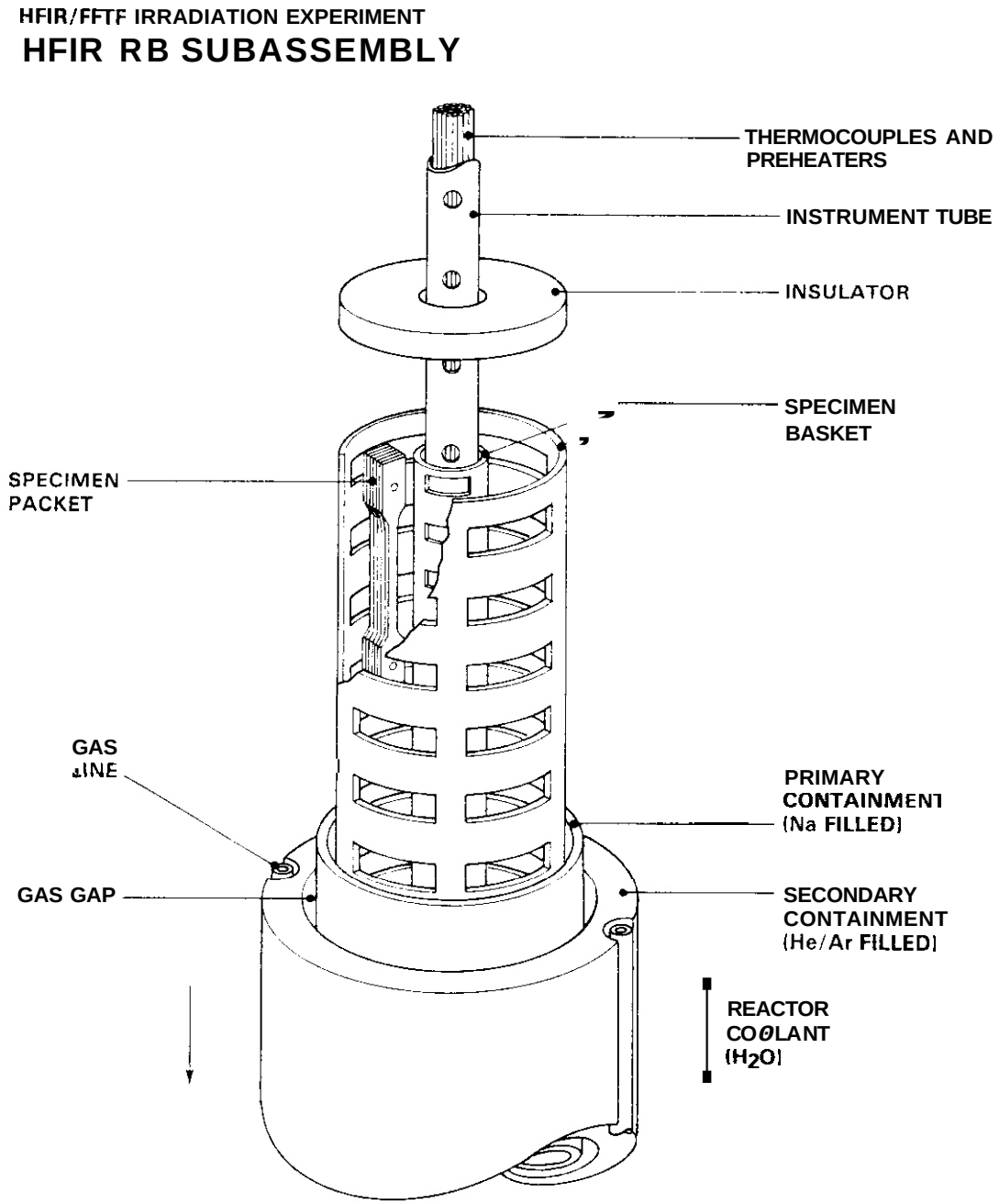

Fig. 2.4.3 Cutaway of a Section of a Proposed HFIR RB Subassembly.

After irradiation in HFIR, the capsule will be shipped to HEDL for specimen removal. Specimens to be irradiated in the FFTF will be inserted into baskets and placed in the Materials Open Test Assembly (MOTA) capsules. Details of the design and operation of MOTA in FFTF are described elsewhere.[3] After irradiation in FFTF, the specimens will be removed at HEDL, and those to be irradiated in HFIR will be inserted into a new RB subassembly.

2.4.4.4 Schedule

A tentative irradiation plan and test schedule is given in Fig. 2.4.4. The helium and dpa values reflect peak reactor values for Path A PCA. The remainder of FY82 will be devoted to the HFIR capsule design with procurement, fabrication and assembly of the capsule scheduled during FY83. The first irradiation in HFIR is planned for the beginning of CY84.

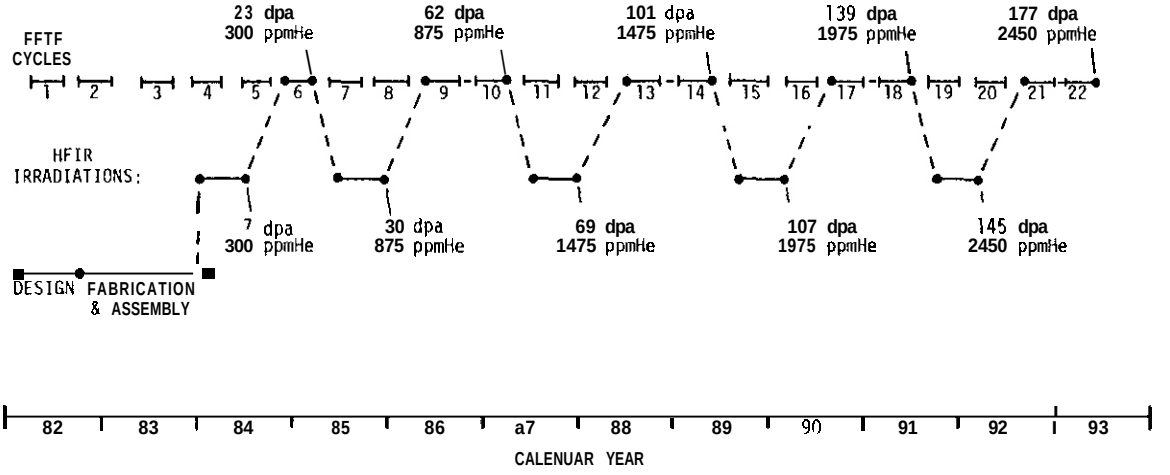

Fig. 2.4.4 Tentative HFIR/FFTF Experiment Test Plan and Schedule (Numbers Refer to Path 1 Irradiation).

2.4.5 Future Work

The remainder of FY82 will be devoted to finalizing the HFIR capsule design with preliminary and final design reviews scheduled during the summer at HEDL, and a safety review before the Reactor Experiments Reivew Committee (RERC) at ORNL in October 1982. Also during FY82, a mock-up of the capsule will be fabricated in order to test the effectiveness of the sodium preheaters. The Path A PCA and LRO test matrices will also be finalized by the end of FY82.

2.4.6 References

1. R. L. Klueh and E. E. Bloom, *Radiation Facilities for Fusion Reactor First Wall and Blanket Structural Materials Development*, OWL-5830, Oak Ridge National Laboratory, Oak Ridge, TN 37830 (December 1981).
2. T. M. Sims and J. H. Swanks, "High Flux Isotope Reactor (HFIR) Experiment Facilities and Capabilities," Oak Ridge National Laboratory, Oak Ridge, TN 37830.
3. R. E. Bauer, "Materials Open Test Assembly in the Fast Flux Test Facility," *Proceedings of the American Nuclear Society Conference on Fast, Thermal, and Fusion Reactor Experiments*, Salt Lake City, Utah (April 1982).

2.5 SPECIMEN SIZE EFFECTS AND FUSION MATERIALS RESEARCH - N. F. Panayotou and E. K. Opperman (Westinghouse Hanford Company)

2.5.1 ADIP Task

The development of design data base and test methods to generate design or engineering data: 1B1-1B7, 1B9-1B11, 1B13-1B15, 1C2, 1C3, 1C6-1C8, 1C10.

2.5.2 Objective

The objective of this report is to quantify the effect of specimen size on the development of design or engineering data bases of interest to the fusion materials community.

2.5.3 Summary

Available data from specimens compatible with the Fusion Materials Irradiation Test (FMIT) facility have been compared with large specimen data to determine and quantify specimen size effects. For most of the properties examined, including properties where size effects are well documented, it was determined that the data obtained from small specimens are in good agreement with, and in some cases indistinguishable from, large specimen data. Small specimens however, require careful attention to the details of design, testing and analysis. Nevertheless, a good approximation of engineering or design quality data can be obtained despite the comparatively limited irradiation volume of fusion spectrum neutron radiation sources such as FMIT.

2.5.4 Progress and Status

2.5.4.1 Introduction

Radiation effects experiments generally employ specimens which are smaller than specimens employed in unirradiated materials testing. Large specimens are undesirable due to large in-reactor temperature and damage gradients, excessive induced radioactivity and limited irradiation space. If the objective of an experiment is to test a prototypic component or to establish relative trends the existence of a specimen size effect can

be ignored or discounted. In many cases, data generated from small specimens is assumed, a priori, to be significantly different from data obtained from larger specimens. However, if this is not the case, data obtained from small specimens may qualify as design or engineering data.

The specimen matrix for the FMIT facility was established based on a concensus of the materials experts of the fusion materials research community.' The initial purpose of this specimen matrix was to ensure that general radiation effects data of interest to the community would be generated in a timely fashion from FMIT. With a few exceptions there was no concerted effort to consider specimens which would also provide engineering or design type data.

The purpose of this report is to evaluate whether or not size effects exist for specimens which are compatible with FMIT. The basic considerations which dictate the size of specimens utilized in the FMIT are reviewed. The material properties of interest are defined and the means of determining each property briefly stated. Finally a comparison is made between small and large specimen data for each property of interest.

2.5.4.2 Facility Restrictions on Specimen Size

There are two fundamental considerations that dictate the size of materials test specimens utilized in the FMIT. The first is nuclear heating. Specimens must be sized so that nuclear heating will not result in large temperature gradients within specimens. Typically acceptable specimen temperature gradients are $<10°C$. The second consideration is damage gradients. The damage produced within a materials specimen is required to be sufficiently uniform to produce representative materials data. The degree of uniformity is very much a function of the portion of the specimen volume that is actually required to produce the materials data. For example, some tensile specimens are about .5 mm thick by 3 mm wide by 40 mm long. The only portion of the tensile specimen requiring neutron damage is the reduced section or the section that actually deforms during the tensile test. This length is typically 5 to 10 mm. Hence, the region requiring uniform irradiation is approximately 10 mm of a 40 mm specimen.

2.5.4.2.1 Nuclear Heating. Specimens irradiated in the highest available FMIT flux will be subjected to nuclear heating rates as high as nine watts per gram of specimen material. The highest rate occurs in the region closest to the neutron source and decreases with distance away from the source (nuclear heating is approximately linear with flux). The heating rate along the beam centerline within the vertical test assembly (VTA) modules 1 and 2 is shown in Fig. 2.5.1.

Generally, temperature gradients across a specimen of up to 10°C are commonly sustained in reactor irradiations. Since the heating rate varies significantly with position in the FMIT the upper limit of specimen size, consistent with intra specimen temperature gradients of $\leq$10°C, will also vary with position. In a solid cylindrical specimen in which the heat transfer is primarily radial (neglect axial heat transfer), the allowable specimen diameter as a function of nuclear heating can be calculated and is shown in Fig. 2.5.2. As seen by Fig. 2.5.2, all of the FMIT test matrix specimens are well within the region of acceptance. From a thermal standpoint, specimens with considerably larger dimensions than those in the FMIT test matrix can be utilized without exceeding a temperature gradient of 10°C across a specimen.

2.5.4.2.2 Damage Gradients. The criteria controlling the maximum allowable damage gradient within a materials test specimen are functions of many variables. The type of data required (engineering, scoping, screening, surveillance, etc.), the type of specimen and the type of test (microscopic examination, tensile test, hardness test, etc.) all must be considered. In large test reactors such as the Experimental Breeder Reactor (EBR)-II and the Fast Flux Test Facility (FFTF) the damage gradients are much less than one percent per mm. In smaller reactor cores such as the high flux isotope reactor (HFIR) at Oak Ridge National Laboratory (ORNL) the gradients are approximately $\leq$.4 percent per mm. However, in the 14 MeV neutron facility, Rotating Target Neutron Source (RTNS)-II gradients exceed approximately 30 percent per mm. The maximum gradient in the FMIT is approximately 12 percent per mm; however, in most of the irradiation volume the gradient is five percent or less per mm.

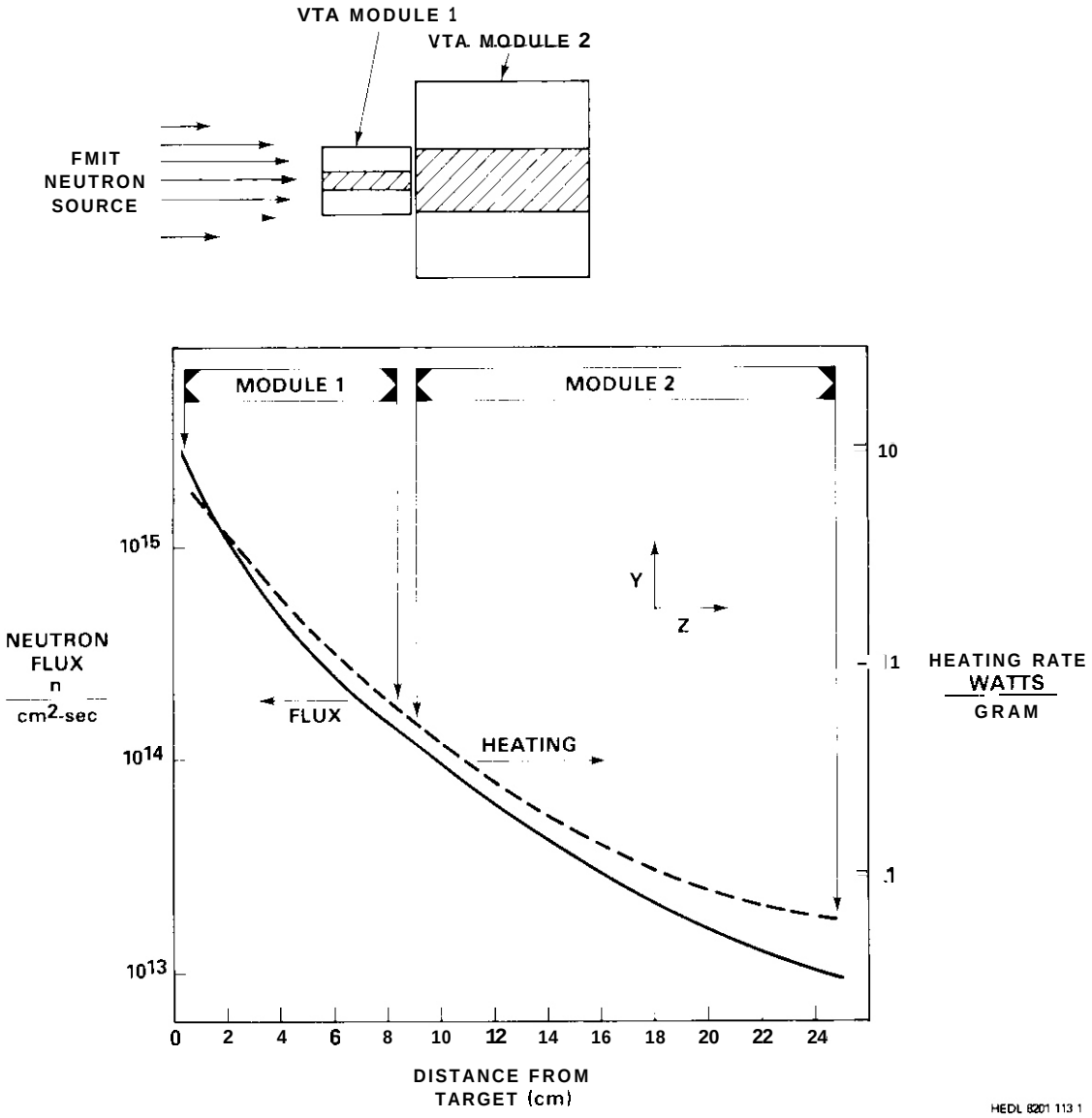

Fig. 2.5.1. Neutron flux and neutron heating within the inner chambers of the high-flux modules of the FMIT vertical test assembly (VTA). Values calculated assuming equal volumes of coolant (NaK) and stainless steel.

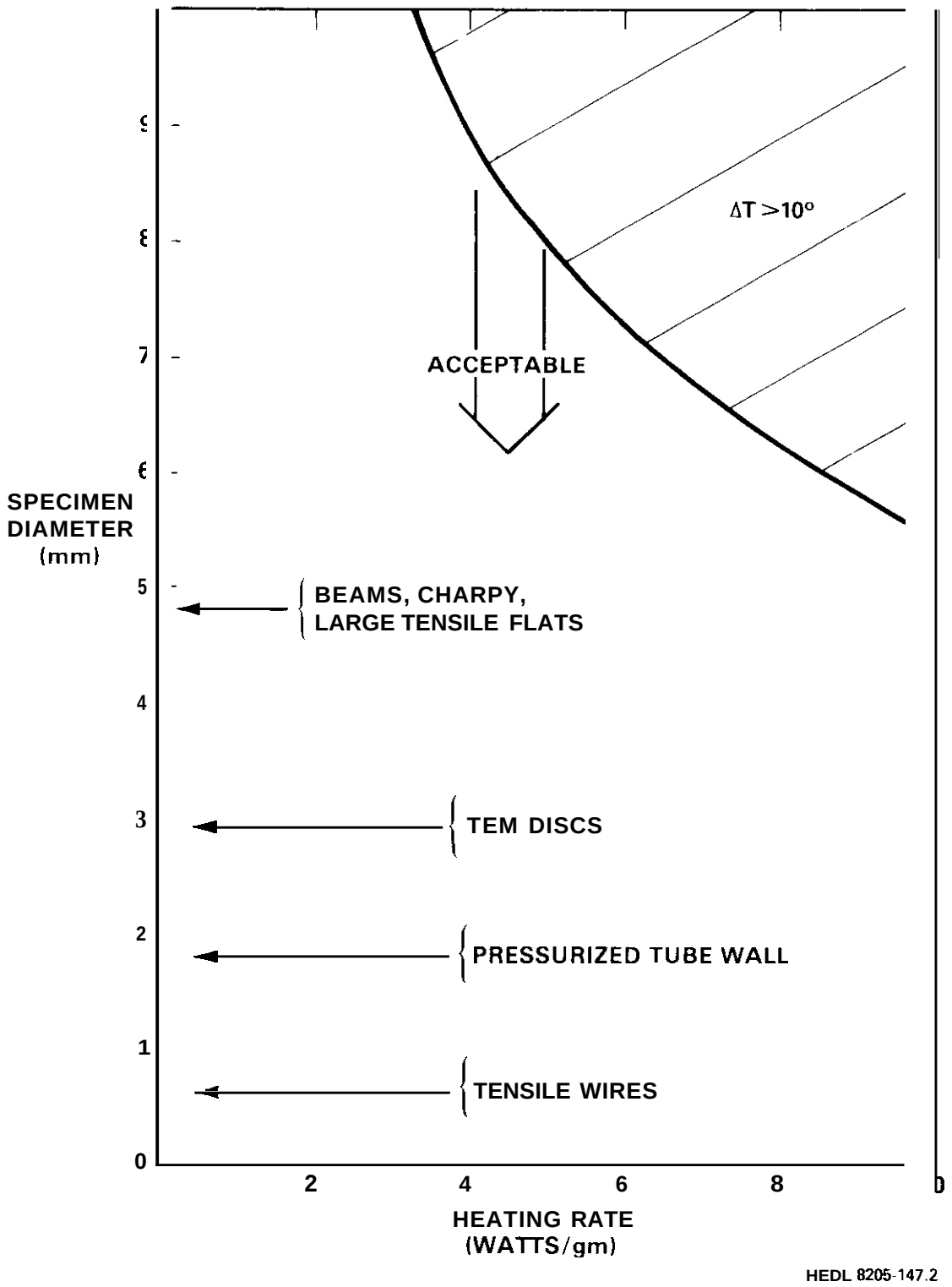

Fig. 2.5.2. Allowable specimen diameter as a function of heating rate (position) in FMIT. Calculation assumes a solid cylindrical rod of stainless steel and neglects axial heat transfer.

The distribution of specimens in the high flux region of the FMIT is shown in Fig. 2.5.3. As seen by Fig. 2.5.3, the specimens close to the target, where gradients tend to be the largest, are transmission electron microscopy (TEM) disks which are 3 mm diameter by .3 mm thick and the tensile wires that have an active gage length of approximately 10 mm (oriented in Y direction) and a diameter of .5 mm (oriented in the Z direction). The maximum gradient in damage occurs across the TEM disks and is approximately 10 to 15 percent. At a distance 5 cm away from the target the intra specimen gradient drops to approximately seven percent for the TEM disks and to one percent for the tensile specimens. These values are considered totally acceptable. As illustrated in Fig. 2.5.3, the FMIT test matrix positions larger specimens further from the target. This is a result of not only gradient (temperature and damage) considerations, but also the optimization of flux magnitude per specimen. Optimization of flux magnitude simply means getting the maximum number of specimens to the highest possible fluence in the least amount of time.

2.5.4.3 Material Properties of Interest

The FMIT test matrix is listed in Table 2.5.1 and a summary of the type of information that will result from completion of the test matrix is given in Table 2.5.2. The FMIT test matrix includes only the types of specimens required to yield the data specified as first priority by the fusion materials community. The subsequent discussion however, will include a broader and more generic review of materials test specimens utilized for irradiation testing.

Data required for radiation damage analysis and materials engineering considerations are as follows:

1. Microstructure
2. Swelling
3. Fracture Toughness
4. Fatigue
5. Fatigue Crack Growth
6. Tensile
7. Creep

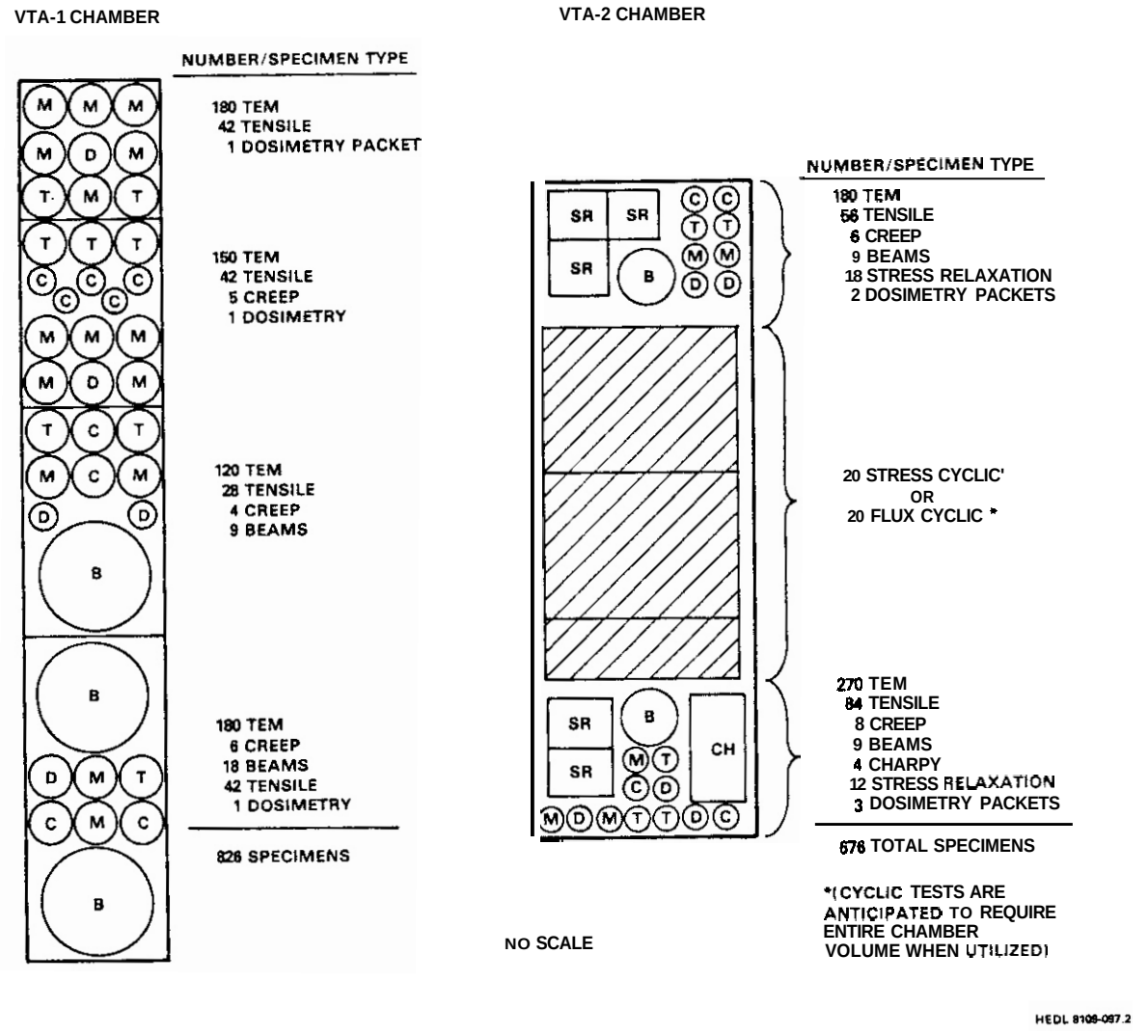

Fig. 2.5.3. Specimen packing arrangement in the inner chambers of VTA Module 1 and 2 of the FMIT. The smallest specimens, TEM (M) disks, tensile and creep specimens are positioned closest to the neutron source. Refer to Fig. 2.5.1 for the relative positions of the neutron source and VTA Module 1 and 2.

TABLE 2.5.1

FMIT High Flux Test Matrix

Test Type	Materials x Duplication	Fluences (dpa)	Irradiation Temperatures (No.)	Total Specimens
TEM (chem, micro, rate)	30 x 4	(5, 10, 20, 50, 100)	4	2400
TEM (flow/rate)	15 x 2	(5, 10, 20, 50, 100)	3	450
Tensile (postirradiation)	10 x 2	(5, 20, 50, 100)	3	240
Creep (rate effect)	5 x 2	(interim to 100)	3	30
Beams (multipurpose)	5 x 2	(5, 20, 50)	3	90
TEM (micro, rate)	15 x 10	(2, 5, 10)	4	1800
TEM (chem)	30 x 6	(2, 5, 10)	4	2160
TEM (flow/rate)	30 x 6	(2, 5, 10, 20)	3	2160
Creep/Rupture	15 x 5	(interim to 50)	3	225
Stress Relax (*in situ*)	15 x 2	(3 preirradiated)	3	270
Beams, preirradiation	10 x 2	(2, 5, 10)	3	180
Tensile (postirradiation and dispensation)	15 x 6	(5, 10, 20, 50)	3	1080
In situ Cyclic Stress (micro)	10 x 2	(5, 20,50)	0	180
Other Materials (micro)	13 x 4	(2, 5, 10)	2	360
Other Materials (postirr., mech/electrical tests)	15 x 4	(2, 5, 10)	2	360
In situ Cyclic Flux	10 x 2	(5, 20, 50)	3	180
TEM (rate effects)	15 x 4	(0.2, 2, 5)	3	580
TEM (correlation RTNSII)	5 x 4	(0.2, 0.5, 2)	3	180
TEM (seed microstructures)	15 x 6	(0.2, 0.5, 2)	3	810
Creep (rate effect)	5 x 2	(interim to 5)	3	30
Tensile (seed microstructures)	15 x 6	(o.2, 0.5, 2)	3	810
			TOTAL	14,575 Specimens

TABLE 2.5.2

Experimentation in FMIT

The High Flux Test Matrix Data

TEM Disc Specimens Microstructural Evolution and Stability Volumetric Swelling Deformation - Strength - Ductility - Hardness Transmutation Products - Solid - Gas	15→30 Alloys at 3→4 Temperatures for ϕt TO 100 dpa
Tensile Specimens (Wire & Flats) Strength - Yield - Ultimate Ductility and **Flow** - Reduction in area - Total Elongation - Uniform Elongation	10 - 15 Alloys 3 Temperatures ϕt To 100 dpa
Creep (Pressurized Tubes, Bent Beams) dpa Rate Effects Spectrum Dependence Creep Rupture Stress Relaxation	5 Alloys 3 Temperatures ϕt→100 dpa
Cyclic Data Minimal Stress & Flux Cycling - Microstructure - Swelling - Phase Stability	10 Alloys 3 Temperatures ϕt→20 dpa

2.5.4.3.1 Microstructure. The universally accepted microstructure specimen is the TEM disk. This is an internationally accepted specimen utilized for both irradiated and unirradiated microstructural examination. The acceptance of the TEM disk is best illustrated by its selection for use in the International Tokamak Reactor (INTOR),[2] the Tandem Spiegelstudie Karlsruhe (TASKA)[3] as well as its current use in the U.S. Breeder Reactor Program and in current fusion materials irradiation experiments.[4] TEM disks comprise approximately *10,000* of the 15,000 specimens in the FMIT test matrix.

2.5.4.3.2 Swelling. In highly irradiated structures swelling, the coalescence of vacancies created by neutron irradiation which results in a net increase in volume, can limit the life of the component. Density determinations performed on TEM disk specimens is the generally accepted method for determining the total volumetric swelling caused by neutron irradiation.

Fig. *2.5.4* compares the swelling measured in both rod (large) and disk (small) specimens of *20* percent cold worked 316 stainless steel, irradiated in three EBR-II experiments at a temperature of about 600°C. Size effects, if they exist, should be evident at this relatively high irradiation temperature. The swelling data obtained from the large (0.09 cm^3) rod specimens are indistinguishable from the data obtained from the smaller *(0.003* cm^3) TEM disk specimens indicating the absence of a specimen size effect for swelling.

2.5.4.3.3 Fracture Toughness. The study of the resistance of a metal to fracture can be divided into two basic areas depending on the rate at which the flawed structure is loaded. Static fracture toughness refers to loading rates in the range 10^{-4} per second while dynamic fracture toughness generally deals with impact type loading rates, 10^3 per second.

Knowledge of quantitative static-type fracture toughness parameters permits the calculation of the maximum safe stress or the maximum safe flaw size for a given material. Linear-elastic fracture toughness parameters are used to describe high strength alloys or structures which by

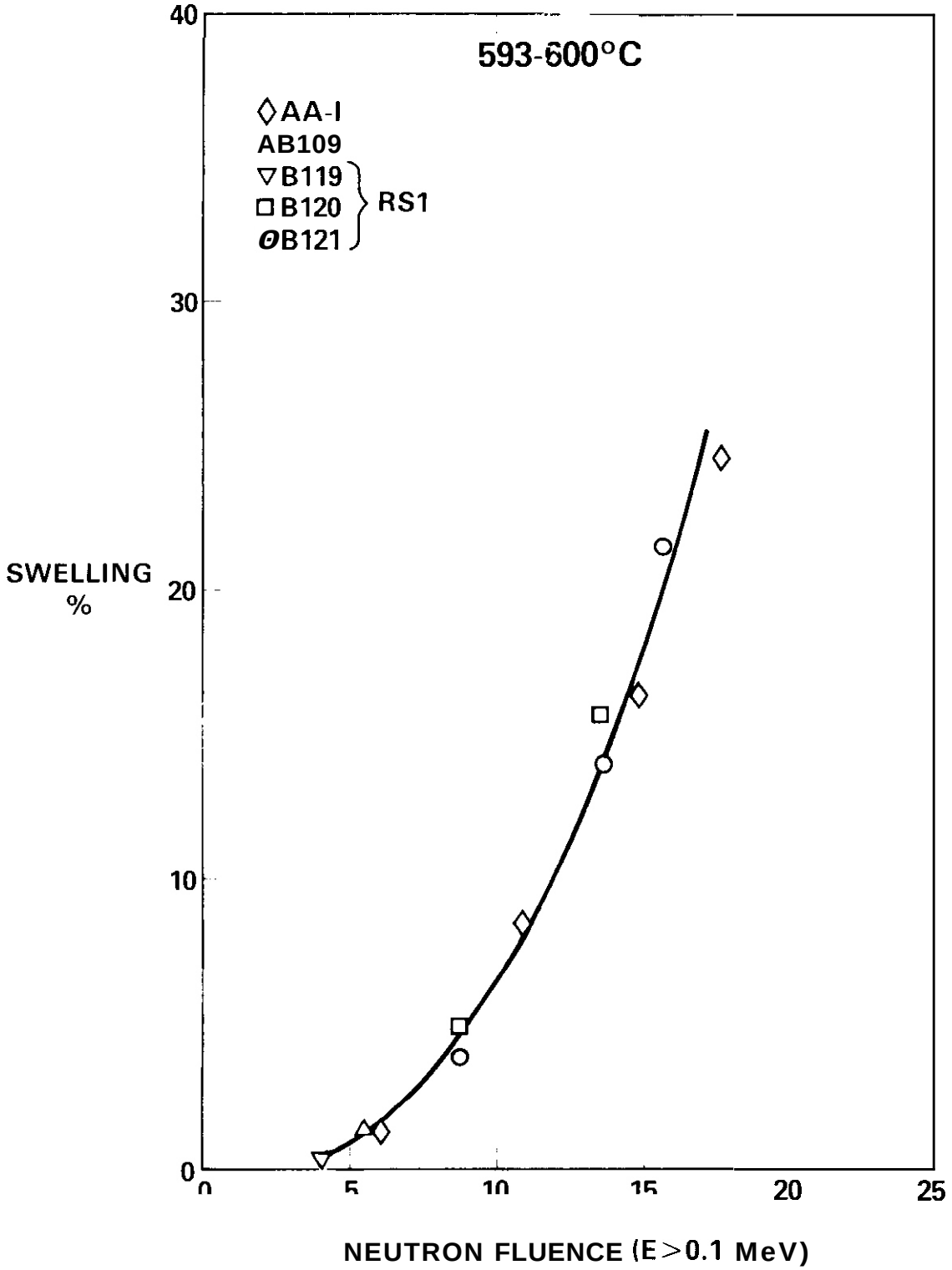

Fig. 2.5.4. Comparison of swelling data from rod (large/AA-I and B109) and TEM disk (small/RS-1) specimens of 20 percent cold worked 316 stainless steel irradiated at about 600°C in three EBR-II experiments; AA-I, B109 and RS-1. Note the consistant trend in the data and therefore the absence of any specimen size effect.

virtue of extensive constraint behave in a linear-elastic manner. Core components for breeder reactors and components for first wall fusion reactor applications are generally ductile metals and/or thin components which exhibit elastic-plastic type deformation. For this case a technology has been developed which can determine the fracture toughness of thin, ductile materials using the J-integral' npproach. The J-integral is defined only for a two dimensional stress state, that is, plane strain conditions. It is generally assumed that the J-integral cannot **be** properly applied to very thin sections where extensive out of plane deformation occurs (plane stress). The existence of a size effect for 3-integral testing is well known.[6] However the issue here is whether or not the .I-integral approach can he applied to structures of interest *to* the breeder and fusion programs. It has been demonstrated that sufficient constraint exists initially, even in 1.02 mm thick specimens, to permit the proper application of the J-integral.[7]

J-integral testing is performed using a compact tension type specimen.[8] Prior to testing the specimens are fatigue precracked following standard procedures to produce a well defined, sharp flaw. Data are obtained by the multiple specimen technique. Specimens are loaded *so* that some crack extension is obtained and then unloaded. Load-deflection data are also recorded. The crack extension is determined by heat tinting the specimen and then pulling the specimen apart to permit a visual measurement to be made. A *3* value is calculated for each specimen, basically by computing the area under the load deflection curve up to the point of unloading. Data are plotted as J versus crack extension, and J_{Ic} is obtained by construction as the value at the intersection ***of*** the blunting line, $2\sigma_{flow} \times \Delta a$ and the least squares fit line through all the points of J versus Δa, where Δa is the crack extension and $\sigma_{flow} = (\sigma_{yield} + \sigma_{ultimate})/2$ (Figs. 2.5.5 and 2.5.6). Whether or not a valid J_{Ic} value has been obtained is determined by the following relationship

$$B \geq 25 \frac{J_c}{\sigma_{yield}}$$

where B is the specimen thickness and J_c is the critical value of J to he validated.[8]

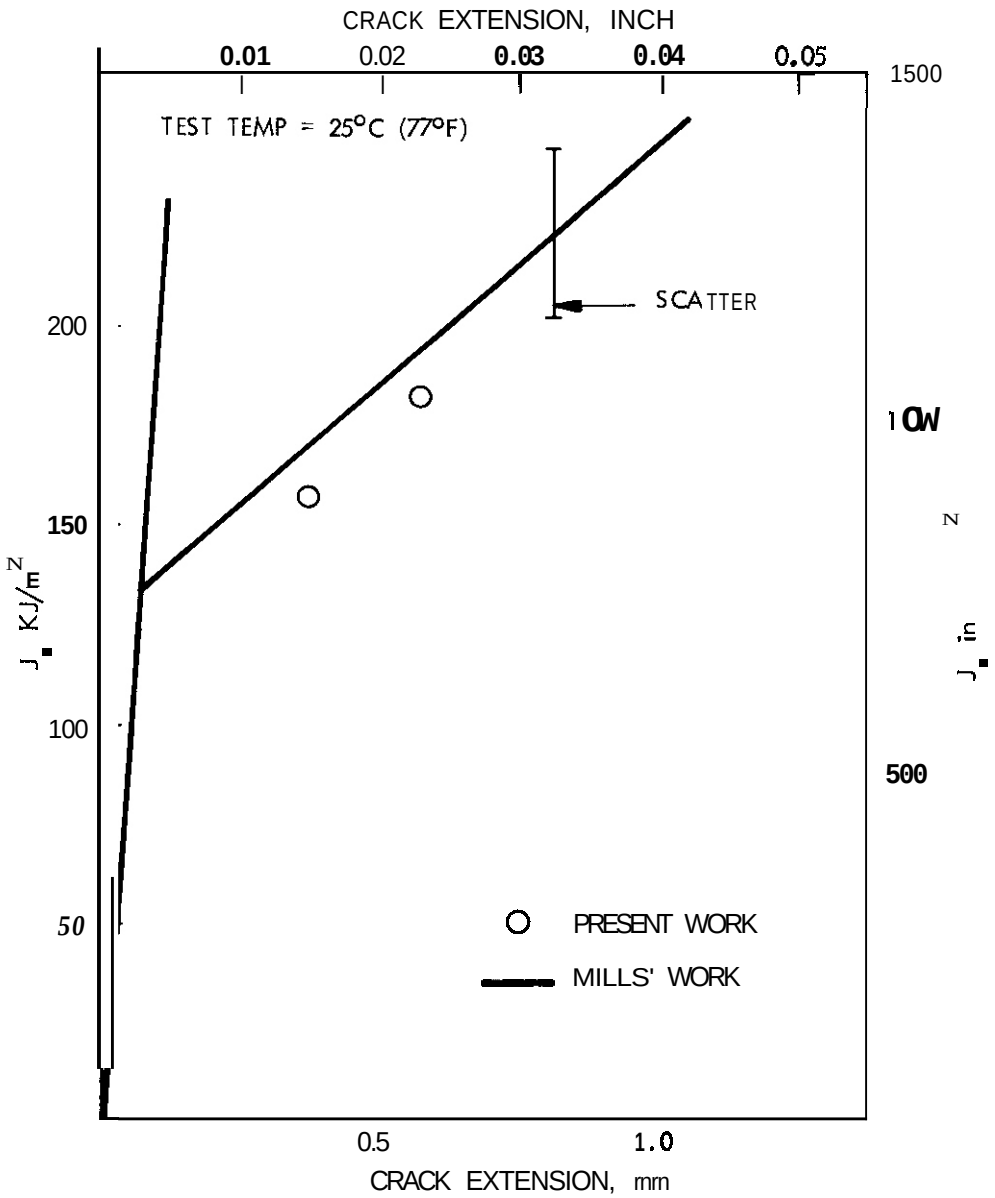

HEDL 7807-099.1

Fig. 2.5.5. J versus Aa tested at 25°C for 3.05 mm thick A286 specimens (present work). Note excellent agreement with large specimen (12.7 mm thick) data (Mills).

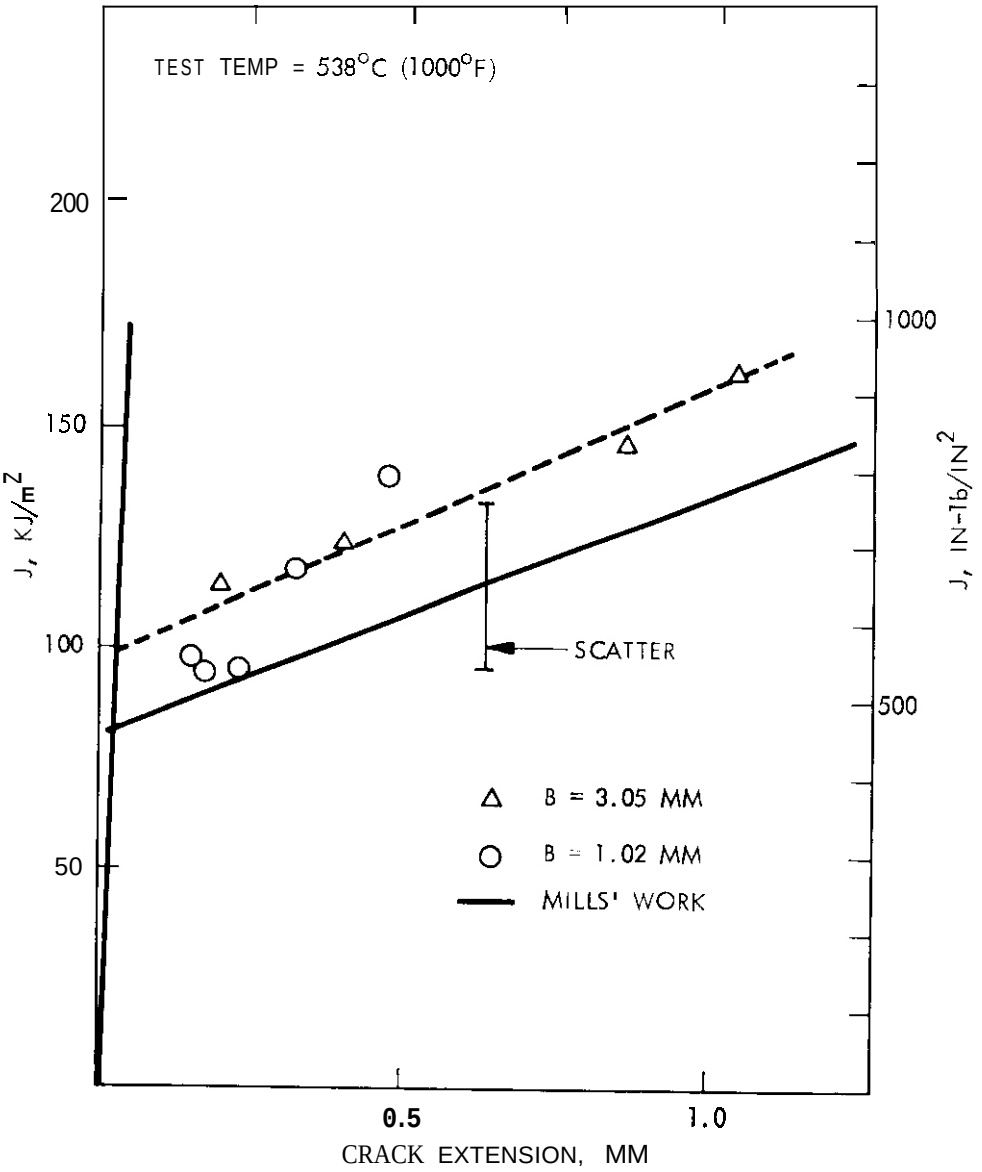

HEDL 7807-099.3

Fig. 2.5.6. **J versus** Δa **tested at 538°C** for **1.02** mm **and 3.05** mm **thick A286 specimens. Note good agreement with large specimen (12.7** mm **thick) data (Hills).**

J-integral testing has been carried out on specimens with thicknesses equal to that of breeder reactor ducts, **1.02** and **3.05** mm.[7] Strictly speaking these specimens do not meet the ASTM criterion for the proper specimen size to obtain a valid J_{Ic} or critical J value. However comparison of the small specimen data with larger, i.e., valid specimen data, indicated very good agreement. Figs. **2.5.5** and **2.5.6** compare the J versus crack extension data obtained for a total of three distinct specimen thicknesses of alloy **A286** which were tested at two temperatures. In all cases the J_c obtained using thin specimens was within **20** percent of the value determined from the ASTM valid **12.7** mm thick specimen. The absence of a significant size effect in this range of specimen thickness has also been observed for **316** stainless steel and the ferritic alloy HT-9. It is important to note that for irradiated metals the valid use of even thinner specimens is possible since irradiation decreases fracture toughness (J_C) while increasing yield strength (σ_{yield}). Recently a single specimen J-integral technique has been developed. By monitoring crack growth using a calibrated electropotential technique an entire J versus Aa curve, which previously required five specimens to define, can be obtained from a single specimen.[9]

Ferritic metals undergo a sharp transition in their dynamic fracture behavior from mostly ductile to mostly brittle when subjected to combinations of dynamic loadings, lowered service temperatures and triaxial stress states. The most common method of quantifying this behavior involves the impact loading of a notched bar known as a Charpy specimen.[10] The energy required to completely break the specimen is determined as a function of temperature. The temperature at which the transition occurs is defined **as** the ductile to brittle transition temperature (DBTT). Strictly speaking the DBTT determined for a metal using a specimen of a certain thickness is only valid for structures of the same thickness. However, it has been determined that the change in DBTT caused by irradiation, for example, is independent of specimen size." Therefore, a specimen conveniently sized for an irradiation experiment can be used to generate radiation effects data which can then be applied to a specific structure merely by determining the absolute DBTT using unirradiated specimens of the appropriate thickness.

A small Charpy type specimen has been developed at Westinghouse Hanford Company (WHC) for the fusion and breeder programs. Fig. 2.5.7 compares this nominally one-half size Charpy specimen (5 mm by 5 mm crossection) to a full size Charpy specimen (10 mm by 10 mm crossection). Even smaller one-third size specimens have been developed and successfully applied in other programs.[11,12] Clearly, specimens must be carefully designed to ensure, for example, that the specimen will fracture and not merely bend upon impact.

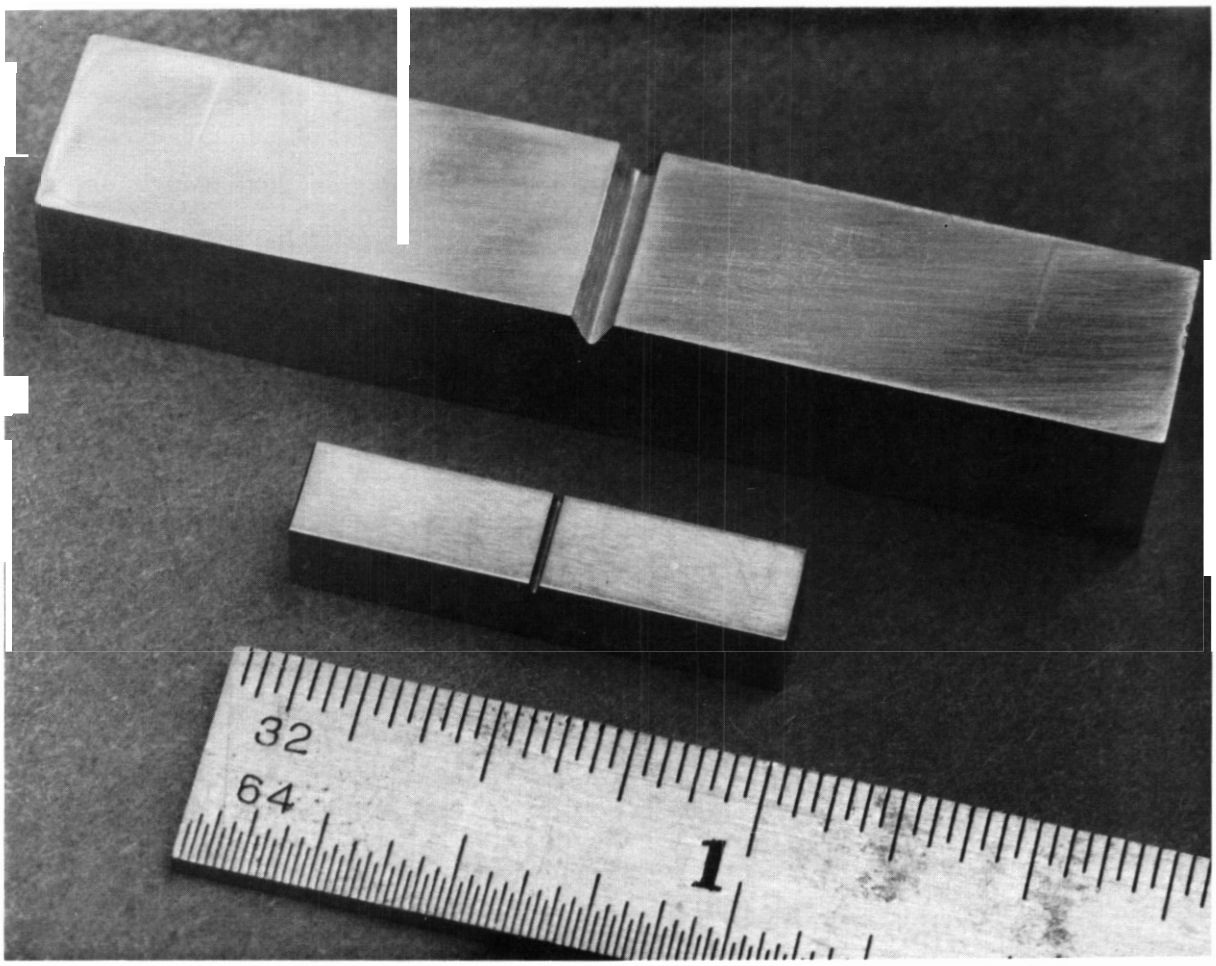

Fig. 2.5.7. Small, half-size and large, full size Charpy type specimens.

A small Charpy type specimen has been developed at Westinghouse Hanford Company (WHC) for the fusion and breeder programs. Fig. 2.5.7 compares this nominally one-half size Charpy specimen (5 mm by 5 mm crossection) to a full size Charpy specimen (10 mm by 10 mm crossection). Even smaller one-third size specimens have been developed and successfully applied in other programs.[11,12] Clearly, specimens must be carefully designed to ensure, for example, that the specimen will fracture and not merely bend upon impact.

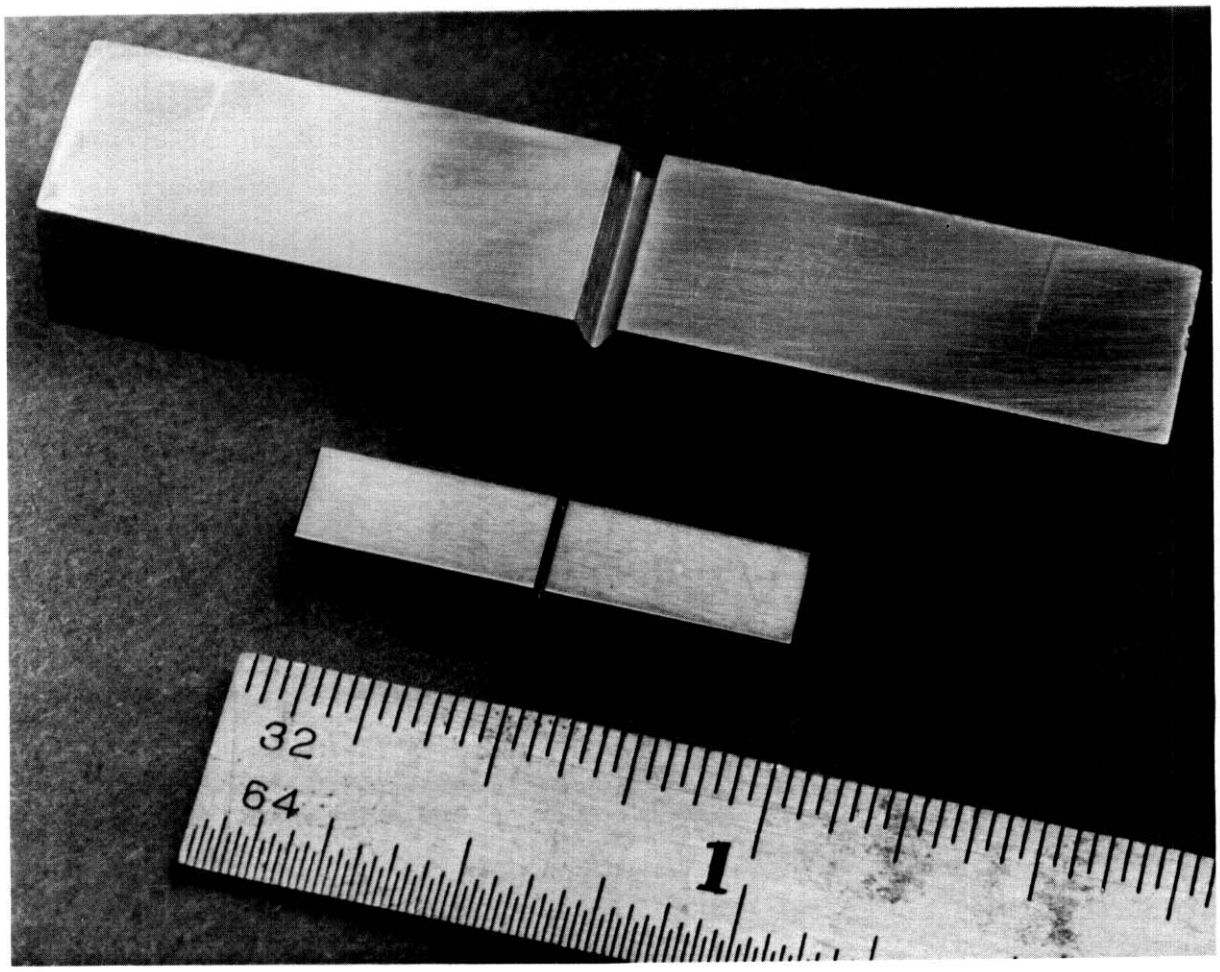

Fig. 2.5.7. Small, half-size and large, full size Charpy type specimens.

Small and large Charpy specimen data are compared in Fig. 2.5.8. In this case excellent agreement has been obtained for the DBTT of HT-9 with no indication of a size effect. However, due to differences in the prior history and specimen orientation of the small and large specimens it was suggested that this result was fortuitous.[13]

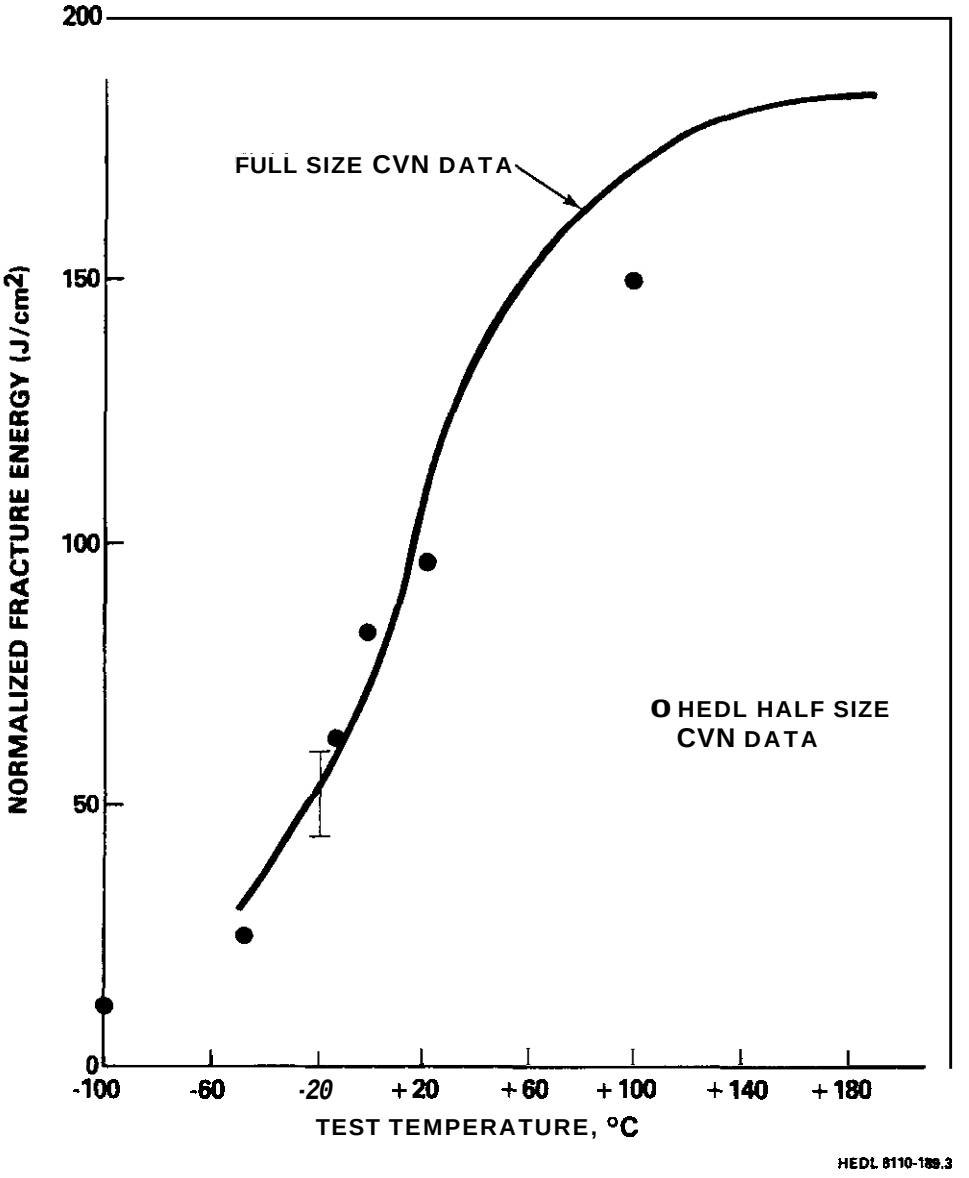

Fig. 2.5.8. Comparison of full size and half-size Charpy specimen data. Excellent agreement for the DBTT was not expected and may be fortuitous (see text).

Recently, in an attempt to extract fracture toughness data from the simple Charpy type impact test, instrumentation has been developed to record the load history of the impact event.[14] This technology has been applied to the testing of half-size Charpy specimens.[13] The results obtained are qualitatively in agreement with other determinations of fracture toughness.

2.5.4.3.4 Fatigue. Fatigue is the tendency for a metal to fail under fluctuating stress levels whose maximum value is less than the monotonic tensile strength of the metal. All structures are subjected to fluctuating stress levels during their lifetimes and designing against fatigue type failures is of great importance. One method of determining the fatigue life of a metal employs an hourglass shaped specimen, Fig. 2.5.9. Specimens are subjected to axial push-pull type loadings at varying total strain levels and the number of cycles required to cause failure at a given strain level is determined.

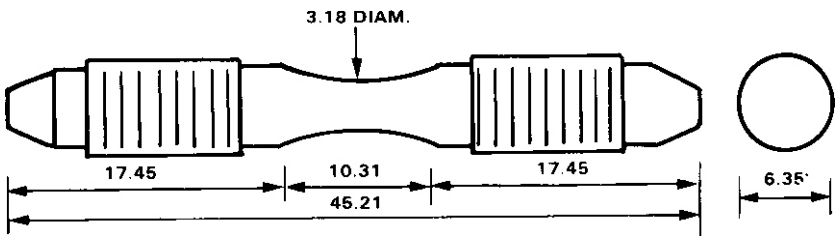

Fig. 2.5.9. Small hourglass shaped specimen for constant strain range axial fatigue type testing.

Size effects are expected for fatigue testing.[15] Decreasing the volume of the test article by using small specimens decreases the available specimen surface area. This decrease in the surface area of the specimen is usually thought to be important since fatigue failures initiate at the specimen surface. However, over the range of minimum specimen diameters allowed by ASTM,[16] 5.1 to 25.4 mm, no size effect has been observed for plain carbon steels.[17] Furthermore, a comparison of available data for 20 percent cold worked 316 stainless steel from two specimen sizes, 5.1 mm diameter (large)[18] and 3.2 mm diameter (small)[19] specimens also does not show any evidence of a size effect, Fig. 2.5.10.

2.5.4.3.5 Fatigue Crack Growth. The methodology of fatigue crack growth (FCG) is basically the application of fracture mechanics to fatigue. Structures are assumed to have pre-existing flaws and the question to be answered is how fast does the flaw grow as a function of the service loading. If these data are obtainable, then safe loads and crack lengths can he specified which will preclude failure over a specified service life. It has been demonstrated that

$$\frac{da}{dn} = A\Delta K^p$$

where da/dn is the crack growth rate, ΔK is the range of stress intensity factor calculated for the fatigue cycle, A is a constant and p depends on the metal and stress level and can range from 1 to 6. For fusion reactors one potential failure mechanism is the growth of a pre-existing flaw to a size equivalent to the thickness of the vacuum boundary. This loss of vacuum integrity could terminate the operation of the device.

In order to assess the resistance of various candidate alloys to FCG the qualification of a center cracked panel type specimen was initiated.** The ideal specimen would be small to conserve irradiation space and would also be thin, that is, prototypic of first wall structures. The result of the development was a small panel 25.4 mm wide and 12.7 mm high which will be irradiated. After irradiation pull tabs will be remotely welded to the irradiated panel for testing. The miniature center cracked tension (CCT) type specimen is shown in Fig. 2.5.11. Larger specimens which were used in the development of the miniature CCT specimen are also shown.

Data obtained from the miniature CCT specimen** are in good agreement with: (1) the larger CCT specimens (Fig. 2.5.12) of 304 stainless steel and six other specimen designs, tested in air at 25°C, Fig. 2.5.12;[21] (2) conventional, i.e., large, compact tension type FCG type specimens of 20 percent cold worked 316 stainless steel tested in air at 25°C, Fig. 2.5.13, and at 315°C, Fig. 2.5.14;[22] and (3) with a conventional single edge notch cantilever (SENC) type specimen of 20 percent cold worked 316 stainless steel tested in air at 593°C, Fig. 2.5.15.[23]

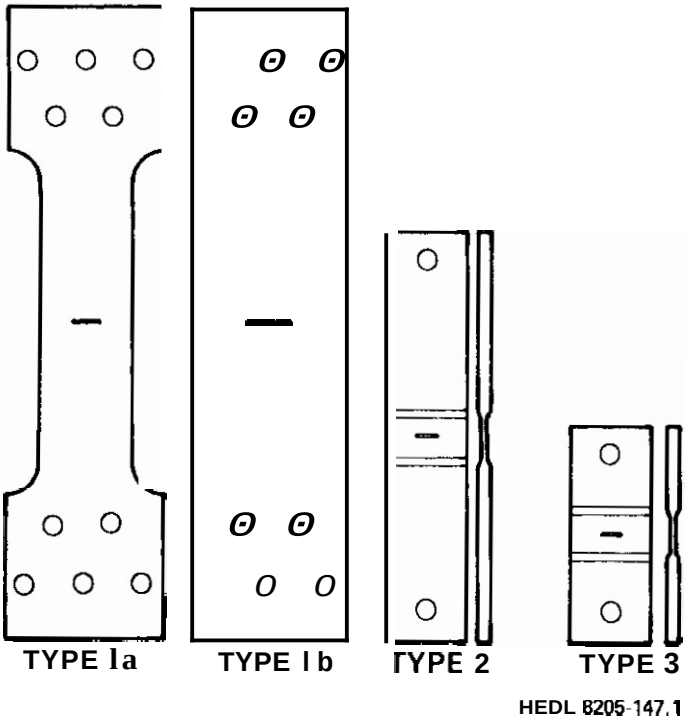

Fig. 2.5.11. Miniature center cracked tension (CCT) specimen development. Type 3 is the optimized miniature specimen design.

There are two major limitations on the use of miniature CCT type specimens. First, an accurate method of following crack growth during a test is required and second, the size of a single miniature specimen permits only a small range of AK to be examined as compared to larger specimens. Both of these limitations have been addressed.

A precise electropotential technique which permits continuous monitoring of crack growth has been applied to miniature CCT FCG testing. The technique eliminates the need to interrupt the test to determine crack extension and is well suited to remote, computerized data acquisition.[24] By connecting several miniature CCT specimens, each precracked to a different initial crack length, in series to form a chain, a large range of ΔK values can be obtained under identical experimental conditions.[24] This novel technique has been used to perform both in-core and ex-core fatigue crack propagation (FCP) type testing. This technique has demonstrated for example, that for 20 percent cold worked 316 stainless steel there is no significant effect of dynamic irradiation on FCP.

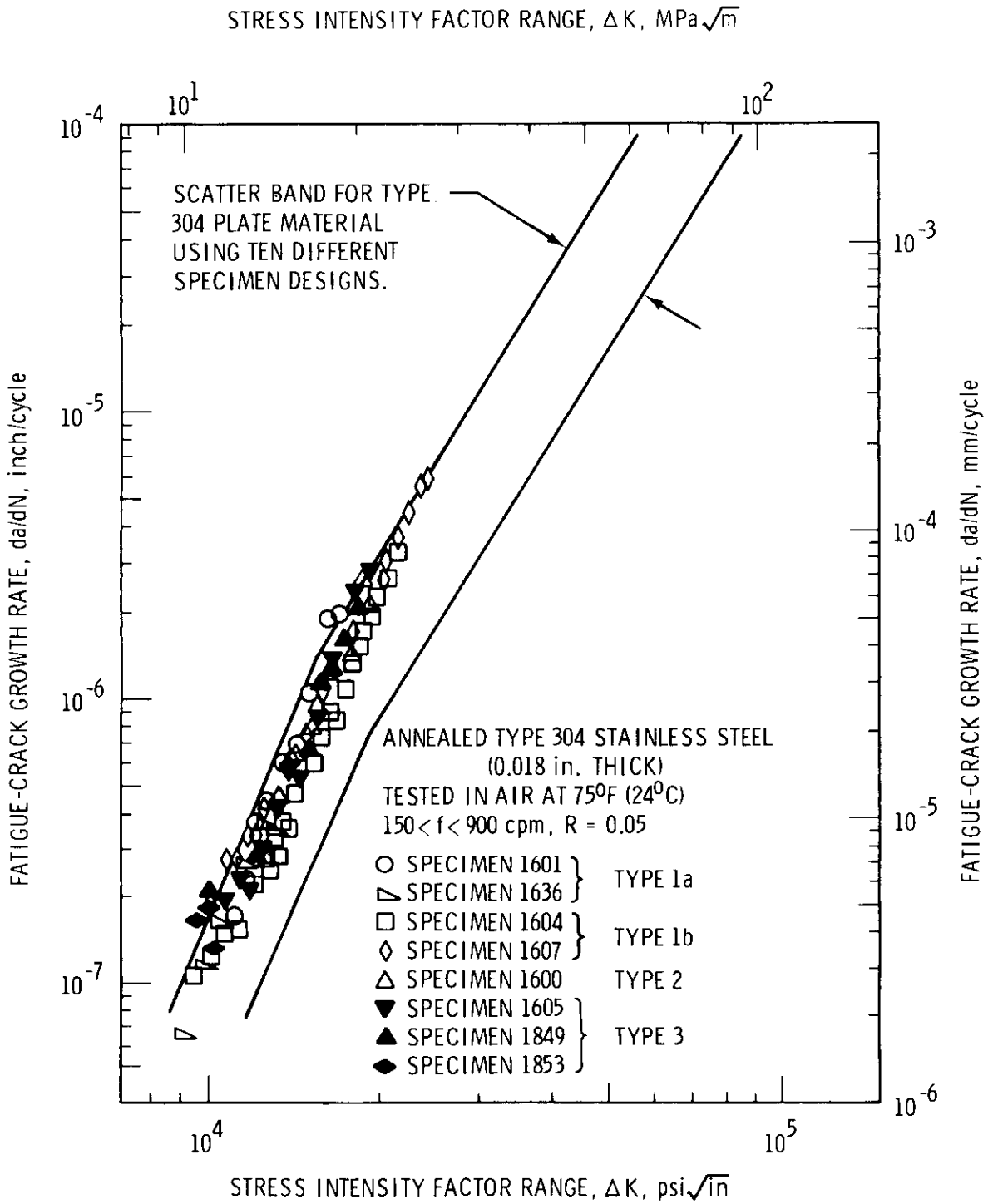

Fig. 2.5.12. Comparison of miniature CCT with developmental CCT specimens and with six other specimen designs.

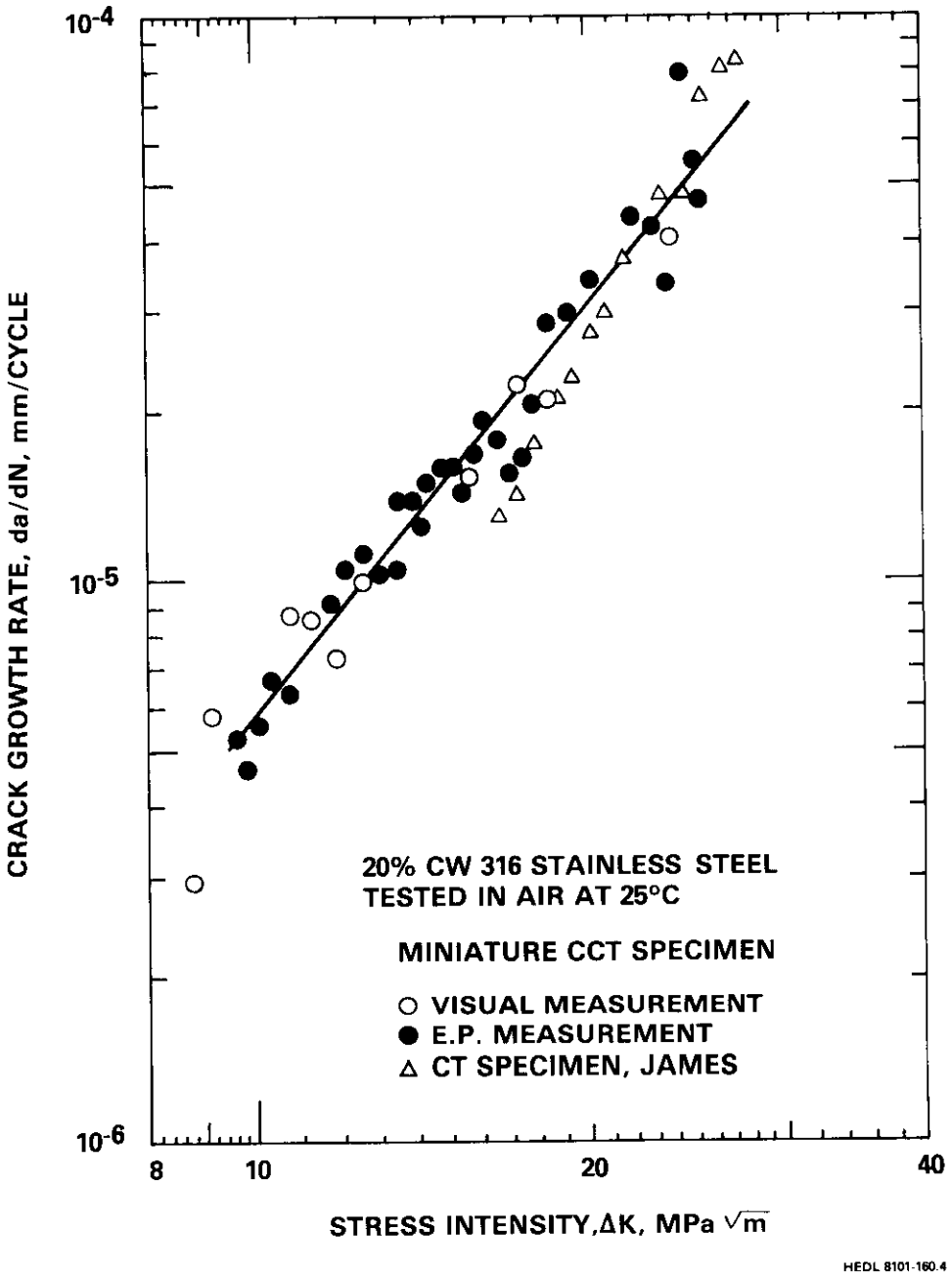

Fig. 2.5.13. Comparison of room temperature fatigue crack growth rates for miniature CCT specimen (e.p. and visual measurements) and the conventional compact tension (CT) specimen (visual).

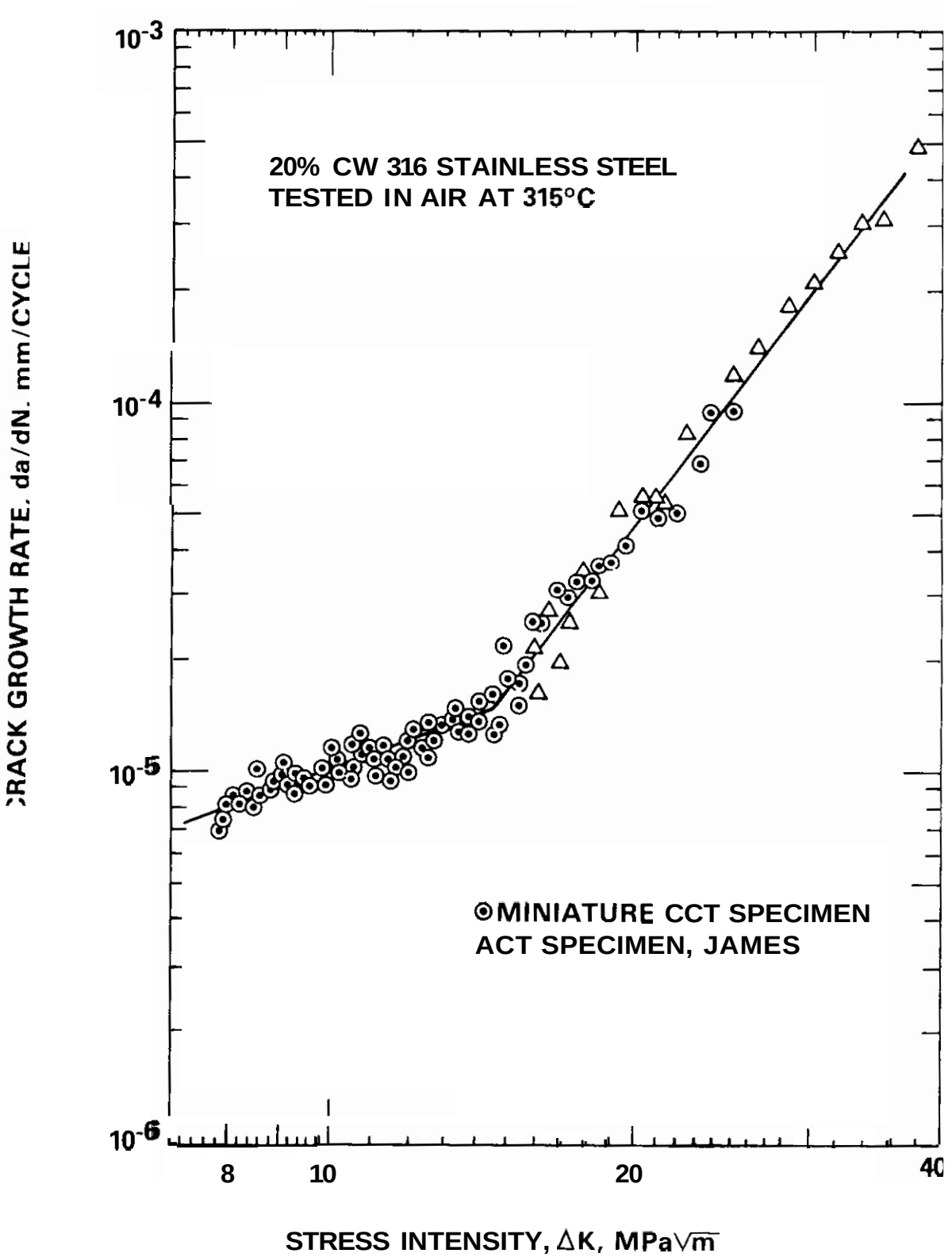

Fig. 2.5.14. Comparison of elevated temperature FCG for miniature CCT specimen (e.p. method) and conventional CT specimen (visual method)

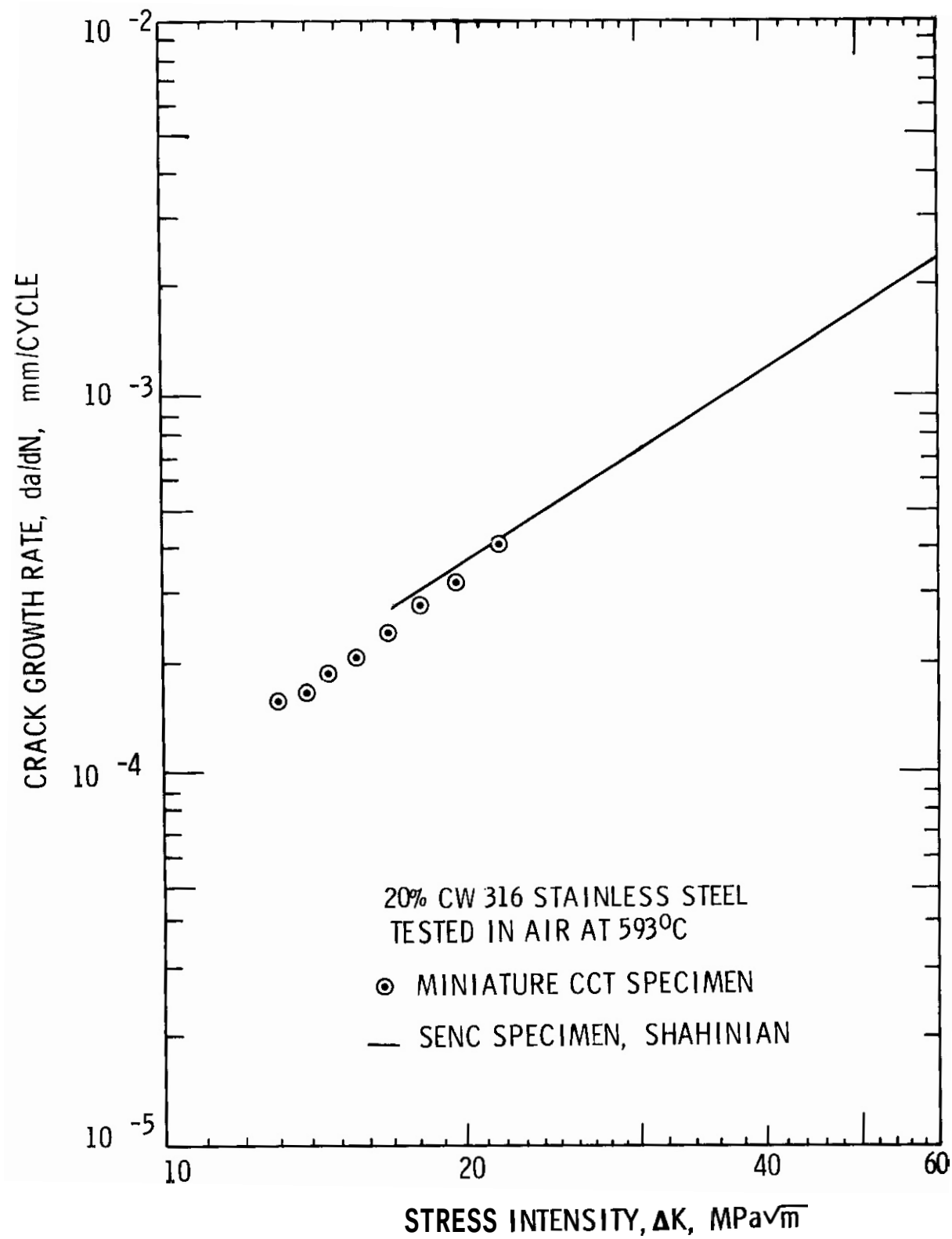

Fig. 2.5.15. **Comparison of elevated temperature FCG for miniature CCT specimen (e.p. method) and SENC specimen (visual method).**

2.5.4.3.6 Tensile. In the tensile test a specimen is subjected to continually increasing uniaxial tensile force while simultaneous observations are made of the elongation of the specimen.[25] The strength and elongation data derived from the tensile test are perhaps the most commonly used means of ranking metals.

Two measures of strength, yield and ultimate and one measure of ductility, percent total elongation, are usually extracted from the tensile test data. While ultimate strength has been the most commonly used parameter for ranking metals it is generally agreed that it is of little fundamental significance.[26] Instead, the use of yield strength is gaining wider acceptance despite the large number of empirical correlations of ultimate strength with properties such as fatigue strength and hardness. Ultimate strength is defined as the onset of plastic instability, or localized deformation, in the tensile specimen and is known to be affected by specimen geometry in general and nonuniformities in the specimen cros-section in particular. Yield strength is defined as the strength at some small designated amount of permanent strain or offset, Yield strength, within limits, is not affected by specimen size. Elongation data are known to be a function of the length of the reduced section of the specimen and data are reported as percent elongation per some specified length. However, elongation data from a small specimen can be scaled to larger sizes by applying Barba's Law which simply states that geometrically similar specimens deform in a similar fashion.[27]

Two small tensile specimens developed for the fusion materials development program by WHC are shown in Fig. 2.5.16. Both specimens are approximately 13 mm in overall length with reduced section lengths of about 6 mm. The diameter of the wire type specimen's reduced section is .25 mm and the sheet type specimen reduced section is 1 by .25 mm. The volume of the reduced section of the wire and sheet type specimens are about 10,000 and 1,000 times less, respectively, than the volume of the reduced section of a standard ASTM bar type specimen.[25] Nevertheless, reasonable agreement is obtained when data from small (wire type) specimens and larger (3.2 mm diameter by 32 mm long reduced section) cylindrical specimens of 20 percent cold worked 316 stainless steel are compared, Fig. 2.5.17.

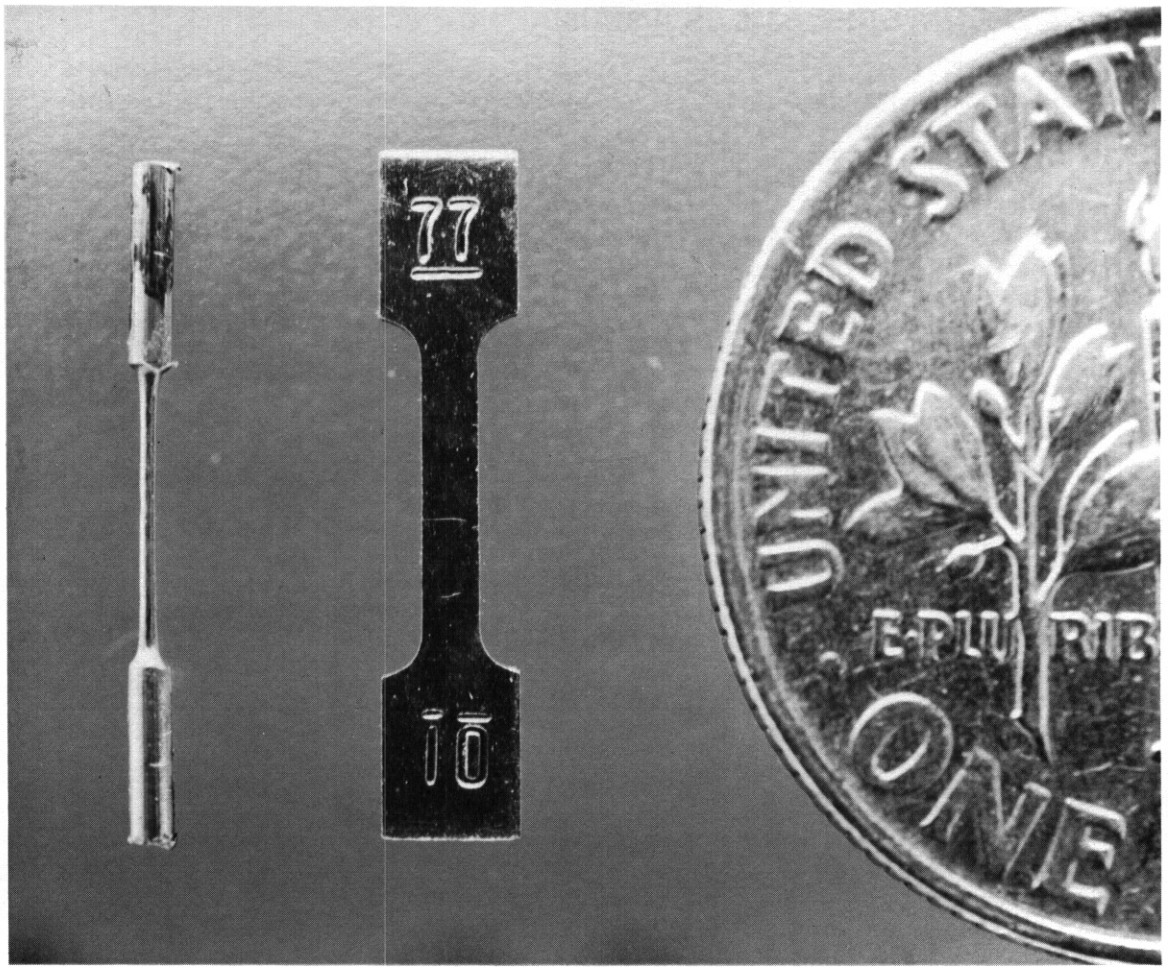

Fig. 2.5.16. Small wire and sheet type tensile specimens.

The grain size of both large and small tensile specimens was identical. Furthermore there were a sufficient number of grains across the reduced section of the small specimen to ensure that bulk material properties would be measured. It is not surprising therefore that the 0.2 percent offset yield strength of large and small specimens is in good agreement. Although similar numbers of specimens were tested for this analysis, the total volume of metal sampled using the wire specimens is, of course, small in comparison to the volume sampled by the large specimens. This would account for the larger spread in the yield strength data observed for large specimens. As reported the crossection of the wire specimens used in this comparison were not exceptionally uniform.[28] It is not surprising that the small and large specimen ultimate strength data are not in close

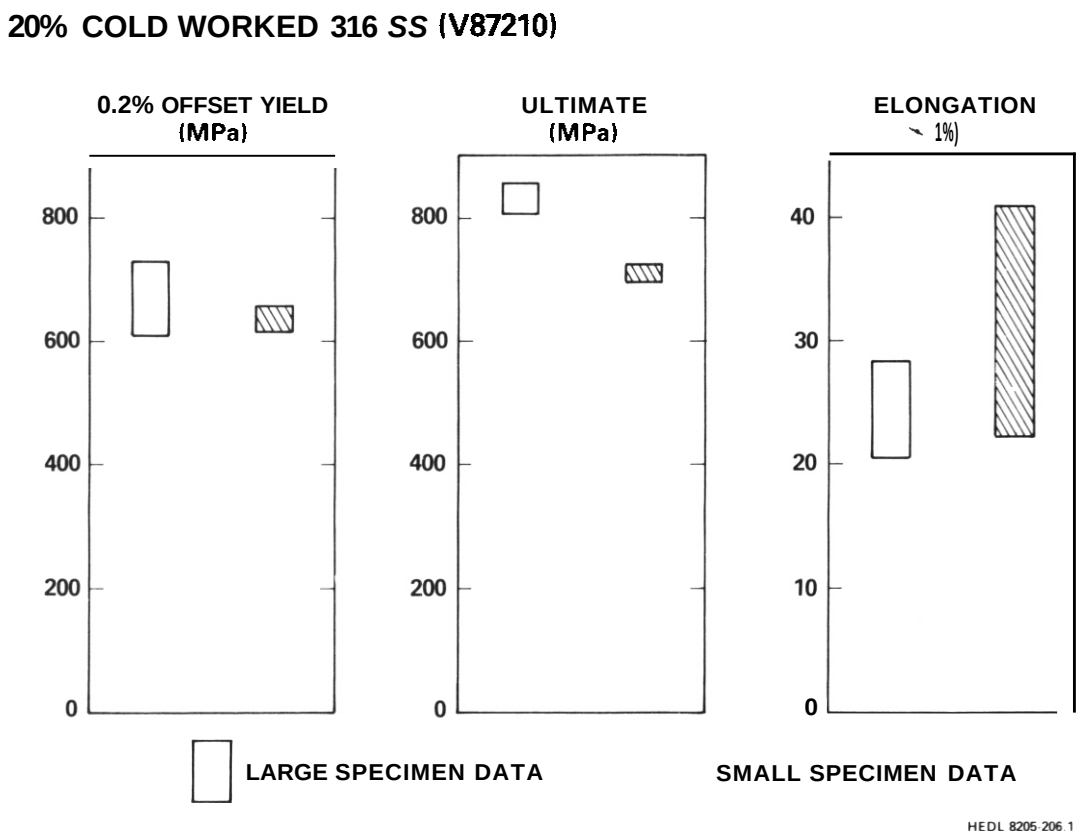

Fig. 2.5.17. Comparison of yield and ultimate strength and elongation for wire (small) and rod (large) specimens of 20 percent cold worked 316 stainless steel.

agreement. In terms of elongation some overlap of small and large specimen data is evident. The large scatter in the small specimen data has been attributed to specimen to specimen variations in the length of the reduced section.[28] Miniature sheet type specimens, which can be produced to more exacting tolerances than wire specimens, were developed partly in response to this large amount of data scatter. The sheet type specimen is based on a similar type specimen designed by workers at ORNL.[4]

2.5.4.3.7 Creep. Creep, the progressive deformation of a metal at a constant stress, is another phenomenon which can limit the life of reactor components. The development of a small creep specimen, the pressurized tube, for the National Cladding/Duct Materials Development Program, was a major achievement for the breeder reactor program.[29,30] This specimen allows a large number of alloys and/or experimental conditions to be

tested in-reactor in the space formerly occupied by a single uniaxial creep test. Specimens to be tested are pressurized to produce the required stress level in the cladding and sealed. After a predetermined amount of in-reactor exposure they are removed and the change in the diameter of each specimen is determined. The procedure is repeated to determine the creep curve, strain versus time, for the metal being tested.

The data obtained from these volume efficient specimens is in good agreement with data from open, i.e., uniaxial tube (5.8 mm diameter by .38 mm wall, 25 to 75 mm gage length) specimens and uniaxial rod type (5.5 mm diameter, 28.6 gage length) specimens of 20 percent cold worked 316 stainless steel as shown in Fig. 2.5.18.[31] The dimensions of the pressurized tubes used in this comparison were 5.84 mm diameter, .38 mm wall and 25.4 mm gage length.

In addition to being the national standard specimen for creep studies for the United States Breeder Reactor Program, the British have recently adopted an analogus specimen and measurement procedure for their breeder program. For FMIT a 2.5 mm outside diameter, .2 mm thick wall pressurized tube has been selected. This new specimen design is currently under development at WHC.

Creep data have also been obtained using small diameter wire type specimens similar to the specimens used for tensile testing. This specimen and a specially designed torsional creep apparatus were used to obtain data on the effect of proton irradiation on creep.[32] The data obtained from this study are in good agreement with data obtained from pressurized tube experiments, Fig. 2.5.19.

2.5.4.3.8 Other Measures of Strength and Ductility

In an effort to maximize the data which can be obtained from the limited irradiation volume of fusion irradiation environments, techniques are being developed to determine properties of interest in novel and in some cases, by pseudo non-destructive means.

Indenter type microhardness is a means of determining the flow properties of a metal. Standard Vickers microhardness data obtained from TEM disk type specimens have been shown to correlate very well with the yield strength of metals. The major advantage of this technique is that

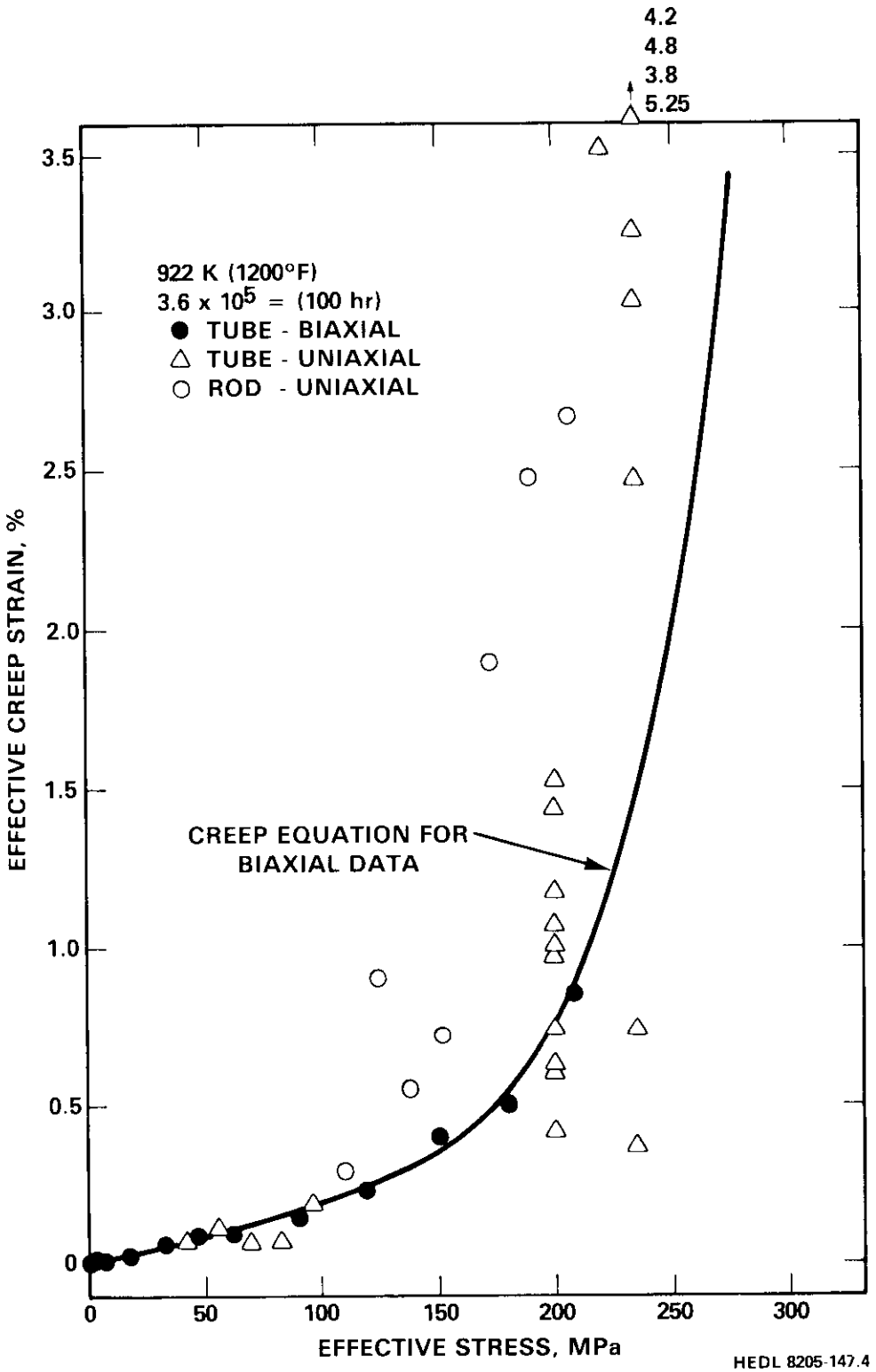

Fig. 2.5.18. Comparison of biaxial (pressurized tube) and uniaxial creep data from open tubes and rod specimens at 922K for a time of 3.6×10^5 s.

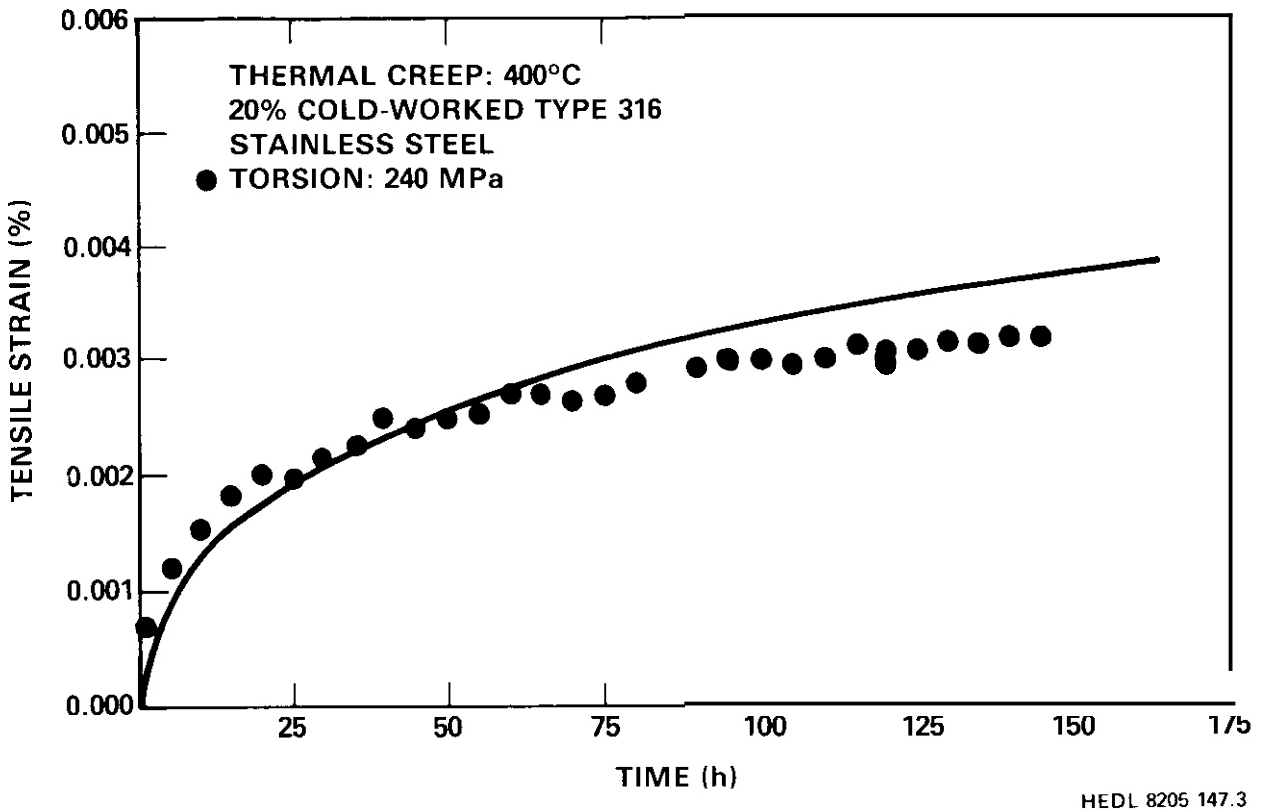

Fig. 2.5.19. Comparison of thermal creep data from torsional and pressurized tube experiments (trend line). Data are normalized to a tensile stress of 240 MPa.

since the deformation associated with the microhardness indent is localized a single specimen can be examined by several analytical techniques or can be repeatedly tested as part of an extended irradiation or postirradiation conditioning program.

In Figs. 2.5.20 and 2.5.21, the increase in the 0.2 percent offset yield strength calculated from hardness data is compared to strength values obtained from tensile specimens, as a function of high energy neutron exposure for pure copper and for 316 stainless steel.[33] Similar correlations between hardness and strength have been obtained for irradiated nickel and 316 stainless steel hardened by cold work.

Lucas, et. al., have employed a ball indenter type hardness test technique to obtain, in a semi-empirical fashion true stress, true strain data from disk type specimens.[34] A comparison of instrumented hardness test data with tensile data is shown in Fig. 2.5.22. In general the agreement is good. Efforts are currently underway to scale the technique so that instrumented hardness data can be obtained from TEM disk specimens.

The primary caution in correlating hardness to strength data is that the parameters of the test must be adjusted so that the volume of the metal sampled by the indenter contains a sufficient number of grains so that bulk properties are being measured. This can be achieved by proper selection of the applied loads and specimen thicknesses.

The bending of TEM disks has been shown to be a valid method of obtaining ductility data.[35] TEM disk specimens are mounted in a die above a hemi-spherical cavity and are centrally loaded with a hydraulically driven punch, Fig. 2.5.23. The edge of the disk initially is simply supported. Load versus punch displacement data are recorded during the test. The ductility measured by this disk bend technique agrees quite well with larger specimen tensile ductilities obtained from the identical metal, Fig. 2.5.24. This technique was originally developed at WHC and is being extended by workers at the Massachusetts Institute of Technology.[36]

2.5.5 Conclusions and Future Work

Data from microstructural, swelling, static and dynamic fracture toughness, fatigue, fatigue crack growth and tensile type specimens which are compatible with FMIT have been compared with data obtained from large

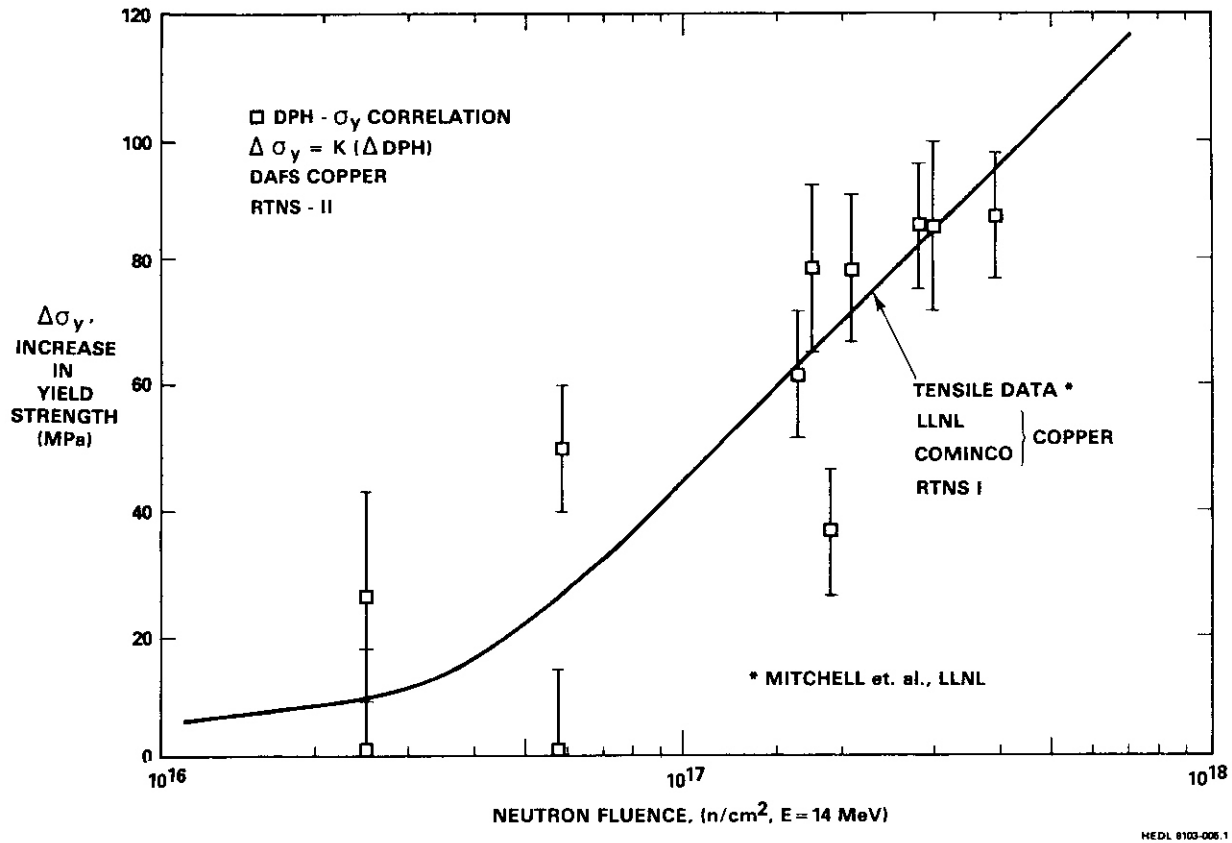

Fig. 2.5.20. Comparison of $\Delta\sigma_y$, the measured increase in the 0.2 percent offset tensile yield strength, of two heats of copper and the strengthening of a third heat of copper calculated from hardness data obtained from TEM disk specimens.

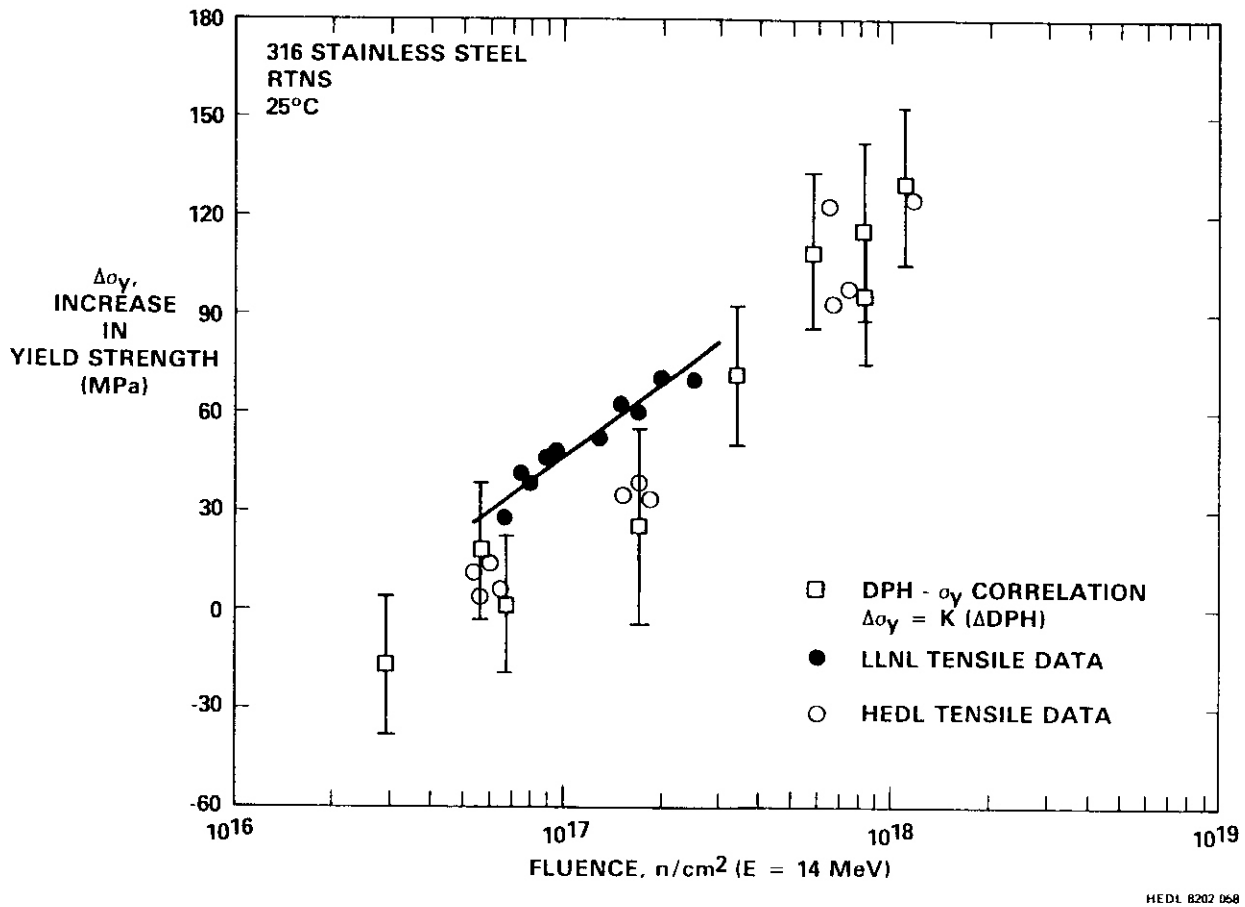

Fig. 2.5.21. Comparison of $\Delta\sigma_y$, the measured increase in the 0.2 percent offset tensile yield strength, of two heats of annealed type 316 stainless steel and the strengthening of a third heat of 316 stainless steel calculated from diamond pyramid hardness (DPH) data.

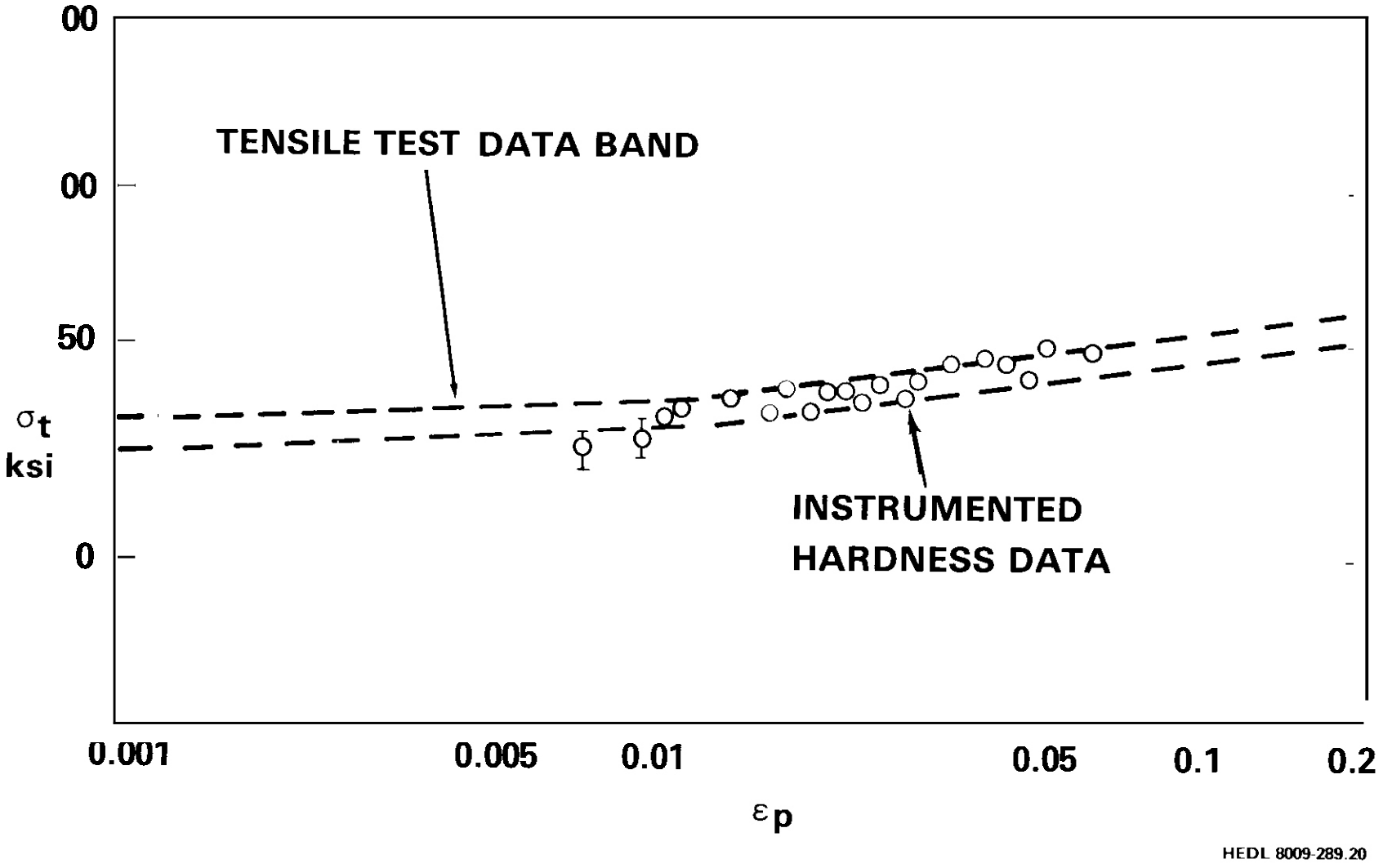

Fig. 2.5.22. Comparison of stress-strain data obtained by an instrumented indenter hardness technique and measured stress-strain data from a tensile specimen.

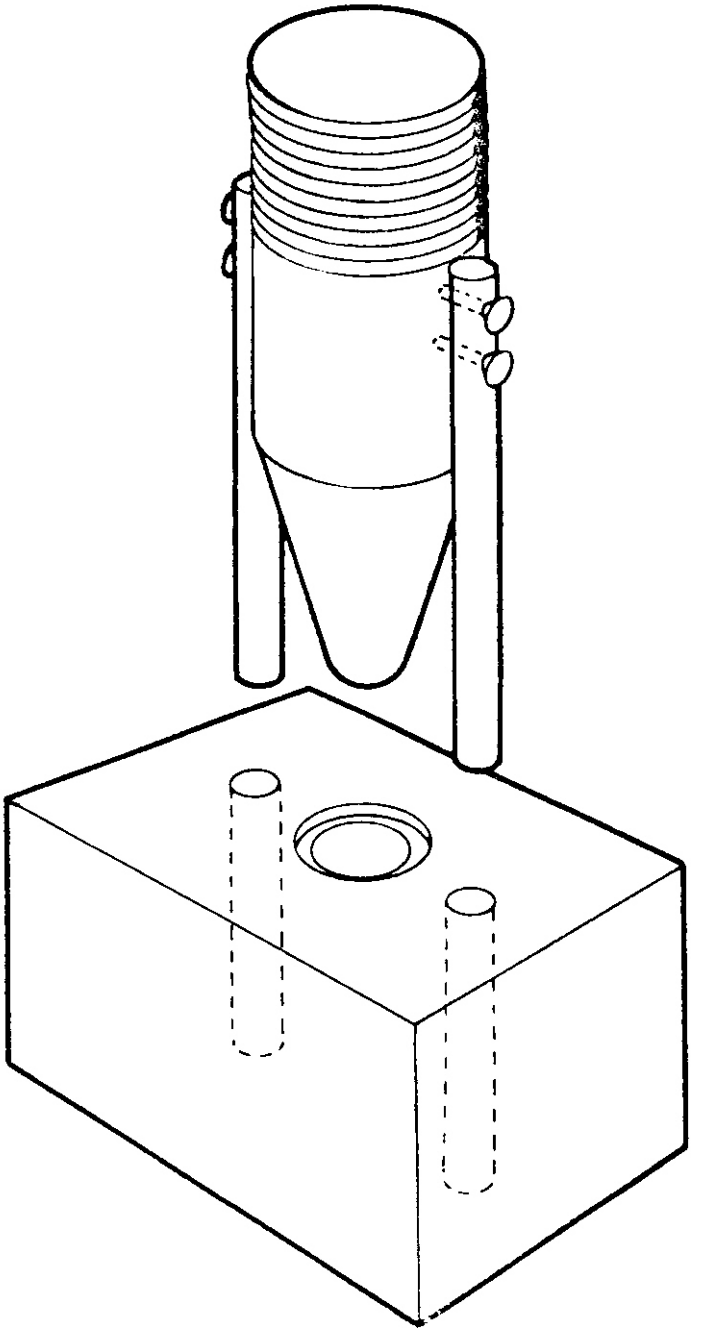

Fig. 2.5.23. Disk **bend test fixture schematic.**

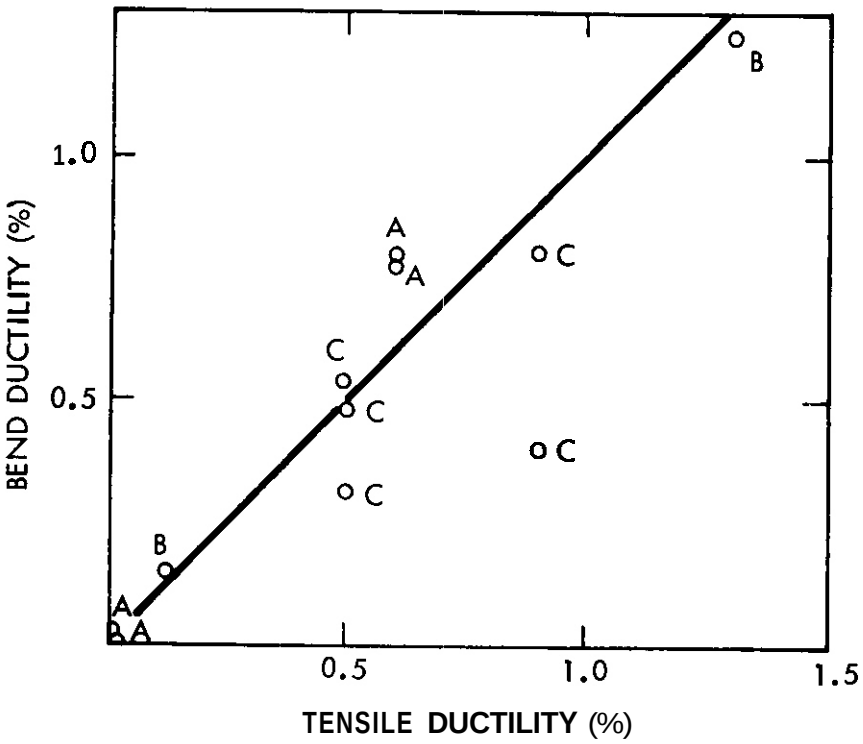

HEDL 8004-320.7

Fig. 2.5.24. Comparison of measured tensile ductility and calculated ductility from the disk bend test.

specimens. In all cases either the absence of a specimen size effect has been demonstrated or a means of utilizing the small specimen data for engineering purposes has been suggested. Pressurized creep tubes for use in F'MIT are under development. Furthermore two hardness techniques and a disk bend technique have been described which allow strength and ductility data to be obtained from small specimen geometries. The data obtained by these novel techniques are also in good agreement with data obtained by more conventional testing techniques. Additional data will be integrated into this comparison and reported.

2.5.6 References

1. R. E. Nygren, "Considerations on Experiments in FMIT," p. 1837 in *IEEE Pub. No. 79CH1441-5NPS*, 1979.
2. W. M. Stacey, Jr., M. A. Abdou, J. A. Schmidt, T. E. Shannon and J. K. Griffith, US *Contribution to the International Tokamak Reactor, Phase I Report," US INTOR REPORT*, Georgia Institute of Technology, Atlanta, GA, INTOR 181-1, 1981.
3. G. L. Kulcinski, G. A. Emmert, C. W. Maynard, J. F. Santarius, M. E. Sawan, W. Heinz, P. Komarek, W. Mauer, A. Supan and E. K. Opperman, "TASKA, A Fusion Engineering Test Facility for the 1990's," *J. Nucl. Mat.* 103 & 104: p. 67 (1981).
4. M. L. Grossbeck and K. R. Thoms, "ORR-MFE-4: A Spectral Tailoring Experiment to Simulate the He/dpa Ratio of a Fusion Reactor in Austenitic Stainless Steel," ADIP *Quart. Prog. Rep. June 1980*, DOE/ER-0045/3, pp. 10-23.
5. J. R. Rice, "A Path Independent Integral and the Approximate Analysis of Strain Concentrations by Notches and Cracks,'' *J. App. Mech.* 35: p. 379 (1968).
6. F. A. McClintock, "Plasticity Aspects of Fracture," pp. 47-225 in *Fracture.* Vol. 3, H. Liebowitz, Ed., Academic Press, New York, 1971.
7. F. F. Huang and G. L. Wire, "Techniques Developed for Elevated Temperature Fracture Toughness Testing of Irradiated Metals in Thin Sections," *J. Eng. Mat. Tech.* 101: p. 403 (1979).
8. American Society for Testing and Materials, "Standard Practice for R-Curve Determination, E561-81," pp. 673-692 in *1981 Annual Book of ASTM Standards,* Part 10, ASTM, Philadelphia, PA, 1981.
9. F. F. Huang and G. L. Wire, "Fracture Toughness Testing of a Ferritic Alloy Using the Electropotential Technique," *J. Nucl. Mat.* 104: p. 1151 (1981).
10. American Society for Testing and Materials, "Standard Methods for Notched Bar Impact Testing of Metallic Materials, E23-81," pp. 273-296 in *1981 Annual Book of ASTM Standards,* Part 10, ASTM, Philadelphia, PA, 1981.

11. M. Grounes, "Review of Swedish Work on Irradiation Effects in Pressure Vessel Steels and on Significance of Data Obtained," pp. 224-259 in *Effects of Radiation on Structural Metals,* ASTM STP 426, American Society for Testing and Materials, Philadelphia, PA, 1967.

12. G. R. Odette and G. E. Lucas, "Small Specimen Test Development," *DAFS Quart. Frog. Rep. Feb. 1981,* DOE/ER-0046/4, pp. 46-64.

13. W. L. Hu and N. F. Panayotou, "Miniature Charpy Specimen Test Device Development and Impact Test Results for the Ferritic Alloy HT-9," *ADIP Semiannual Frog. Rep. Sept. 1981,* DOE/ER-0045/7, pp. 235-251.

14. American Society for Testing and Materials, *Symposium on Instrumented Impact Testing,* ASTM STP 563, ASTM, Philadelphia, PA, 1973.

15. G. E. Dieter, *Mechanical Metallurgy,* Second Edition; McGraw-Hill, New York, pp. 426-427.

16. American Society for Testing and Materials, "Standard Recommended Practice for Constant Amplitude Axial Fatigue Tests of Metallic Materials, E466-76," pp. 631-636 in *1981 Annual Book of ASTM Standards,* Part 10, ASTM, Philadelphia, PA, 1981.

17. C. E. Phillips and R. B. Heywood, *Inst. Mech. Eng.* 165: p. 113 (1951) London.

18. J. M. Beeston and C. R. Brinkman, "Axial Fatigue of Irradiated Stainless Steels Tested at Elevated Temperatures," pp. 419-450 in *Irradiation Effects on Structural Alloys for Nuclear Reactor Applications,* ASTM STP 484, American Society for Testing and Materials, Philadelphia, PA, 1970.

19. M. L. Grossbeck and K. C. Liu, "Fatigue Behavior of Type 316 Stainless Steel Following Neutron Irradiation Inducing Helium," (Summary) Trans. *Am. Nucl. Soc.* 34(TANSAO 34): 186-88 (June 1980).

20. D. A. Mervyn and A. M. Ermi, "Miniature Specimen Technology for Postirradiation Fatigue Crack Growth Testing," p. 1832 in *IEEE Pub. No. 79CH1441-5NPS,* 1979.

21. L. A. James, J. L. Straalsund and R. E. Bauer, "Optimization of Fatigue Crack Growth Testing for First Wall Materials Development Evaluations," J. *Nucl. Mat.* 85 & 86: p. 851 (1979).

22. L. A. James, "Fatigue Crack Growth in 20 Percent Cold Worked Type 316 Stainless Steel at Elevated Temperatures," *Nucl. Tech.* 16: p. 316 (1972).

23. P. Shahinian, "Influence of Section Thickness on Fatigue Crack Growth in Type 316 Stainless Steel," *Nucl. Tech.* 30: p. 390 (1976).

24. A. M. Ermi, R. E. Bauer, B. A. Chin and J. L. Straalsund, "Multispecimen Fatigue Crack Propagation Testing," *J. Eng. Mat. Tech.* 103: p. 240 (1981).

25. American Society for Testing and Materials, "Standard Method of Tension Testing of Metallic Materials, E8-69," pp. 194-213 in 1970 *Annual Book of ASTM Standards,* Part 31, ASTM, Philadelphia, PA, 1970.

26, G. E. Dieter, *Mechanical Metallurgy,* Second Edition; McGraw-Hill, New York, p. 331.

27. W. J. McGregor Tegart, *Elements of Mechanical Metallurgy,* MacMillan Co., New York, p. 24.

28. N. F. Panayotou, R. J. Puigh and E. K. Opperman, "Miniature Specimen Tensile Data for High Energy Neutron Source Experiments," *J. Nucl. Mat.* 103 & 104: p. 1523 (1981).

29. E. R. Gilbert and B. A. Chin, "In-Reactor Creep Measurements," *Nucl. Tech.* 52: p. 273 (1981).

30. A. J. Lovell, B. A. Chin and E. R. Gilbert, "In-Reactor Creep Rupture of 20 Percent Cold Worked AISI 316 Stainless Steel," *J. Mat. Sci.* 16: p. 870 (1981).

31. E. R. Gilbert and L. D. Blackburn, "Creep Deformation of 20 Percent Cold Worked Type 316 Stainless Steel," *J. Eng. Mat. Tech.* 99: p. 168 (1977).

32. E. K. Opperman, J. L. Straalsund, G. L. Wire and R. H. Howell, "Proton Simulation of Irradiation-Induced Creep," Nucl. *Tech.* 42: p. 71 (1979).

33. N. F. Panayotou, "The Use of Microhardness to Determine the Strengthening and Microstructural Alterations of 14 MeV Irradiated Metals," paper presented at International Conference on Neutron Irradiation Effects, Nov. 1981, in press J. Nucl. Mat.

34. G. E. Lucas and N. F. Panayotou, "Microhardness Tests for High Energy Neutron Source Experiments," *J. Nucl. Mat. 103 & 104:* p. 1527 *(1981).*

35. F. F. Huang, M. L. Hamilton and G. L. Wire, "Bend Testing for Miniature Disks," *Nucl. Tech.* 57: p. *234 (1982).*

36. M. P. Manahan, A. S. Argon and O. K. Harling, "The Development of a Miniaturized Disk Bend Test for the Determination of Postirradiation Mechanical Properties," *J. Nucl. Mat. 103 & 104:* p. *1545 (1981).*

2.6 Neutron Source Characterization for Materials Experiments - L. R. Greenwood (Argonne National Laboratory)

2.6.1 ADIP/DAFS Tasks

ADIP Task I.A.2 - Define Test Matrices and Procedures

DAFS Task II.A.1 - Fission Reactor Dosimetry

2.6.2 Objective

To characterize neutron environments in terms of neutron flux, spectra, and fundamental damage parameters (DPA, PKA, transmutation) and to provide these exposure parameters during materials irradiations.

2.6.3 Summary

Data are presented from HFIR-CTR32, EBRII-X287, and the Omega West Reactor. An important new source of damage in nickel arises from the 340 keV ^{56}Fe recoil from the $^{59}Ni(n,\alpha)$ reaction used to produce high helium levels in materials irradiations in a thermal spectrum. The status of all other experiments is summarized in Table 2.6.1.

2.6.4 Progress and Status

2.6.4.1 Dosimetry Results for the HFIR-CTR32 Irradiation

The CTR32 irradiation in the PTP of the High Flux Isotopes Reactor (HFIR) at Oak Ridge National Laboratory was conducted from August 17, 1980 to December 12, 1980 for a total exposure of 124 days (10,863 MWD). Dosimeters were inserted at 12 vertical heights in the experiment. Six of the dosimetry capsules contained radiometric

Table 2.6.1

Status of Reactor Experiments

	Facility/Experiment	Status/Comments
ORR	- MFE1	Completed 12/79
	- MFE2	Completed 06/81
	- MFE4A	Completed 12/81
	- MFE4B, C	Samples Expected 06/82
	- TBC07	Completed 07/80
	- TRIO - Test	Analysis in Progress
HFIR	- CTR32	Completed 04/82
	- CTR30, 31, 34, 35	Irradiations in Progress
	- T1, T2, T3	Irradiations in Progress
	- RB1, RB2, RB3	Irradiations in Progress
	- CTR39, 40, 41, 42, 43	Planning in Progress
Omega West	- Spectral Analysis	Completed 10/80
	- HEDL 1	Completed 05/81
EBR II	- X287	Completed 09/81
IPNS	- LASL 1 (Hurley)	Irradiation 02/82

monitors (Ni, Cu, 0.1% Co-Al, 80%Mn-Cu, Nb, Ti, and Fe). The other six capsules contained helium accumulation monitors supplied by Rockwell International (Fe, Ni, Cu, Nb, Ti). All of the samples were gamma counted at ANL. The helium monitors as well as some of the radiometric samples were then sent to Rockwell for helium analysis.

The radiometric dosimetry results are given in Table 2.6.2. Burnup corrections were applied to all of the reactions, although most corrections were <10 percent. The $^{50}Co(n,\gamma)$ and $^{58}Fe(n,\gamma)$ reactions require significant corrections, 20-30% for cobalt and 10-20% for iron. In the iron case, the largest correction is due to double capture in ^{57}Fe. A self-consistency test insures that these burnup corrections are quite accurate (~2%). This is also confirmed by the excellent agreement between the various thermal neutron reactions. The corrections to ^{54}Mn from the $^{54}Fe(n,p)$ and $^{55}Mn(n,2n)$ reactions are uncertain since the ^{54}Mn thermal cross section is not known (<10 barns). If we assume an average cross section of 5 barns, then the ^{54}Mn corrections have an uncertainty of ±4%. All other corrected activities are accurate to ±2%.

The STAYSL computer code was used to determine flux and spectral values. The activation rates in Table 2.6.2 were used to adjust a HFIR spectrum calculated by Kam and Swanks.[1] Excellent agreement was found between this spectrum and our dosimetry results (Table 2.6.2). The final adjusted spectrum is shown in Figure 2.6.1. Fluence values are listed in Table 2.6.3. Vertical fluence, gradients were also determined from the data in Table 2.6.2 and these gradients are shown in Figure 2.6.2.

Displacement damage rates were computed using the adjusted spectra and our revised displacement damage cross sections which

Table 2.6.2

Activation Rates for HFIR-CTR32

	$\sigma\phi$(atom/atom-s) (100 MW)					
Height, cm	$^{59}Co(n,\gamma)$ (x 10^{-8})	$^{58}Fe(n,\gamma)$ (x 10^{-9})	$^{54}Fe(n,p)$ (x 10^{-11})	$^{46}Ti(n,p)$ (x 10^{-12})	$^{55}Mn(n,2n)$ (x 10^{-13})	$^{63}Cu(n,\alpha)$ (x 10^{-13})
20.8	4.18	1.27	4.13	--	1.23	3.11
16.7	--	1.37	5.22	--	--	--
12.5	5.56	1.70	6.44	9.43	1.94	4.42
4.2	7.21	2.17	6.99	10.46	2.13	4.84
0.0	--	--	--	10.34	--	--
-4.2	7.28	2.19	6.86	10.23	2.10	4.83
-8.3	--	1.87	6.77	--	--	--
-12.5	5.76	1.75	6.08	8.89	1.83	5.11
-16.7	--	--	--	7.28	--	--
-20.8	4.22	1.21	3.86	5.66	1.23	2.88

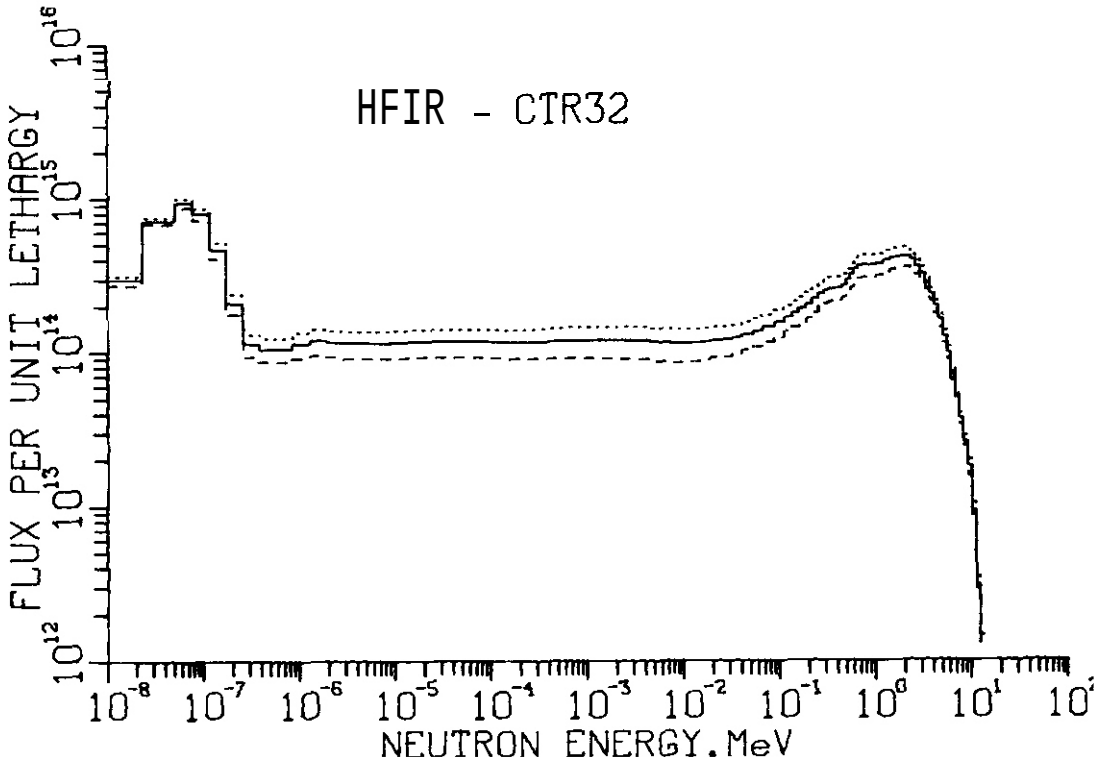

Fig. 2.6.1. Measured neutron spectrum for the HFIR-CTR32 experiment at midplane of the PTP. The dotted and dashed lines show the standard deviations to group fluxes; however, correlations are very strong.

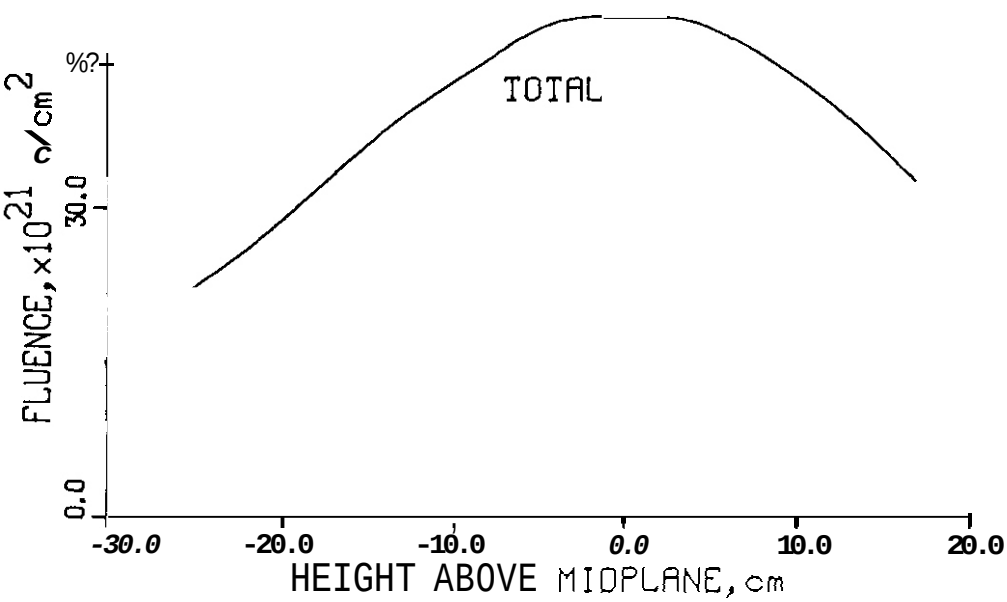

Fig. 2.6.2. Fluence gradients measured during the HFIR-CTR32 irradiation.

Table 2.6.3

Neutron Fluences for HFIR-CTR32

Height, cm	Fluence, x 10^{21} n/cm^2		
	Total (±5%)	Thermal[a] (±5%)	>0.1 MeV (±8%)
-25.0	22.2	9.5	5.7
-20.8	27.5	11.8	7.1
-16.7	33.6	14.0	8.9
-12.5	39.4	16.2	10.6
-8.3	44.1	17.8	12.1
-4.2	48.0	20.5	12.5
0.0	48.7	21.0	12.6
4.2	48.0	20.3	12.6
8.3	44.4	18.7	11.8
12.5	39.4	15.6	10.9
16.7	32.7	12.9	9.1
20.8	28.1	11.8	7.4

[a]Thermal neutrons below 0.5 eV. Multiply values times 0.8862 for equivalent 2200 m/s fluence.

were recently put into the NMFE Computer at Lawrence Livermore Laboratory. The spectral-averaged displacement and helium generation rates are listed in Table 2.6.4. The experimental helium values will be measured by Rockwell International.

The nickel two-step, thermal production of helium was computed assuming the formulation for HFIR of T. Gabriel (ORNL/TM-6361, 1979). The correctness of this procedure is currently being reexamined and the calculations may change slightly. However, experimental values will also be provided by Rockwell.

The thermal neutron capture reaction in nickel also leads to a substantial increase in displacement damage, a point which has been neglected in previous calculations. The Q-value for the $^{59}Ni(n,\alpha)^{56}Fe$ reaction is 5.097 MeV. Hence, thermal neutrons produce a 340 keV ^{56}Fe recoil and a 4757 keV alpha. Using the Lindhard energy partition model and a cut-off of 40 eV, one find that <u>each thermal capture produces 1763 displacements</u> (1701 from ^{56}Fe and 62 from the alpha). If we compute the helium production in nickel, then we can easily determine this extra number of displacements, as follows:

$$\text{DPA}\ (n,\alpha) = \frac{\text{He (appm in Ni)}}{567} \qquad (1)$$

This equation holds for all thermal irradiations and can be used to correct all previous experiments (e.g., in ORR). In the present case at midplane, the usual calculations for Ni gives 9.71 DPA and 41 appm He. Double thermal neutron capture produces 2897 appm He and an additional 5.11 DPA. <u>Hence, neglecting this effect would cause us to underpredict the nickel DPA value by 53%!</u> In 316 SS the effect increases

Table 2.6.4

Damage Parameters for HFIR-CTR32
He in appm, DPA = displacements per atom, (n,γ) included
Values accurate to ±10%

Height, cm:	20.8		12.5		4.2	
Element	DPA	He	DPA	He	DPA	He
Al	9.59	4.67	14.26	6.73	16.21	7.45
Ti	6.03	3.09	9.16	4.67	10.39	5.16
V	6.78	0.15	10.12	0.22	11.49	0.25
Cr	6.01	1.07	8.99	1.57	10.18	1.73
Mn[a]	6.62	0.89	9.81	1.29	11.21	1.43
Fe	5.32	1.82	7.97	2.64	9.01	2.92
Co[a]	6.73	0.93	9.82	1.35	11.43	1.49
Ni[b]	7.80	1196.	11.85	1922.	14.82	2938.
Cu	5.18	1.65	7.73	2.39	8.77	2.64
Nb	5.13	0.35	7.65	0.51	8.66	0.56
316 SS[c]	5.70	121.	8.55	194.	9.82	296.

[a](n,γ) effect is 8.4% for Mn and 27.6% for cobalt; however, corrections for neutron self-shielding effects may be required!

[b]Nickel includes thermal neutron capture helium and DPA effect (see text)

[c]316 SS: Cr(16), Mn(2), Fe(70), Ni(10), Mo(2)

the net DPA value by 4%. In longer irradiations, this effect will be even more important, especially if one is trying to tailor He/DPA ratios to fusion values!

It should also be noted that the DPA rates in Table 2.6.4 include (n,γ) effects, but not beta-decay. This omission will be corrected in our files and new values will be calculated. In any case, great caution must be used with the (n,γ) contributions due to neutron self-shielding effects, especially for Mn and Co.

2.6.4.2 Dosimetry for the EBRII-X287 Irradiation

The EBRII-X287 experiment was irradiated in Row 7 from Jaunary 1977 to November 1978 for a total exposure of 30,496 MWD. Most of the exposure was in position 7A4 during runs 87A-95H (24,000 MWD). The experiment was then moved to position 7E3 for runs 96A-97G (5000 MWD). The average operating power was 62.5 MW.

Twelve dosimetry capsules were irradiated, three each in subassemblies B, C, D, and F. Ten reaction were measured from each dosimetry capsule which contained Fe, Ni, Co, Cu, Nb, Sc, Ti, ^{235}U, and ^{238}U. The activation results are reported in Table 2.6.5.

Burnup corrections were required for the $^{235}U(n,f)$ reaction. The corrections varied from 5-7% depending on the flux at each location. Corrections were also required for the ^{238}U and ^{237}Np fission reactions due to the production and subsequent fission of ^{239}Pu in the samples. In this case, it can be shown that the correction for each fission product has the form:

$$(\sigma\phi)_1 = (\sigma\phi)_0 \, (1 - k_i \, R_i) \qquad (2)$$

Table 2.6.5

ACTIVATION RATES FOR EBRII-X287 EXPERIMENT

Values normalized to 62.5 MW. Accurary ±2% except ^{238}U (±10%) and ^{237}Np (5%).

	σφ (atom/atom-s)					
	D (R = 30 cm)			B (R = 31.6 cm)		
Reaction Z, cm:	-17.1	-0.44	+16.2	-11.4	+5.1	+15.3
$^{59}Co(n,\gamma)^{60}Co$ (x 10^{-11})	18.22	4.87	6.80	--	5.39	--
$^{45}Sc(n,\gamma)^{46}Sc$ (x 10^{-11})	3.24	2.67	2.77	2.86	--	2.69
$^{54}Fe(n,p)^{54}Mn$ (x 10^{-11})	1.13	2.38	1.77	1.73	--	1.54
$^{58}Ni(n,p)^{58}Co$ (x 10^{-11})	1.48	3.26	2.33	2.49	--	--
$^{60}Ni(n,p)^{60}Co$ (x 10^{-13})	2.65	5.90	4.19	4.43	--	--
$^{46}Ti(n,p)^{46}Sc$ (x 10^{-12})	1.33	2.88	2.24	2.16	--	1.73
$^{63}Cu(n,\alpha)^{60}Co$ (x 10^{-14})	6.81	14.42	9.83	10.15	--	10.66
$^{235}U(n,f)$ (x 10^{-9})	2.65	2.46	2.14	2.35	2.41	2.15
$^{238}U(n,f)$ (x 10^{-11})	6.96	11.52	8.38	8.72	10.23	7.42
$^{237}Np(n,f)$ (x 10^{-10})	5.68	8.58	6.38	7.07	7.60	5.45
	F (R = 33.6 cm)			C (R = 34.0 cm)		
Z, cm:	-17.1	-0.44	+16.2	-11.4	+5.1	+15.3
$^{59}Co(n,\gamma)^{60}Co$ (x 10^{-11})	21.22	7.38	10.68	--	--	11.08
$^{45}Sc(n,\gamma)^{46}Sc$ (x 10^{-11})	3.33	2.80	2.91	2.98	2.95	2.84
$^{54}Fe(n,p)^{54}Mn$ (x 10^{-11})	0.88	1.92	1.23	1.39	1.47	1.14
$^{58}Ni(n,p)^{58}Co$ (x 10^{-11})	1.30	2.90	1.96	1.89	2.22	1.75
$^{60}Ni(n,p)^{60}Co$(x 10^{-13})	2.03	4.38	3.10	3.01	3.58	3.45
$^{46}Ti(n,p)^{46}Sc$ (x 10^{-12})	1.14	2.58	1.67	1.63	1.75	1.39
$^{63}Cu(n,\alpha)^{60}Co$ (x 10^{-14})	5.11	10.54	7.48	7.30	7.52	6.60
$^{235}U(n,f)$ (x 10^{-9})	2.62	2.42	1.93	2.48	2.43	2.23
$^{238}U(n,f)$ (x 10^{-11})	6.16	9.47	6.36	7.25	--	6.32
$^{237}Np(n,f)$ (x 10^{-10})	4.72	7.68	5.05	6.09	6.15	4.83

where $(\sigma\phi)_0$ is the uncorrected activation rate, $(\sigma\phi)_1$ is the true reaction rate, R_i is the ratio of fission yields for product i from Pu divided by U, and k is a constant for any given location dependent on the production and fission rates for Pu. Fortunately, three fission products were measured for each reaction, namely ^{106}Ru, ^{137}Cs, and ^{144}Ce. A computer program was then written to vary the parameter k in equation (2) for each case until the three fission products gave values of $(\sigma\phi)_1$ with the smallest standard deviation. The corrections varied smoothly with the flux level and ranged from 0.71 to 0.79 for reactions varied smoothly with the flux level and ranged from 0.71 to 0.79 for $^{238}U(n,f)$ and from 0.85 to 0.97 for $^{237}Np(n,f)$. The absolute accuracy of the correctd activation rates is estimated to be ±10% for ^{238}U and ±5% for ^{237}Np. No other corrections were required for the remaining reactions.

The STAYSL computer code was used to adjust the calculated[2] neutron spectrum at each location. Reasonable fits were obtained using an input spectrum at a radius of 31.0 cm for capsules B and D and one of 33.7 cm for capsules C and F. In each case, these values are within 1 cm of the center of each capsule, Calculations were also available for positions within 1 cm of the vertical height (Z) of each capsule. In all cases, the measurements agreed rather well with the calculated spectra, especially considering the steep flux gradients across the assembly.

The final integral fluence values are listed in Table 2.6.6. A typical adjusted flux spectrum is shown in Figure 2.6.3. Fluence gradients are shown in Figure 2.6.4.

Table 2.6.6

NEUTRON FLUENCES FOR EBRII-X287

Fluence x 10^{22} n/cm^2. Percent errors are listed in parentheses.

	Total Fluence			
	D	B	F	C
Z, cm R, cm:	30.0	31.6	33.6	34.0
-17.1	5.47 (10)	--	5.00 (10)	--
-11.4	--	6.05 (15)	--	5.72 (10)
-0.4	6.73 (8)	--	6.16 (9)	--
+5.1	--	6.76 (15)	--	5.86 (9)
+15.3	--	5.02 (14)	--	4.68 (10)
+16.2	5.14 (9)	--	4.36 (9)	--
	Fluence >0.11 MeV			
-17.1	4.16 (14)	--	3.66 (15)	--
-11.4	--	4.95 (12)	--	4.50 (13)
-0.4	5.75 (11)	--	5.08 (12)	--
+5.1	--	5.1.3 (12)	--	4.69 (13)
+15.3	--	3.93 (13)	--	3.51 (14)
+16.2	4.04 (12)	--	3.25 (13)	--
	Fluence >1.0 MeV			
-17.1	0.82 (13)	--	0.69 (13)	--
-11.4	--	1.08 (12)	--	0.90 (12)
-0.4	1.38 (12)	--	1.15 (12)	--
+5.1	--	1.20 (12)	--	0.97 (13)
+15.3	--	0.86 (12)	--	0.72 (13)
+16.2	0.96 (12)	--	0.74 (12)	--

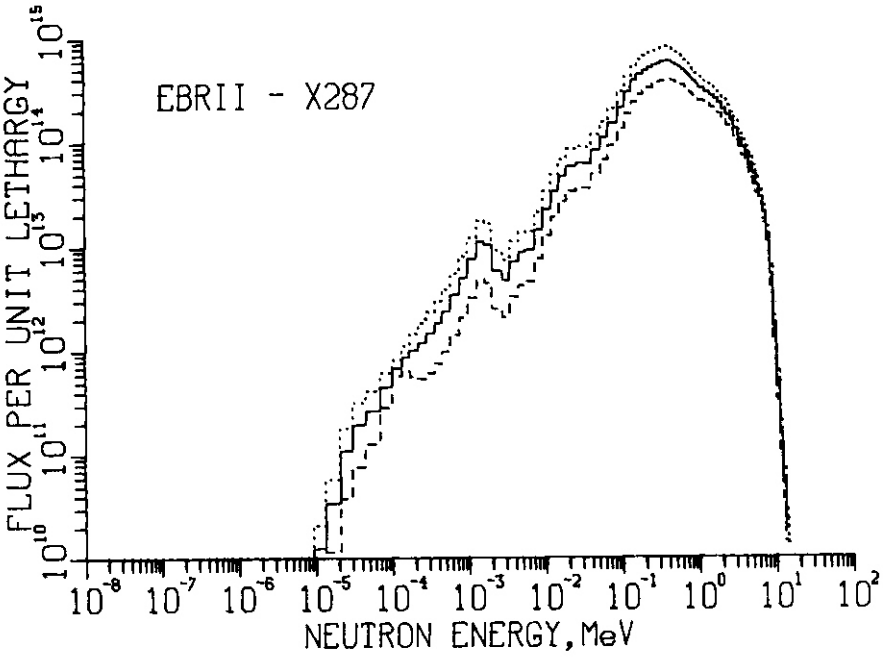
EBRII - X287
FLUX PER UNIT LETHARGY
NEUTRON ENERGY, MeV

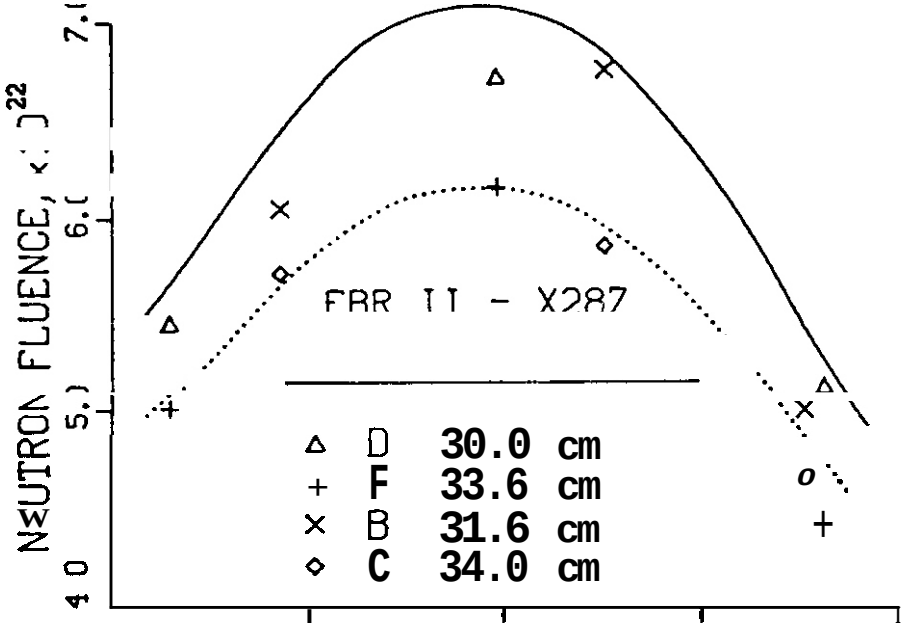
FBR II - X287
NEUTRON FLUENCE
D 30.0 cm
F 33.6 cm
B 31.6 cm
C 34.0 cm

Damage calculations were performed using our recently revised ENDF/B-V cross section file. DPA and helium production rates are given for each dosimetry capsule position in Tables 2.6.7 and 2.6.8. The DPA for 316 SS ranges from 15 to 27 with a corresponding helium production between 3 and 8 appm.

2.6.4.3 Dosimetry Results for the Omega West Reactor

Measurements have been completed for the HEDL-1 experiment (N. Panayotou) in the Omega West Reactor at Los Alamos Scientific Laboratory.

Samples were irradiated in the LLL-HEDL furnace in core position 4F from January 22, 1981 to February 10, 1981. The net exposure was 849.36 MWH with an up time of 106.25 hours at 8.0 MW.

Thin foils of Fe, Ni, Ti, Mn, and Co-A1 (wire) were included with the irradiated samples and at least four of each type of foil was gamma counted. Values were very consistent for each reaction measured indicating that gradients were less than 1% within the experimental capsule.

Seven reaction rates were determined, as listed in Table 2.6.9. These rates are compared to rates measured in October 1980, during a complete (30 reaction) spectral measurement (DOE/ER/0046/4, p. 15, 1981). As shown in Table 2.6.9, the fast reactions agree with the previous measurements within 5%; however, the two thermal reactions indicate about 10% more thermal flux in the present irradiation. This difference is most likely due to small changes in the fuel or reactor operating conditions.

Table 2.6.7

DAMAGE PARAMETERS FOR EBRII-X287

DPA (±10%); He in appm (±15%)

	Capsule D (R = 30.0 cm)					
Z:	-17.1 cm		-0.4 cm		+16.2 cm	
Element	DPA	He	DPA	He	DPA	He
Al	41.1	3.12	50.9	6.33	41.5	4.16
Ti	17.7	4.81	26.7	9.02	19.0	6.47
V	23.4	0.066	34.1	0.13	24.3	0.082
Cr	19.7	0.77	29.4	1.62	20.9	1.13
Mn	21.4	0.60	31.3	1.21	22.3	0.82
Fe	17.7	1.42	26.6	3.03	18.7	2.06
co	19.4	0.66	28.5	1.35	20.1	0.93
Ni	20.4	25.71	29.8	55.86	21.1	39.58
cu	18.3	1.20	27.0	2.49	19.1	1.64
Zr	22.0	0.12	32.2	0.26	22.6	0.17
Nb	20.0	0.29	29.6	0.61	20.7	0.42
Mo	14.7	--	21.1	--	15.1	--
Ta	4.8	--	7.3	--	5.1	--
316 SS	18.3	3.70	27.4	7.99	19.3	5.60

	Capsule B (R = 31.6 cm)					
Z:	-11.4 cm		+5.1 cm		+15.3 cm	
Al	49.8	4.66	53.2	4.53	39.5	4.67
Ti	22.0	6.90	24.7	7.44	17.8	5.77
V	28.6	0.097	31.0	0.095	22.9	0.095
Cr	24.5	1.21	26.5	1.22	19.6	1.15
Mn	26.2	0.91	28.5	0.88	21.0	0.90
Fe	22.0	2.18	23.7	2.16	17.6	2.16
co	23.8	1.03	25.8	1.01	19.0	1.00
Ni	24.9	40.83	26.9	41.91	20.0	37.65
cu	22.5	1.82	24.3	1.76	18.0	1.81
Zr	27.0	0.19	28.8	0.18	21.4	0.18
Nb	24.7	0.45	26.2	0.44	19.6	0.44
Mo	17.8	--	19.4	--	14.3	--
Ta	6.0	--	6.5	--	4.0	--
316 SS	22.7	5.82	24.5	5.92	18.2	5.48

Table 2.6.8

DAMAGE PARAMETERS FOR EBR II-X287

DPA (±10%); He in appm (±15%)

	Capsule F (R = 33.6 cm)					
Z:	-17.1 cm		-0.4 cm		+16.2 cm	
Element	DPA	He	DPA	He	DPA	He
Al	35.8	2.30	51.4	4.50	33.4	3.10
Ti	15.4	3.95	23.0	7.45	15.3	4.80
V	20.4	0.051	29.7	0.091	19.5	0.064
Cr	15.7	0.61	25.6	1.24	16.6	0.84
Mn	18.6	0.45	27.2	0.87	17.8	0.60
Fe	15.3	1.10	23.0	2.22	14.9	1.53
co	16.9	0.51	24.8	0.99	16.2	0.68
Ni	17.8	20.25	25.9	43.74	16.9	29.12
cu	15.9	0.90	23.5	1.79	15.2	1.22
Zr	19.1	0.10	28.0	0.19	18.1	0.13
Nb	17.4	0.22	25.7	0.46	16.5	0.32
Mo	12.a	--	18.5	--	12.1	--
Ta	4.2	--	6.3	--	4.1	--
316 SS	15.6	2.90	23.7	6.14	15.4	4.13

	Capule C (R = 34.0 cm)					
Z:	-11.4 cm		+5.1 cm		+15.3 cm	
Al	44.6	3.26	46.6	3.52	35.0	3.09
Ti	19.3	5.55	20.2	5.98	15.4	4.59
V	25.4	0.07	26.6	0.075	20.2	0.065
Cr	21.6	0.89	22.7	0.96	17.1	0.80
Mn	23.2	0.63	24.3	0.69	18.4	0.60
Fe	19.3	1.54	20.3	1.70	15.3	1.45
co	21.1	0.72	22.1	0.78	16.7	0.67
Ni	22.2	30.03	23.3	32.82	17.6	27.14
cu	20.0	1.26	20.9	1.41	15.8	1.22
Zr	24.0	0.13	25.1	0.15	18.8	0.13
Nb	21.9	0.32	23.0	0.35	17.2	0.30
Mo	15.9	--	16.6	--	12.6	--
Ta	5.3	--	5.5	--	4.2	--
316 SS	20.0	4.24	21.0	4.64	15.8	3.87

Table 2.6.9

ACTIVATION RATES FOR OMEGA WEST - HEDL1

(Irradiation from 1-22-81 to 2-10-81)
(Exposure = 849.36 MWH; Average Power (live) = 8.0 MW)

Reaction	$\sigma\phi$ (atomlatom-s) Position 6	Position 10	Spectral Run[a]	Ratio
$^{59}Co(n,\gamma)^{60}Co$	2.43-9	2.43-9	2.15-9	1.130
$^{58}Fe(n,\gamma)^{59}Fe$	6.88-11	6.75-11	6.29-11	1.083
$^{54}Fe(n,p)^{54}Mn$	2.91 -12	2.91-12	3.07-12	0.948
$^{58}Ni(n,p)^{58}Co$	3.73-12	3.73-12	3.78-12	0.987
$^{46}Ti(n,p)^{46}Sc$	3.94-13	3.94-13	3.99-13	0.987
$^{55}Mn(n,2n)^{54}Mn$	9.01 -15	9.06-15	8.66-15	1.043
$^{54}Fe(n,\alpha)^{51}Cr$	3.00-14	--	2.89-14	1.038

[a]L. R. Greenwood, DOE/ER-0046/4, Volume 1, p. 15 (1981).

Table 2.6.10

FLUX AND FLUENCE VALUES FOR OMEGA WEST - HEDL1

(Fluxes normalized to 8.0 MW)

Energy Range, MeV	Flux $(\times 10^{13})$	Fluence $(\times 10^{19})$	Error, %
Total	19.03	7.27	10
Thermal	8.06	3.08	15
>0.11	5.74	2.19	15
>1.0	2.82	1.08	16
>5.0	0.20	0.076	14
>10.0	0.0047	0.0018	21

The flux spectrum, shown in Figure 2.6.5, was determined using the STAYSL computer code and the seven reaction rates in Table 2.6.9. The input spectrum was taken from our previous spectral measurement. The integral fluxes and fluence values are listed in Table 2.6.10. Damage parameters were then computed using the SPECTER computer code with our recently calculated, ENDF/B-V displacement cross sections and recommended values are listed in Table 2.6.11. The (n,γ) reaction is also included in the damage calculations; however, this effect is generally les than 2%.

Helium calculations for nickel were performed using the total thermal flux (<.5 eV) and the equation recommended by T. Gabriel (ORNL/TM-6361, 1979). This procedure was found to work quite well in previous tests in ORR. It is important to note that for very short irradiations, this equation requires more exact parameters. More accurate values can actually be obtained at low fluence using the first order expansion:

$$He/M(^{58}Ni) = 1/2\ (\phi t)^2\ \sigma_\gamma \sigma_\alpha$$

where ϕt is the thermal fluence, $\sigma_\gamma \sigma_\alpha$ the (n,γ) and (n,α) cross sections for ^{58}Ni and ^{59}Ni, respectively. some helium measurements are now in progress for the OWR by D. Kneff and H. Farrar IV (Rockwell International) and more precise helium values will thus be reported later.

2.6.5 Future Work

The status of other experiments is summarized in Table 2.6.1. Many irradiations are in progress or planning in HFIR. Dosimeters are expected shortly for the second phase of the MFE4 experiment in ORR.

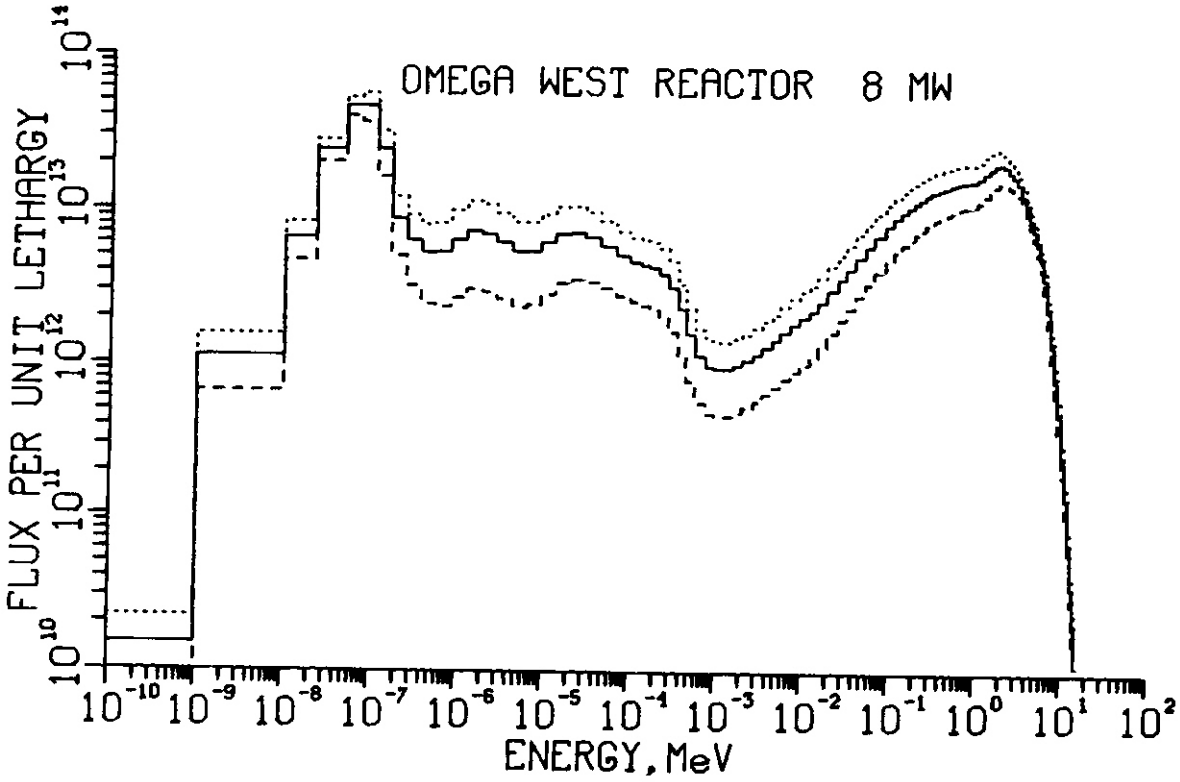

Fig. 2.6.5. **Neutron flux spectrum computed using the STAYSL computer code for the HEDL1 experiment in position 4-F of the Omega West Reactor. Seven reactions were used to adjust a previously measured spectrum. The dotted and dashed lines represent one standard deviation. The flux per unit lethargy is simply energy times flux.**

Table 2.6.11

SPECTRAL-AVERAGED DAMAGE PARAMETERS FOR OMEGA WEST - HEDL1

[Fluence = 7.3 x 10^{19} (2.2 x 10^{19} above 0.11 MeV)]
(Damage cross sections calculated using ENDF/B-V.)

Element	σ_D, keV-b	Damage Energy (eV/atom)	DPA	He (appb)
Al	26.0	1.9	0.028	9.5
Ti	22.7	1.6	0.016	8.5
V	25.8	1.8	0.019	0.31
Cr	23.3	1.7	0.017	2.5
Mn	23.9	1.7	0.017	1.9
Fe	20.8	1.5	0.015	4.1
co	20.9	1.5	0.015	2.0
Ni	21.7	1.6	0.016	66.0
			(0.047)[a]	(83.3)[a]
cu	20.0	1.5	0.015	3.5
Zr	22.3	1.6	0.016	0.38
Nb	20.5	1.5	0.015	0.83
Mo	22.2	1.6	0.01 1	--[b]
316 SS[c]	21.4	1.6	0.016	(11.6)[a]

[a]Thermal process included in parentheses; see equation *(1).*

helium cross section not known.

[c]Composition assumed to be Mn(2), Cr(16), Ni(109, Mo(2), Fe(70); minor elements neglected.

Dosimetry tests have been conducted for the tritium-breeding experiment (TRIO) in ORR.

2.6.6 References

1. F. B. K. Kam and J. H. Swanks, Neutron Flux Spectrum in the HFIR Target Region, ORNL-TM-3322 (1971).

2. F. C. Franklin, E. R. Ebersole, and R. R. Heinrich, "Analysis of EBRII Low-Power Dosimetry Run 78C," ANL-77-76 (1977).

2.6.7 Publications

1. Papers entitled "Neutron Flux and Spectral Measurements for Materials Studies" and "Displacement Damage Calculations with ENDF/B-V" were presented at the Advisory Group Meeting on Nuclear Data for Radiation Damage Assessment and Reactor Safety Aspects in Vienna, Austria, on October 12-16, 1981.

2. L. R. Greenwood, Neutron Flux and Spectral Measurements to Characterize Irradiation Facilities for Fusion Materials Studies, Proceedings of the Fourth ASTM-EURATOM Syposium on Reactor Dosimetry, March 22-26, 1982, National Bureau of Standards, Gaithersburg, MD.

3. L. R. Greenwood, Neutron Source Characterization for Fusion Materials Studies, Jour. Nucl. Mater. 104, 1433 (1982).

2.7 ELEVATED TEMPERATURE IRRADIATION OF FERRITIC STEEL CHARPY SPECIMENS: EXPERIMENTS HFIR-CTR-34 and -35 — J. M. Vitek (Oak Ridge National Laboratory)

2.7.1 ADIP Task

ADIP Task I.A.2, Define Test Matrices and Test Procedures.

2.7.2 Objective

This experiment is intended to evaluate the impact properties of ferritic steels after irradiation at elevated temperatures under conditions which simultaneously produce displacement damage and helium. The samples are nickel-doped 12 Cr-1 MoVW and 9 Cr-1 MoVNb alloys. The transmutation of nickel results in helium production and the influence of helium on the properties will be determined by comparing the properties of alloys with different nickel levels.

2.7.3 Summary

The HFIR-CTR-34 and -35 experiments contain miniature Charpy V-notch specimens of nickel-doped 12 Cr-1 MoVW and 9 Cr-1 MoVNb alloys. Different nickel contents result in different helium levels generated during irradiation in HFIR, to allow for an assessment of the effect of helium on impact properties. Irradiations at 300 and 400°C, to a midplane damage level of 10 dpa, have been completed.

2.7.4 Progress and Status

2.7.4.1 Introduction

By taking advantage of the two-step transmutation reaction of nickel, which results in helium production, increasing levels of helium can be generated during irradiation by increasing the initial nickel content of the alloy. Nickel-doped ferritic alloys[1] with 0.5, 1, and 2% Ni are being studied in order to ascertain the effect of helium at levels expected in fusion reactor service on various material properties. These experiments will provide the first impact property data on the Path E ferritic steels under irradiation conditions that generate both helium and

displacement damage. In addition, they will provide the first moderate-fluence (~6 dpa) data at an irradiation temperature of 300°C. Comparison with results on companion samples irradiated in the EBR-II AD-2 experiment will provide a further means of evaluating the effect of helium on impact properties.

2.7.4.2 Experiment Design

Miniature Charpy V-notch specimens have been used for evaluation of impact properties. The samples are 5 by 5 mm in cross section, and 25.4 mm in length. The notch has a root radius of 0.05 to 0.10 mm and the remaining sample ligament Is 4.24 mm in length. The samples were not precracked. The specimens were cut from 5.3-mm-thick plate with the length parallel to the rolling direction and the notch running through the thickness of the plate.

The specimens are enclosed in stainless steel holders and those holders are inside aluminum sleeves. The outer diameters of the steel specimen holders are adjusted to compensate for the variation in nuclear heating rate along the length of the capsule in order to achieve the desired temperature. Nuclear heating of the specimens and stainless steel holders provides enough heat to raise the sample temperatures to the desired values. A thermal gradient exists from the interior to exterior surface of the specimens, but this has been calculated to be less than 45°C. A schematic drawing of a specimen within a capsule assembly is shown in Fig. 2.7.1.

Two types of temperature monitors have been used. A pure zinc melt wire (melting point 420°C) was inserted into one of the 9 Cr-1 MoVNb-2 Ni samples to be irradiated at 400°C. In addition, SiC temperature monitors were inserted into both capsules in both the 300 and 400°C temperature levels. Three flux monitors were also loaded into each test capsule.

2.7.4.3 Test Matrix and Irradiation Conditions

The miniature Charpy samples were made from four different alloys: two variations of 12 Cr-1 MoVW and two variations of 9 Cr-1 MoVNb. The alloys have been doped with 0 and 2% Ni in order to achieve different

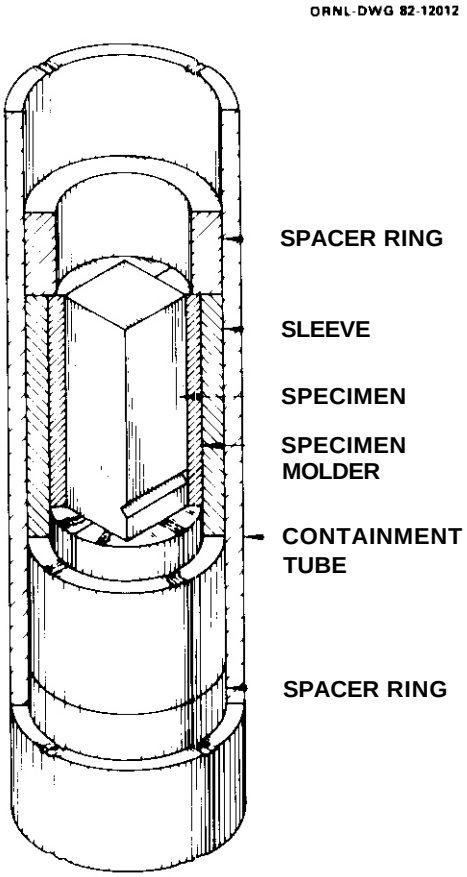

Fig. 2.7.1. Schematic Diagram Illustrating Miniature Charpy V-Notch Specimen within Irradiation Capsule.

helium levels during irradiation. Alloy chemistries have been reported previously.[1] The alloys are in the normalized and tempered condition. Table 2.7.1 lists the alloys and their heat treatments.

The HFIR-CTR-34 capsule contained the 12 Cr-1 MoVW series, whereas the 9 Cr-1 MoVNb alloys were in capsule HFIR-CTR-35. Each capsule contained 16 miniature Charpy V-notch specimens, 8 at 300°C and 8 at 400°C. The matrix for the two capsules is given in Table 2.7.2.

The capsules were irradiated in the HFIR peripheral target positions. Irradiation was for five cycles, yielding a displacement damage level at the experimental midplane of approximately 10 dpa, and approximately 6 dpa at the capsule ends. Calculated helium levels at the midplane are about 10 to 20 at. ppm He in the base alloys and about 85 at. ppm He in the 2% Ni-doped alloys. Irradiation was started in December 1981 and completed in April 1982.

Table 2.7.1. Alloys Irradiated in HFIR-CTR-34 and -35

Alloy	Heat[a]	Normalizing		Tempering	
		(°C)	(h)	(°C)	(h)
12 Cr-1 MoVW	XAA-3587	1050	0.5	780	2.5
12 Cr-1 MoVW-2 Ni	XAA-3589	1050	0.5	700	5
9 Cr-1 MoVNb	XA-3590	1040	0.5	760	1
9 Cr-1 MoVNb-2 Ni	XA-3591	1040	0.5	700	5

[a]Vendor: Combustion Engineering.

Table 2.7.2. Irradiation Matrix for Miniature Charpy V-Notch Specimens in HFIR-CTR-34 and -35

Position	Temperature (°C)	Heat	
		HFIR-CTR-34	HFIR-CTR-35
1	300	XAA-3587	XA-3590
2	300	XAA-3587	XA-3590
3	300	XAA-3587	XA-3590
4	300	XAA-3587	XA-3590
5	400	XAA-3589	XA-3591
6	400	XAA-3589	XA-3591
7	400	XAA-3589	XA-3591
8	400	XAA-3589	XA-3591
9	400	XAA-3587	XA-3590
10	400	XAA-3587	XA-3590
11	400	XAA-3587	XA-3590
12	400	XAA-3589	XA-3591
13	300	XAA-3587	XA-3590
14	300	XAA-3589	XA-3591
15	300	XAA-3589	XA-3591
16	300	XAA-3589	XA-3591

2.7.5 Reference

1. R. L. Klueh and J. M. Vitek, "Characterization of Ferritic Steels for HFIR Irradiation," *ADIP Quart. Prog. Rep.* June 30, 1980, DOE/ER-0045/3, pp. 294–308.

2.8 ELEVATED-TEMPERATURE IRRADIATION OF FERRITIC STEEL TENSILE SPECIMENS: EXPERIMENTS HFIR-CTR-39, -40, and -41 — J. M. Vitek (Oak Ridge National Laboratory)

2.8.1 ADIP Task

ADIP Task I.A.2, Define Test Matrices and Test Procedures.

2.8.2 Objective

This experiment is intended to evaluate the tensile properties of ferritic steels after elevated temperature irradiation in the High Flux Isotope Reactor (HFIR). Irradiation in HFIR of the nickel-doped 9 Cr-1 MoVNb and 12 Cr-1 MoVW alloys will result in simultaneous displacement damage and helium production. The transmutation reaction of nickel leads to helium production, and different nickel levels will allow for an assessment of the effect of helium on tensile properties. A 2 1/4 Cr-1 Mo alloy will also be irradiated.

2.8.3 Summary

The HFIR-CTR-39, -40, and -41 experiments contain rod tensile specimens of the nickel-doped 9 Cr-1 MoVNb and 12 Cr-1 MoVW alloys and the 2 1/4 Cr-1 Mo alloy. Different nickel levels result in different helium levels generated during irradiation. Testing of these alloys will provide data on the effect of helium on tensile properties. Irradiations will be at 300, 400, and 500°C to a midplane fluence equivalent to 12 dpa.

2.8.4 Progress and Status

2.8.4.1 Introduction

As in other HFIR experiments on Path E ferritic steels,[1-3] the two-step transmutation reaction of nickel will be used to produce various levels of helium by adjusting the nickel content of the alloys being irradiated. Nickel-doped ferritic alloys[4] with 0.5, 1, and 2% Ni are being studied in order to ascertain the effect of helium, at levels expected in fusion reactor service, on various material properties. The HFIR-CTR-39, -40, and -41 experiments will be the first experiments to

provide such data on tensile properties after elevated-temperature irradiations. In addition, by comparison with identical alloys in the same heat treated condition presently being irradiated at similar temperatures in EBR-II AD-2, further insight into the effect of helium will be possible.

2.8.4.2 Experimental Design

Each of the three experiments will consist of a column of 11 rod tensile samples. The rod tensile specimen configuration is shown in Fig. 2.8.1. The capsule design used is essentially the same as that used successfully for irradiation of type 316 stainless steel.[5] Samples are held in place by centering spurs. Nuclear heating is used to heat the samples, and a gas gap around the sample gage length and shoulder provide the gradient to achieve the elevated temperatures required. The gas gaps

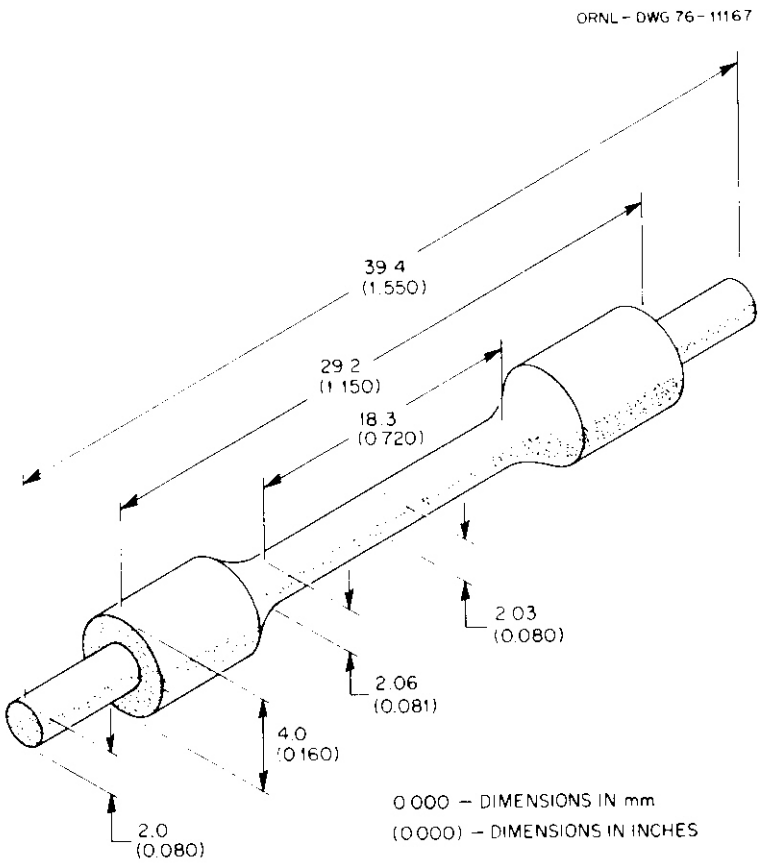

Fig. 2.8.1. Rod Tensile Specimens to be Used for Irradiation in Experiments HFIR-CTR-39, *-40*, and *-41*.

are adjusted for different desired temperatures and different nuclear heating rates along the length of the assembly. The actual gas gap dimensions have been calculated from the most recent data available on the heating rates for these steels in the HFIR-PTP facility.

Silicon carbide temperature monitors will be used to check each of the three irradiation temperatures. The SiC monitors will be inserted into holes drilled in the shoulders of the rod tensile samples. Tests on cold samples have shown that such holes in the shoulder section do not affect the tensile property measurements. Two dosimetry monitors will also be included in each capsule.

2.8.4.3 Test Matrix and Irradiation Conditions

Six different alloys are included in this experiment: three variations of 12 Cr-1 MoVW with 0.5, 1, and 2% Ni, two variations of 9 Cr-1 MoVNb with 0.1 and 2% Ni, and 2 1/4 Cr-1 Mo. Alloy compositions are given in Table 2.8.1. The alloys will be irradiated in the normalized and tempered condition. Table 2.8.2 lists the heat treatments used for each alloy. Eleven tensile specimens will be included in each capsule. The irradiation temperature matrix is given in Table 2.8.3.

Table 2.8.1. Composition of Alloys Included in the HFIR-CTR-39 -40, and -41 Experiments (wt %)

Heat	XAA 3587	XAA 3588	XAA 3589	XA 3590	XA 3591	72768
Cr	11.97	11.92	11.73	8.64	8.54	2.2
Mo	0.94	1.05	1.00	0.97	0.97	0.89
C	0.21	0.20	0.21	0.091	0.070	
N	0.021	0.017	0.018	0.050	0.054	
Ni	0.43	1.13	2.27	0.10	2.18	0.07
Mn	0.51	0.47	0.48	0.35	0.35	0.48
W	0.55	0.53	0.54	0.01	<0.01	
V	0.27	0.31	0.31	0.21	0.22	0.002
Nb	0.024	0.020	0.016	0.064	0.068	
Si	0.18	0.14	0.14	0.07	0.08	0.31
Fe	Bal	Bal	Bal	Bal	Bal	Bal

Table 2.8.2. Alloys, Heat Numbers, and Heat Treatments Used for Samples in Experiments HFIR-CTR-39, -40, and -41

Alloy	Heat	Normalizing		Tempering	
		(°C)	(h)	(°C)	(h)
12 Cr-1 MoVW	XAA 3587	1050	0.5	780	2.5
12 Cr-1 MoVW-1 Ni	XAA 3588	1050	0.5	780	2.5
12 Cr-1 MoVW-2 Ni	XAA 3589	1050	0.5	700	8
9 Cr-1 MoVNb	XA 3590	1040	0.5	760	1.0
9 Cr-1 MoVNb-2 Ni	XA 3591	1040	0.5	700	8
2 1/4 Cr-1 Mo	72768	900	0.5	700	1

Table 2.8.3. Matrix of Irradiation Temperatures for Tensile Specimens in Experiments HFIR-CTR-39, -40, and -41

Position	Temperature (°C)	HFIR-CTR-39	HFIR-CTR-40	HFIR-CTR-41
1 (top)	300	XAA 3587	XAA 3589	XA 3590
2	300	XAA 3587	XAA 3589	XA 3590
3	400	XAA 3587	XAA 3589	XA 3590
4	400	XAA 3587	XAA 3589	XA 3590
5	500	XAA 3587	XAA 3589	XA 3590
6	500	XAA 3587	XAA 3589	XA 3590
7	500	72768	XA 3591	XA 3591
8	400	XAA 3588	72768	XA 3591
9	400	XAA 3588	72768	XA 3591
10	300	XAA 3588	72768	XA 3591
11	300	XAA 3588	72768	XA 3591

Irradiation will be in the HFIR peripheral target positions planned for six cycles, resulting in a displacement damage level of approximately 12 dpa at the midplane and 7 dpa at the capsule extremities. Expected helium levels at the midplane for the base alloys are about 15 to 25 at. ppm He, while the expected helium levels for the 1 and 2% nickel-doped alloys at the midplane are about 50 and 90 at. ppm He, respectively. Insertion into HFIR is scheduled for May 1982, and completion is expected by October 1982.

2.8.5 References

1. J. M. Vitek, R. L. Klueh, M. L. Grossbeck, and J. W. Woods, "HFIR-MFE-T1, -T2, and -RB1: Experiments to Evaluate the Effects of Low-Temperature Irradiation on Ferritic Steels," *ADIP Quart. Prog. Rep. Sept. 30, 1980*, DOE/ER-0045/4, pp. 26–35.
2. J. M. Vitek and J. W. Woods, "Experiment HFIR-MFE-T3 for Low Temperature Irradiation of Miniaturized Charpy V-Notch Specimens of Nickel-Doped Ferritic Steels," *ADIP Quart. Prog. Rep. Sept. 30, 1981*, DOE/ER-0045/7, pp. 36–39.
3. J. M. Vitek and J. W. Woods, "'Experiments HFIR-MFE-RN1, -RB2, and -RB3 for Low-Temperature Irradiation of Path E Ferritic Steels," *ADIP Quart. Prog. Rep. Sept. 30, 1981*, DOE/ER-0045/8, pp. 3C–35.
4. R. L. Klueh and J. M. Vitek, "Characterization of Ferritic Steels for HFIR Irradiation," *ADIP Quart. Prog. Rep. June 30, 1980*, DOE/ER-0045/3, pp. 294–308.
5. M. L. Grossbeck and P. J. Mazlasz, "Tensile Properties of HFIR-Irradiated Types 316 and TiM 316 Stainless Steel at 200 to 1000 at. ppm He," *ADIP Quart. Prog. Rep. Sept. 30, 1978*, DOE/ET-0058/3, pp. 34–51.

3. PATH A ALLOY DEVELOPMGNT — AUSTENITIC STAINLESS STEELS

3.1 SWELLING OF PATH A PCA IRRADIATED TO 10 dpa IN HFIR — P. J. Maziasz and D. N. Braski (Oak Ridge National Laboratory)

3.1.1 ADIP Task

ADIP Tasks I.C.1, Microstructural Stability, and I.C.2, Microstructure and Swelling in Austenitic Alloys.

3.1.2 Objectives

The objective of this work is to evaluate the effect of preirradiation microstructural variation on swelling of Path A PCA irradiated in HFIR. These results will also be compared with results on type 316 and 316 + Ti stainless steels irradiated under similar conditions.

3.1.3 Summary

The Path A PCA with various pretreatments and 20%-cold-worked type 316 stainless steel (CW 316) were irradiated in HFIR at 300 to 600°C to fluences producing up to 9.7 dpa and 620 at. ppm He. Very little swelling was observed at 500°C and below, but swelling at 600°C ranged from 0.2 to 1.2%. Swelling appears coupled to precipitate phase and dislocation microstructural development.

3.1.4 Progress and Status

Previous experiments in HFIR defined the swelling and microstructural development of CW 316 (DO heat) at fluences producing up to 60 dpa and 4000 at. ppm He and of CW 316 + Ti (R1 heat) at up to 16 dpa and 1000 at. ppm He over the irradiation temperature range 55 to about 750°C.[1-8] This report deals with experiment HFIR–CTR–32, intended to survey microstructural development in Path A PCA and two heats of CW 316 (N lot and Heat X15893) during irradiation at 300 to 600°C to neutron fluences producing up to 10 dpa and 500 at. ppm He (ref. 9). Examination of melt–wire capsules has shown much better agreement between these calculated design temperatures and the actual irradiation temperatures than had been obtained in previous experiments.[7] The dpa for these materials range from 8.7 to 9.7 dpa (ref. 10) and the helium content from 440 to 520 at. ppm He in type 316 and 530 to 620 at. ppm He in PCA (ref. 11).

Helium production is about 20% higher in the PCA than in type 316 stainless steel because of the higher nickel content. Compositions of the steels mentioned above (except heat X15893) are given in Table 3.1.1.

The preirradiation microstructures of PCA and thermal mechanical treatments used to produce them are described in Table 3.1.2. These microstructures have been characterized in earlier reports.[12-15] Of the seven microstructures, AI, A2, B1, B2, and C were investigated in this experiment. Microstructure A3 is included in the higher fluence experiments, HFIR-CTR-30 and -31 (ref. 9), and will be examined later.

Disks for transmission electron microscopy (TEM) were thinned with an automatic dual jet Tenupol thinning unit in a hot cell and examined via standard methods in JEM IOOC and IOOCX electron microscopes.

Table 3.1.1. Composition of Austenitic Stainless Steels Included in the HFIR-CTR-32 Irradiation Experiment

Alloy	Alloy Composition (wt %)										
	Fe	Cr	Ni	Mo	Mn	Si	C	Ti	P	S	N
PCA	Bal	14.0	16.2	2.3	1.8	0.4	0.05	0.24	0.01	0.003	0.01
CW 316 + Ti (R1 heat)	Bal	17.0	12.0	2.5	0.5	0.4	0.06	0.23	0.01	0.013	0.006
CW 316 (DO heat)	Bal	18.0	13.0	2.6	19	0.8	0.05	0.05	0.01	0.016	0.05
CW 316 (N lot)	Bal	16.5	13.5	2.5	1.6	0.5	0.05		0.01	0.006	0.006

3.1.5 Results and Discussion

The results of quantitative TEM on the cavity volume fraction (cvf) swelling are given in Table 3.1.3 and plotted as a function of temperature in Fig. 3.1.1. Swelling curves taken from previously reported data[3] on CW 316 (DO heat) and CW 316 + Ti (R1 heat) are also included in Fig. 3.1.1 plotted at irradiation temperatures that have been corrected by +50 to +75°C from those reported previously.

Table 3.1.2. Preirradiation Microstructures of the Path A Prime Candidate Alloy (PCA)

Designation	Description of Microstructure	Thermal-Mechanical Treatment
A	Simple microstructures resulting from	
A1	solution annealing,	25% cold worked plus 15 min at 1175°C
A2	5 to 10% cold working, or	15 min at 1175°C (A1) plus 10% cold worked
A3	20 to 25% cold working.	15 min at 1175°C (A1) plus 25% cold worked
B	Microstructures with both coarse grain boundary MC precipitation and intragranular MC precipitation consisting of	
B1	coarse particles or particle clusters or	Solution annealed (A1) plus 8 h at 800°C plus 8 h at 900°C
B2	fine matrix precipitation.	Solution annealed (A1) plus 8 h at 800°C plus 25% cold worked plus 2 h at 750°C
C	Microstructures with both fine grain boundary MC precipitation and fine intragranular MC matrix precipitation.	Solution annealed (A1) plus 25% cold worked plus 2 h at 750°C
D	Microstructures with both fine grain boundary MC precipitation and fine intragranular MC matrix precipitation plus increased dislocation density.	Solution annealed (A1) plus 10% cold worked plus 2 h at 750°C plus 10% cold worked

Table 3.1.3. Swelling for Path A PCA Microstructural Variants and 20%-Cold-Worked Type 316 Stainless Steel (N lot) after HFIR Irradiation at Up to 9.7 dpa and 620 at. ppm He

Alloy	Condition	Cavity Volume Fraction Swelling (%) at Each Irradiation Temperature (°C)			
		300	400	500	600
PCA	A1	0	0	0.05	0.66
PCA	A2	0	0	0.36	1.08
PCA	C	0	0.25	0.32	0.70
PCA	B2	0	*a*	*a*	0.40
PCA	B1	0	*a*	*a*	1.20
316 (N lot)	20% cold worked	0	*a*	*a*	0.20

[a]Quantitative TEM in progress.

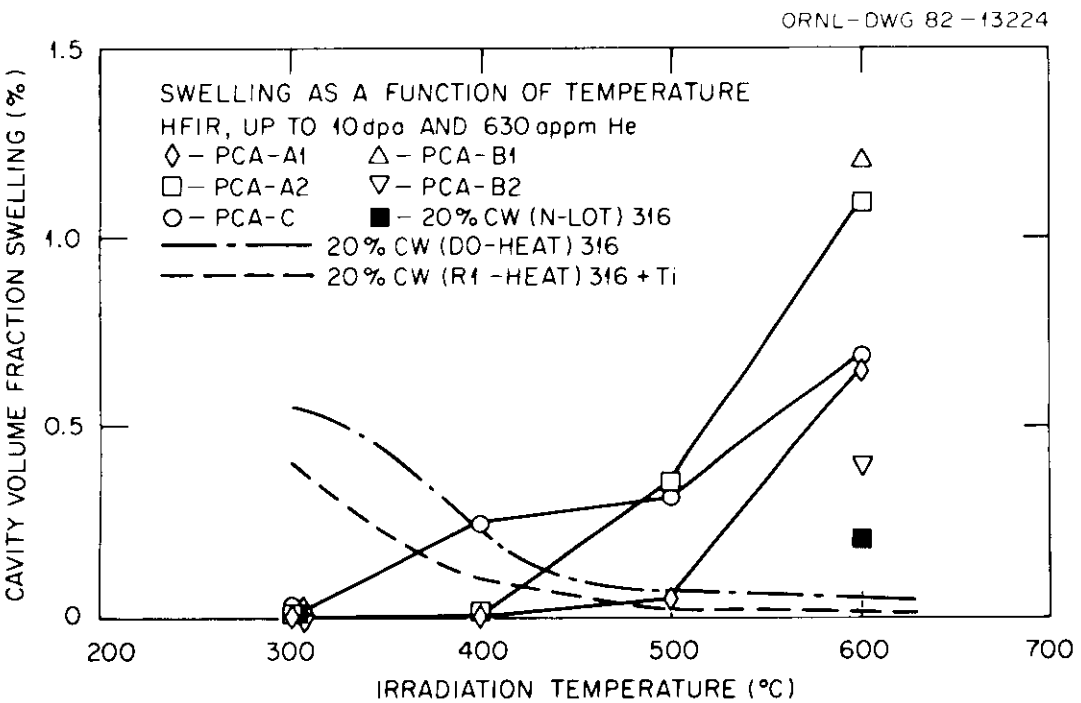

Fig. 3.1.1. Swelling as a Function of Temperature for Various Austenitic Stainless Steels Irradiated in HFIR at up to 10 dpa.

Figure 3.1.1 shows that all samples from HFIR-CTR-32 show temperature-dependent swelling, with the swelling increasing monotonically with increasing irradiation temperature. At 300°C, the various pretreatments of PCA and CW 316 (N lot) show no observable cavitation and hence no cvf swelling. Among the various PCA pretreatments, swelling of microstructure AI remains as low as or lower than the other samples at 500°C and below. At 600°C, the swelling after pretreatments A1 and c is about 0.7%, with microstructure B2 swelling less, about *0.4%.* At 600°C, pretreatments A2 and B1 of PCA show the greatest swelling at 1.1 to 1.2%.

Figure 3.1.2 compares the various pretreatment microstructures before and after irradiation at 600°C. Pretreatments A1 and A2 did not contain MC prior to irradiation. Pretreatments B1 and B2 contained coarse and fine intragranular MC, respectively, prior to irradiation (Table 3.1.2). It is not clear at present whether A1 and A2 contain fine MC after irradiation. The lowest swelling PCA at 600°C, B2, contains fine MC, but there are fewer particles after irradiation than prior to irradiation. The coarse MC present in B1 prior to irradiation **has** dissolved, coincident with B1 showing the maximum swelling. The size distribution of the cavity microstructure of B1 is plotted in Fig. 3.1.3. The sharp, narrow peak in the size distribution represents a high population of fine cavities and the broad tail as size increases represents a diminishing population of much larger cavities. If we discuss this size distribution in terms of the cavity classifications into voids and bubbles given in ref. 8 and typical critical radius bubble-to-void-conversion arguments,[16–18] then the small cavities are most likely bubbles and the very large cavities are most likely voids forming from bubbles that have exceeded their critical radius. Microstructure B2 shows the lowest swelling of the PCA conditions because only a small fraction of the cavities are voids and the cavities are smaller. In all samples, the large cavities identified as voids account for most (80–90%) of the cvf swelling.

If we compare the swelling of CW 316 (N lot) with the various PCA pretreatments (Fig. 3.1.1 and Table 3.1.3), we find that it is similar to pretreatment A1 at 300 to 500°C and is the lowest swelling material at 600°C. Microstructures for CW 316 (N lot) and PCA-A1 are compared in

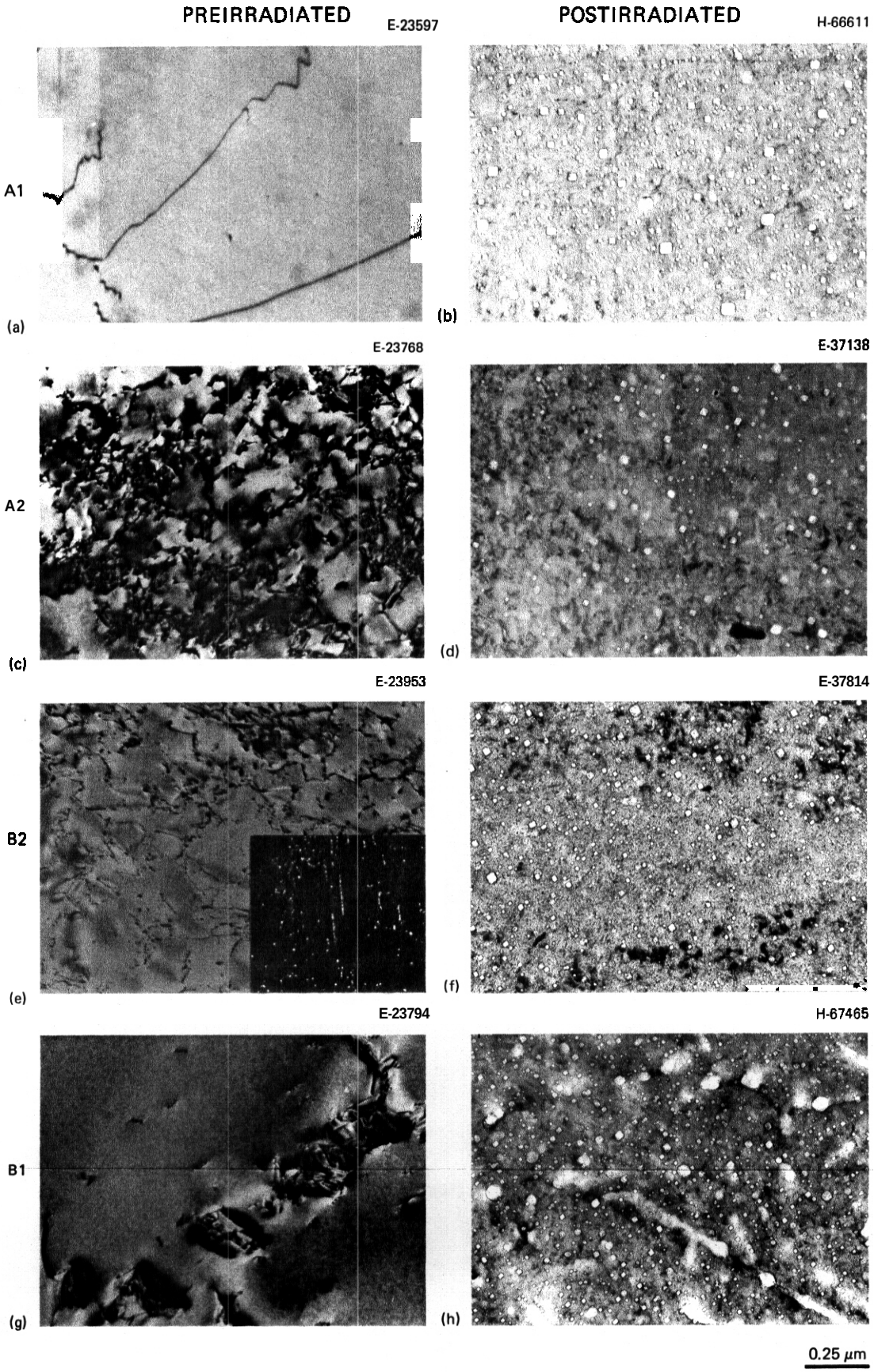

Fig. 3.1.2. A Comparison of Pre- (a,c,e,g) and Post- (b,d,f,h) Irradiation Microstructures for Path A PCA with Various Pretreatments Followed by HFIR Irradiation at 600°C to up to 10 dpa and 620 at. ppm He. Pretreatment designations are indicated. Inlay on (e) is a dark field image of MC precipitation.

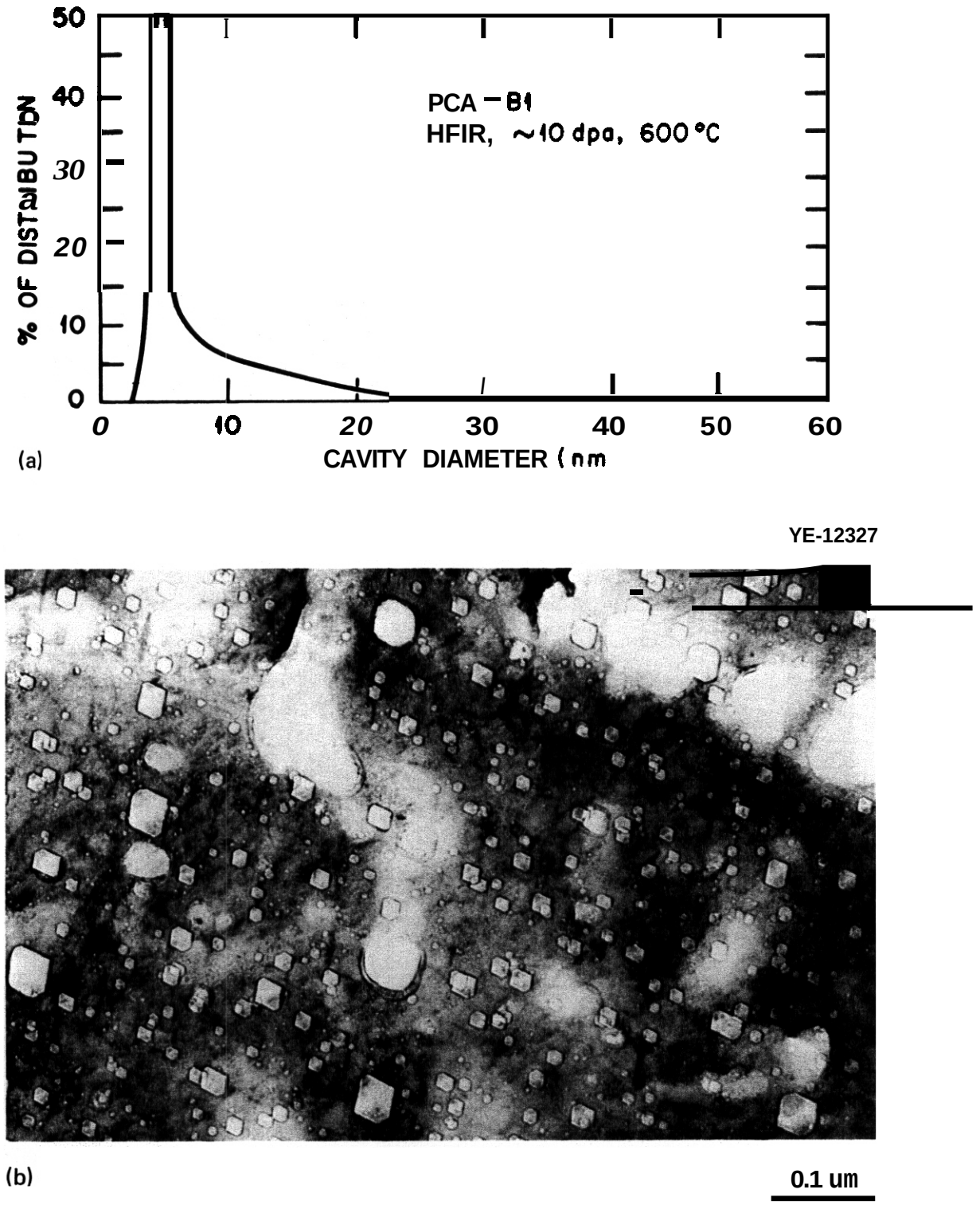

Fig. 3.13. A Plot of Cavity Size Distribution Together with the Microstructure of Path A PCA B1 after HFIR Irradiation at 600°C. The large cavities clearly appear to be voids converting from fine bubbles.

Fig. 3.1.4 for HFIR irradiation at 300 to 600°C to about 10 dpa. This series shows the same temperature dependence of the swelling as illustrated in Fig. 3.1.1. The size distributions of bubbles and voids for the CW 316 irradiated at 600°C are plotted in Fig. 3.1.5(a), together with micrographs representing each cavity component. Unlike the various PCA samples, swelling in the CW 316 (N lot) is very spatially heterogeneous. Fine bubbles are quite uniformly distributed in size and space in all regions, as seen in Fig. 3.1.5. However, swelling varies from about 0.05 to about 0.35% from region to region because of nonuniform conversion of some fraction of the fine bubbles into larger voids. The swelling of 0.2% given in Fig. 3.1.1 and Table 3.1.3 is an area-averaged value.

The present results can be compared with previous HFIR results on CW 316 (DO heat) and CW 316 + Ti (R1 heat) after similar irradiation conditions. The swelling of CW 316 (N lot) and the various pretreatments of PCA is less at 300°C and similar or greater at 400 *to* 600°C than the swelling in the previously studied steels (see Fig. 3.1.1). Figure 3.1.6 compares cavity size distributions at several fluences for CW 316 (DO heat) and CW 316 + Ti (R1 heat) irradiated in HFIR at 600 to 640°C. Representative microstructures for irradiation to 15 dpa are also shown. Comparison can be made with similar results for CW 316 (N lot) (Fig. 3.1.5) and PCA B1 (Fig. 3.1.3). From our previous interpretation concerning voids and bubbles,[8] the CW 316 (DO heat) and CW 316 + Ti (R1 heat) show considerably less swelling than the materials examined in this present work because the cavity microstructures consist of fine bubbles with no significant conversion of these to coarser voids. The CW 316 + Ti (R1 heat) shows less swelling than the CW 316 (DO heat) because the bubble microstructure in the former contains nearly an order of magnitude higher cavity density than does the bubble microstructure in the latter. This refinement effect is due directly to bubble association with fine MC particles in the CW 316 + Ti (refs. 3, 6, 12, 19). Swelling in the CW 316 (DO heat) remains due to bubbles for irradiation in HFIR producing up to *42* dpa and does not show evidence of void formation (Fig. 3.1.6). There is currently controversy about the cavity nature and the fluence dependence of swelling for CW 316 (DO heat) irradiated in HFIR.[20-22]

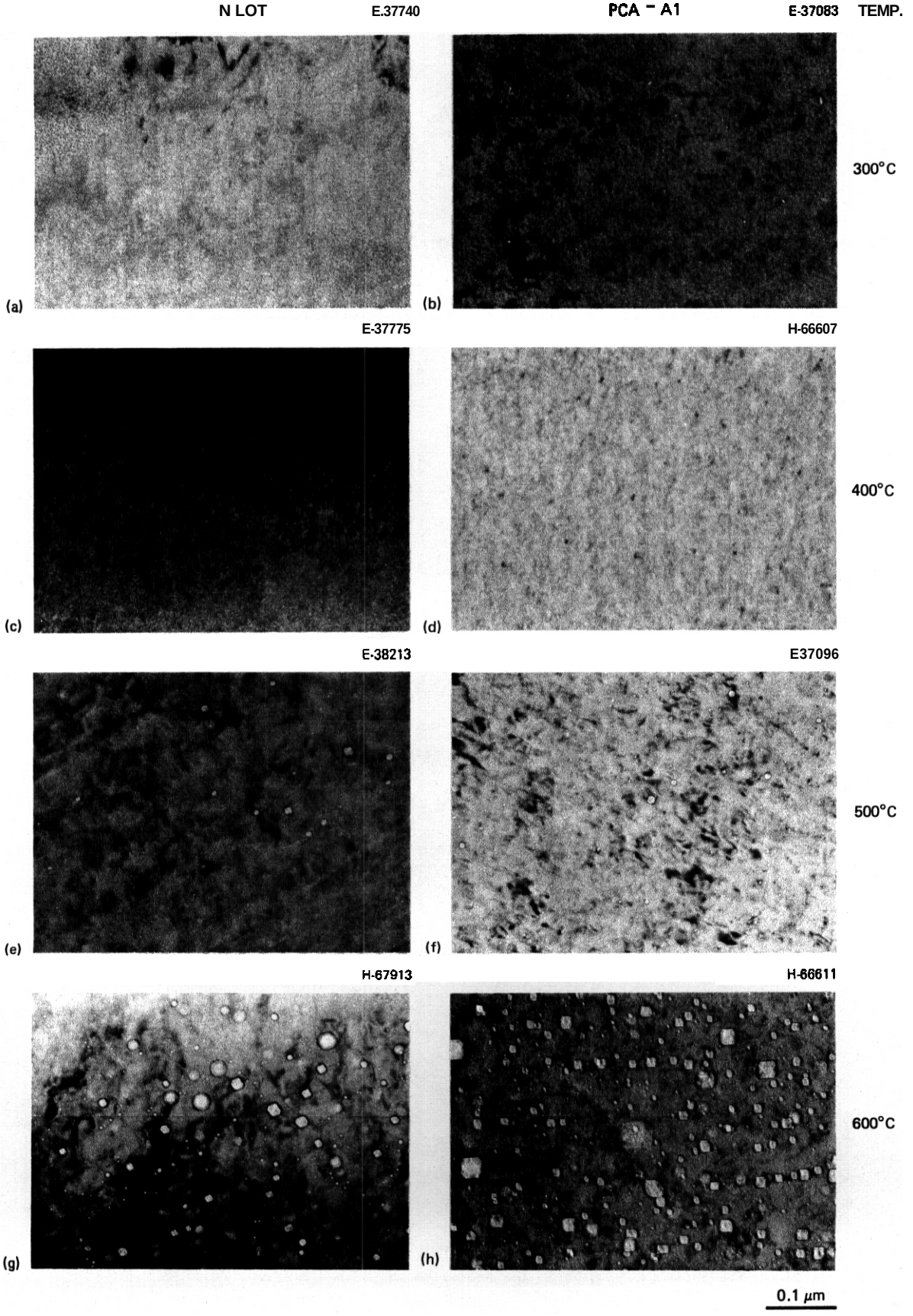

Fig. 3.1.4. A Comparison of Microstructures for 20%-Cold-WorkedType 316 (N Lot) (a,c,e,g) and PCA A1 (b,d,f,h) after HFIR Irradiation at 300 to 600°C to up to about 10 dpa. Irradiation temperatures are indicated.

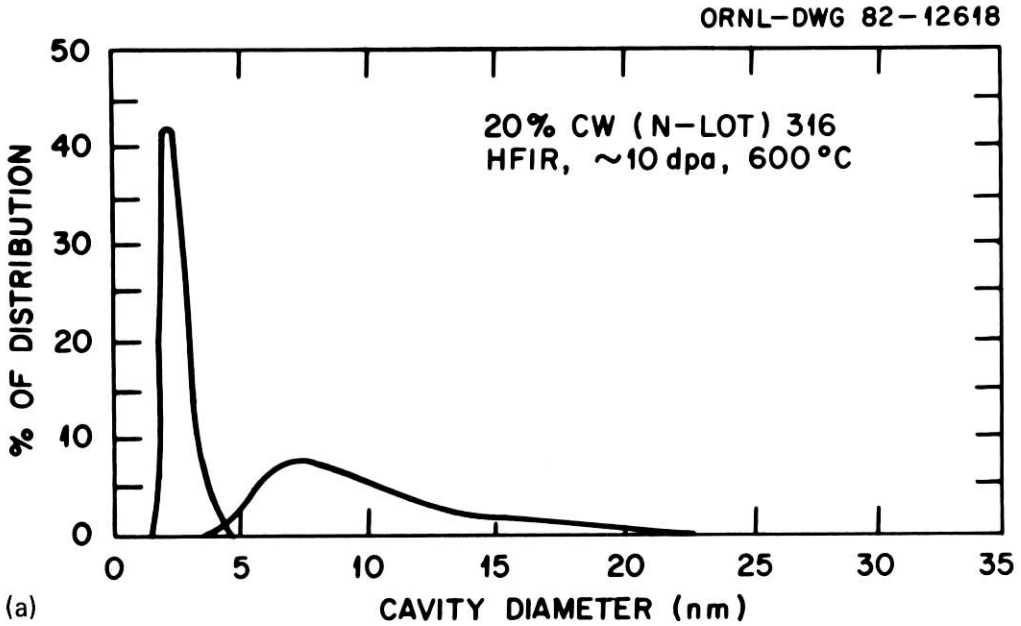

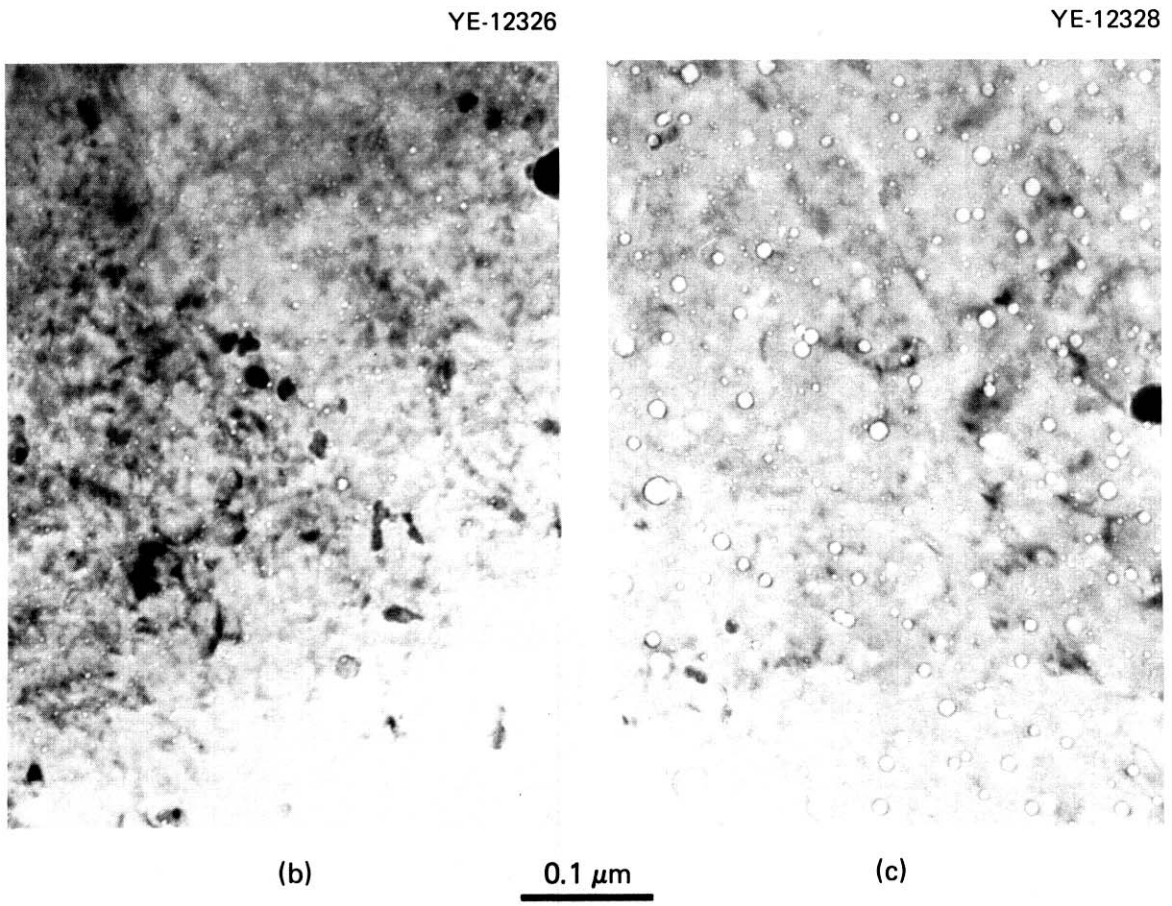

Fig. 3.1.5. A Plot of Size Distribution Together with Representative Microstructures of the Fine (Bubble) Component (b) and Large (Void) Component (c) of the Cavity Microstructure Observed in 20%-Cold-Worked Type 316 (N Lot) after HFIR Irradiation at 600°C to about 10 dpa.

The CW 316 (N lot) and various PCA samples show strong tendencies toward Frank interstitial loop and irradiation-induced γ' precipitate formation during HFIR irradiation at 500 and 600°C, concurrent with the development of void swelling at these conditions. Frank loops are observed in significant proportion over the entire temperature range in all samples examined here. Precipitation of γ' is observed at 600°C in CW 316 (N lot) and PCA A2, B1, and B2. At 500°C γ' is also detected in CW 316. According to our current understanding of void development and swelling, Frank loops help provide an interstitial bias, necessary for void growth,[23] and often coincide with development of irradiation-induced phases.[6,8,24,25] The presence of irradiation-induced phases is also a consequence of a high level of irradiation-induced solute segregation (RISS). A high level of RISS and the presence of irradiation-induced phases most often coincide with substantial void swelling under neutron irradiation.[8,20–25] High RISS will also hinder formation or contribute to instability of phases that are naturally incompatible with the effects of RISS (i.e., nickel- and silicon-poor phases), like tau ($M_{23}C_6$) and titanium-rich MC.[5,6,8,19,24,25] Hence the concurrent formation of voids and the nickel- and silicon-rich γ' precipitate in the alloys irradiated at 600°C in HFIR in this work are mutually consistent. Further, the coincidence of γ' formation and/or lack of MC formation or its dissolution in the various PCA samples is also reasonable.

The following factors affect MC stability under irradiation:

1. homogeneity of titanium and carbon distribution;
2. vacancy availability due to oversized misfit between MC and the matrix;
3. formation of other phases rich in carbon, molybdenum, and titanium;
4. level of RISS (because MC is molybdenum-rich and nickel-, silicon-poor);
5. availability of heterogeneous nucleation sites; and
6. cascade mixing and/or dissolution.

The reasons bubbles do not develop into voids in CW 316 (DO heat) and CW 316 + Ti (R1 heat) during HFIR irradiation, as they do in CW 316 (N lot) and the various PCA pretreatments, appear related both to important differences in dislocation structure development and precipitate phase stability. Both the R1 and DO heats of steel have essentially no Frank interstitial loops after HFIR irradiation above 425 to 450°C (ref. 7).

They also have qualitatively lower concentrations of total dislocation concentration than the N lot or PCA steels examined here. Furthermore, both the precipitate phases and their compositions indicate very low levels of RISS in the DO and R1 heats compared with the high RISS apparent in the N lot and PCA steels. Overall, these observations are consistent with the swelling comparison made above. In general, the swelling in Fig. 3.1.1 at 600°C orders with increased γ' formation and decreased MC stability, for the PCA samples and R1-heat steel. For the DO-heat and N lot steels, the same order is found for considering γ' and tau ($M_{23}C_6$). The PCA B1 and A2 have the highest swelling and most γ'; PCA A1 and C have intermediate swelling and at present show little evidence of either γ' or MC. The PCA B2 and CW 316 (N lot), which have still lower swelling, show only a little γ', and PCA B2 has fine MC formation. Both CW 316 (DO heat) and CW 316 + Ti (R1 heat), which have the lowest swelling because voids are not forming, have no γ' and very little evidence of RISS effects, and the CW 316 + Ti (R1 heat) has a considerable amount of fine titanium-rich MC.

In constrast to the behavior of these materials at 500°C and above, the HFIR results at 400°C and below show more swelling in the R1- and DO-heat steels than in N lot or the various conditions of PCA. The explanation is not as straightforward as at the higher temperatures. Swelling in the CW 316 (DO heat) at low temperatures is due to void formation and coincident dislocation and/or RISS-precipitation effects. Although no voids are present in the R1-heat steel at these temperatures, bubble swelling is greater than in N lot or PCA steels because bubble swelling is low or unresolved in the latter two.

3.1.6 Insight for Future Alloy Development

The purpose of the various pretreatments of PCA was to examine the effect of preirradiation microstructure on microstructural development during HFIR irradiation. The PCA variants and CW 316 (N lot) all show better swelling resistance at 300°C than CW 316 R1 or DO heats. The situation begins to reverse at 400 to 500°C, and at 600°C the swelling is greater in the PCA and N lot steels than in CW 316 DO and R1 heats. The

general phenomenon, in all cases, is swelling due to void development. Swelling reduction requires the prevention of the bubble-to-void conversion. Considering all the results, the principles of increased sink strength and microstructure refinement (i.e., higher bubble, precipitate, and/or dislocation densities) and maximum MC stability with minimum radiation-induced phase formation and RISS effects still appear to be legitimate goals for development of swelling-resistant materials. Varying degrees of resistance to void swelling are observed in the PCA pretreatments and CW 316 (N lot) irradiated at 600°C. Void swelling resistance has also been observed in CW 316 (R1 heat) irradiated at similar conditions. An important result of this work is that the swelling resistance of PCA AI (solution annealed) is at least as good as the other PCA variants (excluding 25% CW PCA A3) and the CW 316 N lot, R1, and DO steels at 500°C and below. This is seldom the case, as void swelling is usually greater in the solution-annealed stainless steels than in cold worked.[8,26] This may be important to the behavior of weld and heat-affected zones, where the initially cold-worked or complex microstructural pretreatments will be erased or perturbed.

Figure 3.1.7 presents schematically the swelling behavior in low and high helium generating irradiation environments, with the swelling phenomena divided into void and bubble swelling regions. Known data trends are also represented. This representation summarizes our previous discussion and projects a direction for future work. Even in EBR-II, void swelling is generally a two-step process, first bubble nucleation and then conversion of the bubbles to voids. In fast reactors, almost all measurable swelling is due to voids. However, in higher helium-producing environments, including fusion, some swelling will be due to bubble formation and maximum swelling will result if bubbles convert to voids. Therefore, the relevant strategy for minimum swelling in a fusion environment is to suppress void formation and manage the helium accumulation. After fast reactor irradiation, the advanced titanium-modified austenitic steels generally show better swelling resistance than unmodified CW 316 because void swelling is being suppressed for the reasons stated above.[25,27] Increased helium generation can present a substantial problem

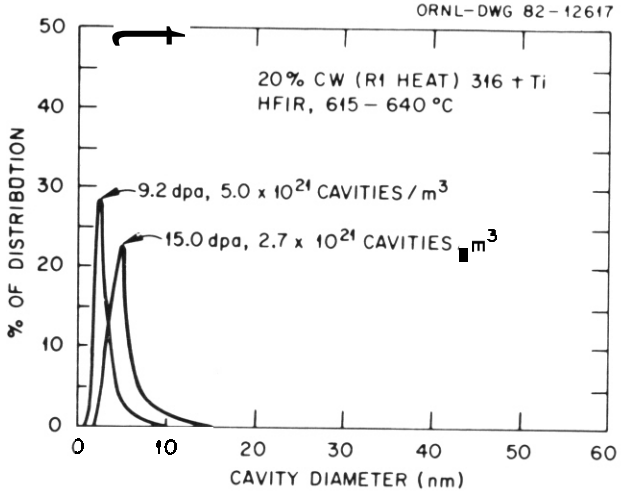

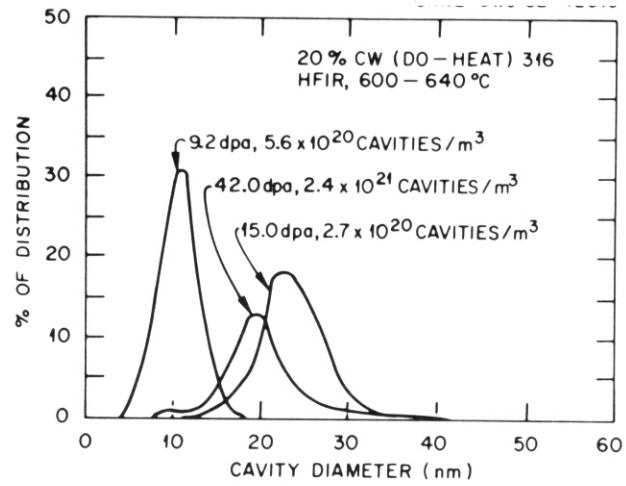

20 % CW 316 + Ti

YE-12118

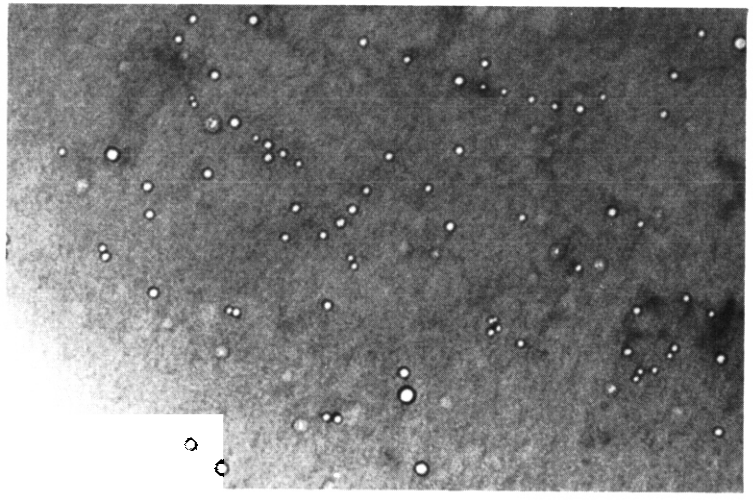

15 dpa

20 % CW 316

Y≤ 12122

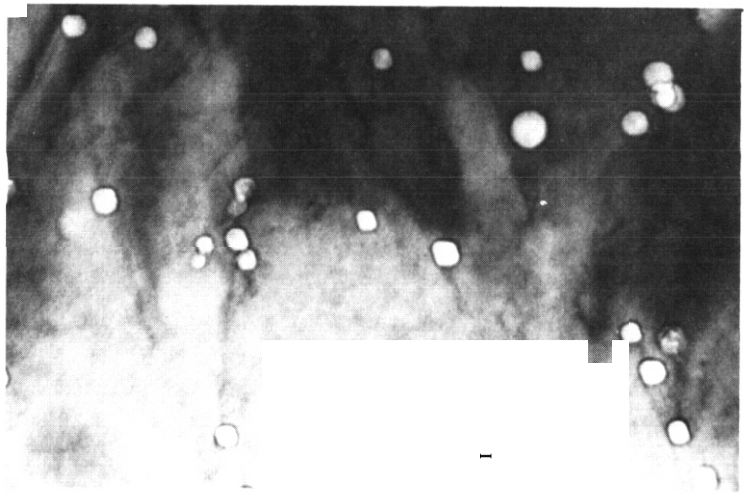

0.1 μm

Fig. 3.1.6. Cavity Size Distribution at Several Fluences for 20%-Cold-Worked Type 316 Stainless Steel (DO Heat) and 20%-Cold-Worked Type 316 + Ti (R1 Heat), and Representative Microstructures (at 15 dpa) for Irradiation in HFIR at 600 to 640°C. Sample designations, fluences, and cavity densities are indicated.

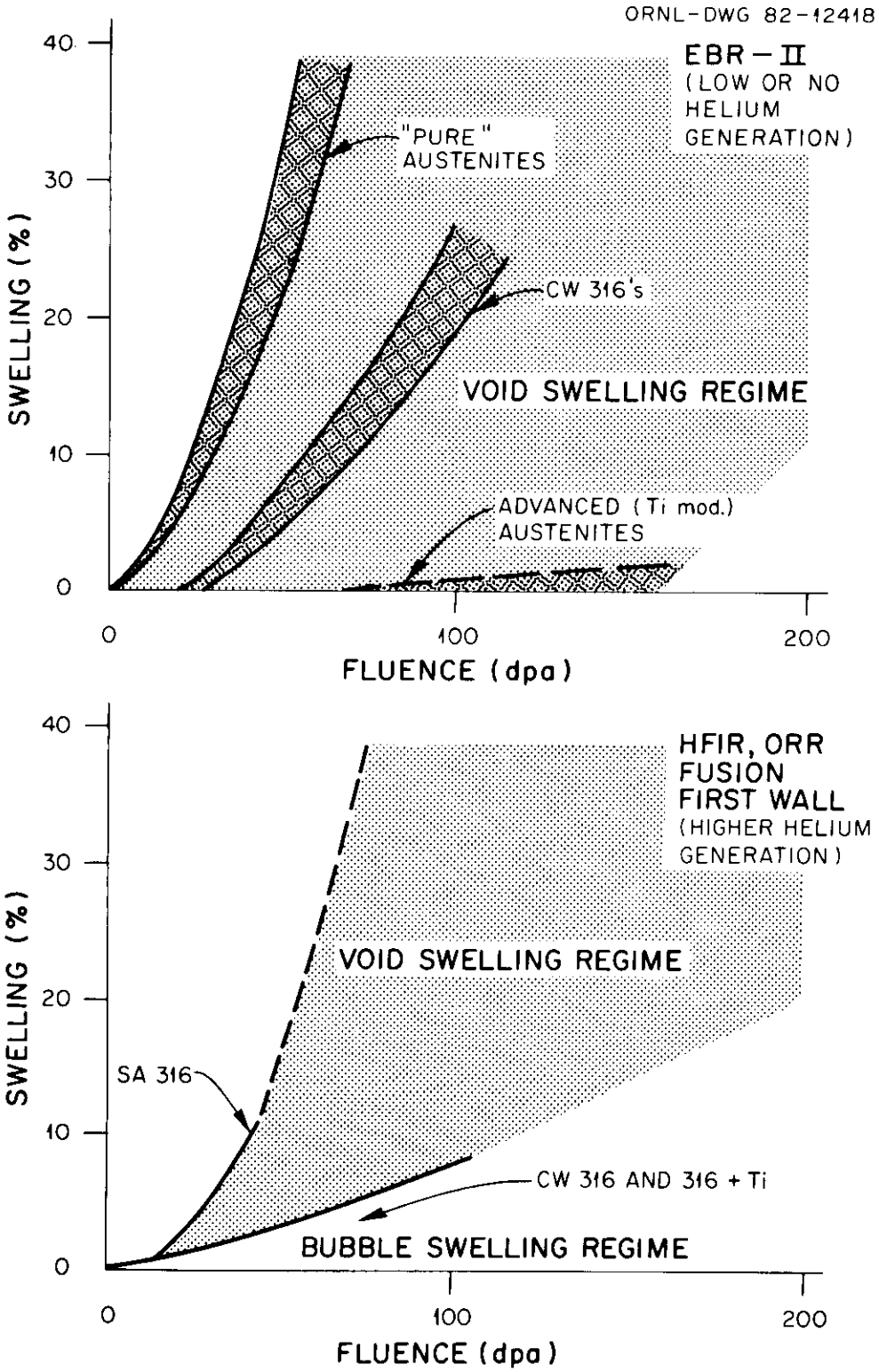

Fig. 3.1.7. A Schematic Representation of Bubble and Void Swelling Regimes in (a) Low Helium (EBR-II) and (b) High Helium (HFIR, Fusion, ORR) Generating Environments. Trend curves for EBR-II data are indicated in (a) and HFIR data are indicated in (b).

for fusion if void swelling is not suppressed.[16,17,20,28] We can have most confidence in the potential for service in a fusion reactor with an alloy that is void swelling resistant in both EBR-II and HFIR.

Under irradiation MC dissolution may be contributing to the void swelling observed in HFIR. In addition to the absence of the beneficial MC-helium interfacial trapping and dislocation pinning, MC dissolution will also contribute excess vacancies to the vacancy supersaturation. Given our understanding of the coupling of these phases to RISS,[8] MC dissolution and instability are certainly consistent with γ' formation. The vacancy effect is a direct result of the large oversized misfit of the MC phase (+0.7 atomic volumes per metal solute atom) that requires absorption of about 0.7 vacancies per solute atom during particle growth. Dissolution will contribute the same vacancies back to the matrix. These may be important during the critical nucleation stage of void development, consistent with the greater swellings of PCA B1 than of PCA C and B2. The maximum stable MC distribution formed under irradiation, as we find in CW 316 + Ti (R1 heat), may not result from the maximum intragranular MC present prior to irradiation, as we thought earlier. Rather, it may result from the most homogeneous, supersaturated solid solution present prior to irradiation. This reasoning would predict lower swelling of PCA A3 and A1 than of PCA A2, B1, C, and possibly B2. Further compositional variations may be necessary for PCA A1 and A3 to influence maximum MC stability <u>under irradiation</u> and to minimize RISS effects.

3.1.7 Conclusions

1. Various pretreatments of PCA and CW 316 (N lot) have been irradiated to produce up to 10 dpa at 300 to 600°C in HFIR. None of the samples swelled at 300°C. Varying amounts of void and bubble swelling (up to 0.2%) are observed at *400* and 500°C and all samples show void swelling at 600°C. Solution-annealed PCA A1 and CW 316 (N lot) are among the lowest swelling at *400* and 500°C. The PCA B1 (coarse precipitate) and A1 (10%-cold worked) are the highest swelling (1.1—1.2%) at 600°C. The PCA A1 and C (fine precipitate) are intermediate (-0.7%) and PCA-B2 (fine matrix precipitate) and CW 316 (N lot) are lowest swelling (0.2—0.4%).

2. Swelling of PCA variants (excluding PCA A3, 25% CW) and CW 316 (N lot) is less than CW 316 (DO heat) and CW 316 + Ti (R1 heat) after irradiation to about 10 dpa at 300 to 400°C, but definitely greater than in those steels at 400 to 600°C. The swelling at 500 and 600°C in the PCA and N lot steels is due to void swelling, whereas bubble formation but no void formation is evident at these conditions in DO- and R1-heat steels.

3. At 500 and 600°C the presence of Frank loops and irradiation-induced γ' (indicating a high level of RISS) appear to be contributing in a complex fashion to the greater void swelling in PCA and CW 316 (N lot) steels than in R1- and DO-heat CW 316 steels. The trend is for maximum γ' formation and/or MC instability to coincide with the highest void swelling.

3.1.8 References

1. P. J. Maziasz, F. W. Wiffen, and E. E. Bloom, "Swelling and Microstructural Changes in Type 316 Stainless Steel Irradiated under Simulated CTR Conditions," pp. 259-88 in *Radiation Effects and Tritium Technology for Fusion Reactors*, CONF-750989, Vol. 1 (March 1976).
2. P. J. Maziasz and M. L. Grossbeck, "Swelling and Microstructure of HFIR-Irradiated 20%-Cold-Worked Type 316 Stainless Steel and 316 + 0.24 wt % Ti," *ADIP Quart. Prog. Rep. Dec. 31, 1980*, DOE/ER-0045/5, pp. 43-69.
3. P. J. Maziasz and M. L. Grossbeck, "Microstructural Development in 20%-Cold-Worked Type 316 Stainless Steel Irradiated in the HFIR: Fluence Dependence of the Cavity Component," *ADIP Quart. Prog. Rep. Mar. 31, 1981*, DOE/ER-0045/6, pp. 28—56.
4. P. J. Maziasz and M. L. Grossbeck, "Swelling Microstructural Development and Helium Effects in Type 316 Stainless Steel Irradiated in HFIR and EBR-II," *J. Nuct. Mater.* 103&104: 987—91 (1981).
5. P. J. Maziasz, "The Precipitation Response of 20%-Cold-Worked Type 316 Stainless Steel to Simulated Fusion Irradiation," *J. Nucl. Mater.* 85&86: 713—17 (1979).

6. P. J. Maziasz, J. A. Horak, and B. L. Cox, "The Influence of Both Helium and Neutron Irradiation on Precipitation in 20%-Cold-Worked Austenitic Stainless Steels," pp. 271–92 in *Phase Stability During Irradiation*, ed. by J. R. Holland, L. K. Mansur, and D. I. Potter, The Metallurgical Society of AIME, Warrendale, Pa., 1981.

7. P. J. Maziasz, "Microstructural Development of 20%-Cold-Worked Types 316 and 316 + Ti Stainless Steels Irradiated in HFIR: Temperature and Fluence Dependence of the Dislocation Component," *ADIP Semiannu. Prog. Rep. Sept. 30, 1981*, DOE/ER-0045/7, p. 54.

8. P. J. Maziasz, "Some Effects of Increased Helium Content on Void Formation and Solute Segregation in Neutron Irradiated Type 316 Stainless Steel," Sect. 3.5 of this report.

9. M. L. Grossbeck, J. W. Woods, and G. A. Potter, "Experiments HFIR-CTR-30, -31, and -32 for Irradiation of Transmission Electron Microscopy Disk Specimens," *ADIP Quart. Prog. Rep. Sept. 30, 1980*, DOE/ER-0045/4, p. 36.

10. T. A. Gabriel, B. L. Bishop, and F. W. Wiffen, "Calculated Irradiation Response of Materials Using Fission Reactor (HFIR, ORR, and EBR-II) Neutron Spectra," ORNL/TM-6361 (August 1979).

11. F. W. Wiffen et al., "The Production Rate of Helium During Irradiation of Nickel in Thermal Spectrum Fission Reactors," to be published.

12. P. J. Maziasz and T. K. Roche, "Preirradiation Microstructural Development Designed to Minimize Properties Degradation During Irradiation in Austenitic Alloys," *J. Nucl. Mater.* 103&104: 797–801 (1981).

13. P. J. Maziasz, "Microstructural Design for Fusion First-Wall Applications and Recommendations for Thermal-Mechanical Preirradiation Treatments," *ADIP Quart. Prog. Rep. June 30, 1979*, DOE/ET-0058/6, p. 48.

14. P. J. Maziasz, B. L. Cox, T. K. Roche, and E. E. Bloom, "Time-Temperature-Precipitation Curve Determination of the Path A Prime Candidate Alloy for Microstructural Design," *ADIP Quart. Prog. Rep. Sept. 30, 2979*, DOE/ET-0058/7, p. 103.

15. P. J. Maziasz and T. K. Roche, "Design and Fabrication of Preirradiation Microstructures in Path A Prime Candidate Alloy," *ADIP Quart. Prog. Rep. Dec. 31, 1980*, DOE/ER-0045/5, p. 25.

16. G. R. Odette and M. W. Frei, "Potential Effects of Interactions Between Transmutants and Displaced Atoms in Controlled Thermonuclear Reactor First Walls," *Proc. First Topical Meeting on the Technology of Controlled Nuclear Fusion,* CONF-740402-P2 (August 1974), p. 485.

17. G. R. Odette and C. S. Langley, "Modeling of Synergistic Effects of Displaced Atoms and Transmutant Damage in Fission and Fusion Environments," p. 395 in *Radiation Effects and Tritium Technology for Fusion Reactors,* CONF-750989, Vol. 1 (March 1976).

18. M. R. Hayns, "The Transition from Gas Bubbles to Void Growth," AERE Harwell Report, AERE-R8806 (May 1977).

19. P. J. Maziasz, "Helium Trapping at Ti-Rich MC Particles in Ti-Modified Austenitic Stainless Steel," p. 477–92 in *Phase Stability During Irradiation,* ed. by J. R. Holland, L. K. Mansur, and D. I. Potter, The Metallurgical Society of AIME, Warrendale, Pa., 1981.

20. G. R. Odette, P. J. Maziasz, and J. A. Spitznagel, "Fission-Fusion Correlations for Swelling and Microstructure in Stainless Steels: Effects of the Helium to Displacement per Atom Ratio," *J. Nucl. Mater.* 103&104: 1289–1303 (1981).

21. H. R. Brager and F. A. Garner, "Comparison of the Swelling and the Microstructural/Microchemical Evolution of AISI 316 Irradiated in EBR-II and HFIR," *J. Nucl. Mater.* 103&104: 993–97 (1981).

22. H. R. Brager and F. A. Garner, "Influence of Neutron Spectra on the Radiation-Induced Evolution of AISI 316," paper presented at International Conference on Neutron Irradiation Effects, Argonne National Laboratory, Argonne, Ill., Nov. 9–12, 1981; to be published in *Journal of Nuclear Materials.*

23. L. K. Mansur, "Void Swelling in Metals and Alloys Under Irradiation: An Assessment of the Theory," *Nucl. Technol.* 40: 5 (1978).

24. E. H. Lee, P. J. Maziasz, and A. F. Rowcliffe, "The Structure and Composition of Phase Occurring in Austenitic Stainless Steels in Thermal and Irradiation Environments," pp. 191–218 in *Phase Stability During Irradiation,* ed. by J. R. Holland, L. K. Mansur, and D. I. Potter, The Metallurgical Society of AIME, Warrendale, Pa., 1981.

25. A. F. Rowcliffe and E. H. Lee, "High Temperature Radiation Damage Phenomena in Complex Alloys," paper presented at International Conference on Neutron Irradiation Effects, Argonne National Laboratory, Argonne, Ill., Nov. 9–12, 1981; to be published in *Journal of Nuclear Materials*.

26. W. K. Appleby, E. E. Bloom, J. E. Flinn, and F. A. Garner, "Swelling in Neutron-Irradiated 300-Series Stainless Steels," pp. 509–27 in *Radiation Effects in Breeder Reactor Structural Materials*, ed. by M. L. Bleiberg and J. W. Bennett, The Metallurgical Society of AIME, New York, 1977.

27. E. H. Lee, A. F. Rowcliffe, and L. K. Mansur, "Precipitation and Cavity Formation in Austenitic Stainless Steels During Irradiation," *J. Nucl. Mater.* 103&104: 1475–80 (1981).

28. R. E. Stoller and G. R. Odette, "A Model Based Fission-Fusion Correlation of Cavity Swelling in Stainless Steel," *J. Nucl. Mater.* 103&104: 1361-65 (1981).

3.2 GRAIN BOUNDARY MICROSTRUCTURE IN PATH A PCA IRRADIATED TO 10 dpa IN HFIR — P. J. Maziasz and D. N. Braski (Oak Ridge National Laboratory)

3.2.1 ADIP Tasks

ADIP Tasks I.C.1, Microstructural Stability, and I.C.2, Microstructure and Swelling in Austenitic Alloys.

3.2.2 Objectives

The objective of this work is to examine and evaluate the effect of thermal–mechanical pretreatments of PCA that are intended to influence grain boundary microstructural development under High **Flux** Isotope Reactor (HFIR) irradiation. This facet of the alloy development was designed to reduce embrittlement on the basis of our understanding of the effects of microstructure on mechanical behavior.

3.2.3 Summary

Path A PCA in several preirradiation grain boundary microstructural conditions was irradiated *in* HFIR at 300 to 600°C to 10 dpa, together with 20%–cold–worked (N lot) type 316 stainless steel (CW 316). None of the samples show significant grain boundary bubble formation at 300 to 500°C. At 600°C, PCA-B1 and -B2, with stable, moderately sized grain boundary MC, have the finest dispersions of grain boundary bubbles.

3.2.4 Progress and Status

3.2.4.1 Introduction

Completion of the first phase of alloy development of the Path A PCA (namely, design and fabrication of various preirradiation microstructures) was reported earlier.[1,2] We are currently in the second phase, which is investigation and evaluation of these pretreated samples. Figure 3.2.1 is a schematic flow diagram indicating categories and interrelationships of the various portions of the overall evaluation effort. The mechanical properties evaluation and their correlation with microstructural effects is an important facet of the overall alloy development effort. In this report we outline the principal ideas behind our approach to developing

ORNL-DWG 82-9818

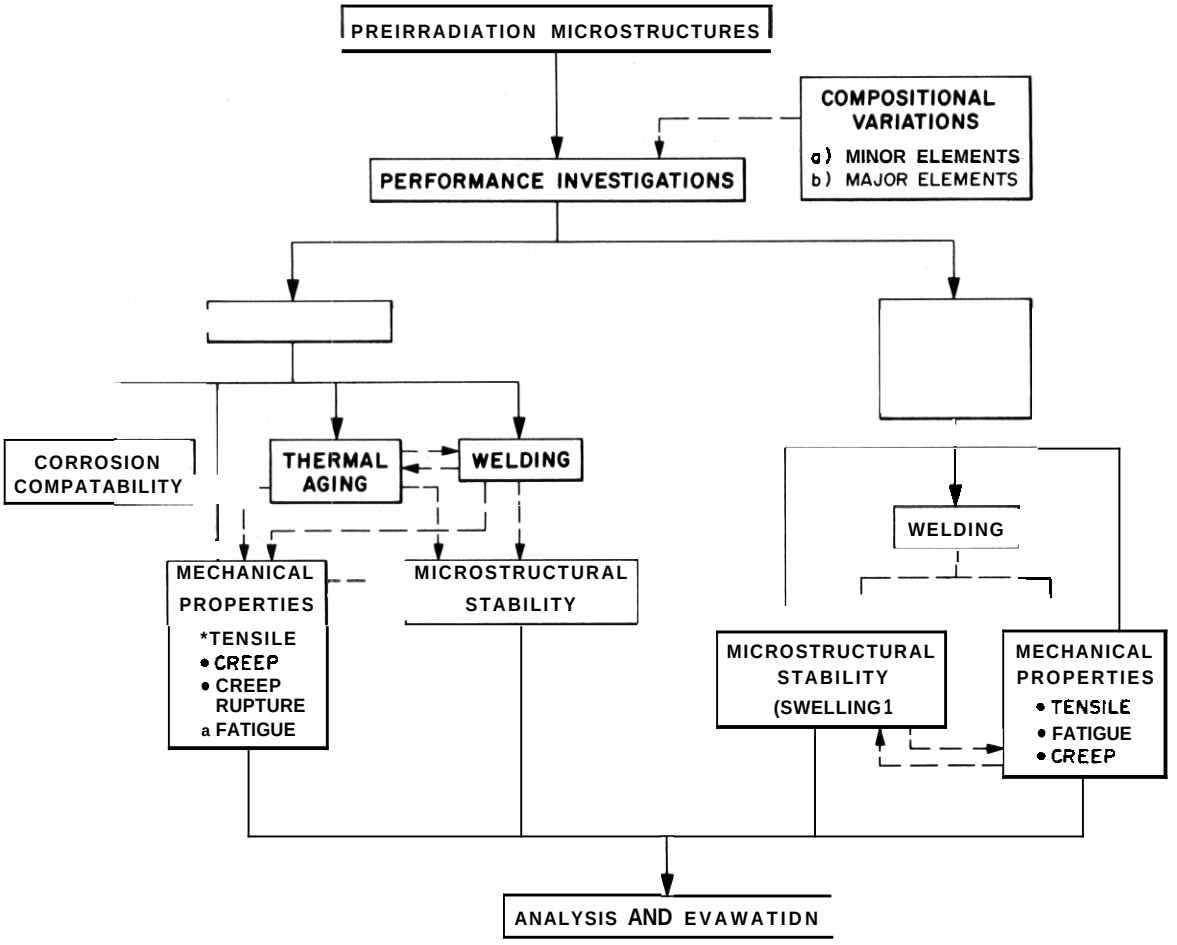

Fig. 3.2.1. Efforts Planned and Under Way to Evaluate the Performance of the Path A PCA and to Guide Further Alloy Development.

embrittlement-resistant alloys. Initial results are presented of the effects of HFIR irradiation on grain boundaries in PCA and CW 316 (N lot).

3.2.4.2 Development of Alloys with Improved Ductility

Embrittlement, in the form of premature failure, can generally be caused by some sufficient amount and/or distribution of helium at the grain boundaries.[3-9] This can occur in stainless steels at about 400 to 500°C and above and is relevant to fusion first walls, which will experience much higher helium generation than fast reactor irradiation.[6,10,11] Embrittlement can be considered for tensile, creep, and fatigue properties. It was shown earlier that embrittlement can occur after low-fluence HFIR irradiation of CW 316 (DO heat). Figure 3.2.2 shows stress-strain curves,

ORNL-PHOTO 274578

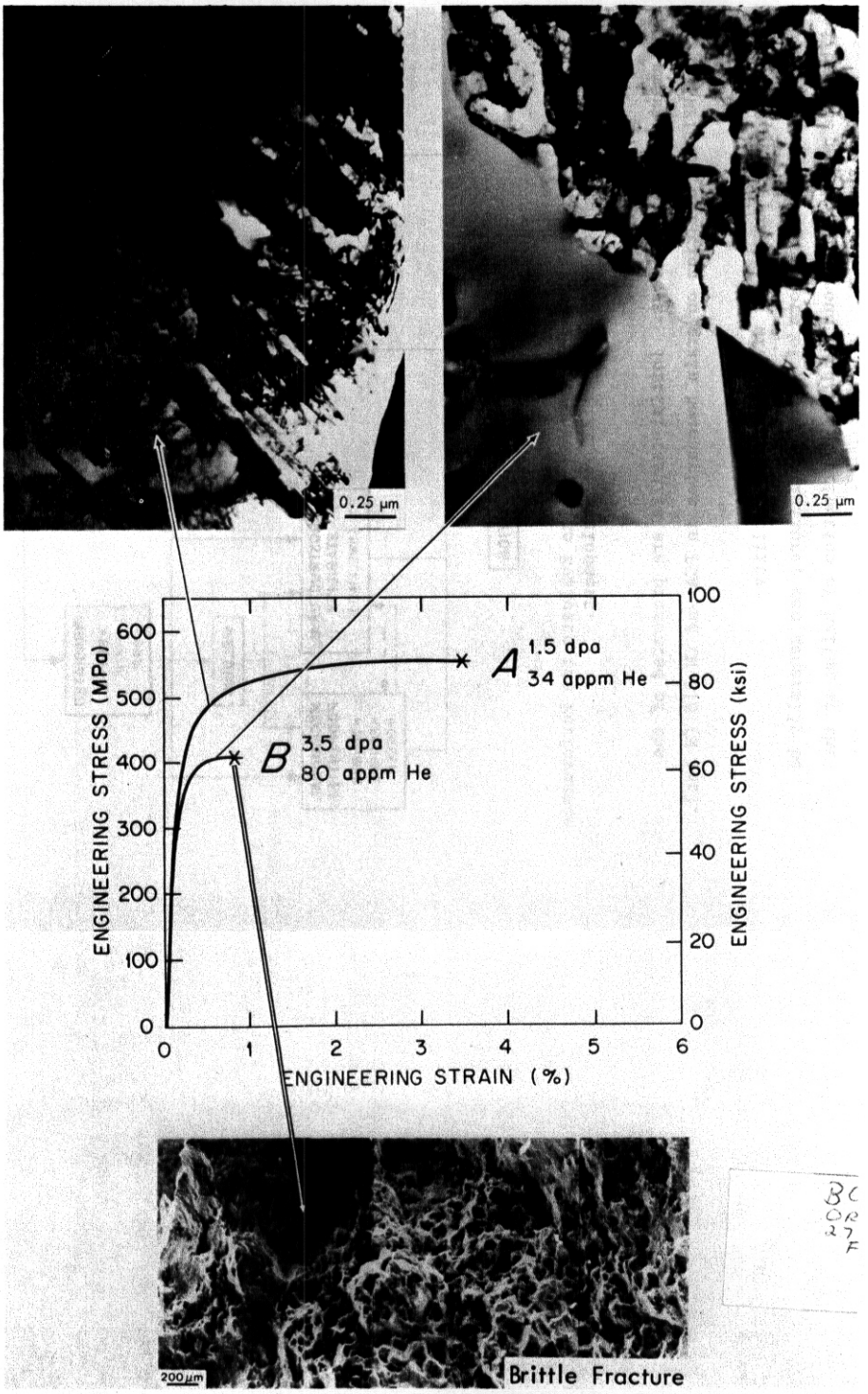

Fig. 322. A Correlation of Tensile Stream-Strain Curves with Hicrostructures and Fracture Surfaces for 20%-Cold-Worked (DO Heat) Type 316 Stainless Steel Irradiated in WIR at 650 to 675°C to the low Pluences Indicated. The test temperature was 575°C. Sample B shows evidence of recrystallization and intergranular failure on the fracture surface.

microstructures, and fracture surfaces for CW 316 (DO heat) irradiated in HFIR to low fluences at 650 to 675°C and then tested at 575°C. Together they demonstrate embrittlement due to helium. Comparison of curves A and B in Fig. 3.2.2 indicates that both strength and ductility are decreasing with increasing fluence. The microstructure for curve B in Fig. 3.2.2 shows evidence of recrystallization. Figure 3.2.3 illustrates at higher magnification the fine boundary bubbles forming as the boundary sweeps and collects helium from the unrecrystallized matrix. This distribution of helium is apparently sufficient to cause brittle intergranular failure at these conditions. By contrast, the same unirradiated material after recrystallization would exhibit a tremendously increased ductility with transgranular ductile failure.[13]

ORNL-PHOTO 6831-81

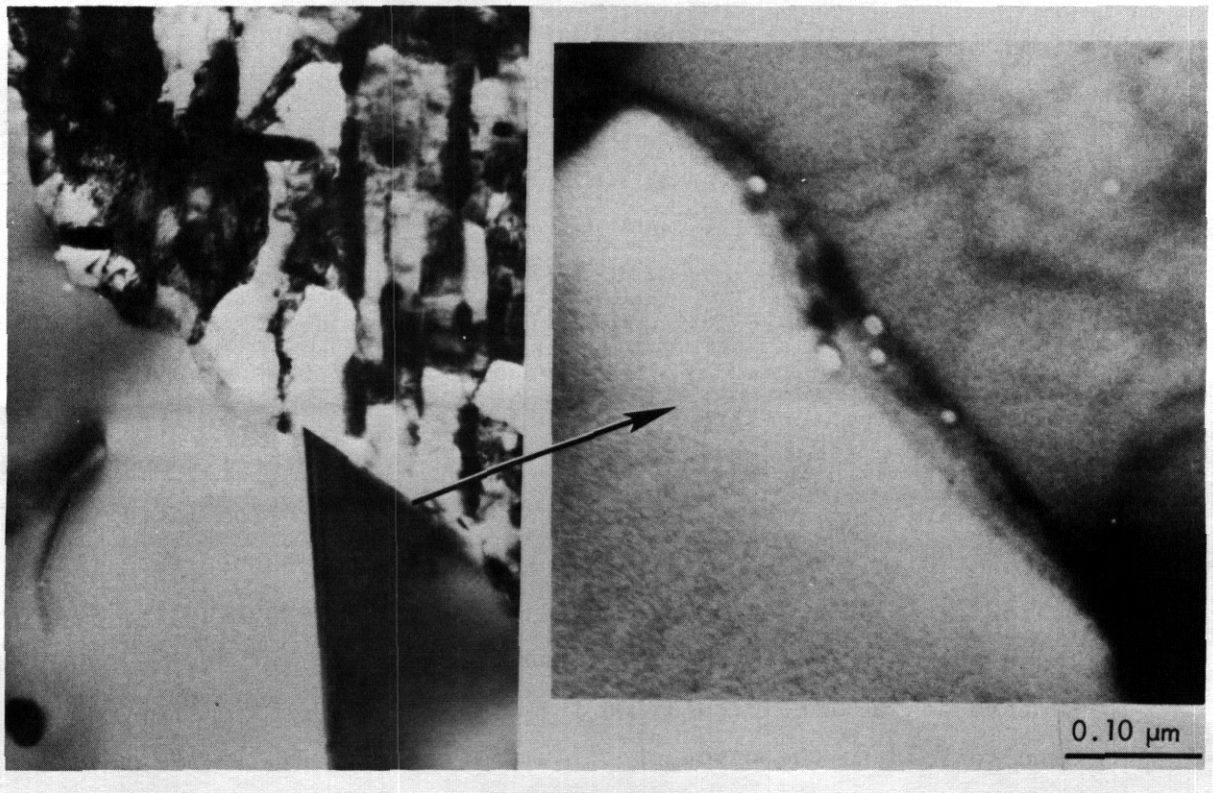

Fig. 3.2.3. Higher Magnification of a Boundary Formed Between a Recrystallized Grain and Recovered Material (from Curve B of Fig. 3.2.2) to Show Helium Bubble Accumulation for HFIR Irradiation of 20%-Cold-Worked (DO Heat) Type 316 Stainless Steel to the Conditions Indicated in Fig. 3.2.2.

Similar low-fluence HFIR irradiation[12] of CW 316 + Ti (R1 heat) does not result in the embrittlement shown for the CW 316 (DO heat), as shown by comparison of Figs. 3.2.4 and 3.2.2. Because both strength and ductility of the CW 316 + Ti (R1 heat) curves are greater than the corresponding properties of CW 316 (DO heat), we interpret these results as embrittlement resistance of the former. The fracture surface comparison supports this interpretation. The microstructural comparison illustrates that the titanium-modified steel shows only slight recovery and no recrystallization compared with type 316 stainless steel. This is due to formation of fine titanium-rich (MC) carbide particles that contribute directly to helium trapping, dislocation pinning, and phase control. However, at higher fluence, the resistance will degrade and embrittlement again begins, coincident with the development of grain boundary bubbles.

We can summarize our understanding of premature failure due to embrittlement with the schematic tensile curves and properties relationships that classify the various stages of embrittlement in Fig. 3.2.5. The normal relationship of strength to ductility is increased strength at the expense of decreased ductility for comparison of unirradiated solution-annealed material (SA) with CW 316. However, progressive embrittlement under irradiation generally involves strength and ductility decreasing together. The earliest stages of embrittlement usually involve the onset of grain boundary bubble formation and a transition from a transgranular ductile to intergranular failure mode. Figure 3.2.6 shows a correlation of grain boundary microstructure with failure mode (in postirradiation tensile tests) for CW 316 (DO heat) irradiated at several temperatures in HFIR. This comparison illustrates the transition from intra- to intergranular failure with increased grain boundary bubble size (which increases as irradiation temperature increases). Concurrently, the amount of grain boundary precipitation of eta (M_6C) and/or tau ($M_{23}C_6$) phases also decreases as the irradiation temperature increases. Both effects combine to lead to the onset of helium embrittlement. Helium bubble formation is irreversible and always presents the potential for premature

ORNL-PHOTO 2747-78

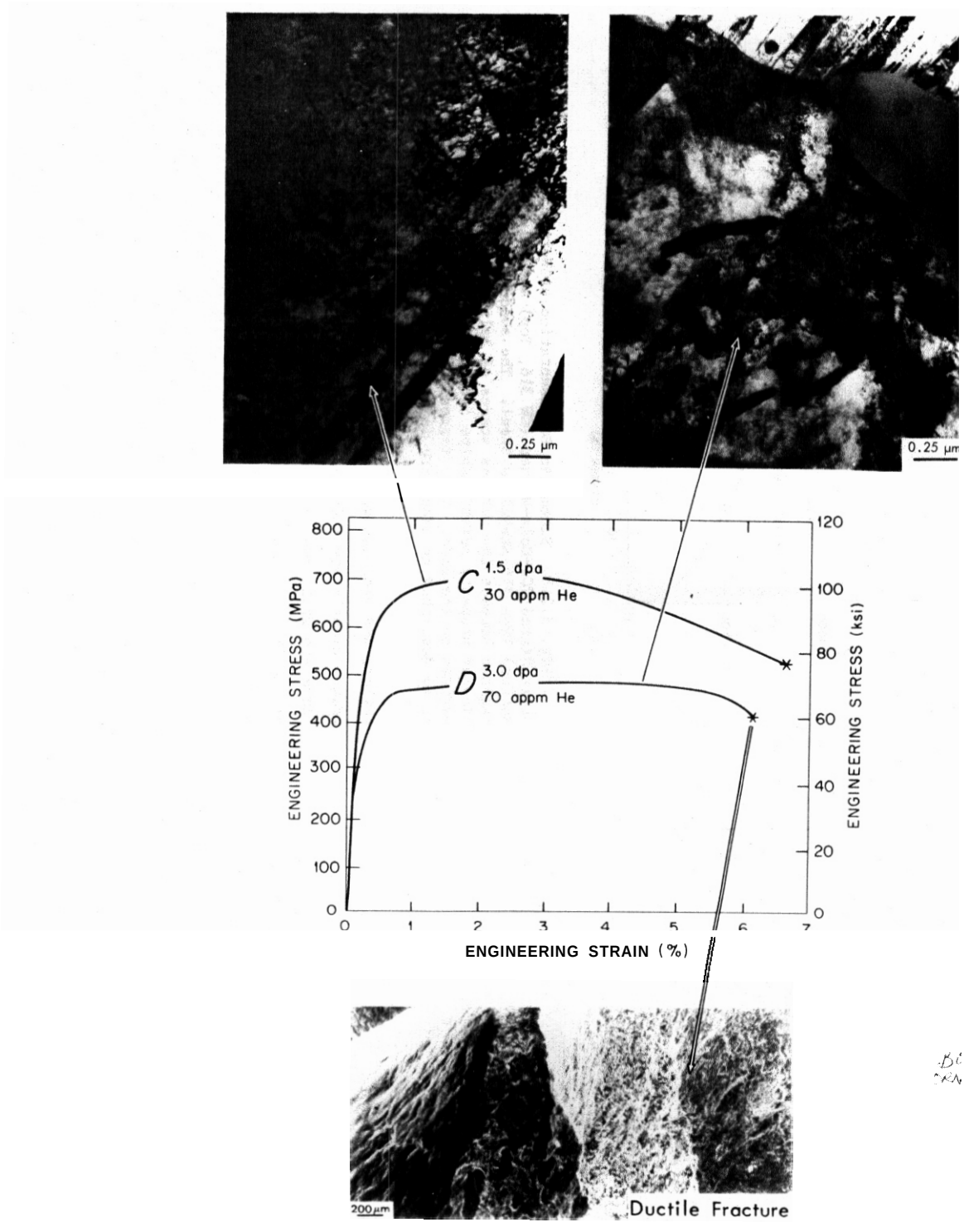

Fig. 3.2.4. A Correlation of Tensile Stress-Strain Curves with Microstructure and Fracture Surfaces for 20%-Cold-Worked (R1 Heat) Titanium-Modified Type 316 Stainless Steel Irradiated in HFIR at 650 to 675°C to the Low Fluences Indicated and Tested at 575°C. Both tensile curves show increased strength and ductility compared with 20%-cold-worked (DO heat) type 316 stainless steel in Fig. 3.2.2. The microstructures show only slight recovery and no evidence of recrystallization. The failure mode is ductile transgranular.

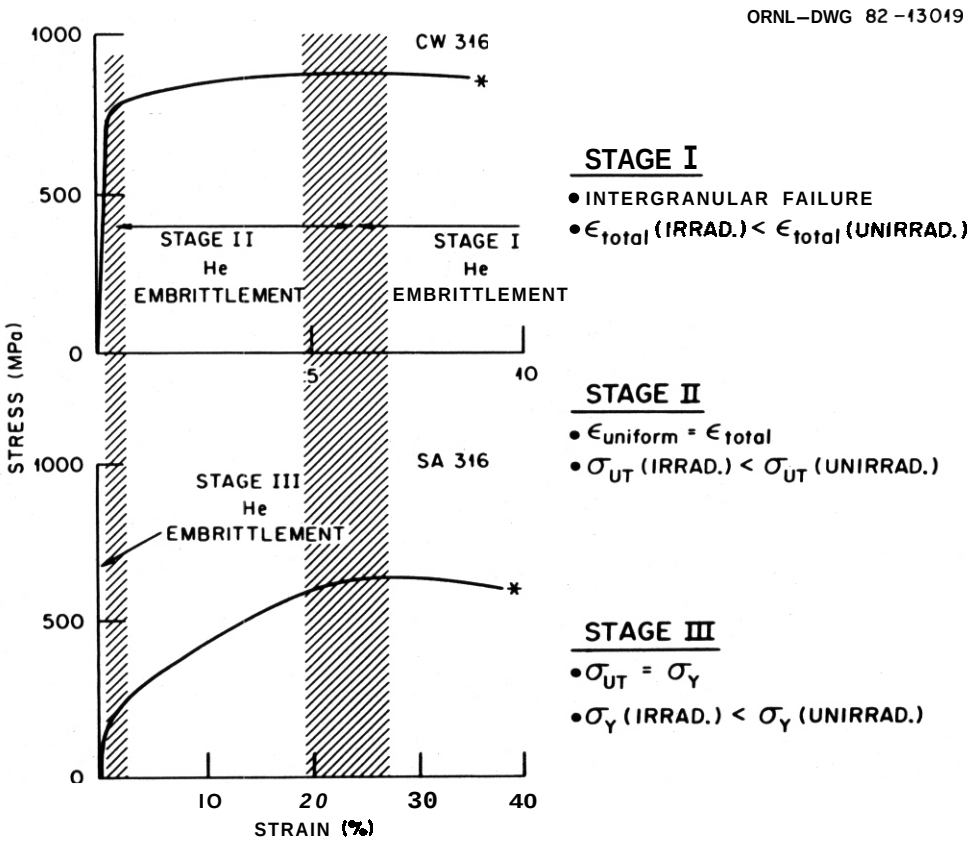

Fig. 3.2.5. Schematic Representation of Normal Tensile Curves for Unirradiated 20%-Cold-Worked (CW 316, Top) and Solution Annealed (SA 316, Bottom) Type 316 Stainless Steel. The shaded areas indicate transition regions between the various stages of helium embrittlement. The particular property relationships for these embrittlement stages are summarized on the side. This representation allows progressive embrittlement to be described as premature failure of either SA or CW 316.

failure and progressively worsening embrittlement. Figure 3.2.7 illustrates clearly how increased helium generation (HFIR compared with EBR-II) increases grain boundary bubble formation for stress-free irradiation of SA and CW 316 at 615 to 640°C.

The current alloy development strategy for fusion, with regard to embrittlement resistance, is either to prevent grain boundary cavitation through stable grain boundary precipitate development or to minimize bubble growth. This is achieved through microstructures with controlled precipitation at the grain boundaries, to optimize the helium accommodation in the boundary.

ORNL-PHOTO 1836-82

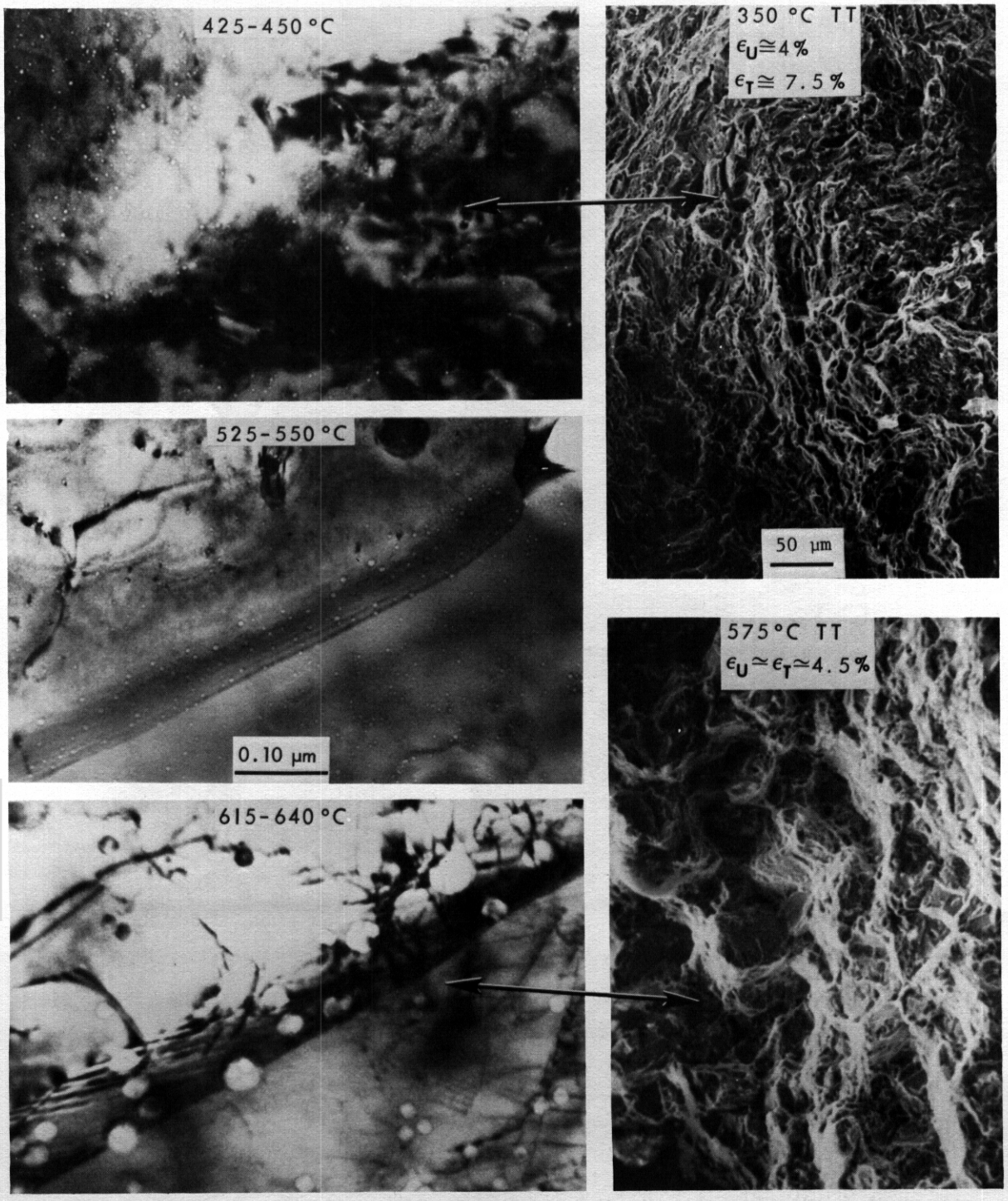

Fig. 3.2.6. Correlation Between Grain Boundary Microstructure and Tensile Fracture Surface for 20%-Cold-Worked (DO Heat) Type 316 Stainless Steel Irradiated in HFIR to 15 to 16 dpa and 880 to 1020 at. ppm He at the Temperature Indicated and Postirradiation Tensile Tested 75 to 100°C Below the Indicated Irradiation Temperature.

ORNL-PHOTO 1837-82

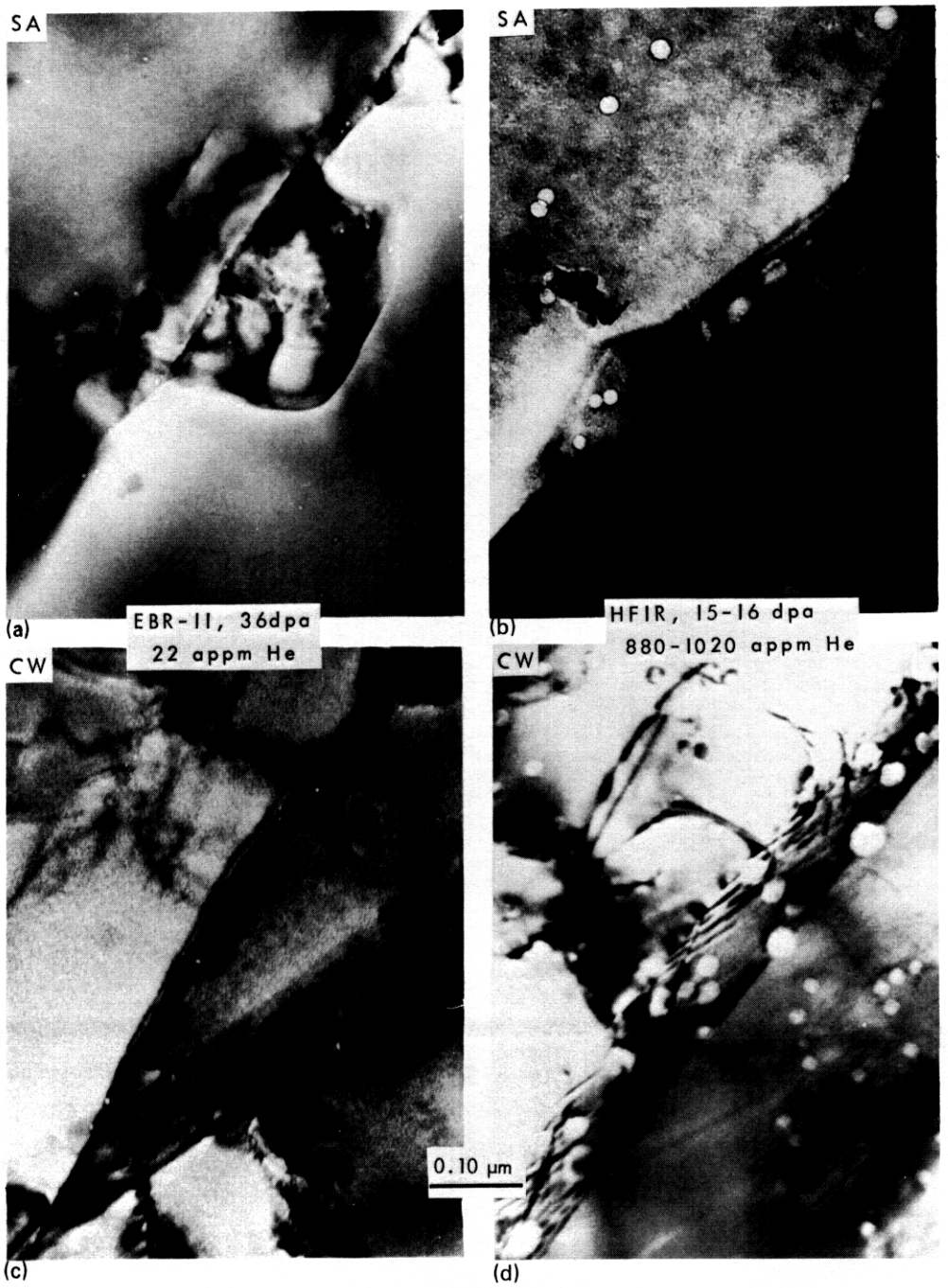

Fig. 3.2.7. A Comparison of Solution Annealed (a,b) and 20%-Cold-Worked (c,d) Type 316 Stainless Steels After EBR-II and HFIR Irradiation to Illustrate the Effect of Increased Helium Generation on Grain Boundary Cavitation. All samples were irradiated at 615 to 640°C. Neutron fluences produced 36 dpa and about 20 at. ppm He for (a) and (c) and 15 dpa and 880 at. ppm He for (b) and (d).

3.2.4.3 Results of HFIR Irradiation of PCA and CW 316 (N Lot)

Toward the goal of achieving embrittlement resistance, preirradiation grain boundary microstructures have been varied through several thermal-mechanical treatments designed for the Path A PCA.[1] A table of the sample designations and microstructural descriptions is found elsewhere in this report.[2] A survey of the various microstructural conditions is shown in Fig. 3.2.8. For the samples irradiated in HFIR-CTR-32, the grain boundary structure of PCA-A1 is representative of a precipitate-free grain boundary and would also describe the preirradiation conditions of boundaries in PCA-A2 and -A3 (not illustrated here; see ref. 2) and CW 316 (N lot). Fine grain boundary MC precipitate is produced by heat treating heavily cold-worked material for 2 h at 750°C, shown for PCA-C in Fig. 3.2.8. Coarse grain boundary MC is produced by heat treating SA material for 8 h at 800°C, as shown for PCA-B1 in Fig. 3.2.8, and is also representative of the preirradiation grain boundary structure in PCA-B2.

After HFIR irradiation to about 10 dpa at 300 to 500°C, virtually no additional grain boundary precipitation is observed in CW 316 (N lot) or in PCA-AI, -A2, or -C. The first three materials contained no grain boundary precipitation prior to irradiation, whereas the PCA-C had fine MC present. At 600°C, PCA-A2 and -C still show no evidence of grain boundary precipitation during Irradiation. At 600°C, CW 316 (N lot) and PCA-A1 show evidence of eta (M_6C) and/or tau ($M_{23}C_6$) precipitation at the grain boundaries. The grain boundary precipitates of PCA-A1 and CW 316 (N lot) are shown in Fig. 3.2.9, and their cavity microstructures, together with that of PCA-C, in Fig. 3.2.10.

The coarse grain boundary MC introduced prior to irradiation in PCA-B1 and -B2 remains stable during HFIR irradiation at all temperatures examined. There are occasional grain boundary eta particles in PCA-B1, somewhat similar to PCA-A1 (Fig. 3.2.9), superimposed on the coarse MC. No bubbles were found in PCA-B2. The grain boundary MC is identical for both samples and apparently independent of the large difference in matrix microstructural development (including MC stability) within the grains for these two samples. Precipitation and cavities at the grain boundary are shown in Figs. 3.2.9 and 3.2.10, respectively, for PCA-B1 as well. Grain boundary cavities are not observed in PCA-B1 and -B2 at 500°C or below.

ORNL-PHOTO 1638-82

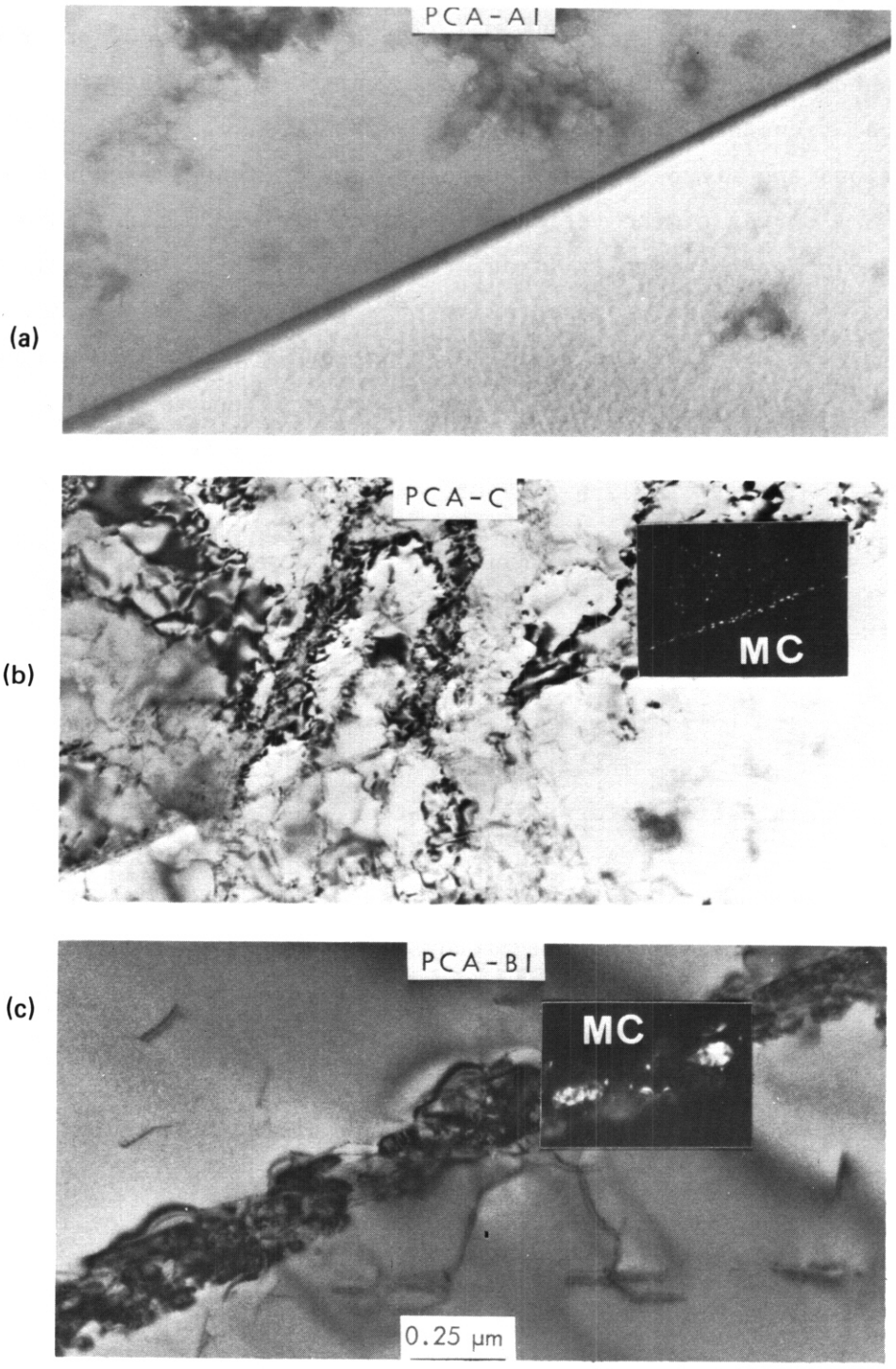

Fig. 3.2.8. A Survey of the Various Preirradiation Grain Boundary Microstructures Developed in the Path A PCA Through Thermal-Mechanical Pretreatment. (a) PCA-A1, solution annealed for 15 min at 1175°C. This clean boundary condition is also representative of PCA-A2 and -A3. (b) PCA-C, 25%-cold-worked and then aged 2 h at 750°C to develop fine grain boundary MC. (c) PCA-B1, solution annealed and then aged for 8 h at 800°C to develop coarse grain boundary MC. Also representative of PCA-B2.

ORNL-PHOTO 1839.82

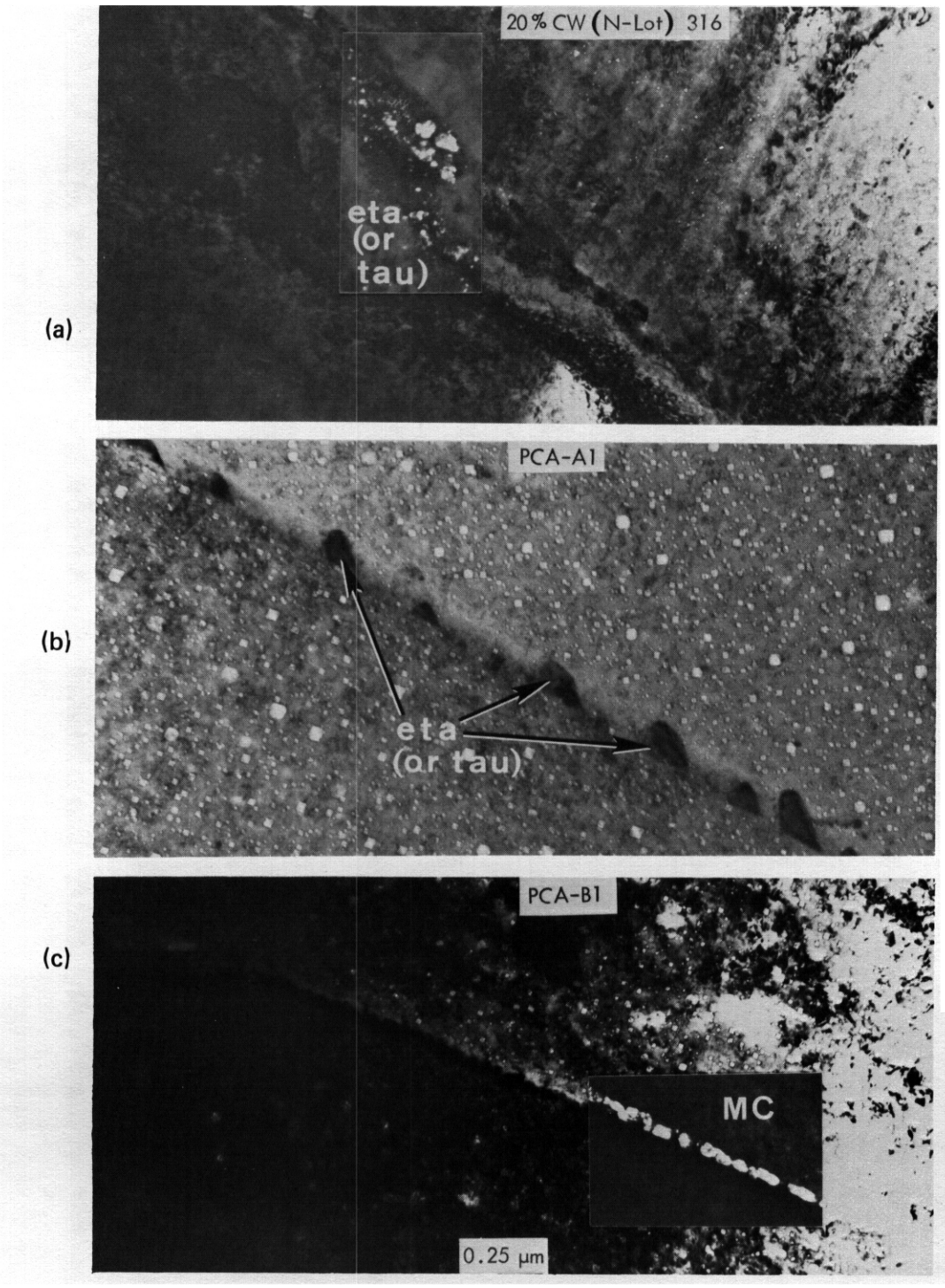

Fig. 3.2.9. A Survey of Grain Boundary Precipitation Microstructure **in** Samples Irradiated **in HFIR** at 600°C to up to 10 dpa and 620 at. ppm He. (a) 20%-cold-worked (N lot) type 316 stainless steel, with a finer, continual distribution of eta (M_6C) and/or tau ($M_{23}C_6$) phase particles (dark-field inlay). (b) PCA-A1, with partial coverage of eta and/or tau at the boundary. (c) PCA-B1, with a continual dispersion of moderate sized MC particles at the boundary (dark-field inlay).

ORNL-PHOTO 1840-82

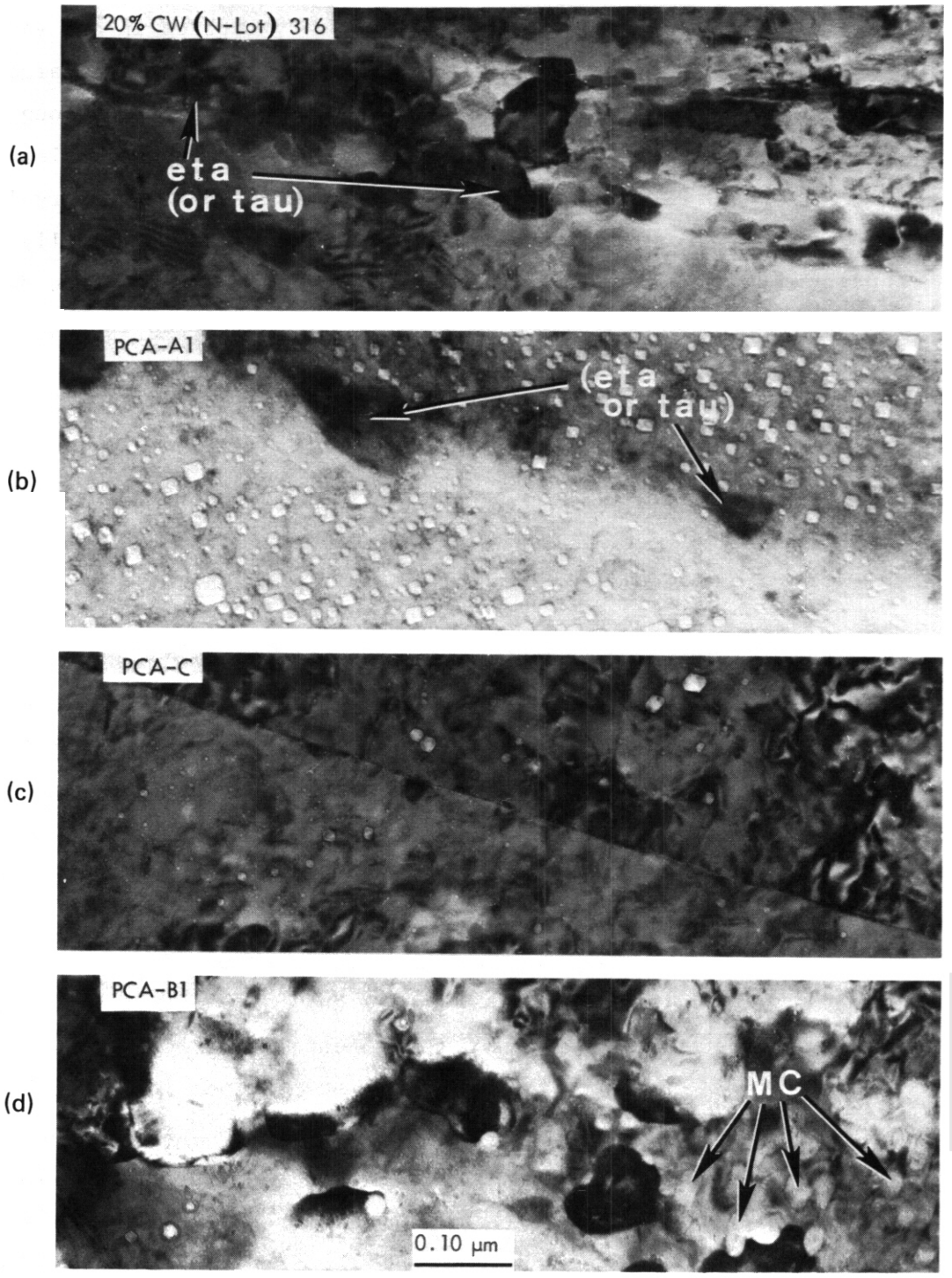

Fig. 3.2.10. A Survey of Grain Boundary Bubble Microstructures Produced by HFIR Irradiation at 600°C to up to 10 dpa and 620 at. ppm He. (a) 20%-cold-worked(N lot) type 316 stainless steel, (b) PCA-AI, (c) PCA-C, and (d) PCA-B1. Note the extremely fine bubble size at the boundary of PCA-B1, which has many MC particles there.

Comparing the grain boundary cavity structures for the several microstructures, Fig. 3.2.10, we see that boundary bubbles in all samples are in general small, with the smallest found in PCA-B1 and the largest in PCA-A1. Both PCA-A1 and -C show continual bubble distribution along the precipitate-free boundary. The CW 316 (N lot) clearly shows bubbles at and between particles along the boundary. Sample PCA-B1 shows very fine bubbles along the interfaces of the many MC particles that virtually cover the boundary, with few bubbles in between. This is similar to the MC interfacial helium trapping observed at matrix MC particles in the R1 heat of CW 316 + Ti.[14]

Coarse grain boundary MC survives in spite of the apparent intragranular MC dissolution that occurs in the PCA at 600°C.[2] Similar titanium-modified steels exhibit MC dissolution or lack of MC formation during EBR-II irradiation at about 500°C and below, *so* that helium may actually be aiding the MC stability in HFIK.[14,15]

3.2.4.4 Discussion

The behavior of grain boundaries in all PCA pretreatments and CW 316 (N lot) are as good as or better than previous results on CW 316 (DO heat) and CW 316 + Ti (R1 heat), for HFIR irradiations at equivalent fluences up to about 450°C. Under these same conditions, swelling resistance of the PCA and CW 316 (N lot) is also as good as or better than CW 316 (DO heat) or CW 316 + Ti (R1 heat), as noted elsewhere.[2]

At 500 and 600°C, the situation begins to reverse. There can be precipitation as well as cavity differences at the boundary that vary from one alloy to another and with pretreatment within any alloy system. During HFIK irradiation at 500 to 550°C, the R1 and DO heats of steel develop grain boundary precipitation of eta and tau in both solution-annealed and 20%-cold-worked conditions. Only PCA-B1 and -B2, with coarser grain boundary MC developed via pretreatment, show any grain boundary precipitation during HFIR irradiation at 500°C. In CW 316 (DO heat), the grain boundary precipitation observed at 525 to 550°C at 10 dpa dissolves by 16 dpa, giving way to the cavitated boundary shown in Fig. 3.2.6. Grain boundary precipitation persists to higher fluence in the CW 316 + Ti (R1 heat) irradiated at 525 to 550°C.[16] The grain boundary bubbles in the CW 316

(DO heat) after 16 dpa at 525 to 550°C in HFIR are larger than in any of the PCAs or CW 316 (N lot) irradiated at 500°C. However, there is no hint of void development in the CW 316 (DO heat), so the swelling resistance is certainly better than in CW 316 (N lot) or the PCA except PCA-A1 (ref. 2). At 625 to 650°C, CW 316 (DO heat) (Fig. 3.2.6) and CW 316 + Ti (R1 heat) have clear grain boundary bubbles that are measurably larger than any of the matrix bubbles, and no grain boundary precipitation is found. The grain boundary microstructures of CW 316 (N lot) and the various PCA microstructures (particularly PCA-B1 and -B2) are clearly better than DO or R1 heats of type 316 stainless steel with regard to bubble size and distribution at the boundary (Figs. 3.2.6 and 3.2.10). However, the swelling of PCA (excluding PCA-A3) and CW 316 (N lot) is greater than that of the CW 316 (DO heat) and CW 316 + Ti (R1 heat). The general observation begins to unfold that the grain boundary microstructure with regard to bubble size and distribution is better when voids are developing in the matrix than when not. This is also the case if we compare PCA-A1, -A2, -C, and CW 316 (N lot). It is also observed in the comparison of grain boundary structures between solution-annealed and CW 316 (DO heat) irradiated in HFIR or EBR-II at higher temperatures (Fig. 3.2.7) and also correlates with tensile properties after HFIR irradiation (at least at 500–550°C test temperature, high fluence) in the case of those same materials.[6] The swelling and void formation are generally greater in the SA type 316 stainless steel than in CW 316. Both PCA-B1 and -B2, with coarser grain boundary MC, are exceptions to this rule. At 600°C PCA-B1 shows the greatest swelling and PCA-B2 the least, and yet the grain boundary microstructure is constant, with an almost undetectably fine bubble dispersion.

On the basis of grain boundary microstructures, none of the PCAs or CW 316 (N lot) show excessive bubble coarseness or growth during HFIR irradiation at 300 to 600°C. From the standpoint of the known beneficial effects of grain boundary precipitation on embrittlement resistance, the CW 316 (N lot) and PCA-B1 and -B2 are good. The coarse grain boundary MC has the finest bubble dispersion associated with it, finer than the CW 316 (N lot). Higher fluence HFIR irradiation will test the stability of the

MC versus the eta and/or tau grain boundary precipitation. From the viewpoint of the design objectives,[1] the coarser grain boundary MC pretreatment is the only successful means of keeping or introducing this phase at the boundary because the MC phase either does not form or dissolves in the other pretreatments. In the other materials, swelling and embrittlement resistance may be tradeoffs. However, in the PCA the coarser grain boundary MC that is developed prior to irradiation, independent of matrix pretreatment, also survives under HFIK irradiation, independent of matrix microstructural development. It may offer the only avenue for obtaining resistance to both embrittlement and void swelling.

3.2.5 Conclusions

1. After HFIR irradiation at 300 to 500°C to 10 dpa, little or no grain boundary precipitation or bubble formation were observed in CW 316 (N lot) or PCA-A1, -A2, or -C.

2. At 600°C, CW 316 (N lot) formed a continual dispersion of eta and/or tau at the grain boundary, and PCA-A1 has widely separated coarse particles of the same phase. Both PCA-A2 and -C show no grain boundary precipitation. All alloy conditions show grain boundary bubble formation, with PCA-A1 having more and larger bubbles than the others.

3. Both PCA-B1 and -B2, which contained coarse grain boundary MC prior to irradiation, maintain the same stable grain boundary structure during HFIR irradiation at 300 to 600°C. At 600°C, only the finest of bubbles are detectable in association with the MC particles at the boundary.

3.2.6 References

1. P. J. Maziasz and T. K. Roche, "Preirradiation Microstructural Development Designed to Minimize Properties Degradation During Irradiation in Austenitic Alloys," J. *Nucl. Muter.* 104(1–3): 797–801 (1981).
2. P. J. Maziasz and D. N. Braski, "Swelling of Path A PCA Irradiated to 10 dpa in HFIR," Sect. 3.1 of this report.

3. E. E. Bloom et al., "The Effect of Irradiation Temperature on Strength and Microstructure of Stainless Steel," *J. Nucl. Mater.* 22(1): 68–76 (April 1967).

4. D. Fahr, E. E. Bloom, and J. O. Stiegler, "Post-Irradiation Tensile Properties of Annealed and Cold-Worked Type 316 Stainless Steel," p. 167–77 in *Irradiation kbrittlement and Creep in Fuel Cladding and Core Components,* British Nuclear Energy Society, London, 1973.

5. E. E. Bloom and J. O. Stiegler, "Effect of Irradiation on the Microstructure and Creep-Rupture Properties of Type 316 Stainless Steel, pp. 360–80 in *Effects of Irradiation on Substructure and Mechanical Properties of Metals and Alloys,* ASTM-STP-529, American Society for Testing and Materials, Philadelphia, 1973.

6. E. E. Bloom and F. W. Wiffen, "The Effects of Large Concentrations of Helium on the Mechanical Properties of Neutron-Irradiated Stainless Steel," *J. Nucl. Mater.* 58: 171–84 (1975).

7. M. L. Grossbeck, J. O. Stiegler, and J. J. Holmes, "The Effects of Irradiation on the Fracture Behavior of Austenitic Stainless Steels," pp. 95–116 in *Radiation Effects in Breeder Reactor Structural Materials,* ed. by M. L. Bleiberg and J. W. Bennett, the Metallurgical Society of AIME, New York, 1977.

8. D. N. Braski, H. Schroeder, and H. Ullmaier, "The Effect of Tensile Stress on the Growth of Helium Bubbles in an Austenitic Stainless Steel," *J. Nucl. Muter.* 83(2): 265–77 (1979).

9. R. L. Fish, N. S. Cannon, and G. L. Wire, "Tensile Property Correlations for Highly Irradiated 20 Cold-Worked Type 316 Stainless Steel," pp. 450–65 in *Effects of Radiation on Structural Materials,* ASTM-STP-683, American Society for Testing and Materials, Philadelphia, 1979.

10. E. E. Bloom et al., "Temperature and Fluence Limits for a Type 316 Stainless Steel Controlled Thermonuclear Reactor First Wall," *Nucl. Technol.* 31: 115–22 (October 1976).

11. E. E. Bloom, "Mechanical Properties of Materials in Fusion Reactor First-Wall and Blanket Systems," *J. Nucl. Mater.* 85&86(II,B): 795–804 (December 1979).

12. P. J. Maziasz and E. E. Bloom, "Mechanical Properties of Type 316 and Titanium-Modified Type 316 Stainless Steel Irradiated in HFIR," *ADIP Quart. hog. Rep. August 31, 1978,* DOE/ET-0058/1, pp. 54-81.

13. D. Fahr, *Analysis of Stress-Strain Behavior of Type 316 Stainless Steel,* ORNL-TM-4292 (November 1973).

14. P. J. Maziasz, "Helium Trapping at Ti-Rich MC Particles in Ti-Modified Austenitic Stainless Steel," pp. 477-92 in *Phase Stability During Irradiation,* (Proc. Symp. Pittsburgh, Oct. 5—9, 1980), J. R. Holland, L. K. Mansur, and D. I. Potter, eds., The Metallurgical Society of AIME, Warrendale, Pa., 1981.

15. E. H. Lee, P. J. Maziasz, and A. F. Rowcliffe, "The Structure and Composition of Phases Occurring in Austenitic Stainless Steels in Thermal and Irradiation Environments," pp. 191-218 in *Phase Stability During Irradiation* (Proc. Symp. Pittsburgh, Oct. 5—9, 1980), J. R. Holland, L. K. Mansur, and D. I. Potter, eds., The Metallurgical Society of AIME, Warrendale, Pa., 1981.

16. P. J. Maziasz and M. L. Grossbeck, "Microstructural Development in 20%-Cold-Worked Type 316 Stainless Steel and Titanium-Modified Type 316 Stainless Steel Irradiated in the HFIR: Fluence Dependence of the Cavity Component, *ADIP Quart. Prog. Rep. March 31, 1981,* DOE/ER-0045/6, pp. 28—56.

3.3 FATIGUE LIFE AT 650°C OF 20%-COLD-WORKED TYPE 316 STAINLESS STEEL IRRADIATED IN THE HFIR AT 550°C — M. L. Grossbeck and K. C. Liu (Oak Ridge National Laboratory)

3.3.1 ADIP Task

ADIP Task I.B.5, Stress–Strain Controlled Fatigue of Austenitic Alloys.

3.3.2 Objective

This study evaluates the effects of simultaneous displacement damage and helium production during irradiation on the low–cycle fatigue life of 20%-cold-worked type 316 stainless steel. The effect of testing at a temperature 100°C higher than the irradiation temperature is investigated.

3.3.3 Summary

Strain controlled fatigue tests were performed in vacuum at 650°C on 20%-cold-worked type 316 stainless steel irradiated in the HFIR at 550°C. Fluences ranged from 0.85 to 1.4 $\times 10^{26}$ neutrons/m^2. Little effect of irradiation was observed, but testing at 650°C failed to show the 10^7-cycle endurance limit observed at 550°C.

3.3.4 Progress and Status

3.3.4.1 Introduction

Since tokamak fusion reactors may operate in a cyclic mode, fatigue of the first wall and blanket structures is a concern. Previous work has examined the effect of simultaneous atomic displacement damage and helium production of fatigue life.[1,2] However, recent studies have raised the possibility of very serious effects on materials during plasma disruptions.[3] Although plasma disruptions are predicted to cause surface melting under certain conditions, armor for the first wall will protect the load–bearing structures. However, such a severe thermal pulse is likely to cause large thermal stresses, again raising the concern for fatigue failure, but now at temperatures higher than the normal operating temperature. Since severe embrittlement has been observed in nickel

alloys tested approximately 100°C above the irradiation temperature,[4] this increment was chosen for testing. Specimens irradiated at 550°C were tested at 650°C.

3.3.4.2 Experimental Procedure

Hourglass specimens with minimum gage diameters of 3.18 mm (0.125 in.) were irradiated in peripheral target positions of the High Flux Isotope Reactor (HFIR). A helium environment was used with a gas gap insulating the specimen to provide the elevated temperature. Details of the irradiation have been previously reported.[5] Testing was performed with a remote servo-hydraulic testing machine equipped for elevated-temperature testing in vacuum. A fully reversed ramp function providing a strain rate of 4×10^{-4}/s was used. Strain was measured at the minimum cross section with a diametral extensometer with ceramic blades and a linear variable differential transformer (LVDT). The diametral signal in turn was converted to an equivalent axial strain through a strain computer for machine control. Details of testing have been previously reported.[2,6]

Following failure, fracture surfaces were studied with a scanning electron microscope (SEM). Results of the fracture studies are incomplete and will be reported subsequently.

3.3.4.3 Results and Discussion

Results of the fatigue tests for both irradiated and unirradiated specimens appear in Table 3.3.1 and are plotted in Fig. 3.3.1. The curves in Fig. 3.3.1 show no significant difference between specimens irradiated at 550°C and tested at 650°C and unirradiated specimens tested at 650°C. However, there were some significant differences observed in the high cycle regime between specimens tested at 550°C and those tested at 650°C. At 550°C an endurance limit (10^7 cycle criterion) was observed at a total strain range of $\Delta\varepsilon_t$ = 0.35% for unirradiated specimens and $\Delta\varepsilon_t$ = 0.30% for irradiated specimens.[1] However, at a test temeperature of 650°C a similar endurance limit at these strain range levels was not observed. All specimens tested at 650°C fractured.

Table 3.3.1. Irradiation and Fatigue Test Parameters for 20%-Cold-Worked Type 316 Stainless Steel Irradiated in the HFIR and Tested at 650°C

Specimen	Fluence (E > 0.1 MeV) (neutrons/m^2)	dpa	Helium (at. ppm)	Total Strain Range (%)	Cycles to Failure
G48	0			2.0	1,462
G47	0			1.0	6,985
AA20	0			1.0	10,354
G37	0			0.70	48,354
AA21	0			0.50	185,000
G36	0			0.30	6,000,000
G62	0			0.25	16,224,790
A79	1.0×10^{26}	7.7	310	2.0	780
A84	1.4×10^{26}	11.0	500	1.0	6,730
A91	1.4×10^{26}	11.0	500	0.50	175,725
A70	0.85×10^{26}	6.6	240	0.35	1,033,800
A77	1.2×10^{26}	9.0	400	0.30	2,500,000

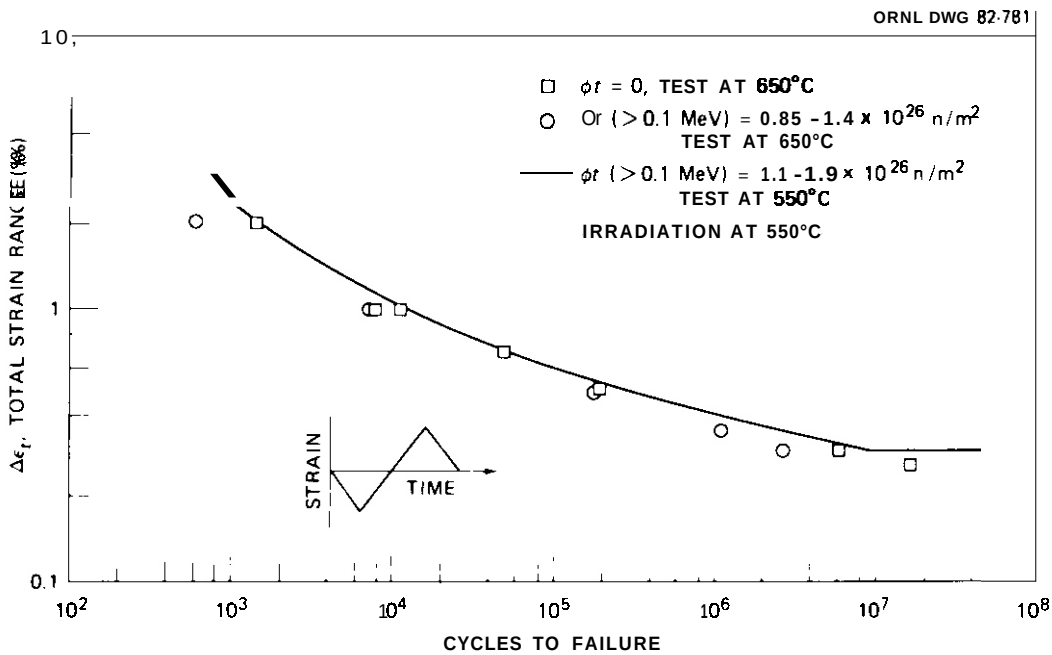

Fig. 3.3.1. Cycles to Failure as a Function of Total Strain Range for 20%-Cold-Worked Type 316 Stainless Steel. Specimens were irradiated in HFIR at 550°C. The solid line represents data from specimens irradiated and tested at 550°C. The horizontal portion of the curve indicates the 550°C endurance limit at $\Delta\varepsilon_t$ = 0.3%.

The absence of an endurance limit or shift to lower strain range values may be a consequence of environmental effects even under the vacuum conditions used in this experiment (10^{-7}–10^{-4} Pa). At 650°C oxide formation on the newly formed fatigue crack surfaces may be sufficiently rapid to prevent rewelding. However, the environment may have an influence prior to crack nucleation. Fresh surfaces formed by intrusion and extrusions may be susceptible to oxygen attack, thus providing nuclei for fatigue cracks. The thermodynamics of the oxide film is now being investigated to determine stability of the oxide film with respect to dissolution.

3.3.5 Conclusions

The low cycle fatigue life of 20%-cold-worked type 316 stainless steel irradiated at 550°C and tested at 650°C appears unchanged from unirradiated material tested at 650°C. For irradiation to 11 dpa and 500 at. ppm He, this indicates that, unlike certain nickel-base alloys, serious embrittlement and fatigue life reduction do not occur. However, the absence of a 10^7 cycle endurance limit at 650°C raises a concern over the effect of environment on the life of the fusion reactor first wall and blanket structures. The effect of oxygen is dependent upon temperature, partial pressure, and exposure time. For materials in contact with liquid lithium, the oxygen partial pressure is expected to be sufficiently low to prevent oxygen attack. However, in structures in contact with other coolants, the slow duty cycles of actual machines may permit oxygen attack with resultant reduced fatigue failure at or above temperatures of 650°C. Further research is being done in this area with investigation of cyclic hold periods. At the present time, sustained operation of type 316 stainless steel at 650°C and higher is not recommended.

3.3.6 References

1. M. L. Grossbeck and K. C. Liu, "High Temperature Fatigue Life of Type 316 Stainless Steel Containing Irradiation Induced Helium," *J. Nucl. Mater.* 103&104: 853–57 (1981).

2. M. L. Grossbeck and K. C. Liu, "Fatigue Behavior of Type 316 Stainless Steel Irradiated in a Mixed Spectrum Fission Reactor Forming Helium," to be published in *Nuclear Technology*.

3. C. A. Flanagan et al., *Initial Trade and Design Studies for the Fusion Engineering Device*, ORNL/TM-7777 (1981).

4. A. F. Rowcliffe and 3. A. Horak, "Tensile Properties and Fracture Behavior of Irradiated Nickel Alloys," *Am. Nucl. Soc.* 38: 266–67 (1981).

5. M. L. Grossbeck and M. J. Kania, "HFIR Irradiation of Hourglass Fatigue Specimens," *ADIP Quart. Prog. Rep. June 30, 1978*, DOE/ET-0058/2, pp. 20–35.

6. K. C. Liu and M. L. Grossbeck, "Status of Fatigue Testing Facility," *ADIP Quart. Prog. Rep. June 30, 1978*, DOE/ET-0058/2, pp. 54–59.

3.4 IRRADIATION RESPONSE OF RAPIDLY SOLIDIFIED PATH A TYPE PRIME CANDIDATE ALLOYS — D. Imeson, C. Tong, M. Lee, J. B. Vander Sande and O. K. Harling (Massachusetts Institute of Technology)

3.4.1 ADIP Task

Task I.C.5, Microstructure and Swelling of Special and Innovative Materials.

3.4.2 Objective

The objective of this study is to present a first assessment of the microstructural response to neutron irradiation shown by Path A alloys prepared by rapid solidification processing. To more fully demonstrate the potential of the method, alloys with increased titanium and carbon content have been used in addition to the Path A prime candidate alloy.

3.4.3 Summary

The microstructural irradiation response of the Path A prime candidate alloy and two similar alloys with increased titanium and carbon content prepared by rapid solidification processing, has been investigated by neutron irradiation to 8.5 dpa (360 appm He) in the HFIR, and by dual ion irradiation to much higher dose (>100 dpa). The results show minor differences between conventionally prepared PCA and PCA prepared by rapid solidification techniques. However, these differences and the characteristic features of the response, the formation of very high densities of small cavities or bubbles and changes in the composition of initially existing TiC particles, are explained by a hypothesis of much importance to the rapid solidification approach. Our results suggest that increasing concentrations of titanium and carbon are beneficial, but only if the elements are initially in solution or present as very small (~ 2 nm) particles of TiC. The only way to practically achieve this for higher TiC contents than in PCA, is by using rapid solidification processing.

3.4.4 Progress and Status

3.4.4.1 Introduction

It has now been demonstrated that void swelling in irradiated Type 316 austenitic stainless steel is considerable, even at relatively low doses.' As the irradiation proceeds, the matrix is depleted in nickel content because of its segregation to vacancy sinks and precipitation as a component in one or more of several possible phases, some only stable under irradiation[2]. In addition, large intergranular $M_{23}C_6$ and MC phases form at lower temperatures, while at higher temperatures the grain boundaries contain a large number of very large cavities[3]. Both effects are seriously deleterious for the mechanical properties of the material, adding to the problem of intragranular cavity swelling, which becomes increasingly more severe as the matrix nickel is reduced. It has been shown[4] that the cavity swelling is generally reduced by the addition of a small amount (0.23 wt%) of titanium to the 316 steel, but that the grain boundary problems remain. The consequent metallurgical modification of this material carried out at ORNL, lowering both Ni and Cr content, gives the Prime Candidate Alloy (PCA) in the Path A approach to alloy development for fusion reactors[5]. The detailed evaluation of this material under neutron irradiation has only recently begun (a 10 dpa HFIR irradiation studied by ORNL is discussed in this report). Our initial results[6] indicate that there is indeed a much improved grain boundary response to irradiation.

The history of improved irradiation response outlined above has been achieved by control of the composition and starting microstructure of the material, in order to beneficially affect future microstructural and microchemical changes. Rapid solidification processing (RSP) is capable of producing a wide range of metastable alloy states, offering substantial control of elemental composition and distribution in the matrix and in other phases, including states that cannot be achieved by conventional methods. RSP could thus be a valuable tool in achieving the optimum composition and microstructure, whereby the best irradiation response for a particular type of alloy could be attained. This report

is concerned firstly with investigating the irradiation response of the PCA alloy when prepared by rapid solidification methods as compared to when prepared by conventional means. It is also concerned with the irradiation response of some modified alloys prepared by RSP that may more clearly show the potential of the RSP technique. Lastly, the optimum microstructure and composition for these alloys is far from being well understood, and results such as these may eventually add a little to that understanding.

We should make it clear before proceeding that although the final arbiter of "irradiation response" must be the change in the bulk mechanical properties, these bear an intimate relationship to microstructure and microchemistry, wherein lies an understanding of the mechanical properties. We shall here be concerned only with the microstructural and microchemical response brought about by irradiation and not at all with mechanical property measurements (which are, however, being pursued as a separate part of our total effort).

3.4.4.2 Experimental and Irradiation Procedures

Prime Candidate Alloy, in ingot form, was provided by Oak Ridge National Laboratory[7], with composition in w/o: Ni 16.6, Cr 14.3, Mo 1.96, Mn 1.62, Si 0.53, Ti 0.32, C 0.046, Co 0.015, P 0.014, N 0.008, S 0.002, Fe bal. This material was rapidly solidified from the melt by means of a roller quencher to thin foils which were then hot extruded at 1040°C. The alloy was subsequently cold worked and recrystallized by annealing at 850°C, to form the Alloy PA-1. PA-2 and PA-3 alloys were similarly prepared except that extra titanium and carbon was added to the PCA melt to double and to triple, respectively, the TiC content. The materials were irradiated either as-annealed, or annealed plus cold work to 20% reduction in area, except in the case of PCA used in the dual ion irradiations to be described, where as-solution-annealed at 1150°C and annealed plus cold work to 25% R.A. material was used (as provided by ORNL).

Our primary irradiation test is by neutron irradiation in one of a number of research reactors. The results to be described for PCA based materials show the response to irradiation in the High Flux

Isotope Reactor at Oak Ridge, at nominal temperatures of 500°C and 600°C, and to 6.2 dpa (210 appm He) or 8.5 dpa (360 appm He). [There are indications from temperature calibrations made at ORNL that these temperatures are too high by 50-75°C.] In addition to these neutron irradiations, some results will be described of examination of samples irradiated simultaneously with 4.8 MeV Fe and 0.2-0.4 MeV He ions at ORNL, to a range of doses exceeding 100 dpa maximum at 550°C and 650°C. These irradiations will be referred to as either 'neutron' irradiation or 'ion' irradiation, for brevity.

Specimens were prepared for electron microscopical examination using standard electropolishing procedures, following, in the case of ion irradiations, electrochemical removal of 0.7 ± 0.05 μm of material from the irradiated surface (which was polished prior to irradiation). Specimens were examined in either a Siemens Elmiskop 101, or a JEOL 200CX TEM. Analytic microscopy was performed using a VG HB5 STEM.

3.4.4.3 Void Swelling in PA-1 and PCA Alloys

Use of both neutron and ion irradiations. In this section, and throughout, results of studies performed on specimen8 from both the neutron and ion irradiations will be described. The reason for the use of ion irradiation data here is to provide some information about the high dose irradiation response, supplementing the information available from the more important, but far lower dose, neutron irradiations. We do not wish to justify mixing results in this way on the basis that the ion irradiations adequately simulate neutron irradiation to higher doses, but rather because we are concerned mostly with comparative responses between materials. The results will be clearly separated and attributed to the appropriate irradiation in every case. However, the general features of the microstructures observed suggest that the same fundamental mechanisms operate in both cases, and therefore that comparison of materials response at high ion doses has some relevance. An important possible exception to this is the observation of microchemical changes during ion irradiation, described in detail below. There is insufficient evidence yet available from neutron irradiation testing to confirm the presence or absence of similar changes. Since studies in other materials suggest a different behavior

during neutron irradiation,[9] the response to ion irradiation at very high doses (100 dpa, here), which depends strongly on earlier microchemical changes, will not be discussed.

Examination and comparison of RS and conventionally processed alloys. A basic objective in this work is the comparison of the irradiation performance of the rapidly solidified PA-1 with that of the conventionally processed PCA. At the low dose levels presently attained and studied in the neutron irradiation tests, there do not appear to be large differences in microstructure between the two materials. Neither does the response to ion irradiation differ noticeably, at doses up to about 50 dpa, in terms of cavity population. However, there is observed some difference in microchemical behavior under ion irradation and in the cavity population development at higher doses ($\sim$100 dpa). Because these phenomena are almost certainly linked, and because of the uncertainty about whether the microchemical effects are reproduced in neutron irradiations, we shall not consider further the ion irradiations to doses higher than about 50 dpa. We describe the microchemical effects in Section 3.4.4.4 below. Figures 3.4.1 through 3.4.5 illustrate the similarity of the PA-1 and PCA response, and these will now be described in detail.

Figures 3.4.1 and 3.4.2 show microstructures of the alloys after neutron irradiation at 500°C and 600°C to 6.2 dpa (210 appm He), and at 500°C to 8.5 dpa (360 appm He), respectively. The samples were placed in the reactor in the as-annealed state. Data is also available for samples irradiated at 300°C and 400°C, but neither show any cavity swelling, just a high density of faulted dislocation loops. These loops are also seen at the higher temperatures, with density decreasing and size increasing with temperature so that at 600°C they do not form a large component of the total dislocation density. Cavities are evenly distributed throughout the specimens examined, with density, average size and the calculated volume fraction swelling given in Tables 3.4.1 and 3.4.2 for the 6.2 dpa irradiation. Although some differences between the two alloys can be inferred from the figures and tables, it is difficult to confer statistical significance to these small variations. Prior to irradiation the PA-1 alloy contained

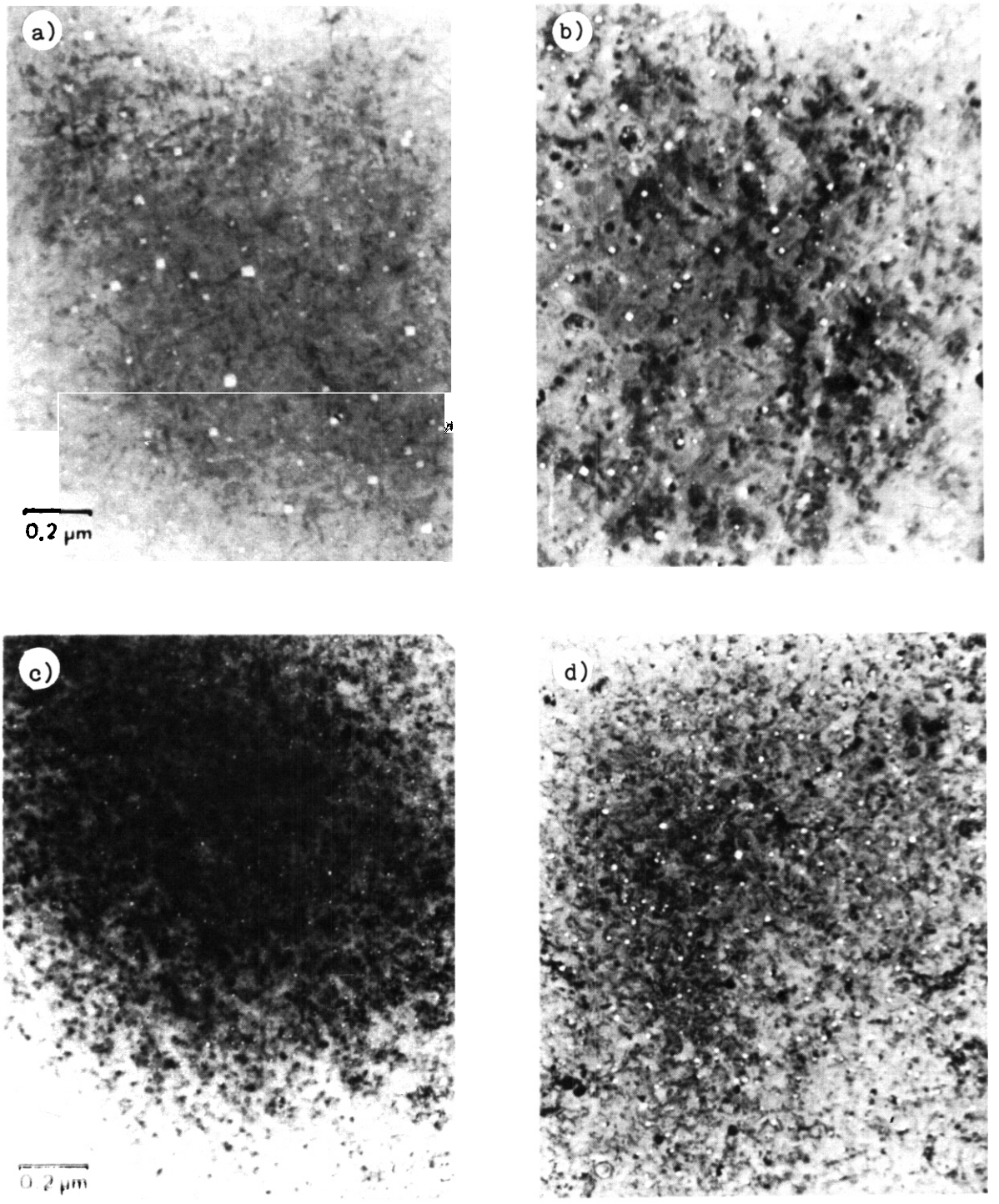

Fig. 3.4.1. Micrographs illustrating the void population observed in neutron irradiated annealed PA-1 and PCA alloys. Foil thicknesses are similar in each case. Dose 6.2 dpa, 210 appm He. (a) PCA irradiated at 600°C, (b) PA-1 at 600°C, (c) PCA at 500°C, (d) PA-1 at 500°C.

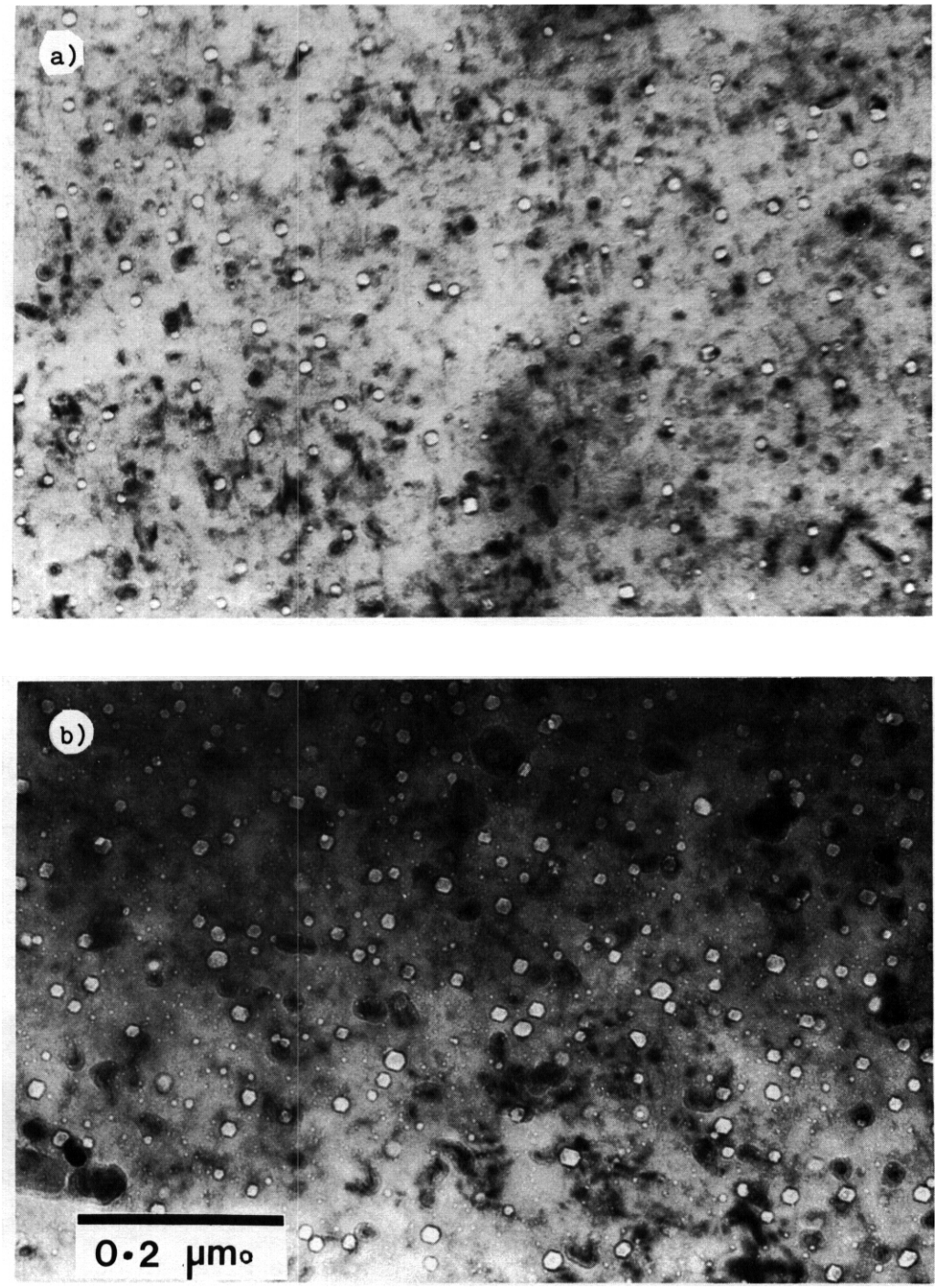

Fig. 3.4.2. The micrographs show void population in (a) annealed PCA and (b) PA-1 alloys after neutron irradiation to 8.5 dpa, 360 appm He, at 500°C.

Table 3.4.1. Quantitgtive Analysis of Void Size and Density at 500 C, 6.2 dpa, 210 appm He

ALLOY	Average Size (diameter) in nm	Density X $10^{21} m^{-3}$	Swelling $\Delta V/V$ %
PA-1, Ann.	7.5 ± 0.5	2.7 ± 0.8	0.09
PCA, Ann.	6.0 ± 0.3	3.6 ± 0.9	0.05
PA-1, CW	6.0 ± 0.7	1.5 ± 0.5	0.036
PCA, CW	5.0 ± 0.7	2.0 ± 0.5	0.026

Table 3.4.2. Quantitgtive Analysis of Void Size and Density at 600 C, 6.2 pda, 210 appm He

ALLOY	Average Size (diameter) in nm	Density X $10^{21} m^{-3}$	Swelling $\Delta V/V$ $
PA-1, Ann.	8.2 ± 1.0	1.3 ± 0.3	0.09
PCA, Ann.	11.0 ± 1.5	1.0 ± 0.3	0.17
PA-1, CW	8.5 ± 2.0	0.06 ± 0.05	0.002

a high density (approximately 1 x 10^{21} m^{-3}) of TiC particles, as confirmed by analytical electron microscopy, with average size of about 16.0 nm[8]. After neutron irradiation the particles still contain a high percentage of titanium. The particles have also become enriched to some extent in the elements Mo and Ni, however, as shown by energy dispersive X-ray analysis. Their size has not changed significantly nor, apparently, has their density, although this is very difficult to determine due to their not being coherent, their small size, and the complexity of the microstructure. Further discussion is given in Section 3.4.4.4 below.

Figure 3.4.3 shows the microstructure obtained after neutron irradiation of samples cold worked before irradiation, to 6.2 dpa at 500°C. As shown in Table 3.4.2, the cavity density at 600°C was very low. Few dislocation loops were seen in the cold worked samples. Again there

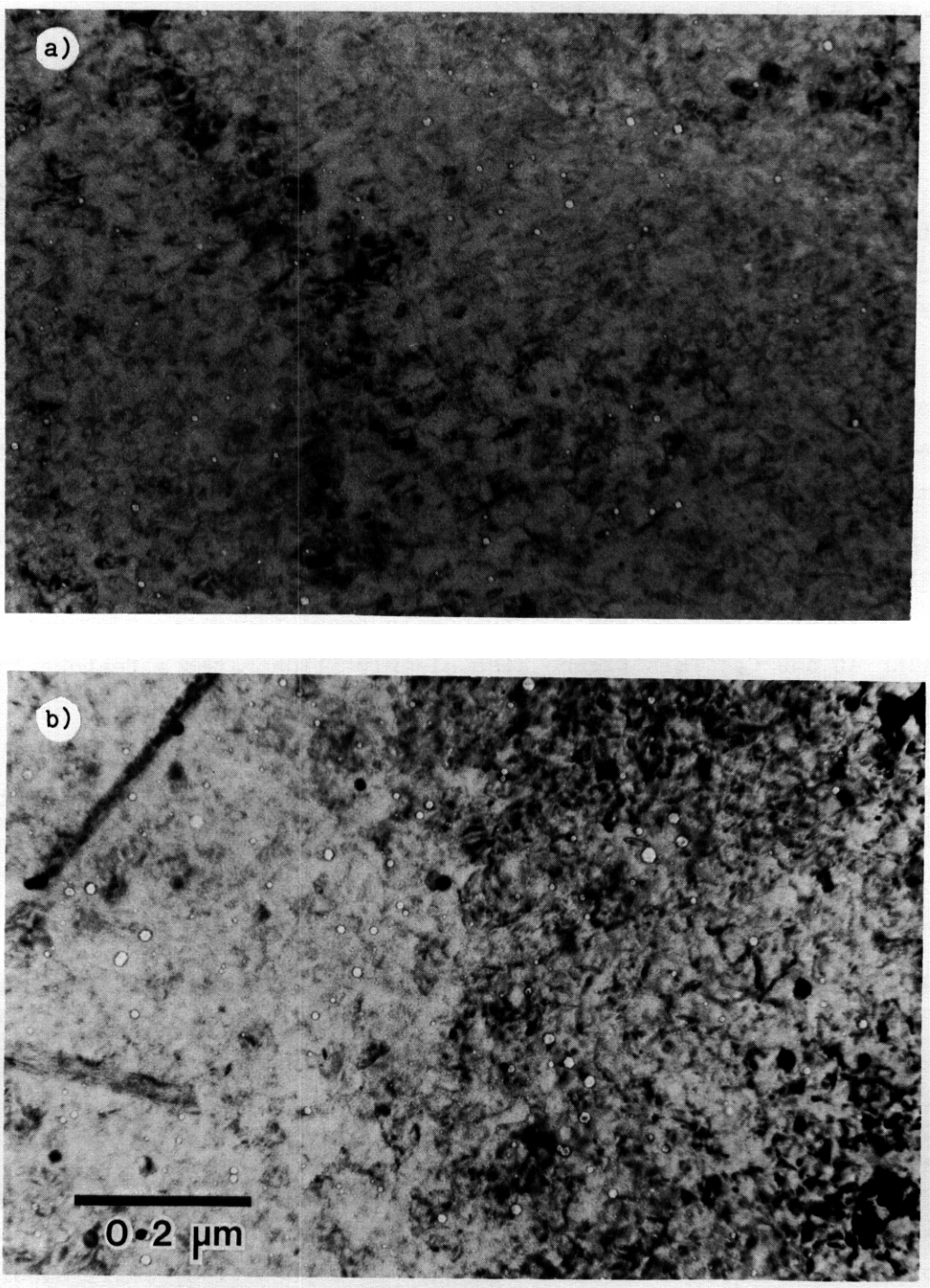

Fig. 3.4.3. Micrographs comparing void populations in 20% cold worked (a) PCA and (b) PA-1 alloys neutron irradiated at 500°C. Dose 6.2 dpa, 210 appm He.

are no marked differences between the PA-1 and PCA alloys. Additional results and discussion on the 6.2 dpa neutron irradiations have been published[6], including the observation that there does not exist significant cavity swelling at grain boundaries in any of these materials at this dose, which was a primary concern in the alloy design.

Figures 3.4.4 and 3.4.5 show microstructures of PA-1 and PCA alloys, both cold worked prior to irradiation, after ion irradiation to about 50 dpa (760 appm He) at 550°C and to about 35 dpa (587 appm He) at 650°C. At 550°C, the cavity populations are seen to be quite similar, as is the dislocation density. A large number of particles can be seen to exist in the PA-1 alloy, as compared with only a few for the PCA alloy. These particles are irradiation induced, having a different composition from the initial TiC. This will be discussed further below. The particle density can vary quite widely between different areas of the sample, and these particles are often associated with voids.

As shown in Figure 3.4.5, the cavity populations are also quite similar at 650°C. This figure also clearly illustrates a feature common to all the microstructures examined. There exist a very large number of small cavities in all of the samples, from both neutron and ion irradiation, with sizes extending down to the practical resolution limit of approximately 1.0-1.5 nm. It is difficult under these circumstances to obtain a reliable estimate of the true void density. This bimodality in the cavity size distribution is clearly shown in Figure 3.4.6. The small cavities or bubbles (of helium) are often apparently associated with particles, but particularly appear to line up along dislocations of the network.

3.4.4.4 Particles and Microchemistry

The ability of the titanium modified Type 316 steels to resist swelling during neutron irradiation has been accounted for by the action of titanium carbide particles[9]. In this interpretation, small bubbles form at the titanium carbides and accommodate helium, preventing or reducing the rate of void nucleation elsewhere. The particles are therefore of central interest, both in elucidating their role in more detail, and in terms of their stability under irradiation. We shall consider this second question first.

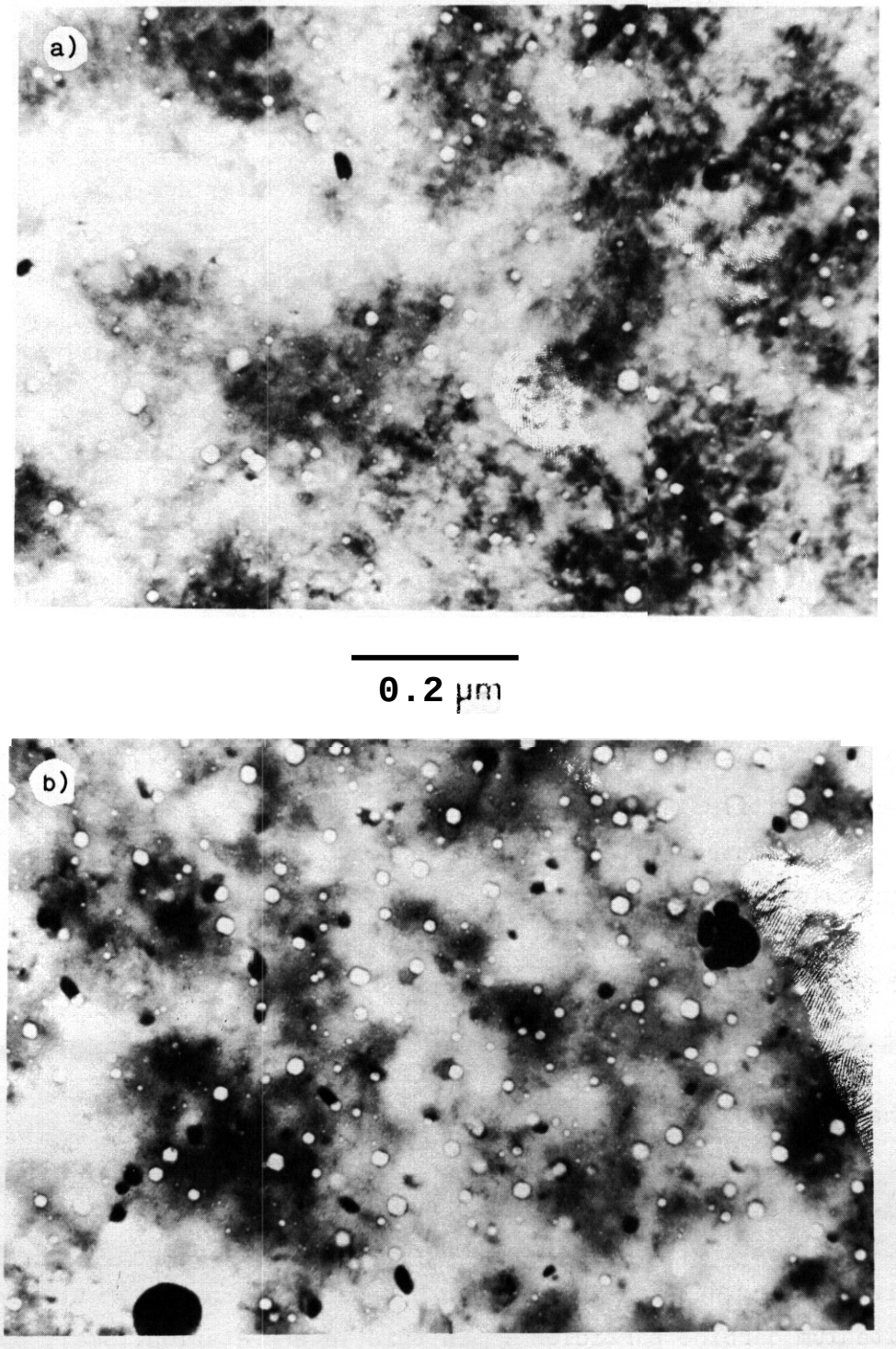

Fig. 3.4.4. The micrographs show void populations after dual ion irradiation to about 50 dpa at 550 °C, and compare (a) cold worked PCA (52 dpa, 760 appm He) with (b) cold worked PA-1 (49 dpa, 760 appm He).

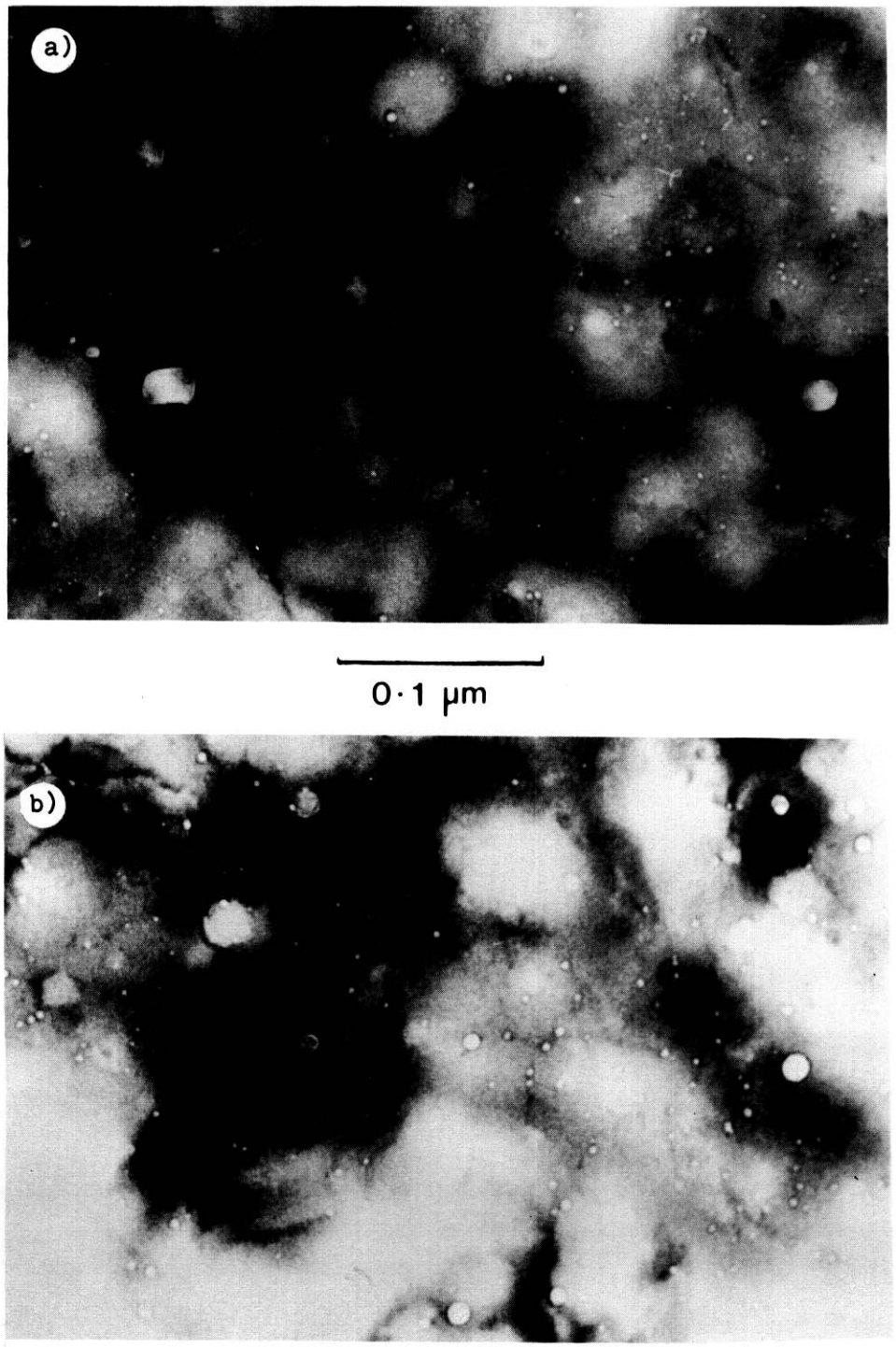

Fig. 3.4.5. Void populations after dual ion irradiation at 650°C, comparing (a) cold worked PCA (33 dpa, 587 appm He) with (b) cold worked PA-1 (38.5 dpa, 587 appm He).

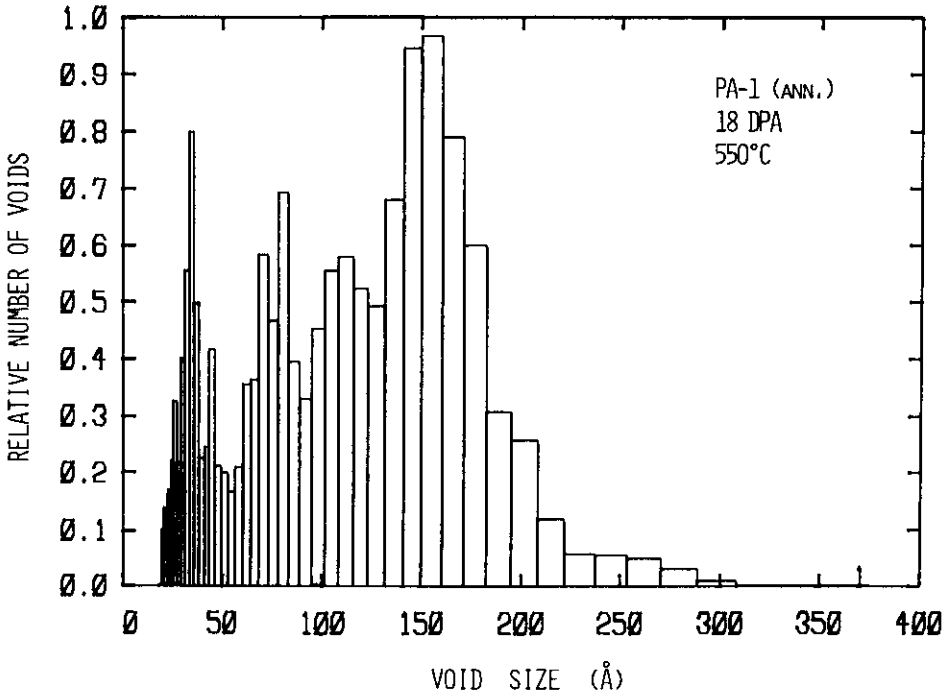

a)

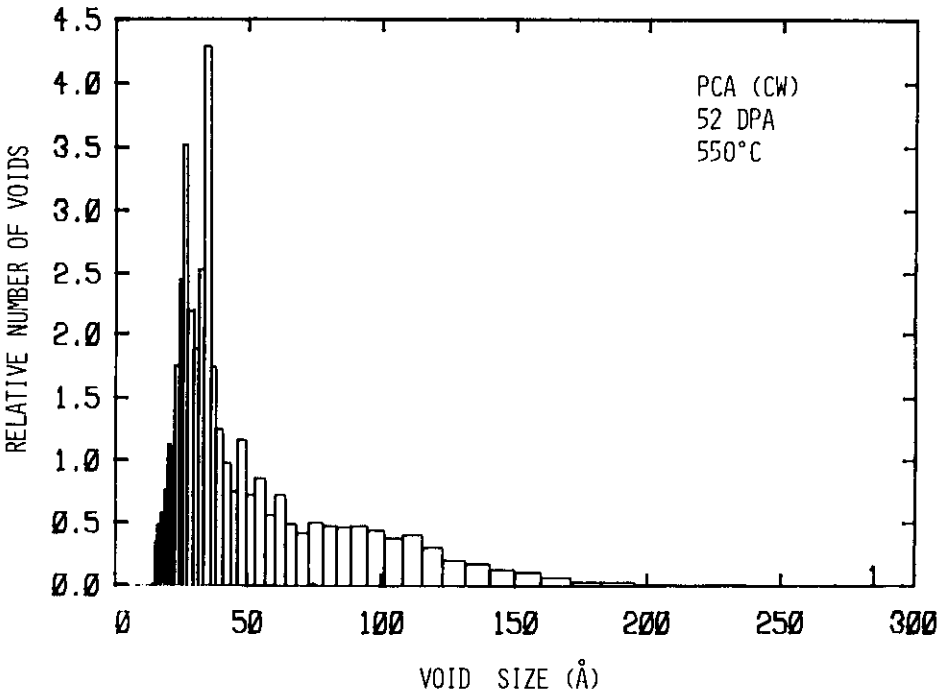

b)

Fig. 3.4.6. Caption overpage

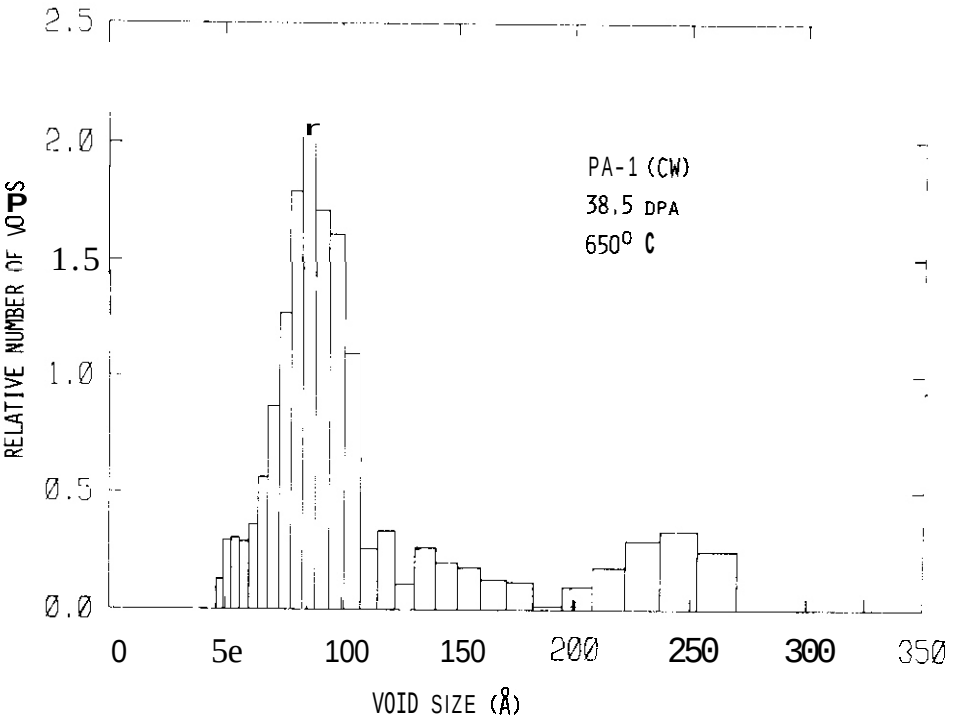

c)

Fig. 3.4.6. Void size distributions measured in three samples with differing ion irradiation and material conditions. Note that all show a bimodal distribution, most pronounced at the higher temperature. (a) PA-1 annealed, irradiated to 18 dpa, 259 appm He at 550°C, (b) PCA cold worked, irradiated to 52 dpa, 700 appm He, at 550°C, and (c) PA-1 cold worked, irradiated to 38.5 dpa, 587 appm He, at 650°C.

In previously published work" the observation was reported that previously existing, TiC particles are dissolved after ion irradiation of PA-1 alloy to about 50 dpa at 550 and 650°C, while a nickel and silicon rich phase has precipitated out. No small (< 50 nm) Ti rich particles were found. In the previous study, the only other data obtained were after 7 dpa ion irradiation, when the original TiC particles were found to be little changed apart from an enrichment in Mo. Further results have now been obtained at the intermediate doses of 18.1 dpa and 38.5 dpa, both at 550°C. At 18 dpa the particle composition as determined by energy dispersive X-ray analysis includes mostly Ti but also Mo and a significant amount of Ni. Figure 3.4.7 compares the spectra obtained, in situ, from a typical particle with that from the matrix nearby. At 38.5 dpa, the nickel content has risen substantially, and some silicon can now be detected, as can be seen in Figure 3.4.8. In

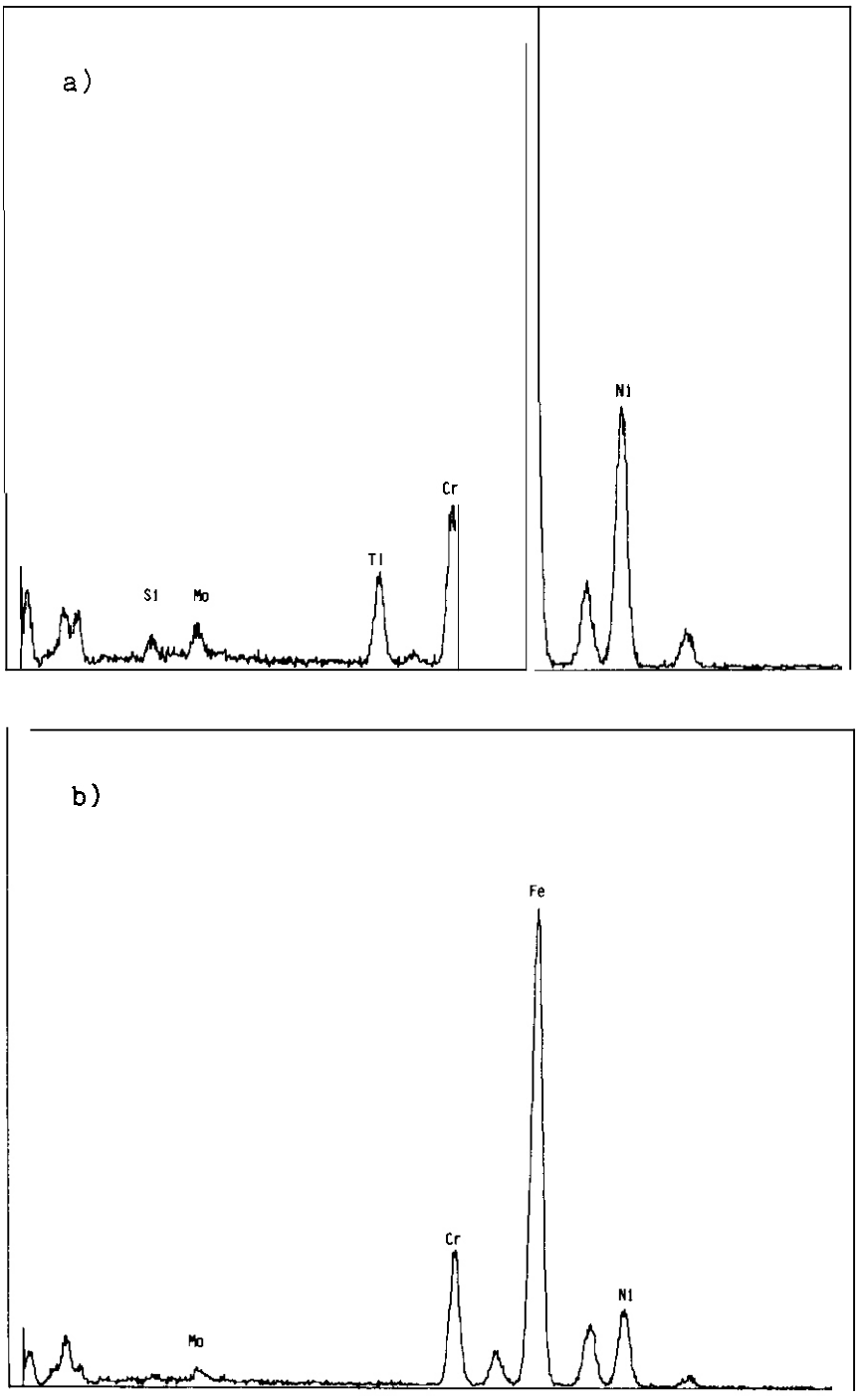

Fig. 3.4.7. X-ray energy dispersive spectra of (a) a small particle and the surrounding matrix and (b) the nearby matrix alone, in cold worked **PA-1** alloy ion irradiated to 15.6 dpa, 288 appm He, at 650°C. Note the presence of increased Ni, Mo, and Si peaks from the particle, as well as the Ti peak showing it was originally TiC.

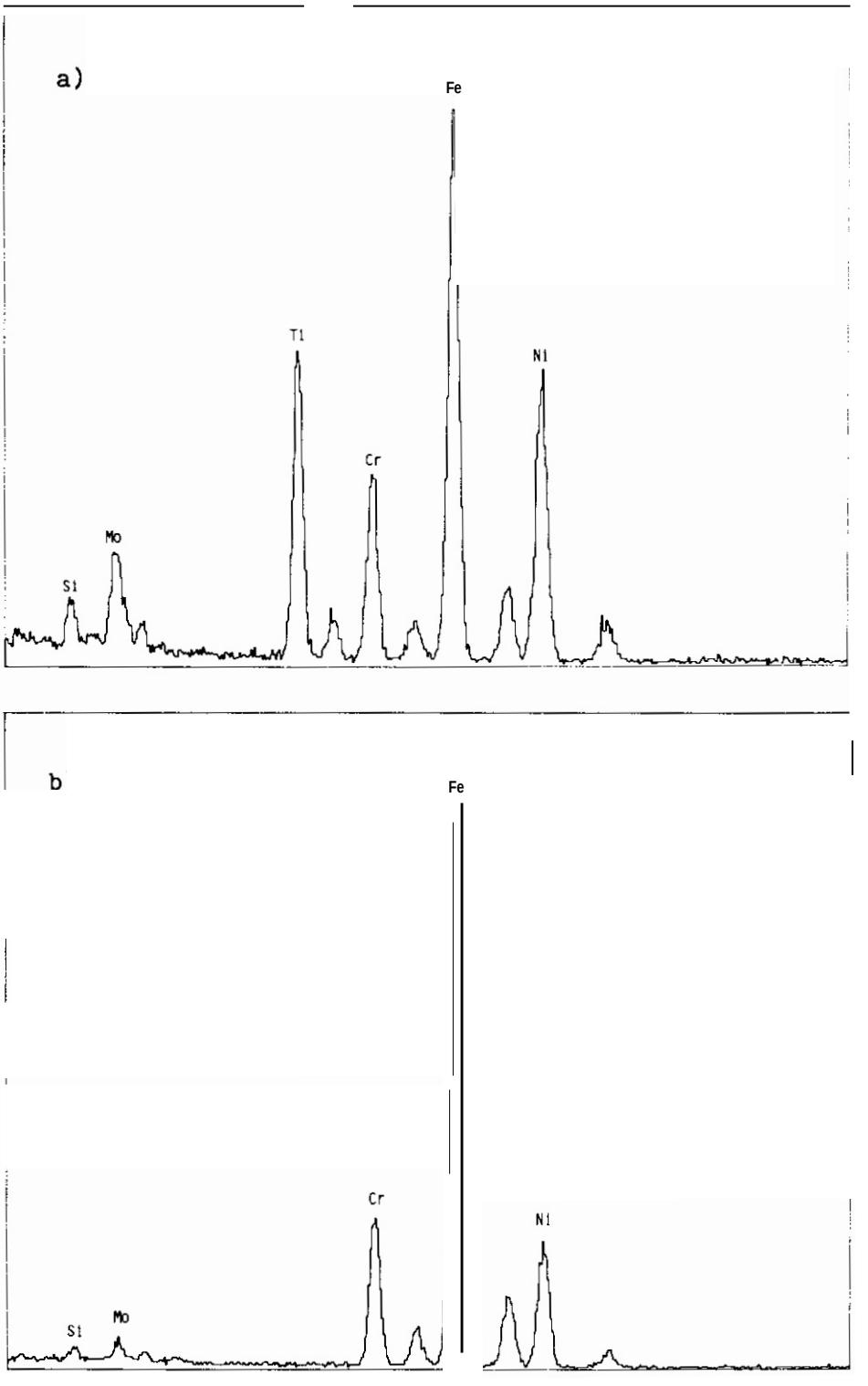

Fig. 3.4.8. As for Figure 3.4.7, except that now ion irradiation has been carried out to higher dose, 38.5 dpa and 587 appm He. (a) spectrum from particle and matrix and (b) spectrum from the matrix alone. Irradiation temperature 650°C.

this specimen it was observed that the larger the particle, the larger was the Ti fraction. It was also noticed, however, that there appeared to be a much lower density of particles in this specimen. These results show that the particles initially present gradually change composition toward a Ni and Si rich phase. This might be achieved either by diffusional replacement of atoms or by nucleation of the (Ni,Si) phase on a TiC particle. Since the particle density does not remain constant, and because of the distribution of the (Ni,Si) particles at high doses in both the **PA-1** and PCA alloys (e.g., see Figure 3.4.4), it would seem likely that the new phase preferentially nucleates on TiC particles, but can also form elsewhere, for example on voids, which are often associated with these particles. This would occur at the same time as the TiC particles are dissolving, which would account for the variations in particle densities. The dissolution probably proceeds by the process of recoil resolution.[11]

The extent to which the effects seen under ion irradiation will occur during neutron irradiation is not known. Some evidence that similar effects will indeed take place is illustrated in Figure 3.4.9, an energy dispersive X-ray spectrum taken from a particle after neutron irradiation to 6.2 dpa/210 appm He at 600°C. The intrinsic X-ray signal produced by radioactive decay processes in the specimen, in fact the "hole count", has been overlaid on the recorded spectrum in addition to the two being shown separately. In addition to Ti, small Ni and Mo peaks can be seen. The contribution of matrix elements to the spectrum is small since the particle was found in a very thin region.

In addition to the disappearance of pre-existing TiC particles at high doses in ion irradiations, we believe that TiC is also precipitated out of solution during irradiation. Figure 3.4.10 shows bright field and dark field micrographs of a region of PA-1 alloy, neutron irradiated in the as-annealed condition at 600°C to 8.5 dpa/360 appm He. The dark field utilizes a {220} reflection attributable to the TiC crystal lattice. In the bright field micrograph clusters of very **small** cavities can be seen, as arrowed. As indicated by the dark field micrograph, these clusters appear to be associated with TiC particles, as has been observed previously by other workers.' However, there exists

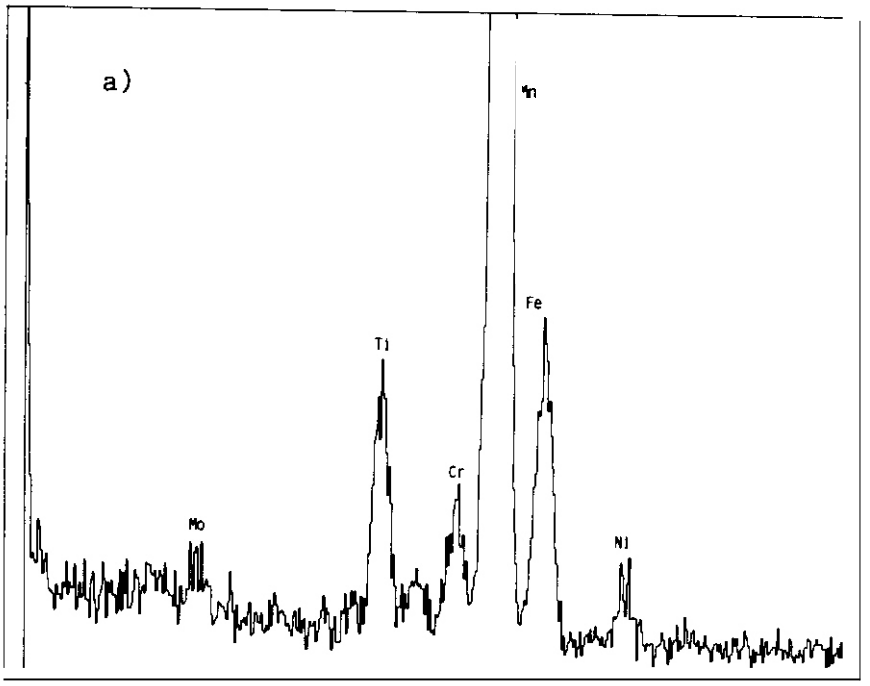

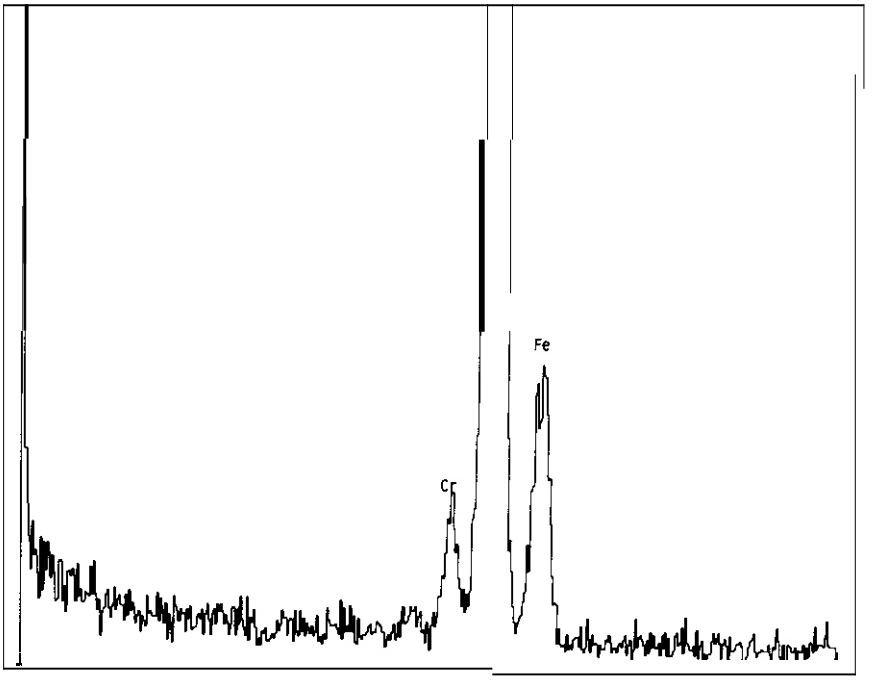

Fig. 3.4.9. Caption overpage

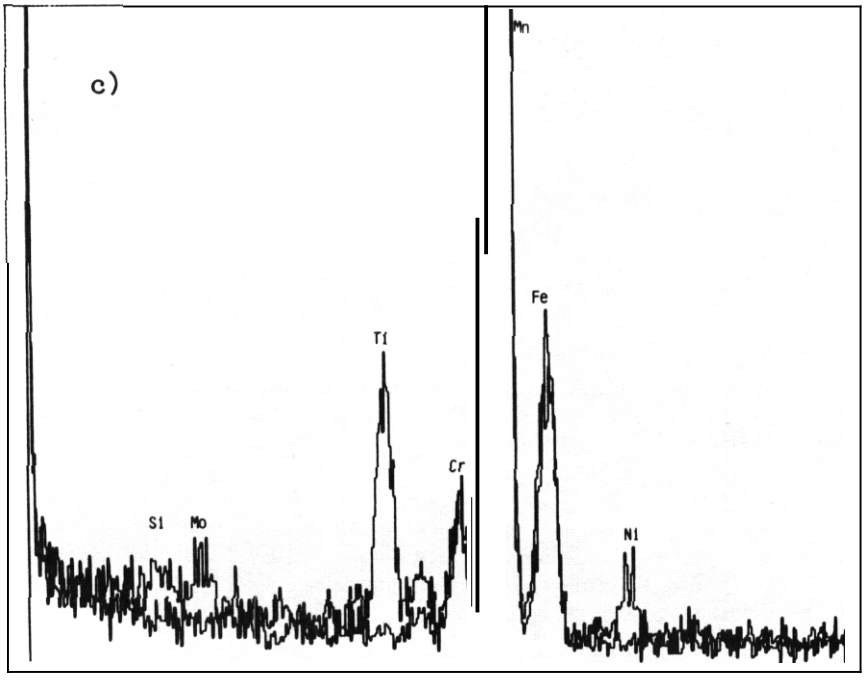

Fig. 3.4.9. Energy dispersive X-ray spectra obtained from a neutron irradiated PA-2 alloy sample irradiated to 6.2 dpa, 210 appm He, at 600°C. (a) shows the spectra from a particle near the edge. Superimposed on this is the intrinsic X-ray emission from radioactive decay in the sample, shown alone in (b), the "hole" count. (c) shows the two spectra superimposed, clearly showing the Ti, Ni and Mo peaks originating from the particle alone.

in general in all specimens an evenly distributed, very high density of small cavities in addition to those clustered at particles, as an examination of Figures 3.4.1 through 3.4.5 shows. It is very difficult, using the dark field technique, to detect very small particles in significant numbers unless they possess coherence with the matrix, since otherwise only those particles that have the exactly favorable orientation will be seen, and then only if they give rise to sufficient intensity above background. Dark field studies have appeared to indicate the presence of very small TiC particles, however, although their exact size cannot be determined. Diffraction patterns taken of these materials clearly show a diffuse ring pattern in addition to the strong matrix spot pattern. The ring radii correspond to a cubic lattice with lattice parameter 0.424 nm, which suggests that they arise from many small crystallites of TiC. The width of the rings suggests a size of about 1 nm

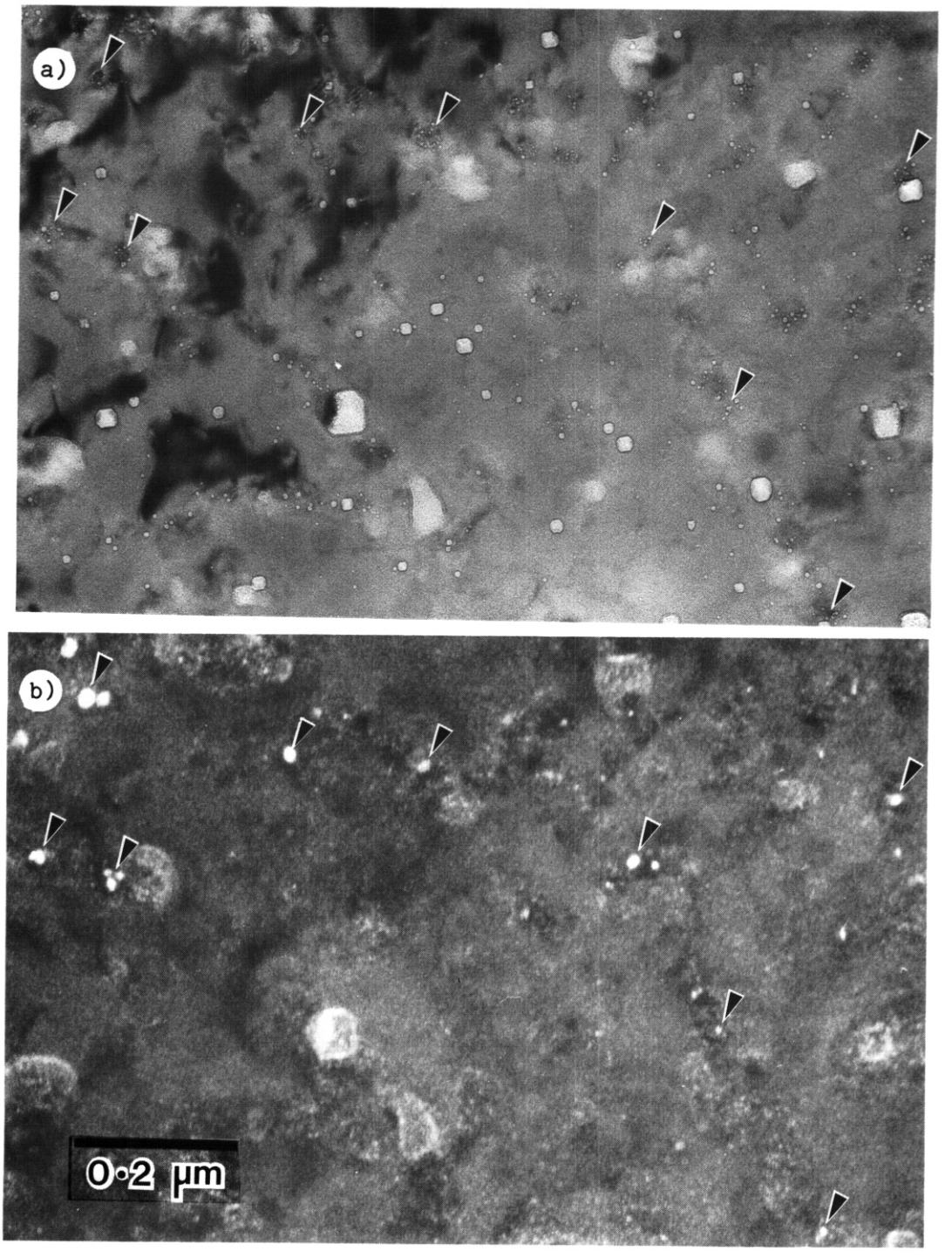

Fig. 3.4.10. Clusters of small cavities, arrowed, are seen in (a) bright field micrograph of annealed PA-1 neutron irradiated to 8.5 dpa, 360 appm He at 600°C. In (b) a dark field micrograph is shown of the same area taken with a TiC {220} reflection. Strongly diffracting particles (bright spots) are seen to be associated with the small cavity clusters.

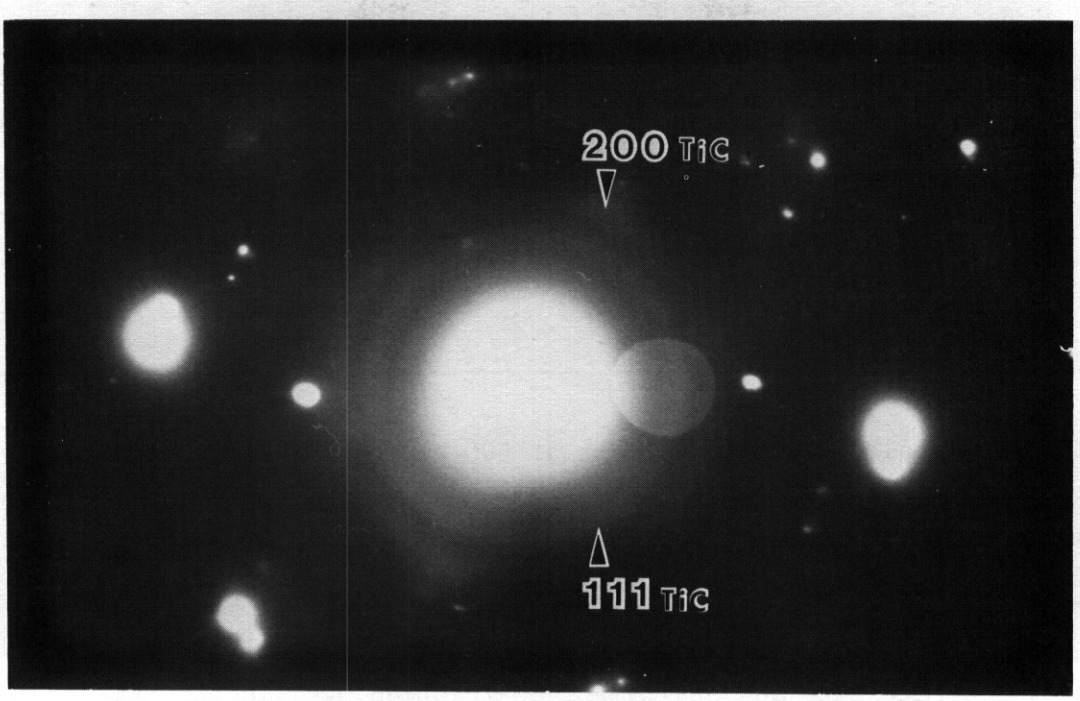

Fig. 3.4.11. Diffraction pattern of ion irradiated PA-1 alloy (18 dpa at 650°C) showing faint rings corresponding to TiC {111} and {200} reflections.

to 2 nm for these particles. A typical pattern is shown in Figure 3.4.11. These results are tentative as yet, but suggest that the TiC either originally in solution, or put into solution from the dissolution of larger particles, comes out as small particles, almost certainly on dislocations. It is attractive to connect the small cavities, which are also often seen to be formed on dislocations, with small particles acting as nucleants. Further work is in progress on this topic.

3.4.4.5 The Effect of Increased Titanium and Carbon Content

Using rapid solidification processing, the amount of titanium and carbon added to the base alloy PCA can be increased well beyond the practical limit for conventional processing. Irradiation testing has been carried out on PA-2 alloy, which has been irradiated in HFIR in

Table 3.4.3. Quantitative Analysis of Voids in PCA, PA-1 and PA-2 at 500°C, 6.2 dpa, 210 appm He

ALLOY	Average Size (diameter) in nm	Density X 10^{21} m^{-3}	Swelling Δ v/v %
PCA, Ann.	6.0 ± 0.3	3.6 ± 0.9	0.05
PA-1, Ann.	7.5 ± 0.5	2.7 ± 0.8	0.09
PA-2, Ann.	8.6 ± 1.0	1.0 ± 0.3	0.05

the as-annealed state to 6.2 dpa at 500 and 600°C, and on cold worked PA-3 alloy, ion irradiated to various dpa at 550°C and 650°C. At the lower temperature in each case, the cavity component of the microstructure is quite similar to that seen in PA-1 or PCA alloy irradiated in the same state, under the same conditions. Table 3.4.3 shows void density, average size and cavity volume fraction swelling for PA-2, PA-1 and PCA alloy at 500°C. The densities tabulated do not include the large number of very tiny cavities presumed to be gas bubbles, because of our inability to confidently count them. There is a slight trend toward a more narrow size distribution, but with a larger average size and lower density, in the PA-2 alloy. Under ion irradiation PA-1 and PA-3 alloys behave similarly at 550°C. At very high doses (about 100 dpa) a slight difference is observed, with PA-3 showing a lower cavity volume fraction swelling.

At higher temperature both PA-2 and PA-3 alloys show heterogeneous cavity populations. Although in some few areas a quite high void component is found, in much of the PA-3 samples ion irradiated at 650°C the void component is almost completely suppressed, leaving just the small bubbles. Figure 3.4.12 illustrates this, and shows a typical area in PA-1 alloy for comparison.

The particle distribution in PA-2 and PA-3 alloys is rather different to that seen in PA-1 since, in both cases, much of the TiC is precipitated during extrusion as quite large particles. These larger (100-200 nm) particles are also found in PA-1, but much less frequently. The density of smaller (– 20 nm) TiC particles is thus not proportionately

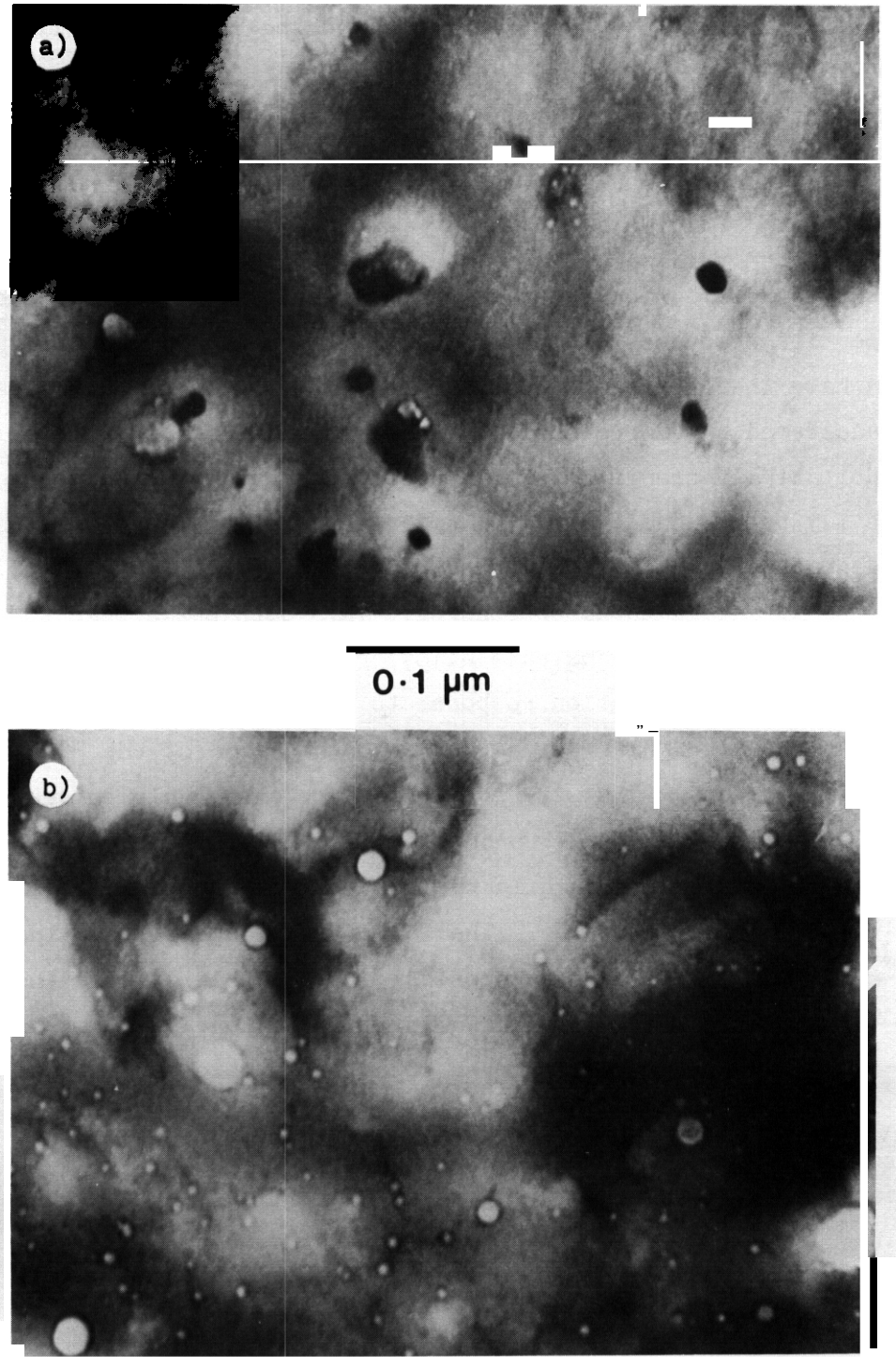

Fig. 3.4.12. Showing in (a) the cavity distribution obtained in PA-3 alloy ion irradiated at 650°C to 18 dpa, 290 appm He. Small cavities are seen but almost no larger cavities are found, unlike the PA-1 alloy, shown in (b) ion irradiated to higher dose, 33 dpa, at 650°C.

larger in PA-2 and PA-3 alloys, with two and three times the TiC content, than in PA-1 alloy. The density may also vary from area to area more strongly, which could lead to some of the observed effects. Further work is in progress to quantify these suggestions.

3.4.4.6 Discussion

Rapid solidification processing can give an alloy improved mechanical properties compared to when it is conventionally prepared. Irradiation can have these relative consequences: the response may be essentially unaltered by RS processing or the response may be qualitatively and quantitatively changed, in which case an improved, or a degraded, response may be obtained. Only when the irradiation response is significantly degraded, as compared to conventionally prepared material, will there be no advantage to RS processing. This does not appear to be the case with the prime candidate alloy, rapid solidification seeming not to affect the irradiation response to a significant degree, although there are certainly differences seen in the behavior of the PCA and PA-1 alloys. These alloys were not completely comparable before irradiation, however, since the RS processed material contained a high density of small TiC particles while the PCA alloy was irradiated in the as-solution-annealed condition. The following paragraphs outline the role of the TiC as we see it at present, and how this affects the rapid solidification approach to optimum alloy fabrication.

It has previously been observed' that TiC particles nucleate small cavities, presumed to be He gas bubbles, upon neutron irradiation. Our results, see Figure 3.4.10 for example, also provide for this. We do see, however, a very large number of small cavities that are not associated with observable TiC particles. Previous work has also shown that small TiC particles may be precipitated during irradiation.[12] When TiC precipitates, it will normally do so on dislocations, as observed in annealing studies.[8] We suggest then that the bimodal cavity distribution observed is due in large part to the action of very many small TiC precipitates forming on dislocations and subsequently, or simultaneously, allowing a small He gas bubble to form. The dynamics of this must be governed by the combined sink strengths of particle,

dislocation and gas bubble. It is conceivable that as the particle and bubble grow, they change the total sink strength in such a way as to slow, and eventually prevent, further growth. The bimodal cavity distribution consists then firstly of a distribution of gas bubbles and secondly of a distribution of voids formed by the growth of bubbles left when their nucleating dislocation has moved away, by climb for example, and thus changed the sink strength in favor of vacancy absorption.

The supply of Ti and C for TiC precipitation must be either the amount originally in solution, or that driven into solution by the irradiation induced dissolution of larger TiC particles. Frost[11] has shown that recoil resolution will occur, at a rate depending on the matrix concentrations of Ti and C. Thus constant precipitation on dislocations drives the constant dissolution of larger particles, since the amount in solution is kept very low. This explains the disappearance of intermediate size TiC particles observed here.

The microchemical changes can also be explained. In the process of dissolution the particle is also continually being 'reconstituted' by diffusion back into it. In this process it would seem likely that Mo could be used to replace some of the lost Ti and hence the Mo content of the particle will be enriched. Diffusion of Ni and Si will also take place since the particle is a vacancy sink, vacancies being structurally necessary in TiC growth. If this Ni and Si precipitate out as a separate phase, nucleating on the TiC, then as the process continues the TiC particle, initially enriched with Mo, will gradually be replaced by the other Ni and Si rich phase (which contains no, or little, Mo), giving the results obtained.

This schema explains our observations in PA-1 and PCA alloy. In the alloys with higher TiC content the same processes occur. However, the greater number of large (100-200 nm) TiC particles, and their variation from area to area, means that it is difficult to directly establish the amount of 'available' TiC in any area. It is tempting to suggest that areas where the large void component of the size distribution is suppressed correspond to areas where there is a large amount of TiC in the form of small particles, a high number of gas bubbles and strongly

pinned or weakly biased (or both) dislocations. If this is the case then it suggests firstly that increasing the TiC content may be beneficial if it is evenly distributed, in very small particles or preferably in solution in a cold worked material, and secondly that RS processing may be valuable in producing a much improved irradiation response, since it enables such an alloy to be produced (which is not possible by conventional means). If the TiC is present in large enough particles to nucleate the Ni and Si rich phase, however, the response at high dose will be much degraded due to the depletion of these elements and the consequent acceleration of swelling.

3.4.5 Conclusions

1. Path A prime candidate alloy has been prepared using a standard method of rapid solidification processing, including consolidation by hot extrusion, in a first attempt at obtaining an improved irradiation response through RS technology. This initial run of alloy PA-1 shows quite similar, but not identical, neutron and dual ion irradiation response to that of the same material conventionally prepared using ingot techniques, in irradiation tests to low neutron doses (~ 10 dpa) but high dual ion doses (~100 dpa). The slight differences that exist are attributed to the differing preirradiation distributions of TiC in the materials. The results on these alloys, and on alloys containing increased amounts of Ti and C, strongly suggest ways in which the use of RS technology might be optimized to indeed give an improved irradiation response.

2. All the alloys examined characteristically contain a bimodal distribution of cavities, showing a high density of very small cavities thought to be gas bubbles, in addition to a larger cavity component, thought to be voids, using accepted terminology. The small bubbles are thought, without substantial evidence, to be associated with the formation of very small TiC particles on network dislocations.

3. Microchemical changes have been observed in ion irradiated alloys, showing initial enrichment of TiC particles with molybdenum followed by a decrease in the titanium, and molybdenum content. At the same time, the elements Ni and Si become increasingly present at

the particle, eventually dominating. It is thought that the TiC dissolves by recoil resolution, while nucleating another phase rich in nickel and silicon. It is this dissolution of TiC that is the source of material for precipitation on dislocations, which in turn helps drive the process of recoil resolution by depleting the matrix concentration.

4. *Our* results suggest that TiC addition to austenitic stainless steel has both beneficial and deleterious effects on irradiation response. The benefical effects arise, in our interpretation, from TiC in solution or present as very small particles on dislocations. Larger TiC particles appear to act as nucleating agents for a phase rich in nickel and silicon. The removal of nickel from solution is deleterious, as swelling will increase markedly. Rapid solidification processing may prove essential in producing an alloy with as much TiC as possible, present either in solution or as extremely small particles. Experiments with PA-2 and PA-3 alloys with increased TiC content are promising, but have not yet come close to showing the full potential of the rapid solidification method.

3.4.6. References

1. S. Wood, J. A. Spitznagel, W. J. Choyke, N. J. Doyle, J. N. McGruer, and J. R. Townsend, "Cavity Alignment and Precipitation in Solution Annealed 316 SS During Dual Ion Bombardment," Scripta Met. 14: 211-214 (1980).
2. F. A. Garner, "The Microchemical Evolution of Irradiated Stainless Steels," paper presented at AIME Symposium on Irradiation Phase Stability, Pittsburgh, PA, Oct. 5-9, 1980.
3. P. J. Maziasz, "Microstructural Design for Fusion First-Wall Applications and Recommendations for Thermal-Mechanical Preirradiation Treatments," ADIP Quart. Prog. Rep. June 1979, pp. 48-56, DOE/ET-0058/6.
4. P. J. Maziasz, and E. E. Bloom, "Comparison of Titanium Modified and Standard Type 316 Stainless Steel Irradiated in HFIR - Swelling and Microstructure," ADIP Quart. Prog. Rep. Jan.-Mar. 1978, pp. 40-55, DOE/ET-0058/1.

5. U. S. Department of Energy, The Fusion Reactor Materials Program Plan, DOE/ET-0058/1 (July 1978).

6. L. Arnberg, J. Megusar, D. Imeson, H. J. Frost, J. B. Vander Sande, O. K. Harling, and N. J. Grant, "The Microstructure of Neutron Irradiated Rapidly Solidified Path A Prime Candidate Alloys," J. Nucl. Mater. 103 and 104: 1005-1009 (1981).

7. P. J. Maziasz, and T. K. Roche, "Fabrication of Homogeneous Path A Prime Candidate Alloy," ADIP Quart. Prog. Rep. Sept. 1979, pp. 83-102, DOE/ET-0058/7.

8. J. Megusar, L. Arnberg, J. B. Vander Sande, and N. J. Grant, "Microstructures of Rapidly Solidified Path A Prime Candidate Alloys," J. Nucl. Mater. 103 and 104: 1103-1107 (1981).

9. P. J. Maziasz, "Helium Trapping at Ti-Rich MC Particles in Neutron Irradiated Type 316+Ti Stainless Steel," Scripta Met. 14: 1251-1256 (1980).

10. L. Arnberg, J. B. Vander Sande, H. J. Frost, and O. K. Harling, "The Microstructure of Rapidly Solidified Path A Prime Candidate Alloys Following Irradiation with Fe and He Ions," J. Nucl. Mater. 103 and 104: 1069-1073 (1981).

11. H. J. Frost and K. C. Russell, "Recoil Resolution and Particle Stability under Irradiation," J. Nucl. Mater. 103 and 104: 1427-1431 (1981).

12. J. A. Spitznagel, S. Wood, and W. J. Choyke, "Dual-Ion Irradiation of Titanium Modified 316 SS," DAFS Quart. Prog. Rep. Aug. 1980, pp. 103-120, DOE/ER-0046/2.

3.5 SOME EFFECTS OF INCREASED HELIUM CONTENT ON VOID FORMATION AND SOLUTE SEGREGATION IN NEUTRON-IRRADIATED TYPE 316 STAINLESS STEEL — P. J. Maziasz (Oak Ridge National Laboratory)

3.5.1 ADIP Tasks

ADIP Tasks I.C.l, Microstructural Stability, and I.C.2, Microstructures and Swelling in Austenitic Alloys.

3.5.2 Objective

The objective of this work is to determine the effects of helium on swelling and microstructural evolution during irradiation. The results may serve to guide alloy development and, with complementary modeling tasks, to lead to a correlation of irradiation effects in fission and fusionlike facilities.

3.5.3 Summary

During EBR-II irradiation of solution-annealed (SA) and 20%-cold-worked type 316 stainless steel (CW), void formation and swelling are often coupled to radiation-induced solute segregation (RISS). A refined sink structure, including a high cavity concentration, results if helium is preinjected before EBR-II irradiation or produced during HFIR irradiation. This can suppress both the void swelling and the RISS.

3.5.4 Progress and Status

3.5.4.1 Introduction

Fast breeder reactors (FBRs) were operating before the effects that dominate the studies of the radiation damage community today were discovered. The first Experimental Breeder Reactor (EBR-I) began operation in 1951, the Dounreay Fast Reactor (DFR) in 1959, and EBR-II in 1964. The phenomenon of swelling due to void formation was not discovered until postirradiation examination by Cawthorne and Fulton' in 1966 of austenitic stainless steel cladding from a fuel element used in the DFR. In complex engineering multicomponent alloys like austenitic stainless steels, phase

instability and solute redistribution are also very important effects. Radiation-induced solute segregation was anticipated in 1971 by Anthony[2] and then observed experimentally by Okamoto and Wiedersich in 1974.[3] Radiation-induced solute segregation has since been studied both theoretically and experimentally by many investigators.[4-10] Brager and Garner were pioneers in relating void swelling, precipitation behavior, and RISS effects in austenitic stainless steel under neutron irradiation.[11,12] They were also among the first to apply x-ray energy dispersive spectroscopy (EDS) together with conventional transmission electron microscopy (CTEM)[11-13] for irradiated materials. They have also undertaken an effort to explain many aspects of void swelling behavior in FBR irradiated steels in terms of microcompositional roles of the various solutes like carbon, nickel, and silicon.[13-15]

Unlike the FBR programs, the Magnetic Fusion Energy (MFE) materials development program does not have the actual irradiation environment presently available. Much has been written about the parameters that will make fusion irradiation damage different from FBR damage, particularly increased helium generation for the former.[16-20] Water-moderated fission reactors with highly enriched fuel, like the High Flux Isotope Reactor (HFIR), have both fast and thermal neutron populations near the fuel and are able to generate displacement damage and helium together in nickel-bearing alloys like austenitic stainless steels. Comparison of the same material irradiated in HFIR and EBR-II can be used to determine the response of physical and mechanical properties to changes in helium-to-dpa ratio and damage rate.

This report presents the results of an investigation of the influence of helium generation rate on the microstructural and microcompositional evolution of CW and SA 316 irradiated in EBR-II and HFIR. The effects of preinjected helium in SA 316 irradiated in EBR-II are also presented. It includes a more complete and better characterized baseline of aged 316 samples than previous work on the subject, particularly for interpreting compositional changes in precipitate phases.[11-15] Data are presented to support the idea that the primary coupling between RISS and precipitation is "microalloy" formation. A "microalloy" is used here to describe

compositional changes to small regions of austenite. The phases in these regions are similar in type and composition to those expected if one simply aged samples having the composition of the microalloy. Finally we show that both void swelling and RISS can be significantly reduced or suppressed if the total sink strength of the microstructure is increased and maintained above a minimum level. Helium, through the cavity microstructure, plays a critical role in the microstructural and microcompositional evolutionary path that the material follows under irradiation.[20–27]

3.5.4.2 Experimental

Results are presented on SA and CW 316 samples that were irradiated to a range of neutron fluences in several HFIR and EBR-II experiments at 510 to 550°C (refs. 23, 28—30). Calculations and/or measurement details for helium and displacement damage have been reported.[27] To investigate special conditions, samples preinjected with 110 at. ppm He at about 20°C were irradiated side by side with uninjected SA 316 to neutron fluences producing 8.4 dpa in EBR-II at 500 to 625°C. To provide baseline phase stability data, pieces of the same heat of SA and CW 316 (DO heat) were thermally aged at 470 to 650°C for 2770 to 10,000 h. Details have been reported previously for the preinjected[23] and the aged samples.[23,25,29] Sufficient data are available now to assign nominal irradiation temperatures that are 50 to 75°C higher than the originally calculated irradiation temperatures.[29] The nominal HFIR irradiation temperatures are still probably uncertain by ±25 to 50°C.

Specimens were thinned for CTEM analysis by either a two-stage manual or Tenupole automatic electropolishing technique. Both JEM 100C and 100CX electron microscopes were used for observation and analysis of specimens. A Hitachi 1MV microscope was used for thick section examination, particularly in samples having very large voids after high-fluence EBR-II irradiation. The details of quantitative CTEM analysis, including diffraction analysis of precipitate phases, have been reported previously.[21–25,27,29,31] For x-ray EDS of quantitative analytical electron microscopy (AEM), the details of specimen preparation, data analysis and choice of measurements (in-foil versus extracted precipitates;

compositional gradients versus simple phase compositional differences) can affect interpretation of results. In this work, we chose to emphasize accurate phase identification and composition as our desired observables, and thus extraction replicas were made on all samples. The replica technique was designed to obtain matrix-free precipitates as well as an imprint of the surface microstructure. The samples were cleaned by electropolishing; then the samples were electrolytically etched for surface relief before depositing an electron-transparent amorphous carbon film. The samples were then etched again slowly at —10 to —30°C to remove the films, which were then secured on beryllium grids. Analytical electron microscopy was performed on the JEM 100CX, modified and optimized for x-ray EDS by Bentley et al.[32] Data reduction to obtain quantitative compositional information through the standardless analysis method used computer programs developed by Zaluzec.[33,34] These programs are capable of calculation for the full range of atomic number (Z), absorption (A), and fluorescence (F) effects that can be encountered even if the "thin film" criterion is violated for any element in the multicomponent phase.[34] Except for very small particles, where scanning transmission electron microscopy (STEM) was used, the minimum beam diameter in CTEM was used for most precipitate analysis to minimize contamination.

3.5.4.3 Results

3.5.4.3.1 <u>CW 316 Microstructural Evolution</u>. The behavior baseline for precipitation in CW 316 under irradiation was found by thermally aging the same material over a range of conditions. Microstructures produced by aging at 560 and 600°C are shown in Fig. 3.5.1. Details of the microstructure for aged material are also summarized in Tables 3.5.1 and 3.5.2. No precipitation was found after 4400 h at 470°C. A small amount (—0.3 vol %) of fine (~30—40 nm in size) tau ($M_{23}C_6$) phase particles are found after aging 2770 h at 560°C; no observable additional changes occurred after 4400 h. Substantially more (~2.5—3 vol %) precipitation of coarser (50—200 nm in size) eta (M_6C) and Laves phase particles was found after 2770 h at 600°C, and these phases showed little change thereafter up

Table 3.5.1. A Summary of Matrix Microstructural Information (Cavity and Dislocation Components) on 20%-Cold-Worked Type 316 Stainless Steel (DO Heat) After Thermal Aging and EBR-II and HFIR Irradiations

Exposure Conditions (°C, Aging Time or Reactor, dpa, at. ppm He)	Cavity Component			Dislocation Component	
	Diameter (nm)	Density (m^{-3})	Comments	Density (m/m^3)	Comments
470, aged 4400 h		None		3–5	No recovery
560, aged 4400 h		None		0.8–	Network recovery
600, aged 4400 h		None		5.6	Network recovery
600, aged 10,000 h		None		5.6	Network recovery
650, aged 10,000 h		None		3–4	Network recovery plus small fraction of recrystallization
500, EBR-II, 8.4, ~5		None			Network recovery; no loops
525, EBR-II, 36, ~22	2–5 (bubbles) 70–170 (voids)	$0.5–1 \times 10^{21}$ $0.4–2 \times 10^{19}$	Fine bubbles on dislocation lines and precipitates. Only a few of the largest voids are attached to precipitates; most are in the matrix. ~0.1% or less swelling.		Network; no loops
510, EBR-II, 69, ~41	100–300 (voids)	$2–8 \times 10^{19}$ [a]	Many voids, some as large as 400 nm diam; many are attached to precipitates; ~10 to 11% swelling.		Network; no loops
525–550, HFIR, 6.9, 290	2–3 (bubbles)	$>10^{22}$ [a]	Very fine and uniformly distributed in size and space; less than 0.1% swelling.		Network; no loops; many faulted bands are forming
525–550, HFIR, 10, 500 [b]	7–8 (bubbles)	$2–3 \times 10^{21}$	Uniformly distributed, but uniformly coarser than at 6.9 dpa. Less than 0.1% swelling.		Network; no loops
525–550, HFIR, 16, 1020	2–3 (bubbles)	$1–3 \times 10^{22}$	Not uniformly distributed spatially; in clusters along dislocations and near precipitates. Less than 0.1% swelling.		Network plus a few large prismatic loops
515–540, HFIR, 54, 3660	17 (bubbles)	$6–7 \times 10^{21}$	2.2% swelling. Coarsening compared to 16 dpa; slightly less uniform, but no coarse voids.		measured [c]

[a] Work is still in progress on either a particular microstructural component or the sample in general.

[b] Two identical samples, irradiated at exactly the same conditions, were examined and gave similar results.

[c] Dislocation density was not measured because sample was taken from gage of tensile specimen that had been postirradiation tensile tested at 75 to 100°C below the irradiation temperature.

Table 3 5 2 A Summary of Matrix Microstructural Information (Precipitate Component) on 20%-Cold-Worked Type 316 Stainless Steel (DO Heat) After Thermal Aging and HFIR Irradiation

Exposure Conditions (°C, aging time or reactor, dpa, at. ppm He)	Phases[a]	Size (nm)	Density (m^{-3})[b]	Comments
470, aged 4400 h		None		
560, aged 4400 h	Tau ($M_{23}C_6$)	30–40	~5 × 10^{20}	~0.3 vol %
600, aged 4400 h	Tau, eta (M_6C)	50–200	1–5 × 10^{20}	(2.5–3 vol %) Laves is about 60% of total precipitation, tau about 25%, and eta about 10%.
600, aged 10,000 h	Same plus sigma	50–200	1–5 × 10^{20}	Same as above plus occasional coarse sigma phase particles.
650, aged 10,000 h	Tau, eta, Laves, sigma	100–300	<1 × 10^{20}	More than found at 600°C.
500, EBR-II, 8.4, ~5	Eta	15–25	<5 × 10^{18}	Less than 0.001 vol %.
525, EBR-II, 36, ~22	Eta, Laves, tau	70–350	~5–7 × 10^{19}	(1.5–2 vol % total precipitation.) Eta is major portion, present as blocky particles. Laves is in the form of very narrow, long or thin laths.
510, EBR-II, 69, ~41	Eta, Laves, γ′, G phase	10–250	Greater than above	About the same amount as above or slightly less. Eta portion remains the same, and tau is no longer found. γ′ is very fine and very small fraction of total precipitation. Laves and G phase are medium-sized blocky particles found almost completely associated with voids. Only a small amount of G phase is found. Laves laths that existed at lower fluence are not found.
525–550, HFIR, 6.9, 290	Tau and possibly some eta	~50	~3 × 10^{20}	About 0.6 vol % total with dominantly tau phase. Smaller particles in the matrix and stacking faults are heavily decorated with precipitates.
525–550, HFIR, 10, 500[b]	Eta, Laves, and tau	20–50 (tau) 50–500 (Laves, eta)	3 × 10^{20} 1–2 × 10^{20}	About 2 vol % total precipitation. Tau particles are fine and a small fraction of total. Eta particles are blocky and Laves particles are long laths. Fairly equal portions of Laves and eta. Tau at faulted bands has coarsened.
525–550, HFIR, 16, 1020	Eta, Laves, (tau?)[c]	50–200	0 [illegible]	About 0.7 to 1.0 vol % total precipitation. There appear to be partial dissolution of eta and Laves particles (reduced particle size and density) and almost complete disappearance of fine tau phase particles, particularly at stacking faults.
515–540 HFIR, 54, 3660	Eta, tau, and Laves	20–50 (tau) 50–400 (Laves, eta)	~3 × 10^{20} 3 × 10^{20}	About 4.4 vol % total precipitation. Laves and eta have increased and coarsened; fine tau [illegible] reprecipitated.

[a] Phases identified through electron diffraction or x-ray EDS on replicas.

[b] Identical samples, irradiated at exactly the same conditions were examined and gave similar [illegible]

[c] Work is still in progress on either [illegible]

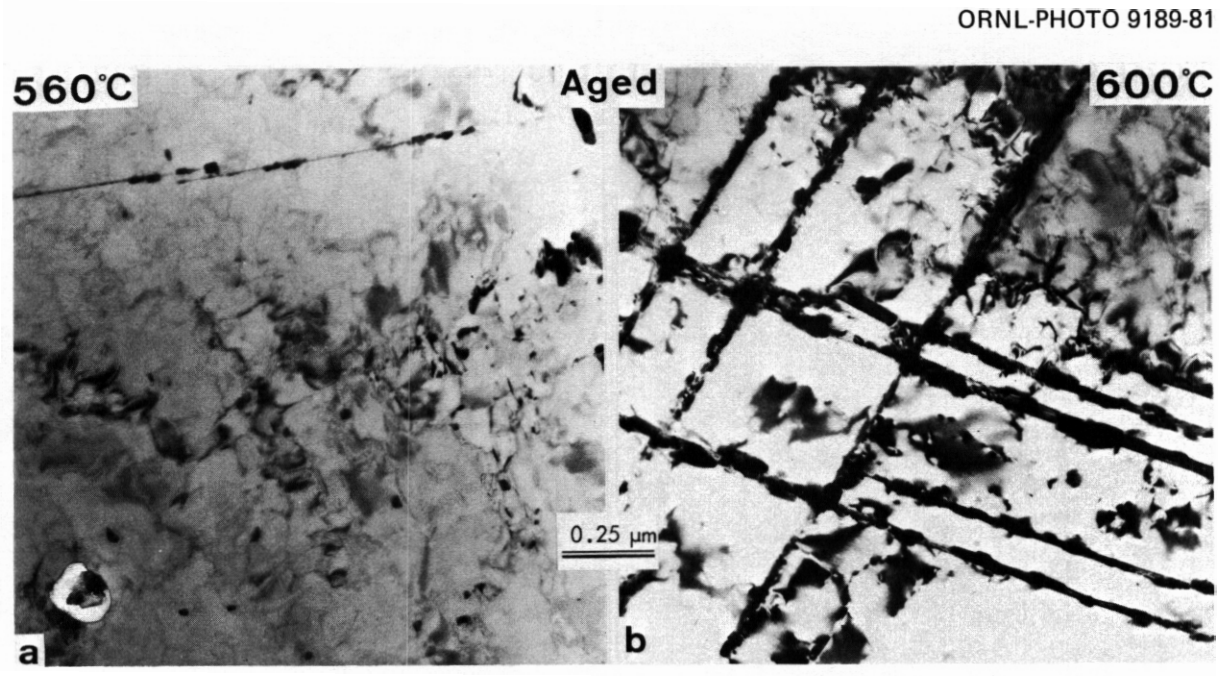

Fig. 3.5.1. Cold-Worked (20%) Type 316 Stainless Steel (DO Heat) Aged at (a) 560°C and (b) 600°C for 2770 h. These microstructures do not change significantly with further aging for *4400* h at 560°C or 10,000 h at 600°C (ref. 23). The precipitate phases present are (a) a small amount of tau and (b) a much larger amount of tau, eta (M_6C), and Laves phases (ref. 23).

to 10,000 h. One minor change with increasing time was detection of a small amount of sigma phase after 10,000 h at 600°C. Sigma phase was not observed after aging for *4400* h. A large volume fraction and coarser distribution of the same phases were observed after 10,000 h at 650°C.[22,31] More detail on these samples can be found elsewhere.[22,23,31]

The main focus of this work is the connection between development of precipitate and cavity (void or bubble) components of the total microstructure under irradiation and the possible influence of large differences in helium generation rates. Material irradiated in EBR-II at 500°C (start) to 550°C (finish) (525°C average) to 36 dpa and then reirradiated an additional 33 dpa at 510°C to achieve 69 dpa total was supplied to this author courtesy of H. R. Brager, HEDL. Microstructural development in CW 316 over a range of fluences at 500 to 525°C in EBR-II is compared with that developed in CW 316 on irradiation at 510 to 555°C in HFIR. Very substantial differences are found between the two reactors in cavity and

precipitate type, nature, and development. A summary of microstructural information after EBR-II irradiation is found in Tables 3.5.1 and 3.5.2. Low-fluence micrographs are shown in Fig. 3.5.2 and higher fluences in Fig. 3.5.3.

ORNL-PHOTO 9190-81

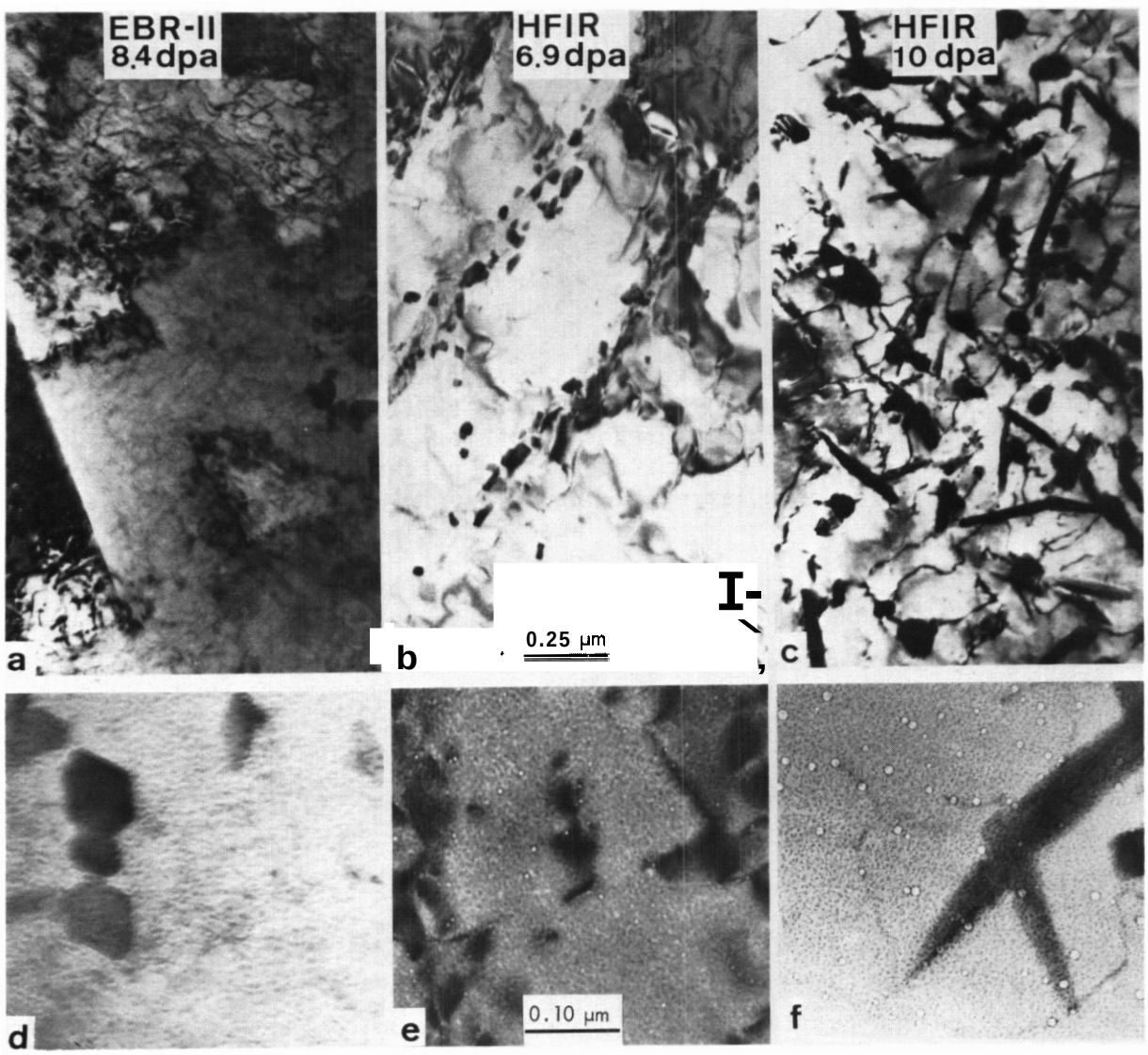

Fig. 3.5.2. Cold-Worked (20%) Type 316 Stainless Steel (DO Heat) Irradiated at 500 to 550°C in EBR-II and HFIR to the Indicated Fluences. (a), (b), and (c) are lower magnifications to show precipitate and dislocation structure; (d), (e), and (f) are high-magnification, kinematical, underfocused micrographs of the same materials for maximum small cavity visibility. Helium contents are (a) 5, (b) 300, and (c) 500 at. ppm He.

ORNL-PHOTO 9191-81

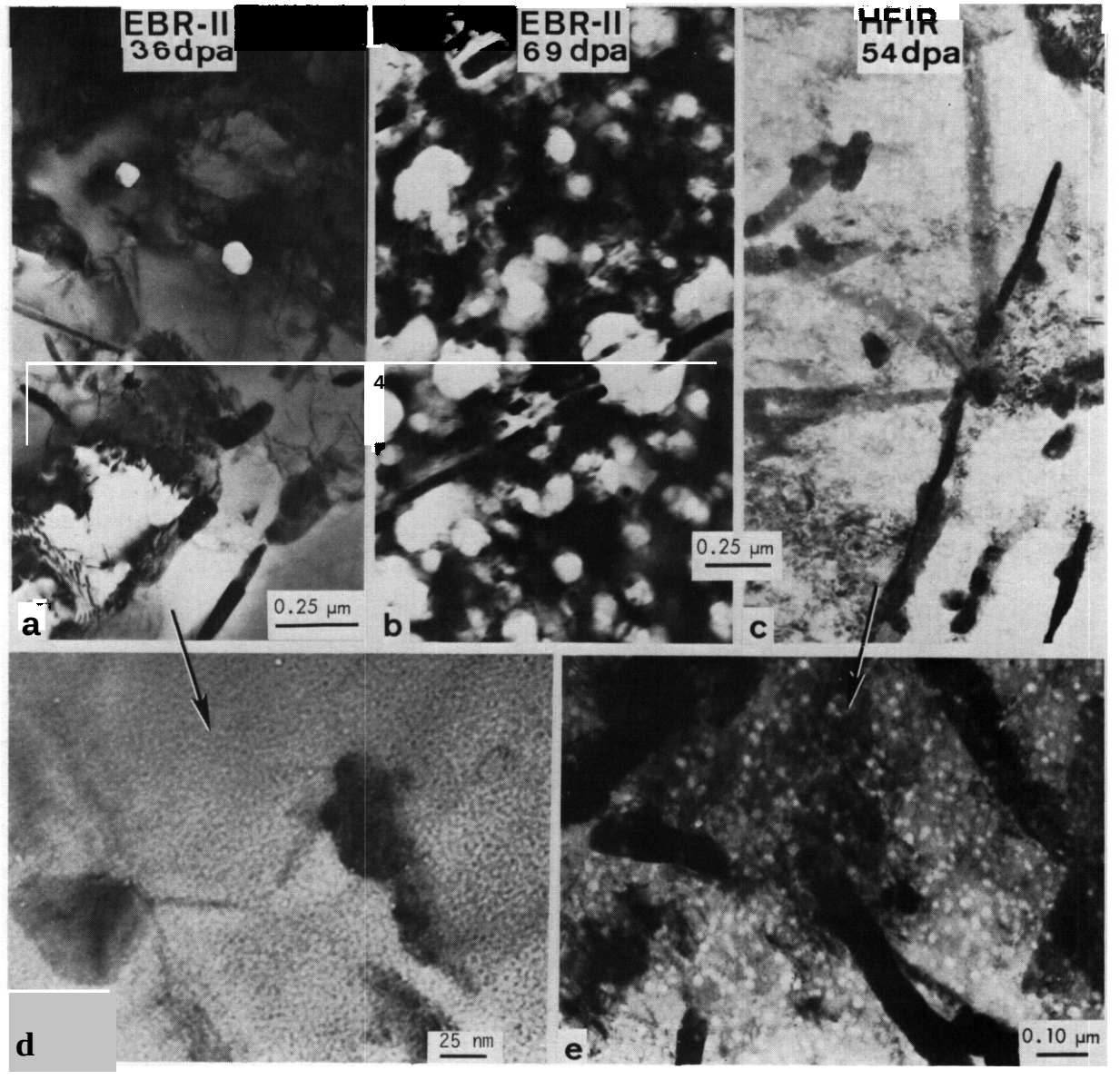

Fig. 3.5.3. Cold-Worked (20%) Type 316 Stainless Steel (DO Heat) Irradiated at 510 to 535°C in EBR-II and HFIR to the Indicated Fluences. (a), (b), and (c) are lower magnifications to show void, precipitate, and dislocation structures; and (d) and (e) are higher magnifications of (a) and (c), respectively, imaged to show cavity structures [note magnification difference between (d) and (e)].

In EBR-II irradiated samples, the cold-worked dislocation density recovered rapidly to 3×10^{14} m/m^3 at 8.4 dpa and then remained quite constant with increasing fluence up to 69 dpa. A substantial amount of faulted bands formed between 8.4 and 36 dpa and persisted to 69 dpa. Only

a few small eta (M_6C) particles were found after *8.4* dpa, but substantial precipitation of eta and Laves phases (–2 vol %) occured between *8.4* and 36 dpa. Eta **is** the major portion **in** blocky particles distributed both along faulted bands and **in** the matrix. The Laves particles found in the matrix occur as very long, thin laths. A few blocky tau ($M_{23}C_6$) particles were also found mixed with eta particles. The amount of precipitation **is** the same or slightly less after 69 dpa. The major changes occurring between 36 and 69 dpa were disappearance of tau, precipitation of medium to small blocky Laves and G–phase particles, and a small amount of fine γ' (see Table 3.5.2). The Laves phase laths found at 36 dpa appear to have dissolved at 69 dpa.

No fine bubbles were observed at *8.4* dpa. However, many *(–4-6* **x** 10^{20} m^{-3}) fine (2–4 nm diam) bubbles[26] were observed at the intermediate fluence of 36 dpa, and these are located along dislocations and at precipitate particle interfaces [about 2 to 5 bubbles per particle; see Fig. **3.5.3(d)].** No voids were found at *8.4* dpa [Fig. **3.5.1(a)];** a few voids that range **in** diameter from 20 to 140 **vv** (~70–80 nm av) are nonuniformly distributed in the matrix between precipitate–laden (eta) faulted bands after 36 dpa. **It is** important to attempt to distinguish between cavities that are bubbles and those that are voids, and a summary of some criteria used for making the distinction **is** found **in** Table 3.5.3. Even though there are fine bubbles at precipitate interfaces, most of the initial voids are not attached to the precipitate particles present. A higher density and more uniform distribution of voids, ranging **in** diameter from about 100 to 300 **vv, was** found after 69 dpa, and at this high fluence **no** fine bubbles were found among the voids. A large increase in swelling compared with 36 dpa **is** seen by comparing Figs. 3.5.3(a) and **(b).** The swelling after 69 dpa **was reported**[30] to be **11%.** Most of the voids after 69 dpa have a precipitate particle attached, with many of the particles considerably smaller than the voids. Very large voids [see Pig. **3.5.3(b)]** were observed along the precipitate–laden faulted bands. Comparing low– and high–fluence microstructures, these precipitates, which are intercepted by large (and presumably growing) voids, appear to be dissolving.

Table 3.5.3. Some of the Factors that Help to Distinguish Between Bubbles and Voids in the Cavity Microstructure

Definitions

- Cavity — any general observable collection of vacancies and gas atoms.
- Void — acavity that is virtually empty.
- Bubble — a cavity that contains nearly the equilibrium[a] amount of gas (helium in our case).

Distinguishing Features of Each Type of Cavity[b]

Feature	Bubble	Void
Size (at about 650°C or below)	Small, usually 3 to 30 nm in diameter	Large, usually 15 to 500 nm in diameter
Size distribution	Very narrow	Very broad
Microstructural location	Precipitate interfaces, dislocation lines, matrix, and at grain boundaries[c]	Matrix, precipitate interfaces
Ratio of calculated gas concentration for material from cavity microstructure to that calculated or measured from transmutations[d]	~1 or more	Much less than 1

[a] $P = 2\gamma/r$ is the condition for mechanical equilibrium, where P = internal gas pressure, γ = surface energy, and r = cavity radius, all in consistent units.

[b] one should include consideration of all of these and if there is still ambiguity resort to postirradiation annealing. Handling for such an operation is a particular problem for the highly radioactive HFIR stainless steel specimens.

[c] At least theoretically, without stress, cavities should not exist at boundaries without stabilizing gas; hence these are the most likely cavities to be bubbles of any found in the microstructure. For a distribution of equilibrium bubbles in the matrix and at grain boundaries, experience shows that the largest bubbles are found at the boundary. These provide, then, an easy visual reference point. Matrix cavities smaller than these are most probably bubbles; cavities much larger are probably voids.

[d] In most cases the gas content is calculated with a nonideal equation of state and integrated over the cavity size distribution (ref. 27).

Very different microstructural behavior was observed after HFIR irradiation of the same steel compared with that described above for EBR-II irradiation. Summaries of observations are also found in Tables 3.5.1 and 3.5.2. Compared with the sluggish evolution found in ERR-11, considerable precipitation and a high concentration of fine bubbles developed rapidly during HFIR irradiation at 525 to 550°C (ref. 26). Many fine (2–5 nm diam) bubbles can be seen in Fig. 3.5.2(e) after 6.9 dpa in HFIR. At this fluence tau (and possibly some eta) phase particles (~0.7 vol %) are precipitated along faulted bands in the matrix [Fig. 3.5.2(b)]. The bubbles coarsen to about 7 to 8 nm diam after 10 dpa [Fig. 3.5.2(f) and Table 3.5.11, but the size distribution is very narrow, and several TEM disks taken from the same specimen show the microstructure to be spatially homogeneous. Also by 10 dpa considerable amounts of coarser eta and Laves precipitates form in addition to the previous smaller fraction of tau phase to yield about 2.5 to 3 vol % total precipitate [Fig. 3.5.2(c) and Table 3.5.21. Many bubbles are found at dislocations and precipitate interfaces.

At 16 dpa, considerable refinement of the cavity structure and a reduction in the amount of precipitate due to dissolution were observed.[26,35] Multiple disks were examined from the 16-dpa sample to confirm these observations. Apparently the changes seen at 16 dpa are complicated but transient effects, because the cavity structure coarsened and an increased amount (~4.5–5 vol %) of eta, Laves, and tau phases were found after HFIR irradiation to 54 dpa. The evidence (see Table 3.5.3) supports the cavities still being bubbles at 54 dpa as opposed to voids.[26,27] These bubbles are about 17 nm in diameter and have a concentration of about 7×10^{21} m^{-3}. They are 10 times smaller and about 50 to 70 times more dense than the voids found after EBR-II irradiation. Although coarse precipitate particles of eta and Laves phases have bubbles at their interfaces, precipitate-assisted void formation has not occurred. Swelling is therefore only 1 to 2% after 54 dpa in HFIR. This result together with the lower fluence HFIR data shows that swelling develops at a much slower rate than the swelling in EBR-II (see Table 3.5.1).

3.5.4.3.2 CW 316 Precipitate Compositional Information. There are several ways to monitor the microcompositional redistributions in irradiated materials that occur as a consequence of RISS. The precipitate and matrix chemical changes are, of course, complementary in a conservative system.[31] A small amount of vanadium is produced from manganese transmutation during HFIR irradiation of type 316 stainless steel.[36] However, we believe the vanadium **has** only a minor, if any, influence on cavity and precipitation behavior.[20,26] The bases for the phase identifications have been given previously.[24,31]

Representative x-ray EDS spectra with the results of quantitative compositional analysis for each spectrum are shown for eta, Laves, and tau phases in Figs. 3.5.4 through 3.5.6, respectively. The compositions of

ORNL-PHOTO 9192-81

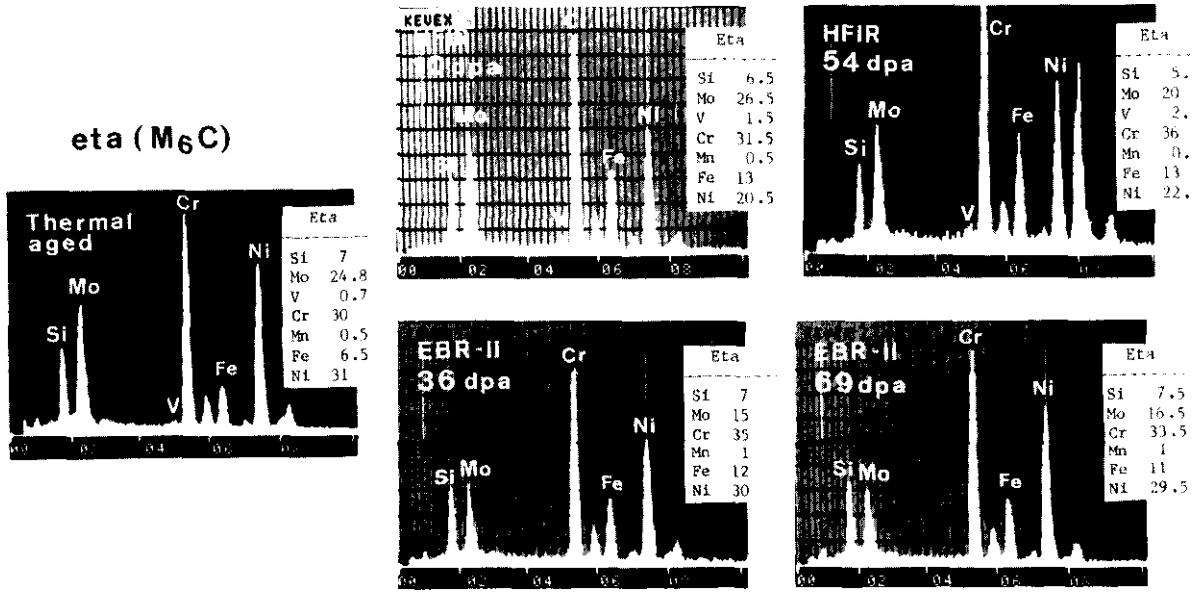

Fig. 3.5.4. Representative X-ray EDS Spectra (Abscissa is in keV) with Quantitative Compositional Data for Eta (M_6C) Phase Formed in CW 316 (DO heat) Either by Thermal Aging at 500 to 550°C or in the Reactor and to the Fluence Indicated. All spectra were taken from extraction replicas and on Be grids except for the HFIR 54-dpa sample, which was on a Cu grid and hence **has** a Cu Ka peak next to Ni. Element peaks present are labeled. In these spectra Mn $K\alpha$ are not labeled because they are obscured by Cr $K\beta$. Note the similarity between spectra.

ORNL-PHOTO 9193-81

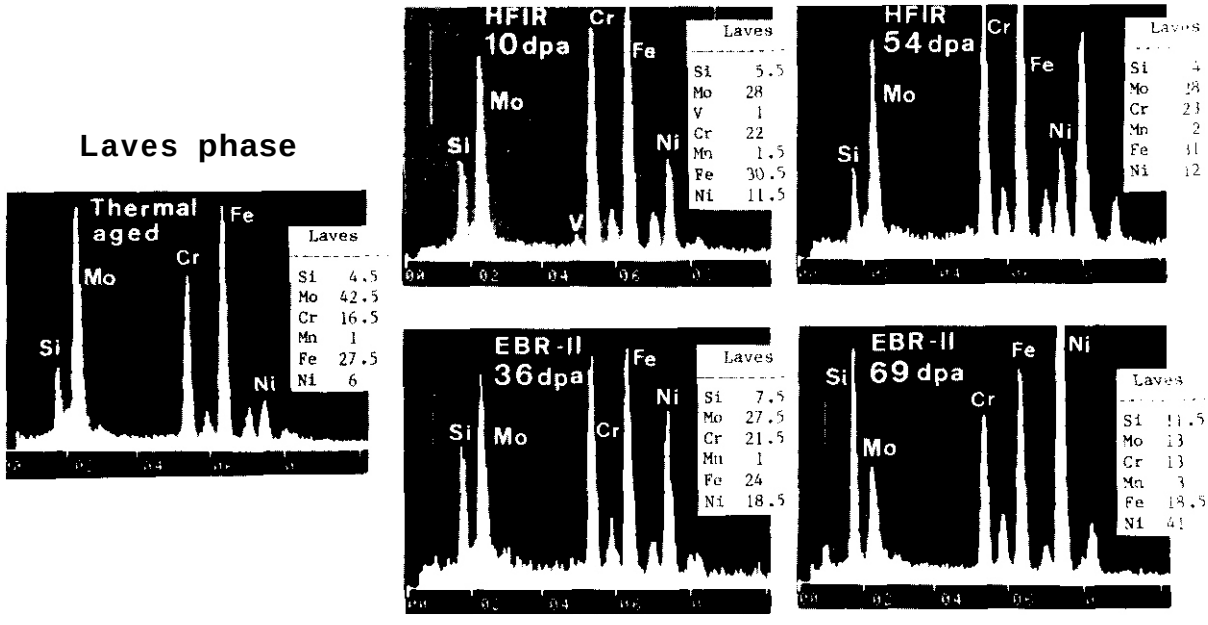

Fig. 3.5.5. Representative X-ray EDS Spectra and Compositional Data for Laves Phase from the Same Replicas Described in Fig. 3.5.4. (Thermally aged at 600°C and EBR-II or HFIR irradiated at 500–550°C, as indicated.) Element peaks present are labeled. Note Ni and Mo differences between spectra.

these phases are also given in Table 3.5.4. This section will focus on the details that are believed to be important for establishing the links among precipitate formation, RISS, and cavity development. The baseline for comparison is the thermal aging behavior of these phases.

As mentioned before, precipitation in CW 316 during thermal aging at 560 to 800°C is dominated by formation of eta, Laves, and tau phase particles.[20–24,31] Eta phase contains nearly 30 wt % each of Cr and Ni, and about 25% Mo and 7% Si (Table 3.5.4 and Fig. 3.5.4). The eta phase is considerably depleted in iron relative to the matrix. The Laves phase in aged material has the highest molybdenum content of the various phases (~40–45 wt %), is rich in Si at about 4.5 wt %, has about half the Fe content (~25–30 wt %) (Table 3.5.4 and Fig. 3.5.5) and close to the same Cr content as the matrix (which is normally 16–18 wt %). The Ni content in the Laves phase is low, at 5 to 6 wt %. Tau is morphologically and crystallographically similar to eta phase and often shares a common

ORNL-PHOTO 9194-81

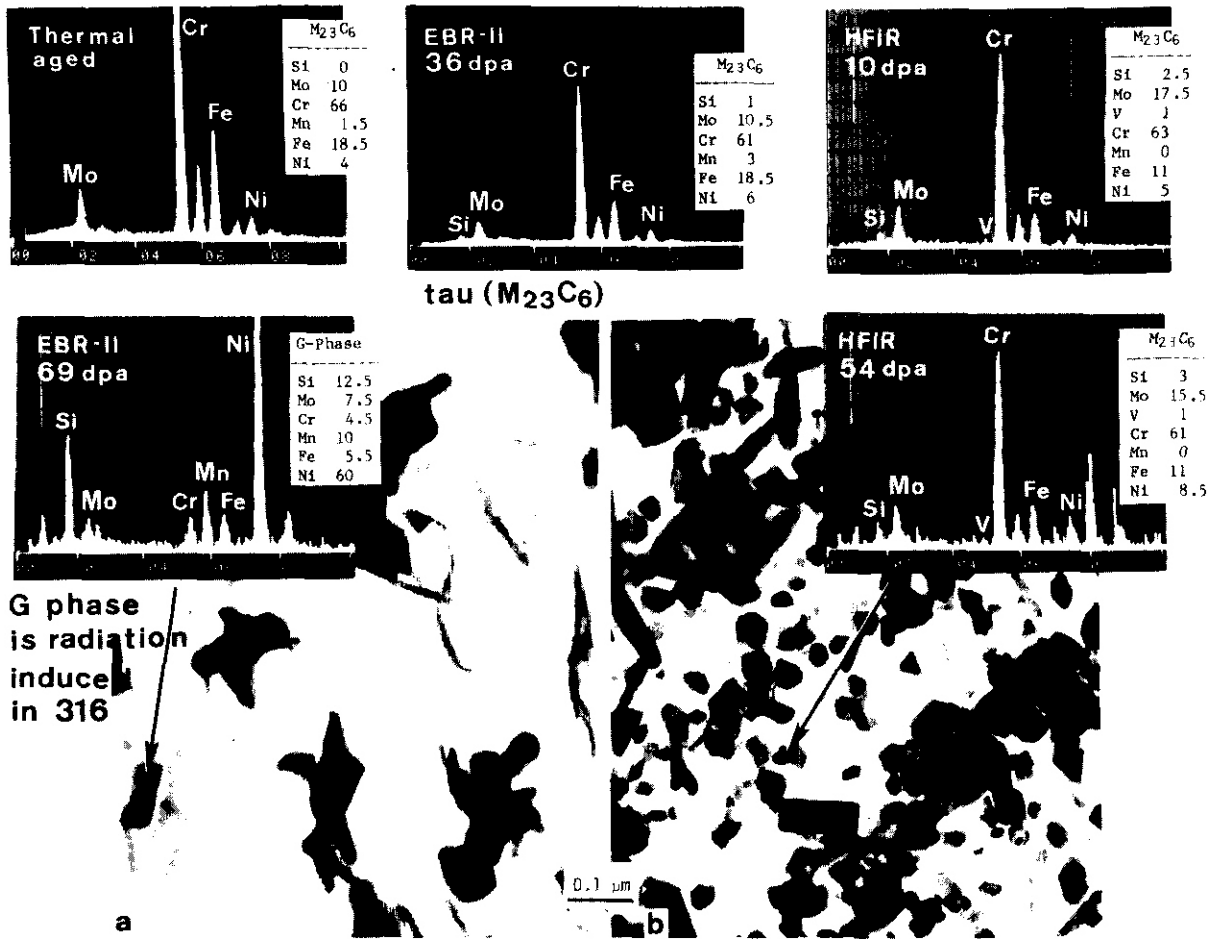

Fig. *3.5.6.* Representative X-ray **EDS** Spectra and Compositional Data for Tau ($M_{23}C_6$) Phase and G Phase from the Same Replicas Described **in Fig.** 3.5.4. (Thermally aged at 600°C and EBR-II **or** HFIR irradiated at 500–550°C, as indicated). Transmission electron microscopy of replicas after (a) EBR-II irradiation at 69 dpa and (b) **HFIR** irradiation at ***54*** dpa are included with spectra so that the reader can appreciate size, scale, and relative phase amounts. The G phase is radiation induced **in** type 316 srainless steel. Note the similarity **among** the various tau phase spectra and the striking difference **in Si** and Ni levels between G and tau phases.

interface. However, tau phase is clearly different **in** composition from eta **phase.**[21-24,31] Tau is enriched in Cr to about ***60*** to 70 **wt** % and **has** low Ni (3–5 **wt** %) and very low or no Si (0–1 **wt** %) (Table ***3.5.4*** and **Fig.** *3.5.6).*

After either EBR-II or **HFIR** irradiation at 500 to 550°C, the eta, Laves, and tau phases are the dominant phases, but the relative amount of tau **is** much less than after aging (see Table 3.5.2). Very **minor** amounts

Table 3.5.4. Quantitative AEM Compositional Analysis of Matrix Phases Produced in 20%-Cold-Worked Type 316 Stainless Steel (DO Heat)

Temperature (°C)	Damage Level (dpa)	Content (at. ppm)	Phase	Composition (wt %)								Comments
				Si	Mo	Ti	V	Cr	Mn	Fe	Ni	
600			Eta (M_6C)	7	24.8	*b*	0.7	30	0.5	6.5	30.5	Tau, eta, and Laves are major phases in roughly similar proportions.
			Tau ($M_{23}C_6$)	*b*	10	*b*	*b*	66	1.5	18.5	4	
			Laves	4.5	42.5	*b*	*b*	16.5	1	27.5	6	
			EBR-II Irradiated									
500	8.4	~5	Eta (M_6C)	5	15	*b*	0.5	43.5	2	13	20	Only a few small particles (some occasionally contain ~1 wt % P).
525	36	~22	Eta (M_6C)	7	15	*b*	*b*	35	1	12	30	Primarily eta with small amounts of Laves (only occasionally tau found between other eta particles at faulted bands).
			Tau ($M_{23}C_6$)	1	10.5	*b*	*b*	61	3	18.5	6	
			Laves	7.5	27.5	*b*	*b*	27.5	1	24	18.5	
510	69	~41	Eta (M_6C)	7.5	16.5	*b*	*b*	33.5	1	11	29.5	Eta and Laves in roughly equal portions; very minor amounts of G and γ′ phases.
			Laves	11.5	13	*b*	*b*	13	3	18.5	41	
			G Phase	12.5	7.5	*b*	*b*	4.5	10	[illegible]	[illegible]	
			HFIR Irradiated									
525–550	10	500	Eta (M_6C)	6.5	26.5	*b*	1.5	31.5	0.5	13	20.5	Eta and Laves are dominant in roughly equal portions; many small particles of tau are a minor portion.
			Tau ($M_{23}C_6$)	2.5	17.5	*b*	1	63	*b*	11	5	
			Laves	5.5	28	*b*	1	22	1.5	30.5	11.5	
510–535	54	3600	Eta (M_6C)	5.5	20	*b*	2.5	36	0.5	13	22.5	Similar to above.
			Tau ($M_{23}C_6$)	3	15.5	*b*	1	61	*b*	11	8.5	
			Laves	[illegible]	[illegible]	[illegible]	[illegible]					

Metallic elements heavier than aluminum, normalized to 100%.

Not detected.

of radiation-induced γ' and G phases[24] are found after EBR-II irradiation at 69 dpa, but neither of these are found after HFIR irradiation to 54 dpa. The various phases are also clearly distinguishable.[24,31] Tau and eta phases produced by irradiation show almost no compositional changes relative to these phases produced by aging. However, Laves phase can show substantial systematic variation of Si, Mo, and Ni levels, which will later be shown to depend upon the coupling to RISS.

Figure 3.5.4 is set up for easy visual comparison of HFIR and EBR-II irradiation effects on the composition of the eta phase as fluence increases, with the thermally aged composition as a reference point. Table 3.5.4 presents the compositions of the phases for sample-to-sample comparison for various exposure conditions. In general, there are only small systematic differences between the spectra and composition for eta produced by HFIR irradiation at 10 and 54 dpa and that found after aging at 600°C (which, in turn, is quite representative of eta phase over its entire range of observation after thermal aging[23,31]). The Si and Ni contents are slightly lower, Fe content about double, and Cr slightly increased after HFIR irradiation compared with aging. It is important to note that the V content increases during HFIR irradiation, consistent with the reported V production due to transmutation of Mn in HFIR.[36] Eta phase will scavenge and greatly concentrate even a minor amount of V present or produced in the matrix.[22,24,31] The eta phase composition shows little dependence on neutron fluence after HFIR irradiation. The composition and EDS spectrum "fingerprint" of the eta phase after EBR-II irradiation (8–69 dpa) is similar to the composition of the eta phase produced by thermal aging and by HFIR irradiation. The Si and Ni contents after EBR-II irradiation are almost identical to those found after aging; Cr is slightly higher and Fe almost double. For EBR-II irradiation, little or no V is found (consistent with previous measurements at lower fluence[31]) and the Mo is reduced by almost a factor of 2.

Figure 3.5.5 shows the comparison of the elemental composition of Laves phase for HFIR- and EBR-II irradiated materials and for aged material. The compositions are also found in Table 3.5.4. Irradiation apparently can affect the Laves composition much more than it does the eta

(Fig. 3.5.4) and tau (Fig. 3.5.6) phases. The HFIR irradiation does not substantially alter the Si and Mn contents and only slightly increases Cr and Fe contents relative to thermal aging. Vanadium is detected sporadically and at lower contents in Laves phase than in eta phase after HFIR irradiation. The largest changes are a reduction in Mo to 28 to 30 wt % (from 40–45 wt % found after aging) and a doubling of the Ni content to approximately 12 wt % after HFIR irradiation. Surprisingly little variation is found with increasing fluence from 10 to 54 dpa in HFIR, and particle-to-particle variations in composition are very small. Prior work[24,31] indicated about 20 to 25 at. % Ni in Laves phase in the HFIR sample irradiated to 54 dpa. However, the initial replica was quite poor, and only a few measurements were made. Possibly eta and Laves particles were superimposed because a very good second replica was made to recheck that result. Eta phase was found to be the only nickel-rich phase, and all the Laves particles were similar to the composition shown in Fig. 3.5.5. Fine tau ($M_{23}C_6$) phase was not found previously either, but its presence on the new replica was consistent with the low nickel content of the Laves phase.

In EBR-11-irradiated material, Laves phase is clearly distinguishable from the other phases by the "fingerprint" spectra of Fig. 3.5.5. In addition, Laves phase has an internal stacking fault structure and diffraction behavior that makes it easily distinguishable from the other phases, even without x-ray EDS.[24,31] In this study (and previous work[26]), Laves phase was clearly identified at 36 and 69 dpa in EBR-11-irradiated material. The amount of Laves is quite small at 36 dpa but is increased substantially by 69 dpa, and there are also considerable differences in composition as the neutron fluence increases (see Table 3.5.2). After 36 dpa in EBR-II, the Si content is higher, the Ni content nearly triple, the Cr slightly greater, and Fe slightly less than the levels of these same elements in the same phase produced by thermal aging (see Table 3.5.4). After 69 dpa the Si content is still higher (11–12 wt % compared to 4–5%), Mo reduced to about a third, and Ni almost seven times greater than after thermal aging. After the EBR-II irradiation Cr and Fe show only small reductions.

Details in Table 3.5.2 show that in EBR-II after 36 dpa the Laves particles in the form of fine laths constitute only a small volume fraction of the precipitation, with virtually no void association. After EBR-II irradiation to 69 dpa, the Laves particles have a blocky morphology, which usually has a different crystal habit than the lath morphology.[31] The blocky Laves particles are almost completely associated with voids, and the volume fraction of Laves has moderately increased from 36 to 69 dpa. These observations favor interpretation as dissolution and reprecipitation rather than any type of infiltration-exchange mechanism.[13-15]

The final portion of this section deals with tau phase and the radiation-induced G and γ' phases. Figure 3.5.6 again shows spectra and compositional information for tau phase after irradiation, with the thermal composition and EDS spectrum as a visual reference point. Figure 3.5.6 and Table 3.5.4 include an analysis of G phase, found after EBR-II irradiation at 69 dpa. Transmission electron microscopy of the carbon extraction replicas after EBR-II irradiation to 69 dpa [Fig. 3.5.6(a)] and after HFIR irradiation to 54 dpa [Fig. 3.5.6(b)] are included so that the reader can appreciate the scale, amounts, and spatial distributions of the phases identified and the very obvious difference between the EBR-II and HFIR irradiations. Tau phase, in very small portions, is observed after 8.4 dpa (refs. 26 and 31) and 36 dpa in EBR-II, but none is found after 69 dpa. Only a very small fraction of γ' was detected, primarily by Moirë fringe imaging in bright field and the combination of diffraction analysis plus dark-field imaging with superlattice reflections. Many of the small particles found between voids appear to be Laves and G-phase particles in addition to γ'. The "fingerprint" of tau phase is very distinct and clearly similar to the fingerprints of the thermally produced phase and the phase produced by HFIR irradiation at both fluences and EBR-II irradiation at 36 dpa. After EBR-II irradiation, tau contains slightly more Si and Ni but is otherwise compositionally identical to its thermal counterpart. After HFIR irradiation, tau has a little more Si, slightly more Ni, a noticeable amount of V, more Mo, and less Fe than the thermal

phase, and virtually no compositional fluence dependence (see Table 3.5.4). We do not observe much enrichment of Si and never observe Ni enrichment of tau phase relative to the matrix under any aging or irradiation condition[21-24,26,31] in contrast to both early and recent work by Brager and Garner (and co-workers)[11-15,30,37,38] on this DO heat and other heats of type 316 stainless steel. The G-phase spectrum and composition are included in Fig. 3.5.6 for comparison of an irradiation induced phase with a naturally Ni- and Si-poor phase like tau. The Si and Ni contents of G phase are the highest observed in any of the phases in Figs. 3.5.4 through 3.5.6, and the Mn enrichment is unique to this phase in type 316 stainless steel.[26,38] Its distinctive "fingerprint" cannot be confused with any of the other phases, including γ' (ref. 26). One distinct correlation here is that tau phase is not observed where irradiation-induced phases are present and vice versa (Tables 3.5.2 and 3.5.4).

3.5.4.3.3 SA 316 Microstructural Evolution. We will not go into the microstructural or microchemical detail for the SA material that we did for the CW 316 because research is still in progress. There are, however, several interesting, easy comparisons that are important to further illustrate and help reinforce points made previously. Summaries of microstructural observations are given in Tables 3.5.5 and 3.5.6.

Previous work shows that there are distinct precipitation differences between thermally aged SA and CW 316.[24,31,39,40] Tables 3.5.5 and 3.5.6 summarize microstructural observations for the aged SA 316 samples. Figure 3.5.7 shows the SA 316 microstructure that developed after aging for 10,000 h at 600°C [compare with CW 316 in Fig. 3.5.1(b)]. Tau is the only phase formed during the aging, and these coarse laths are fully developed after 2770 h and remain unchanged on further aging to 10,000 h. The microstructure is nearly identical after aging for 2770 and 4400 h at 560°C, and no precipitates are observed after 10,000 h at 500°C. Considerable precipitation of coarser tau and Laves develops after 10,000 h at 650°C.

Table 3.5.5. A Summary of Matrix Microstructural Information (Cavity and Dislocation Components) on Solution-Annealed Type 316 Stainless Steel (DO Heat) After Thermal Aging and EBR-II and HFIR Irradiations

Exposure Conditions (°C, aging time or reactor, dpa, at. ppm He)	Cavity Component			Dislocation Component	
	Diameter (nm)	Density (m^{-3})	Comments	Density (m/m^3)	Comments
500, aged 10,000 h[a]		None		<10[illegible]	
560, aged 4400 h[a]		None		About same as above	
600, aged 2770 h[a]		None		About same as above	
600, aged 10,000h[a]		None		Same as above	
650, aged 10,000 h[a]		None		Slightly greater than above	
500, EBR-II, 8.4, ~5[a]	20–100 (voids)	Close to 10^{19}	Very few fine bubbles are found; most voids are associated with precipitates and swelling is several tenths of percent or less.	a	Many Frank loops plus network
500, PI[b]	2–3 (bubbles)	Much greater than 10^{22}	A few very fine bubbles are observable, most are probably below resolution limit of microscope; there are no voids.	a	Very many small prismatic loops, no network.
525, EBR-II, 36, ~22[a]	20–100 (voids)	~5 × 10^{19}	Very few fine bubbles, increased void population, and most are attached to precipitates.	a	Network, very few loops.
625, EBR-II, 8.4, ~5[a]	2–5 (bubbles) 20–400 (voids)	Very low 5–7 × 10^{18}	A few very fine bubbles are seen along dislocations and at precipitate interfaces; nearly all voids are attached to precipitates.	a	Network plus a few large Frank loops.
625, PI[b] EBR-II, 8.4, ~110	2–8 (bubbles)	>10^{22}	A very uniform size and spatial distribution of fine bubbles in the matrix, along dislocations, and at precipitate interfaces.	a	Loose network, no loops
515–540, HFIR, 11, 600[a]	2–5 (bubbles) 10–20 (voids?)	0.5–1 × 10^{22}	A fine uniform dispersion of bubbles with a distinct bimodal population of larger matrix cavities at a much lower concentration. These may be early voids.	a	Loose network, no loops
530–555, HFIR, 42, 3000	30–60 (voids) 90–120 [illegible]	[illegible] 10^{22}	Very few fine bubbles are found; smaller voids are in the matrix and larger voids are attached to precipitate particles.	Not measured[c]	

[a]Work is still in progress on either a particular microstructural component or the sample in general.

[b]PI = 110 at. ppm He injected at 20°C prior to irradiation.

[c]Dislocation density was not measured because sample was taken from gage of tensile specimen that had been postirradiation tensile tested at 75 to 100°C below the irradiation temperature.

Table 3.5.6. A Summary of Matrix Microstructural Information (Precipitate Component) on Solution-Annealed Type 316 Stainless Steel (DO Heat) After Thermal Aging and EBR-II and HFIR Irradiations

Exposure Conditions (°C, aging time or reactor, dpa, at. ppm He)	Phases[a]	Size (nm)	Density (m^{-3})	Comments
500, aged 10,000 h[b]	None			
560, aged 4400 h[b]	Tau	100–500	$<2 \times 10^{19}$	Small volume fraction of swordlike laths, many nucleated in clusters of two, three, and four.
600, aged 2770 h[b]	Tau	Similar to above	$\sim 2 \times 10^{19}$	
600, aged 10,000 h[b]	Tau	Same as above		Slightly larger amount (laths are a little thicker); otherwise, same as above.
650, aged 10,000 h[b]	Tau, Laves	100–1000	$0.5–1 \times 10^{19}$	Coarse laths and blockly particles of tau and Laves. Many particles appear clustered, possibly indicating sympathetic nucleation.
500, EBR-II, 8.4, ~5[b]	Eta, Fe_2P, γ'	10–200	*b*	Fe_2P is fine laths; only a small amount of fine γ', and most of the precipitation is blocky eta phase.
500, PI[c] EBR-II, 8.4, 110[b]	None			
525, EBR-II, 36, ~22[b]	Eta, Fe_2P *b*	10–200	More than at 8.4 dpa	There does not seem to be any γ', and the amount of precipitation is several times greater than at 8.4 dpa because of a greater number of eta particles.
625, EBR-II, 8.4, ~5[b]	Eta, Laves, Fe_2P	100–500	*b*	Laves and especially Fe_2P-type particles are very long, thin narrow laths. Eta phase is dominant portion as blocky particles.
625, PI[c] EBR-II, 8.4, 110	Eta, Laves, and tau	100–500	*b*	Particle density is similar, but volume fraction appears about double that found in the uninjected sample because of thicker particles, particularly because of switchover from Fe_2P to Laves as dominant lath-shaped phase. Laves dominates and a small amount of tau ($M_{23}C_6$) is found.
515–540, HFIR, 11, 600[b]	Eta, Laves	100–200	*b*	Primarily blocky eta phase particles with some smaller Laves laths.
530–555, HFIR, 42, 3000[b]	Eta, Laves	100–200	$1–2 \times 10^{20}$	Similar, or maybe a little coarser than above.

[a]Phase identified through electron diffraction or x-ray EDS an replicas.

[b]Work is still in progress on either a particular microstructural component or the sample in general.

[c]PI = 110 at. ppm He injected at 20°C prior to irradiation.

ORNL-PHOTO 9198-81

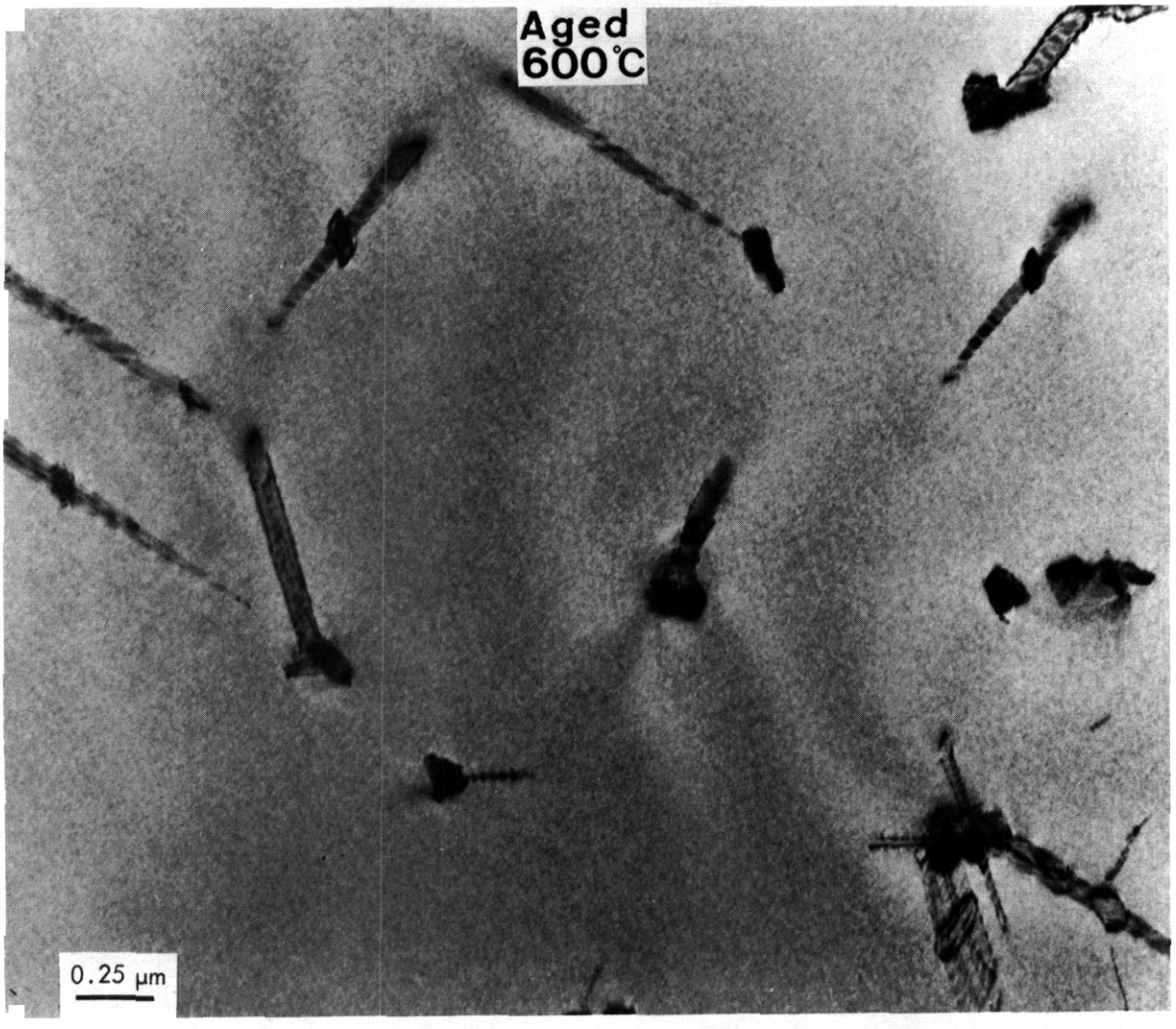

Fig. 3.5.7. Solution Annealed Type 316 Stainless Steel (DO Heat) Aged at 600°C for 10,000 h. The only precipitate formed is tau ($M_{23}C_6$) phase in the swordlike lath morphology.

Figure 3.5.8 shows microstructures developed at lower and higher fluences after EBR-II and HFIR irradiation of DO heat SA 316 at 500 to 555°C. Tables 3.5.5 and 3.5.6 also contain microstructural descriptions for these samples. These illustrate, by intercomparison, microstructural differences that correlate with the large change in helium generation rate. They also illustrate the couplings between precipitate *and* cavity development and the importance of relative development rates among the various microstructural components. Figure 3.5.8(a) and (b) shows the

ORNL-PHOTO 919581

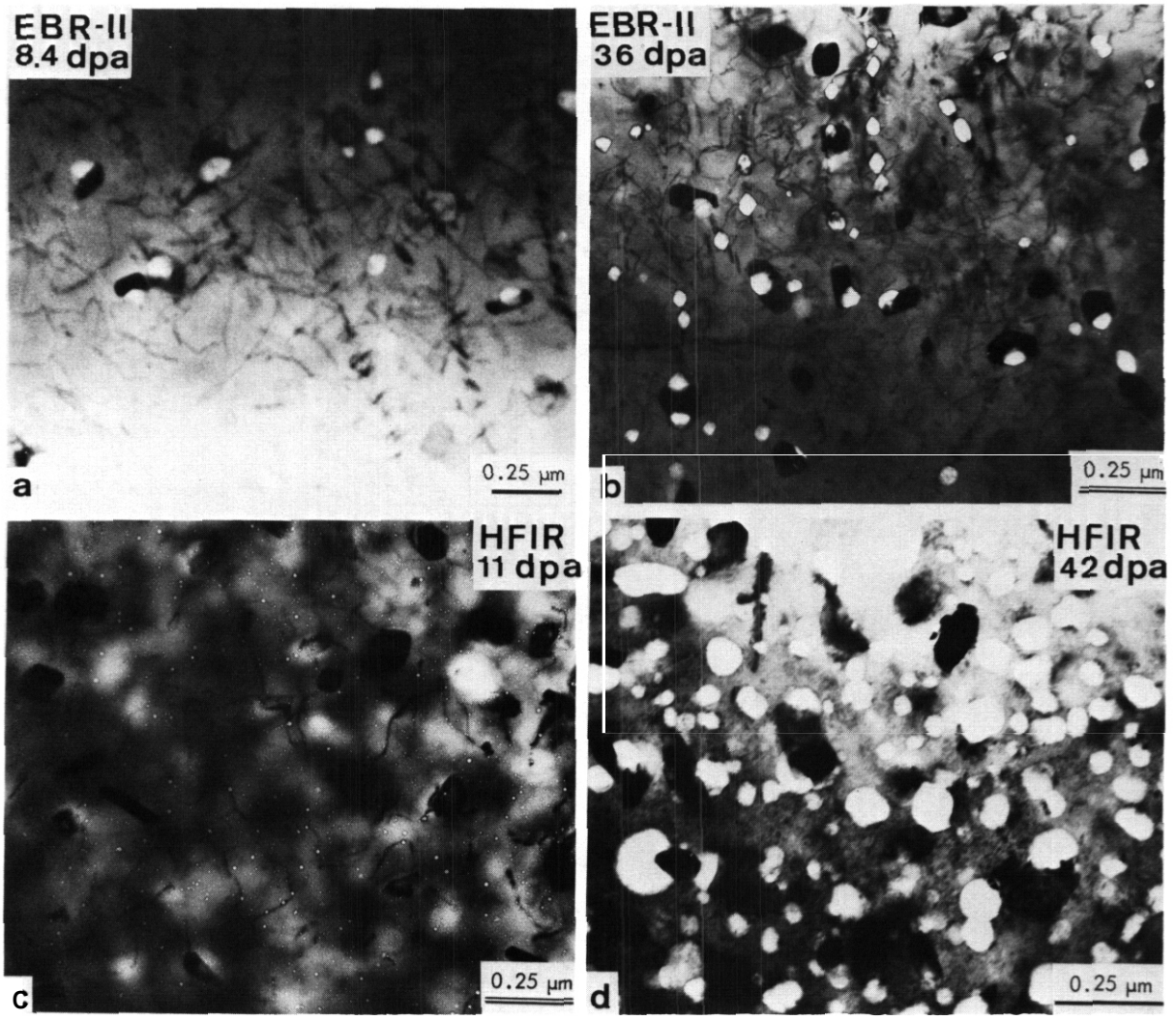

Fig. 3.5.8. Solution Annealed Type 316 Stainless Steel (DO Heat) Irradiated in EBR-II at (a) 500°C and (b) 525°C and in HFIR at (c) 515 to 540°C and (d) 530 to 555°C to the Fluences Indicated. The helium generation rate is about 100 times greater in the HFIR-irradiated samples. The sequence and amount of void development together with precipitate development are clearly being affected by differences in helium generation rate.

slow and continuous development of an increasing number of voids and precipitate particles (eta, Laves, plus small amounts of irradiation-induced phases) with increasing fluence in EBR-II (see Tables 3.5.5 and 3.5.6). There are very few resolvable bubbles (see Table 3.5.5). Apparently, as helium bubbles form they quickly convert to voids. A few voids are observed in the matrix after 36 dpa, but most of the larger

voids are attached to precipitate particles. Figure 3.5.8(c) and (d) shows that a moderately high concentration of bubbles and a significant amount of precipitates develop rapidly after 11 dpa in HFIR, and abundant void formation is observed both in the matrix and in association with precipitate particles after 42 dpa. After 11 dpa, a bimodal distribution of matrix cavities [see Table 3.5.5 and Fig. 3.5.8(c)] is observed. This bimodal development could be the early stage of matrix void formation.[20] After 42 dpa, the largest voids are clearly those associated with various precipitate particles. Void swelling clearly develops earlier in EBR-II than in HFIR at low fluence but is then accelerated in HFIR at higher fluence. Swelling after 36 dpa in EBR-II is about 0.5%, due to 5×10^{19} m^{-3} of voids that range from 20 to 100 nm in diameter (Table 3.5.5).[27] Swelling is 8 to 9%, by the same measure, after 42 dpa in HFIR due to about 1.5×10^{21} m^{-3} of voids that range from 20 to 120 nm in diameter (Table 3.5.5).[27] Clearly the microstructural evolution is different in EBR-II and HFIR in Fig. 3.5.8. The direct role of increased helium generation is increased bubble nucleation. However, subsequent development of bubbles into voids, if they grow beyond their critical radius,[16] appears very complicated and related to development of other microstructural components as well. At least some coupling to RISS is obvious in comparing thermal with irradiated precipitation behavior.

Finally, consider some helium-preinjected (110 at. ppm) samples of SA 316 irradiated side by side with uninjected material in EBR-II to 8.4 dpa. Results from these samples help to make clear the coupling of system sink strength to precipitation formation through the various mechanisms of RISS. Figure 3.5.9 shows the microstructure of the helium-preinjected counterpart of Fig. 3.5.8(a) after 8.4 dpa at 500°C in EBR-II. No voids and some barely resolvable bubbles are observed, and matrix precipitation is not found (see Table 3.5.6). The only features are a high concentration of prismatic loops that have developed from the fine black spot damage present after the 20°C helium preinjection. Figure 3.5.10 has the same comparison of uninjected and preinjected SA 316 after 8.4 dpa at 625°C in EBR-II. Figure 3.5.11 shows the microstructure of the preinjected sample at higher magnification. In the samples without

ORNL-PHOTO 9196-81

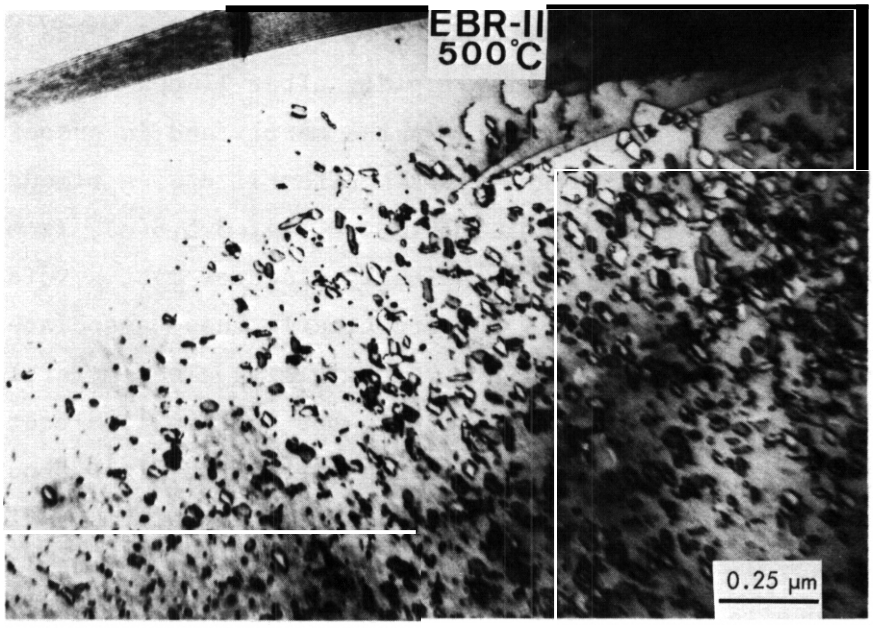

Fig. 3.5.9. Solution Annealed Type 316 Stainless Steel (DO Heat) Irradiated in EBR-II at 500°C to 8.4 dpa after 110 at. ppm He Had Been Preinjected at 20°C. Prismatic loops are found with virtually no observable voids, bubbles. or precipitation.

ORNL-PHOTO 9199-81

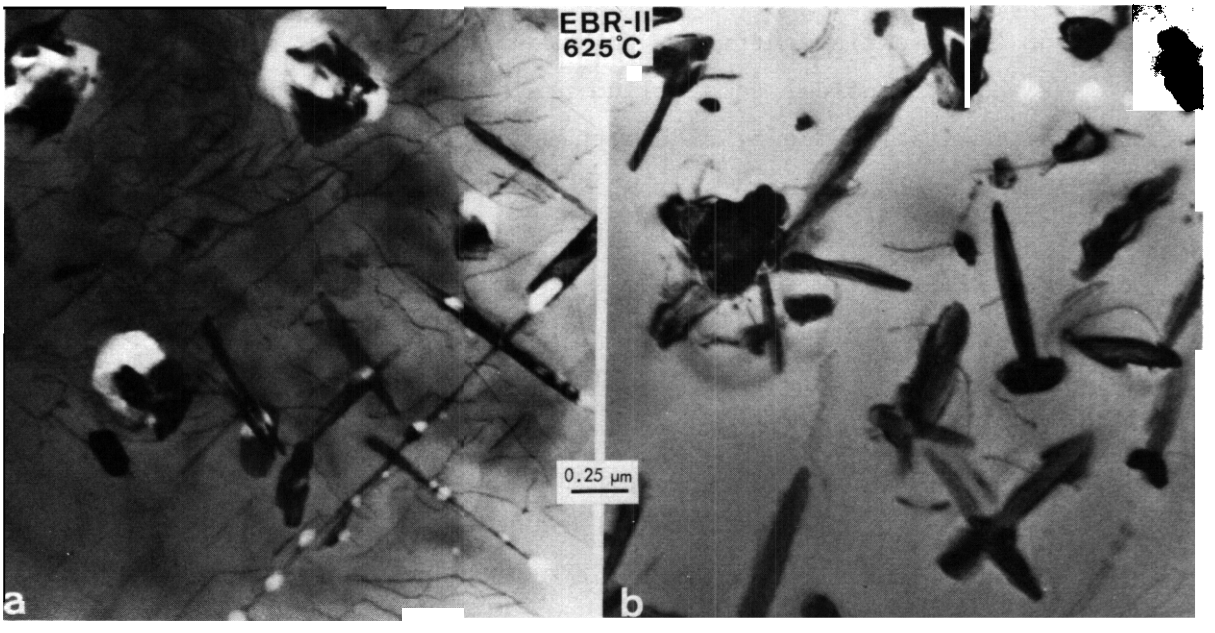

Fig. 3.5.10. Solution Annealed Type 316 Stainless Steel (DO Heat) Irradiated in EBR-II at 625°C to 8.4 dpa. (a) Uninjected and (b) with 110 at. ppm He preinjected at 20°C. Precipitation is increased but void swelling completely suppressed.

ORNL-PHOTO 9197-81

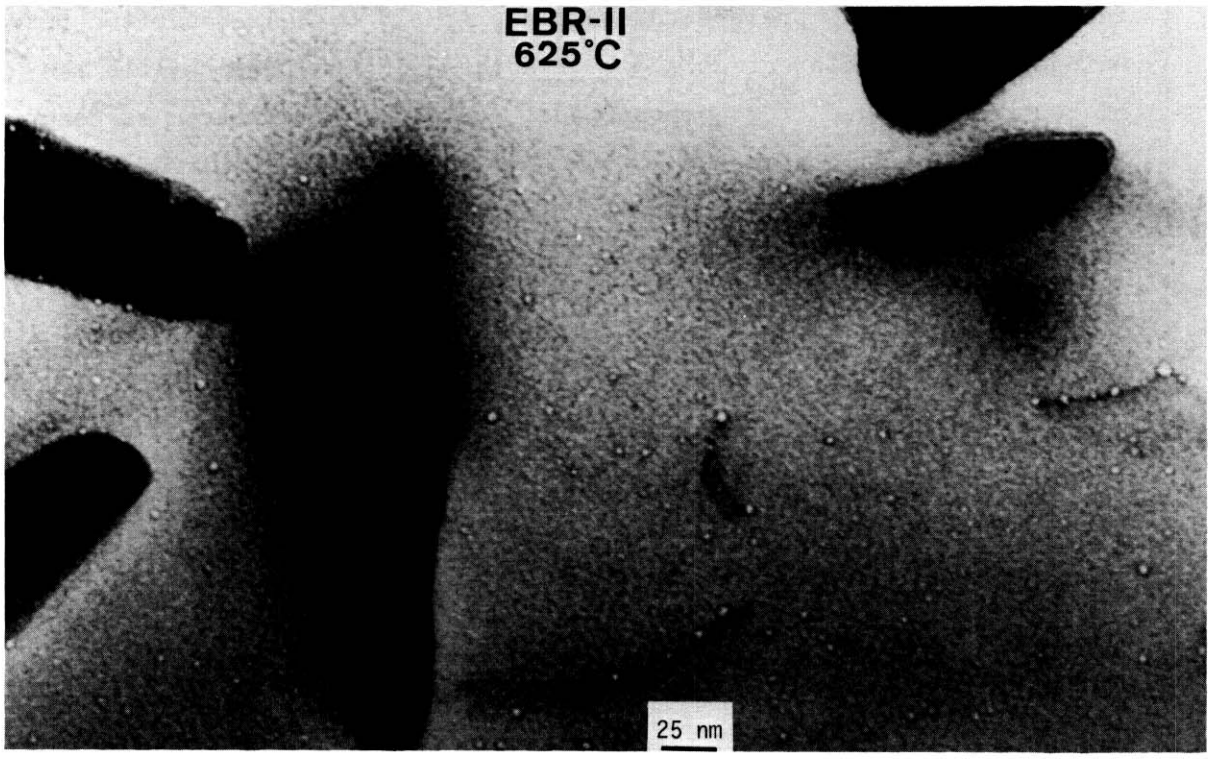

Fig. 3.5.11. Higher Magnification of SA 316 Irradiated in EBR-II at 625°C with 110 at. ppm He Preinjected at 20°C [Fig. 3.5.10(a)] Shows the Very High Concentration of Fine Helium Bubbles in the Matrix, at Dislocations and Precipitate Interfaces that Coincide with and Are Thought Responsible for the Suppressed Swelling Shown in Fig. 3.5.10.

preinjection [in Fig. 3.5.10(a)], both large and small voids can be seen in association with some portion of the equally coarse precipitation (Tables 3.5.5 and 3.5.6). By comparison, the helium-preinjected sample has no observable voids as well as more and coarser precipitate particles than the uninjected material. Early phase identification and compositional x-ray EDS studies show that the precipitation in the preinjected sample is nearer the thermal behavior for this material, with eta, Laves, and sigma being found thus far (Table 3.5.6). By contrast, the precipitation in the uninjected sample contains a significant fraction of irradiation-induced phases. This combined with higher nickel in Laves phase indicates a much higher level of RISS. Figure 3.5.11 shows clearly the very high concentration ($>10^{22}$ m^{-3}) and uniform (size and spatial) dispersion of fine

bubbles in the matrix, along dislocations and across precipitate interfaces in the helium-preinjected sample. At 625°C, the comparison between uninjected and preinjected SA 316 irradiated in EBR-II parallels the microstructural and microcompositional evolutionary differences described in Sect. 3.5.4.3.1 between CW 316 irradiated in HFIR and irradiated in EBR-II at 500 to 550°C. This agreement leads us to suspect that some more general underlying principles can reconcile these observations.

3.5.4.3.4 Microstructural Data Correlation and Summary of the Effects of Helium.

CW 316, EBR-II and HFIR. The data show that altering the helium level or generation rate can affect development of both cavity and precipitate components of the microstructure. First we will deal with the cavity microstructure. At the low helium generation rate found in EBR-II, the entire microstructure of CW 316 develops slowly and progressively at 500 to 525°C. Fine bubble formation and significant precipitation precede the early stages of void formation from 8.4 to 36 dpa. The bubbles convert[16] to a coarser distribution of voids, in conjunction with further development of the precipitate structure as fluence increases (including some dissolution and redistribution). During irradiation of the same CW 316 at similar conditions in HFIR with its much higher helium generation rate, fine bubbles and precipitation develop much more rapidly than in EBR-II irradiation. In HFIR, the cavity microstructure continues to grow slowly, as a fairly uniform size distribution of bubbles, and resists development into coarse voids up to 54 dpa.

There are also important differences between precipitation in CW 316 irradiated in HFIR and in EBR-II. The behavior of aged CW 316 provides a baseline for precipitation that helps us understand the nature of these differences. Much more eta and more Laves are found after irradiation in either reactor than after aging (see Table 3.5.2). Tau is a major phase during aging, a minor phase in HFIR, and very sparse in EBR-II. In EBR-II, irradiation encourages formation of the naturally Si- and/or Ni-rich thermal phases (only Si-rich in the case of Laves) and discourages

formation of phases poor in both elements. The G and γ' phases found after EBR-II irradiation are not normally found in aged SA or CW 316. When these phases are found after aging in other austenitic or Fe-Cr-Ni-Mo-Si alloys, they are also naturally Ni- and Si-rich.[24,41]

The compositional fluence dependence varies from phase to phase during EBR-II irradiation. Eta phase remains compositionally unchanged over the entire fluence range. Tau phase, found over a smaller fluence range, also remains constant. Compositionally, Laves phase is more flexible in Ni concentrations than the other phases. It is found substantially enriched in Ni at the early stages of development in ERR-I1 at 36 dpa, and it is found even richer in Ni at 69 dpa. The important point, however, is that Laves phase development with increasing fluence appears to involve both redistribution through dissolution and reprecipitation, as well as particle growth and coarsening.

Precipitation in CW 316 irradiated in HFIR differs from that in EBR-11-irradiated material and falls closer in character to aged CW 316. Substantial amounts of eta and Laves develop in HFIR, but a fine dispersion of Ni- and Si-poor tau ($M_{23}C_6$) particles is the minor phase. This is in contrast to the small particles of the irradiation-induced Ni- and Si-rich G and γ' phases found in ERR-11. These fine tau-phase particles are the first precipitate phase to develop and are still present (and Ni- and Si-poor) after 54 dpa. The volume fraction of Laves phase is greater and it forms with much less Ni in HFIR than in EBR-II. It remains compositionally unchanged and low in Ni over the entire fluence range, in contrast to the high Ni and continuously increasing enrichment observed in EBR-II.

SA 316, EBR-11 and HFIR. Considering first SA 316 in EBR-II at 500 to 525°C, void swelling and precipitation develop after 8.4 dpa, and the number of voids and the number of precipitate particles increase with increasing fluence up to 36 dpa. Both precipitate size and void size, however, are fairly constant over this fluence range, indicating that, once nucleated, each microstructural feature rapidly grows to a stable size. Compared with the CW 316 at the same conditions and low helium

generation rate in ERR-11, void formation and precipitation are greater in the SA 316 and very few fine bubbles are observed. At 36 dpa there is much more precipitate-assisted void growth in SA 316 than in CW 316. Precipitate formation in the ERR-11-irradiated SA 316 is greater than that in aged material and is dominated by eta (M_6C) phase. Small amounts of irradiation-induced γ' and/or Fe_2P-type phases are observed at 8.4 to 36 dpa.[24] The only phase found in aged SA 316 is Ni- and Si-poor tau phase ($M_{23}C_6$) up to 600°C, so that the presence of these other phases under EBR-II irradiation indicates substantial RISS in conjunction with the void swelling.

At the higher helium generation rate in HFIR, the precipitates and voids develop independently in SA 316, compared with the coupling we find in EBR-II. Precipitate development is rapid in HFIR, and after 11 dpa the particle size and number density at 510 to 550°C are nearly equivalent to those found after 36 dpa in EBR-II. The HFIR precipitation contains no irradiation-induced phases. Cavity nucleation is rapid in SA 316 in HFIR and consists of fine bubbles rather than the coarse voids found in EBR-II. However, the HFIR sample exhibits a distinct bimodal distribution shown in Fig. 3.5.8(c), which indicates the earliest stage of bubble-to-void conversion. These first voids forming in HFIR are in the matrix and not at eta particles (which are both coarse[42] and Ni- and Si-rich[**]) as in EBR-II. In contrast with the lower fluence comparison, void formation and swelling are considerably greater at higher fluence in HFIR than in EBR-II [see Fig. 3.5.8(b) and (d)]. The swelling is greater because voids are about 50 times more numerous at the higher fluence in HFIR than in EBR-II. Both matrix and precipitate-assisted void formation contribute to the high swelling in HFIR. Cavity concentration is reduced with increasing fluence in HFIR because of void and bubble coalescence, in contrast to the increasing void plus bubble concentrations found in EBR-II with increasing fluence.

SA 316, EBR-11, With and Without Preinjected Helium. The bubble concentration in preinjected SA 316 irradiated at 625°C to 8.4 dpa is much higher than the void plus bubble concentrations in any of the uninjected

SA and CW 316 irradiated in EBR-II or HFIR. The preinjected SA 316 has smaller bubbles, which are barely resolvable and are at least as numerous as those found at 625°C. In addition, the loops add significantly to the total sink density at 500°C. Preinjection suppresses void swelling completely at both temperatures. The precipitate results contrast because helium preinjection coincides with elimination of precipitation at 500°C but considerable increase at 625°C. However, the high sink strength also suppresses RISS; thus preinjection, which increases the sink strength; will also suppress RISS. In the absence of RISS the alloy will behave just like a thermally aged alloy. No thermal precipitation is found in aged SA 316 at 500°C, but significant precipitation is seen at 625 to 650°C (refs. 31, 39, and 40). The phases identified thus far in the preinjected SA 316 irradiated at 625°C are similar to those found in aged material.

3.5.4.4 Discussion

3.5.4.4.1 Helium Effect on Void Formation. The condensation and correlation of the data reveal several general principles and insights about helium effects on void and precipitate development. This data for a commercial, complex alloy like type 316 stainless steel under neutron irradiation indicates that helium is very important to the nucleation stage of void formation. Void development appears to be a two-step process that involves initial helium bubble formation and subsequent conversion of the bubbles to voids. The conversion depends, at least in part, on location in the microstructure — that is, association with precipitates — and either local or total sink structure and strength. There has been a great deal of discussion over the years as to exactly how voids form. Cawthorne and Fulton envisioned bubble formation as a prerequisite to void formation in their earliest work.[1] This is also exactly the sequence of events envisioned in theoretical critical radius arguments for bubble-to-void conversion.[16,20,43] Recent heavy-ion irradiation work by Kenik and Lee[44] demonstrates that in complex austenitic stainless steels coarse precipitation and RISS alone are not sufficient for void formation. They find that helium is essential.

Increased helium level or generation rate usually increases the helium bubble population, and these bubbles in turn affect the bubble-to-void conversion by their contribution to the total sink strength of the system. At the extreme, if the cavity nucleation rate is very high, cavities (as opposed to dislocations and precipitates) can become the dominant sinks in the system. Differences in fine bubble distribution certainly contribute to differences in void formation between SA and CW 316 irradiated in EBR-II.

The combined data for HFIR and EBR-II irradiation of SA and CW 316 stainless steel indicate a sink strength at which bifurcation occurs in the possible evolutionary paths for the cavity microstructure with increased fluence. If the stable sink strength is above this level, a low-swelling path of continued bubble growth is followed, but if sink strength falls below this level a high-swelling void growth path is pursued. Our data indicate that this sink strength is a level between the strength of sink structures found in the SA and CW 316 irradiated in HFIR. This same principle is seen in the beneficial effects that fine, stable dispersions of titanium carbide (MC) particles afford to Ti-modified austenitic stainless steels. These particles refine the bubble microstructure and suppress void formation in both EBR-II and HFIR.[35,45,46]

A recent review by Odette et al.[20] of both ion and reactor swelling data for type 316 stainless steel also supports such bifurcation of the microstructural evolutionary path. The fact that the point of divergence falls between the sink structures and cavity densities produced by irradiation of SA and CW 316 in HFIR causes problems for projecting the swelling of CW 316 in a fusion environment from the existing EBR-II and HFIR data sets. Stoller and Odette[47] calibrate their model to fit the HFIR and EBR-II data sets for CW 316 (DO heat) for the appropriate He/dpa ratios and then set the He/dpa ratio at the fusion level, which is between the EBR-II and HFIR ratios. They then find that fusion swelling can fall between the swelling found in the two reactors or can be greater than either, depend on whether voids develop or whether cavities are constrained to grow as bubbles. The data thus far does not allow us to determine which way CW 316 will behave for fusion but does help to understand why the dilemma exists.

3.5.4.4.2 Helium Effects on Precipitation. The fact that helium also affects precipitation in type *316* is puzzling because helium is an inert gas and its atoms cannot enter directly into the solid state chemical reactions responsible for precipitation the way that other solid transmutants or alloy solutes can. We believe that helium affects precipitation through its effect on increasing bubble nucleation, which in turn increases the total sink strength of the system. This increased sink strength decreases **RISS** and thereby changes precipitation under irradiation. Although this picture is complicated, a conclusion from our data is that development of all the various microstructural components is intimately coupled. Our data also show bifurcation with respect to microcompositional evolution at about the same level of total sink strength as that for the cavity component of the microstructure. The presence of tau ($M_{23}C_6$) or irradiation-induced phases like γ', G, and the Fe_2P-type phases and the Ni level of Laves phase are good indicators as to whether or not RISS is substantial or minimal. Throughout our data, RISS is low when void swelling is suppressed and high when void swelling ensues.

The focus of the rest of our discussion will be to understand how RISS affects precipitation and why changes in sink strength, mitigated by helium, affect both. Later, we will compare both our data and our interpretations with those of others in the literature.

Summary of ***RISS*** *Mechanisms.* The effects of RISS have been extensively studied, both experimentally and theoretically,[4-9] for simple alloys and more recently for model stainless steels.[6,8,10] Several separable mechanisms contribute to the overall effects of **RISS.** Undersized atoms (like Si and Ni in type 316 stainless steel) can be associated with interstitial atoms in the dumbbell configuration, leading to their enrichment at sinks. Inverse Kirkendall effects lead to enrichment of slowly diffusing atoms (like Ni) and depletion of rapidly diffusing atoms (like Si, Mo and Cr)[48,49] at defect sinks for vacancy flow to sinks. Thus, Ni enrichment and Cr and Mo depletion are expected at point defect sinks, as confirmed experimentally.[10] From the above, silicon can enrich or deplete, but the results of Sethi and Okamoto generally indicate substantial enrichment.[10] No **RISS** effects for C, V, Ti, Mn, and other trace residuals in steel are well-known at present.

Several features of RISS theory are important for our consideration of its effect on precipitation and how it is affected by helium. Radiation-induced solute segregation is a result of point defect flows, so that generally some sinks would be expected to be present for significant solute enrichment to occur. The enrichment can be opposed through normal diffusion. The highest possible local solute buildups are usually required to produce irradiation-induced phases; lesser levels enhance or modify thermally stable phases. Finally, we must remember that long-range diffusion' of the appropriate point defects are required to obtain substantial solute redistribution on a scale that is microstructurally relevant (tens to hundreds of nanometers). Increased bulk recombination prevents long-range diffusion and thereby suppresses RISS effects.[6] Point defect annihilation at highly concentrated, small sinks, such as bubbles, is analogous to bulk or trap recombination of defects, so that very close spacing of the sinks will similarly reduce the buildup of significant RISS.

Description of *"Microalloying."* There are a variety of phases, each with a multitude of unique elemental requirements or solubility limits, to consider for type 316. Radiation-induced solute segregation is not the only effect to be considered for precipitate formation. For this reason, we felt it extremely important to consider the response of the alloy to both irradiation and thermal aging. As made clear in the review by Lee et al.,[24] the phases found in a particular type 316 alloy after irradiation are not new but are the precipitate phases possible via aging in other regions of that multicomponent phase diagram. The precipitate phases in a particular heat of type 316 under irradiation will be different from those produced via aging of that particular alloy to the extent that RISS causes small regions of the material to depart from their original composition. Another way to describe this process is "microalloying" as a result of RISS. Williams and Titchmarsh[42] performed aging experiments with a similar concept in mind. They prepared macroalloys for aging that were intended to simulate the compositional changes due to RISS at sinks in their base alloy, FV 548. They added enough Si to exceed the solubility limit for that element upon aging at 650 to 750°C and varied C content by a factor of 10 to go far below and far above the

normal C concentration of that steel. In the low-C, high-Si alloy they produced G-phase and no carbides; and in the high-C, high-Si alloy they produced the tau ($M_{23}C_6$) (always Si-poor) and eta (M_6C) phases. Silicon-rich Laves phase was found in both alloys. Both G and eta phases produced in the aged alloys are very similar compositionally to those same phases produced in FV 548 under irradiation in DFR. That observation is similar to ours for eta and tau phases produced in HFIR or EBR-II and supports our model.

In our model, RISS changes the composition of the "microalloy" until some solubility limit is exceeded. The precipitate phase formed will be compatible with the composition at that temperature of the "microalloy" rather than the bulk alloy. However, predicting the exact precipitate phase formed or even the particular "microalloy" formed is beyond our ability at present because one must consider more than just the effects of RISS. First, complex alloys, whether SA or CW, generally decompose during aging into several different phases, which often complement each other in terms of enrichment and depletion. Second, for the same general RISS effects, namely Si, Ni enrichment and Cr, Mo depletion, the specific "microalloy" formed depends upon the rate, order, and combination in which solutes are enriched or depleted. Third, the phases themselves, once nucleated, are also distinct thermodynamic entities, with their own well-defined elemental requirements or solubility limits. Their growth will depend on how well they match the combined effects of RISS.

The most important concept of the "microalloy" model is the connection between these microalloys and sinks. Radiation-induced solute segregation will occur to the greatest extent around point defect sinks. From the previous discussion on RISS effects, the sinks must be spaced sufficiently far apart to allow long-range diffusion for RISS. Solute changes can occur very rapidly and will be appreciable, even if equal numbers of vacancies and interstitials recombine or annihilate without net growth of the sink. A very satisfying feature of the "microalloy" concept is that it allows for intimate spatial and temporal coupling of development of the various microstructural components, particularly voids and RISS-assisted or -induced precipitation, as we so often observe.

All active sinks will experience RISS and hence microalloying adjacent to themselves. Small bubbles in type 316 stainless steel should develop some sort of surface coating, most probably enriched in Ni and Si. Mansur and Wolfer[50] envision this effect to aid void formation. Further, the nucleus of any precipitate particle will also begin to experience "microalloying" adjacent to its interface as it begins to grow and act as a sink itself, particularly if it is not forming inside the "microalloy" of some other sink. Initially, nuclei of several different phases may occur in any unstable region of the alloy, with only those nuclei growing to stable size whose solute requirements are compatible with the "microalloying" (in general, enrichment of Ni and Si, and depletion of Cr and Mo). The type 316 alloy is unstable under aging, and Ni- and Si-poor tau ($M_{23}C_6$) phase is normally the initial dominant precipitate phase. Tau phase particles may also attempt to nucleate under irradiation, but RISS will oppose further development because they do not easily dissolve the excess Si and Ni. Thermally induced phases (e.g., eta and Laves phases) must balance their intrinsic solute requirements with the enrichments and depletions of RISS. Eta in particular requires Si and Ni, but it also is substantially enriched in Mo and Cr, which are depleted by RISS. It is obvious that thermal diffusion can supply Mo and Cr flows to the interface, in response to chemical potential differences between precipitate and matrix, in spite of the effects of RISS. But it is also obvious that Mo has lower enrichment levels in eta when RISS is high. A similar effect is observed in Laves phase, with the high Ni enrichment apparently being tolerated rather than required. Apparently higher levels of RISS make possible formation of these phases that are kinetically more sluggish, and they form at temperatures lower than they would under thermal aging. They are often forced to form parasitically coupled to other sinks when RISS is too high. The primary constituents of irradiation-induced phases like G, γ', and the Fe_2P-type phases are Ni and Si. Thus they require the greatest degree of "microalloying" via RISS and are often completely associated with other sinks.

Coupling of "Microalloying" to the Effects of Helium on Sink Strength. We have developed a model for coupling RISS to precipitate development through compatibility and "microalloying" effects, and the effects of changes in helium level, distribution, or continuous generation rate are easily incorporated. Increased helium level or generation rate will significantly increase bubble nucleation, which in turn will both increase cavity and total sink strength level and tremendously hinder or cut down long-range diffusion of point defects because of the very close sink spacing. If the sink strength only suppressed point defect concentrations through mutual annihilation, swelling would be reduced, but RISS buildup would still continue. However, a high concentration of closely spaced sinks both increases sink strength and drastically cuts down the long-range diffusion to reduce both RISS and swelling by partitioning point defects and solute to many more sites. As the level of RISS and microalloying is reduced, the phase types, phase compositions, spatial arrangement, and kinetics of precipitation will progressively move from the severely irradiation affected toward the normal thermal aging behavior. This reasoning is quite consistent with our observations. The EBR-II-irradiated samples show the greatest effects of RISS, the HFIR SA 316 intermediate, and the HFIR CW 316 and helium-preinjected EBR-11-irradiated SA 316 the least. At least in the type 316 alloy, the bifurcation in the microcompositional-microstructural evolutionary path with regard to stable critical sink strength and structure occurs between those produced in SA and CW 316 in HFIR. In our model of microstructural and microcompositional evolution, void swelling and RISS-affected precipitation phenomena will most often be coupled. However, they are separable mechanisms and can uncouple and definitely can vary in order of occurrence. Further, the model allows for an effect of helium on both processes.

Comparison of Data and Model with Those Found in the Literature. Controversy and differences exist between portions of the data and interpretations presented here and elsewhere[20-27,31,35,40,43-47,51,52] and the work of Brager and Garner[11-15,30,36-38] with regard to the effect of matrix microchemical changes on microstructural evolution and the effects

of helium. Statements on both sides of the controversy can be found in the literature.[20,53] Brager and Garner[53] indicate that reaching critical low matrix levels of Si, Ni, or C is responsible and necessary for void development. The attainment of these low levels eventually results in microstructures that are independent of starting microstructure or temperature and have the same swelling rate. If helium plays any role at all in their model, it is a transient effect. Their model apparently does not allow for effects of helium on steady-state swelling rate or continued suppression of void formation and RISS effects.[53,54] The reasons for the differences in interpretation are complicated because they involve both data and mechanism differences. We will address the former and only comment on the latter.

Aging results for SA and CW 316, both microstructural and compositional, are consistent with previous results on a number of heats of type 316 stainless steel and related austenitic alloys.[39,42,55-57] The major contributions that these and other recent quantitative AEM results have made is finding eta (M_6C) formed during thermal aging and measuring Si contents of all the phases.[21-24,31,40,42,55-57] The major work in this area prior to AEM was that of Weiss and Stickler,[39] and they did not find eta (M_6C) in type 316 nor did they measure Si in precipitate phases or matrix. Formation of eta phase (M_6C) during aging is important to irradiation studies because this is the only phase that is substantially enriched in both Si and Ni during aging. There are many morphological and crystallographical similarities between tau ($M_{23}C_6$) and eta (M_6C), and the techniques for distinguishing between them are well documented.[21,24,31,38,40,55,57,58] Apparently eta (M_6C) is not formed in every heat of type 316 but is found in most.[38] Thermally formed Laves is also found to be quite rich in Si, and chi and sigma can contain Si as well. Tau ($M_{23}C_6$) is found to be both Si- and Ni-poor, and the only other phase with similar Si and Ni depletion characteristics is titanium carbide (MC) in Ti-modified steels.[24,25]

For a long time, many investigators did not adequately identify precipitate phases in steel under irradiation because of lack of adequate AEM capabilities.[27,28,40,59,60] Brager and Garner[11] were the first to find

that most of the precipitate particles produced under irradiation are substantially Ni- and Si-rich. However, they, identified the phase as "$M_{23}(C,Si)_6$" and did not until recently find eta (M_6C).[30,38] Therefore, they envisioned tau to form initially Ni- and Si-poor and then to become Ni- and Si-rich progressively during the irradiation. They also included Laves phase in this behavior pattern, and now with Mo depletion as well, termed this an "infiltration-exchange," that is, interdiffusion across the precipitate particle interface. They consider thermally formed Laves to be Si-poor,[37,38] even though their own measurements previously[12] showed the same level of Si enrichment that we show. Our data and that of others[24,42,52,58] would suggest some confusion in their earlier identifications of eta (M_6C) and tau ($M_{23}C_6$) phases. These details are, however, quite important to the concepts of Brager and Garner's particular model describing the effects of "microchemical" changes on void formation. According to their model, at some point after or during the precipitate microstructural development, depletion of Ni, Si and C to critical low solute levels in the matrix triggers void swelling and launches the material into its steady state swelling regime.[12] Further, they indicate that these depletions are inevitable, the same for a variety of irradiation conditions,[11] and ultimately unaffected by helium.[30,52,54] In the model presented here, by comparison, high swelling and RISS are not inevitable (although always possible) and indeed are separable phenomena. Also, we easily envision helium affecting both.

Our observations and those of Brager and Garner are often on different heats of type 316 but do coincide in the case of the CW 316 (DO heat) irradiated in EBR-II at 36 and 69 dpa and described here. Our samples are pieces of the same specimens they used and can therefore be compared directly. Our cavity microstructure measurements are similar to theirs, but we show somewhat higher concentrations of fine bubbles and larger voids at 36 dpa[26,30] and show larger voids at 69 dpa. The latter is most certainly due to the use of the 1 MV electron microscope for thick-section examination. Our dislocation data are similar.[29,30] The greatest disparity is in the precipitate results. At 36 dpa, Brager and Garner do not find tau ($M_{23}C_6$) or Laves phase,[30] which we show in Figs. 3.5.5 and 3.5.6. At 69 dpa, they report coarse G phase and small particles

of γ', whereas we find a mixture of medium to small Laves and G phase particles with only a small amount of γ' as the smallest particles (see Table 3.5.2). They also find no Laves but find tau ($M_{23}C_6$) and two different eta (M_6C) phases, distinguished on the basis of composition and crystal habit (also see ref. 38). We show Laves at 69 dpa (Fig. 3.5.5), find no tau ($M_{23}C_6$), and find only one type of eta phase (M_6C) with one composition (Fig. 3.5.4). Eta (M_6C) is capable of several different orientation relations for the same phase.[24,31,40]

Application of This Work to Future Alloy Development for Fusion. For the austenitic stainless steels, helium effects are shown to be important in estimating microstructural and microcompositional evolution, which in turn govern swelling. Helium effects are an important concern for both swelling and mechanical behavior of CW 316 operating as a fusion first wall. Our results indicate uncertain fusion swelling behavior for CW 316 because of the couplings of sink strength, RISS, and precipitation and the effect of helium on cavity sink strength. Swelling can definitely be high if voids develop but can be low if the sink strength constrains bubble growth and suppresses RISS. However, CW 316 is a behavior reference point for judging the improvements to be expected from advanced austenitic alloys being developed for fusion applications. Our understanding of helium effects in type 316 will also factor into the alloy development strategy and confidence we can place in the advanced alloys for fusion application. The current Path A Prime Candidate Alloy (PCA) of the ADIP effort is a 14 Cr–16 Ni–2 Mo–0.25 wt % Ti austenitic stainless steel.[61] Finely dispersed titanium carbide (MC) formation in Ti–modified austenitic stainless steels often has the beneficial effect of suppressing void swelling during either EBR-II or HFIR irradiation.[23,25,35,45,52] The reasons for this void suppression involve the combined contributions of direct helium trapping by MC particles to promote very fine helium bubble dispersions, of MC–dislocation pinning, and of MC formation coinciding with reduced precipitation of coarse, undesirable phases. All these have been factored into the philosophy and strategies of alloy development in the PCA.[61] The couplings of sink strength, RISS, precipitation, and the

effect of helium through the bubble component of the cavity sink strength would lend more confidence, at this point, to use of alloys like PCA than CW 316 for fusion. It is clear, however, that behavior for fusion is not certain at this point and that understanding helium effects is important to both alloy development and alloy selection for fusion.

3.5.5 Conclusions

From direct TEM and x-ray EDS analysis, we observe the following:

1. In CW 316 irradiated in EBR-II at 500 to 525°C, voids develop slowly at first, converting from tiny helium bubbles previously nucleated on matrix dislocations and precipitate interfaces. Voids develop more rapidly at higher fluence.

2. Precipitation in CW 316 during EBR-II irradiation at 500 to 525°C generally reflects a high degree of RISS. Compared with aged material as a baseline, eta formation (naturally Ni-, Si-rich) is increased, Laves (naturally Ni-poor, Si-rich) is modified and its formation increased, and tau (naturally Ni-, Si-poor) is quite retarded. After 69 dpa, a small fraction of radiation-induced γ' and G phases is found.

3. Irradiation in HFIR of the same CW 316 at 510 to 550°C very rapidly produces a high density of tiny bubbles and extensive precipitation, compared with EBR-II irradiation. The cavities are sufficiently dense that they remain bubbles and resist converting to voids up to at least 54 dpa.

4. Precipitation in CW 316 during HFIR irradiation reflects a much lower level of RISS and corresponds more nearly to thermally induced precipitation than that produced during EBR-II irradiation. After 54 dpa, fine tau (Ni-, Si-poor) particles are found instead of the radiation-induced phases found after EBR-II irradiation.

5. Irradiation in HFIR of SA 316 at 525 to 550°C initially produces a dense bubble structure, which suppresses void formation relative to EBR-II irradiation. However, at higher fluence this bubble concentration is not sufficient to suppress void formation, which is then accelerated relative to EBR-II irradiation.

6. Helium preinjection of SA 316 at 20°C produces a high density of bubbles, which prevent void formation and drastically reduce the effects of RISS on precipitation during EBR-II irradiation at 500 to 625°C, compared with irradiated but uninjected material.

We interpret these observations to indicate the following:

7. The coupling between RISS and precipitation under irradiation appears to be "microalloy" formation near point defect sinks. The precipitation under irradiation is then similar to simply aging these "microalloys," rather than the uniform bulk alloy, at or near the irradiation temperature. Generally RISS results in enrichment of Si and Ni and depletion of Mo and Cr at point deflect sinks. The level of RISS will generally be indicated by the increase in eta phase, the production of radiation-induced phases (γ', G phase), the modification of Laves phase, and the retardation or elimination of tau phase.

8. In general, increased helium content, either preinjected or through an increased continuous generation rate, directly increases the nucleation of fine helium bubbles. Helium effects on other microstructural components are then reflected in the level of sink strength achieved in the cavity component of the microstructure. If the total sink strength is high enough, void formation can be suppressed together with RISS being considerably reduced.

3.5.6 References

1. C. Cawthorne and E. J. Fulton, "The Influence of Irradiation Temperature on the Defect Structures in Stainless Steel," pp. 446–60 in *The Nature of Small Defect Clusters,* (vol. II of Report of a Consultants Symposium held at A.E.R.E., Harwell, July 4-6, 1966). AERE-R 5269 (1966).
2. T. R. Anthony, "Solid Segregation and Stresses Generated Around Growing Voids in Metals," pp. 630–46 in *Radiation-Induced Voids in Metals,* ed. by J. W. Corbett and L. C. Ianniello, *AEC Symp. Ser.* 26, CONF-710601 (April 1972).
3. P. R. Okamoto and H. Wiedersich, "Segregation of Alloying Elements to Free Surfaces During Irradiation," *J. Nuct. Mater.* 53(1): 336–45 (1974).

4. R. A. Johnson and N. Q. Lam, "Solute Segregation in Metals Under Irradiation," *Phys. Rev. B* 13(10): 4364–75 (1976).

5. R. A. Johnson and N. Q. Lam, "Solute Segregation Under Irradiation," *J. Nucl. Mater.* 69&70(1): 424–33 (1978).

6. P. R. Okamoto and L. E. Rehn, "Radiation-Induced Segregation in Binary and Ternary Alloys," *J. Nucl. Mater.* 83(1): 2–23 (1979).

7. H. Wiedersich, P. R. Okamoto, and N. Q. Lam, "A Theory of Radiation-Induced Segregation in Concentrated Alloys," *J. Nucl. Mater.* 83(1): 98–108 (1979).

8. H. Wiedersich and P. R. Okamoto, "Effects of Radiation-Induced Segregation," pp. 23-41 in *Phase Stability During Irradiation* (Proc. Symp., Pittsburgh, Pa., Oct. 5–9, 1980), ed. by J. R. Holland, L. K. Mansur, and D. I. Potter, The Metallurgical Society of AIME, Warrendale, Pa., 1981.

9. G. Martin et al., "Dose Rate Effects on Solid Solution Stability," pp. 43–62 in *Phase Stability During Irradiation* (Proc. Symp., Pittsburgh, Pa., Oct. 5–9, 1980), ed. by J. R. Holland, L. K. Mansur, and D. I. Potter, The Metallurgical Society of AIME, Warrendale, Pa., 1981.

10. V. K. Sethi and P. R. Okamoto, "Radiation-Induced Segregation in Complex Alloys," pp. 109–21 in *Phase Stability During Irradiation* (Proc. Symp., Pittsburgh, Pa., Oct. 5–9, 1980), ed. by J. R. Holland, L. K. Mansur, and D. I. Potter, The Metallurgical Society of AIME, Warrendale, Pa., 1981.

11. H. R. Brager and F. A. Garner, "Swelling as a Consequence of Gamma Prime (γ') and $M_{23}(C,Si)_6$ Formation in Neutron Irradiated 316 Stainless Steel," *J. Nucl. Mater.* 73(1): 9–19 (1978).

12. H. R. Brager and F. A. Garner, "Dependence of Void Formation on Phase Stability in Neutron-Irradiated Type 316 Stainless Steel," pp. 207–32 in *Effects of Radiation on Structural Materials, ASTM Spec. Tech. Publ.* 683, American Society for Testing and Materials, Philadelphia, 1979.

13. H. R. Brager and F. A. Garner, *DAFS* Quart. *Prog. Rep. March 1980,* DOE/ER-0046/1, p. 157.

14. H. R. Brager and F. A. Garner, "Microchemical Evolution of Neutron-Irradiated Stainless Steel," pp. 470–83 in ***Effects of Radiation on Materials, ASTM Spec. Tech. Publ.*** 725, ed. by David Kramer, H. R. Brager, and J. S. Perrin, American Society of Testing and Materials, Philadelphia, 1981.

15. F. A. Garner, "The Microchemical Evolution of Irradiated Stainless Steels," pp. 165–89 in ***Phase Stability During Irradiation*** (Proc. Symp., Pittsburgh, Pa., Oct. 5–9, 1980), ed. by J. R. Holland, L. K. Mansur, and D. I. Potter, The Metallurgical Society of AIME, Warrendale, Pa., 1981.

16. H. R. Brager and F. A. Garner, "Microchemical Evolution of Neutron-Irradiated Stainless Steel," pp. 470–83 in ***Effects of Radiation on Materials, ASTM Spec. Tech. Publ.*** 725, ed. by David Kramer, H. R. Brager, and J. S. Perrin, American Society of Testing and Materials, Philadelphia, 1981.

17. J. A. Spitznagel, F. W. Wiffen, and F. V. Nolfi, "Microstructures Developed in 'Simulated' Fusion Irradiations," ***J. Nucl. Mater.*** 85&86(II,B): 629–46 (1979).

18. J. J. Holmes and J. L. Straalsund, "Irradiation Sources for Fusion Materials Development," ***J. Nucl. Mater.*** 85&86(Part A): 447–51 (1979).

19. R. E. Gold et al., "Materials Technology for Fusion: Current Status and Future Requirements," ***Nucl. Technol./Fusion*** 1: 169–237 (1981).

20. G. R. Odette, P. J. Maziasz, and J. A. Spitznagel, "Fission-Fusion Correlations for Swelling and Microstructure in Stainless Steels: Effect of the Helium to Displacement Per Atom Ratio," ***J. Nucl. Mater.*** 104(1–3): 1289–1303 (1981).

21. P. J. Maziasz, "The Formation of Diamond-Cubic Eta (η) Phase in Type 316 Stainless Steel Exposed to Thermal Aging or Irradiation Environments," ***Scr. Metall.*** 13(7): 621–26 (1979).

22. P. J. Maziasz, "The Precipitation Response of 20%-Cold-Worked Type 316 Stainless Steel to Simulated Fusion Irradiation," ***J. Nucl. Mater.*** 85&86(II,B): 713–17 (1979).

23. P. J. Maziasz, J. A. Horak, and B. L. Cox, "The Influence of Both Helium and Neutron Irradiation on Precipitation in 20% Cold-Worked Austenitic Stainless Steel," pp. 271–92 in ***Phase Stability During Irradiation*** (Proc. Symp., Pittsburgh, Pa., Oct. 5–9, 1980), ed. by J. R. Holland, L. K. Mansur, and D. I. Potter, The Metallurgical Society of AIME, Warrendale, Pa., 1981.

24. E. H. Lee, P. J. Maziasz, and A. F. Rowcliffe, "The Structure and Composition of Phases Occurring in Austenitic Stainless Steels in Thermal and Irradiation Environments," pp. 191–218 in ***Phase Stability During Irradiation*** (Proc. Symp., Pittsburgh, Pa., Oct. 5–9, 1980), ed. by J. R. Holland, L. K. Mansur, and D. I. Potter, The Metallurgical Society of AIME, Warrendale, Pa., 1981.

25. P. J. Maziasz and M. L. Grossbeck, "Swelling and Microstructure of HFIR Irradiated 20%-Cold-Worked Type 316 Stainless Steel and 316 + 0.23 wt % Ti," ***ADIP Quart. Prog. Rep. Dec. 31, 1980,*** DOE/ER-0045/5, pp. 43–69.

26. P. J. Maziasz and M. L. Grossbeck, "Swelling, Microstructural Development and Helium Effects in Type 316 Stainless Steel Irradiated in HFIR and EBR-II," ***J. Nucl. Mater.*** 104(1–3): 987–91 (1981).

27. P. J. Maziasz, F. W. Wiffen, and E. E. Bloom, "Swelling and Microstructure Changes in Type 316 Stainless Steel Irradiated under Simulated CTR Conditions," pp. 259–88 in ***Radiation Effects and Tritium Technology for Fusion Reactors,*** CONF-750989, Vol. I (March 1976).

28. E. E. Bloom and J. O. Stiegler, "Effect of Irradiation on the Microstructure and Creep-Rupture Properties of Type 316 Stainless Steel," pp. 360–82 in ***Effects of Radiation on Substructures and Mechanical Properties of Metals and Alloys, ASTM Spec. Tech. Publ.*** 529, American Society for Testing and Materials, Philadelphia, 1973.

29. P. J. Maziasz, "Microstructural Development on 20%-Cold-Worked Types 316 and 316 + Ti Stainless Steels Irradiated in HFIR: Temperature and Fluence Dependence of the Dislocation Component," ***ADIP Semiannu. Prog. Rep. Sept. 30, 1981,*** DOE/ER-0045/7, pp. 54–109.

30. H. R. Brager and F. A. Garner, "Comparison of the Swelling and the Microstructural/Microchemical Evolution of AISI 316 Irradiated in EBR-II and HFIR," *J. Nucl. Mater.* 104(1–3): 993-97 (1981).

31. P. J. Maziasz, "Composition and Microstructure of Precipitate Phases in Austenitic Stainless Steels," *ADIP Quart. Prog. Rep. June, 30, 1980,* DOE/ER-0045/3, pp. 75–129.

32. J. Bentley et al., "Optimization of an Analytical Electron Microscope for X-Ray Microanalysis: Instrumental Problems," pp. 581-94 in *Scanning Electron Microscopy* (Proc. Washington, D.C., April 16–20, 1979), SEM, Inc., AMF O'Hare, Ill., 1979.

33. N. J. Zaluzec, "Chap. 4, Quantitative X-Ray Microanalysis Instrumental Considerations and Applications to Materials Science," pp. 121-67 in *Introduction to Analytical Electron Microscopy,* ed. by J. J. Hren, J. I. Goldstein, and D. C. Joy, Plenum Press, New York, 1979.

34. N. J. Zaluzec, "Elemental Microanalysis Using Analytical Electron Microscopy," pp. 141–64 in *Phase Stability During Irradiation* (Proc. Symp., Pittsburgh, Pa., Oct. 5–9, 1980), ed. by J. R. Holland, L. K. Mansur, and D. I. Potter, The Metallurgical Society of AIME, Warrendale, 1981.

35. P. J. Maziasz and M. L. Grossbeck, "Microstructural Development in 20%-Cold-Worked Type 316 Stainless Steel and Titanium-Modified Type 316 Stainless Steel Irradiated in the HFIR: Fluence Dependence of the Cavity Component," *ADIP Quart. Prog. Rep. March 31, 1981,* DOE/ER-0045/6, pp. 28–56.

36. J. F. Bates, F. A. Garner, and F. M. Mann, "The Effect of Solid Transmutation Products on Swelling in 316 Stainless Steel," *J. Nucl. Mater.* 104(1–3): 999–1003 (1981).

37. H. R. Brager and F. A. Garner, "Radiation-Induced Evolution of the Austenite Matrix in Silicon-Modified AISI 316 Alloys," pp. 219–35 in *Phase Stability During Irradiation* (Proc. Symp., Pittsburgh, Pa., Oct. 5–9, 1980), ed. by J. R. Holland, L. K. Mansur, and D. I. Potter, The Metallurgical Society of AIME, Warrendale, Pa., 1981.

38. W.J.S. Yang, H. R. Brager, and F. A. Garner, "Radiation-Induced Phase Development in AISI 316," pp. 257–69 in *Phase Stability During Irradiation* (Proc. Symp., Pittsburgh, Pa., Oct. 5-9, 1980), ed. by J. R. Holland, L. K. Mansur, and D. I. Potter, The Metallurgical Society of AIME, Warrendale, Pa., 1981.

39. B. Weiss and R. Stickler, "Phase Instabilities During High Temperature Exposure of 316 Austenitic Stainless Steel," *Metall. Trans.* 3: 851–66 (1972).

40. P. J. Maziasz, "Precipitation Response of Austenitic Stainless Steel," pp. 160–80 in *The Metal Science of Stainless Steel*, ed. by E. W. Collins and H. W. King, The Metallurgical Society of AIME, New York, 1979.

41. L. K. Mansur, "Theoretical Evaluation of a Mechanism of Precipitate-Enhanced Cavity Swelling during Irradiation," to be published in *Philosophical Magazine.*

42. T. M. Williams and J. M. Titchmarsh, "Silicon-Rich Phases in Austenitic Alloys," *J. Nucl. Mater.* 98(1&2): 223–26 (1981).

43. G. R. Odette, "Modeling of Microstructural Evolution Under Irradiation," *J. Nucl. Mater.* 85&86(Part A): 533–45 (1979).

44. E. A. Kenik and E. H. Lee, "Influence of Injected Helium on Phase Instability," pp. 493–503 in *Phase Stability During Irradiation* (Proc. Symp., Pittsburgh, Pa., Oct. 5–9, 1980), ed. by J. R. Holland, L. K. Mansur, and D. I. Potter, The Metallurgical Society of AIME, Warrendale, Pa., 1981.

45. P. J. Maziasz, "Helium Trapping at Ti-Rich MC Particles in Ti-Modified Austenitic Stainless Steel," pp. 477–92 in *Phase Stability During Irradiation* (Proc. Symp., Pittsburgh, Pa., Oct. 5–9, 1980), ed. by J. R. Holland, L. K. Mansur, and D. I. Potter, The Metallurgical Society of AIME, Warrendale, Pa., 1981.

46. A. F. Rowcliffe and E. H. Lee, "High Temperature Damage Phenomena in Complex Alloys," to be published in *Journal of Nuclear Materials* (1982).

47. R. E. Stoller and G. R. Odette, "A Model Based Fission-Fusion Correlation of Cavity Swelling in Stainless Steel," *J. Nuct. Mater.* 104(1–3): 1361–65 (1981).

48. P. J. Alberry and C. W. Haworth, "Interdiffusion of Cr, Mo, and W in Iron," pp. 407–12 in *Metal Science*, Vol. 8, ed. by J. S. Bristow, The Metals Society, 1974.

49. M. A. Kirshtal and A. M. Mokrova, *Uch. Zap. Tul. Gos. Pedogog. Inst. Fiz-Tekhn. Nauki* 93 (1967).

50. L. K. Mansur and W. G. Wolfer, "Influence of a Surface Coating on Void Formation," *J. Nucl. Mater.* 69&70(1): 825–29 (1978).

51. P. J. Maziasz, "Microstructural Development and the Effects of Helium in Type 316 Stainless Steel Irradiated in HFIR and in EBR-II, *ADIP Quart. Prog. Rep. March 31, 1981*, DOE/ER-0045/6, pp. 70-92.

52. E. H. Lee, A. F. Rowcliffe, and L. K. Mansur, "Precipitation and Cavity Formation in Austenitic Stainless Steels During Irradiation," *J. Nucl. Mater.* 104(1–3): 1475–80 (1981).

53. H. R. Brager and F. A. Garner, *DAFS Quart. Prog. Rep. Sept. 30, 1981*, DOE/ER-0046/7, p. 127.

54. F. A. Garner and D. L. Porter, *DAFS Quart. Prog. Rep. Aug. 31, 1981*, DOE/ER-0046/6, p. 176.

55. C. G. Bolten et al., *Mechanical Behavior of Materials*, Pergamon, 1979, p. 183.

56. M. Waldenström, "An Experimental Study of Carbide–Austenite Equilibria in Iron–Base Alloys with Mo, Cr, Ni, and Mn in the Temperature Range 1173 to 1373 K," *Metall. Trans.* 8A(12): 1963–77 (1977).

57. K. E. Cooke, N. Evans, L. Stoter, and J. W. Steeds, "Accurate Crystallographic Information from Precipitates in 316 and Related Stainless Steels," *Inst. Phys. Conf. Ser.* 41: 195 (1978).

58. T. M. Williams and J. M. Titchmarsh, "The Occurrence of a Silicon-Rich Phase of the M_6C Type in Neutron–Irradiated FV 548 Steel," *J. Nucl. Mater.* 87(2&3): 398–400 (1979).

59. J. I. Bramman et al., "Void Formation in Cladding and Structural Materials," pp. 125–41 in *Radiation-Induced Voids in Metals*, ed. by J. W. Corbett and L. C. Ianniello, *AEC Symp. Ser.* 26, CONF–710601 (April 1972).

3.6 APPLICATION OF QUANTITATIVE ELECTRON ENERGY LOSS SPECTROSCOPY TO ANALYSIS OF THE TITANIUM CARBIDE PHASE IN AUSTENITIC STAINLESS STEELS — P. J. Maziasz (Oak Ridge National Laboratory) and N. J. Zaluzec (Argonne National Laboratory)

3.6.1 ADIP Task

ADIP Task I.C.1, Microstructural Stability.

3.6.2 Objective

The objective of this work is to understand the precipitate phase behavior in Path A alloys. This information can be used to develop compositional variations to optimize irradiation stability of the MC phase.

3.6.3 Summary

Quantitative analytical electron microscopy employing both x-ray energy dispersive spectroscopy (XEDS) and electron energy loss spectroscopy (EELS) was used to determine the carbon content of carbide particles in the Path A PCA. These results show that the experimental techniques must be adequate to resolve the Mo M and C K shell edges before quantitative measurement of carbon content is possible. Precipitate particles of different sizes had different metal-to-carbon ratios, which could be related to their titanium and molybdenum contents.

3.6.4 Progress and Status

The intent of this work is to study the light element (C,N,O) contents, particularly C, of individual particles of the titanium MC carbide phase. Analytical electron microscopy (AEM) studies can employ either EELS or XEDS with ultra-thin-window detectors to detect these elements, but we will show that because MC contains substantial molybdenum and carbon, the former method is better. The alloy studied is the PCA austenitic stainless steel. The microstructure studied was designed for scoping the resistance of this material to fusion irradiation.[1] The key to this application is stability of the MC phase, and composition is very important to stability. However, such studies cannot be undertaken without the advanced techniques and equipment development of EELS, and we will focus on the interfacing of the latter with the metallurgical system studied.

The microstructure of MC in the PCA is shown in Fig. 3.6.1. The material was solution annealed for 15 min at 1100°C and aged for 8 h at 800°C followed by 8 h at 900°C, all in vacuum. The heat treatment produced two types of MC particles: coarse particles about 200 nm diam and a distribution of small particles less than 50 nm diam. Both EELS and XEDS were performed on clean, thin foils with a Philips *400* AEM, operated at 120 kV, at Argonne National Laboratory (ANL). The EELS spectrometer is a π/2 magnetic sector designed by Zaluzec. The MC particles near the foil edge were examined, and this microstructure allowed uses of larger than minimum probe size, about 30 to 50 nm on average. For EELS measurements, incident beam convergence and scattering half-angles were 2 and 5.6 mrad, respectively, while energy resolution was set at *4* to 5 eV. The larger probe size, clean foils and vacuum system of the Philips 400 allowed EELS measurements without detectable carbon buildup through contamination. (The contamination was checked by measurements in the matrix adjacent to precipitates.) The EELS and XEDS spectra were recorded and stored on an ORTEC EEDII multichannel analyzer and analyzed with programs developed by

YE-12426

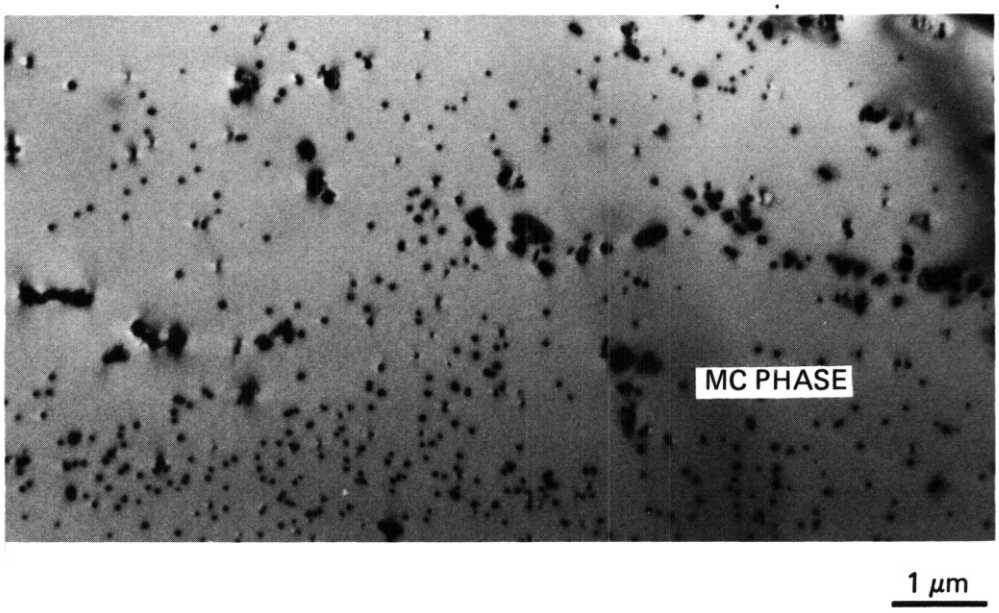

Fig. 3.6.1. Microstructure of Aged Path A PCA Showing Coarse- and Fine-Scale Distributions of Titanium-Rich MC Precipitate Particles.

Zaluzec. Recently calculated K and L cross sections from Egerton[2,3] for Ti and C, respectively, were used to convert integral intensities into compositional information. Details of EELS spectra calibration and measurement considerations are the same as recently reported by Zaluzec et al.[4] The EELS compositional measurements of standards of NiO, BN, Al_2O_3, and MnO indicate satisfactory results with K and L shell cross sections, and results are thus believed accurate to ±20% of reported values.[5]

For analysis of the EELS spectra, the spectra for the M shell of pure Mo was obtained from a library file,[6] aligned in energy with the MC EELS spectra, scaled down to fit the portion of Mo M shell edges visible underneath the C K edge, and then stripped away. More detail on this technique can be found elsewhere.[7] The Mo spectrum is shown in Fig. 3.6.2.

The XEDS and EELS spectra (after background stripping) are shown in Fig. 3.6.3 for the two different types of MC particles found. Both XEDS and EELS spectra show more Mo in smaller MC particles analyzed (a, b) than in larger particles (c, d). Relative metal atom concentrations, including

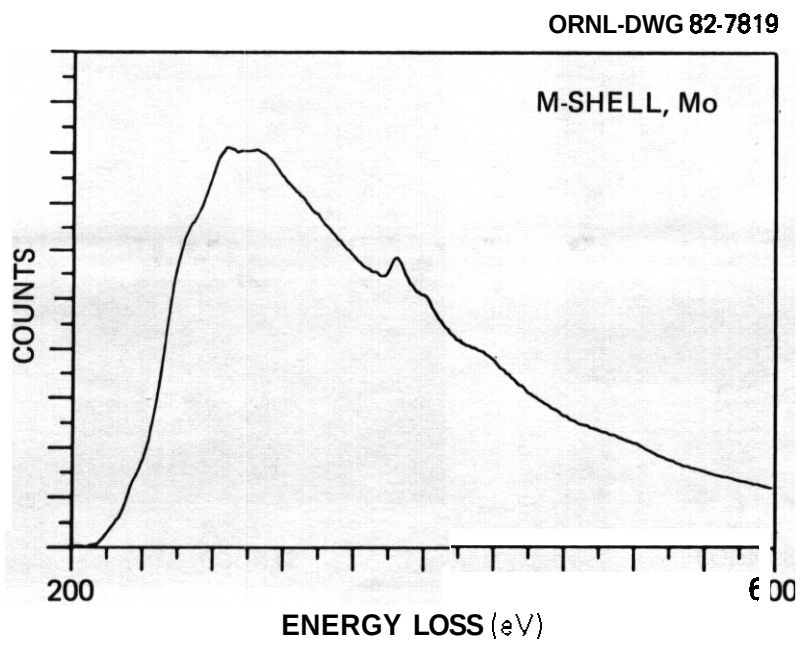

Fig. 3.6.2. EELS Spectrum of the M Shell of Molybdenum Used for Stripping the Molybdenum Signal from the Total EELS Spectra from Precipitate Particles.

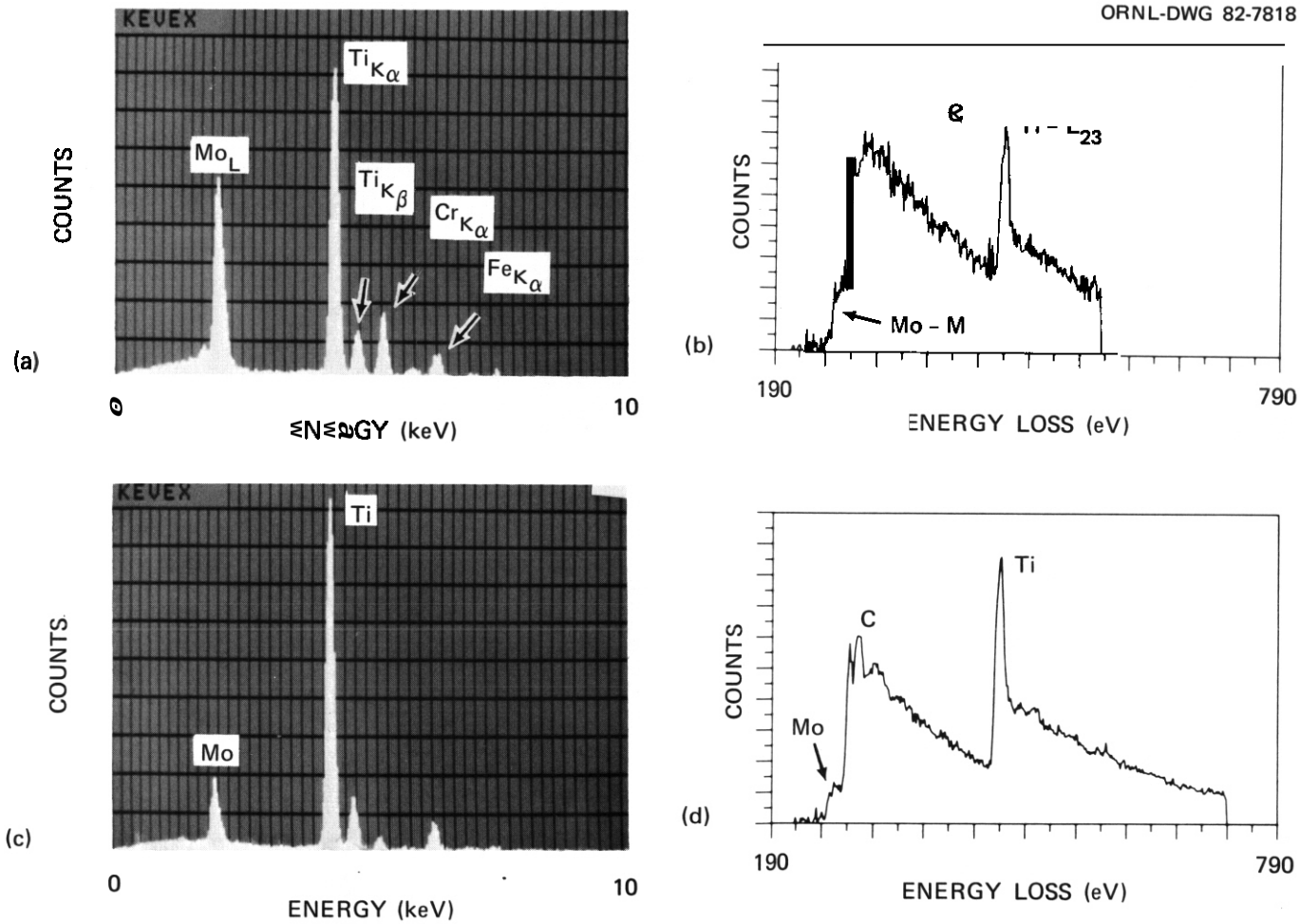

Fig. 3.6.3. Analysis results generated by AEM of Precipitates in the Path A PCA Alloy. (a) XEDS and (b) EELS spectra of small MC particle that contains considerable molybdenum, and (c) XEDS and (d) EELS spectra of larger MC particle with much less molybdenum. These spectra illustrate that Mo, Ti, and C contents can vary in the same phase.

atoms/mole

Mo, were obtained from the XEDS spectra. The normalized contents of metallic elements are 54.5 Ti-31 Mo-10 Cr-4 Fe-0.5 Ni (at. %) for the small MC particles and 78 Ti-13 Mo-2.5 Cr-6 Fe-0.5 Ni for the large MC particles.

Quantitative analysis of the EELS spectra yielded a Ti-C atom ratio of 0.6 ± 0.12 for the small MC particle and 1.1 ± 0.2 for the large MC. Together with XEDS data to include the other metallic elements we obtain molybdenum-carbon ratios of 0.9 ± 0.2 for the small particle with more molybdenum and 1.5 ± 0.3 for the large particle with less molybdenum. Although preliminary, these results suggest that the large particle is nearly stoichiometric TiC, with the other elements being dissolved to yield carbon-deficient MC. Conversely, the small particles are deficient in titanium with respect to TiC but the other elements substitute to yield nearly stoichiometric MC.

These results would not be possible without EELS techniques sufficiently advanced to resolve overlap between Mo M and C K shell edges. This consideration will be very important for the carbon determination in the other phases in type 316 stainless steel because all contain substantial molybdenum.

3.6.5 Future Work

Future work will continue to examine the MC phase to confirm these results and then extend the investigation to the other phases in steel. This information combined with compositional information on the heavier elements in precipitate particles, will help guide compositional variations of PCA.

3.6.6 References

1. P. J. Maziasz and T. K. Roche, "Preirradiation Microstructural Development Designed to Minimize Properties Degradation During Irradiation in Austenitic Alloys," *J. Nucl. Mater. 104:* 797–801 (1981).
2. R. F. Egerton, *Ultramicroscopy 4:* 169 (1979).
3. R. F. Egerton, "Design of a Parallel-Detection System for EELS," pp. 368–69 in *Proc. Electron Microscopy Society of America, 39th Annu. Meet., 2981,* ed. by G. W. Bailey, Claitor's, Baton Rouge, La.

Ti/M = 54/44 = 1.2 M/C = 44/27 Ti/C = M/C = 1.1

4. N. J. Zaluzec, T. Schober, and P. G. Westlake, "Application of EELS to the Study of Metal–Hydrogen Systems," pp. 194–95 in *Proc. Electron Microscopy Society of America, 39th Annu. Meet., 1981*, ed. by G. W. Bailey, Claitor's, Baton Rouge, La.

5. N. J. Zaluzec, unpublished research, Argonne National Laboratory (available upon request).

6. *Library of Energy Loss Spectra*, being compiled by N. J. Zaluzec at Argonne National laboratory.

7. N. J. Zaluzec, molybdenum stripping technique in paper to be published.

3.7 DYNAMIC POWDER COMPACTION OF RAPIDLY SOLIDIFIED PATH A ALLOY WITH INCREASED CARBON AND TITANIUM CONTENT — J. Megusar, D. Imeson, J. B. Vander Sande and N. J. Grant (Massachusetts Institute of Technology)

3.7.1 ADIP Task

Task I.C.5, Microstructure and Swelling of Special and Innovative Materials

3.7.2 Objective

The objective of this study is to show the potential of the dynamic powder compaction technique to consolidate rapidly solidified Path A alloys and to develop microstructures with improved irradiation performance in the fusion environment. Samples of rapidly solidified and dynamically compacted Path A alloy with increased carbon and titanium content have been included in alloy development irradiation experiments.

3.7.3 Summary

Different techniques for consolidation of rapidly solidified alloys which are available or are under study at the present time include conventional consolidation techniques (hot extrusion, HIP,...), high velocity consolidation of atomized partially solidified particulates and dynamic powder compaction (DPC). This report describes the results of dynamic compaction of Path A alloy with increased carbon and titanium content. The microstructure of the as-compacted alloy is highly complex, evidencing an extreme degree of deformation. TEM revealed very high dislocation and twin density reflecting high hardness of the as-compacted alloy. Annealing studies revealed that recovery and recrystallization processes in dynamically compacted alloy are slower than in conventionally treated materials. High dislocation density appears to be an intrinsic property of the dynamic compaction process and it may be potentially useful in developing materials for irradiation performance. Other potential applications of dynamic compaction include preparation of graded materials and ceramic materials.

3.7.4 Progress and Status

3.7.4.1 Introduction

Rapid solidification involves cooling rates in the order of 10^3-10^7 K/sec and this allows for structural and compositional modifications of existing alloys as well as for the development of new classes of alloys – for example, metallic glasses. These high cooling rates are obtained by the production of fine powders, foils, flakes, ribbons, etc., such that one dimension is finer than about 50 μm, and sometimes in the near-micron-size range; this is accomplished by gas or water atomization, roll quenching, splatting against high conductivity substrates, and by melt spinning and melt extraction. Consolidation is therefore an important step in developing rapidly solidified alloys for applications such as alloy development for improved irradiation performance. Different consolidation techniques which are available or are under study at the present time include conventional consolidation techniques (such as hot extrusion, hot isostatic pressing, etc.), high velocity consolidation of atomized partially solidified particulates and dynamic powder compaction.

In high velocity consolidation of atomized partially solidified particulates, the molten alloy is atomized at high velocity to produce fine droplets in a narrow range of fine sizes. A high conductivity metallic substrate is provided and the partially solidified droplets are impacted at high velocity first against a metallic substrate, and subsequently on previously deposited layers of quenched alloy. Thicknesses of the order of 5-10 mm can be deposited by using this technique. Additional thermomechanical treatments may be required with some alloys to obtain fully dense material and to optimize the structure and properties. This technique allows for processing short-cuts but the secondary cooling rates (in the solid state) will not be as high as those for rapidly solidified foils or powders.

Dynamic powder compaction techniques are applied by the closely controlled passage of shock waves through the particulate materials in powder, foil or ribbon form. The shock wave throws the particles so violently together that enough heat is generated at the surfaces

of each particle to lead to film melting while the particle interiors remain cool; this leads to complete bonding and densification. Different dynamic powder compaction (shock wave compaction) techniques which are being developed include explosive compaction' and compaction under impact by projectiles launched by compressed air[2]. In this report, we are presenting the results on the dynamic powder compaction of rapidly solidified Path A alloy with increased carbon and titanium content. Microstructures of the as-compacted material have been examined and annealing studies have been carried out to show the recovery and recrystallization processes in highly deformed material. Furthermore, we are discussing the applicability of the dynamic compaction process in developing materials for improved irradiation performance.

3.7.4.2 Experimental Procedure

Prime Candidate Alloy (PCA) was provided by Oak Ridge National Laboratory. It was remelted, adding extra titanium and carbon to triple the normal amount of carbon and titanium (0.17 wt% C and 0.92 wt% Ti). Rapid solidification was performed in a roller quenching apparatus. A fine stream of metal was rapidly solidified in contact with two counter-rotating rolls. The foils obtained were typically 5-10 cm long, 1 cm wide and 80-160 μm thick. The estimated cooling rate was 10^5 °C/sec.

Dynamic powaer compaction (DPC) was performed at the Institut Cerac, Ecublens. A two-stage "high speed" gun was used which is capable of approaching 8000 m/sec. Compaction is effected by the shock wave which is produced by impact of the projectile on the powder. During the passage of the shock wave the pressure rises extremely rapidly, remains at this high value for some time and later falls as the pressure release occurs. Calculations showed[3] the following relation between the shock speed, particle velocity and the internal energy imparted to the material: steel powder of approximately 50% loose density compacted to shock pressure of 5 GPa, gives a shock velocity of 1600 m/sec, particle velocity of 800 m/sec and internal energy change of 3 x 10^5 J/kg. This energy change corresponds to a

temperature rise of 600°K and if the energy is considered to be deposited predominately at the powder particle surface, values for energy density and power density of 2×10^4 J/m^2 and -2×10^{11} W/m^2 are deduced. This value corresponds to the upper end of the laser glazing processing.

Rapidly solidified foils were cut into pieces with a length to a thickness ratio less than 30 to 1 and were then compacted with the gun speed 1200 m/sec. The diameter of compacted material was 5 cm and the height was 1 cm.

The microstructure of as-compacted material was examined by transmission electron microscopy. The alloy samples were thinned by electropolishing in a 10% $HClO_4$ in CH_3OH solution at -50°C and 25 V. Nearly all specimens were thinned additionally by using ion milling.

Dynamically compacted material was annealed for 1/2 hr in the temperature interval of 650-1000°C. Specimens for microstructural examination were prepared for each annealing condition and Knoop microhardness measurements were made to determine the softening curve.

3.7.4.3 Microstructure of Dynamically Compacted Path A Alloy

The microstructure of the as-compacted alloy is highly complex, evidencing an extreme degree of deformation, so much so that it is difficult to analyze further. A typical area is shown in Figure 3.7.1. A banded substructure is seen together with an extremely high dislocation density. The bands seem to be formed of twins and dislocation conglomerates which additionally show internal microtwinning and a high dislocation density, reminiscent of martensitic microstructures. We have not been able as yet to clearly isolate these components in any sensible fashion. Selected area diffraction patterns arising from such regions also evidence the high degree of deformation of the metal lattice, as shown in Figure 3.7.2. A proliferation of diffraction spots arising from twinning, double diffraction, and sub-grain misorientations can be seen along with the fundamental lattice reflections, themselves strongly streaked due to strain effects (dislocations) and stacking or twin faults. The organization of the dislocations connected with the banded structures might lead to some significant

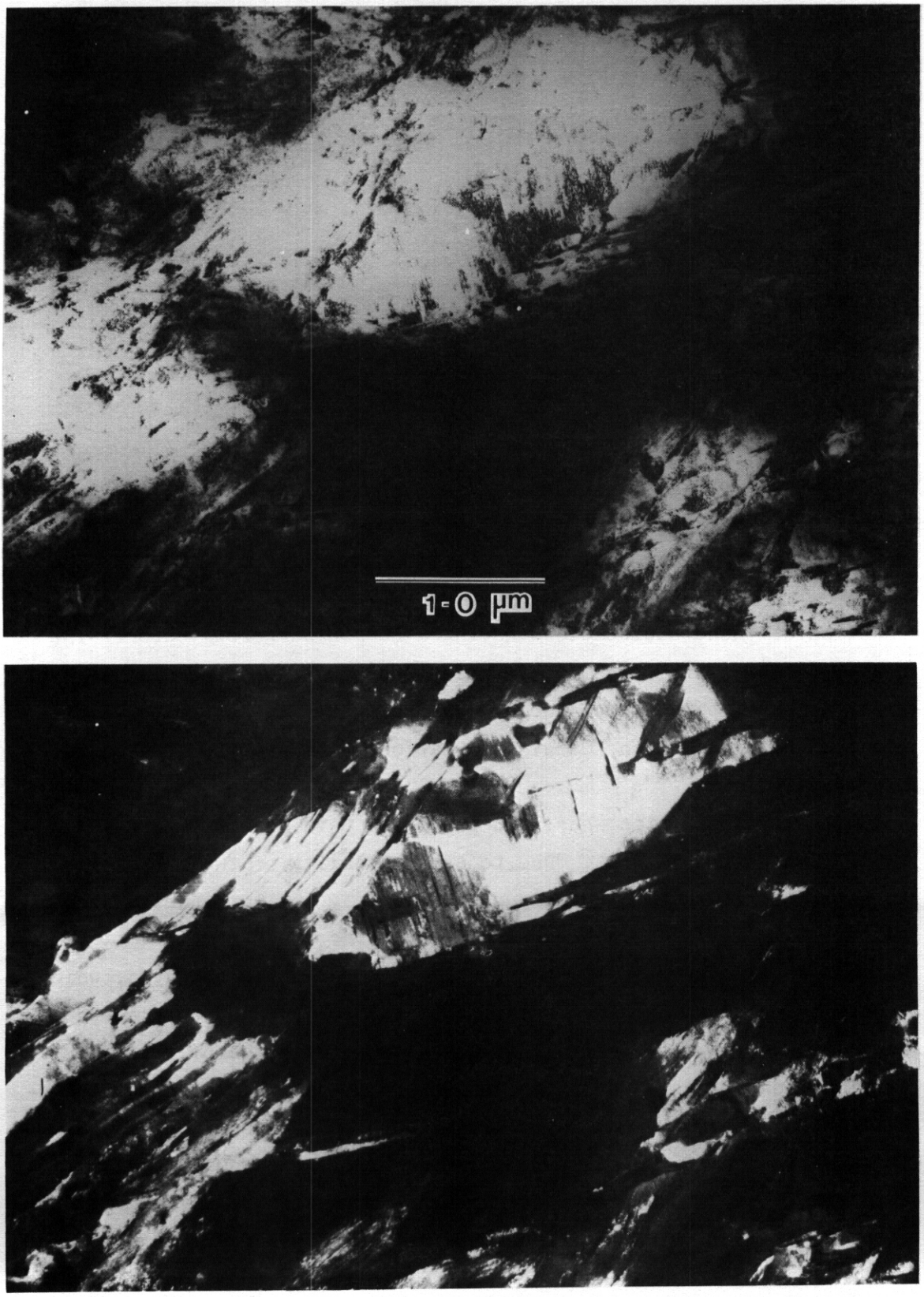

Fig. 3.7.1. A typical area in rapidly solidified and dynamically compacted Path A alloy (with increased carbon, 0.17 wt%, and titanium, 0.92 wt%, content). (a) bright field and (b) dark field using the diffraction conditions shown in Fig. 3.7.2.

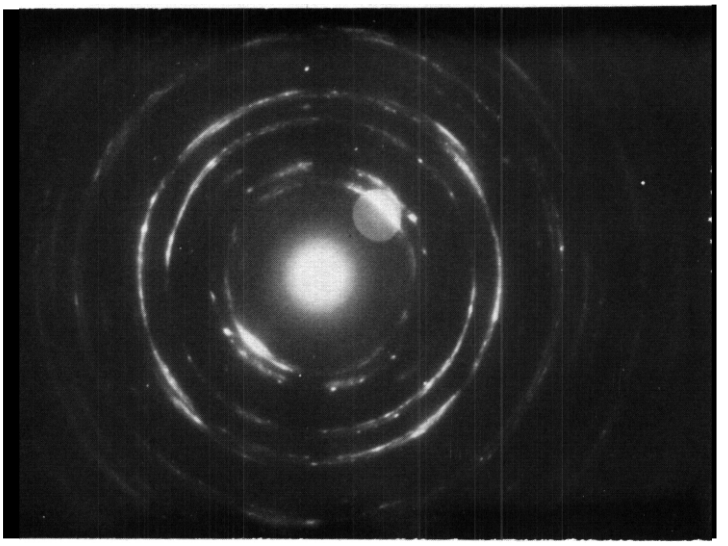

Fig. 3.7.2. Selected area diffraction pattern of the area shown in Fig. 3.7.1. The objective aperture is superimposed in the position used for the image in Fig. 3.7.1 (b).

fraction of these dislocations having a common Burgers' vector. The degree of streaking of the diffraction spots will be dependent on the orientation of this common Burgers' vector with respect to the incident electron beam direction, causing variations from area to area as is indeed seen.

The bonding region where two particles have been welded together is of particular interest. Due to the complexity of the microstructure it is difficult to unambiguously identify the interparticle regions. In a study of an explosively compacted superalloy[4] similar banded substructures to those reported here have been observed, which were attributed to the inner regions of particles. A structure was also seen in the interparticle melt region, identified by optical examination of the TEM specimen, which was characterized as microcrystalline and which showed ring-like diffraction patterns. We see similar areas, shown in Figure 3.7.3, in our alloy, but would suggest that ring-like diffraction patterns such as that shown in Figure 3.7.2 might be due in some cases largely to deformation effects in just a few grains, as discussed above, rather than to the much larger number of grains that would be thought of as microcrystalline. We do see,

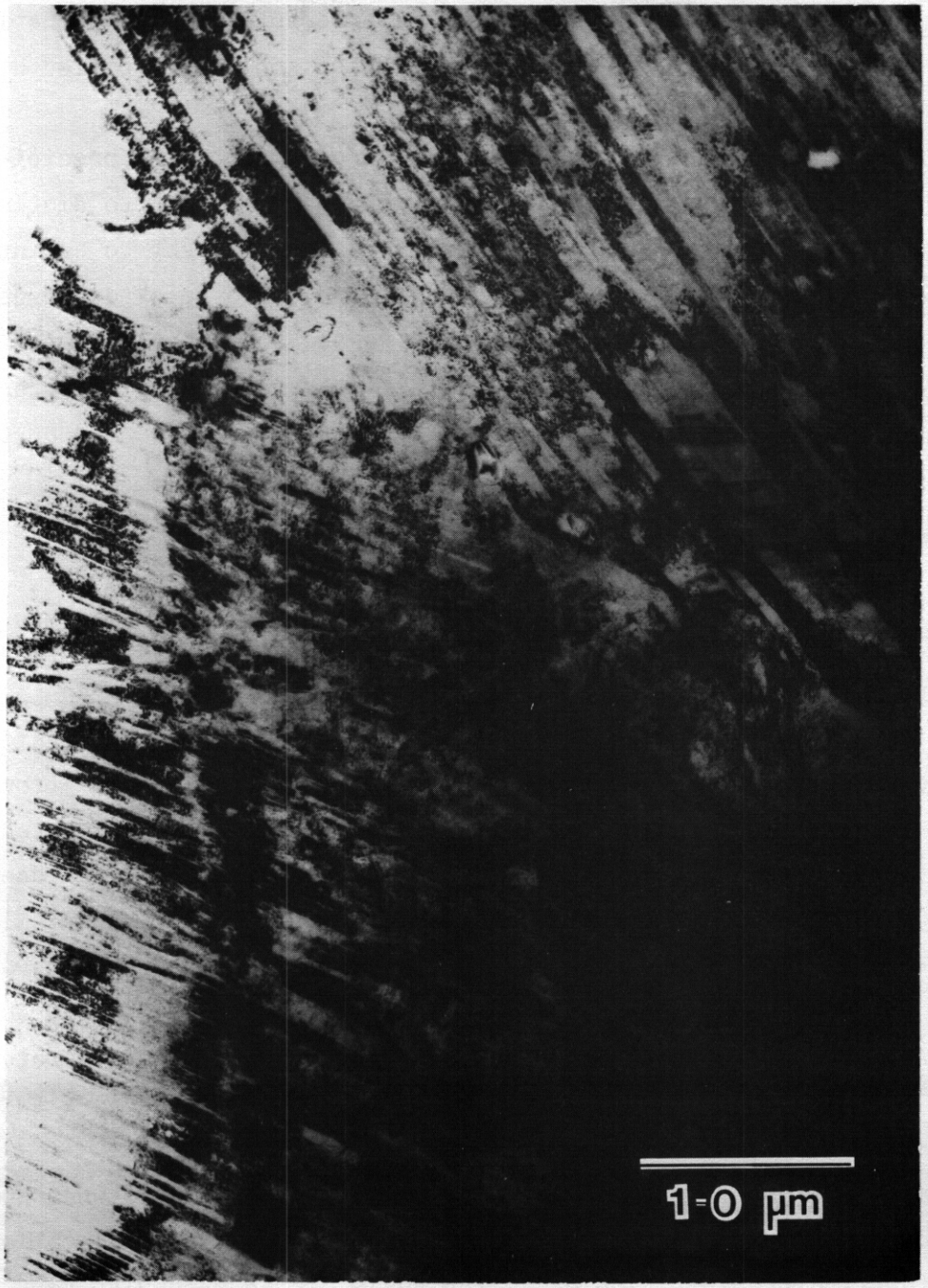

Fig. 3.7.3. This micrograph shows an area interpreted as the boundary between two particles, fused together during dynamic compaction. Note the banded nature of the microstructure away from the boundary.

however, some evidence for a degree of microcrystallinity in the inter-particle melt regions, which have been melted and re-solidified at an extremely high cooling rate.

Lastly, we see no evidence in the micrographs of any precipitation in the material, although this would be difficult to distinguish, except for a few particles at the regions thought to be inter-particle boundaries (see Figure 3.7.3), which could be oxide or debris from the original surfaces. Neither do we see any clear evidence of precipitation throughout the material in the diffraction patterns, although again the interpretation of the patterns is obscured by their complexity.

3.7.4.4 Recovery and Recrystallization of Dynamically Compacted Path A Alloy

The recrystallization curve for dynamically compacted material (Figure 3.7.4) was determined from measurements of Knoop hardness as a function of annealing temperature (1/2 hr anneal). As dynamically compacted material shows extremely high hardness values (480); for comparison, rapidly solidified Path A alloy which was consolidated by hot extrusion and subsequently 60% cold worked has Knoop hardness of 320. Furthermore, hardness of dynamically compacted Path A alloy (see Figure 3.7.4) decreases gradually by annealing in the temperature range 650° to 1000°C; the hardness of the extruded and 60% cold worked Path A alloy on the other hand decreased abruptly in the temperature range 750° to 800°C and a 1/2 hr anneal at 850°C resulted in a fully recrystallized structure.[5]

Examination of a sample annealed at 700°C for 1/2 hr, when some softening has taken place, reveals some recovery of the dislocation structure and precipitation on a fine scale, in an otherwise very similar looking microstructure to the as-compacted samples. No recrystallization was detected. Again because of the complexity of the microstructure, it is difficult to describe or analyze its recovery, which is evidenced in images only as a slightly increased sense of familiarity! The recovery is more clearly seen in diffraction patterns from most, but not all, areas, showing more normal-looking spot

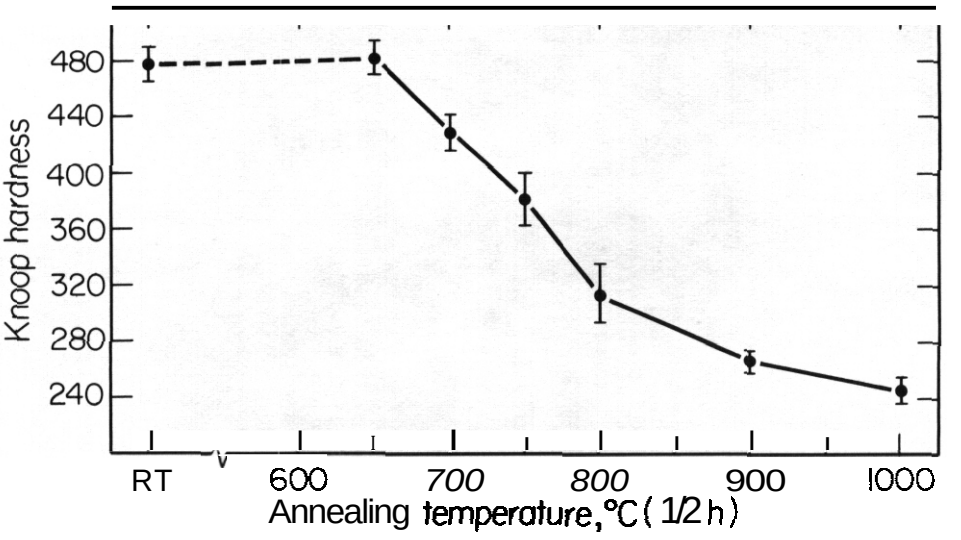

Fig. 3.7.4. Softening curve for rapidly solidified and dynamically compacted Path A alloy. Plot of Knoop hardness versus annealing temperature (1/2 hr anneal).

patterns, primarily because of a reduced magnitude of the characteristic streaking seen in the as-compacted material which we believe arises from severe strain effects. That is, recovery is evidenced in a reduction of the deformation induced strain, without appearing to greatly change the gross features of the microstructure. Figure 3.7.5 shows a micrograph and its associated diffraction pattern, illustrating these points. However, a new feature has appeared in the diffraction pattern which should not be confused with the ring-like patterns of Figure 3.7.2. In addition to the major reflections characteristic of a <110> orientation, 'polycrystalline' rings can be seen. These are modulated in intensity around the ring, with greatest intensity near to the matrix reflections. The modulated rings are interpreted as arising from many small coherent or semi-coherent particles of TiC, which is known to precipitate out of solution at about this annealed temperature, from previous studies of rapidly solidified and extruded Path A alloys.[5] The micrograph in Figure 3.7.5 shows many small regions of interference fringes, most clearly seen in the {200} type bend contour crossing the image. These fringes, with spacing 1.57 ± 0.1 nm, are interpreted as Moiré patterns arising from the

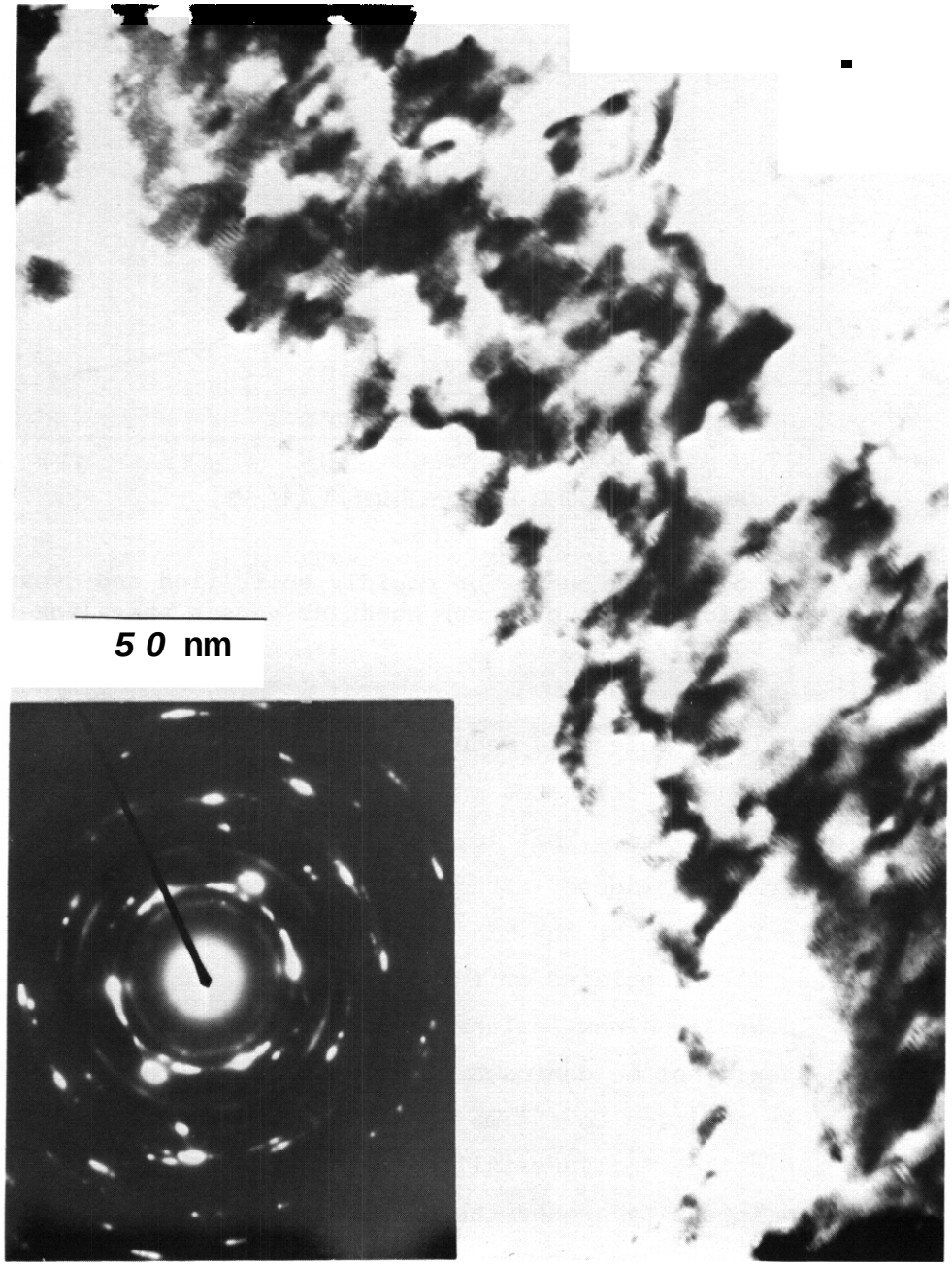

Fig. 3.7.5. An area in dynamically compacted alloy annealed at 700°C for 30 min, shown at high magnification. The very high contrast is an unfortunate consequence of the complex microstructure. A {200} bend contour crosses the picture, in which small areas showing fringe patterns can be seen. The diffraction pattern from this area is also shown. The modulated ring passing just inside the matrix {200} reflections and through the matrix {111} reflections arises from TiC {200} reflections. The inner ring is TiC {111} and the outer clear ring is from TiC {220} reflections.

mismatch of the particle and matrix lattices, with lattice parameters 0.425 ± 0.005 nm and 3.358 ± 0.004 nm respectively, as measured from the diffraction pattern. The product of these lattice parameters should give the Moiré fringe spacing, which, within the error expectancy, it does. The particles seem to be elliptical in shape and are generally 10 nm or less in size.

After annealed at 750°C for 1/2 hr, most of the material showed little apparent change in microstructure, although the recovery processes will have continued. However, there were now observed a few recrystallized grains, with considerable intragranular precipitates. This trend continued after annealing at 800°C for 1/2 hr, when now a larger fraction of the area observed was composed of recrystallized grains, the rest still showing the banded, highly deformed microstructure. This is illustrated in Figure 3.7.6. The recrystallized grains, in both 750°C and 800°C annealed samples, showed similar features, principally a high density of precipitate particles. A typical region is shown in Figure 3.7.7 in bright field and dark field conditions, using a precipitate reflection as shown in the diffraction pattern. The precipitate reflections seen in the diffraction pattern are consistent with the particles being composed of TiC, as would be expected and as has been observed in annealing studies of this alloy consolidated using hot extrusion. They appear from the diffraction pattern to be coherent or semi-coherent with the matrix. They are approximately spherical and have sizes generally in the 10 to 20 nm range, but perhaps the most striking feature is that they often form in linear arrays, as can be seen in Figure 3.7.7. This presumably reflects their formation in the banded structures prior to recrystallization.

In brief, then, the annealing studies showed evidence of recovery and recrystallization seeming to proceed much as in conventional highly cold worked materials, but with these processes strongly retarded in their onset as the annealing temperature is increased in some areas of the material. This effect explains the gradual decrease in hardness shown in Figure 3.7.4, with the fraction of recrystallized to recovered but still highly deformed areas gradually increasing with annealing temperature.

Fig. 3.7.6. An area in dynamically compacted alloy annealed at 800°C for 30 min, showing the coexistence of the banded, highly deformed but recovered structure and recrystallized areas.

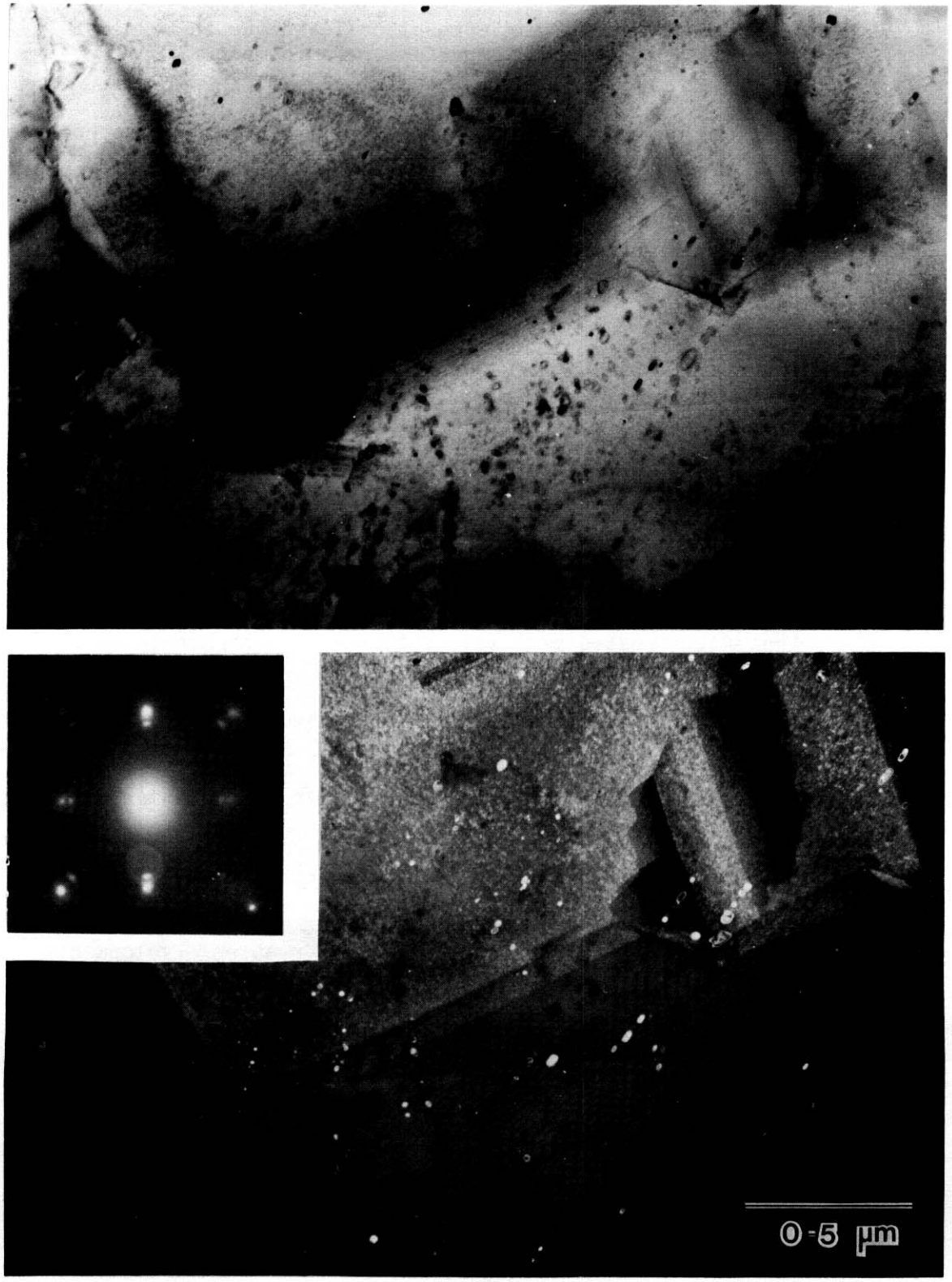

Fig. 3.7.7. An area in the dynamically compacted and annealed at 800°C alloy, which has recrystallized and in which copious precipitate (TiC) formation can be seen. (a) shows the bright field image, in which 'stringers' of particles are clearly seen and (b) shows a dark field image using a TiC {200} reflection as indicated in the selected area diffraction pattern.

3.7.4.5 Applicability of Dynamic Compaction Technique in Developing Materials with Improved Irradiation Performance

As shown in this report, dynamic compaction of Path A alloy with increased carbon and titanium content resulted in a microstructure with high dislocation and twin density and in the retention of carbon and titanium in solid solution. Extremely high hardness values are furthermore indicative of high mechanical strength. High dislocation density appears to be an intrinsic property of the dynamic compaction process and it may be potentially useful in developing materials for irradiation performance, as it has been shown that dislocations are effective trapping sites for helium.[6] It is not known, however, to what extent very high dislocation density may have an effect on precipitation reactions in stainless steel and on the microchemical evolution during neutron irradiation.

Annealing studies showed that recovery and recrystallization processes are slower in dynamically compacted material than in conventional mechanically treated material; this suggests higher thermal stability of dynamically compacted materials. Comparison of the annealed and 20% CW austenitic stainless steel showed that equilibrium dislocation density obtains with increasing flux regardless of the initial state of the material.[7] Retention of high dislocation density in dynamically compacted material at elevated service temperature (possibly by using dispersoids such as oxides and carbides) is therefore a challenging possibility.

Surface effects and corrosion problems may require development of graded, clad or coated first wall materials. Dynamic compaction allows for the preparation of graded material, with the advantage that bonded mixtures of (normally) chemically or thermally incompatible material are possible, without formation of brittle intermetallic phases. For example, dynamic compaction has formed strong aluminum-steel bonds without formation of intermetallics.[2]

Ceramic materials are also potential electrical insulators and first wall materials. In production of ceramic materials, alternative densification methods, which produce bodies of high density while avoiding the limitations imposed by additives or hot pressing

are being sought. It has been shown that explosive compaction is such a technique[1]; microstructural examination of explosively compacted AlN showed similar features as observed in dynamically compacted metallic alloys and discussed in this report.

3.7.5 Conclusions and Future Work

Consolidation is an important step in developing rapidly solidified microcrystalline and amorphous alloys for applications such as alloy development for improved irradiation performance. Dynamic powder compaction (shock wave compaction) is one of the consolidation techniques which are presently under study.

Microstructural examination of as dynamically compacted Path A alloy with increased carbon and titanium content showed an extreme level of deformation including very high dislocation and twin density.

Recovery and recrystallization processes seem to proceed much as in conventional highly cold worked materials. Future work will include detailed studies of recovery processes in dynamically compacted materials.

Neutron irradiation is currently in progress to determine irradiation response of rapidly solidified and dynamically compacted Path A alloy with increased carbon and titanium content.

3.7.6 References

1. W. H. Gourdin, C. J. Echer, C. F. Cline and L. E. Tanner, "Microstructure of Explosively Compacted Aluminum Nitride Ceramic," pp. 233-41, Proceedings 7th Int. Conf. on High Energy Rate Fabrication, Univ. of Leeds, 14-18 Sept. 1981.
2. D. Raybould, D. G. Morris, G. A. Cooper, "A New Powder Metallurgy Method," J. Mat. Sci., 14: 2523-26 (1979).
3. D. G. Morris, "Dynamic Compaction of Metallic Glasses and Microcrystalline Materials," pp. 372-84, in Rapid Solidification Processing, Principles and Technologies," Proc. Int. Conf., 2nd, 1980, Clairtor's Publishing Div., 1980.
4. M. A. Meyers, B. B. Gupta and L. E. Murr, "Shock-Wave Consolidation of Rapidly Solidified Superalloy Powders," J. Metal: 21-26 (Oct. 1981).

5. J. Megusar, L. Arnberg, J. B. Vander Sande and N. J. Grant, "Optimization of Structure and Properties of Path A PCA Alloy by Rapid Solidification," J. Nucl. Mater., 99: 190–202 (1981).

6. P. J. Maziasz and E. E. Bloom, "Comparison of Titanium-Modified and Standard Type *316* Stainless Steel Irradiated in HFIR–Swelling and Microstructure," ADIP Quart. Prog. Rep., 40-53 (Jan.-March 1978).

7. F. A. Garner, "The Microchemical Evolution of Irradiated Stainless Steels," paper presented at AIME Symposium on Irradiation Phase Stability, Pittsburgh, Pa., Oct. 5–9, 1980.

3.8 MECHANICAL PROPERTIES AND STRUCTURE OF Y_2O_3 DISPERSION STABILIZED, RAPIDLY SOLIDIFIED 316 TYPE STAINLESS STEEL – A. I. Ibrahim, J. Megusar and N. J. Grant (Massachusetts Institute of Technology)

3.8.1 ADIP Task

Tasks I.C.5 and I.B.16 and I.8.12, Microstructure and Swelling of Special and Innovative Materials, Tensile and Stress Rupture Properties.

3.8.2 Objective

The objective of this work was to prepare an oxide dispersion stabilized 316 austenitic stainless steel in order to study the effect of oxide dispersion on swelling resistance and mechanical behavior of 316 austenitic stainless steels under neutron irradiation. Samples of oxide dispersion stabilized 316 stainless steel have been included in alloy development irradiation experiments.

3.8.3 Summary

An oxide dispersion stabilized 316 stainless steel has been prepared by mechanical alloying of a few 100 Å size yttria powders with attrited flakes of 316 stainless steel prealloyed with 1 ut% aluminum. Alloys with 4 vol% and 5 vol% yttria additions have been prepared and they show significant improvements in microstructural stability. Austenitic stainless steel containing 4 vol% yttria showed very high room temperature YS and UTS, with sufficient ductility. Stress rupture testing at 650°C as a function of different thermomechanical treatments is currently in progress.

3.8.4 Progress and Status

3.8.4.1 Introduction

In a previous work[1,2] an aluminum oxide dispersed 316 stainless steel has been developed; surface oxidation has been chosen as a preferred method in order to minimize formation of less stable chromium oxides. For this purpose, an ultra low C+N stainless steel was alloyed

with 1 wt% Al, rapidly solidified to produce fine powders and attrited to approximately 0.5 μm thick flakes to provide for surface oxidation. SAM analysis revealed an approximately 100 Å thick surface layer enriched in oxygen, aluminum and chromium similar to that determined for rapidly solidified powders. Internal oxidation of the attrited flakes has not been carried out in order to minimize formation of less stable chromium oxides and the attrited flakes were instead directly hot extruded. The oxide layer which formed on the surface of the flakes during the attrition process broke up during the extrusion process to form discrete oxide particles. TEM showed that oxide particles were uniformly distributed in the extruded material. Their size was about 1000-1500 Å and the interparticle spacing was 3000-5000 Å. The composition of oxide particles was obtained by STEM and most oxides were identified as Al oxides, based on the energy dispersive X-ray spectrum, which showed a strong Al line and on the electron energy loss spectrum, showing an oxygen peak. Microstructural stability studies showed that aluminum oxide dispersion retarded recrystallization and that it effectively inhibited grain growth up to 1150°C (1 hr anneal); at 1250°C the grain size increased from 5 to 10 μm. Mechanical testing showed that aluminum oxide dispersion improved room temperature tensile properties.

This work showed that prealloying of 316 stainless steel with aluminum results in preferential formation of aluminum oxide particles in the presence of high chromium content. This is an important result since the aluminum oxides show much higher thermal stability than the chromium oxides. However, the average oxide particle size exceeded 1000 Å and it was considered too coarse to obtain optimum high temperature structural and mechanical properties. As a continuation of this research, alternate techniques of preparing oxide dispersion stabilized austenitic stainless steel are being studied, such as mechanical alloying of fine refractory oxides with fine rapidly solidified powders. It has been attempted to further increase structural and mechanical stability by reducing the average oxide particle size and interparticle spacing and by increasing the volume fraction of oxide particles. This report describes the preparation of Y_2O_3 dispersion stabilized 316 stainless steel by using the mechanical alloying technique. It also includes preliminary

results on mechanical testing and microstructural examination of these alloys.

3.8.4.2 Experimental Procedure

The ultra low C+N 316 stainless steel was provided by Allegheny Ludlum Company and had the following chemical composition (in wt%): 16.36 Ni; 16.76 Cr; 2.26 Mo; 1.25 Mn; 0.51 Si; 0.0027 C; 0.003 N; 0.0027 S; bal. Fe. This alloy was remelted and modified by the addition of 1 percent aluminum. Rapid solidification was performed by means of high velocity jets of nitrogen and argon to produce fine powders.

Size fraction +53, -106 was comminuted in an attritor, using stainless steel balls; 200 g lots of powders were attrited under isopropyl alcohol at 180 rpm for 72 hours to produce fine flakes. The accumulated flakes were decanted and dried in air.

Flakes were mixed with yttria powder particles, in the amounts of 4 and 5 vol% to prepare yttria dispersion stabilized 316 stainless steel Alloy I and Alloy 11, respectively. The size of the commercially available yttria powders was specified in the range of 200-400 Å. A mixture of stainless steel flakes and yttria powders was mechanically alloyed in a ball mill in an argon atmosphere. This process has been chosen to assure a uniform distribution of yttria in the material. A charge of 200 g was ball milled at a time. The ball mill was run 72 hrs for Alloy I and 48 hrs for Alloy 11. Powders were then cold compacted, degassed by heating to about 450°C under vacuum, and hot extruded at about 1150°C at an area reduction ratio of 16:1, resulting in 1.27 cm diameter bars.

Rapidly solidified powders, flakes and mechanically alloyed powder particles were examined in SEM and TEM. The microstructure of the consolidated material was examined in TEM; samples were thinned by electropolishing in a 10% $HClO_4$-90%CH_3OH solution at -50°C and 25V. Nearly all specimens were thinned additionally by using ion milling.

Microhardness testing was performed with a Tukon Tester with a 200 gm load. Room temperature tensile tests were performed on an Instron machine at a crosshead speed of 0.05 cm/min. Stress rupture tests were done at 650°C in air by using a lever load applicator system. Specimens

were machined to ASTM specifications; the test bar had a gage diameter of 0.406 cm and gage length of 1.905 cm.

The extruded materials were thermomechanically processed. Samples were isothermally annealed at various temperatures to study microstability, hardness and tensile properties. Samples were cold worked, with intermediate annealing: the process involved pre-annealing at 1200°C for 1 hr, followed by cold working in steps of 20% and 15% for Alloys I and II, respectively, plus annealed at 850°C, until cracks were observed in the samples.

3.8.4.3 Microstructures

The morphology of the rapidly solidified powder particles of 316 stainless steel as-atomized is shown in Figure 3.8.1. The particles are spherical and previous work[1] showed that the dendrite arm spacing is typically 1-3 μm suggesting a cooling rate of about 10^4 °C/sec. Segregation could not be observed in the interdendrite spaces.

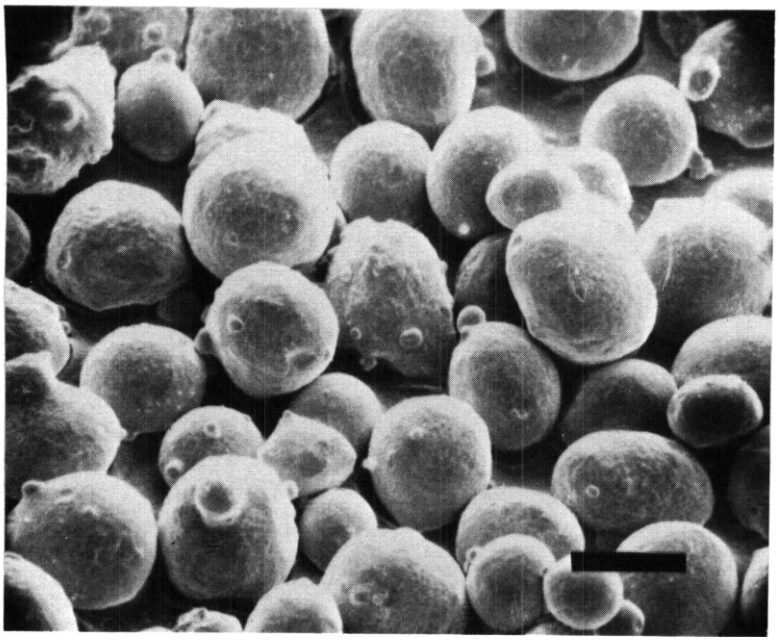

Fig. 3.8.1. SEM micrograph showing the morphology of rapidly solidified powders of 316 stainless steel (with 1% Al). Length of the marker is 75 μm.

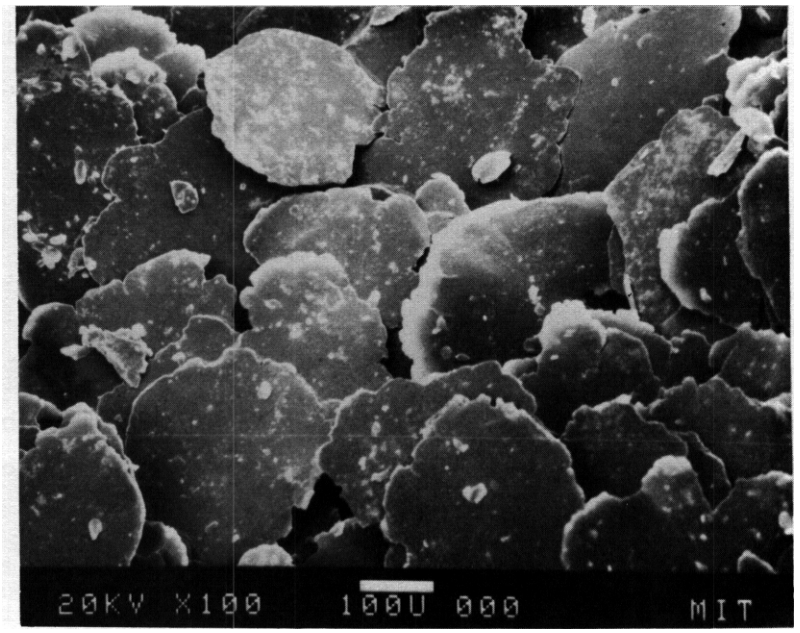

Fig. 3.8.2. SEM micrograph showing the morphology of the attrited flakes.

Table 3.8.1. Average Flake Dimensions as a Function of Attrition Time

Attrition Time hrs	Flake Thickness	Flake Width µm
48	7.5	250
72	1.5	250

Figure 3.8.2 shows the morphology of the attrited flakes. The thicknesses of the flakes decreased with increasing attrition time as shown in Table 3.8.1. The final flake size, produced after 72 hours of attrition, has an average area-to-volume ratio of 1.35 compared to that of the original powder particles, which is about 7.5 x 10^{-2}. This should allow for most of the aluminum in the alloy to be oxidized. The flake thickness of 1.5 µm which was obtained after 72 hrs of attrition was considered sufficiently small to allow for a uniform distribution of yttria particles in the material during the subsequent ball milling operation.

The efficiency of mechanical alloying in uniformly distributing yttria powder particles was determined by varying ball milling time (24, 48 and 72 hrs) and starting size and shape of stainless steel powders (as-atomized powders, 1.5 μm thick flakes). Microstructural examination in SEM and TEM (carbon extraction replica technique) of ball milled powder particles which were prepared metallographically and etched in glycerol regia showed that 48 and 72 hr ball milling produced a uniform dispersion of yttria in stainless steel powders provided that yttria has been mixed with 1.5 μm thick stainless steel flakes. Mechanical alloying of as-atomized stainless steel powders did not produce, however, a uniform yttria dispersion after 48 and 72 hrs.

Microstructural examination (SEM, TEM) of the extruded Alloy I which was annealed 1 hr at 1200°C showed more or less uniform distribution of oxide particles in the austenitic matrix. The average oxide particle size was 413 Å and estimated interparticle spacing was 1000-2000 Å. Particle size and interparticles spacing in Alloy I is considerably smaller than in previously developed aluminum oxide dispersion stabilized austenitic stainless steel. Detailed STEM analysis has been planned to identify the composition and structure of different oxides present: a) yttrium oxides which were added to stainless steel; b) aluminum oxides which formed from oxide surface film on the attrited flakes during ball milling and hot extrusion; and c) possibly smaller amounts of chromium oxides. The longitudinal and transverse grain sizes, d_1 and d_2 respectively, were shown by SEM to be of the order of 12 and 0.85 μm, respectively. The grain aspect ratio, GAR, defined as the ratio d_1/d_2 is thus of the order of 16, and the grain size, d, defined as $(d_1 d_2)^{\frac{1}{2}}$, is of the order 3 μm. The GAR is greater than 3, the minimum required to produce substantial improvement in high temperature properties.[3]

3.8.4.4 Microstructural Stability and Response to TMT's

Figure 3.8.3 shows stability curves for the as-extruded oxide dispersion stabilized Alloys I and 11. Knoop hardness (200 g load) was plotted as a function of annealing temperature (1 hr anneal). Hardness of the as-extruded material remained unchanged after 1 hr anneal to 1100°C for Alloy I. Relative to the alumina dispersion stabilized alloy,[1]

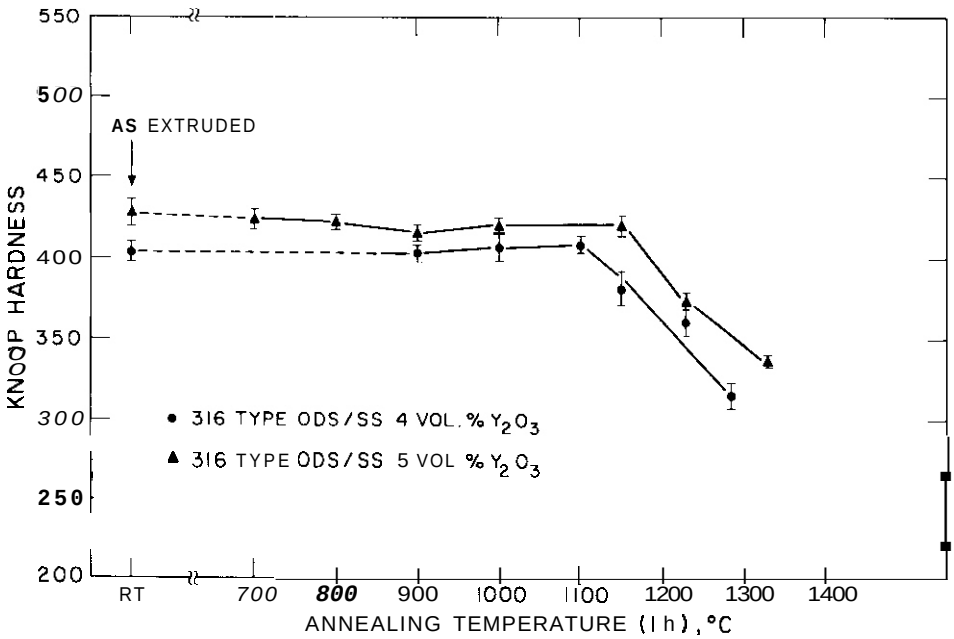

Fig. 3.8.3. Stability curves for the as-extruded OD alloys I and II. Plots of Knoop hardness versus annealing temperature (1 hr anneal).

the hardness is much higher, almost doubled. A similar stability curve plotted for Alloy II, Figure 3.8.3, showed that the hardness can be increased further by increasing the amount of finely dispersed Y_2O_3 and that the hardness remained unchanged to 1150°C.

However, the increase in hardness at this amount of oxide dispersion (5 vol% addition) would be detrimental to the ductility of the alloy. This was evident in room temperature working by swaging performed on Alloys I and 11. Alloy I cracked after 40% CW while Alloy II cracked after 33% CW. Intermediate annealing (IA) at 850°C performed on the alloys resulted in 60% CW for Alloy I and only about 30% for Alloy 11. Cold swaging plus intermediate annealing of OD alloys has the effect of rearranging dislocations into low single boundaries, thereby permitting further cold working before cracking.' This is evident in the increase of ability to cold work Alloy I from 40 to 60%; however, this is not true with Alloy II and this suggests the possibility of having exceeded the optimum content of oxide in 316 stainless steel.

Table 3.8.2. Room Temperature Tensile Properties of OD Alloy I

ALLOY CONDITION	Yield Strength (0.2% offset) MPa	UTS MPa	Elongation %
As extruded	930.0	1031.3	15.32
As extruded + 1130°C anneal	965.3	1076.5	13.15
As extruded + 1230°C anneal	885.5	1010.5	16.15
As extruded + 1330°C anneal	628.5	868.1	20.78

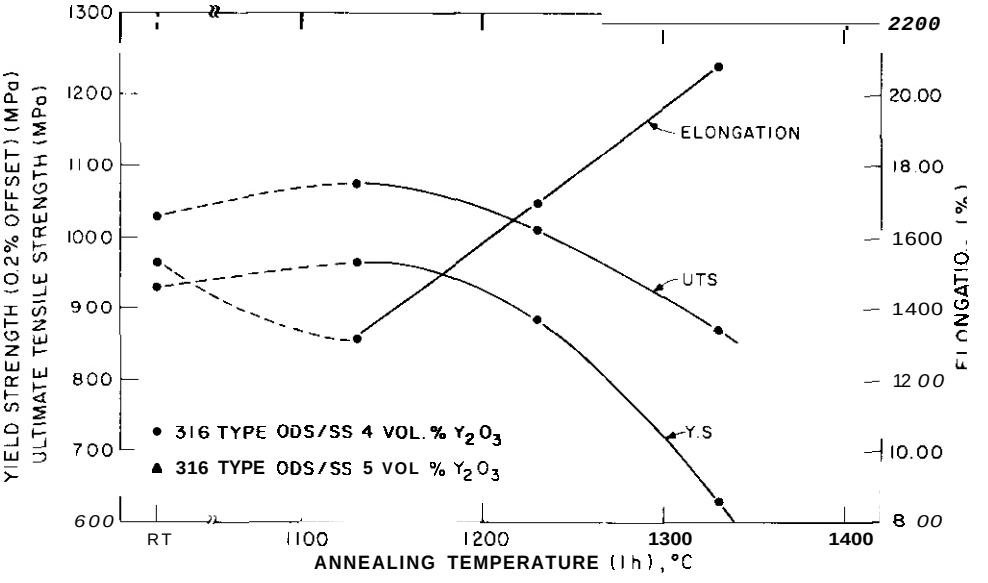

Fig. 3.8.4. Room temperature tensile properties for OD alloy I.

3.8.4.5 Room Temperature Tensile Properties

The tension testing performed on Alloy I showed a substantial improvement in the room temperature properties, as shown in Table 3.8.2. The yield strength increased from 379 MPa for the Al_2O_3 OD alloy to 980 MPa for Alloy I; the UTS increased from 604 MPa for the Al_2O_3 OD alloy to 1031 MPa for Alloy I. Ductility is, however, lowered to 15.3% compared with 30.5% for the Al_2O_3 OD alloy.

Figure 3.8.4 shows the effect of annealing for 1 hr at temperatures near the recrystallization point. An annealing condition of 1 hr at 1130°C resulted in the highest strength and the lowest ductility, which decreased and increased, respectively, at higher temperatures. This suggests grain growth coupled with recrystallization since, according to the work of Scott and Spruielli on the effect of grain size on hardness and tensile properties for a 316 type stainless steel,[5] the hardness, YS and UTS all decrease as the grain size increases. The structure is probably recrystallized at about 1350°C. Working opens voids at particle/matrix interfaces and the voids elongate with increased working. These voids heal during high temperature annealing.[6] This accounts for the higher strength of the alloy annealed at 1130°C before recrystallization. Detailed microstructural and fractography studies are currently underway on Alloy I as a function of different thermomechanical treatments.

3.8.4.6 Stress-Rupture Tests at 650°C

Stress-rupture testing of Alloy I at 650°C has been initiated. The stress-rupture time plot for the as-extruded material shows an exponent of 12 and the extrapolation of the plot predicts that the alloy is capable of withstanding a load of 220 MPa (32 KSi) without failure up to 100 hrs, and a load of 180 MPa (26 KSi) without failure up to 1000 hrs. The curve after 1200°C, 1 hr anneal exhibits the same exponent of 12 but the strength is lower by about 20 MPa (2.9 KSi) which may be understood as a consequence of the reduction of dislocation density due to 1200°C anneal as compared to the as-extruded material.

Stress rupture testing of Alloy I (4 vol% yttria) which is currently in progress includes the following thermomechanical treatments: a) 20-30% cold work (with an intermediate annealing at 850°C after 10-15% CW) which is a reference condition for fusion materials research; b) annealing at temperatures above 1200°C to allow for recrystallization and grain growth; and c) directional recrystallization to increase the grain aspect ratio.

3.8.5 Conclusions and Future Work

Based on this and previous works[1,2,7], mechanical alloying by attrition followed by ball milling is a powder metallurgy technique that can be used efficiently to generate an inert oxide dispersion in 316 stainless steels. The thin flakes provide a large surface area to volume ratio to enhance surface oxidation of aluminum and generate fairly uniform distribution of Al_2O_3 and Y_2O_3 oxides. The milling involved cold welding of the consituents, dividing and uniformly distributing of oxide particles in the interior of each alloy particle.

Alloys with 4 vol% and 5 vol% yttria additions have been prepared and they show significant improvements in microstructural stability.

Austenitic stainless steel containing 4 vol% yttria showed very high room temperature YS and UTS, with sufficient ductility.

Stress rupture tests at 650°C on the 4 vol% yttria alloy in the as-extruded material showed favorable high temperature behavior. Future work will include detailed studies of the effect of different thermo-mechanical treatments on high temperature strength and ductility of oxide dispersion stabilized rapidly solidifed stainless steel.

Samples of oxide dispersion stabilized 316 stainless steel will be included in alloy development irradiation experiments.

3.8.6 References

1. J. Megusar, L. Arnberg, J. B. Vander Sande and N. J. Grant, "Microstructure of Rapidly Solidified Al_2O_3 Dispersion Strengthened Type 316 Stainless Steel," J. Nucl. Mater., 103 & 104: 1109-13 (1981).
2. E. Y. Ting, "Properties of an Oxide Dispersion Stabilized 316 Stainless Steel through a Powder Metallurgy Approach," M.S. Thesis, Dept. of MSE, M.I.T., 1980.
3. B. A. Wilcox and A. H. Claner, "Dispersion Strengthening," Chapter 7 in the Superalloys, John Willey & Sons, Inc., 1972.
4. J. G. Rasmussen and N. J. Grant, "ThO_2 Dispersion Strengthened Ni and Ni-Mo Alloys Produced by Selective Reduction," Powd. Metall., 8: 92-113 (1965).

5. J. A. Scott and J. E. Spruielli, "Tensile Properties of Thermal-Mechanically Pretreated Type 316 Austenitic Stainless Steel Alloy," Met. Trans., 5: 1695-97 (1974).

6. B. A. Wilcox and A. H. Claner, "The Role of Grain Size and Shape in Strengthening of Dispersion Hardened Nickel Alloy," Acta Metall., 20: 743-57 (1972).

7. W. F. Schilling, "Dispersion Strengthened FeCrAlY Alloy by Flake-Powder Processing," pp. 373-83 in Superalloys, Metallurgy and Manufacture, Proc. Int. Symp., 13th, 1976, Clairton's Publishing Div., 1976.

3.9 MICROSTRUCTURES DEVELOPED IN AUSTENITIC STAINLESS STEELS IRRADIATED IN HFIR AT 55°C — P. J. Maziasz (Oak Ridge National Laboratory)

3.9.1 ADIP Tasks

ADIP Tasks I.C.1, Microstructural Stability, and I.C.2, Microstructures and Swelling in Austenitic Alloys.

3.9.2 Objective

The objective of this task is to determine the effects of displacement damage and helium generation on microstructural development at lower water coolant temperatures.

3.9.3 Summary

Samples of solution annealed types 316 and 347 stainless steel (SA 316 and SA 347) and 20%-cold-worked type 316 stainless steel (CW 316) have been irradiated in the High Flux Isotope Reactor (HFIR) at 55°C. No voids or bubbles were detected. All samples contained a fine "black spot" component of the dislocation structure. Both SA 316 and SA 347 contained a high concentration of Frank interstitial loops (14—30 nm diam) but no dislocation networks, whereas CW 316 shows network recovery with few Frank loops.

3.9.4 Progress and Status

Early work on fusion first-wall lifetime limitations indicated that irradiation temperatures should not exceed 550 to 600°C, according to HFIR irradiation swelling and ductility data for type 316 stainless steel.[1] Recent work by Wiffen[2] has indicated minimal properties degradation after HFIR irradiation of type 316 at 55°C, and recent design studies[3] have considered first wall temperatures near 300°C. However, very recent HFIR data[4] indicate that a swelling maximum may be present between 55 and 300°C in CW 316, indicating that the lower temperature microstructural and swelling behavior of these steels in not well-known. Fast breeder reactor irradiation produces data on the effects of displacement without much helium generation at temperatures above about 370°C. Light water reactor

irradiation produces helium with very little accompanying displacement damage at lower temperatures. The present study was motivated by the lack of data at low temperature and HFIR's ability to produce helium and displacement damage at 55°C.

Transmission electron microscopy (TEM) of the as-irradiated microstructures of both SA and CW 316 shows only dislocations, with no evidence of precipitation and no resolvable cavities. Irradiation parameters are given in Table 3.9.1. Quantitative dislocation information for both unirradiated and as-irradiated material is also given in Table 3.9.1. Solution-annealed type 316 stainless steel had a very low ($<10^{12}$ m/m^3) density of line dislocations randomly distributed prior to irradiation. High Flux Isotope Reactor irradiation at 55°C produced a high total dislocation concentration (1.6×10^{14} m/m^3) that consisted of a large concentration (3.6×10^{22} m^{-3}) of about 14-nm-diam Frank interstitial loops. There is also fine black spot damage that appears to be loops, in the background, as indicated in Table 3.9.1. However, the vacancy or interstitial character of these has not yet been determined. They contribute little to the total equivalent line dislocation density.

Table 3.9.1. Dislocation Information for Austenitic Stainless Steels Irradiated in HFIR at 55°C

Material, starting Microstructure	Displacement Damage (dpa)	Helium Content (at. ppm)	Network Dislocation concentration (m/m^3)	Dislocation Loops		Total Dislocation concentration (m/m^3)
				Average Diameter (nm)	concentration (m^{-3})	
316, SA	0	0	10^{10}–10^{12}		0	10^{10}–10^{12}
	7.3	290	$<10^{10}$	14[a]	3.6×10^{22}	1.6×10^{15}
				3.7[b]	3×10^{22}	
316, 20% CW	0	0	3–5×10^{15}		-0	3–5×10^{15}
	10.8	520	5×10^{14}	23[a]	-1.0×10^{21}	1.5×10^{15}
				3.5[b]	7.7×10^{22}	
347, SA	-0	-0	3–4×10^{13}		0	3–4×10^{13}
	~1[c]	~2500[d]	$<10^{10}$	-305	-5×10^{22}	-5×10^{15}
				2–6[b]	3–4×10^{22}	

[a]Frank interstitial loops.

[b]Small defect clusters, tentatively identified as loops, but vacancy or interstitial nature not yet determined.

[c]Calculated, based on fast fluence of 1.1×10^{25} neutrons/m^2 ($E > 0.1$ MeV).

[d]Calculated, based on thermal fluence of 7×10^{26} neutrons/m^2 and 13 wt % Ni, as measured by quantitative x-ray EDS.

Under the same irradiation conditions CW 316 develops quite differently from SA 316. The CW 316 shows network dislocation recovery from about 3 to 5 x 10^{15} m/m^3 prior to irradiation to about 5 x 10^{14} m/m^3 after irradiation. The CW 316 shows a much lower concentration of Frank loops, but about three times more black spot damage than the SA 316. In CW 316, the loop component contributes about twice as much as the network to the total dislocation density of 1.5 × 10^{15} m/m^3, which is the same as the total density in the SA 316.

Examination of a segment of SA 347 tubing irradiated in another part of HFIR at about 55°C helps shed more light on the mechanisms involved and the role of helium. The SA 347 saw service for five years as a pneumatic tube located in the beryllium reflector outside the core. The neutron spectrum was primarily thermal, with a small fast fraction. The irradiation produced approximately 1 dpa and 2500 at. ppm He. Transmission electron microscopy of unirradiated and irradiated portions of the tube is shown in Fig. 3.9.1, and dislocation information is included in Table 3.9.1. There are nearly ten times as many dislocations in the network of the unirradiated SA 347, probably due to a stabilization treatment to produce the NbC precipitates observed in Fig. 3.9.1(a). Irradiation in HFIR to only 1 dpa produces several times more total dislocation density than SA 316 irradiated to about 7 dpa. There are more and larger Frank interstitial loops in the SA 347, with essentially the same black spot damage as the SA 316. The SA 347 contains approximately eight times more helium than the SA 316, generated continuously in both samples during the irradiation.

Postirradiation annealing of the SA 347 for 1 h at 650°C developed a very high concentration (2 to 3 x 10^{23} m^{-3}) of fine (2 to 3 nm diam) helium bubbles, shown in Fig. 3.9.2(a). These can easily account for all of the helium in equilibrium and would indicate that helium and vacancies were trapped on a very fine scale to nucleate such a high concentration of bubbles during annealing. The loop structure is also annealing to form some network in Fig. 3.9.2(b). At these low temperatures, there are essentially no equilibrium vacancies, and there must be one vacancy surviving recombination for every interstitial that is incorporated into a

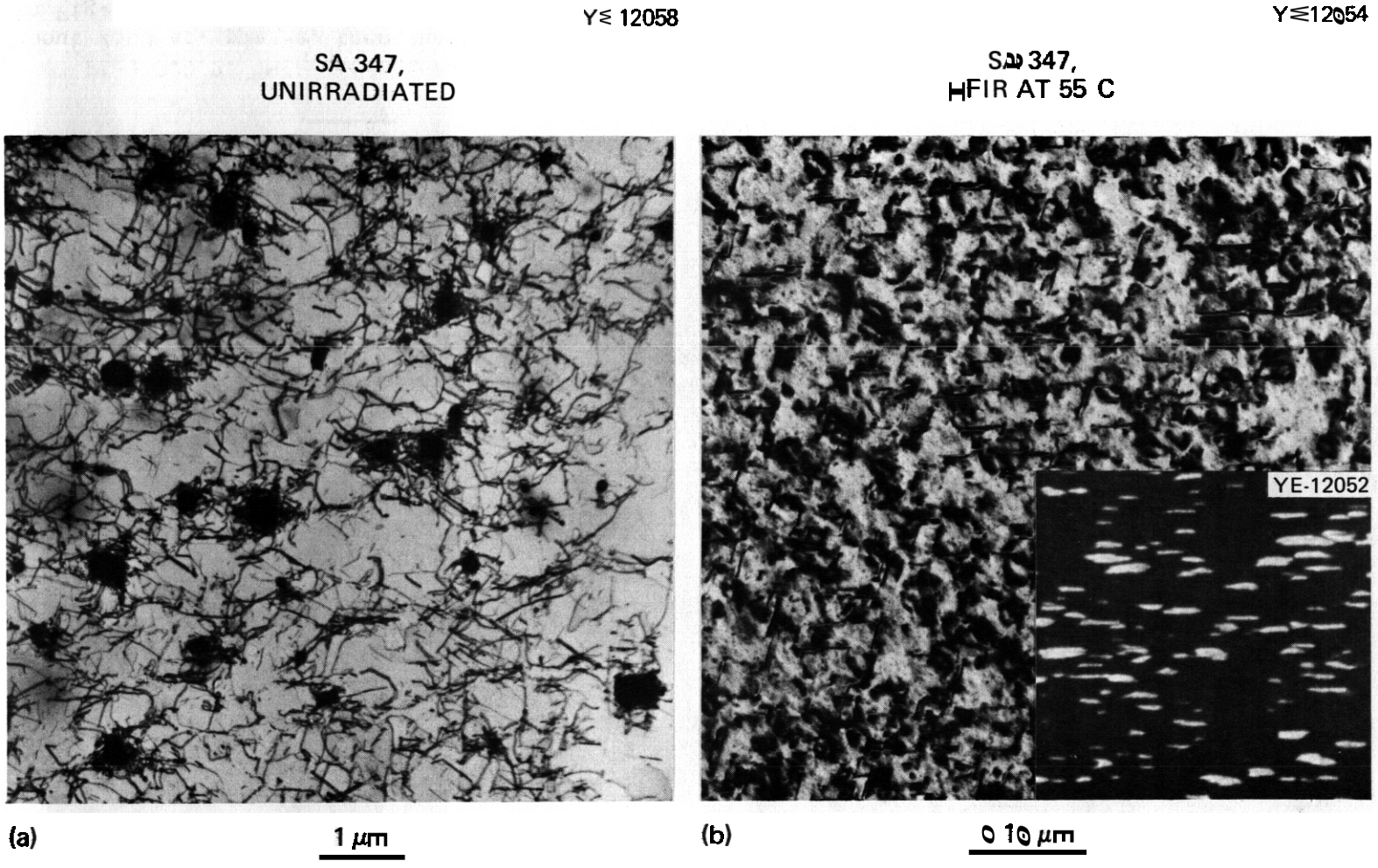

Fig. 3.9.1. Microstructural Comparison of SA 347 (a) Unirradiated, (b) After HFIR Irradiation at 55°C to About 1 dpa and About 2500 at. ppm He. Inlay on (b) shows Frank imaged in dark field using <111> stacking fault satellites near (200) reflections.

H-63682

H-63676

SA 347, HFIR AT 55°C
POSTIRRADIATION ANNEALED
FOR 1 h AT 650°C

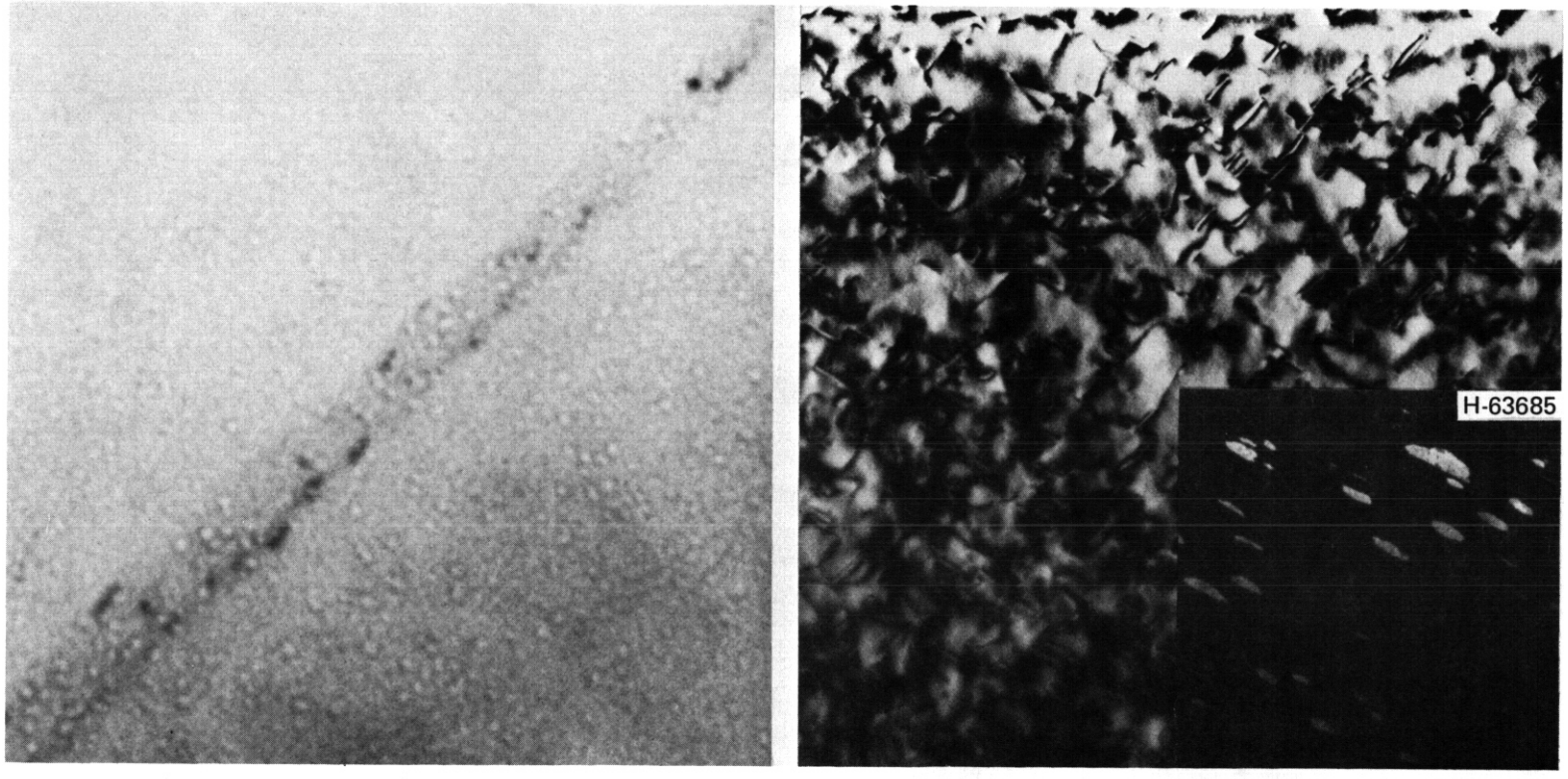

(a) 20 nm (b) 0.10 μm

Fig. 3.9.2. Microstructure of SA 347 Irradiated in HFIR at 55°C to Produce About 1 dpa and About 2500 at. ppm He, then Annealed for 1 h at 650°C. Inlay on (b) shows Frank loops imaged as in Fig. 3.9.1(b).

Frank loop or that causes a line dislocation to climb. Helium atoms are also strongly bound to vacancies, and if they prevent some fraction of recombination, they could reasonably contribute to formation and development of dislocation sinks for the interstitials.

3.9.5 Conclusions

Although prior low-irradiation-temperature work showed only black spot damage from 90 to 300°C (ref. 5), this study showed a more extensive development of dislocation microstructures. The amount of microstructural development and difference between CW 316 (network) and SA 316 (all loops) should be important for sorting out loop nucleation and growth mechanisms and may be important to the irradiation creep behavior at these temperatures. The work also points to the importance of helium to microstructural (and hence properties) development, even at these low temperatures.

3.9.6 References

1. E. E. Bloom, F. W. Wiffen, P. J. Maziasz, and J. O. Stiegler, "Temperature and Fluence Limits for a Type 316 Stainless-Steel Controlled Thermonuclear Reactor First Wall," *Nucl. Technol.* 31: 115–22 (October 1976).
2. F. W. Wiffen, "The Effects of Irradiation at About 55°C on Type 316 Stainless Steel," *ADIP Quart. Prog. Rep. March 31, 1978*, DOE/ET-0058/1, pp. 89–93.
3. C. C. Baker and M. A. Abdou, *STARFIRE — A Commercial Tokamak Fusion Power Ptant Study*, ANL/FPP-80-1, Argonne National Laboratory, Argonne, Ill. (September 1980).
4. P. J. Maziasz and M. L. Grossbeck, "Swelling and Microstructure of HFIR-Irradiated 20%-Cold-Worked Types 316 Stainless Steel and 316 + 0.23 wt % Ti," *ADIP Quart. Prog. Rep. Dec. 31, 1980*, DOE/ER-0045/5, pp. 43–69.
5. E. E. Bloom, W. R. Martin, J. O. Stiegler, and J. R. Weir, "The Effect of Irradiation Temperature on Strength and Microstucture of Stainless Steel," *J. Nuct. Mater.* 22(1): 68–76 (April 1967).

3.10 STATISTICAL ANALYSIS OF THE MFE-5 IN-PEACTOR FATIGUE CRACK GROWTH EXPERIMENT RESULTS - A. M. Ermi (Westinghouse Hanford Company)

3.10.1 *ADIP* Task

ADIP Task I.B.1, "Fatigue Crack Growth in Austenitic Alloys" (Path A).

3.10.2 Objectives

An in-reactor fatigue crack propagation experiment was conducted in the ORR on the Path A Reference Alloy, 20% cold-worked 316 stainless steel. The effects of dynamic irradiation on crack growth behavior were evaluated by comparing the results with thoseof alaboratory thermal control test.

3.10.3 Summary

Results fromthe in-reactor fatigue crack propagation experiment and thermal control test have been quantitatively analyzed using statistical comparisons of the data. The analysis showed that at the 95% confidence limits, thein-reactor growth rates exceeds the thermal control by at most a factor of about two. However, the average growth rates in-reactor were less than that for the thermal controls, but statistically there were no significant differences between the crack growth rates from the two tests.

3.10.4 Progress and Status

3.10.4.1 Introduction

Fatigue crack propagation (FCP) in the first wall of a magnetic fusion reactor may be a limiting quantity governing reactor lifetimes. Previous studies of irradiation effects on FCP have all been conducted out of reactor on materials pre-irradiated in the unstressed condition. The ORR-MFE-5 experiment was designed to investigate FCP during irradiation, where dynamic irradiation may effect crack growth characteristics.

3.10.4.2 Test Background

The MFE-5 experiment was conducted in the ORR, being inserted in Nov. 1980, and scheduled to run for 200,000 cycles (approximately 6 months). After nearly 60,000 cycles (2 months), a problem with the stress cycling system developed, apparently caused by a lengthening somewhere in

the specimen chain. This prompted removal of the experiment during the Feb. 1981 end-of-cycle shutdown. The initial concern when the test was terminated was whether there was any damage to the specimens due to an overload, thus invalidating the results. Post-test examination of all specimens discounted this possibility:

(a) There were no measurable specimen elongations which could account for the apparent specimen chain lengthening;

(b) there was no evidence of gross plastic deformation at the crack tips which its obvious in overloaded specimens.

(c) scanning electron microscopy revealed no anomalies along the crack front of any specimens; and

(d) the fact that crack growths were observed for all specimens verifies that an overload did not occur, at least up until the final reactor startup when the problem suddenly developed and the test was halted.

Post-test examination of the test hardware and design led to the conclusion that the most probable cause of the chain lengthening was a loosening of a specimen pin clamp, thus allowing the pin to slip partially out of a specimen support link. The only impact of early termination on the data was that very small crack extensions were available for analysis. The final MFE-5 test matrix is detailed in Table 3.10.1 while the results for both the in-reactor test and the thermal control test are listed in Tables 3.10.2 and 3.10.3 respectively.

Table 3.10.1 MFE-5 EXPERIMENT TEST MATRIX

Specimen:	Miniature Center-Cracked Tension
Material:	Path A 20% Cold-Worked 316 SS
Peak Temperature:	460^0C
Environment:	Sodium
Frequency/Waveform:	1 cycle/min; triangular
Stress Intensity:	8 to 13 Mpa m
Stress Ratio:	min. load/max. load, R = 0.10
Reactor:	ORR, Position C-7
Fast Flux:	3×10^{14} n/cm^2-s (E > 0.1 MeV)
Duration of Test:	∿ 60,000 cycles

TABLE 3.10.2 MFE-5 IN-REACTOR FATIGUE TEST RESULTS

Peak Load: 1490 N (335 lbs)

R = 0.10 Frequency: 1 cycle/min.

N = 58,197 cycles

Spec. #	Width, w (mm)	Thick. t (mm)	Initial Crack, 2a (mm)	Final Crack, 2a (mm)	Crack Growth (mm)	Growth Rate, da/dN (mm/cycle)	Stress Intensity Range, ΔK (Mpa$\sqrt{m}$)
AE-11	25.375	0.568	4.587	4.684	0.097	8.29×10^{-7}	8.10
AE-01	25.382	0.569	5.690	5.702	0.013	1.09×10^{-7}	9.05
AE-06	25.405	0.568	4.684	4.719	0.036	3.05×10^{-7}	8.15
AE-05	25.397	0.568	6.952	7.054	0.102	8.73×10^{-7}	10.2
AE-03	25.405	0.563	5.598	5.652	0.053	4.58×10^{-7}	9.07
AE-07	25.420	0.552	4.580	4.742	0.163	1.40×10^{-6}	8.34
AE-02	25.387	0.588	8.796	9.030	0.234	2.01×10^{-6}	11.5
AE-04	25.362	0.538	9.634	9.914	0.279	2.40×10^{-6}	13.4

TABLE 3.10.3 MFE-5 THERMAL CONTROL FATIGUE TEST RESULTS

Peak Load: 1490 N (335 lbs)

R = 0.10 Frequency: 1 cycle/min

N = 58,346 cycles

Spec. #	Width, w (mm)	Thick t (mm)	Initial Crack 2a (mm)	Final Crack, 2a (mm)	Crack Growth (mm)	Growth Rate da/dN (mm/cycle)	Stress Intensity Factor, ΔK (MPa $\sqrt{m}$)
AE-17	25.395	0.566	4.591	4.721	0.130	1.11×10^{-6}	8.14
AE-14	25.430	0.556	5.518	5.685	0.167	1.43×10^{-6}	9.17
AE-09	25.405	0.541	4.516	4.688	0.173	1.48×10^{-6}	8.46
AE-10	25.392	0.539	6.375	6.664	0.289	2.48×10^{-6}	10.3
AE-15	25.418	0.536	5.113	5.166	0.053	4.55×10^{-7}	9.07
AE-16	25.430	0.554	4.596	4.647	0.052	4.42×10^{-7}	8.27
AE-18	25.413	0.567	8.328	8.445	0.117	1.00×10^{-6}	11.4
AE-12	25.413	0.538	9.629	9.715	0.086	7.38×10^{-7}	13.3

3.10.4.3 Statistical Analysis

Both tests consisted of eight specimens which were precracked to different initial crack lengths, and cycled between fixed load limits. The crack lengths and loads chosen were based on previous testing in sodium, and were designed to give crack extensions from approximately 1.0mm (0.040 in) to approximately 5.0 mm (0.200 in). However, due to (a) the shortened duration of the test and (b) the relatively lower crack growth rates than anticipated, the crack extensions for all sixteen specimens were very small, ranging from 0.01 nun to 0.29 mm. To overcome the problem associated with measurement errors of small crack extensions which can lead to large errors for an individual specimen, results from all eight specimens in each chain were combined to obtain accurate overall crack growth rates. As expected, considerable scatter in the crack growth plots are produced, much of which is attributed to the uncertainties in measuring (Figures 3.10.1 and 3.10.2).

In order to establish a basis for comparing the two tests, a slope of 2.5 was fixed for both curves, and the intercepts for the best fit determined. The slope was chosen to match that of the room temperature curve (nearly equivalent to the high temperature sodium curve) which was used as a basis for the design. It should be emphasized that the purpose of the slope selection was only to describe the data sets in a physically meaningful fashion so that additional comparisons fo the data sets could be made. It should be noted also that the choice of the particular slope does not significantly alter the conclusions.

A plot of the 95% confidence intervals for the crack growth curves for both tests are included in Figures 3.10.1 and 3.10.2, and are compared in Figure 3.10.3. The t test was used to test the hypothesis that the equations were the same, and to determine by how much the in-reactor crack growth rate could exceed the thermal control test:

(1) To test the hypothesis that the equations are the same at the 95% confidence limit, compute

$$t = \frac{\vec{\alpha}_1 - \bar{\alpha}_2}{s_0 \, (1/n_1 + 1/n_2)^{1/2}} \qquad (1)$$

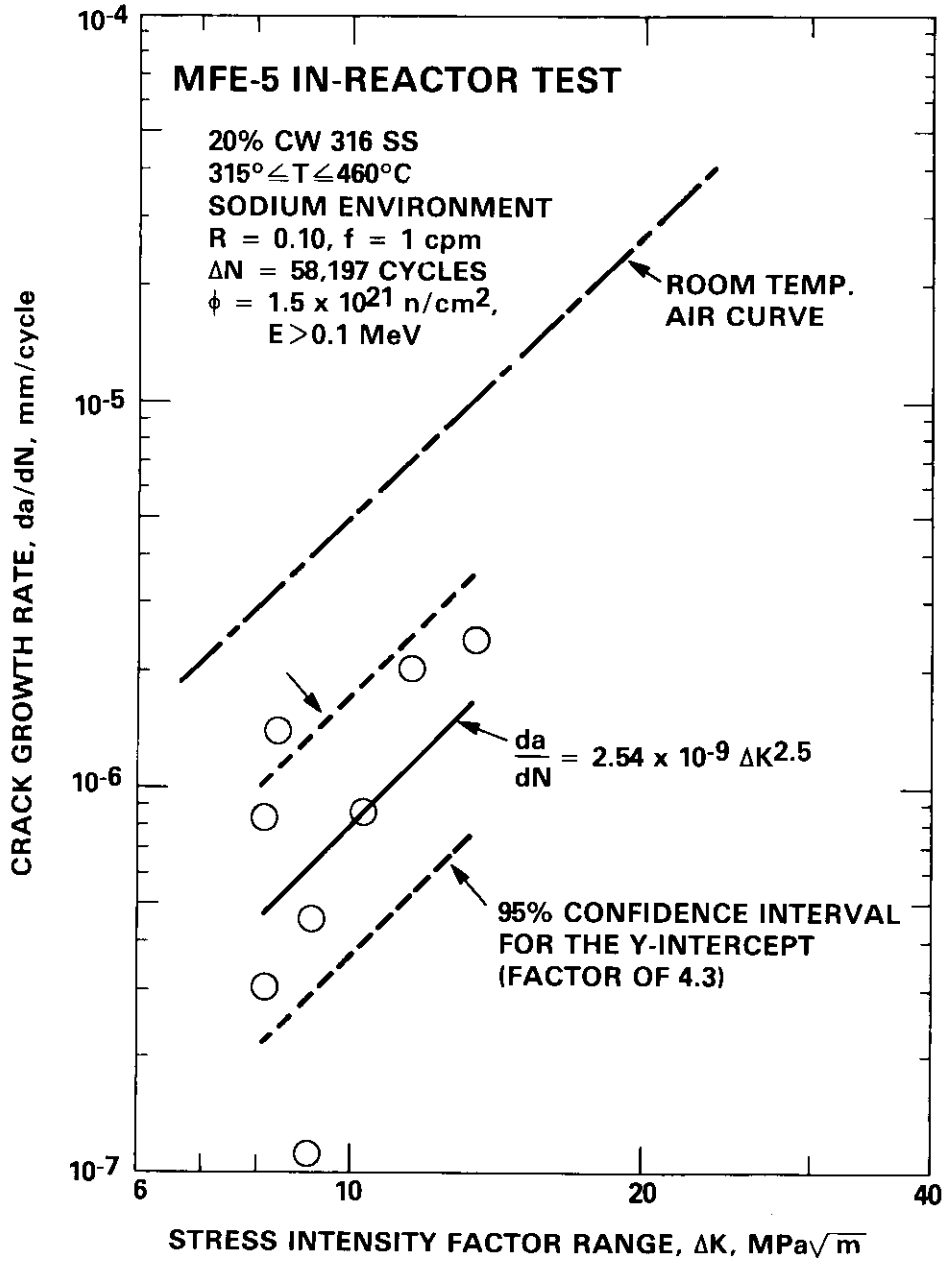

Figure 3.10.1 Crack growth rate results of in-reactor tested 20% cold-worked 316 stainless steel.

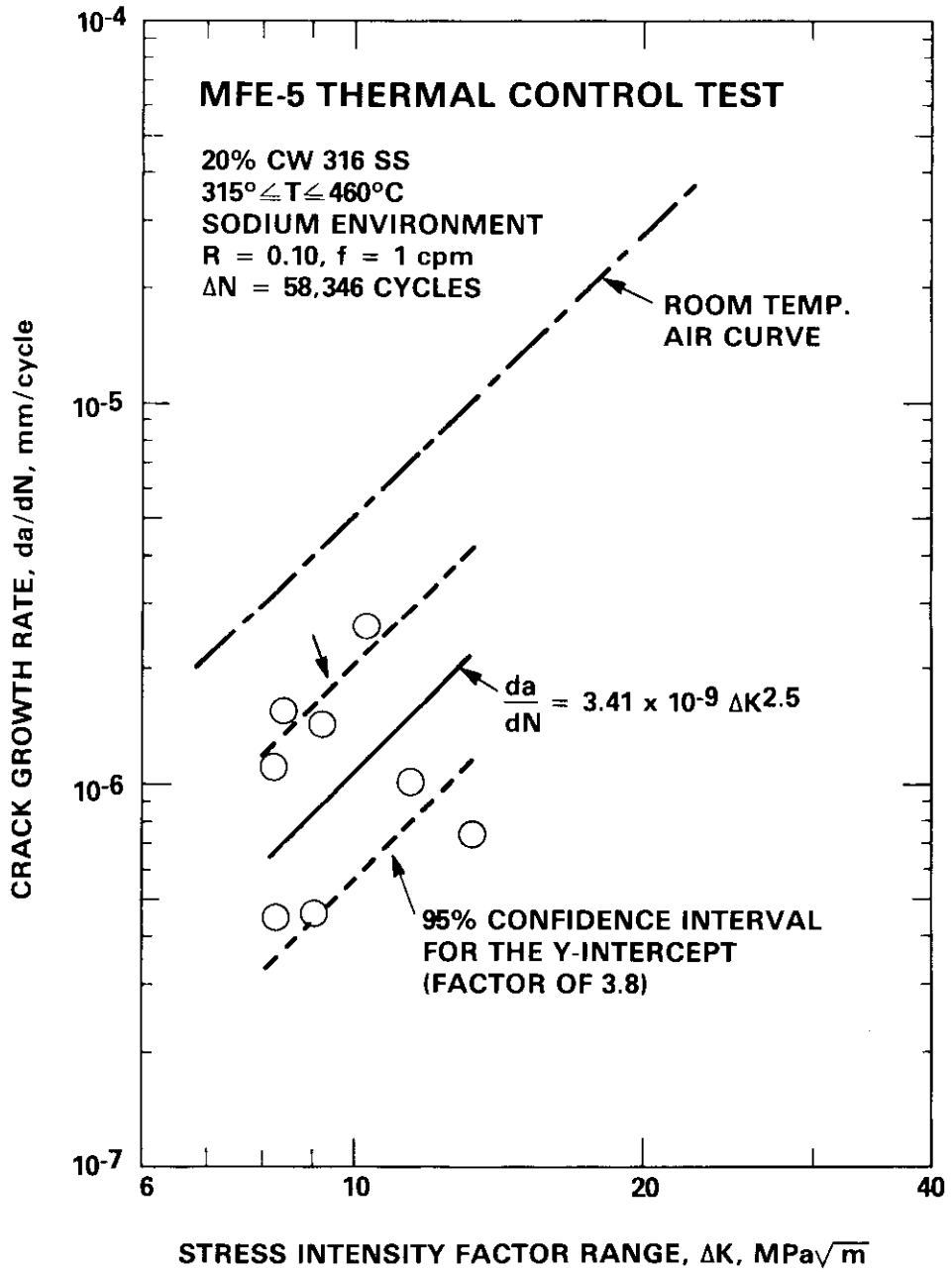

Figure 3.10.2 Crack growth rate results of the thermal control tested 20% cold-worked 316 stainless steel.

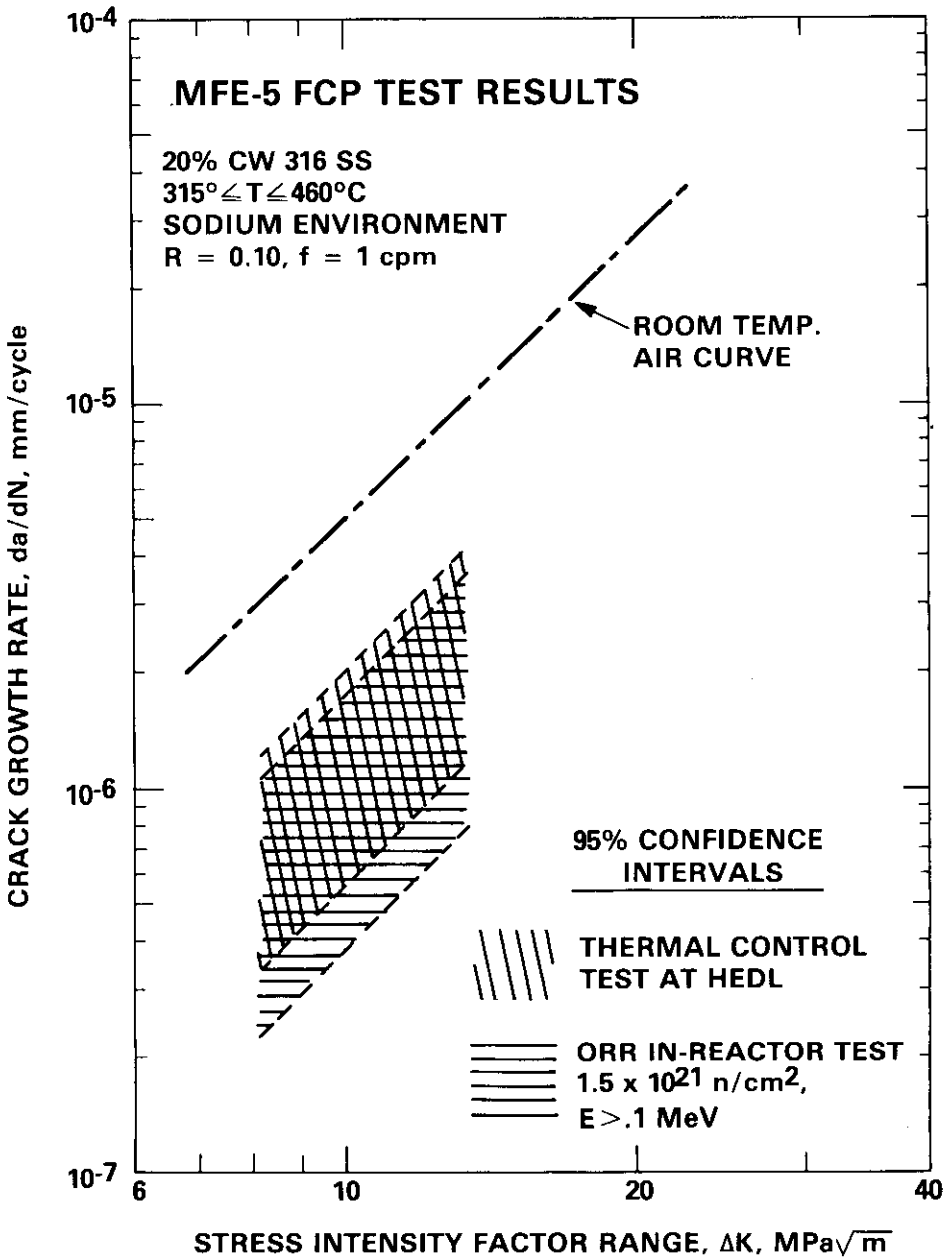

Figure 3.10.3 Statistical comparison of the fatigue crack growth behavior of unirradiated and in-reactor tested 20% cold-worked 316 stainless steel.

where $\bar{\alpha}_1$, $\bar{\alpha}_2$ = in-reactor and thermal control test mean intercepts,

s_o = pooled standard deviation and,

n_1 , n_2 = sample sizes

Using the information from Table 3.10.4, t is computed as 0.740 which is less than 2.145 for 100 (1-a) = 95%. Therefore, the hypotheses is accepted, and there are no significant differences in the equations.

Table 3.10.4 Statistical Parameters for the MFE-5 Test[a]

	In-Reactor	Thermal Control
Mean Intercept, $\bar{a}$:	$\bar{\alpha}_1$=-8.5944	$\bar{\alpha}_2$=-8.4675
Standard Deviation, s:	s_1 =0.3727	s_2=0.3102
Sample Size, n:	n_1 =8	n_2=8
Pooled Standard Deviation, s_o:	s_o = 0.3429	
$t_{\alpha/2,\ n_1+n_2-2}$:	$t_{0.25,14}$ = 2.145	

[a]Values are computed from log (da/dN) and log (ΔK) data.

(2) To determine how much the in-reactor crack growth rate could exceed the thermal control rates use,

$$t_{\alpha/2,n_1+n_2-2} = \frac{(\bar{\alpha}_1 + d) - \bar{\alpha}_2}{s_o\ (1/n_1 + 1/n_2)^{1/2}} \qquad (2)$$

where d is the amount thein-reactor rate could exceed the thermal control rate at the 100 (1-α)% confidence limit.

Solving for d yields d = 0.2409, and converting from logarithmic to linear units, 10^d = 1.74. The in-reactor crack growth rate is no more than a factor of 1.74 greater than the thermal control crack growth rate

at the 95% confidence limit. This is within the normal scatter band for fatigue crack growth and is therefore considered insignificant.

3.10.4.4 Conclusions and Recommendations

Based on the above analysis, it is evident that there were no significant effects of dynamic irradiation for 20% cold-worked 316 stainless steel at the test conditions investigated. Consequently, a second in-reactor test conducted under similar conditions is not warranted. This does not mean that in-reactor FCP testing need not be pursued further. The recommendation is that once materials have been narrowed down for a particular fusion reactor first wall application, and the operating conditions defined, additional in-reactor FCP testing should then be carriedoutto obtain the precise design data required for final material selection. In the meantime, irradiation effects on FCP for design studies and alloy selection will be ascertained through the more economical postirradiation test techniques.

3.10.5 Future Work

This concludes the work on the MFE-5 in-reactor FCP test. There are no plans to conduct any follow-on tests at this time.

3.11 TENSILE PROPERTIES OF U.S.S.R. AUSTENITIC STAINLESS STEEL AFTER LOW-TEMPERATURE HIGH FLUX ISOTOPE REACTOR IRRADIATION — R. L. Klueh and M. L. Grossbeck (Oak Ridge National Laboratory)

3.11.1 ADIP Task

ADIP Task I.B.13, Tensile Properties of Austenitic Alloys.

3.11.2 Objective

The United States and the U.S.S.R. have agreed to develop common physical points of reference (in materials and tests) to which irradiation-effects research and development studies may be related. The first step of this agreement was the exchange of a stock of austenitic stainless steels. The objective of this task is to irradiate and test the material supplied by the U.S.S.R., and to compare the results with results on similar U.S. materials.

3.11.3 Summary

Two tensile specimens of the U.S.S.R. low-nickel, high-manganese stainless steel EP-838 were irradiated in the High Flux Isotope Reactor (HFIR) at about 55°C to produce about 5.2 dpa and 63 at. ppm He. The tensile properties at room temperature and 300°C of the irradiated and unirradiated 20%-cold-worked steel were quite similar to the properties of 20%-cold-worked type 316 stainless steel (CW 316) that was similarly irradiated.

3.11.4 Progress and Status

The HFIR-CTR-33 irradiation experiment was primarily designed to determine the effect of transmutation helium on the tensile properties of ferritic steels.[1] In addition to these steels, CW 316 was included for comparison. Two specimens of the U.S.S.R. low-nickel, high-manganese stainless steel EP-838 obtained in the U.S.-U.S.S.R. exchange agreement[2] were also irradiated and tested. In this report the tensile properties of the unirradiated and irradiated 20%-cold-worked EP-838 and similar properties for CW 316 will be presented.

3.11.4.1 Alloys Irradiated

The compositions of the EP-838 and CW 316 are given in Table 3.11.1; the type 316 stainless steel is from the fusion reference heat (X15893). There are several major composition differences between the steels, most notably, the Ni, Mn, Cr, Mo, and Al.

Specimens of both steels were machined from 0.76-mm-thick sheet that was in the 20%-cold-worked condition. Before the EP-838 sheet was rolled to the final thickness, it was annealed 0.83 h at 1160°C.[2] The type 316 stainless steel was annealed 1 h at 1050°C prior to the final deformation.

Table 3.11.1. Chemical Composition of Austenitic Stainless Steels

Element	Chemical Composition (wt %)	
	U.S.S.R. Manganese Stainless Steel	Type 316 Stainless Steel
Cr	11.6	17.28
Mn	13.5	1.70
Ni	4.2	12.44
Mo	0.9	2.10
co	0.003	0.3
cu	0.1	0.3
Si	0.42	0.67
Nb		<0.05
V	0.01	
Ta	0.01	<0.05
Ti	≤0.018	<0.05
Al	0.72	
B	0.001	0.0004
Ce	0.04	
La	0.007	
Nd	0.008	
Pr	0.001	
C	0.02	0.061
S	0.02	0.018
P	0.003	0.037
Fe[a]	68.4	63.9

[a]Iron is approximate, by balance.

3.11.4.2 Experimental Procedure

Sheet tensile specimens were of an SS-1 type, with a reduced gage section 20.3-mm long by 1.52-mm wide by 0.76-mm thick (Fig. 3.11.1). Two specimens of EP-838 and ten CW 316 specimens were irradiated[3] at HFIR coolant temperature (about 55°C). Although the maximum total fluence for HFIR-CTR-33 was 5×10^{26} neutrons/m^2 and the maximum fast fluence was 1.3×10^{26} neutrons/m^2 (>0.1 MeV), the EP-838 specimens were at the ends of the capsule and received about 0.63×10^{26} neutrons/m^2 (>0.1 MeV) (the minimum value).[3] Type 316 stainless steel specimens were irradiated over the full range of fluence values.[3]

After immersion density measurements, the specimens were tensile tested at room temperature and 300°C. Tests were conducted in a vacuum chamber on a 44-kN capacity Instron universal testing machine at a strain rate of 4.2×10^{-5}/s.

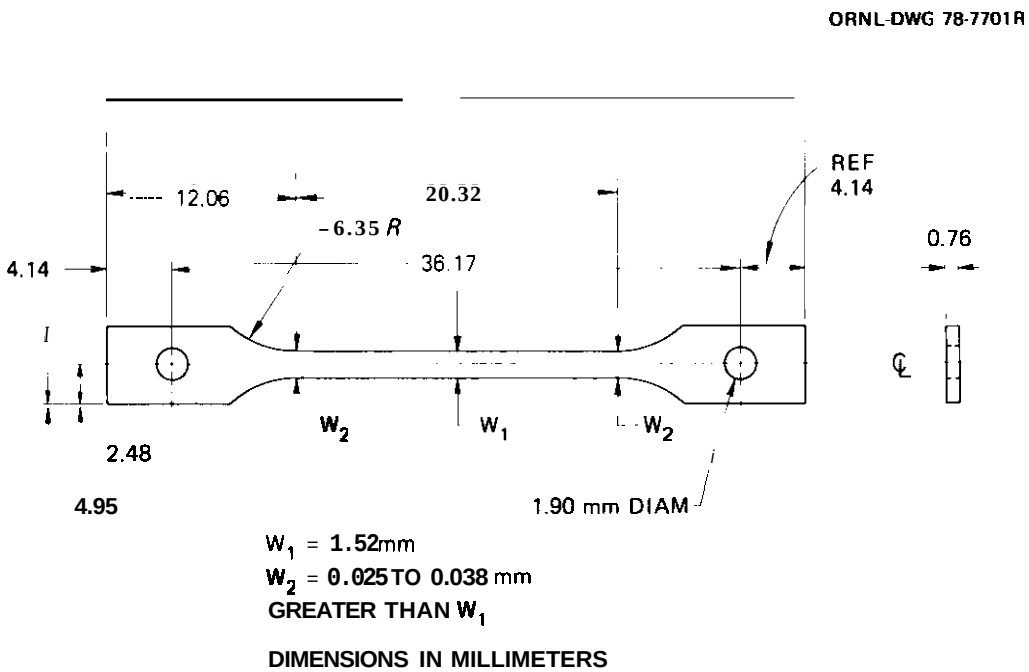

Fig. 3.11.1. The SS-1 Type Tensile Specimen.

3.11.4.3 **Results**

There was no detectable change in the density of the EP-838 or the type 316 stainless steel as a result of the irradiation.

Although there were some notable differences in the unirradiated tensile properties of the EP–838 and CW 316, the irradiated properties were quite similar (Table 3.11.2 and Figs. 3.11.2 through 3.11.4). The 0.2%-yield strength of the unirradiated CW 316 at room temperature and 300°C was greater than that of the EP–838 (Fig. 3.11.2). There was little difference in the unirradiated ultimate tensile strength (Fig. 3.11.3). The room temperature uniform and total elongations of EP–838 were considerably greater than those for the CW 316; however, there was little difference at 300°C (Fig. 3.11.4).

Table 3.11.2. Tensile Properties of Unirradiated and Irradiated[a] 20%-Cold-Worked U.S.S.R. EP–838 and Type 316 Stainless Steels

Fluence, >0.1 MeV (neutrons/m^2)	Displacement Level (dpa)	Helium Concentration[b] (at. ppm)	Test Temperature (°C)	Strength (MPa)		Elongation (%)	
				Yield	Ultimate	Uniform	Total
			EP–838				
0			25	571	751	21.9	25.9
0.63×10^{26}	5.2	63	25	883	910	0.8	6.9
0			300	460	594	2.1	5.0
0.63×10^{26}	5.2	63	300	720	732	0.5	2.5
			Type 316 Stainless Steel (Heat X15893)				
0			25	665	143	11.1	14.9
0.63×10^{26}	5.2	159	25	854	867	0.8	8.6
1.3×10^{26}	9.5	416	25	892	905	0.8	7.1
0			300	595	645	1.8	4.4
1.1×10^{26}	7.8	305	300	123	131	0.6	3.3

[a]Irradiation was in HFIR at about 55°C.

[b]Calculated level of helium from transmutation of ^{58}Ni and ^{10}B.

After irradiation there was very little difference in tensile properties. Both of the EP–838 specimens were irradiated to 5.2 dpa (–63 at. ppm He). Two CW 316 specimens irradiated to 5.2 dpa (–159 at. ppm He) and 9.5 dpa (–416 at. ppm He) were tested at room temperature. Although the specimen irradiated to 9.5 dpa was slightly stronger, the difference was less than 5%, indicating that a saturation level of hardening is probably being approached at this fluence. The yield strength and ultimate tensile strength for EP–838 were almost

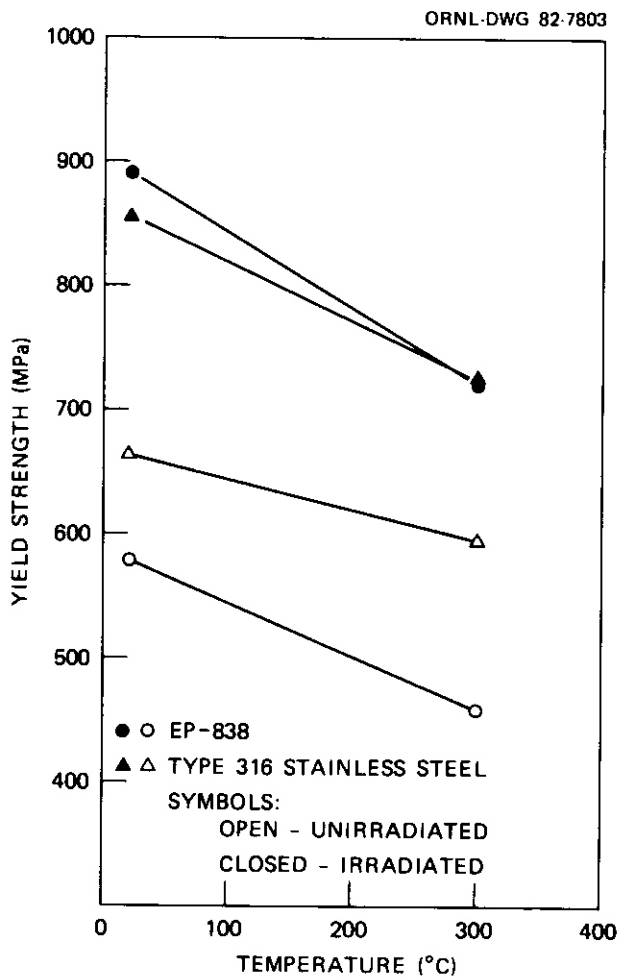

Fig. 3.11.2. The 0.2% Yield Strength Plotted Against Test Temperature for 20%-Cold-Worked EP-838 and Type 316 Stainless Steels, Unirradiated and After HFIR Irradiation at about 50°C.

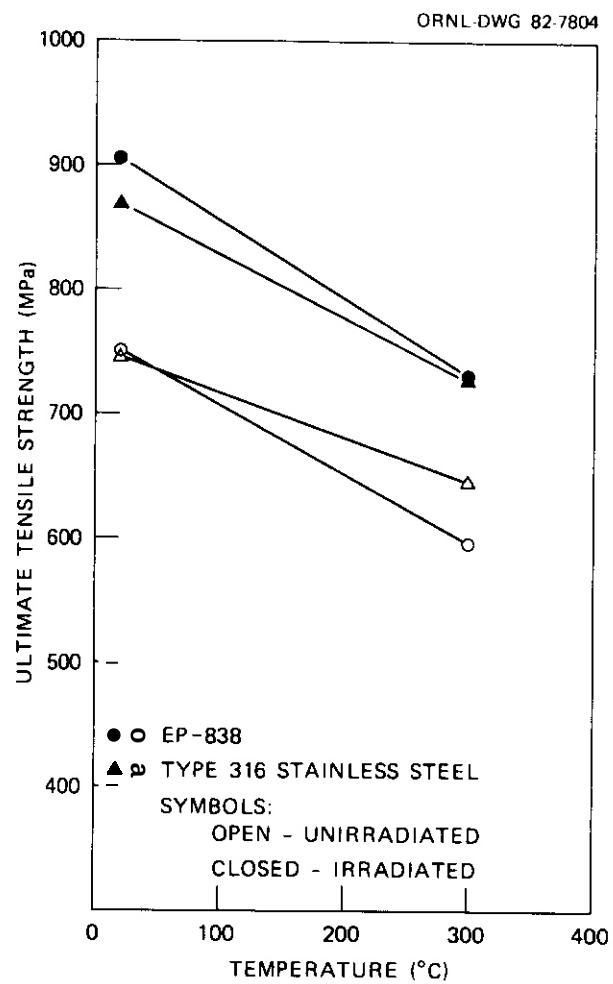

Fig. 3.11.3. The Ultimate Tensile Strength Plotted Against Test Temperature for 20%-Cold-Worked EP-838 and Type 316 Stainless Steels, Unirradiated and After HFIR Irradiation at about 50°C.

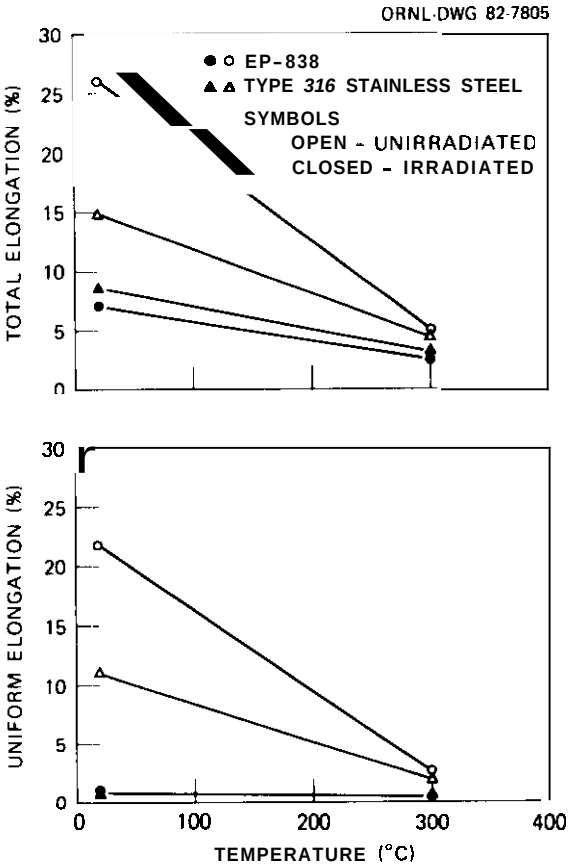

Fig. 3.11.4. The Uniform and Total Elongation Plotted Against Test Temperature for 20%-Cold-Worked EP-838 and Type 316 Stainless Steels Unirradiated and After HFIR Irradiation at about 50°C.

identical to those for the CW 316 specimen irradiated to 9.5 dpa (Table 3.11.2; the values for CW 316 shown in Figs. 3.11.2 through 3.11.4 are for the specimen irradiated to 5.2 dpa). At 300°C, there is essentially no difference in any of the properties for the EP-838 at 5.2 dpa and the CW 316 at 7.8 dpa (Figs. 3.11.2 through 3.11.4).

The large increase in strength and decrease in uniform and total elongation that result from irradiation of EP-838 are easily seen when the tensile curves are examined (Fig. 3.11.5). Likewise, the similar behavior of EP-838 and type 316 stainless steel at room temperature [Fig. 3.11.6(a)] and 300°C [Fig. 3.11.6(b)] is seen when the tensile curves for these two materials are compared. Except for the larger unirradiated ductility of the EP-838 at room temperature, there is essentially no difference in the two steels.

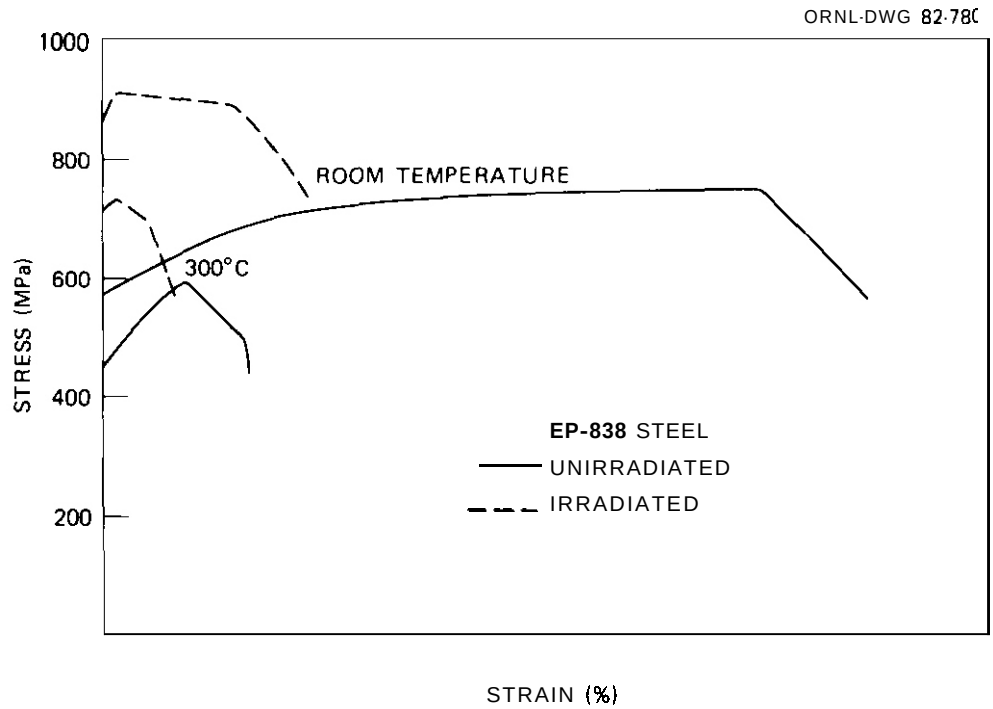

Fig. 3.11.5. Engineering Stress-Strain Curves at Room Temperature and 300°C for Unirradiated and HFIR-Irradiated 20%-Cold-Worked EP-838 Steel.

The low uniform elongation of these steels after irradiation seems to be characteristic of materials irradiated and tested at low temperatures. Similar decreases were noted for ferritic steels irradiated at the HFIR coolant temperature. In Fig. 3.11.7 the unirradiated and irradiated tensile curves for 9 Cr-1 MoVNb steel at room temperature and 300°C are shown, and the similarity in behavior to the austenitic steels is obvious. At room temperature the ferritic steels show a more rapid decrease in stress at strains above the ultimate tensile strength than do the austenitic steels, while the drop appears more rapid for the austenitic steels at 300°C. Stress-strain curves with a low uniform elongation, followed by a rapid decrease in stress beyond the ultimate tensile stress, are indicative of a type of localized deformation that has been termed channel deformation. One difference between the ferritic and austenitic steels is that the uniform elongation for the ferritic steels at 300°C is greater than at room temperature,[4] whereas the uniform elongation for the austenitic steels at 300°C was below that at room temperature.

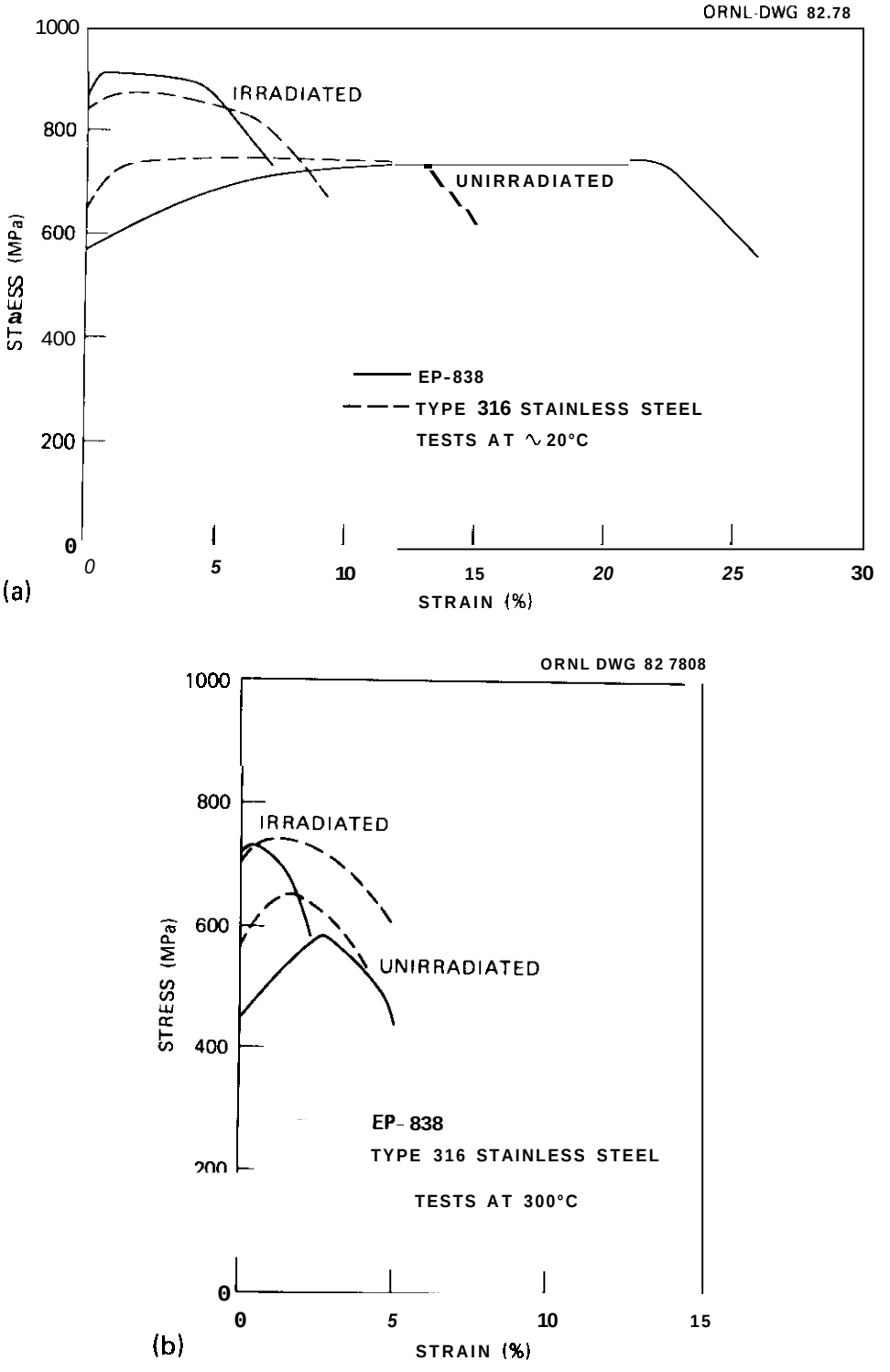

Fig. 3.11.6. Engineering Stress–Strain Curves at (a) Room Temperature and (b) 300°C for Unirradiated and Irradiated 20%–Cold–Worked EP–838 and Type 316 Stainless Steels.

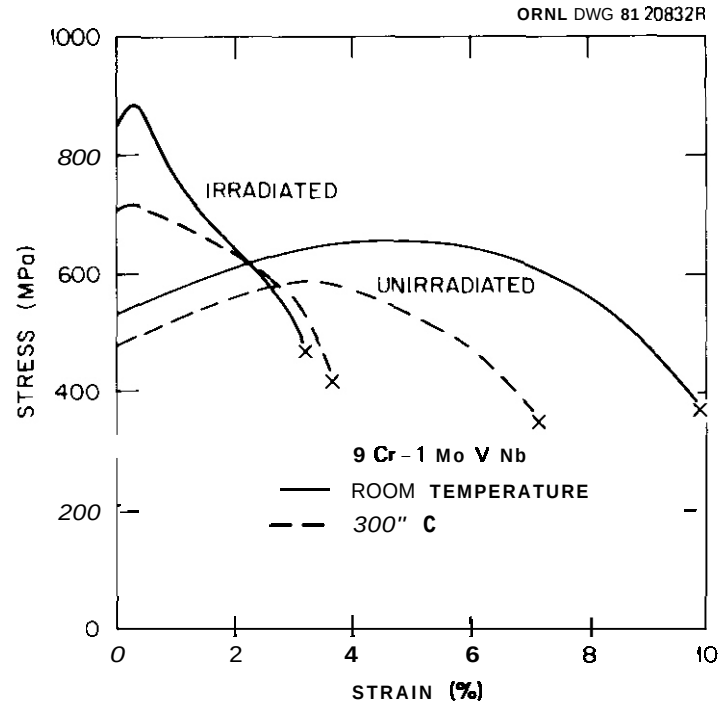

Fig. 3.11.7. Engineering Stress–Strain Curves at Room Temperature and 300°C for Unirradiated and Irradiated 9 Cr-1 MoVNb Steel.

Votinov et al. compared the effect of irradiation on the behavior of EP–838 and type 316 stainless steel in the solution–annealed condition.[5] After irradiation to a fluence of 2.5 x 10^{24} neutrons/m^2 (>0.1 MeV), unirradiated and irradiated specimens were tensile tested over the range 20 to 750°C. The authors concluded, "The nature of the load–elongation curves and similar elongation values, in the original as well as the irradiated states, are evidence of identical deformation and fracture modes before and after irradiation."[5] This statement also summarizes our observations on the comparison of the 20%–cold–worked EP–838 and type 316 stainless steel. It should be kept in mind, however, that these conclusions follow from a very limited set of test conditions.

3.11.5 References

1. M. L. Grossbeck, V. K. Sikka, T. K. Roche, and R. L. Klueh, "Preparation of Nickel–Doped Ferritic Alloys for HFIR Irradiation to Produce Helium," ADIP *Quart. Prog. Rep. Dec. 31,* 1979, DOE/ER-0045/1, pp. 100–04.

2. T. K. Roche, "The Exchange of Austenitic Stainless Steels Under the U.S.-U.S.S.R. Fusion Reactor Materials Agreement," *ADIP Quart. Frog. Rep. June 30, 1980,* DOE/ER-0045/3, pp. 38-41.

3. M. L. Grossbeck and J. W. Woods, "An Irradiation Experiment to Scope the Tensile Properties of Ferritic Alloys — HFIR-CTR-33," ADIP Quart. Prog. Rep. June 30, 1980, DOE/ER-0045/3, pp. 3C—34.

4. R. L. Klueh and J. M. Vitek, "Tensile Properties of Ferritic Steels After Low-Temperature HFIR Irradiation," *ADIP Semiannu. Prog. Rep. Sept. 30, 1981,* DOE/ER-0045/7, pp. 275—83.

5. s. N. Votinov et al., "Effects of Neutron Irradiation on Mechanical Properties of EP-838 and 316 Steels," pp. 50—52 in *Fizika i Khimiya Obrabotki Materialov,* No. 1, 1981; ORNL-tr-4812 (1982).

4. PATH B ALLOY DEVELOPMENT — HIGHER STRENGTH Fe–Ni–Cr ALLOYS

No contributions.

5. PATH C ALLOY DEVELOPMENT — REACTIVE AND REFRACTORY ALLOYS

5.1 MECHANICAL PROPERTY EVALUATIONS OF PATH C VANADIUM SCOPING ALLOYS - R. E. Gold (Westinghouse Electric Corporation)

5.1.1 ADIP Tasks

I.B.11. Stress-Rupture Properties of Reactive/Refractory Metal Alloys (Path C)

I.B.15 Tensile Properties of Reactive/Refractory Metal Alloys (Path C)

5.1.2 Objective

The objective of this program is to examine the effects of controlled levels of nonmetallic (oxygen) contamination on the tensile and stress-rupture properties of the unirradiated Path C vanadium-base Scoping Alloys [V-20Ti, V-15Cr-5Ti, VANSTAR-71.

5.1.3 Summary

Nominal oxygen impurity levels of 600 and 1200 wppm, above the residual content of the alloys, have been introduced by gas-metal reaction into 0.76 mm sheet specimens of vanadium-base alloys. Tensile tests have been performed on each alloy at RT, 500, and 700°C and the results compared to previous tests on noncontaminated specimens. The oxygen contamination affected both strength and fracture behavior; these effects varied for the three alloys.

5.1.4 Progress and Status

The Path C vanadium-base Scoping Alloys which were prepared for the ETM Research Materials Inventory, sited at the Oak Ridge National Laboratory, are the subject of this evaluation. These include: (compositions in weight percent)

V-20Ti

V-15Cr-5Ti

VANSTAR-7 (V-9Cr-3.3Fe-1.2Zr-0.054C)

Efforts during the preceding fiscal year (PI 81) focused on establishing the tensile and stress-rupture behavior for the unirradiated alloys. In addition, because nonmetallic impurities are known to have significant effects on the mechanical behavior of refractory metal alloys, a procedure was developed for introducing controlled levels of oxygen into mechanical property specimens. The results of these efforts were reported previously.[1-2] Evaluations for the current fiscal year are focused on determination of the tensile and stress-rupture properties of intentionally contaminated specimens.

Specific tasks associated with the FY 82 efforts are:

Task 1. Material Procurement
Task 2. Initial Specimen Preparation and Heat Treatments
Task 3. Contamination Exposures for Mechanical Test Specimens
Task 4. Tensile Evaluations
Task 5. Creep/Stress-Rupture Testing
Task 6. Chemical and Microstructural Characterizations

Tasks 1 through 4 have been completed. Task 5 has been started and the Task 6 fractography has been performed on the tensile specimens. These efforts are summarized in the following subsections.

5.1.4.1 Material Identification and Condition (Tasks 1 and 2)

The analyzed chemical compositions for the three Path C vanadium Scoping Alloys are presented in Table 5.1.1.[3] Prior to initiating any of the experimental work, all alloys were given a one hour heat treatment at temperatures determined previously to produce a fully recrystallized, equiaxed (grain size ∿30 μm) microstructure. These temperatures are 1100, 1200, and 1350°C for the V-20Ti, V-15Cr-5Ti, and VANSTAR-7 alloys, respectively.

Table 5.1.1
Chemical Analysis of Path C Vanadium Alloy Sheet

	ELEMENTAL ANALYSIS (w/o)						
ALLOY	Ti	Cr	Fe	Zr	C	O	N
V-20Ti	19.7				0.029	0.045	0.056
V-15Cr-5Ti	15.3	5.0			0.017	0.023	0.052
VANSTAR-7		9.7	3.4	1.3	0.064	0.028	0.052

An identical specimen design was utilized for both tensile and creep-rupture testing for this program. A sketch of this pin-loaded specimen was shown in a previous report.[1]

5.1.4.2 Contamination Exposures for Mechanical Test Specimens (Task 3)

An ultrahigh vacuum microbalance system was used to introduce controlled levels of non-metallic impurities into vanadium alloy specimens. This system, depicted schematically in a previous report,[2] is constructed of stainless steel and quartz with copper gasket seals; it is completely bakeable with the exception of the microbalance. The UHV microbalance system was assembled previously for studies of gas-metal reactions between the refractory metals and their alloys and reactive gases such as oxygen and nitrogen. During the FY 81 research period, the system was reassembled and used to perform preliminary "demonstration-of-capability"experiments on the vanadium-base alloys of interest to the present program.

Following the same procedures used for the FY 81 experiments,' a total of eighteen (18) contamination runs were carried out; six specimens of each of the three Scoping Alloys were exposed. In order to minimize the total number of contamination exposures, the 0.76 mm thick sheet specimens were approximately 25 mm wide x 150 mm long. Each of these blanks was large enough to provide two mechanical test specimens. The test specimens machined from the top half of each blank were designated by the suffix-A,

whereas the suffix-B was used for the specimens from the lower half. All tensile specimens were prepared from -A specimens while creep specimens were machined from the -B halves. A reaction temperature of 700°C was used for all exposures.

The results of the oxygen exposures are summarized in Table 5.1.2. Only nominal (calculated) oxygen gains are indicated since post-exposure chemical analyses have not been completed. These analyses will be useful in interpreting the mechanical property test results. Hardness measurements (Vickers, DPH, 10 kg load) were made on all test specimens in order to roughly monitor the uniformity of reaction. While some variation is expected to occur over the approximate 150 mm length of the exposure blanks no systematic variations could be detected from the hardness data.

5.1.4.3 Tensile Evaluations (Task 4) and Fractographic Examinations (Task 6)

Tensile tests were conducted on sheet specimens of each of the three vanadium alloys at room temperature, 500, and 700°C. For each alloy, at each test temperature, specimens which contained nominal oxygen levels of 600 wppm and 1200 wppm above that of the starting material were evaluated. A constant strain rate of 3.3 x $10^{-4}s^{-1}$ was used throughout all tests; testing at 500 and 700°C was performed in a vacuum environment, maintained below about 1 x 10^{-5}torr throughout the tests. The results of these tests, and associated fractography, are presented below for each of the three alloys.

V-20Ti. The results of the tensile tests are presented in Table 5.1.3. Included are results at the same test temperatures for noncontaminated specimens (from FY 81 test results, Reference 1). The major effect of the additional oxygen on the strength of this alloy was seen at 500°C and, for the 1200 wppm specimen, at room temperature. Effects on the strength at 700°C were insignificant. The increase at 500°C is at least partially due to dynamic strain aging;

Table 5.1.2 Results of 700°C Oxygen Exposures with Vanadium-Base Scoping Alloys

Alloy	Specimen Ident. No.	Mass Initial(g)	Mass Gain(mg)	Oxygen Pickup (wppm) Target	Oxygen Pickup (wppm) Measured[a]
V-20Ti	VT-82-1A,B	16.8161	10.10	600	601
	-2A,B	16.4905	19.90	1200	1207
	-3A,B	16.7047	10.10	600	605
	-4A,B	16.4.473	19.76	1200	1201
	-5A,B	16.9742	10.14	600	597
	-6A,B	17.0373	20.28	1200	1190
V-15Cr-5Ti	VCT-82-1A,B	18.7478	11.15	600	595
	-2A,B	18.7125	22.56	1200	1206
	-3A,B	18.5927	11.24	600	604
	-4A,B	18.6091	22.40	1200	1204
	-5A,B	16.0210	9.62	600	600
	-6A,B	18.7432	22.00	1200	1174
VANSTAR-7	VS-82-1A,B	19.1518	12.00	600	626
	-2A,B	18.5703	22.32	1200	1202
	-3A,B	18.9948	11.40	600	600
	-4A,B	19.2227	23.20	1200	1207
	-5A,B	19.2191	11.48	600	597
	-6A,B	18.5763	22.80	1200	1227

(a) From microbalance recordings during exposures.

Table 5.1.3 Tensile Test Results for the V-20Ti Alloy.

Specimen Ident. No.	Test Temp. (°C)	Nominal[a] O_2 Content (wppm)	0.2% Y.S. (MPa)	UTS (MPa)	Elongation (%) Unif.	Total
VT-1,2	RT	0	577	675	19.0	22.4
-82-1A	RT	600	572	672	14.8	18.9
-82-2A	RT	1200	625	742	12.9	17.5
VT-3,4	500	0	356	575	14.6	17.7
-82-3A	500	600	443	677	10.8	13.2
-82-4A	500	1200	443	679	12.9	14.4
VT-11,12	700	0	373	505	10.4	18.0
-82-5A	700	600	405	527	10.1	22.6
-82-6A	700	1200	397	519	9.6	21.4

(a) Additional oxygen content; i.e. above the initial concentration of 450 wppm.
All values for noncontaminated specimens are the average of two tests [Ref. 1].
All tests at a strain rate of $3.3 \times 10^{-4} s^{-1}$ throughout.

serrated yield was observed on the stress-strain curves of these specimens.

Fracture of the noncontaminated material had been by ductile shear at all of these temperatures. However, despite reasonably high values of both uniform and total strain, the specimens which had been oxygen-exposed demonstrated a mixed failure mode consisting of a small amount of cleavage and intergranular separation; ductile shear was still the dominant mechanism, Figure 5.1.1. The fracture surfaces of the 500°C and 700°C specimens exhibited only dimpled, ductile rupture, Figures 5.1.2 and 5.1.3.

V-15Cr-5Ti. The tensile test data are presented in Table 5.1.4; data for noncontaminated specimens are also provided for comparison. At room temperature the yield strength was increased with little change in the ultimate tensile strength and a dramatic decrease was observed in the tensile elongation of the oxygen-contaminated specimens. Moreover, these specimens failed at the maximum load point on the stress-strain curve so that uniform and total elongation values were identical. The uniform strain value is meaningless in any event since inspection of the gage length of these specimens indicated very heavy transverse cracking had occurred; very little "uniform" strain is apparent, either along the gage section or at the fracture, Figure 5.1.4. The fracture surface of the room temperature specimens displayed only transgranular cleavage and intergranular fracture with cleavage being the dominant process, Figure 5.1.5.

At 500°C, both the yield and ultimate tensile strengths were increased by the higher oxygen levels, the effects being slightly greater for the 1200 wppm specimen. The fracture mode appeared to vary across the width of the specimen. In general, it was by ductile shear near the center, with increasing evidence of intergranular and cleavage fracture near the surfaces, Figure 5.1.6. At 700°C, minor strengthening was observed with a corresponding decrease in tensile ductility. The

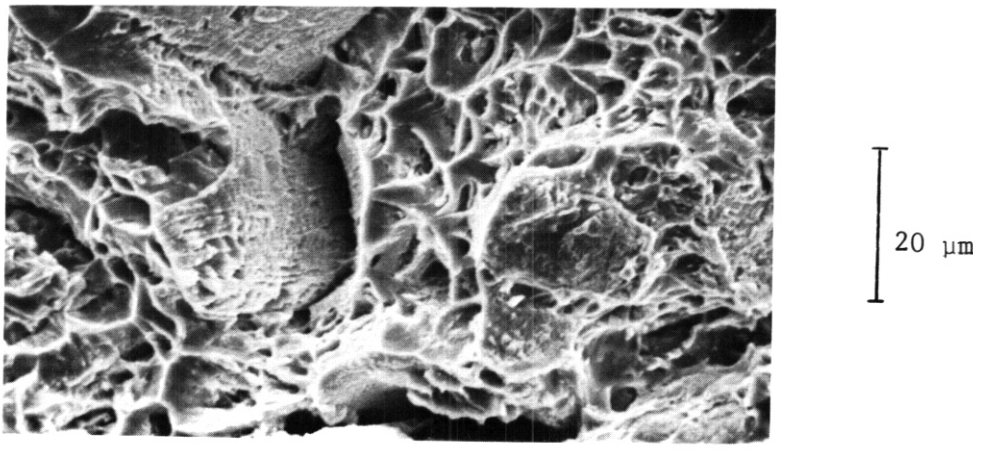

Figure 5.1.1 V-20Ti Tensile Tested at Room Temperature [Nominal Additional Oxygen Content - 1200 wppm]

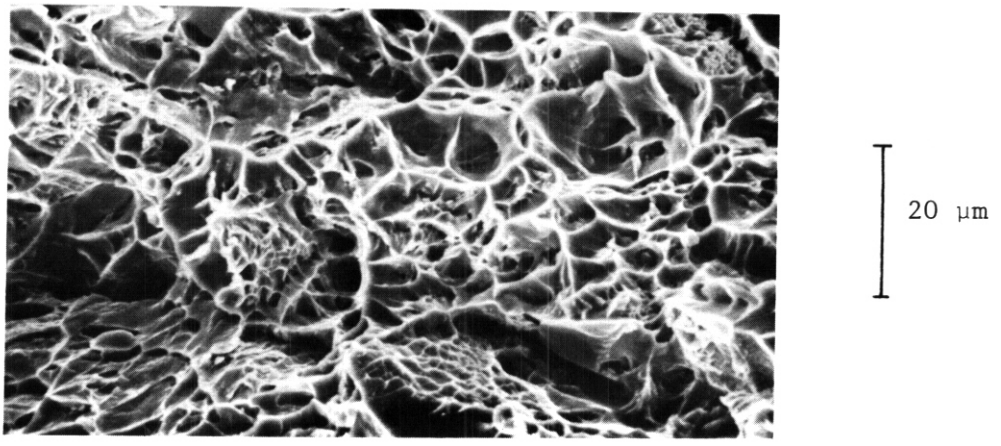

Figure 5.1.2 V-20Ti Tensile Tested at 500°C [Nominal Additional Oxygen Content - 600 wppm]

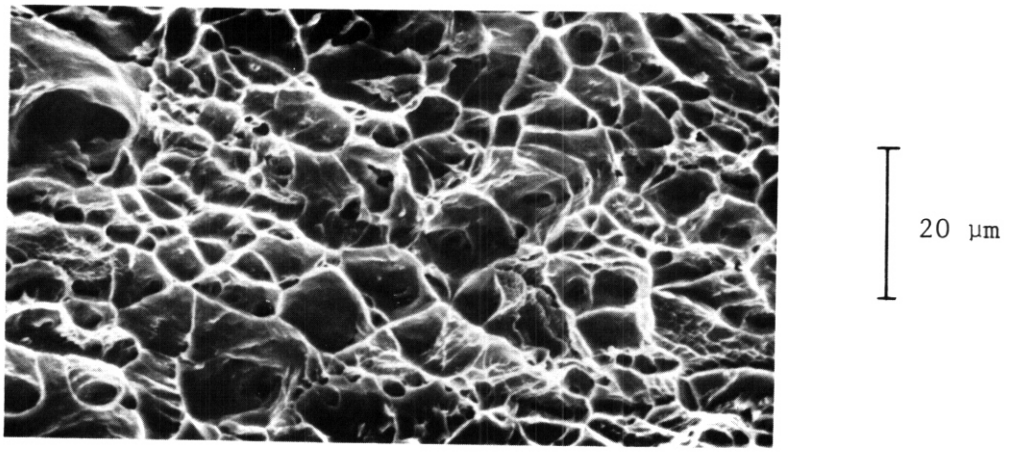

Figure 5.1.3 V-20Ti Tensile Tested at 700°C [Nominal Additional Oxygen Content - 600 wppm]

Table 5.1.4 Tensile Test Results for the V-15Cr-5Ti Alloy.

Specimen Ident. No.	Test Temp. (°C)	Nominal[a] O_2 Content (wppm)	0.2% Y.S. (MPa)	UTS (MPa)	Elongation (%) Unif.	Total
VCT-1,2	RT	0	489	687	22.9	27.8
-82-1A	RT	600	557	678	11.2	11.2
-82-2A	RT	1200	565	686	11.9	11.9
VCT-3,4	500	0	318	532	14.0	17.1
-82-3A	500	600	367	604	11.6	14.2
-82-4A	500	1200	396	643	9.2	10.9
VCT-11,12	700	0	308	586	15.8	19.1
-82-5A	700	600	(b)	(b)	(b)	(b)
-82-6A	700	1200	345	641	13.0	14.0

(a) Additional oxygen content; i.e. above the initial concentration of 230 wppm.

(b) Testing machine and furnace malfunctioned; no data.

All values for noncontaminated specimens are the average of two tests [Ref. 1].

All tests at a strain rate of $3.3 \times 10^{-4} s^{-1}$ throughout.

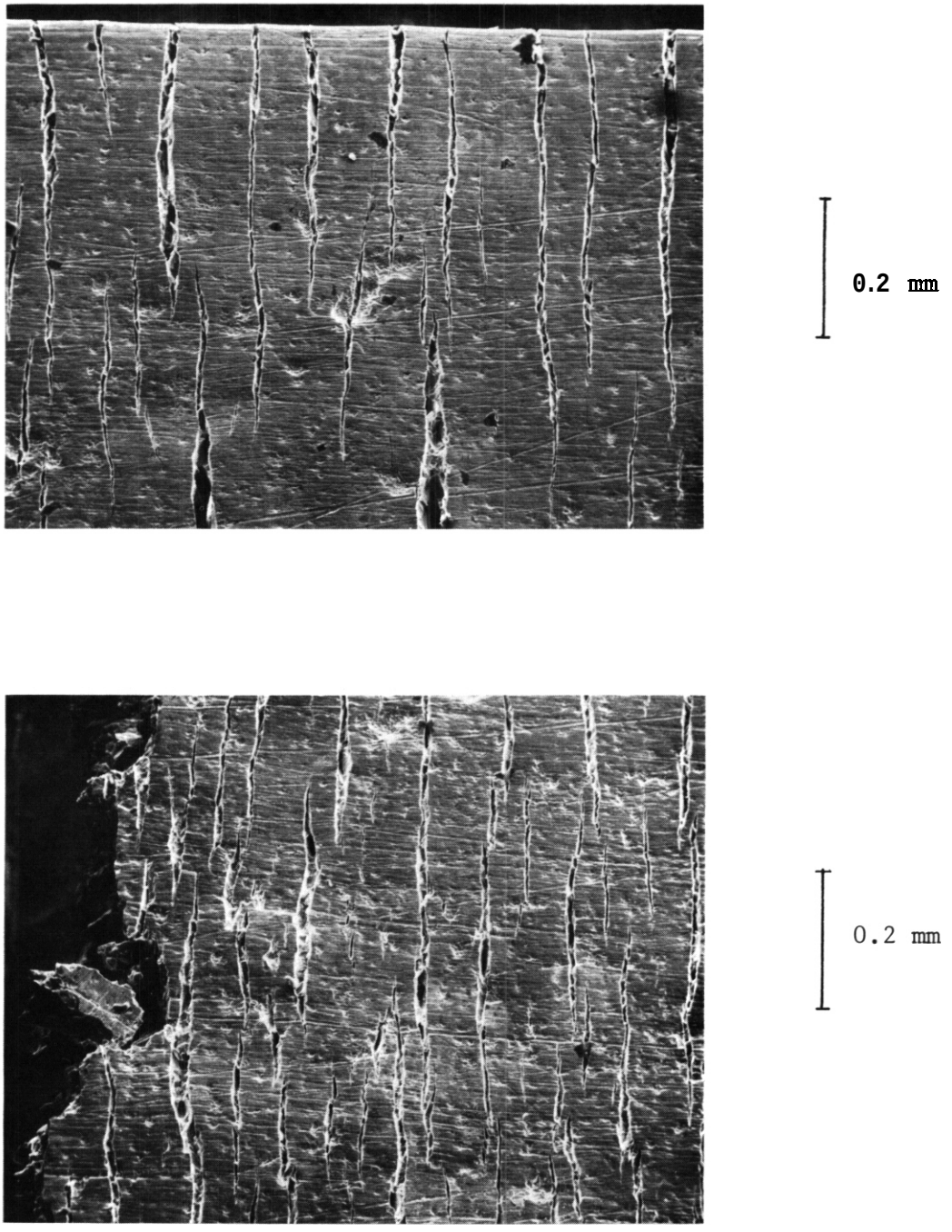

Figure 5.1.4 V-15Cr-5Ti Tensile Tested at Room Temperature [Nominal Additional Oxygen Content - 1200 wppm]

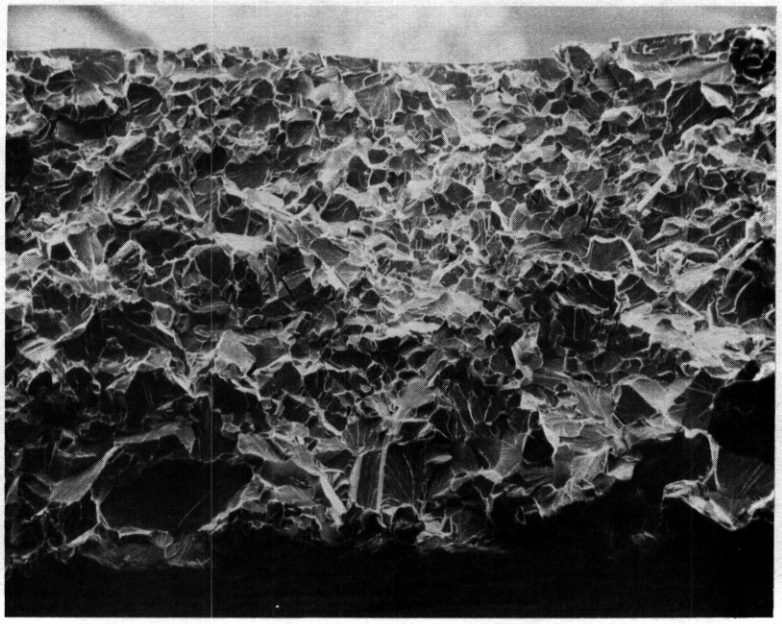

0.2 mm

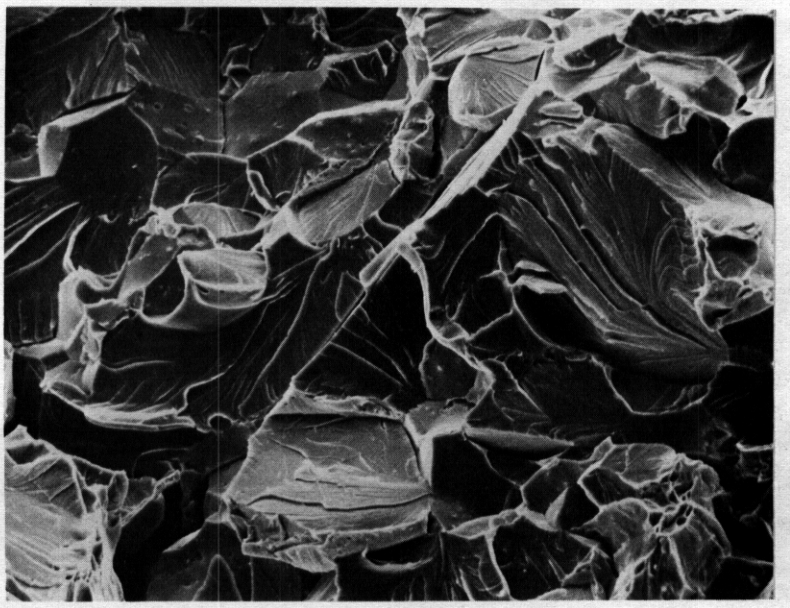

40 μm

Figure 5.1.5 V-15Cr-5Ti Tensile Tested at Room Temperature
[Nominal Additional Oxygen Content - 1200 wppm]

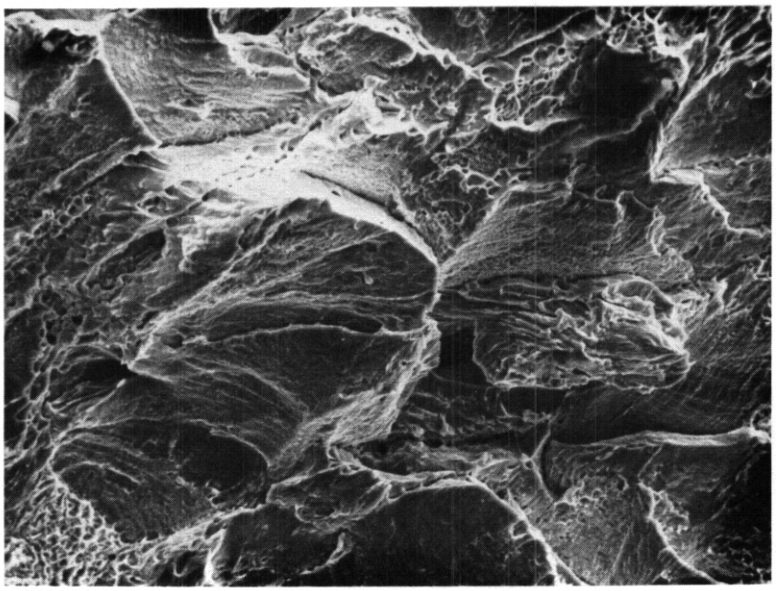

40 μm

Near Surface

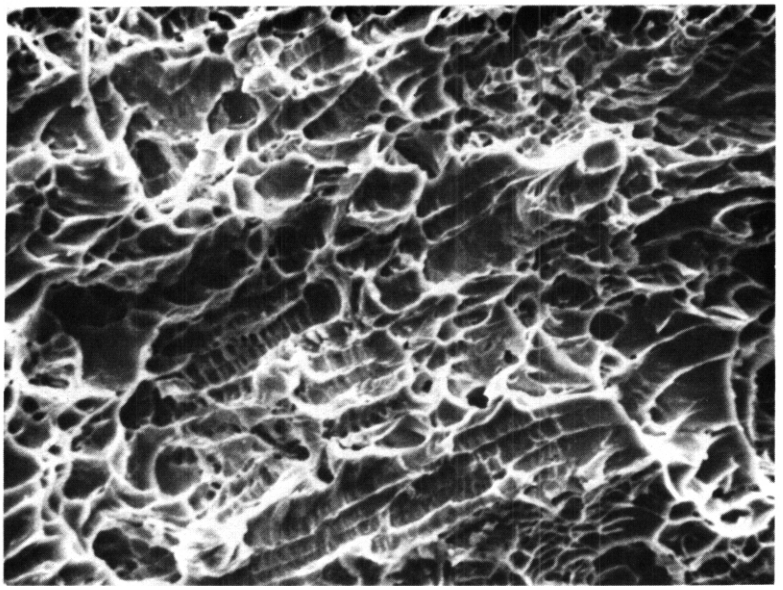

20 μm

Figure 5.1.6 V-15Cr-5Ti Tensile Tested at 500°C [Nominal Additional Oxygen Content – 1200 wppm]

fracture surface was typical of ductile rupture, except very near the surface where some intergranular separation was obvious. Typical fracture morphologies are shown in Figure 5.1.7; note the precipitates associated with the near-surface region.

VANSTAR-7. The tensile test results for the VANSTAR-7 alloy are presented in Table 5.1.5; again, data for noncontaminated specimens are also tabulated. All tensile tests conducted previously on noncontaminated VANSTAR-7 specimens throughout the temperature range from room temperature to 750°C had resulted in ductile fracture. For the current series of tests on oxygen-contaminated specimens this was not the case; cleavage became a prominent feature on the fracture surfaces, particularly for the room temperature tests. From Table 5.1.5 it is apparent that changes in tensile strength were not regular or extreme. The most significant effects are the decreases in tensile elongation noted for the room temperature and 500°C tests.

During room temperature testing a series of transverse striations could be seen to develop along the gage section. When a new striation intersected the surface an audible "click" could be heard. Post-test examination with scanning electron microscopy revealed these striae to be small, uniformly spaced cracks which extended about 75 to 150 μm into the surface of the specimen. At that depth the crack would be arrested by the tough interior and slip would occur at an angle of approximately 45° until the back surface was approached and a surface crack would again result. The process continued in this fashion along the entire gage length until fracture occurred along one of the heavily deformed slip bands. Scanning electron micrographs of these specimens are shown in Figures 5.1.8 and 5.1.9. The only noticeable difference between the specimens containing nominally 600 and 1200 wppm oxygen was the uniformity of crack spacing; hence micrographs of each are used to illustrate general features.

Examination of the fracture surfaces of the room temperature-tested

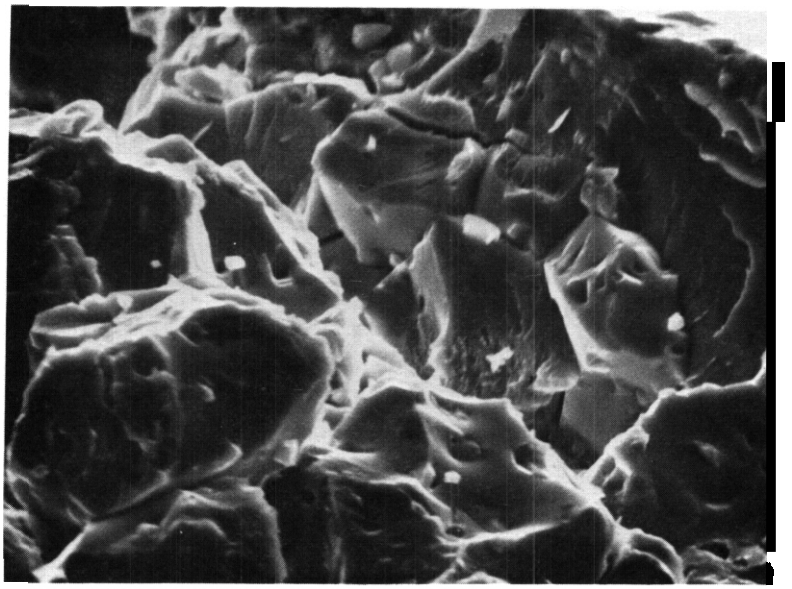

10 μm

Near Surface

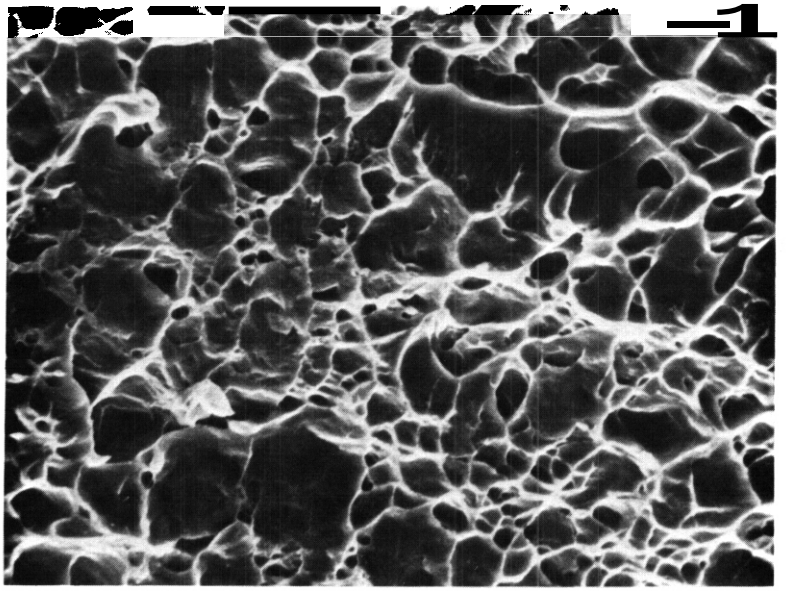

10 μm

Figure 5.1.7 V-15Cr-5Ti Tensile Tested at 700°C [Nominal Additional Oxygen Content - 1200 wppm]

Table 5.1.5 Tensile Test Results for the VANSTAR-7 Alloy

Specimen Ident. No.	Test Temp. (°C)	Nominal[a] O_2 Content (wppm)	0.2% Y.S. (MPa)	UTS (MPa)	Elongation (%) Unif.	Elongation (%) Total
VS-1,2	RT	0	423	578	20.0	24.3
-82-1A	RT	600	435	530	12.0	13.2
-82-2A	RT	1200	474	513	7.9	9.2
VS-3,4	500	0	248	427	16.5	18.5
-82-3A	500	600	283	472	10.8	12.9
-82-4A	500	1200	286	407	3.7	4.8
VS-11,30	700	0	234	416	13.4	16.9
-82-5A	700	600	266	411	15.7	25.0
-82-6A	700	1200	271	399	12.4	23.9

(a) Additional oxygen content; i.e. above the initial concentration of 280 wppm.

All values for noncontaminated specimens are the average of two tests [Ref. 1].

All tests at a strain rate of $3.3 \times 10^{-4} s^{-1}$ throughout.

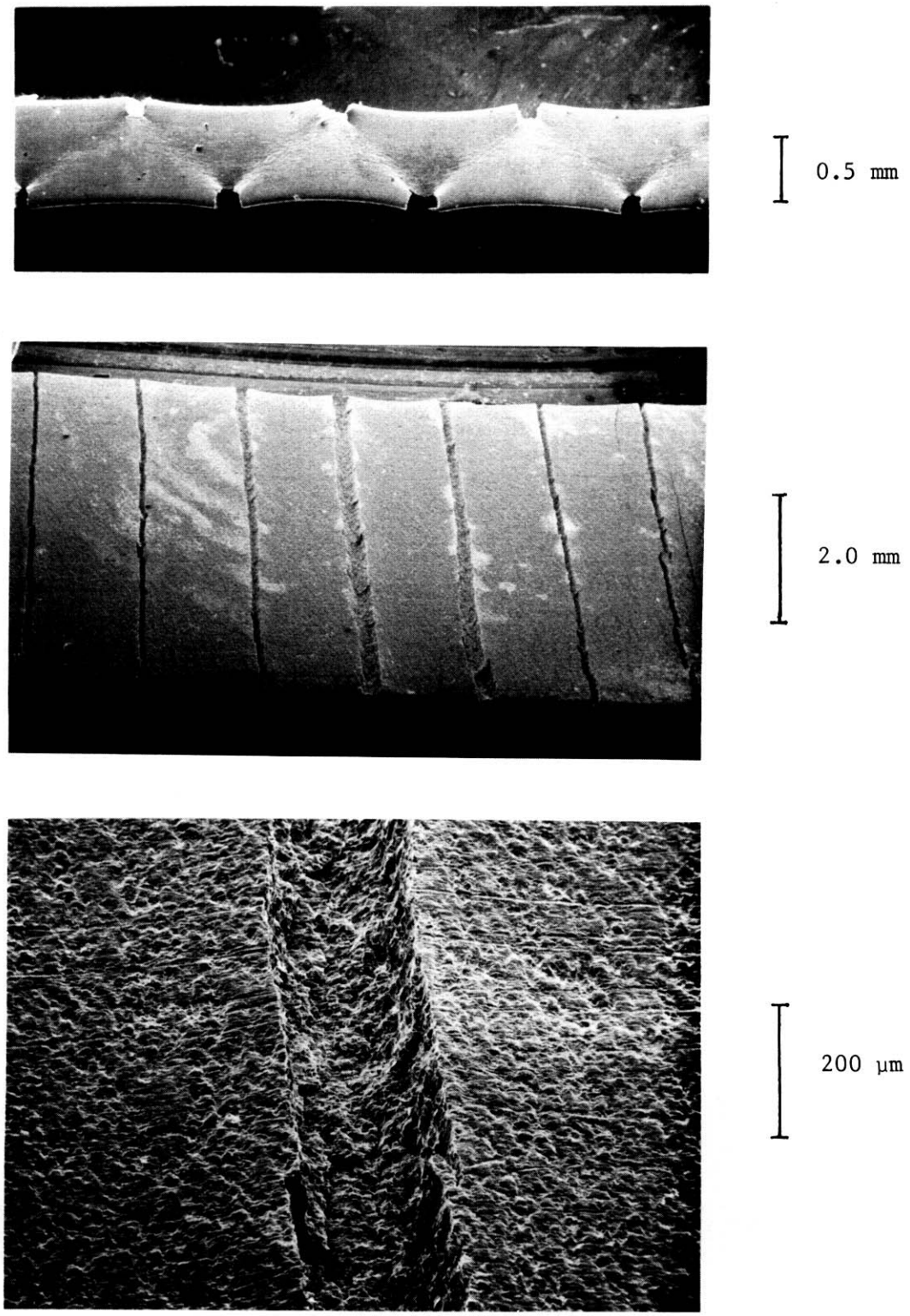

Figure 5.1.8 VANSTAR-7 Tensile Tested at Room Temperature
[Nominal Additional Oxygen Content - 1200 wppm]

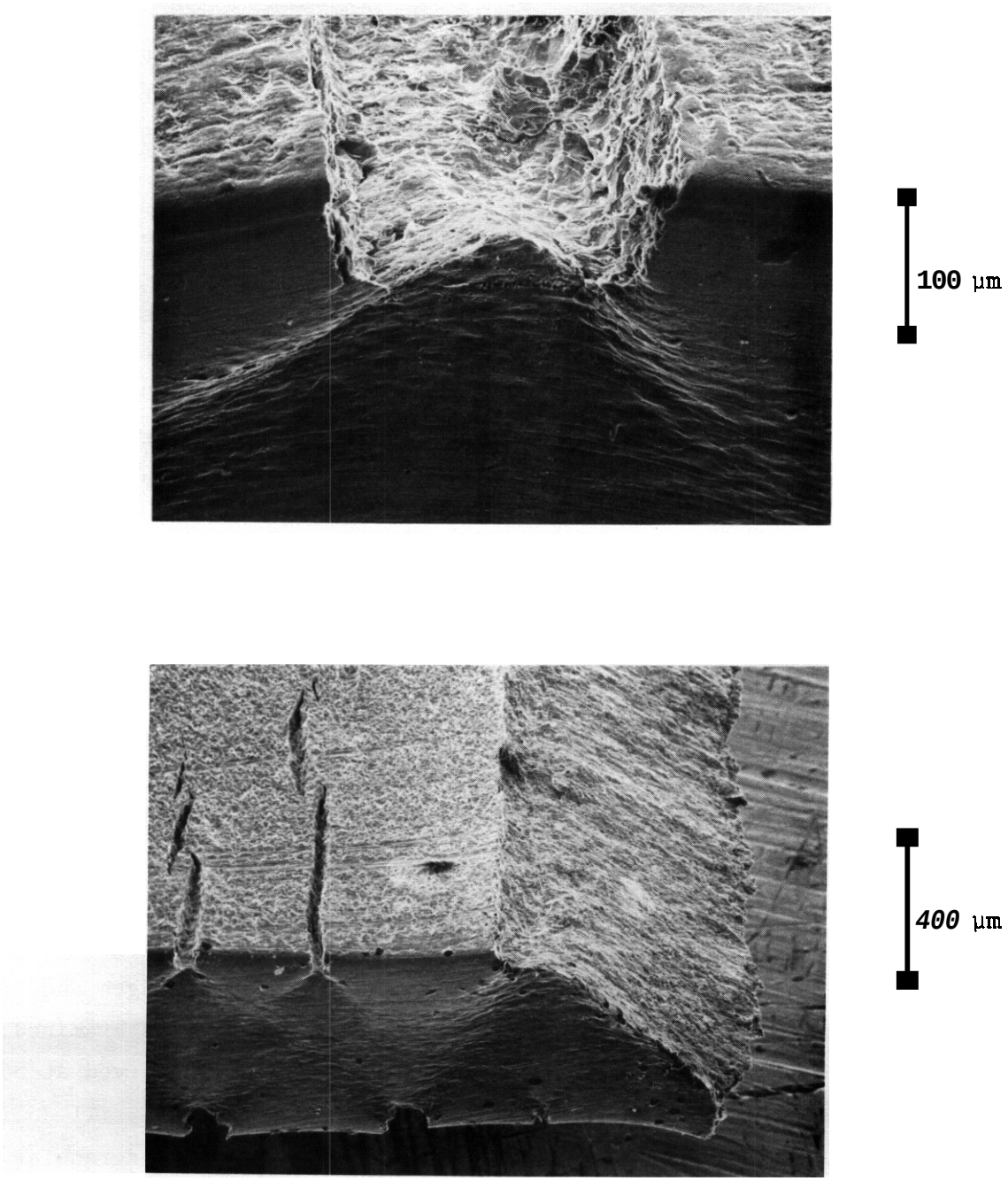

Figure 5.1.9 VANSTAR-7 Tensile Tested at Room Temperature [Nominal Additional Oxygen Content - 1200 wppm (top), 600 wppm (bottom)]

specimens revealed two distinctly different zones. At the top and bottom surfaces, cleavage dominated the fracture while the "tough" inner zone was characterized completely by ductile, dimpled rupture, Figures 5.1.10 and 5.1.11.

Testing at 500°C produced results which were similar to those obtained at room temperature. Surface cracking along the gage section was much less uniform, however, and intergranular fracture became more common in the embrittled surface regions, Figure 5.1.12. At 700°C there was no evidence of any effect of the oxygen on either the strength or the fracture mode. The entire surface exhibited only dimpled rupture.

5.1.4.4 Creep/Stress-Rupture Testing (Task 5)

A series of stress-rupture tests have been initiated to examine the effects of oxygen contamination on the time-dependent deformation of the vanadium alloys. These tests will be performed in ultra-high vacuum creep test stands and will be run using temperatures and stresses similar to those previously used (Reference 2) for noncontaminated specimens.

5.1.5 Discussion of Results

The effects of oxygen contamination on the tensile strength and fracture characteristics vary for the three vanadium-base alloys examined. For the V-20Ti alloy the only major strength change was observed at 500°C, where dynamic strain aging occurred. Although fracture was still dominantly by ductile shear, a small amount of cleavage and intergranular fracture occurred at room temperature. Fracture at 500 and 700°C remained as it had been for noncontaminated specimens - by transgranular shear.

The V-15Cr-5Ti alloy responded to the oxygen increases with modest increases in the tensile strength but with noticeable changes in the fracture mode. At room temperature the gage section displayed extensive transverse cracking and the fracture was completely due to cleavage and

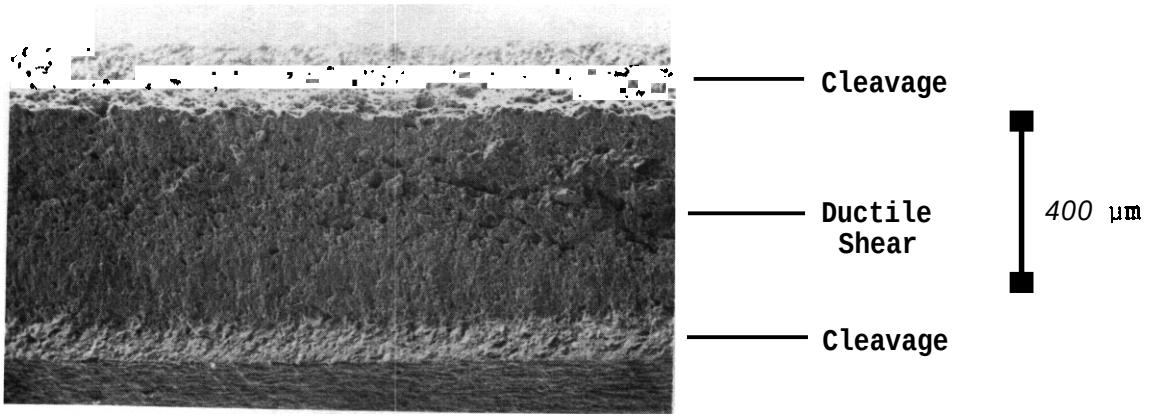

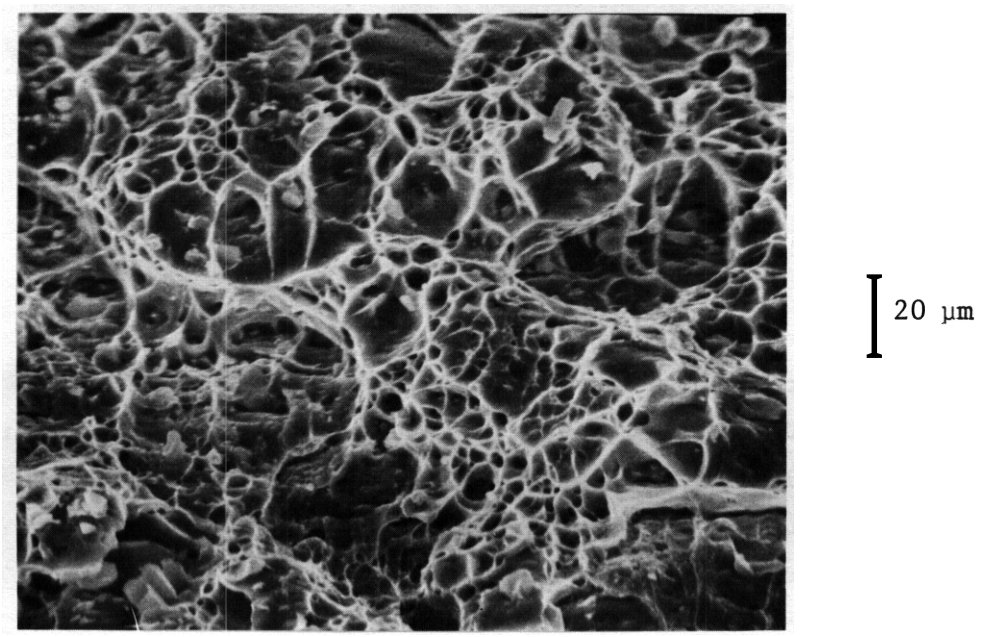

Figure 5.1.10 VANSTAR-7 Tensile Tested at Room Temperature
[Nominal Additional Oxygen Content - 1200 wppm]

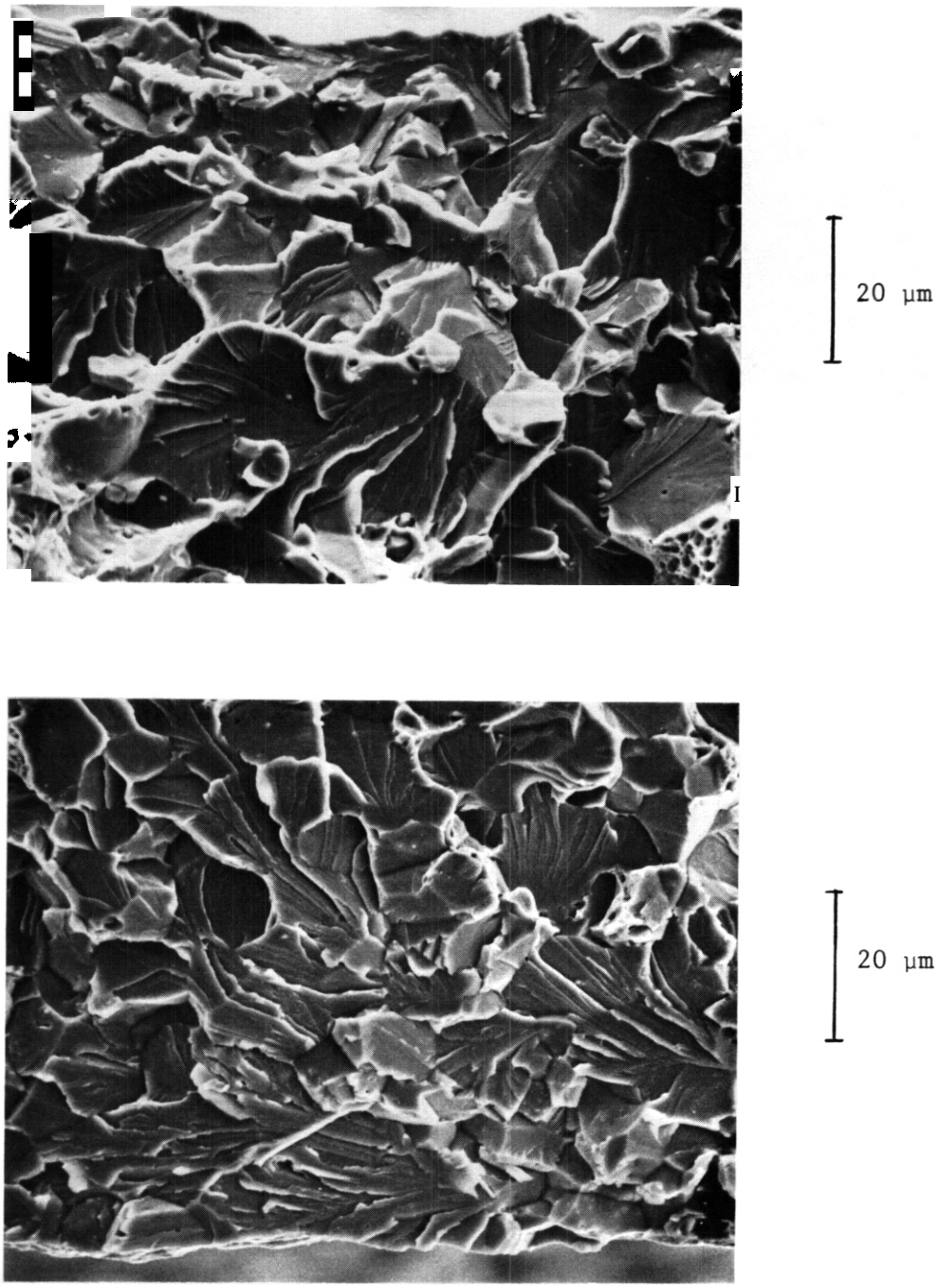

Figure 5.1.11 VANSTAR-7 Tensile Tested at Room Temperature [Nominal Additional Oxygen Content - 600 wppm]; Near-Surface Regions of Fracture

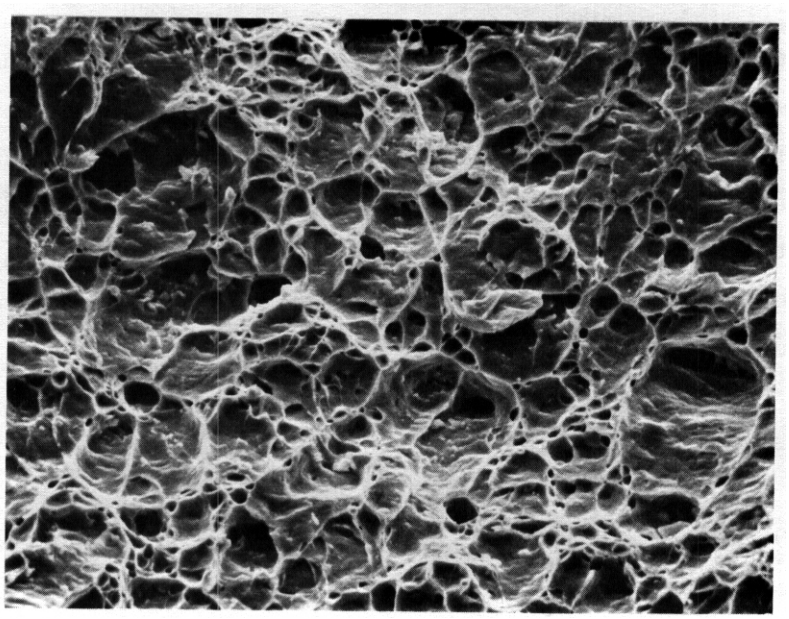

20 μm

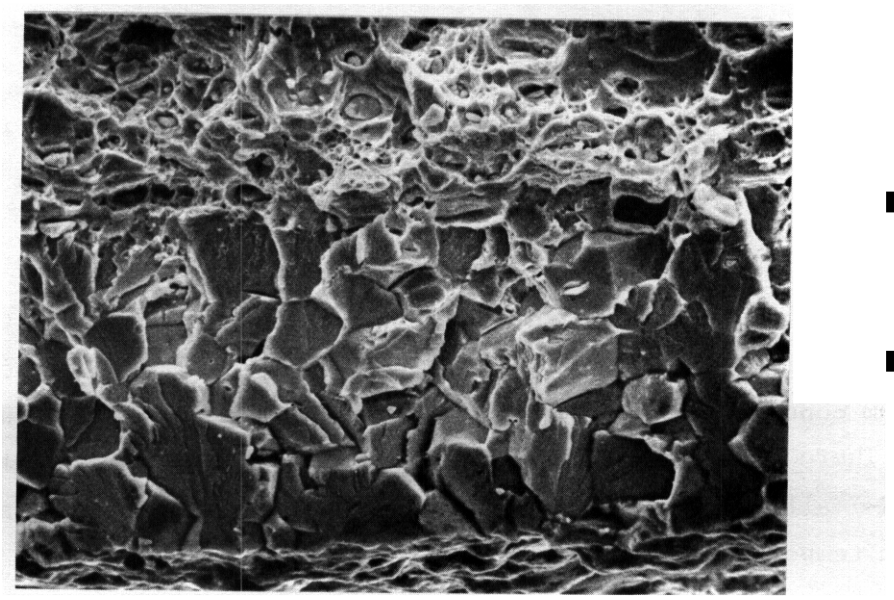

20 μm

Figure 5.1.12 VANSTAR-7 Tensile Tested at 500°C [Nominal Additional Oxygen Content - 1200 wppm]

intergranular separation. At 500 and 700°C the fracture behavior was characterized by mainly ductile shear except very near the surfaces where some intergranular separation occurred. This difference seems to reflect the fact that, while the surface layers are embrittled by the oxygen at all temperatures examined, at the higher temperatures the core region is tough enough to blunt the brittle cracking and permit shear deformation to become the dominant process.

For VANSTAR-7 the brittle nature of the surface was amply demonstrated by the ∿100 μm deep cleavage cracking which was observed for room temperature and 500°C tests. The inner volume of these specimens was tough enough to completely arrest these cracks and permit the specimen to deform such that the final fracture was dominated by transgranular shear. At 700°C, only ductile shear-type fracture was observed.

For virtually all specimens, the differences between specimens containing nominally 600 wppm and 1200 wppm oxygen were subtle. Any attempt, however, to interpret any differences must clearly await the results of oxygen analysis to establish the actual, rather than nominal, oxygen contents.

Based on these limited results, the V-20Ti alloy appears to be the least sensitive to oxygen contamination. This may reflect the greater titanium content which may influence the homogeneity of oxygen distribution. There seems to be little to choose from between the V-15Cr-5Ti and VANSTAR-7 alloys although the latter alloy exhibited better "toughness" at room temperature.

5.1.6 References

1. R. E. Gold and R. L. Ammon, "Mechanical Property Evaluations of Path C Vanadium Scoping Alloys," Alloy Development for Irradiation Performance, Qtrly. Progress Report for Period Ending March 31, 1981, DOE/ER-0045/6, p. 96 (July 1981).

2. R. E. Gold, "Mechanical Property Evaluations of Path C Vanadium Scoping Alloys,'' Alloy Development for Irradiation Performance, Semiannual Progress Report for Period Ending September 30, 1981, DOE/ER-0045/7, p. 122 (March 1982).

3. R. L. Ammon, "Melting and Processing of Niobium and Vanadium Alloy Sheet and Rod," Report AESD-M-FR-79-004, Westinghouse Advanced *Energy* Systems Division, Pittsburgh, PA (October 1979).

5.2 SWELLING IN NEUTRON IRRADIATED TITANIUM ALLOYS - D. T. Peterson (Westinghouse Hanford Company)

5.2.1 ADIP Task

Task Number I.C.4 – Microstructures and Swelling in Reactive/Refractory Alloys (Path C).

5.2.2 Objective

The objective of this work is to characterize the swelling and microstructural response of titanium alloys during neutron irradiation.

5.2.3 Summary

Immersion density measurements have been performed on a series of titanium alloys irradiated in EBR-I1 to a fluence of 5 x 10^{22} n/cm^2 (E >0.1 MeV) at 450 and 550°C. The materials irradiated were the near-alpha alloys Ti-6242s and Ti-5621S, the alpha-beta alloy Ti-64 and the beta alloy Ti-38644. Swelling was observed in all alloys with generally the greater swelling being observed at 550°C. Preliminary microstructural examinations revealed the presence of voids in all alloys. Ti-38644 was found to be the most radiation resistant. Ti-6242s and Ti-5621s also displayed good radiation resistance, whereas considerable swelling was observed in Ti-64 at 550°C.

5.2.4 Progress and Status

5.2.4.1 Introduction

Titanium alloys have been proposed for fusion reactor structural material applications below 500°C. Titanium alloys are attractive candidates because of their high strength-to-weight ratio, good crack growth properties and thermal properties which lead to low thermal stresses.[1] Unfortunately, very little is known about the effects of irradiation on the microstructure and mechanical properties of titanium alloys.

The first titanium alloy scoping study by the ADIP program examined the creep properties of four alloys.' The alloys studied were Ti-6242s Ti-5621S, Ti-15333 and Ti-64. The specimens were irradiated in EBR-II

at 450°C to a fluence of 4 x 10^{22} n/cm^2 (E >0.1 MeV). Ti-6242s and Ti-5621s were found to be the most creep resistant with creep rates comparable to cold worked AISI 316.

A more comprehensive EBR-II experiment was subsequently designed to study the effects of higher fluence irradiation on the properties of titanium alloys. The alloys irradiated were the near-alpha alloys Ti-6242s and Ti-56215, the alpha-beta alloy Ti-64 and the beta alloy Ti-38644. The experiment included tensile, fatigue, crack growth, pressurized tube and swelling disk specimens. The specimens were irradiated at 395, 450 and 550°C to fluences up to 5 x 10^{22} n/cm^2 (E >0.1 MeV).[3] The present study reports the swelling and microstructural behavior of these alloys at 450 and 550°C.

5.2.4.2 Experimental Procedure

Disk specimens for swelling and microstructural examinations were fabricated from 0.30 mm thick sheet stock provided by the McDonnell Douglas Astronautics Company. The compositions of the materials are listed in Table 5.2.1. Their heat treatments are listed in Table 5.2.2.

The specimens were irradiated in three isothermal capsules in Rows 2 and 4 of EBR-II. The 395°C capsule attained a fluence of 4.2 x 10^{22} n/cm^2 (E >0.1 MeV) while the 450 and 550°C capsules attained a fluence of 5.0 x 10^{22} n/cm^2 (E >0.1 MeV). More details of the irradiation are given in Reference 3.

Prior to immersion density measurements the specimens were chemically polished at 0°C in a solution of 65 percent nitric acid, 18 percent hydrofluoric acid and 17 percent water. The density of the specimens were determined by hydrostatic weighing in air and an immersion liquid. The swelling was determined by comparing the densities of unirradiated control specimens with the irradiated specimens. The accuracy of the swelling determination is ±0.15 percent.

Specimens for microstructual examination were initially chemically polished as described above. Electropolishing to perforation was performed at 30V in a -40°C solution of 60 percent methyl alchol, 36 percent n-butyl alchol and 4 percent perchloric acid.

Table 5.2.1. Compos'tions of the Alloys Examined (Wt %)

Alloy	Heat Number	Al	V	Zr	Mo	Sn	Cr	Si	C	N	O	H
Ti-6242S	Timet N-983Z	5.8	ND*	4.0	1.9	1.3	0.001	0.030	0.043	0.005	0.10	0.008
Ti-5621S	RMI 802881	4.7	ND	1.8	0.73	5.3	ND	0.23	0.02	0.009	0.090	0.009
Ti-38644	RMI 801008	3.4	8.2	4.0	4.0	ND	6.2	ND	0.02	0.012	0.084	0.0137
Ti-64	RMI 831352	6.4	3.9	ND	ND	ND	ND	ND	0.0	0.010	0.122	0.0065

* ND = Not Determined

Table 5.2.2. Specimen Heat Treatments*

Alloy	TMT
Ti-6242S	900°C/0.5 hr/AC + 790°C/0.25 hr/AC + 720°C/4 hr in vacuum/ArC
Ti-5621S	975°C/1 hr/AC + 595°C/2 hr/AC + 955°C/0.25 hr in vacuum/ArC + 595°C/2 hr in vacuum/ArC
Ti-38644	815°C/0.25 hr/AC + 825°C/0.5 hr in vacuum/ArC + 620°C/8 hr in vacuum/ArC
Ti-64 Duplex Anneal	790°C/0.25 hr/AC + 940°C/10 min in vacuum/ArC + 675°C/4 hr in vacuum/ArC
Ti-64 Beta Anneal	790°C/0.25 hr/AC + 1040°C/0.5 hr in vacuum/ArC + 700°C/2 hr in vacuum/ArC
Ti-64 Mill Anneal	790°C/0.25 hr/AC + 720°C/4 hr in vacuum/ArC

* AC = Air Cool ArC = Argon Cool

5.2.4.3 Results and Discussion

Immersion density measurements were performed on the specimens irradiated at 450 and 550°C. The results are presented in Table 5.2.3. It should be noted that the density results include contributions from both void swelling and precipitation reactions. Preliminary microstructural examinations were performed on the specimens to determine whether the observed swelling was due to voids. The results of these examinations are summarized in Table 5.2.4.

Table 5.2.3. Immersion Density Results

Alloy	Swelling ($\Delta V/V_o$, %) 550°C	450°C
Ti-6242s	0.27	0.55
Ti-5621s	0.66	0.36
Ti-38644	0.50	1.50
Ti-64 Duplex Anneal	3.52	-0.20
Ti-64 Beta Anneal	4.85	0.56
Ti-64 Mill Anneal	1.50	0.35

Voids were observed in all the specimens examined. With the exception of Ti-38644, the immersion density measurements are consistent with the void swelling observed. In Ti-38644 very few voids were observed. However the transformation from the beta to alpha phase produces a decrease in density. The swelling observed by immersion density is attributed to the increased alpha precipitation observed following irradiation.

The results of other irradiation experiments on titanium alloys are summarized in Table 5.2.5. As previous neutron irradiations attained very low fluences it is not surprising that voids were not observed. Only in ion irradiations have voids previously been observed in titanium alloys.

To discuss the ion irradiation results it is necessary to account for the shift in swelling behavior due to differences in displacement rate. This can be accomplished by shifting the temperature down by 40°C for every decade increase in displacement rate.[15] Using a displacement rate of 10^{-6} dpa/sec for EBR-II, temperature shifts of -100°C, -150°C

Table 5 2 ? Results of Microstructural Examinations

Alloy	Preirradiation Microstructure	550°C	450 C
Ti-6?42S	Equiaxed primary alpha grains with some transformed beta.	Inhomogenous void distribution with low density of voids along alpha boundaries. Fine structure in alpha grains.	Not amined
Ti-5621S	Equiaxed primary alpha grains with some transformed beta.	Very low density voids in alpha grains. Inhomogenous distribution of voids along alpha boundaries. Fine structure in alpha grains.	Low density voids in alpha grains. Fine structure in alpha grains.
Ti-38644	Beta matrix with fine alpha precipitates.	Only isolated voids observed. Coarse alpha precipitation.	Isolated voids. Extensive fine alpha precipitates.
Ti-64 Duplex Anneal	Equiaxed primary alpha grains with transformed beta.	Extensive void formation. Some blocky beta precipitates	Not examined.
Ti-64 Beta Anneal	Acicular alpha plates.	Extensive void formation. Some blocky beta precipitates	Few scattered voids.
Ti-64 Mill Anneal	Equiaxed primary alpha grains with transformed and intergranular beta.	Extensive void formation. Some blocky beta precipitates	Not examined.

Table 5 2 5 Summar iiation Experiments on Titanium

	Alloy	Irradiation		Exposure	Results
	Ti	Neutron		1.3×10^{20} n/cm^2 (E >1 MeV)	Black spots.
	Ti	Neutron		3×10^{21} n/cm^2 (E >0.1 MeV)	Dislocation loops
	Ti	Neutron		3.9×10^{19} n/cm^2 (E >1 MeV)	Dislocation loops
	Ti-64, Ti-6242S, Ti-5621S, Ti-38644, Ti-15333	Neutron		3×10^{21} n/cm^2 (E >0.1 MeV)	Beta precipitation and dislocation loops in Ti-64. Dislocation loops in Ti-6242S and Ti-5621S. Alpha precipitation in Ti-38644 and Ti-15333.
	Ti-64	17.5 MeV Cu^{4+}		1.5 dpa 1.5 dpa 1.5 dpa	Precipitation and dislocation loops. Precipitation and dislocation loops. Beta precipitates and dislocation loops.
	Ti-64	z 4 MeV V^{+}		25 dpa 12 dpa 25 dpa	Beta precipitation. Beta precipitation. Course beta precipitates and voids (∿0.07% ΔV/V).
	Ti-6[illegible]	5 MeV Ni^{+} ~00 KeV He^{+}	, 5 , 6	50 dpa	Beta precipitation and discloca-tion network.
	Ti-70A		, 5 630	50 dpa 50 dpa	Dislocation loops. Black spots.
Erck[14]	Ti-1[illegible] at % Al	3 MeV N^{+}	570 670	13 dpa [illegible] 6.3, 14.7	No voids. Voids with 0.6% ΔV/V at dpa.

and -150°C were calculated for the irradiations of Wilkes,[11] Erch[14] and Jones.[13] As Agarwal[12] did not publish the displacement rate for their titanium irradiation a rate of 3 x 10^{-3} dpa/sec was assumed based upon the rate for their austenitic alloy irradiation reported in the same article. This resulted in a temperature shift of -140°C. Using these temperature shifts we find that in Erck's study of Ti-14Al[14] voids were observed at approximately 520°C at 1.3 dpa with 0.6 percent swelling at 15 dpa. No voids were observed at temperatures less than 450°C to 14 dpa. In Agarwal's study of Ti-64[12] voids were observed in single ion irradiated specimens at approximately 520°C with 0.7 percent swelling at 25 dpa. No voids were observed at temperatures less than 400°C to 25 dpa. In Jones' study of Ti-64 and Ti-70A[13] no voids were observed for irradiation to 50 dpa at 480°C and below. Although the adjusted irradiation temperatures must be taken as only approximations these three studies form a consistent picture with voids only being observed above 500°C. This is consistent with the observation of peak swelling at 550°C in the present study.

5.2.5 Future Work

The microstructural examination of the specimens will be continued in depth.

5.2.6 Conclusions

The titanium alloys Ti-62425, Ti-5621S, Ti-38644 and Ti-64 have been irradiated to 5 x 10^{22} n/cm^2 (E >0.1 MeV) at 450 and 550°C. Swelling was observed in all alloys with generally greater swelling at 550°C. Although voids were observed in all alloys the swelling observed in Ti-38644 is attributed to alpha precipitation. Ti-36644 was found to be the most radiation resistant. Ti-6242s and Ti-5621s also displayed good radiation resistance whereas considerable swelling was observed in Ti-64 at 550°C. The swelling in Ti-64 was also found to be sensitive to pre-irradiation heat treatment.

5.2.7 References

1. J. W. Davis and G. L. Kulcinski, "Assessment of Titanium for Use in the First Wall/Blanket Structure of a Fusion Power Reactor," EPRI-ER-386, Electric Power Research Institute, Palo Alto, CA, April 1977.
2. R. E. Nygren, *Journal of Nuclear Materials*, 85 and 86, 861 (1979).
3. R. J. Puigh and E. K. Opperman, Alloy Development for Irradiation Performance Quarterly Progress Report, DOE/ER-0045/1, Dec. 1979, p. 58.
4. Y. Higashiguchi, H. Kagano and S. Yajima, *Journal of Nuclear Science and Technology*, 13, 454 (1976).
5. J. L. Brimhall, G. L. Kulcinski, H. E. Kissinger and B. Mastel, *Radiation Effects*, 9, 273 (1971).
6. A. Jostons, R. G. Blake and P. M. Kelly, *Philosophical Magazine A*, 211, 903 (1980).
7. J. A. Sprague and F. A. Smidt, Jr., Alloy Development for Irradiation Performance Quarterly Progress Report, DOE/ER-0058/4, March 1978, p. 67.
8. J. A. Sprague and F. A. Smidt, Jr., Alloy Development for Irradiation Performance Quarterly Progress Report, DOE/ER-0058/5, March 1979, p. 79.
9. S. M. L. Sastry, J. E. O'Neal and J. M. Davis, Alloy Development for Irradiation Performance Quarterly Progress Report, DOE/ER-0058/4, March 1978, p. 72.
10. S. M. L. Sastry, J. W. Davis and J. E. O'Neal, Alloy Development for Irradiation Performance Quarterly Progress Report, DOE/ER-0058/5, March 1979, p. 42.
11. P. Wilkes and G. L. Kulcinski, *Journal of Nuclear Materials*, 78, 427 (1978).
12. S. C. Agarwal, G. Ayrault, D. I. Potter, A. Taylor and F. V. Nolfi, Jr., *Journal of Nuclear Materials*, 85 and 86, 653 (1979).
13. R. H. Jones and L. A. Charlot, *Journal of Nuclear Materials*, 91, 329 (1980).
14. R. A. Erck, D. I. Potter and H. Wiedersich, *Journal of Nuclear Materials*, 80, 120 (1979).
15. F. A. Garner and J. J. Laidler, in proceedings of the workshop in Correlation of Neutron and Charged Particle Damage, CONF-760673, Oak Ridge National Laboratory, 1976, p. 177.

6. INNOVATIVE MATERIAL CONCEPTS

6.1 MICROSTRUCTURES OF IRON-BASE LONG-RANGE-ORDERED ALLOYS BOMBARDED TO 70 dpa WITH NICKEL IONS — D. N. Braski (Oak Ridge National Laboratory)

6.1.1 ADIP Task

ADIP Task I.C.5, Microstructure and Swelling in Special and Innovative Materials.

6.1.2 Objective

The objective of this research is to define the response of $(Fe,Ni)_3V$ long-range-ordered (LRO) alloys to ion irradiation. The overall goal is to determine the potential use of this alloy class as a structural material for fusion energy systems.

6.1.3 Summary

Disks of LRO-37-5 in the as-ordered and 20%-cold-worked conditions were bombarded with 4-MeV nickel ions to 70 dpa at temperatures from 570 to 680°C. Both conditions retained order for bombardment below the critical ordering temperature of about 650°C, and cold work improved the swelling resistance, especially above T_c. Both conditions showed better resistance to swelling than 20%-cold-worked type 316 stainless steel.

6.1.4 Progress and Status

A heat of the LRO alloy LRO-37 has been fabricated to serve as a link between research and commercial-size heats. This heat, LRO-37-5, has the nominal composition of LRO-37 (ref. 1) but was melted with less expensive ferrovanadium feedstock. The use of ferrovanadium increased the carbon content of the alloy from about 100 to 240 wt ppm. The purpose of this experiment was to determine if the cheaper alloy fabrication technique would have any deleterious effects on the alloy's resistance to swelling. Previous experiments indicated that LRO-37 was relatively low-swelling.' A second goal was to measure the amount of added swelling resistance which might be gained by cold working the alloy. Such a technique is known to be effective in increasing the swelling resistance of austenitic stainless steel.

The melting and fabrication of the alloy was by the same method as described previously.[2] The composition and heat treatments for LRO-37-5 and type 316 stainless steel are given in Table 6.1.1. The procedure for irradiating the disks was also described in ref. 2, except that the bombardment temperatures in this experiment were 570, 625, 650, and 680°C. As before, the dose was 70 dpa and the helium and deuterium ions were simultaneously injected at rates of 8 and 28 at. ppm/dpa, respectively. The TEM specimens were prepared in the same manner and the cavity size distributions were determined by the same method as described in ref. 2. Precipitate phases were electrolytically extracted from bulk specimens in a 10 vol % solution of HCl in methanol with an applied dc voltage of 1.5 V. The extracted phases were placed on silicon substrates and analyzed by x-ray diffraction.

Table 6.1.1. Alloy Composition and Heat Treatment

Alloy and Condition	Nominal Composition (wt %)								Heat Treatment
	Fe	Ni	V	Ti	Cr	Mo	Mn	C	
LRO-37-5 As-ordered	38	40	22	0.4				0.024	Annealed 20 min at 1100°C, quenched into water, aged at 650°C for 5.5 d, followed by 18 h at 600°C and 48 h at 500°C.
LRO-37-5 20%-cold-worked	38	40	22	0.4				0.024	Annealed 20 min at 1100°C, quenched into water, aged at 650°C for 5.5 d. followed by 18 h at 600°C and 48 h at 500°C plus cold worked 20%.
Heat DO 316 stainless steel 20%-cold-worked	65	13		0.005	18	20	1.9	0.050	Solution annealed plus cold worked 20%.

The unirradiated microstructures of LRO-37-5 in the as-ordered and cold-worked conditions are shown in Fig. 6.1.1. The as-ordered microstructure [Fig. 6.1.1(a)] consists of an ordered matrix and three precipitate phases. Titanium nitride (TiN) particles were geometric in shape and were mostly dispersed throughout the matrix. The TiN particles appeared to contain about 20 wt % V, as revealed by energy dispersive x-ray spectroscopy (EDS) in the electron microscope. The TiN particles punch out dislocations at their interfaces and the dislocations were usually

YE-12374

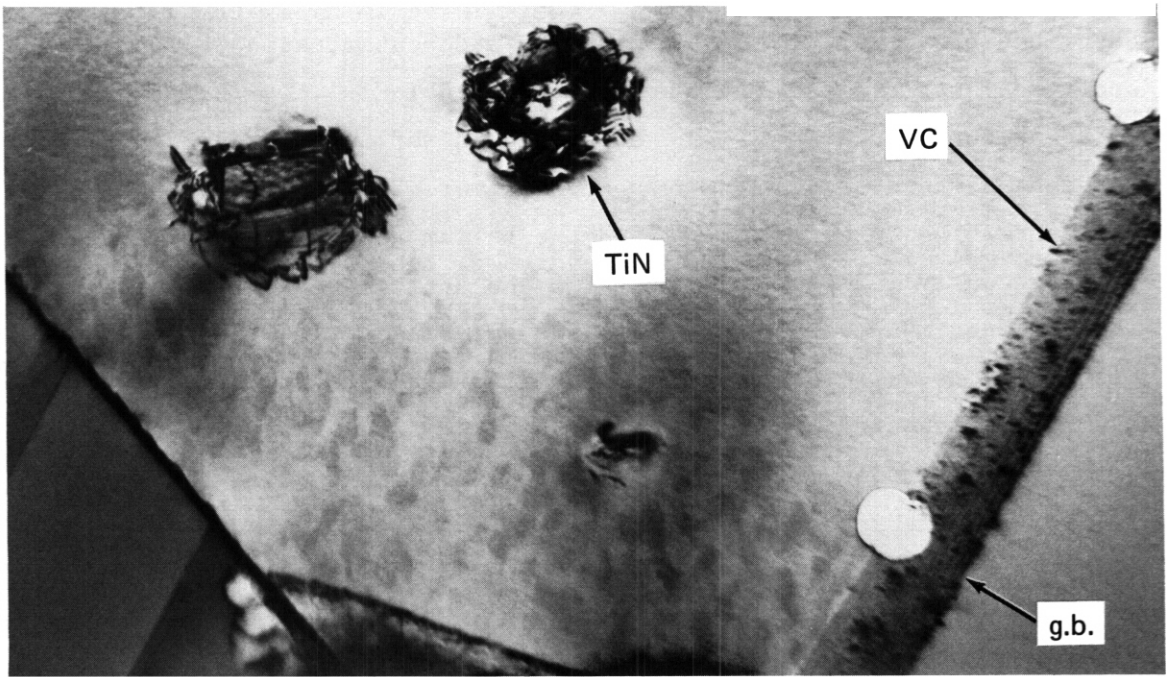

(a)

YE-12375

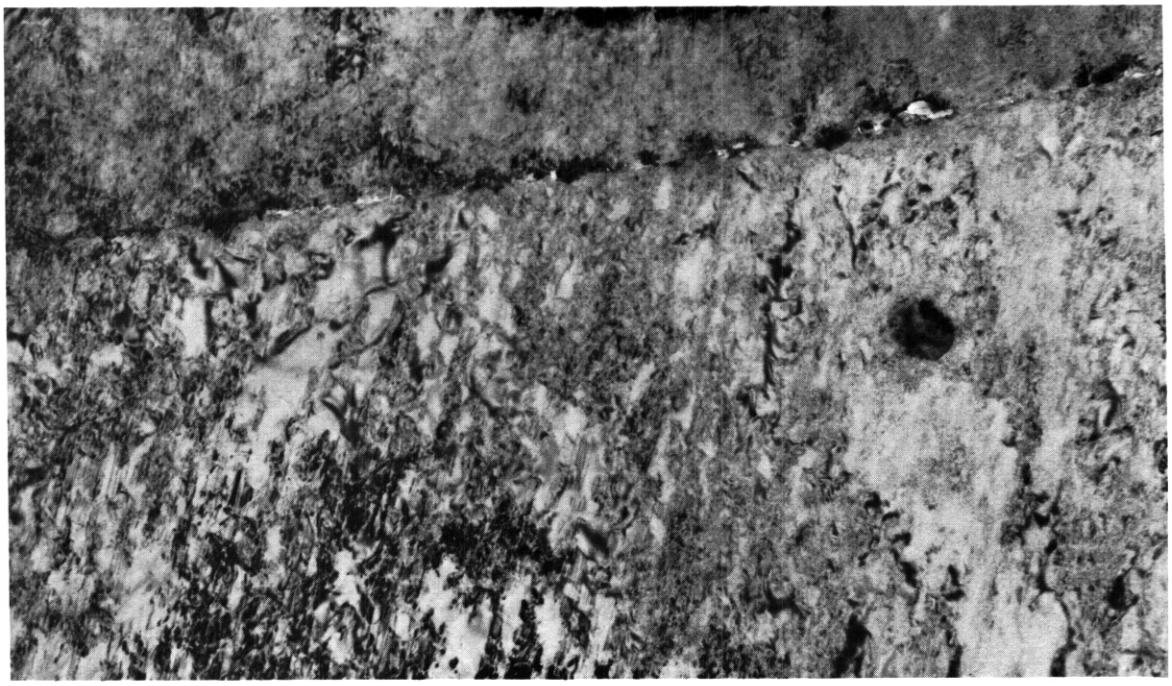

(b)

0.2μm

Fig. 6.1.1. Unirradiated Microstructure of (a) As-Ordered LRO-37-5 Showing Large TiN and Smaller VC Particle, and (b) 20%-Cold-Worked LRO-37-5 Showing the Dislocation Structure Introduced by the Cold Work.

decorated with small VC particles. Small VC particles also line the grain boundaries as shown in Fig. 6.1.1(a). It is not known whether the larger, etched-out particles on the grain boundary were TiN or VC particles. The third phase was present as rounded or "kidney-shaped'' particles several times larger than the TiN particles. These could not be identified. However, information from EDS analyses showed that the unknown phase was rich in titanium and contained smaller amounts of vanadium, nickel, and iron. The unknown phase was rather widely dispersed throughout the matrix but does not appear in Fig. 6.1.1(a). The unirradiated cold-worked LRO-37-5 microstructure [Fig. 6.1.1(b)] was the same as that just described, with the addition of a dense forest of dislocations that were introduced by the cold work.

The ion bombardment produced interstitial (Frank) loops, dislocations, and cavities in both conditions of the LRO alloy. All of the LRO alloy disks bombarded below T_c (~650°C) remained ordered. Measurements of cavities yielded swelling curves for both LRO conditions and the 20%-cold-worked type 316 stainless steel standard (Fig. 6.1.2). The swelling

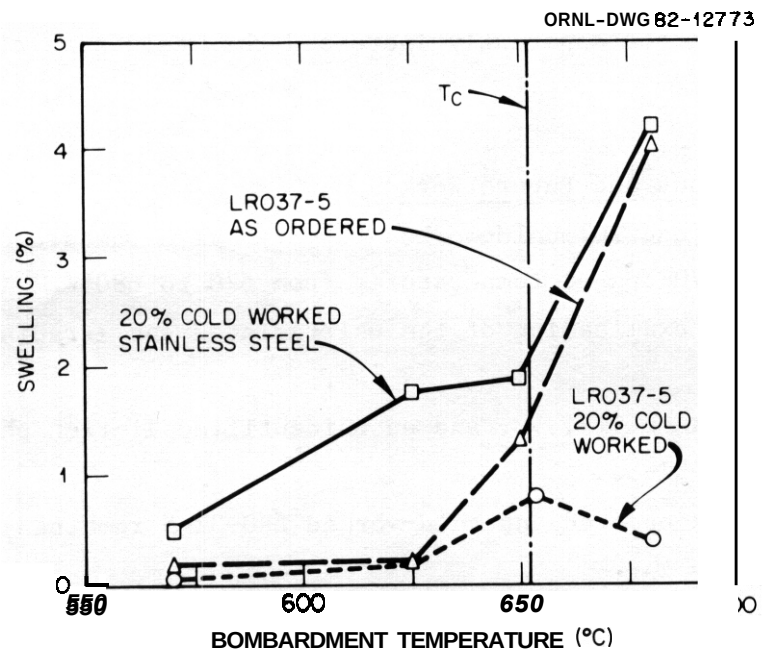

Fig. 6.1.2. The Temperature Dependence of Swelling in LRO-37-5 (As-Ordered and 20%-Cold-Worked) and 20%-Cold-Worked Type 316 Stainless Steel. Specimens bombarded with 4-MeV nickel ions to 70 dpa, with simultaneous injection of 560 at. ppm He and 1960 at. ppm D.

behavior of the as-ordered LRO-37-5 alloy was similar to other iron-base LRO alloys investigated previously,[3] i.e., the swelling was relatively low below the critical ordering temperature (T_c) of about 650°C, and increased markedly above this temperature. On the other hand, the 20%-cold-worked LRO-37-5 showed only a modest increase in swelling just above T_c and swelling was significantly reduced at 680°C. Both conditions of the LRO alloy performed better than the cold-worked type 316 stainless steel below T_c, but only the cold-worked LRO-37-5 was better at the highest irradiation temperature. Figure 6.1.3 shows the cavities present in all three alloys after the bombardment to 70 dpa at 650°C. Fewer of the medium to large size cavities ($\gtrsim$10 nm diameter), which account for a greater portion of the total swelling value, were present in the two LRO alloys. However, the difference between the as-ordered LRO-37-5 and 20%-cold-worked type 316 stainless steel was not large. Figure 6.1.4 shows the microstructure of 20%-cold-worked LRO-37-5 after bombardment at 680°C. A higher number density of small cavities and only a few medium-sized cavities were observed. The cavities were located preferentially on the dislocations, forming a cavity network. No recovery of the dislocation structure was observed after the 3-h bombardment at 680°C. Cold working prior to irradiation apparently increased the resistance of the LRO alloy to swelling.

6.1.5 Conclusions and Future Work

As-ordered and 20%-cold-worked LRO-37-5 were bombarded with 4 MeV nickel ions to 70 dpa at temperatures from 570 to 680°C. The results of microstructural examination of the unirradiated and irradiated material showed that:

1. The phases TiN, VC, and an unidentified Ti-rich phase exist in the ordered LRO-37-5.

2. Both as-ordered and cold-worked LRO-37-5 remained ordered when irradiated below T_c.

3. Both alloy conditions showed less swelling below T_c than 20%-cold-worked type 316 stainless steel bombarded under identical conditions.

4. Cold working improved the resistance of the LRO-37-5 alloy to swelling, especially for bombardment temperatures above T_c.

YE-12376

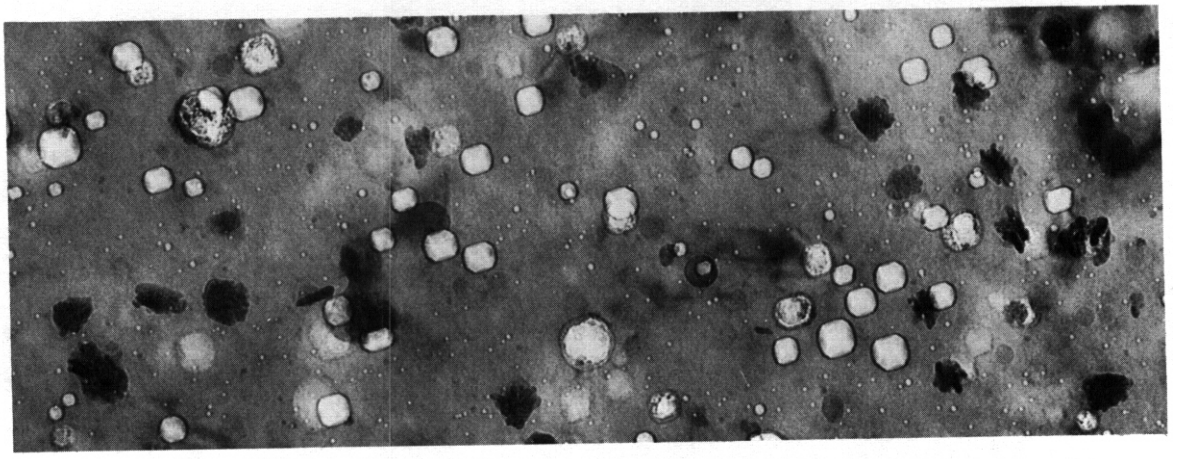

(a)

YE-12377

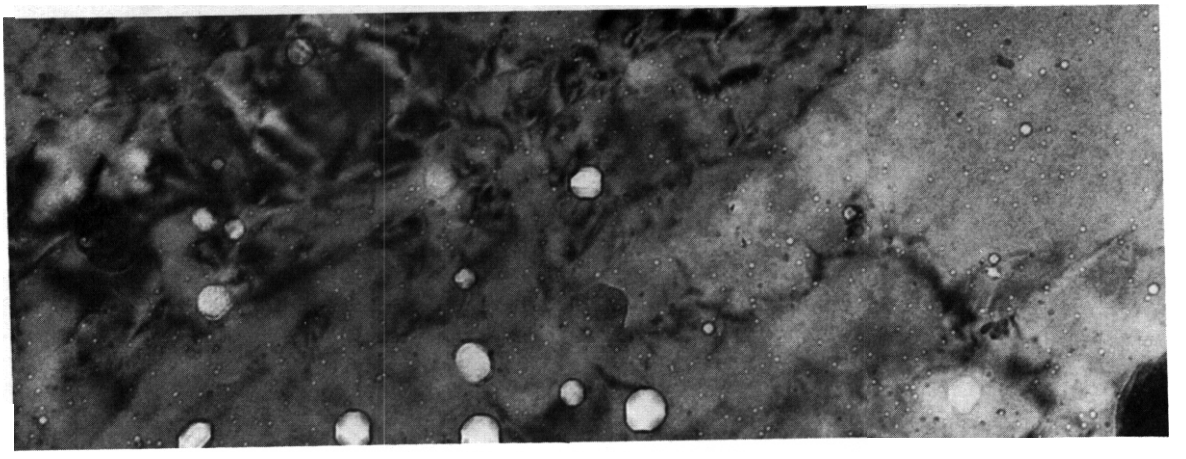

(b)

YE-12378

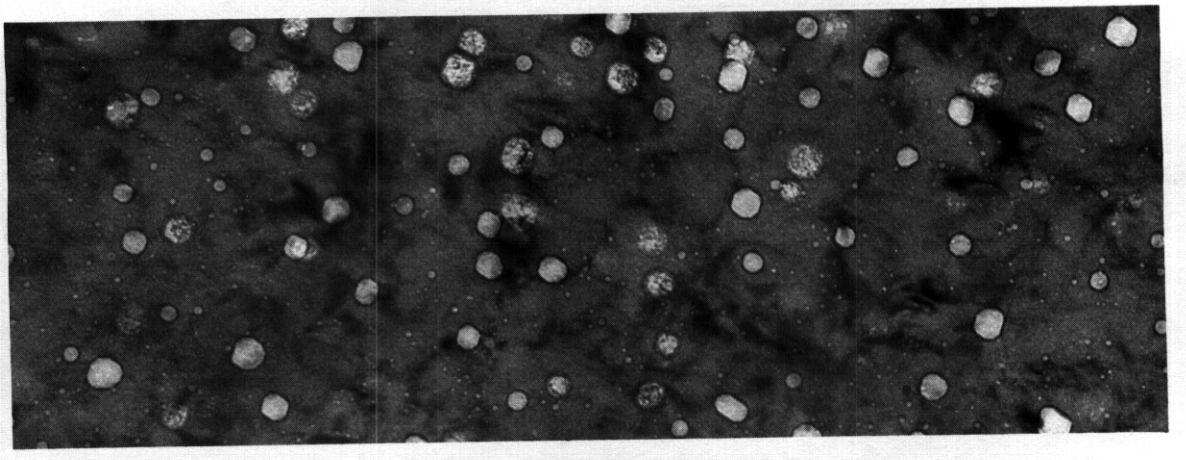

(c)

0.1 μm

Fig. 6.1.3. Microstructure After Bombardment with 4-MeV Nickel Ions to 70 dpa at 650°C for (a) As-Ordered LRO-37-5, (b) 20%-Cold-Worked LRO-37-5, and (c) 20%-Cold-Worked Type 316 Stainless Steel.

YE-12379

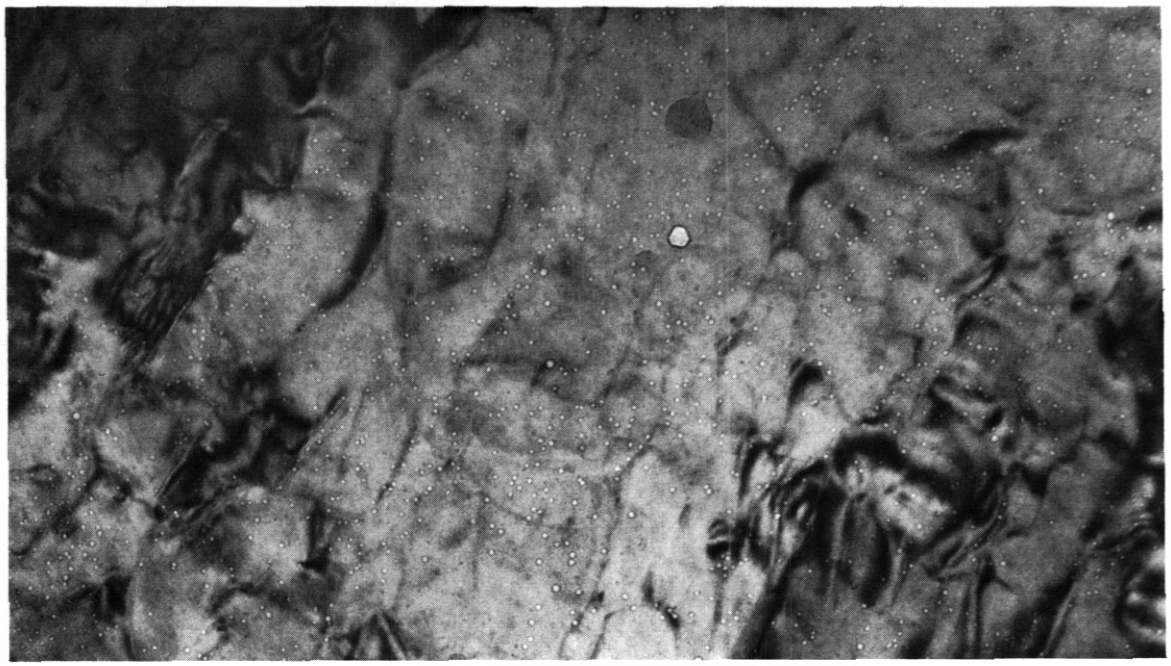

Fig. 6.1.4. Microstructure of 20%-Cold-Worked LRO-37-5 After Bombardment at 680°C with 4-MeV Nickel Ions to 70 dpa Plus 560 at. ppm He and 1960 at. ppm D. Small cavities can be seen located on the dislocations.

6.1.6 References

1. D. N. Braski, "The Effect of 4-MeV Nickel Ion Irradiation on the Microstructure of $(Fe,Ni)_3V$ Long-Range-Ordered Alloys," *ADIP Quart. Prog. Rep. Sept. 30, 1980*, DOE/ER-0045/4, pp. 114-21.
2. D. N. Braski, "The Effect of 4-MeV Nickel Ion Irradiation on the Microstructure of $(Fe,Ni)_3V$ Long-Range-Ordered Alloys," *ADIP Quart. Prog. Rep. June 30, 1980*, DOE/ER-0045/3, pp. 162-73.
3. D. N. Braski, "The Effect of 4-MeV Nickel Ion Irradiation on the Microstructure of $(Fe,Ni)_3V$ Long-Range-Ordered Alloys," *ADIP Quart. Prog. Rep. Dec. 31, 1980*, DOE/ER-0045/5, pp. 119-21.

6.2 STATUS OF SCALE-UP OF AN IRON-BASE LONG-RANGE-ORDERED ALLOY — T. K. Roche and C. T. Liu (Oak Ridge National Laboratory)

6.2.1 ADIP Tasks

ADIP Tasks I.A.5, Perform Fabrication Analyses, and I.D.1, Materials Stockpile for Magnetic Fusion Energy Programs.

6.2.2 Objective

The objective of this work is to perform semiproduction scale-up of an iron-base long-range-ordered (LRO) alloy to gain some commercial experience with this class of developmental alloy. The activity will provide material for irradiation, mechanical property, compatibility, and other property tests to evaluate the potential of the alloy class for use in fusion energy systems.

6.2.3 Summary

The semiproduction scale-up of an iron-base LRO alloy is under way by a commercial source. Three 18-kg ingots have been produced by two different melt practices. Chemical analyses indicate that the compositions of the ingots are near the alloy specifications. Specimens from the ingots were successfully cold rolled at room temperature and hot rolled at 1100°C. Further evaluation of alloy homogeneity and distribution of second phases is in progress.

6.2.4 Progress and Status

Long-range-ordered alloys of the system $(Fe,Ni)_3(V,Ti)$ have been developed on a laboratory scale at ORNL. These alloys have unique properties which make them attractive as structural materials for advanced energy systems. The alloy development program has reached the important phase of alloy scale-up.

Semi-production scale-up of the alloy, LRO-37 (Fe—39.4 wt % Ni—22.4 wt % V—0.43 wt % Ti), is being carried out at the facilities of High Technology Materials Division, Cabot Corporation. Stage I involving ingot preparation has been completed. A total of three ingots, each

weighing approximately 18 kg (40 lb) have been produced by two different melt practices — vacuum induction melting plus electron beam remelting using high purity materials (one ingot, LRO-37-HP), and vacuum induction melting plus electroslag remelting using commercial grade materials (two ingots, LRO-37-CG). The principal difference between the HP and CG ingots, other than melt practice, was the grade of vanadium melt stock. Very high purity vanadium was used for making the HP alloy, and more economical, but lower purity, ferrovanadium was used for the CG alloy. Melt stock for the other additions was the same for all ingots. A small amount of cerium was added to the ingots to improve their high-temperature properties.

Results of chemical analyses by both the vendor and ORNL are shown in Tables 6.2.1 and 6.2.2. The results were from a sample cut from the bottom of the electron beam melted HP ingot, and samples from the vacuum

Table 6.2.1. Chemical Analysis of Electron Beam Remelted Iron-Base Long-Range-Ordered Alloy, LRO-37-HP

Element	Composition (wt %)[a]		
	Target	Vendor	ORNL
Al	<0.03	0.02	
C	<0.03	0.006	0.0022
co	<0.03	0.02	
Cr	<0.03	<0.1	
cu	<0.03	<0.01	
Fe	Bal	36.65	37.18
Mg	<0.03	0.001	
Mn	<0.03	<0.01	
Mo	<0.03	<0.01	
N	<0.02	0.013	0.0172
Ni	39.4	38.78	38.51
O	<0.02	0.023	0.017
P	<0.002	0.005	
S	<0.002	0.002	
si	<0.03	0.05	0.042
Ti	0.43	0.51	0.48
V	22.4	23.51	23.75
W	<0.03	0.03	

[a]Significant figures are as listed on analysis reports, and do not imply accuracy limits.

Table 6.2.2. Chemical Analysis of the Electroslag Remelted Iron-Base Long-Range-Ordered Alloy, LRO-37-CG

Element	Composition (wt %)[a]						
	Target	Vendor			ORNL		
		Electrode	Ingot Top	Ingot Bottom	Electrode	Ingot Top	Ingot Bottom
Al	<0.5	0.05	<0.01	0.11	0.029	0.44	1.23
C	<0.06	0.031	0.035	0.045	0.0325	0.0321	0.0438
Co	<0.06	0.02	0.02	0.05			
Cr	<0.06		0.06	0.06			
Cu	<0.06	0.01	0.05	0.08			
Fe	Bal	35.94	35.95	36.18	37.93	37.95	38.48
Mg	<0.06	0.001	<0.001	<0.001			
Mn	<0.06	0.04	0.05	0.06			
Mo	<0.06	0.04	0.07	0.06			
N	<0.05	0.05	0.054	0.053	0.0555	0.0574	0.0580
Ni	39.9	40.45	39.57	40.01	39.75	38.85	38.68
O	<0.05	0.049	0.005	0.015	0.0155	0.0161	0.0098
P	<0.005	0.009	0.009	0.01			
S	<0.005	0.005	0.003	0.002			
Si	<0.5	0.43	0.43	0.45	0.37	0.4	0.41
Ti	0.43	0.33	0.16	0.11	0.36	0.22	0.13
V	21.2	21.87	21.86	21.83	21.99	21.95	21.80
W	<0.06	0.07	0.09	0.09			

[a]Significant figures are as listed on analysis reports, and do not imply accuracy limits.

induction melted CG electrode and top and bottom of one of the electroslag remelted CG ingots. In general there is very good agreement between the analyses performed at the two locations, and the analyzed chemistries are reasonably close to the goal composition, except for the titanium loss seen in the CG alloy. Since ferrovanadium characteristically has a high oxygen content, it is postulated that the loss of titanium during vacuum induction melting of the CG electrode was through oxidation. Additional losses from electroslag remelting might have occurred through reaction with the slag. Nevertheless, it is felt that sufficient titanium was retained in the CG alloy for the material to be acceptable.

Specimens from the same locations as those analyzed chemically were examined metallographically. Results are presented in Figs. 6.2.1 and 6.2.2. Second phase(s), believed to be carbides, sigma phase, or both, are evident in the alloys. A degree of inhomogeneity was indicated in the HP alloy since some areas of the examined specimen were relatively free of

Y-184216

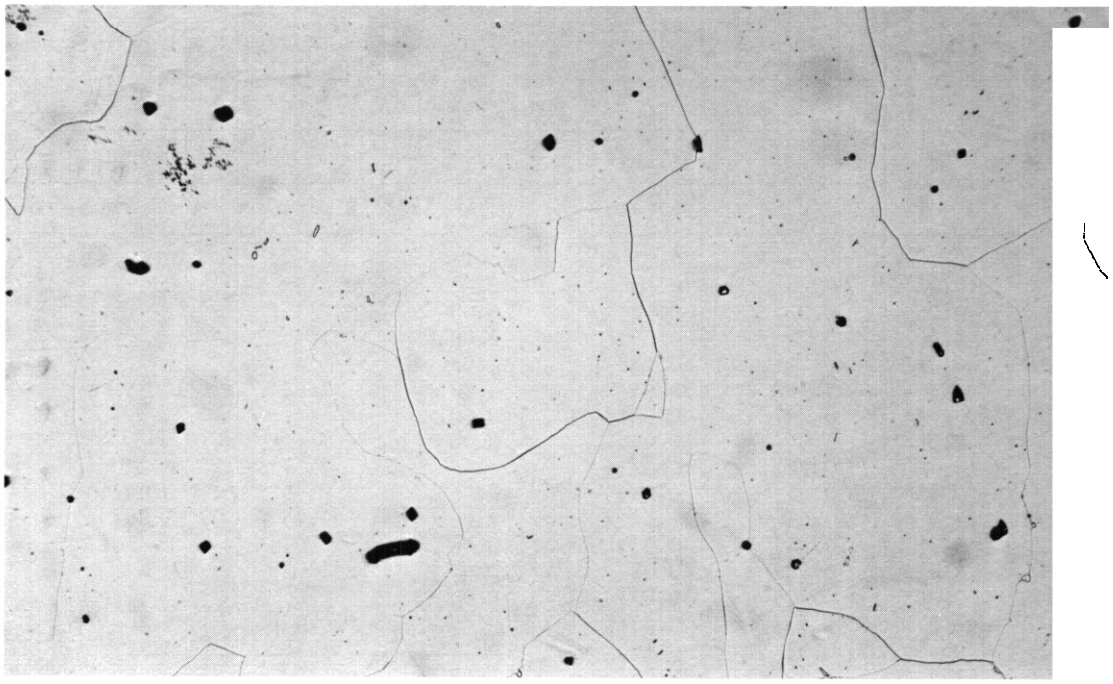

(a)

Y-184217

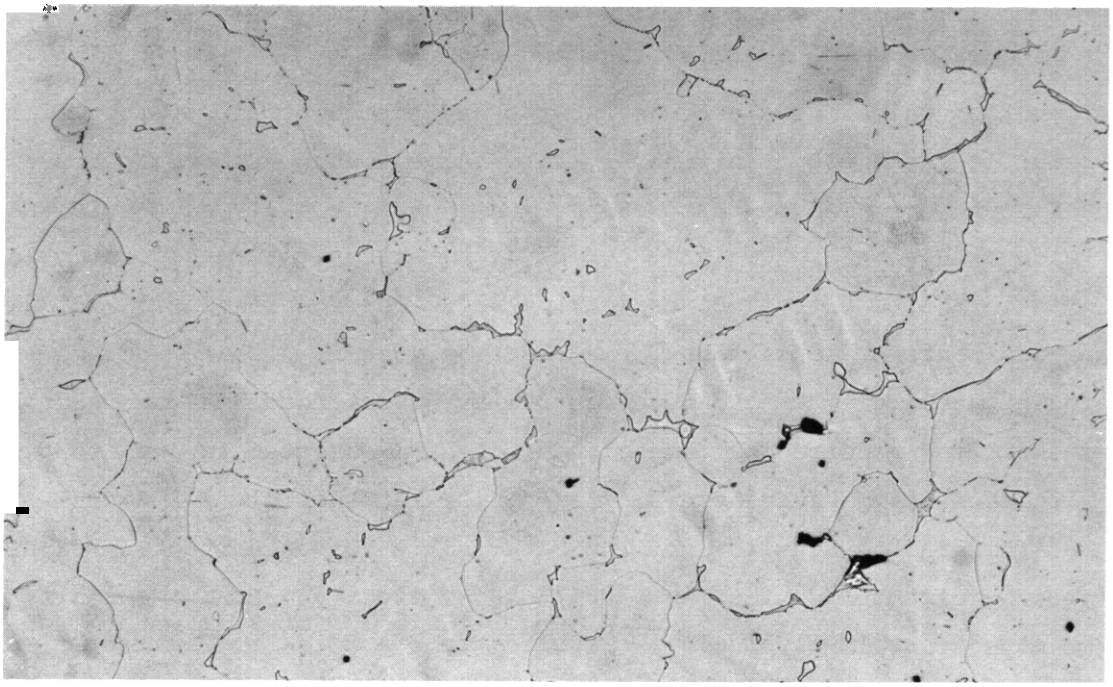

(b)

200 μm

Fig. 6.2.1. Microstructure of Electron Beam Remelted Iron-Base Long-Range-Ordered Alloy, LRO-37-HP. The sample has been etched with modified aqua regia. (a) Little second phase precipitation. (b) Second phase precipitation.

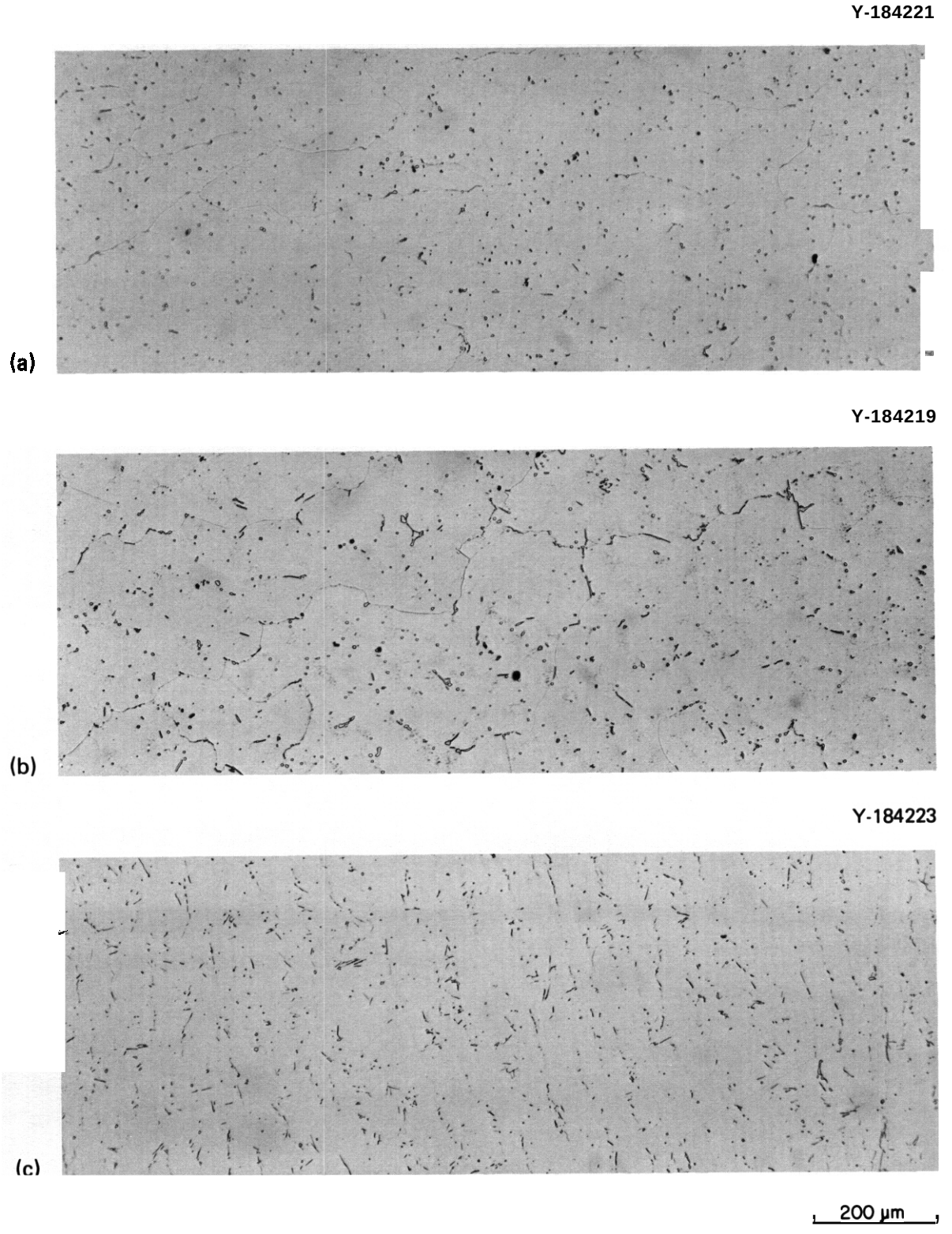

Fig. 6.2.2. Microstructure of Iron-Base Long-Range-Ordered Alloy, LRO-37-CG. Etched with modified aqua regia. (a) Vacuum induction melted electrode. (b) Top of electroslag remelted ingot. (c) Bottom of electroslag remelted ingot.

precipitation. This can be seen by comparing Fig. 6.2.1(a) with Fig. 6.2.1(b). Microstructures (Fig. 6.2.2) of the electrode and top and bottom of the electroslag remelted ingot of the CG alloy were all similar. Studies are underway to determine if the observed precipitates in the alloys can be redissolved by heat treatment.

Fabrication tests were also conducted on specimens from the HP and CG ingots. All could be hot rolled at 1100°C for a total area reduction of approximately 75% and cold rolled for a total reduction of approximately 50%, with no difficulty. Thus, no problems are expected in proceeding with the planned fabrication schedule of hot forging followed by hot and cold rolling of the ingots.

6.3 MICROSTRUCTURES OF IRON-BASE LONG-RANGE-ORDERED ALLOYS IRRADIATED TO 10 dpa IN HFIR — D. N. Braski (Oak Ridge National Laboratory)

6.3.1 ADIP Task

ADIP Task I.C.5, Microstructure and Swelling in Special and Innovative Materials.

6.3.2 Objective

The objective of this research is to define the response of $(Fe,Ni)_3V$ long-range-ordered (LRO) alloys to neutron irradiation. The overall goal is to determine the potential use of this alloy class as a structural material for fusion energy systems.

6.3.3 Summary

The LRO-16, -20, and -37 alloys were irradiated in HFIR at 300 to 600°C to approximately 8.3 dpa and 1000 at. ppm He. All three remained ordered, and interstitial loops, dislocation segments, and cavities formed in the microstructure. Cavities grew preferentially on {111} loops, and helium bubbles formed on grain boundaries at the higher temperatures. Swelling in LRO-20 and -37 was low; LRO-16 swelled more than annealed PCA.

6.3.4 Progress and Status

Preliminary results are presented showing the microstructural response of three LRO alloys to neutron irradiation in the temperature range of 300 to 600°C.

Disks of each alloy (3 mm diameter x 0.25 mm thick) were punched from sheet material and subsequently heat treated to produce the fully ordered condition (see Table 6.3.1). The disks were irradiated in the experiment HFIR-CTR-32 at 300, 400, 500, and 600°C to produce nominal displacement and helium levels of 8.3 dpa and 1000 at. ppm, respectively. After the disks were electropolished in a 12 vol % solution of concentrated H_2SO_4 in methanol (−10°C, 100 mA), they were examined in a transmission electron microscope (TEM).

The LRO alloys remained ordered after irradiation at all four temperatures. However, the superlattice reflections observed in electron

Table 6.3.1. Long-Range-Ordered Alloy Compositions and Heat Treatments

Alloy	Composition (wt %)				Heat Treatment
	Fe	Ni	V	Ti	
LRO-16	46.0	31.0	23.0		10 min at 1170°C, water quenched, aged at 640°C for 4 d, 600°C for 12 d, and 500°C for 6 d.
LRO-20	37.6	39.5	22.9		15 min at 1200°C, water quenched, aged at 650°C for 4 d, 600°C for 1 d, and 500°C for 2 d.
LRO-37	37.6	39.5	22.4	0.4	15 min at 1200°C, water quenched, aged at 650°C for 4 d, 600°C for 1 d, and 500°C for 2 d.

diffraction patterns were noticeably weaker for specimens irradiated at 300°C than for unirradiated, ordered material. A technique of measuring the degree of order in a TEM specimen by convergent beam electron diffraction (CBED) has been developed[1] and it will be used to measure this parameter in the irradiated specimens. The size of the ordered domains increased with increasing irradiation temperature, as was observed previously in LRO-16 irradiated in the ORR (ref. 2) and in LRO-1 (cobalt-base) irradiated with nickel ions.[3] Small loops and dislocation segments observed in the microstructure are shown in Fig. 6.3.1 for LRO-16 irradiated at 300°C. The loops were interstitial (Frank), and their size increased with increasing irradiation temperature. The larger loops were faulted and displayed fringe contrast. Cavities were observed to grow preferentially on these faulted loops as shown in Fig. 6.3.2 for the LRO-20 specimen irradiated at 600°C. Since the loops lie on {111} planes, rows of cavities were often observed in directions corresponding to these planes in the foil. Such alignment is seen in Fig. 6.3.3, where cavities along the $(11\bar{1})$ and (111) planes are parallel to each other when the electron beam was oriented near the [112] direction in the crystal.

Small cavities were also found in the grain boundaries of all three LRO alloys after irradiation at the higher temperatures. Occasionally, relatively large cavities were also found, as shown in Fig. 6.3.4 for

YE-12380

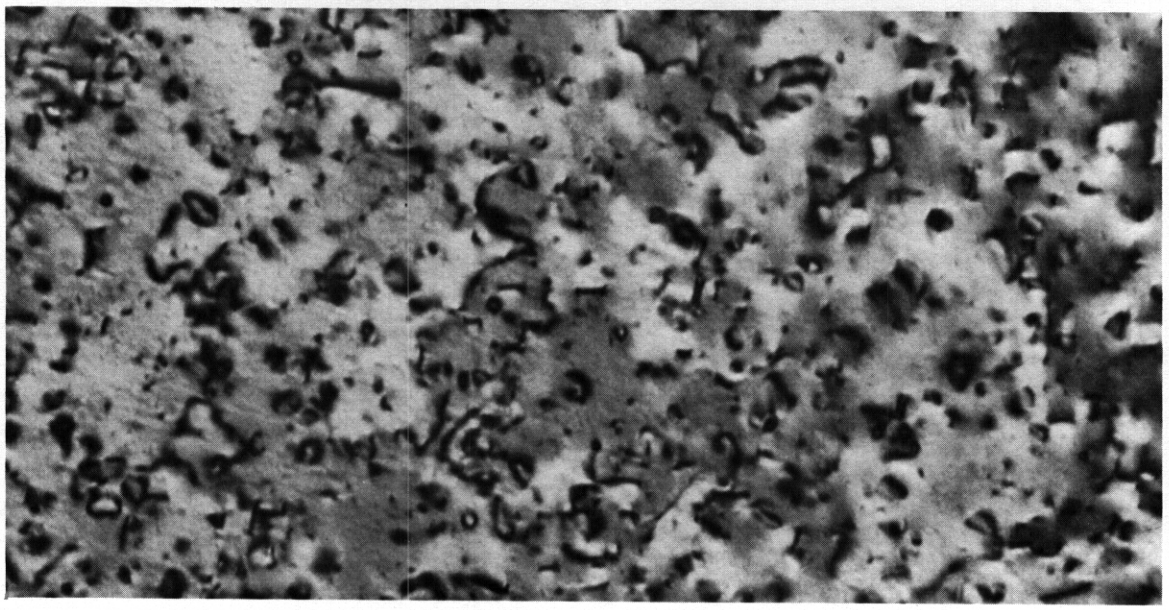

0.1 μm

Fig. 6.3.1. Small Loops and Dislocation Segments Produced in LRO-16 by Irradiation in High Flux Isotope Reactor to about 8.3 dpa at 300°C.

YE-12381

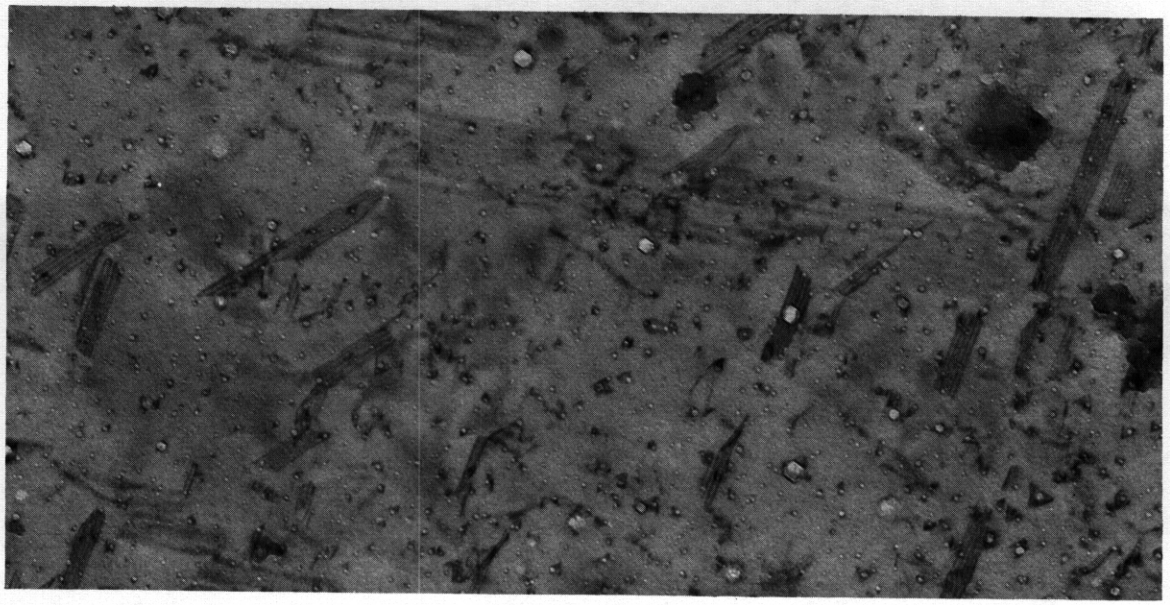

0.1 μm

Fig. 6.3.2. Cavities Along Faulted Loops and in Matrix of LRO-20 after Irradiation in High Flux Isotope Reactor to about 8.3 dpa at 600°C.

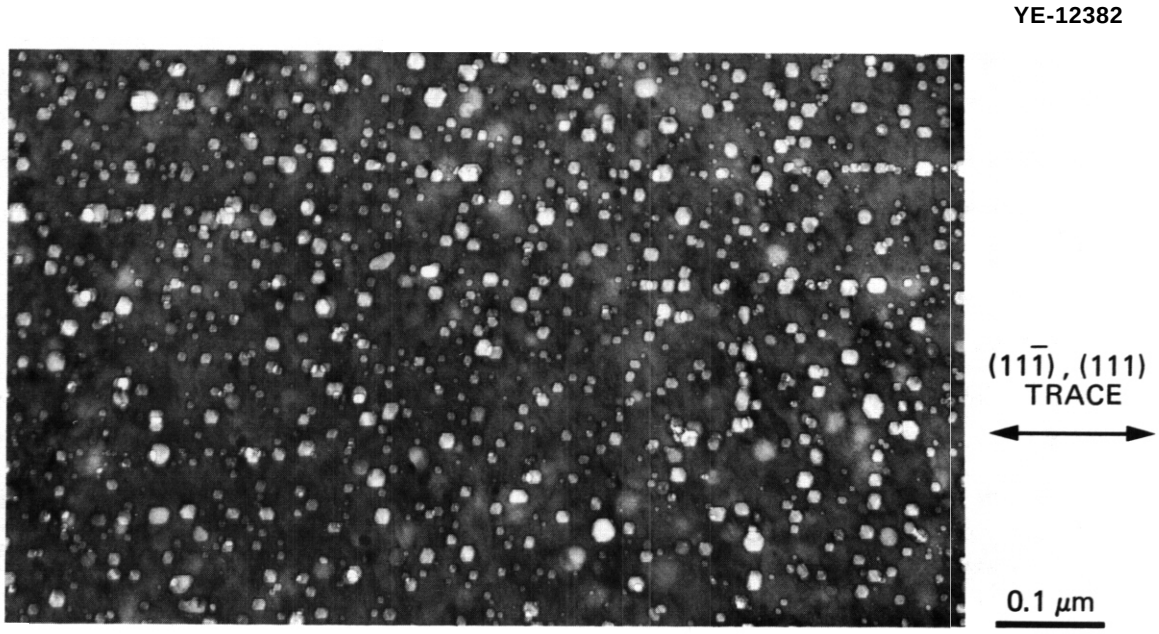

Fig. 6.3.3. Alignment of Cavities Which Lie Preferentially on (11$\bar{1}$) and (111) Planes in LRO-16 Irradiated in High Flux Isotope Reactor to about 8.3 dpa at 600°C. Beam direction is nearly parallel to [112].

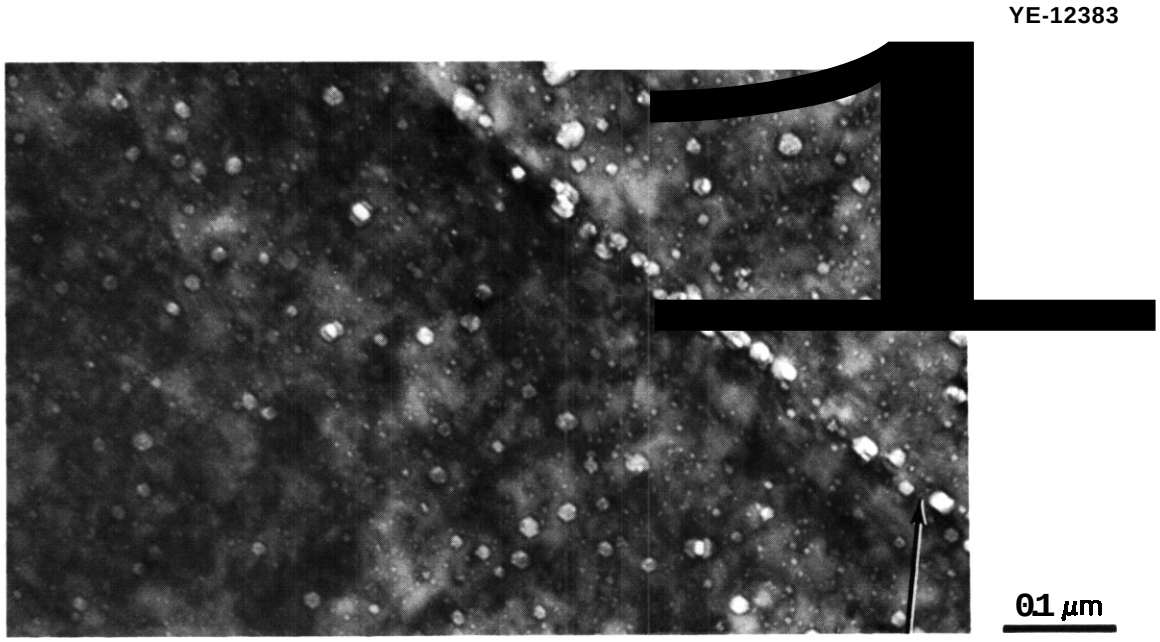

Fig. 6.3.4. Relatively Large Cavities (Presumed to Be Helium Bubbles) on High Angle Grain Boundary in LRO-16 Irradiated in High Flux Isotope Reactor to Produce about 8.3 dpa and 1000 at. ppm He at 600°C.

LRO–20 irradiated at 600°C. These cavities at the grain boundaries are assumed to be helium bubbles. Our experience with LRO-16 irradiated in the ORR indicates that this helium in the grain boundaries will probably have a deleterious effect on the mechanical properties of the alloy. Perhaps the effect can be measured in bend tests that will be conducted on disks of these alloys.

Measurements of the cavities have yielded values of swelling, which are plotted in Fig. 6.3.5. Recent results for the PCA stainless steel in the solution–annealed condition (see P. J. Maziasz and D. N. Braski, this report)[4] are also included for purposes of comparison. The LRO–16 alloy, which has a lower nickel content and contains sigma phase, showed the highest swelling, followed by LRO–37 and –20. The LRO–37 alloy has essentially the same composition as LRO–20 but also contains a small titanium addition. The titanium addition did not markedly alter the response of the alloy to neutron irradiation for the conditions examined in this experiment.

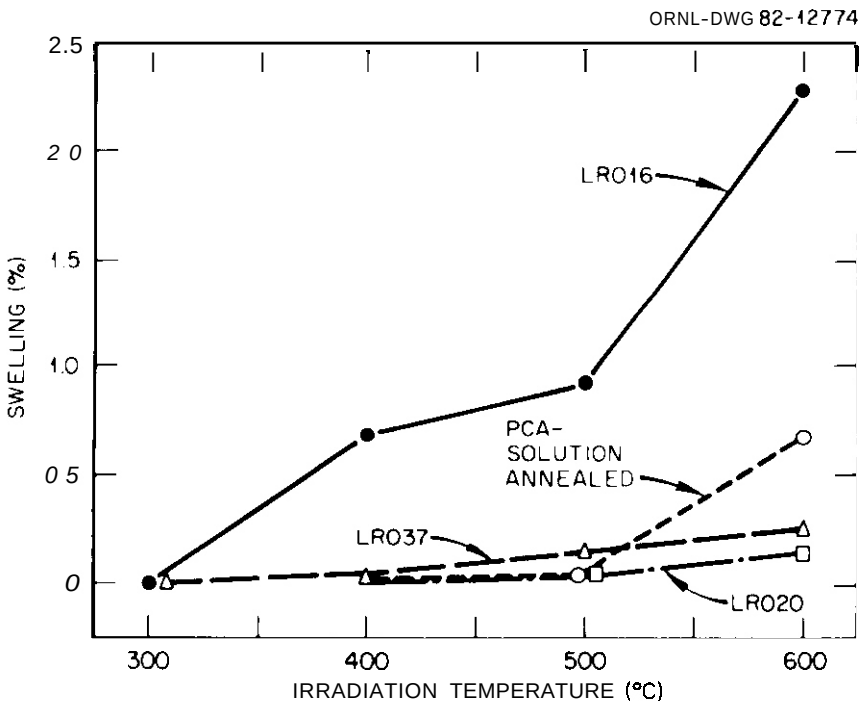

Fig. 6.3.5. Swelling of LRO Alloys and PCA Stainless Steel Produced by Irradiation to 8.3 dpa in HFIR.

The LRO–16 alloy is less resistant to swelling than the PCA stainless steel in the solution–annealed conditions, while LRO–20 and –37 were somewhat more resistant at 600°C. At 500°C, the swelling in PCA, LRO–20, and –37 was about the same.

6.3.5 Conclusions and Future Work

The LRO alloys, LRO–16, –20, and –37, were irradiated in HFIR to produce about 8.3 dpa and 1000 at. ppm He at 300 to 600°C. It was concluded that:

1. The LRO alloys remained ordered after the irradiation.
2. Ordered domain size increased with increasing irradiation temperature.
3. Faulted interstitial loops were produced by the irradiation and their size increased with increasing irradiation temperature.
4. Cavities grew preferentially along the faulted loops, which had {111} habit planes.
5. Cavities, assumed to be helium bubbles, were also found in the grain boundaries after irradiation at the higher temperatures.
6. Both LRO–20 and –37 had somewhat better resistance to swelling at 600°C than solution–annealed PCA, while LRO–16 was less resistant.
7. The small titanium addition to the LRO–20 composition (the LRO–37 alloy) had little effect on swelling.

Future work will include determination of degree of order and post–irradiation bend ductilities for the irradiated LRO alloys. Microstructural response, swelling, and bend ductilities will also be determined for the same alloys after irradiation to approximately 20 dpa in HFIR.

6.3.6 References

1. D. N. Braski, J. Bentley, and J. W. Cable, "Measurement of Degree of Order in Ordered Alloys by Convergent Beam Electron Diffraction Patterns," to be presented at the 40th ESMA Meeting, Washington, D.C., August 9–13, 1982.

2. D. N. Braski, "Microstructure and Tensile Properties of Neutron-Irradiated $(Fe_{0.61}Ni_{0.39})_3V$ Alloy," to be presented at 11th International Symposium on Effects of Radiation on Materials, ASTM, Scottsdale, Ariz., June 28–30, 1982.

3. D. N. Braski and K. Farrell, "Radiation Damage Structure in Ordered $(Co_{0.78}Fe_{0.22})_3V$ Alloy," Proceedings of 1980 EUREM Conference, The Hague, Netherlands, *Electron* Micros. 1: 284–85 (1980).

4. P. J. Maziasz and D. N. Braski, "Swelling of Path A PCA Irradiated to 10 dpa in HFIR," Sect. 3.1, this report.

7. PATH E ALLOY DEVELOPMENT — FERRITIC STEELS

7.1 POSTIRRADIATION NOTCH DUCTILITY AND FRACTURE TOUGHNESS BEHAVIOR OF AOD HEAT OF ALLOY HT-9 - J. R. Hawthorne (Naval Research Laboratory)

7.1.1 AOIP Task

The Department of Energy (DOE)/Office of Fusion Energy (OFE) has stated the need to investigate ferritic alloys under the AOIP program task. Ferritic Steels Development (Path E).

7.1.2 Objectives

Objectives of the present research task were to irradiate an Alloy HT-9 plate from the Fusion Ferritic Program reference heat at two temperatures, 93° and 288°C, and to perform postirradiation notch ductility and dynamic fracture toughness tests to assess the relative magnitude of radiation embrittlement produced at the two exposure temperatures.

7.1.3 Summary

Alloy HT-9 is being evaluated for potential application as a first wall material in magnetic fusion reactors. One objective of the current studies is the assessment of material notch ductility and fracture toughness in the pre- and postirradiation conditions.

Charpy-V (C_v) and fatigue precracked Charpy-V (PCC_v) specimens of a 1.7 cm thick plate from the HT-9 reference melt (AOD process) were irradiated at 93° and at 288°C to 7.8 X 10^{19} n/cm^2, E> 0.1 MeV, in a water-cooled test reactor. The C_v transition temperature elevation produced by the 93°C irradiation was more than three times that produced by the 288°C irradiation. The 93°C irradiation data showed the alloy to be unacceptable for 93°C service unless (only) elastic fracture resistance is acceptable. Good agreement was observed between C_v and PCC_v determinations of radiation-induced embrittlement.

7.1.4 Progress and Status

7.1.4.1 Introduction

The ferritic stainless steel compositions, HT-9 and 9Cr-1Mo (Mod.),

are being assessed for possible first wall applications in magnetic fusion reactors by the Magnetic Fusion Materials Program and for duct applications in liquid metal fast breeder reactors by the Cladding/Duct Alloy Development Program of the Department of Energy. For these proposed uses, fracture resistance properties before and after elevated temperature irradiation are being investigated. Specimen types include C_v specimens for notch ductility determinations, PCC_v specimens for dynamic fracture toughness (K_J) determinations and compact tension (CT) specimens for static fracture toughness determinations.

Current studies are aimed at exploratory evaluation of the radiation resistance of Alloy HT-9 plate material as a function of service temperature, using C_v and PCC_v specimens irradiated in controlled temperature assemblies in the water cooled reactor at the State University of New York at Buffalo (UBR). The plate was produced from the Fusion Ferritic Program reference heat (Electralloy Corporation Heat No. 9067) representing AOD processing. Plate heat treatment is described in reference 1. Specimens were taken in the longitudinal (LT, strong) test orientation only. Miniature PCC_v specimens (half standard size) and 2.54 mm thick CT specimens (0.5T size except for thickness) were included in the irradiation assemblies also; plans for these specimens are indicated below.

7.1.4.2 Material Irradiation

The specimens were contained in two, individually controlled irradiation assemblies. The assemblies were irradiated in tandem in a fuel lattice position of the UBR. Temperatures were monitored continuously by means of thermocouples welded to the specimens (approximately 50 percent specimen coverage). Neutron fluences were determined using iron neutron dosimeter wires placed within the specimen array and are reported here on the basis of a calculated neutron energy spectrum developed by the Hanford Engineering Development Laboratory under contract.' The total time at temperature was 798 hours; the target neutron fluence (E> 0.1 MeV) was 8×10^{19} n/cm^2.

7.1.4.3 Postirradiation Results

Postirradiation notch ductility determinations are illustrated in Fig. 7.1.1; postirradiation fracture toughness (K_J) determinations by the PCC_V test method are shown in Fig. 7.1.2. The K_J values are based on energy absorbed to maximum load corrected for specimen and test machine compliance, and were developed using the J-integral assessment procedures. (Note: K_J based on maximum load implies an absence of stable (i.e., rising load) crack extension and thus may overestimate the actual K_J at crack "initiation").

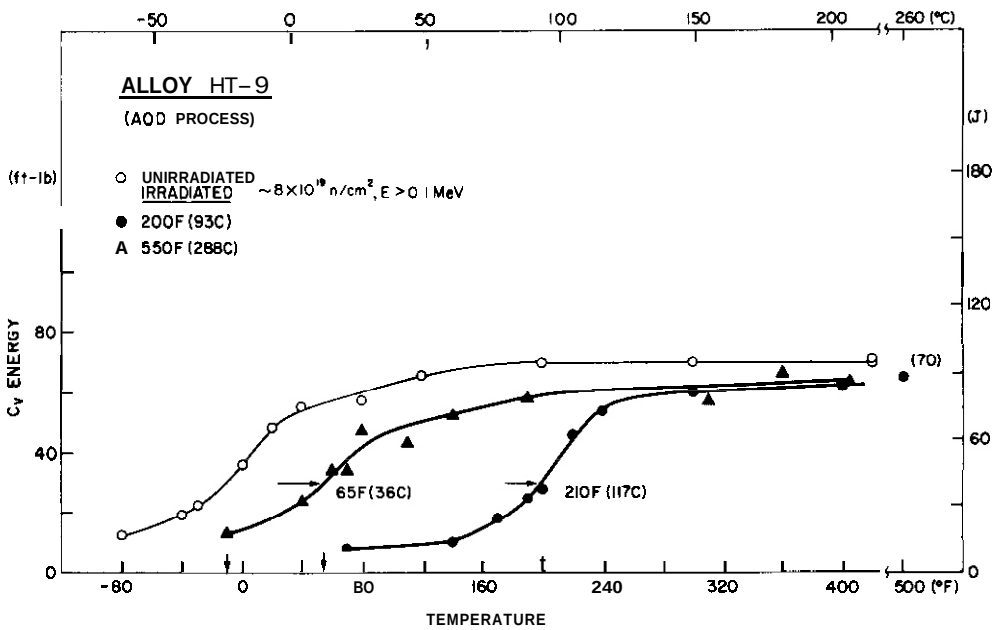

Fig. 7.1.1. Notch Ductility of Alloy HT-9 Plate (AOD Reference Melt) Before and After Irradiation at 93°C and at 288°C. Iron Neutron Dosimeter Wires Included in the Irradiation Assembly Showed Fluences ($E > 0.1$ MeV) to be 7.3×10^{19} n/cm^2 and 8.1×10^{19} n/cm^2, respectively.

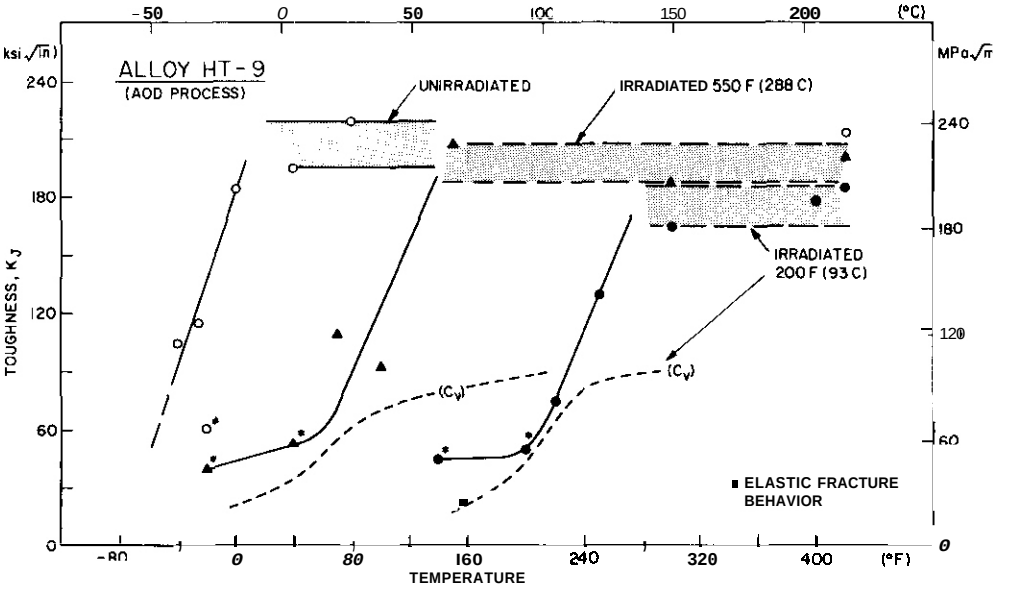

Fig. 7.1.2. Dynamic Fracture Toughness (K_J) of Alloy HT-9 Plate (AOD Reference Melt) Determined by the PCC_V Test Method Before and After Irradiation at 93° and at 288°C. The Dashed Lines Indicate Postirradiation C_V Test Behavior from Fig. 7.1.1. The PCC_V and C_V Specimens were Commingled in the Irradiation Units.

Several observations can be made from the results. Referring first to the C_V data (Fig. 7.1.1), the transition temperature elevation (415 index) produced by the 93°C irradiation was more than three times that produced by the 288°C irradiation. Accordingly, the radiation embrittlement resistance of Alloy HT-9 is quite exposure temperature dependent in this range. Equally important, the 93°C irradiation raised the 415 transition temperature up to the irradiation temperature even though the fluence is low, compared to expected service fluences. This result indicates that the alloy is unacceptable for 93°C service unless the designer is willing to accept (only) elastic fracture resistance. In contrast to the 93°C irradiation data, the data for the 288°C irradiation condition show a significant margin of toughness against further fluence accumulation. Because a trend of decreasing embrittlement buildup with increasing fluence has been observed in

other steels at fluences greater than ~ 2 to 3 x 10^{19} n/cm^2 , this toughness reserve suggests that a relatively high, total fluence accumulation may be possible before the transition temperature of the alloy closely approaches the 288°C irradiation temperature. For both the 288°C and the 93°C irradiation conditions, good upper shelf level retention is indicated by the data.

In general, the PCC_v test results (Fig. 7.1.2) support the C_v indications; that is, the postirradiation K_J 100 MPa$\sqrt{m}$ temperatures differ by about the same amount as the postirradiation C_v 41J temperatures. Furthermore, the upsweep in K_J toughness occurs at about the same temperature as the upturn in C_v notch ductility. The reductions in K_J upper shelf toughness by the irradiations also were small. Accordingly, C_v performance can be taken as a good indicator of PCC_v performance for this alloy for the irradiated condition. For the unirradiated condition, the limited K_J data presently available place the K_J transition curve somewhat below the C_v transition curve. Additional PCC_v tests are now planned to verify this indication. PCC_v versus C_v tests of another HT-9 material (separate melt) suggest that the displacement to lower temperature may simply be a manifestation of biased data scatter.

7.1.4.4 Postirradiation Evaluation of Miniature C_v and CT specimens

Tests of the miniature C_v specimens from the 93° and the 288°C irradiation assemblies are not to be conducted at NRL; rather, the plan called for the specimen tests to be made at a site (to be selected) with the necessary equipment installed or under construction. The irradiated specimens and a limited number of control specimens are available for immediate shipment.

Tests of the CT specimens (static mode) are planned for the next reporting period. Test temperatures will be chosen to bracket the brittle-to-ductile transition region suggested by PCC_v and C_v test results. J-R curves will be developed, test temperatures permitting. Test plans include examination of selected fracture surfaces by SEM; SEM examinations of C_v fracture surfaces are currently underway.

7.1.5 Conclusions

The experimental results show that the radiation resistance of Alloy HT-9 plate is highly dependent on the choice of irradiation temperature (93° vs 288°C). Furthermore, the results indicate that the alloy is unacceptable for 93°C high fluence service except for cases where elastic fracture resistance levels are allowable. For 288°C service, the alloy does show considerable promise for applications having lifetime fluences well in excess of 8×10^{19} n/cm^2.

Comparisons of C_v and PCC_v measures of radiation-induced embrittlement in HT-9 indicate good agreement.

7.1.6 References

1. J. R. Hawthorne, "Preparation of Alloy HT-9 and Modified Alloy 9Cr-1Mo Reference Plates for Unirradiated and Irradiated Condition Fracture Resistance Studies," Alloy Development for Irradiation Performance, Quarterly Progress Report for the Period Ending 31 Mar 1981, DOE/ER-0045/6, pp. 148-156.
2. Private communication, E. P. Lippencott, et al, to J. R. Hawthorne, Naval Research Laboratory, Letter Report, "Buffalo Light Water Reactor Calculation," dated Nov. 15, 1977.

7.2 IMPACT TEST RESULTS FOR IRRADIATED FERRITIC ALLOYS — W. L. Hu (Westinghouse Hanford Company)

To be reported in the next semiannual report.

7.3 MICROSTRUCTURAL EXAMINATION OF HT-9 AND 9Cr-1Mo CONTAINED IN THE AD-2 EXPERIMENT - D. S. Gelles and L. E. Thomas (Westinghouse Hanford Company)

7.3.1 ADIP Task

The Department of Energy (DOE)/Office of Fusion Energy (OFE) has cited the need to investigate ferritic alloys under the ADIP program task, Ferritic Steels Development (Path E). The tasks involved are akin to task number 1.C.2, Microstructures and Swelling in Austenitic Alloys and task number 1.C.1, Microstructural Stability.

7.3.2 Objective

The objective of this work is to provide guidance on the applicability of martensitic stainless steels for fusion reactor structural materials.

7.3.3 Summary

The microstructures of HT-9 and modified 9Cr-1Mo have been examined before and after irradiation in EBR-II in the AD-2 experiment to a fluence of 2.5 x 10^{22} n/cm^2 (E>0.1 MeV) at temperatures from 400 to 550°C. The precipitate structure of unirradiated HT-9 consists of $M_{23}C_6$ which forms at martensite lath and prior austenite grain boundaries. 9Cr-1Mo shows much less $M_{23}C_6$ at grain boundaries, but contains finely-dispersed (Nb,V,Cr)C within grains. Irradiation of both alloys at 400°C causes extensive additional precipitation, formation of a dislocation substructure, and, in 9Cr-1Mo, void formation. The irradiation-induced precipitate in HT-9 was identified as G-phase, a nickel silicide with fcc crystal structure and lattice parameter of 1.12 nm. Only very small additions of nickel are required in ferritics to promote the formation of G-phase. 9Cr-1Mo irradiated at 400°C formed rod-shaped Cr_2C. Above 450°C, the HT-9 formed additional $M_{23}C_6$, whereas the 9Cr-1Mo formed additional MC and a phosphide with Fe, Cr, and Mo. No voids were observed above 450°C in the 9Cr-1Mo alloy. The formation of finely-dispersed G-phase in HT-9 and Cr_2C in 9Cr-1Mo during irradiation below 450°C is

believed to contribute to observed irradiation hardening and increased DBTT.

7.3.4 Progress and Status

7.3.4.1 Introduction

A major part of the Path E effort to identify the applicability of ferritic alloys for a fusion reactor first wall has been irradiation of the AD-2 experiment in EBR-II.[1] This experiment covers the temperature range 400 to 550°C and has now reached a fluence of 2.5 x 10^{22} n/cm^2 (all fluences are given as E>0.1 MeV) or 11 dpa. The present effort is intended to provide microstructural information on two materials contained in that experiment: HT-9 the candidate Path E alloy and modified 9Cr-1Mo an alternate Path E alloy. The purpose is to relate microstructural changes to bulk properties.

7.3.4.2 Experimental Procedure

Specimens examined in this work were transmission electron microscopy (TEM) disks irradiated in the AD-2 experiment. Irradiation conditions are given in Table 1 and alloy chemistries are provided in Table 2. Specimen heat treatment conditions were HT-9: 40% CW + 1038°C/5min/air cool (AC) + 760°C/0.5 hr/AC and 9Cr-1Mo: 40% CW + 1038°C/1 hr/AC + 760°C/1 hr/AC. These specimen conditions were selected because they most closely matched the heat treatment conditions for mechanical properties test specimens which are being irradiated in the AI-2 experiment.

Both TEM foils and carbon extraction replicas were prepared from each specimen in order to allow complete precipitate identification during microstructural examination. The extraction technique, known as a "carbide" extraction procedure, involved electolytic etching in 10% HCl-90% methanol (operating conditions: 1 sec at 2V) followed by carbon coating and electrolytic stripping of the carbon film. Thin foils were prepared using a twin jet electropolishing device which had been altered for remote handling. The electrolyte was 5% perchloric acid - 95% butyl alcohol and operating conditons were YOV, 250 to 300 mA and moderate pump speed.

TABLE 1

Martensitic Stainless Steel Specimen Conditions Examined Following Irradiation in the AD-2 Experiment

Alloy	Specimen ID	Irradiation temperature °C	fluence (E>0.1 MeV) x 10^{22} n/cm^2
HT-9	2HCK	400	2.3
	2HCL	450	2.3
	2HCN	500	2.3
	2HCJ	550	2.5
9Cr-1Mo	2RCK	400	2.3
	2RCN	500	2.3
	2RCJ	550	2.5

TABLE 2

Compositions of Martensitic Stainless Steels

Alloy	Heat No.	C	Mn	Si	Ni	Cr	Mo	V	W	Nb	Cu	N	P	S
HT-9	91354	0.22	0.45	0.22	0.52	12.07	1.01	0.38	0.51	----	0.05	0.005	.008	.003
9Cr-1Mo	30182	0.087	0.37	0.17	0.10	8.45	0.89	0.23	----	0.08	0.03	0.05	.012	.003

TEM examinations were performed on an analytically equipped JEOL 100CX microscope operating at 100KV in transmission mode, and replica analyses were done on both the JEOL 100CX and a HB-501 microscope operating in scanning transmission mode. The HB-501 was equipped with an ultrathin window (UTW) KEVEX detector which provides analysis for elements with atomic numbers as low as carbon whereas the JEOL 100CX was equipped with a standard detector. For quantitative energy dispersive X-ray (EDX) microanalysis, a ratio method was used. In this method, the integrated counts in one X-ray peak for each element to be analyzed are multiplited by experimentally determined correction factors (K-factors)

and normalized to yield concentrations in weight percent. A digital filter method provided the peak integration above background, and correction was made for overlapping Kα and Kβ X-ray peaks for elements having adjacent atomic numbers. The elements routinely analyzed included Al, Si, Ti, V, Cr, Mn, Fe, Ni, Mo, Nb. (Carbon was not analyzed because the replicas were carbon coated.) For a few special cases, S and P were also analyzed. Visual inspection of the X-ray spectra showed no elements other than those analyzed. No correction was made for X-ray absorption or fluorescence in the extracted particles although such effects would have affected analyses of some particles thicker than 50-100 μm.

7.3.5 Results

7.3.5.1 HT-9 The preirradiation microstructure of HT-9 has been described previously[illegible]) and consists of tempered lath martensite with a recovered dislocation structure and $M_{23}C_6$ precipitates decorating lath and prior austenite grain boundaries.

Following irradiation, the HT-9 preirradiation microstructural features were retained. However, further microstructure changes were readily identified. Following irradiation at 400°C to 2.3 x 10^{22} n/cm^2, the dislocation structure was altered by the formation of irradiation induced dislocation loops and tangles. Precipitation of $M_{23}C_6$ on boundaries appeared to be more extensive (but no attempt was made to quantify the difference). Also, a high density of equiaxed precipitates on the order of 8 nm in diameter had developed in the matrix.

Following irradiation at 450°C to 2.3 x 10^{22} n/cm^2, the microstructure was quite different. Examples of both irradiation induced dislocation formation and fine precipitation in the matrix could be found, but the densities were much lower. In fact, the precipitate was only present between very widely spaced martensite lath boundaries and no dislocation loops were seen.

Following irradiation at 500°C to 2.3 x 10^{22} n/cm^2 and following irradiation at 550°C to 2.5 x 10^{22} n/cm^2 the microstructures looked much the same. The $M_{23}C_6$ particles at lath and prior austenite grain boundaries

had coarsened and additional $M_{23}C_6$ formed within subgrains. However, the change in precipitate distributions is not expected to alter bulk properties significantly. The dislocation structures observed in the 550°C specimen showed extremely well developed subgrain tilt boundaries typical of recovery.

Examples of these HT-9 microstructures from TEM are provided in Figures 1 and 2. Figure 1 shows low magnification micrographs of the unirradiated structure (a), the structure following irradiation at 400°C (b), at 450°C (c), and at 550°C (d). The micrographs were selected to show both prior austenite boundary and subgrain structures. Figure 2 provides comparison of the irradiated microstructures at higher magnification. The micrographs were selected to show both precipitate and dislocation structures. In Figure 2a, showing the specimen irradiated at 400°C, the small spherical precipitates are imaged by strain contrast and appear as dark features, the $M_{23}C_6$ particles present prior to irradiation appear as elongated particles and examples of dislocation loops can be found. Following irradiation at 450°C, a region with the equiaxed precipitate particles is shown in Figure 2b and examples of the structures developed at 500°C and 550°C are shown in Figures 2c and 2d.

Extraction replicas confirmed these results. Evidence for the large $M_{23}C_6$ particles and the fine equiaxed particles which formed at 400°C could be found. Examples are given in Figure 3. Figures 3a and b shown examples of the replica from the 400°C irradiation condition a) at low magnification and b) at high magnification. However, diffraction patterns of areas which contained the fine equiaxed particles showed very few diffraction spots and EDX analysis of such areas gave no compositional information. The images in Figure 3b are therefore castings of the particles in the carbon coating and the particles themselves had disappeared. Figures 3c and d provide low magnification examples of the 500 and 550°C irradiation condition. Both contain a number of particles in regions away from martensite lath and prior austenite grain boundaries. Such particles probably formed during irradiation, as indicated by the larger sizes observed in the 550°C condition. EDX analysis of the HT-9 extraction replicas only showed $M_{23}C_6$ with composition similar to the $M_{23}C_6$

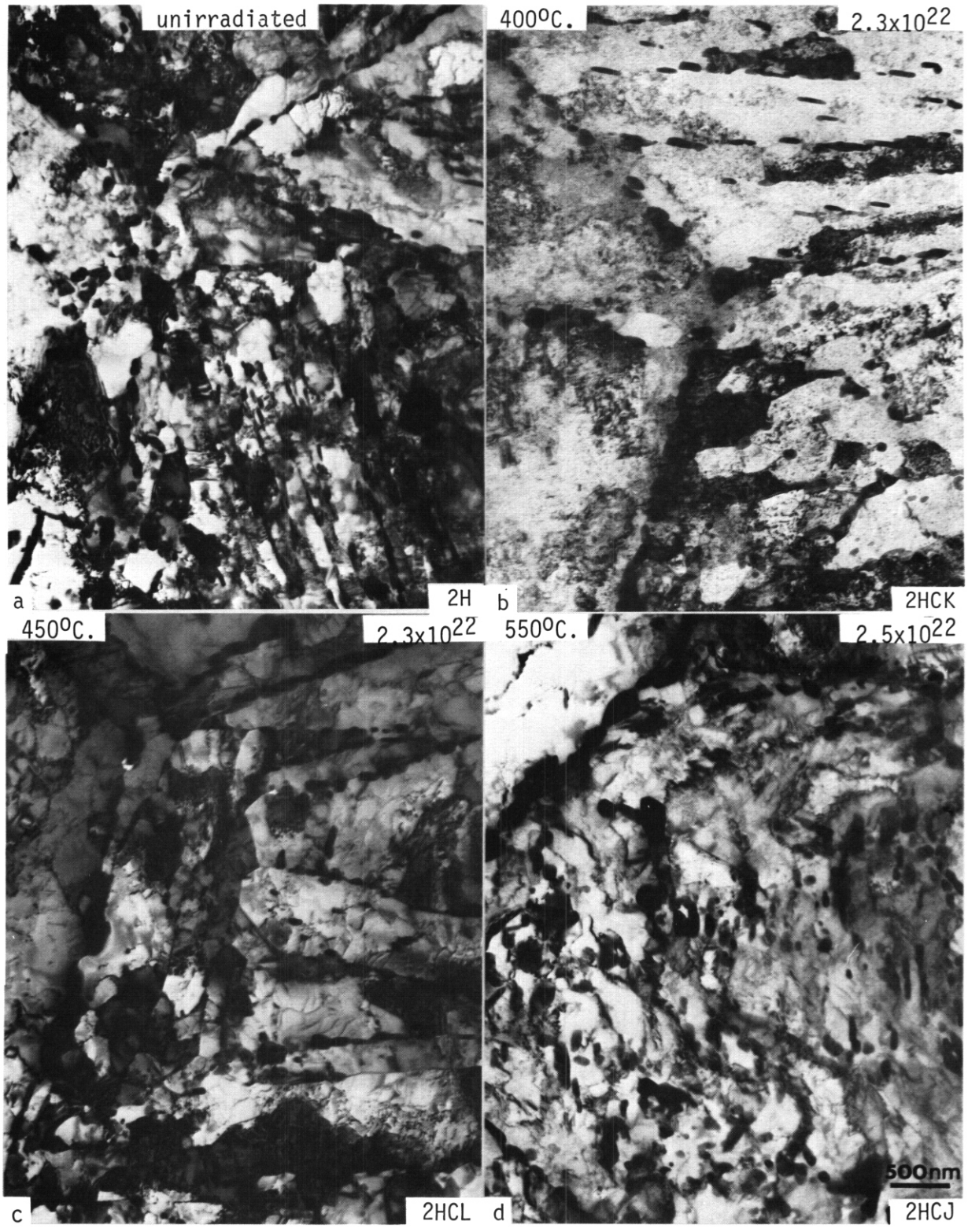

Figure 1 – Low Magnification Micrographs of HT-9

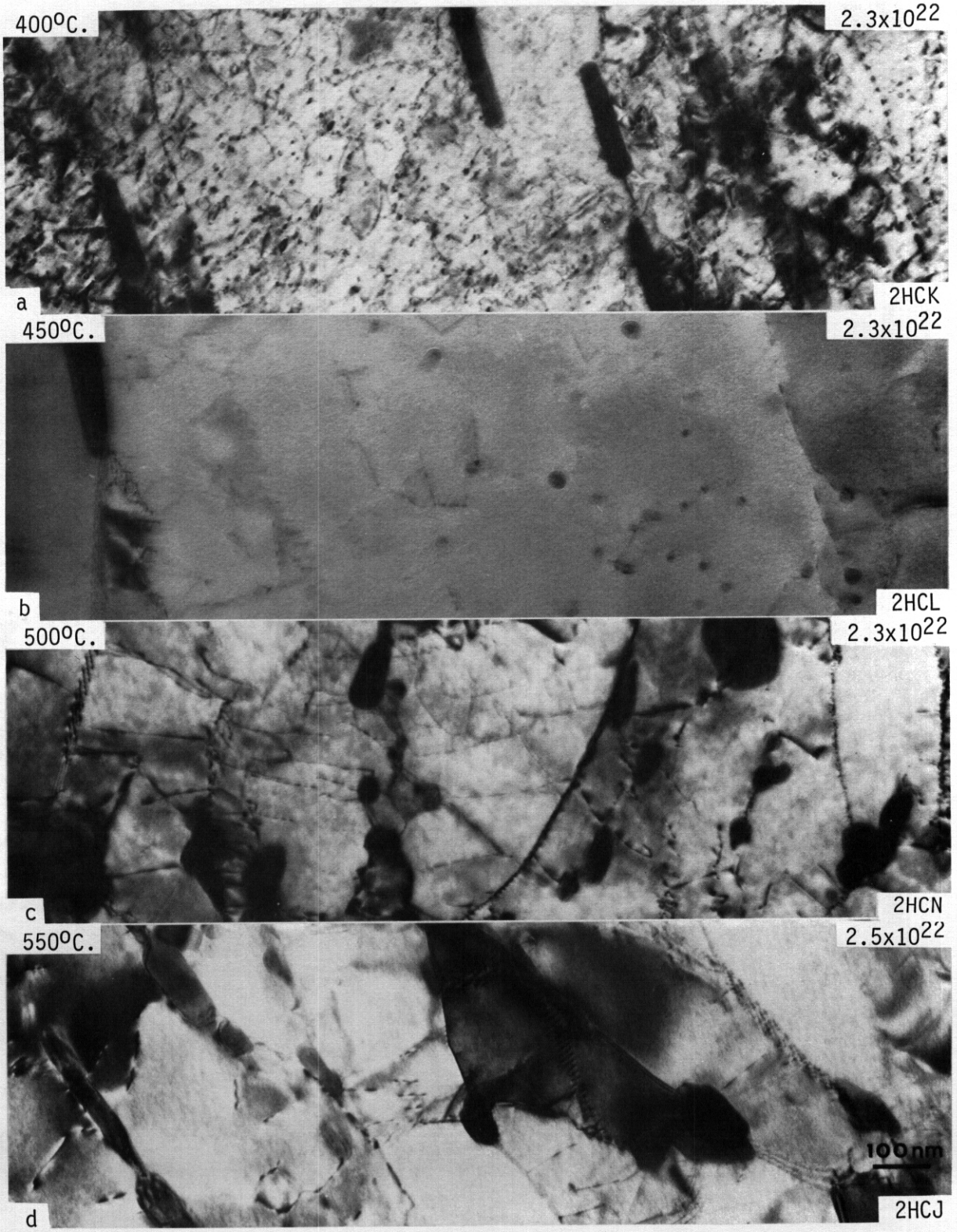

Figure 2 - Microstructures of HT-9 at Higher Magnification

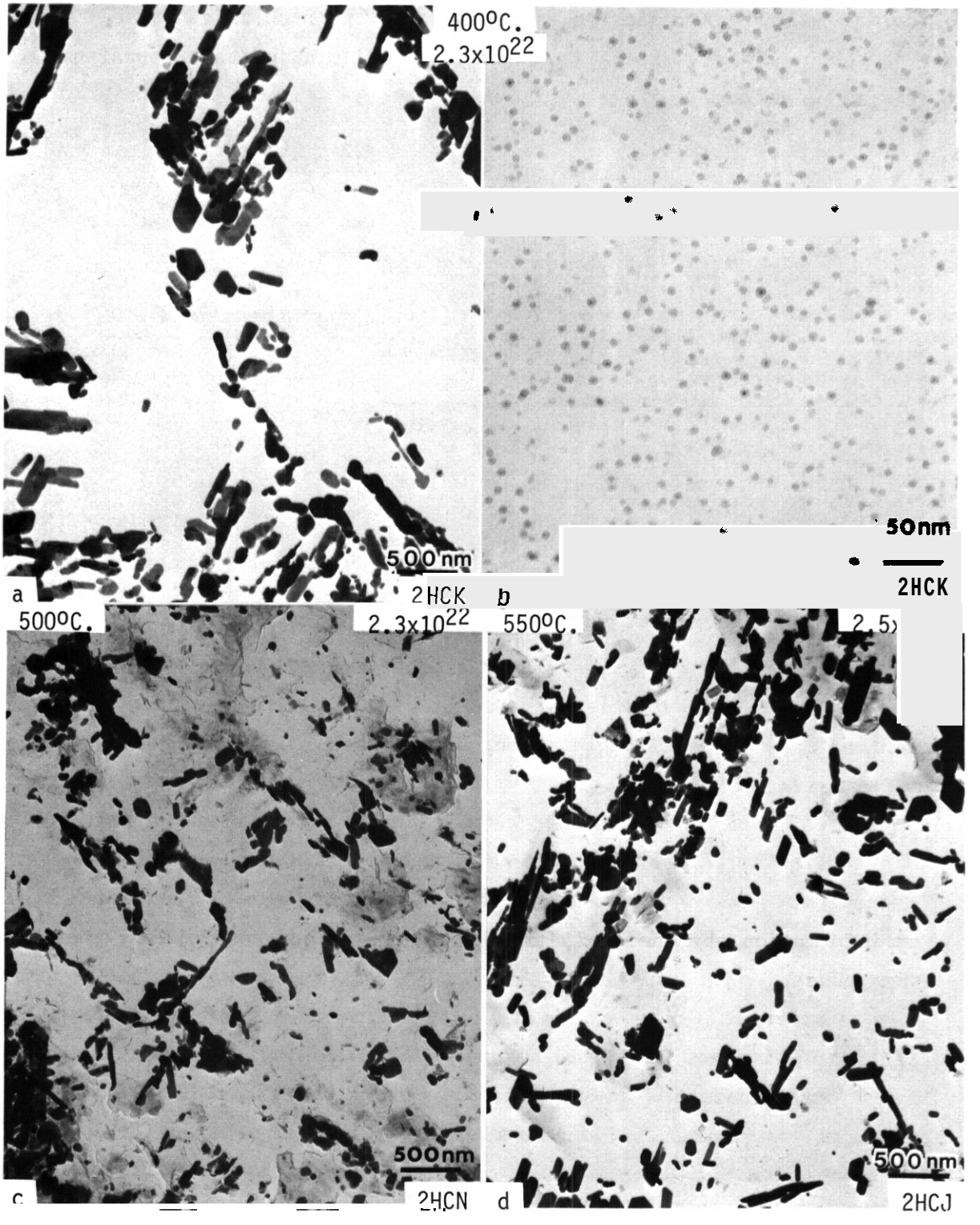

Figure 3 - Extraction Replicas of HT-9

formed prior to irradiation as is shown by the results given in Table 3. Thus all of the $M_{23}C_6$ particles, including those apparently formed in reactor had similar compositions.

TABLE 3

Second-phase Compositions (Wt %) in HT-9 Specimens from the AD-2 Test

HT-9 "Carbide" extraction replica (only $M_{23}C_6$ extracted)

Alloy Code/Conditions	Si	V	Cr	Fe	Mo	no other elements detected
2H unirradiated	0.8	1.4	60.1	29.8	7.9	
2HCK 400°C Irrad.	1.0	1.4	59.9	32.0	5.7	
2HCL 450°C Irrad.	1.2	1.3	60.5	30.7	6.3	
2HCN 500°C Irrad.	0.8	1.0	67.8	22.4	8.0	
2HCJ 550°C Irrad.	0.5	1.6	71.1	20.0	6.8	

The phase which forms in HT-9 at 400°C proved to be very difficult to identify. The particles were small. This resulted in weak electron diffraction information. A strong orientation relationship existed between the particles and the ferrite matrix. This resulted in strong double diffraction and created further ambiguity in interpreting diffraction patterns. Extraction techniques failed to isolate the precipitate and so no phase composition was available. Therefore, based on information obtained only from HT-9, it was not possible to identify this phase.

However, the phase which was observed in HT-9 gave diffraction patterns which had been seen before. AISI 416 contained this phase following irradiation at 425°C to 5.1 x 10^{22} and 15.8 x 10^{22} n/cm^2. Also, an experimental alloy known as E102 with composition (Fe-1.27Ni-2.79 Cr-1.76Mo-0.35S, -0.37Mn -0.15C) contained this phase following irradiation at 425°C to 9.8 x 10^{22} n/Cm^2. The E102 specimen contained larger particles so that it was possible using EDX to obtain a composition determination for particles on the edge of a thin foil. The phase was found to be rich in nickel, iron, silicon and manganese with approximate

composition Ni-24.1 Fe-12.7 Si -8.7 Mn -3.8 Mo-1.9Cr. The phase was therefore highly enriched in nickel, silicon and manganese. The tentative identification of the phase as Gphase, an fcc phase with lattice parameter 1.1198 nm of formula $Ti_6Ni_{16}Si_7$ (or $Mn_6Ni_{16}Si_7$) [4], was found to be consistent with electron diffraction patterns. This is demonstrated in Figure 4 which shows electron diffraction patterns of HT-9 irradiated at 400°C to 2.3 x 10^{22} n/cm^2. Patterns for foil orientations of (011) (001) and (112) are shown and the G-phase spot patterns are indexed for each. The lattice parameter measured from these patterns is 1.12 nm. Therefore, neutron irradiation results in strong partitioning of G-phase forming elements in martensitic steels at low temperature. G-phase forms in HT-9, AISI 416 and E102 because there is sufficient nickel and silicon, and the amount present is directly proportional to the amount of nickel present. The phase does not form in modified 9Cr-1Mo because the nickel content is purposefully limited in that alloy.

7.3.5.2 9CR-1Mo

The preirradiation microstructure of modified 9Cr-1Mo was similar in several ways to that in HT-9. Lath and prior austenite grain boundaries contained large blocky $M_{23}C_6$ but the particles were smaller and less numerous in the 9Cr-1Mo. The dislocation structure was recovered into subgrain boundaries. Unlike the HT-9 however, 9Cr-1Mo contained a high density of small, intragranular MC carbides. The metal content of the MC particles included mainly Nb, V, and Cr, with individual particles varying widely in the proportions of these elements (see Table 4).

Following irradiation, the preirradiation microstructural features were retained but several changes in microstructure were found. The specimen irradiated to 400°C developed a high density of irradiation-induced dislocations. Both dislocation loops and tangles were found. Also, faceted voids were formed at 400°C. The number density of voids was quite low and the largest voids were 20 nm in diameter. Therefore the resulting density change was negligible, although higher swelling may be anticipated at higher fluence. In addition, small rod-shaped precipitates formed during irradiation at 400° C. EDX analysis showed

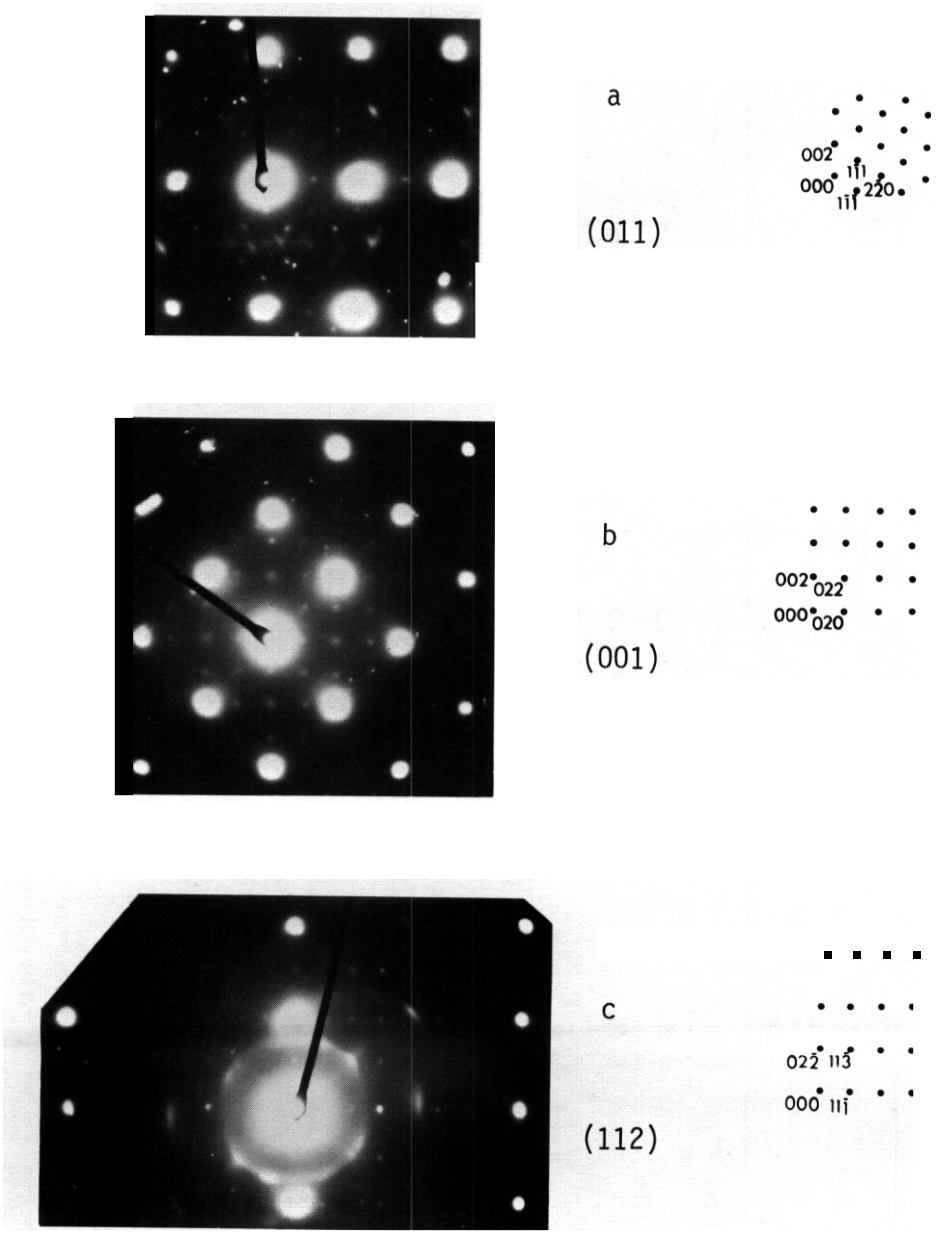

Figure 4 - Diffraction Patterns of G-Phase in HT-9 Irradiated at 400°C. The Corresponding Gphase Patterns are Shown Indexed.

TABLE 4 Phase Compositions (Wt %) in Fe-9Cr-1Mo Specimens from the AD-2 Test

Alloy Code/Condition	Phase	Si	V	Cr	Mn	Fe	Ni	Mo	Nb	Other
2R Unirradiated alloy *	Matrix	--	1.0	9.2	--	89.8	--	--	--	--
	$M_{23}C_6$	--	0.3	53.7	--	39.0	--	6.9	--	--
2R Unirradiated **	$M_{23}C_6$	--	1.0	56.4	--	35.4	--	7.2	--	--
	MC	--	48.5	8.1	--	--	--	--	43.4	--
	MC	--	7.1	1.0	--	--	--	--	91.9	--
2RCK 400°C Irradiated **	$M_{23}C_6$	--	1.3	57.4	--	33.9	--	7.4	--	--
	MC	--	21.0	18.5	--	--	--	--	60.5	--
	MC	--	47.5	52.5	--	--	--	--	--	--
	Cr_2C	--	--	96.5	--	1.5	--	2.0	--	--
2RCN 500°C Irradiated **	$M_{23}C_6$	--	1.3	58.4	--	33.1	--	7.2	--	--
	MC	--	29.3	12.3	--	--	--	--	58.5	--
	MC	--	58.1	10.7	--	5.0	--	--	26.2	--
	MC	--	13.8	3.0	--	--	--	--	83.2	--
2RCJ 550°C Irradiated **	MC	--	26.2	4.5	--	--	--	--	69.3	--
	Fe_2Mo-Laves	2.2	1.0	13.4	0.6	52.2	--	30.6	--	--
	MnS	--	1.6	2.3	49.0	--	--	--	--	47.1S***
	FeCrPMo	--	3.6	18.5	--	43.2	--	16.2	--	18.5P

* Electropolished TEM disk
** Extraction replica
*** Analyses for P and S used calculated correction factors (K-factors); all others K-factors were measured.

primarily chronium with no nitrogen or oxygen and electron diffraction ring patterns gave a consistent identification as Cr_2C. Therefore, the irradiation induced phase formed in 9Cr-1Mo at 400°C is identified as Cr_2C.

Following irradiation at 500°C, the microstructure of modified 9Cr-1Mo was more typical of the preirradiation structure. The dislocation density between martensite laths was low and typical of a recovered structure. Preirradiation precipitate phases were retained but further MC precipitation had developed.

Following irradiation at 550°C, the dislocation structure was recovered and the precipitates formed prior to irradiation were retained. Some subgrain growth may have occurred (but this was very difficult to prove due to the variable subgrain structure of the preirradiation microstructure). In-reactor precipitation was of two types: MC containing various amounts of vanadium, chromium and niobium, and a phosphide phase rich in iron, chromium and molybdenum. The phosphide was of lath morphology and was very non-uniformly distributed. Bands of phosphide particles were found widely scattered through the replica specimen. Also local regions containing concentrations of MnS and Fe_2Mo - Laves phase particles were found. Therefore, it appears that the modified 9Cr-1Mo material used in this study (heat number 30182) was not well-homogenized.

Examples of the microstructures found in modified 9Cr-1Mo are shown in Figures 5 and 6. Figure 5 provides low magnification micrographs of the preirradiation microstructure (a) and the structures following irradiation at 400°C (b), 500°C (c) and 550°C (d). Both prior austenite grain boundaries and typical lath martensite structures are shown. Figure 6 provides higher magnification examples of the microstructure found following irradiation. Figure 6a, the 400°C irradiation condition was selected to show the faceted voids in this material. The dislocation structure is in weak contract and examples of elongated Cr_2C and equiaxed MC can be identified. Figures 6b and c provide examples of the dislocation structures in higher contrast. Following irradiation at 500 and 550°C the dislocation arrays which can be seen are typical of

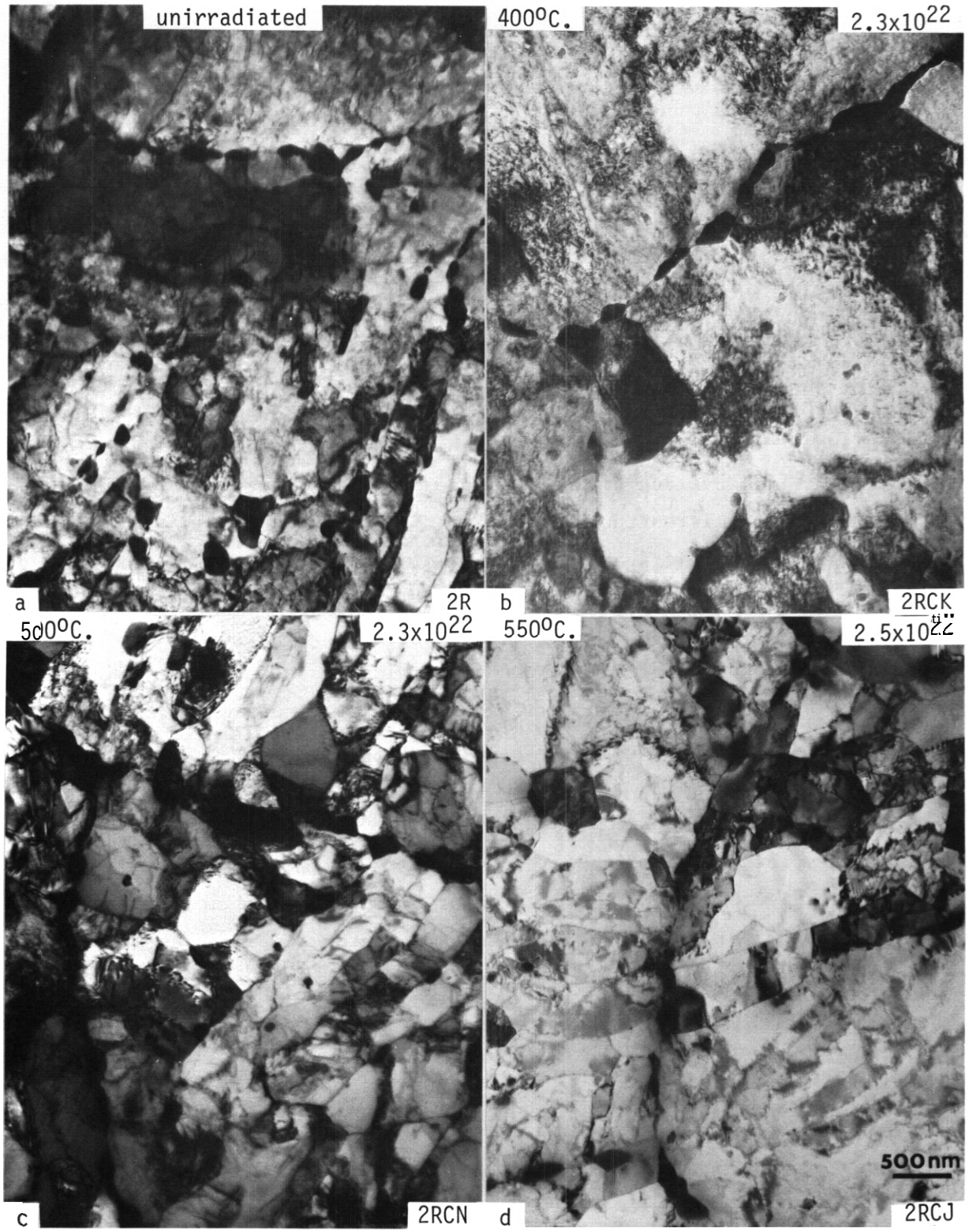

Figure 5 - Low Magnification Micrographs of Modified 9Cr-1Mo

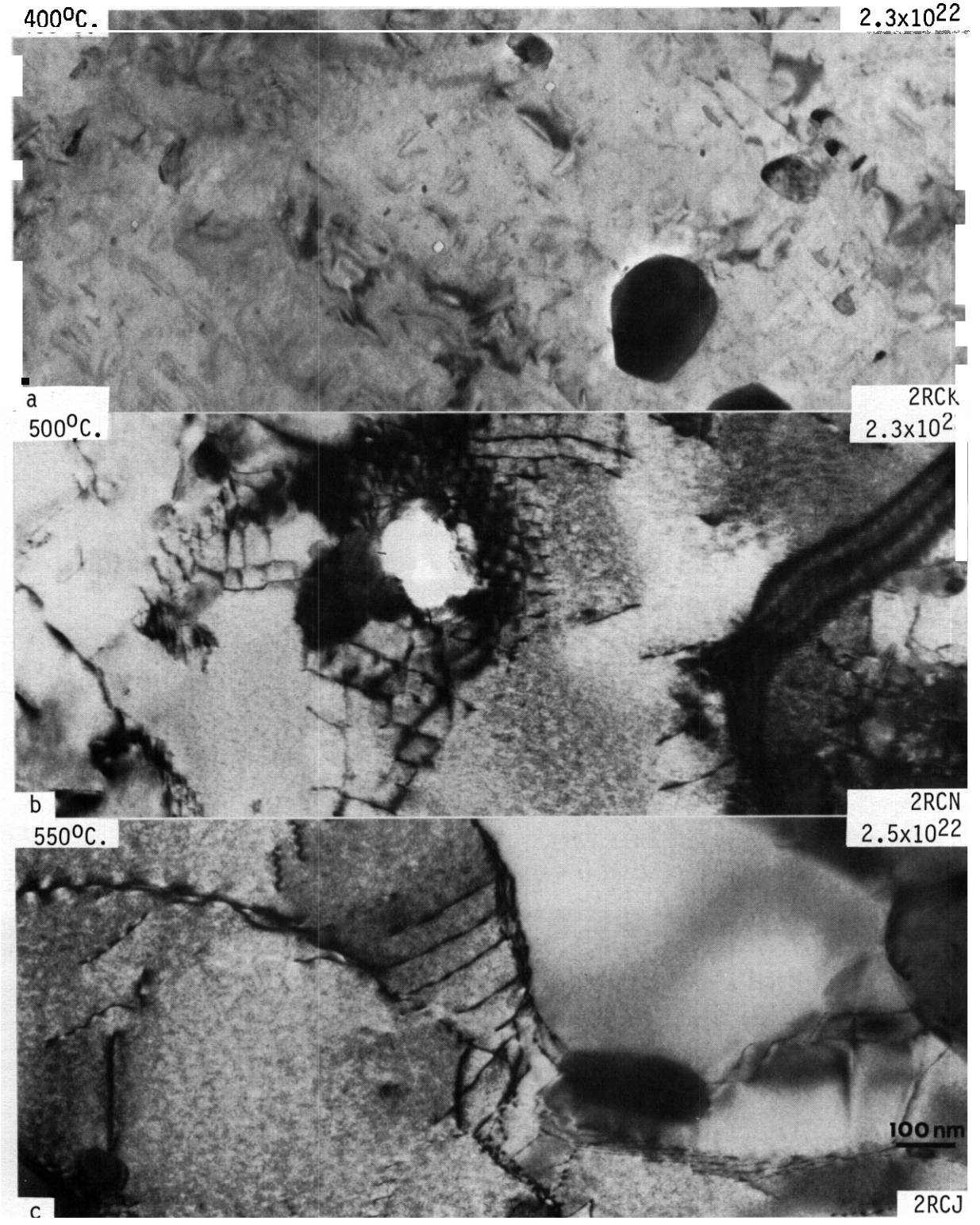

Figure 6 - Microstructures of Modified 9Cr-1Mo at Higher Magnification

subgrain boundary dislocation networks.

Extraction replica micrographs of 9Cr-1Mo are given in Figure 7 for the 400°C, 500°C and 550°C conditions. The high magnification example of the 400°C condition shows the typical highly elongated morphology of the Cr_2C structure, and an example of the Cr_2C electron diffraction pattern is inset. Figure 7d provides an example of the phosphide particles and a typical phosphide diffraction pattern is inset. The phosphide particles in Figure 7d are the lath shaped features whereas the MC particles are more equiaxed. Typical compositions of the phases are given in Table 4.

7.3.6 Discussion

The present work further demonstrates the tendency of martensitic stainless steels to develop precipitates during irradiation [4]. High densities of small precipitate particles which form at 400°C are apparently responsible for observed irradiation hardening and DBTT increases [5]. Phase identification therefore provides important further understanding which could be used for guidance on alloy composition specifications. The phases which form following irradiation at 400°C have been identified as G-phase in HT-9 and Cr_2C in 9Cr-1Mo.

7.3.7 Consequences of G-Phase

G-phase precipitates are believed to be responsible for the large shift in ductile brittle transition temperature (DBTT) found in HT-9 following irradiation to 1.1×10^{22} n/cm^2 at 425°C[5]. A similar conclusion was reached in a thermal aging study of a 12%Cr-4%Ni steel [6]. In that study hardening occurred within 100 hours when aged at 450°C and led to a concurrent increase in DBTT. The precipitation hardening phase was found to be fcc with lattice parameter 1.115 nm and composition Ni-15.5Cr-13.3Si-10.0Fe-8.Mn and therefore was the same as the G-phase found in this work.

It must therefore be anticipated that additions of nickel and silicon to martensitic stainless steel will promote Gphase formation (both in and out-of-reactor) which will alter mechanical properties.

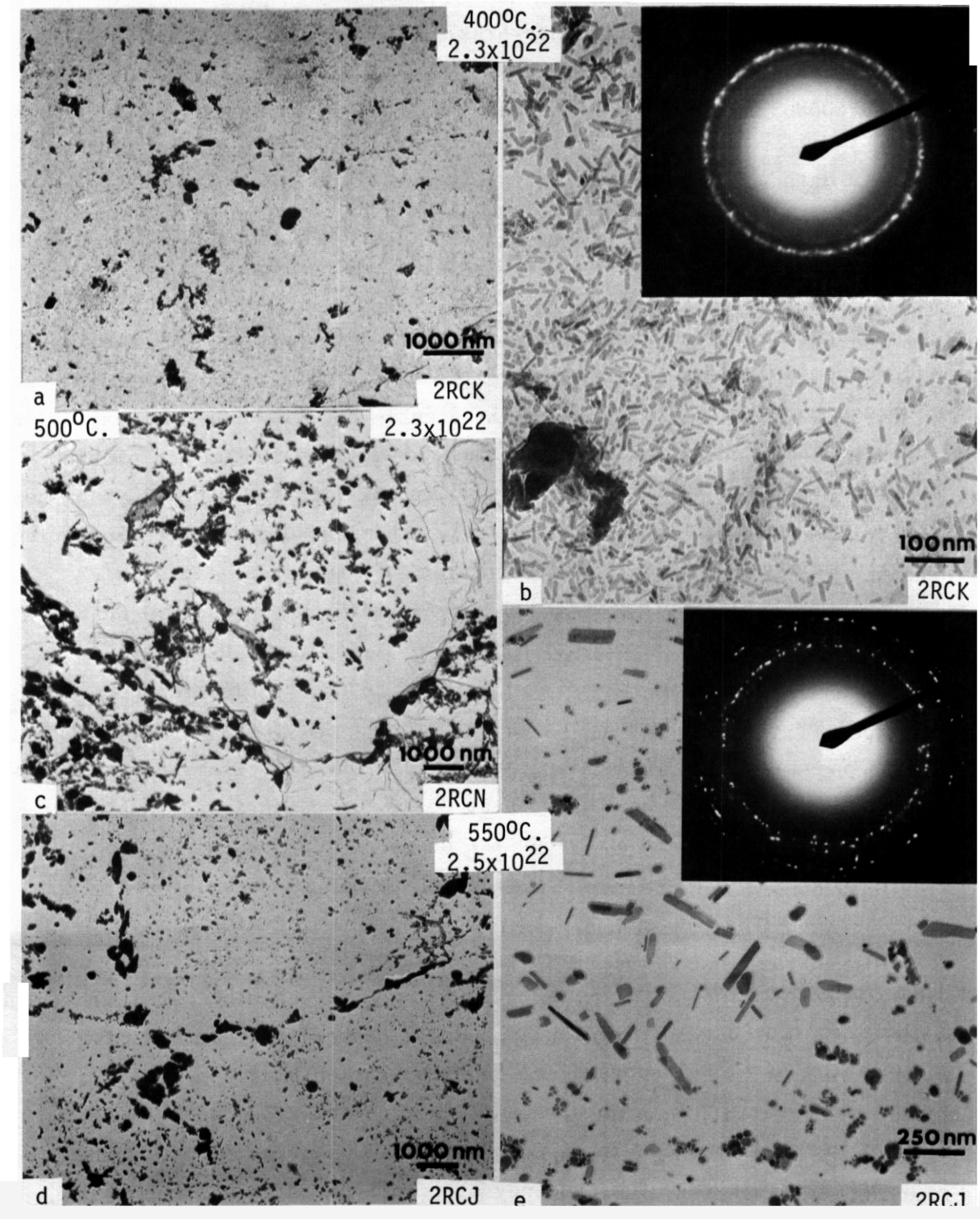

Figure 7 - Extraction Replicas of Modified 9Cr-1Mo. Examples of Diffraction Patterns for Cr_2C (b) and Phosphide (e) are Inset.

The experimental alloys designed to study effects of helium generation on mechanical properties following irradiation in HFIR [7] can also be expected to develop G-phase. Precipitation strengthening due to Gphase formation is likely responsible for large increases in post-irradiation tensile data [8,9] and strength increases should not be attributed only to displacement damage.

7.3.8 Effects of Precipitation

Although HT-9 and modified 9Cr-1Mo are both martensitic steels, alloy chemistries are sufficiently different so that microstructural response to irradiation is quite different. Modified 9Cr-1Mo was designed to purposefully limit nickel additions and employ vanadium and niobium additions to form MC carbides prior to irradiation. HT-9 employs higher nickel and carbon additions in order to minimize delta ferrite formation, and its main carbide formers are chromium and tungsten. Thus, HT-9 forms mainly $M_{23}C_6$ whereasmodified 9Cr-1Mo forms MC carbides. When nickel and silicon are present, G-phase will form. If G-phase does not form, some other phase probably will, such as Cr_2C. Different precipitation sequences can lead to different properties. G-phase formation appears to inhibit void swelling in ferritic steels. Examples are found in AISI *416* [4], E102 and the present work. In comparison, most other ferritic steels develop voids but few do so at fluences as low as $2x10^{22}n/cm^2$. Modified 9Cr-1Mo therefore appears to possess poor irradiation resistance. (This is not expected to be a problem with regard to swelling because the ferritic alloy class swells slowly even when voids are present.) Gphase formation also contributes to radiation hardening. The data of references 8 and 9 show a straightforward correlation of nickel content and postirradiation yield strength. Conversely, if nickel is not present irradiation hardening is reduced. Similar correlations can be expected for DBTT behavior. These correlations can arise from the tendency of relatively small additions of Ni and Si to promote Gphase formation in ferritic steels.

7.3.9 Conclusions

Specimens of HT-9 and modified 9Cr-1Mo have been examined following irradiation in EBR-II over the temperature range 400 to 550°C to fluences of 2.5 x 10^{22} n/cm^2. The following is found:

1) Irradiation at 400°C promotes extensive dislocation and precipitate development in both alloys. The dominant irradiation induced phase in HT-9 at 400°C is G-phase, a nickel silicide. In 9Cr-1Mo it is Cr_2C. Voids had formed in 9Cr-1Mo.

2) At higher temperatures, microstructural changes were not as extensive. Further carbide precipitation occurred and dislocation development was mostly of a recovery nature. Phospide precipitates were identified in 9Cr-1Mo at 550°C.

3) Irradiation at temperatures of 450°C and below can be expected to have the greatest effect on postirradiation mechanical properties.

7.3.10 Future Work

Specimens of HT-9 will be examined following irradiation in HFIR to 10dpa at 300 and 400°C.

7.3.11 References

1. RJ Puigh & NF Panayotou, "Specimen Preparation and Loading for the AD-2 Ferritics Experiment" DOE/ER-0045/3 (4-6/1980) 261.
2. DT Peterson "Microstructural Examination of HT-9 Archive Material from the AD-2 Test" DOE/ER-0045/5 (10-12/1980) 212
3. DS Gelles "Microstructural Examination of Several Commercial Ferritic Alloys Irradiated to High Fluence" J Nuc Mat 103 & 104 (1982) 975
4. EI Gladyshevskii, PI Kripyakevich, Yu. B. Kuz'ma and M.Yu. Teslyuk Sov. Alloys Cryst 6 (1962) 615
5. FA Smidt, Jr., JR Hawthorne and V Provenzano "Fracture Resistance of HT-9 After Irradiation at Elevated Temperature" Effects of Radiation on Materials: Tenth Conference ASTM STP 725, 1981, p.269
6. GT Brown & RT Allsop "Embrittlement of a 12%Cr-4%Ni Steel" JISI (1960) 435
7. RL Klueh &JM Vitek "Characterization of Ferritic Steels for HFIR Irradiation" DOE/ER-0045/3 (4-6/1980) 294
8. RL Klueh and JM Vitek "Tensile Properties of Ferritic Steels after Low Temperature HFIR Irradiation DOE/ER-0045 (10-12/1980) 218
9. RL Klueh & JM Vitek "Tensile Properties of Ferritic Steels after Low-Temparature HFIR Irradiation" DOE/ER-0045/6 (103/1981) 139.

7.4 THE PROCUREMENT AND CHARACTERIZATION OF THE ELECTROSLAG REMELTED NATIONAL FUSION PROGRAM HEAT OF 12Cr-1Mo STEEL - T. A. Lechtenberg (General Atomic Company)

7.4.1 ADIP Task

The Department of Energy (DOE)/Office of Fusion Energy (OFE) has stated the need for this investigation under the ADIP program task. Ferritic Steels Development.

7.4.2. Summary

Previously it was reported that a 30.000 lb heat of a 12Cr-1Mo steel melted to the specifications of Sandvik HT-9 was procured by General Atomic Company from Electralloy Corporation for the Ferritic Steel Program(1). This heat of argon-oxygen decarburized (AOD) 12Cr-1Mo steel has. since. been electroslag remelted (ESR) by Universal Cyclops Corporation in Pittsburg. and converted to plate and bar stock. This remelted heat (No.9607R2) was within the chemical specification requirement of HT-9. The remelted ingot was homogenized at 1100C for 16 hrs prior to conversion to the product forms. After conversion to plate and bar stock. each form was given a stress relief at 700C for 6 hrs. Subsequent mechanical property analysis on the 0.625 in (1.58 cm) plate has shown that it meets the strength and tensile elongation specifications. The UTS was 121 ksi (835 MPa), the yield stress was 87.5 ksi (604 MPa), and the elongation was 21%. The upper shelf energy determined on standard Charpy impact specimens was 85 ft-lbs (115J) as compared to the upper shelf of the AOD heat of 66 ft-lbs (89J). Microstructural examination showed a uniform tempered martensitic structure with a delta ferrite content less than 1%.

7.4.3. Remelting and Conversion to P

The AOD ingots were shipped to Universl Cyclops in Pittsburg for

electroslag remelting. The slag contained CaF, CaO, and Al_2O_3. The castings were two 20 inch rounds. These were hot-topped (3% from tops and 1% from bottoms of the castings). and slowly cooled in a lime pit. The castings were transferred to a soaking pit and homogenized at 1200C for 16 hrs. The castings were descaled and rough ground.

One casting was shipped to Bridgeport. PA where it was reheated to a rolling temperature of 1050-1090C (first to 650-750C for 30 minutes. then brought to temperature) for 4 hours and bloomed to 8 in x 13 in x roll length. cooled and cut with an abrasive saw. These were then reheated by the same process to 1050-1090C and held as before. then bloomed to 4 in x 15 in x roll length. and furnace cooled. The slabs were annealed at 1050-1090C as before with the same preheat cycle. These were furnace cooled. and cut into mults for the final hot rolling. The mults were reheated as before to 1050-1090C and all plates were rolled in one pass to their final dimensions. excepting the 0.125 inch which was brought to 0.635 inch. reheated to 1050-1090C then final rolled to 0.125 inch. The plates were annealed for 2 hours at 850C, cooled at 5C/hr to 700C, and then held for 6 hours. and air cooled for stress relief. The plates were then inspected with ultrasound. ground and deburred.

The bar stock was shipped to the Titusville plant and treated similarly to that converted to plate. The casting was heated to 1050-1090C in stages of 650-750C and held for 30 minutes then to the rolling temperature of 1050-1090C. These were bloomed to a 4 inch billet, cut in thirds. reheated and rolled to the 2 and 3 inch bar. Some of the 2 inch bar was reheated. then bloomed to the 1 inch bar. All these were cooled slowly as for the plate. then given the stress relief as for the plate. These were cut to final lengths and centerless ground.

So, plate and bar were in the stress relieved condition. and prior to testing, require a standard heat treatment of 1050C for 1/2

hour, and 760 for 2-1/2 hrs both followed by an air-cool for a tempered martensite structure.

7.4.4. Characterization of the ESR 12Cr-1Mo

Chemical analysis was performed by International Nickel on the ESR heat of 12Cr-1Mo steel after being received at General Atomic. The results are given in Table I along with the AOD chemistry and other heats of HT-9 for comparison. All of the elemental amounts were within the DIN 17175-79 specification, Werkstoff 1.4935. for Sandvik HT-9. The chemistry also compared well with the specifications for 12Cr-1Mo dictated by the Breeder program. The levels of several embrittling specie were lower than those values found in the AOD heat prior to remelting. and were significantly lower than the Breeder program specifications in titanium and sulphur. The phosphorous content decreased from the AOD heat to 0.016 wt% (Breeder specified at 0.02 wt%).

Material for tensile and Charpy impact specimens were heat treated at 1050C for 30 minutes. and 760C for 2.5 hrs, both followed by an air-cool in the 0.625 inch plates form. Specimens were machined. The tensile properties for the ESR heat (9607R2) in Table II and compared to the National Fusion AOD (9607) and Breeder ESR (91354) heats of 12Cr-1Mo. The UTS was 121.0 ksi. the yield stress was 87.5 ksi, and the total tensile elongation was 21.0%. The UTS is at the high end of the Sandvik specifications. being 110/122 ksi. The yield strength was greater than the specification of 71 ksi minimum. and similar to that measured on the breeder heat No. 91354 which was 88 ksi.

Impact transition curves were determined for the ESR heat in the longitudinal (L-T) and transverse (T-L) rolling directions. The data is compared in Figure 1 to the AOD heat and to the ESR Breeder heat (No. 91354). All the material was in the standard heat treated condition. that is 1050C for 1/2 hr. followed by 2.5 hrs at 760C, both followed by an air-cool. The upper shelf energies for the Fusion ESR heat are 85

TABLE I

A SUMMARY OF CHEMICAL COMPOSITION

FOR HEATS OF HT-9

HEAT	CHEMICAL COMPOSITION LIMITS													
	C	Si	Mn	P	S	Cr	Mo	Ni	V	W	N	Al	Ti	Other (Max.)
DIN SPEC (1.4935)	.17/ .23	.1/ .50	.3/ .80	0.035 (max)	0.035 (max)	11.0/ 12.5	0.8/ 1.20	.3/ .80	.25/ .35	.4/ .6				
AOD (9607	.20	[illegible]	57	0 01[illegible]	0 007	11 6[illegible]	1.01	52	30	57	.044	009	< 01	O_2 .0[illegible]3, C[illegible] 0.01 Cu .0[illegible], Co 0.09, As 0.004 Z[illegible] .002, B 0.001, P[illegible] .001, S[illegible] 0.001, Sb trace
ESR (960[illegible]R[illegible])	.20	1[illegible]	57	[illegible] 016	[illegible] 003	12 1	1 0[illegible]	51	2[illegible]	[illegible]5	.02[illegible]	.006 .007	0[illegible]1	Cu .07, Co <0.05, As [illegible].003 O_2 .002, [illegible] <.001, Bi <.001 Pb <.0001, [illegible]b 0.00[illegible]5 Sn 0.004, C[illegible] <.001
Breeder (91354)	.17/ .23	.2[illegible] .3[illegible]	.4[illegible] .7[illegible]	0.020 (max)	0.010 (max)	11.0/ 12.5	0.8[illegible] 1.2[illegible]	.3[illegible] .8[illegible]	.25/ .35	.4[illegible] .6[illegible]	.010	.050 (max)	.050 (max)	Cu .10, As 0.030, Ta 0.020, Co 0.05 B 0.001

TABLE II

TENSILE PROPERTIES OF THE ESR 12Cr-1Mo HEAT COMPARED TO OTHER HEATS AND SPECIFICATIONS

HEAT	ωTS (ksi)	0.2% YS (ksi)	ELONGATION (%)
ESR (9607R2)	121.0	≡7.5	21.0
AOD (9607)	114.4	80.2	22.5
ESR Breeder (91354)	110	≡8.0	11 ≡
Sandvik Specification	110/121	71 0 ωιν	17.0 ωιν.

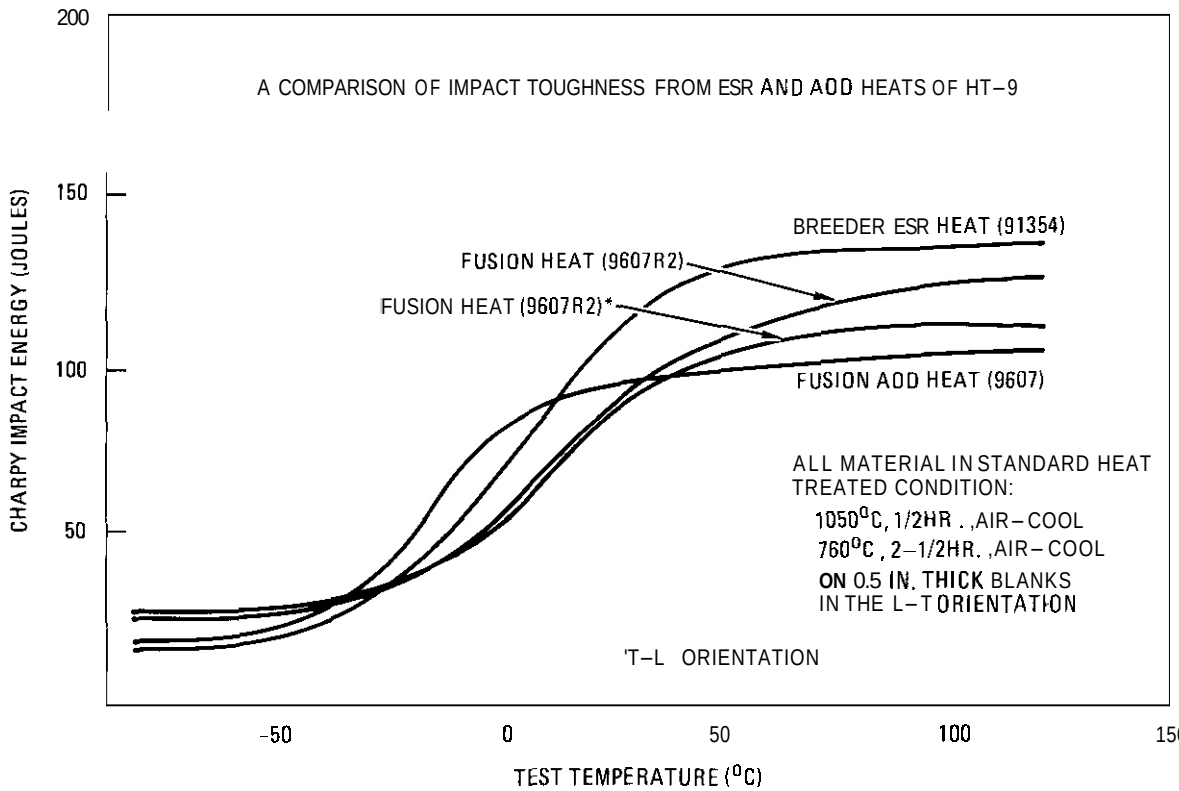

Figure 1. A comparison of the Charpy Impact toughness values of the National Fusion heat of ESR 12Cr-1Mo and other heats.

ft-lbs in the L-T orientation and 76 ft-lbs in the T-L orientation. This compares favorably with the Breeder program heat of No. 91354 with an upper shelf energy of approximately 90 ft-lbs[2]. The breeder heat of HT-9 may have a higher upper shelf energy because it's in a bar form. not plate as for the ESR fusion product form tested. heat. A comparison of the toughness of the bar form is being made. The fusion AOD heat of HT-9 has an upper shelf of about 65 ft-lbs.

7.4.5. Summary

The AOD ingots of HT-9 purchased in FY80 from Electralloy were electroslag remelted at Universal Cyclops and fabricated into plate and bar stock. The plates sizes were the same as procured from the AOD ingots previously. while the bar was in 1.0, 2.0 and 3.0 inch rounds. A comparison of the ESR material with the AOD and Breeder ESR heat No. 91354 shows favorable properties.

7.4.6 References

1. Lechtenberg. T., et al, ADIP Quarterly for the period ending 31 March 1980, DOE/ER-0045/2, pg. 109.

2. Hawthorne. R., ADIP Quarterly for the period ending 31 March 1981. pg. 155.

3. Hawthorne. R., ADIP Quarterly for the period ending 31 December 1980, pg. 127.

7.5 THE WELDABILITY OF HT-9: PREHEAT *AND* POSITION EFFECTS — T. A. Lechtenberg and W. Stack (General Atomic Company)

To be reported in the next semiannual report.

7.6 THE TOUGHNESS OF SIMULATED HEAT-AFFECTED ZONE MICROSTRUCTURES IN A 12Cr-1Mo-0.3V MARTENSITIC STAINLESS STEEL -

J. C. Lippold (Sandia National Laboratories, Livermore, CA)

7.6.1 ADIP Task

The Department of Energy (DOE)/Office of Fusion Energy (OFE) has stated the need for these data under the ADIP program task, Ferritic Steels Development (Path E).

7.6.2 Objective

The weld heat-affected zone (HAZ) of HT9 exhibits a variety of microstructures whose properties may differ considerably from those of both the fusion zone and quench-and-tempered base metal. Unfortunately, the evaluation of HAZ properties is confounded by the difficulty of identifying and, in turn, testing a particular microstructure. The objective of this study was to simulate four previously identified HT9 HAZ microstructures using the Gleeble and to determine the notch toughness of the individual microstructures by means of Charpy V-notch tests.

7.6.3 Summary

The four distinct HAZ microstructures which were identified in HT9 GTA welds (Ref. 1) were simulated in the Gleeble in order to produce bulk microstructural Charpy V-notch samples suitable for evaluation of notch toughness. Samples both transverse and longitudinal to the rolling direction (R.D.) of AGD melt plate stock were evaluated. Following the Gleeble thermal treatment the samples were given a postweld heat treatment (PWHT) for 1 hour at 760°C. Charpy tests of the individual microstructures were performed over the temperature range from -60 to 200°C. The toughness values of samples oriented transverse to the rolling direction (notch aligned parallel to R.D.) fell in a wide scatterband which enclosed the base metal toughness at low temperatures and was slightly less

than the base metal value on the upper shelf. When samples oriented parallel to the R.D. (notch transverse to R.D.) were evaluated the toughness of three of the microstructural regions was again equivalent to that of the base metal. The fourth region, which contained a fine prior austenite grain size exhibited superior toughness properties with respect to both the ductile-to-brittle transition temperature (DBTT) and the upper shelf energy.

7.6.4 Progress and Status

During fusion welding of martensitic steels variety of microstructures are developed in the HAZ as a consequence of the austenite-to-martensite transformation. In an earlier report, four distinct microstructures were identified and characterized in the HAZ of GTA welds in HT9 (Ref. 1). The microstructures which develop and their relationship to the Fe-Cr-C pseudo-binary diagram are summarized in Fig. 1. Since a large portion of the HAZ exhibits untempered martensite in the as-welded condition a postweld heat treatment (PWHT)is required to obtain adequate mechanical properties in the weld region. From a structural standpoint it is particularly important to determine the notch toughness of these materials over a range of possible reactor operating temperatures. Unfortunately, because of the microstructural gradient which is inherent in the HAZ of most martensitic materials it is impossible to locate a notch in an actual weld HAZ which will propagate a crack through a uniform microstructure. As a result, toughness values may be artificially high if the crack is not precisely located or propagates out of a low toughness microstructure region into one which exhibits higher toughness. In order to eliminate this ambiguity the Gleeble (a progammable thermo-mechanical simulator) has been employed to simulate the microstructure of the four HT9 HAZ regions in bulk samples such that notch location is facilitated and crack propagation occurs within a uniform microstructural region.

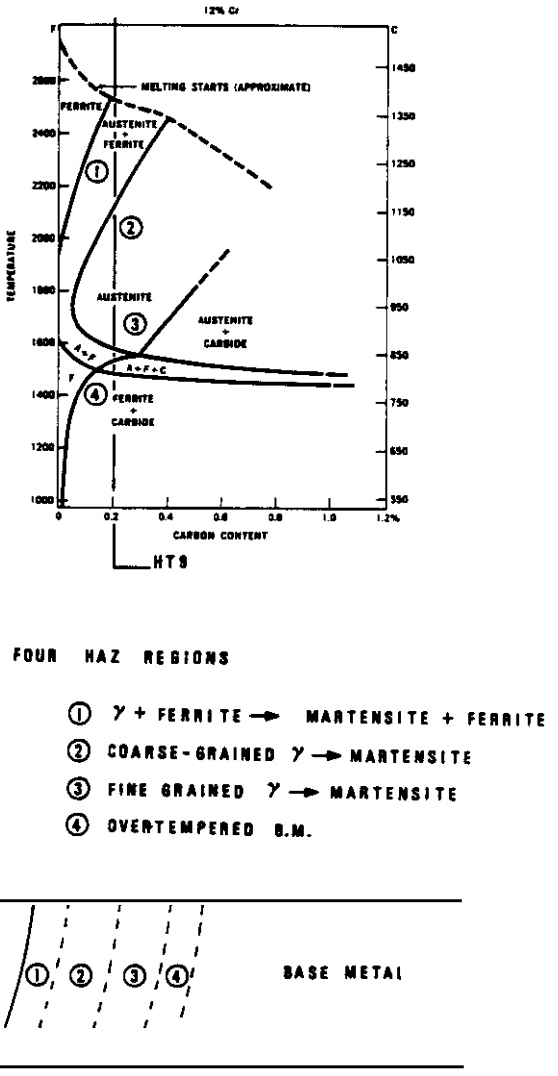

Figure 1. Schematic illustration of the four distinct microstructures produced in the HAZ of HT9 fusion welds and the relationship of these structures to the Fe–Cr–C pseudo–binary equilibrium phase diagram.

7.6.4.1 Experimental Approach

The composition of the National Fusion Heat (AOD melt) used in this investigation is listed in Table 1. The material in the form of 15 mm (5/8 in.) thick plate was austenitized for 0.5 hour at 1040 C, air cooled and then tempered at 760 C for 1 hour. Gleeble blanks 11 x 11 x 100 mm were machined both longitudinal and transverse to the R.D. of the plate. The blanks were then thermally

cycled in the Gleeble to produce the four distinct HAZ microstructures. The temperature-time history of the four cycles is shown in Figure 2. Following Gleeble cycling the samples were subjected to a PWHT of 760 C for 1 hour. Finally, standard Charpy V-notch samples 10 x 10 x 50 mm were machined from the heat treated blanks with the notch in the simulated HAZ region of the sample.

Table 1

Chemical Composition (wt %)

Cr	Ni	Mo	W	V	Si	Mn	C	P	S
12.14	0.53	0.64	0.50	0.24	0.25	0.63	0.15	.015	.010

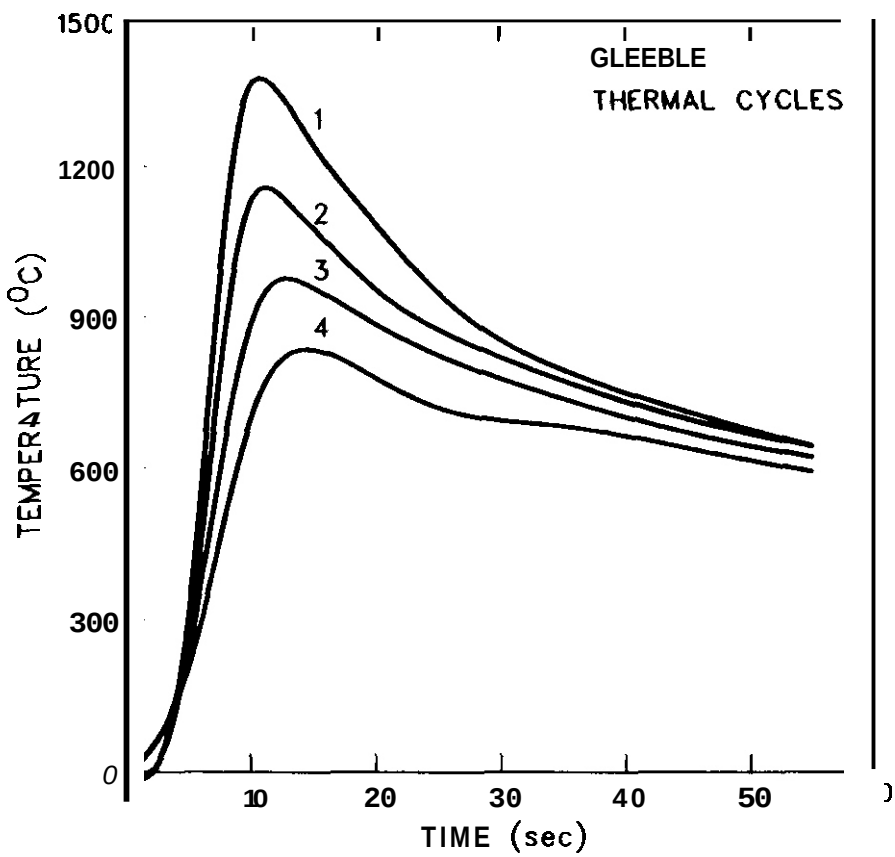

Figure 2. Gleeble thermal cycles used to simulate the HAZ microstructures.

Charpy tests were performed over the temperature range from -60 to 200°C. The small number of samples available allowed only one or two tests to be performed at a particular temperature for each microstructural region. Following testing selected samples were metallographically mounted, polished, and etched with Vilella's reagent to reveal microstructural features. The scanning electron microscope (SEM) equipped with an energy dispersive spectrometer (EDS) was utilized to determine the fracture mode and to identify particles located on the fracture surface.

7.6.4.2 Simulated Microstructures

The resultant HAZ microstructures following Gleeble cycling and subsequent PWHT are shown in Fig. 3. Although the PWHT has effectively homogenized the distinctive features of the as-welded microstructure, subtle differences still remain which may affect the properties of the material. For instance, the prior austenite grain size of the HAZ #3 structure is significantly smaller than that of structures 1, 2, and 4. The refinement in prior austenite grain size is related to the relatively low austenitizing temperature which the material experienced during the Gleeble heat treatment. This low temperature limits the growth of newly formed austenite grains which nucleate upon heating above the upper critical temperature (~ 960°C). Since both HAZ #1 and HAZ #2 are heated to much higher temperatures (Figs. 1 and 2) austenite grain growth is more significant. The prior austenite grain size of HAZ #4 in Fig. 3 is representative of the quench-and-tempered heat treatment since this structure is not reasutenitized during the Gleeble cycle. In general, the microstructure of all four HAZ regions following PWHT consists of untempered martensite and alloy carbides.

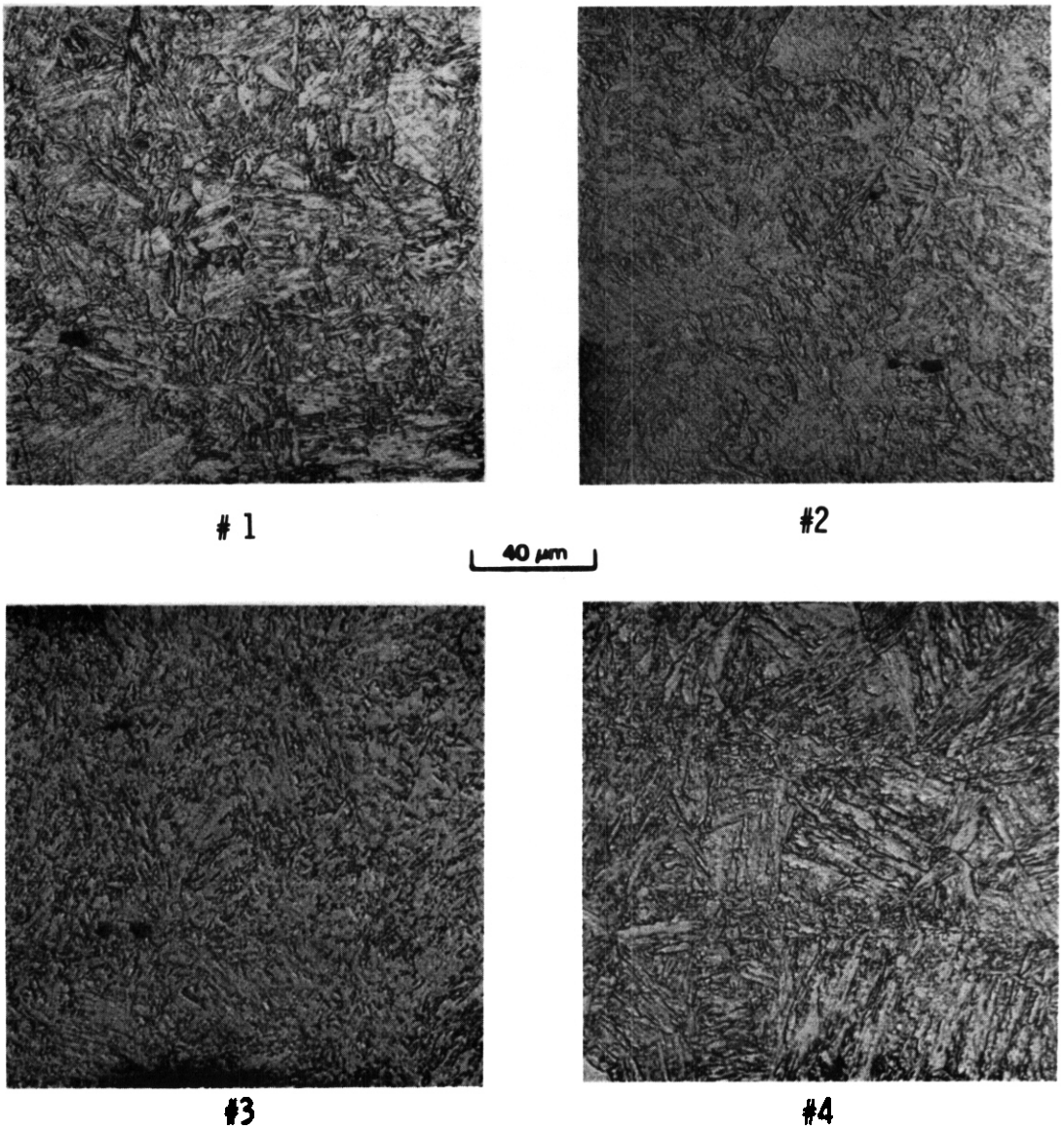

Figure 3. Gleeble simulated HAZ microstructures following a PWHT at 760°C for 1 hour.

7.6.4.3 Charpy V-notch Test Results

The Charpy V-notch toughness measured in terms of energy absorbed (ft-lbs) versus temperature in the range from -60 to 200°C (-76 to 392°F) for samples oriented transverse to the R.D. is presented in Figure 4. Base metal toughness values for AOD material in the quench-and-tempered condition is superimposed over the HAZ data. Note that the toughness data for all four microstructures falls in a broad band which overlaps the base metal curve at lower temperatures. The upper shelf energy of the HAZ microstructures lies slightly below that of the base material. Despite the range of toughness behavior, HAZ #3 values fall consistently in the upper part of the band while HAZ #2 data lie in the lower part of the band. The DBTT for both base metal and HAZ microstructures are approximately the same.

The Charpy toughness for HAZ samples oriented parallel to the R.D. (notch transverse to R.D.) is shown in Fig. 5. Again, the behavior of HAZ regions 1, 2, and 4 are confined within a band. The toughness of HAZ region #3, however, is significantly greater than the other three HAZ regions and the base metal. The DBTT of the HAZ #3 microstructure is nearly 20°C lower than the other structures and the upper shelf energy has increased by over 20 ft-lbs. The dramatic increase in notch toughness is a result of both the orientation of the sample relative to the R.D. and the refined prior austenite grain size.

7.6.4.4 Metallographic Evaluation of Charpy Samples

Inspection of the fractured Charpy samples revealed a significant variation in fracture behavior as a function of test temperature. A photomacrograph of a series of HAZ #2 samples is shown in Fig. 6a. Note that at low temperatures (-60, -20, and 0°C) the fracture surface appears faceted and the samples exhibit little lateral reduction (Poisson effect). Above 0°C the fracture appears more fibrous and the lateral contraction increases. The fracture behavior of the HAZ #3 samples similar (Fig. 6b) although the

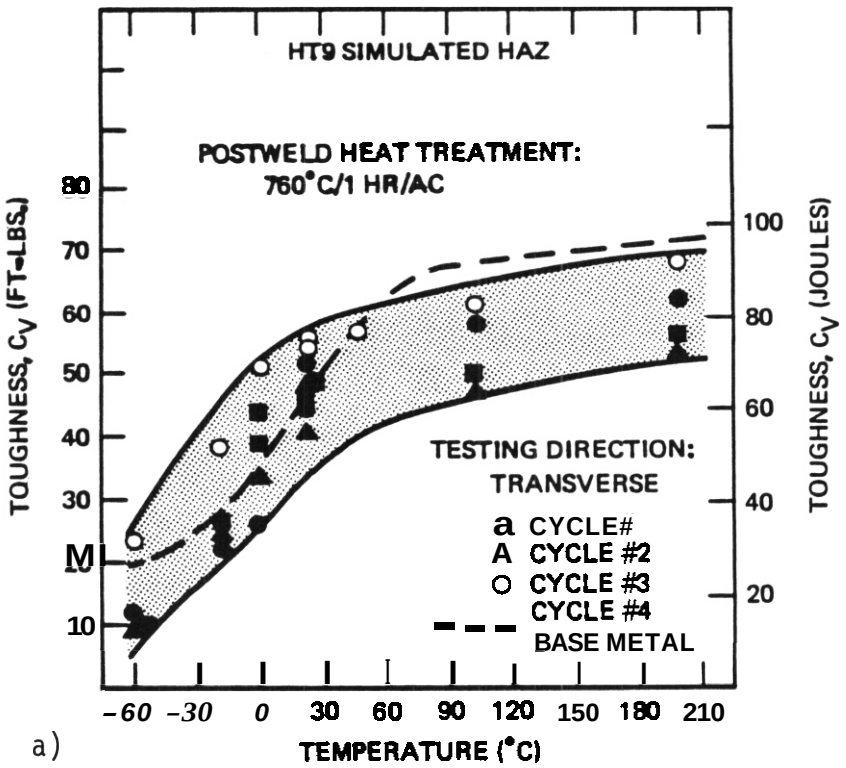

a)

Figure 4. Toughness of simulated HAZ microstructures tested transverse to the rolling direction of the original plate.

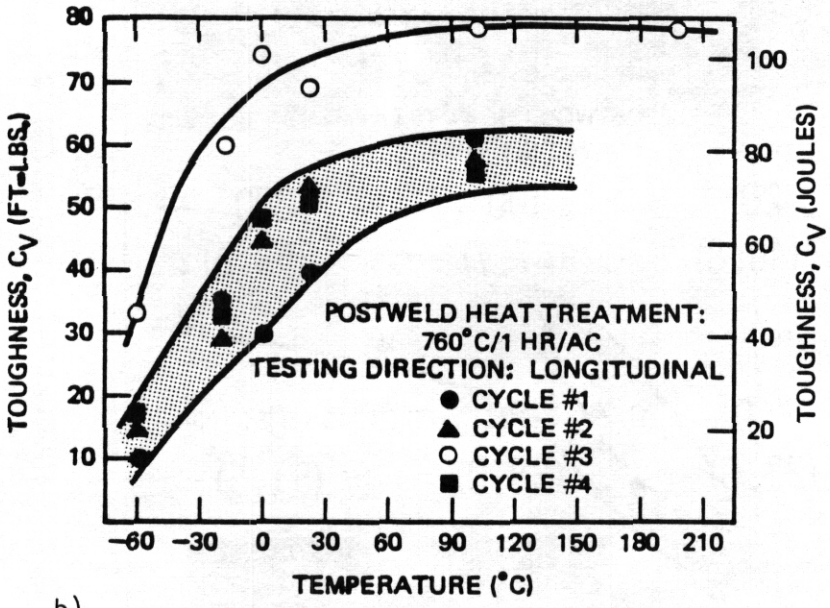

b)

Figure 5. Toughness of simulated HAZ microstructures tested longitudinal to the rolling direction of the original plate.

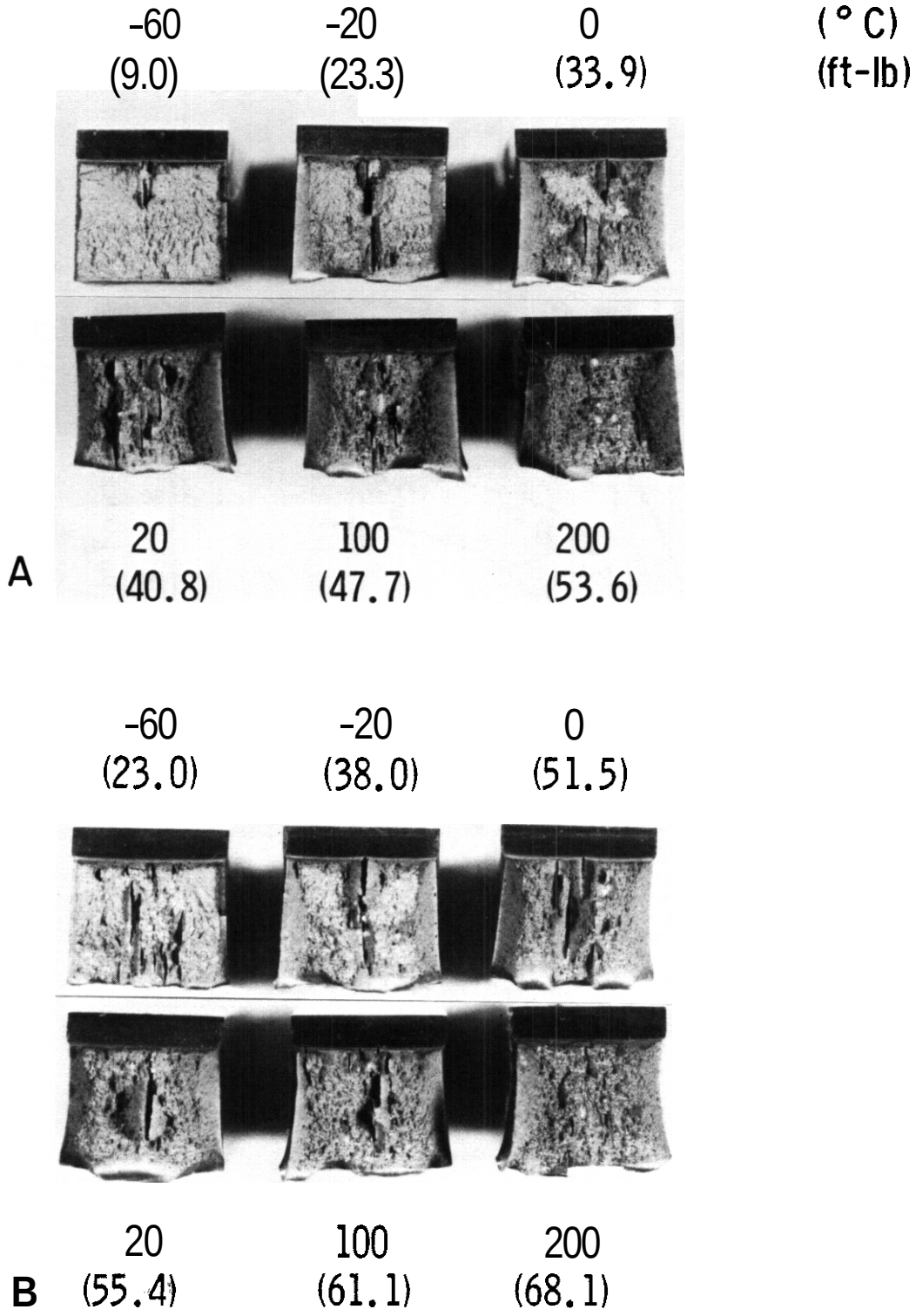

Figure 6. Macrograph illustrating the effect of temperature on the toughness and fracture appearance of simulated HAZ microstructures, a) Cycle #2, b) Cycle #3.

individual toughness values of samples tested at the same temperature are significantly higher. Note that all the samples, except those tested at 200°C, exhibit substantial secondary cracking perpendicular to the direction of primary crack growth. The behavior of HAZ #1 and #4 samples was similar to that portrayed by HAZ #2 and #3 in Fig. 6.

The nature of the secondary cracks can be determined by examining metallographic cross sections near the fracture surface. Typical sections for HAZ regions 1 and 2 are shown in Fig. 7. Note that the secondary cracks appear to propagate along stringers which run perpendicular to the main fracture plane. At higher magnification in Fig. 8, it can be seen that secondary fracture is associated with ferrite which was prevalent along rolling bands in the AOD material.

7.6.4.5 Fracture Morphology

The variety of fracture morphologies which are observed in the temperature range from -60 to 100°C can be illustrated by the fractographs of HAZ #1 samples in Fig. 9. At -60°C the sample absorbed approximately 10 ft-lbs. of energy and exhibited the interlath cleavage failure mode shown in Fig. 9. In the transition region (20°C) the fracture exhibits a mixed failure mode consisting of regions of interlath and ductile rupture, At room temperature and above the fracture was primarily dimpled rupture with average dimple spacings on the order of 2-3 microns or less.

In general, the fracture mode transition in the other three HAZ regions was analogous to the behavior of HAZ #1, although the transition to ductile rupture occurred at somewhat lower temperatures in HAZ region #3. Anomalous behavior of samples from the HAZ #1 lot was related to partial melting along ferrite stringers which occurred during the Gleeble thermal cycle. This melting is manifested by the fractographs in Fig. 10. Note the large amount of secondary cracking observed at low magnification (upper left). At higher magnification regions associated with the

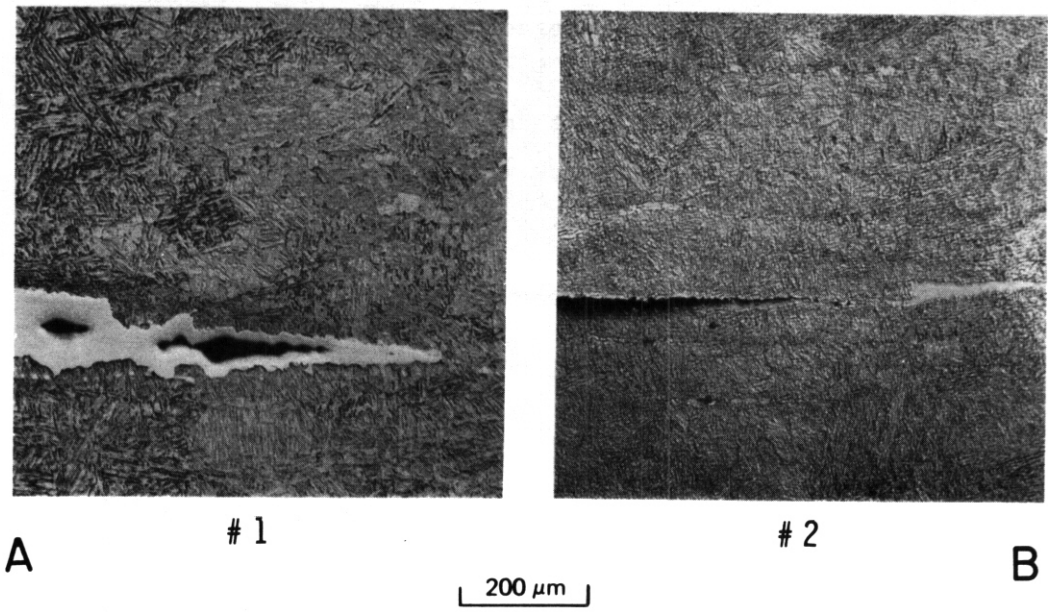

Figure 7. Microstructure near the fracture surface of Charpy samples, a) Cycle #1, b) Cycle #2. Unetched region surrounding crack represents Ni-plate used to protect fracture surface.

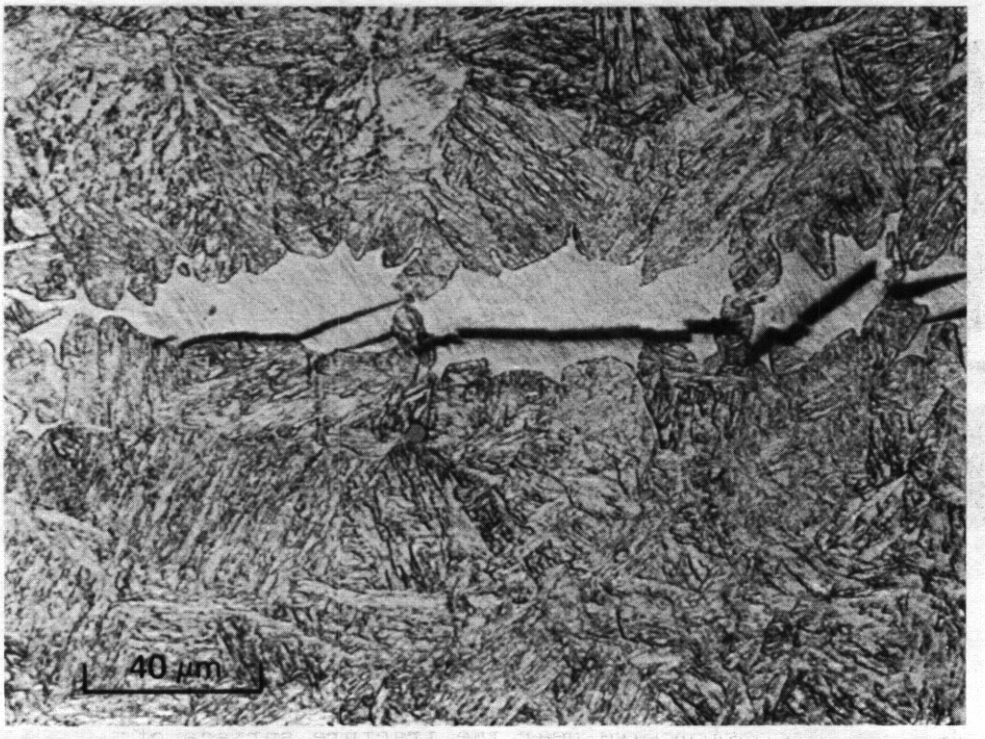

Figure 8. Fracture through ferrite stringer in HAZ Region #1 Charpy sample.

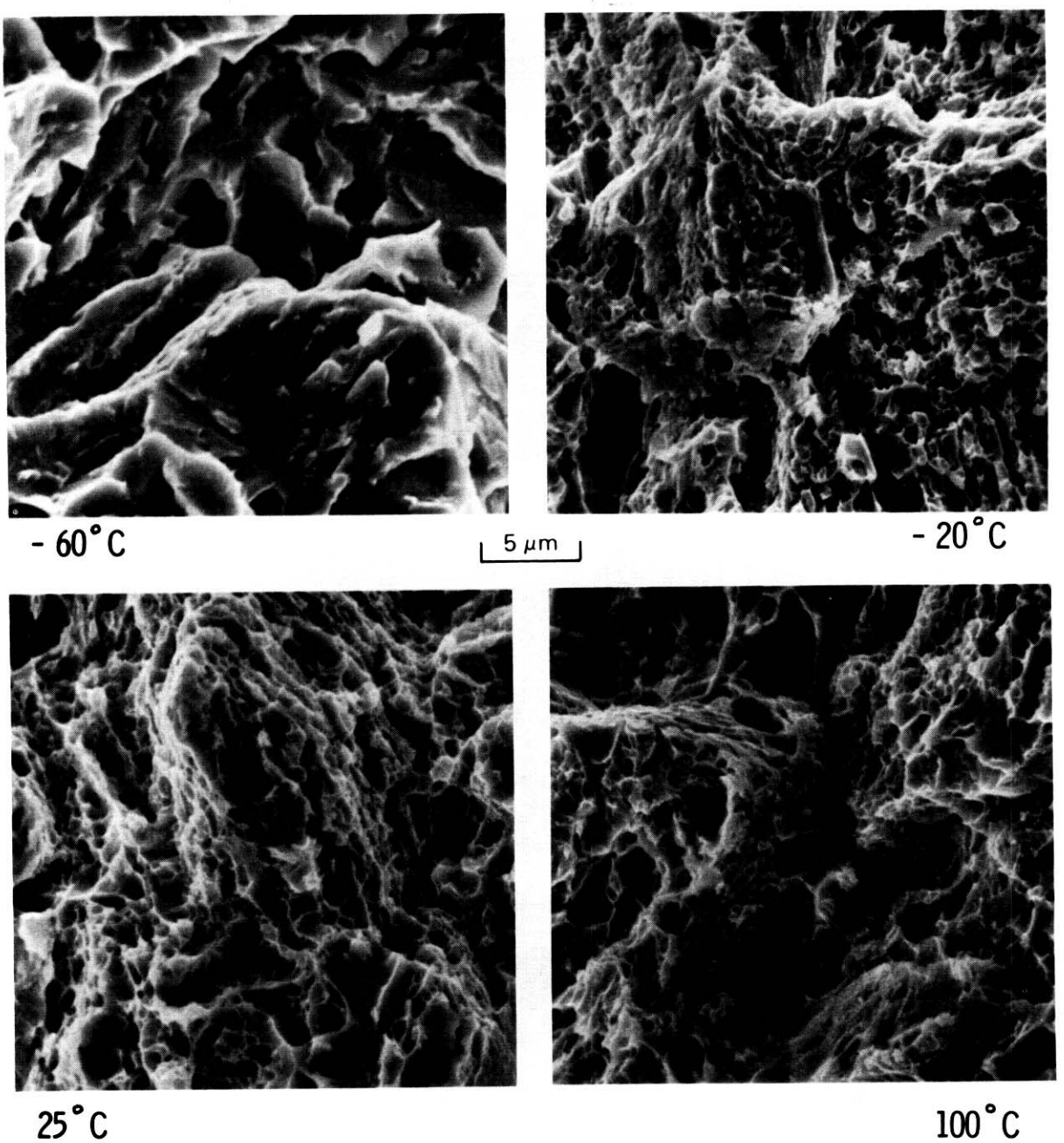

Figure 9. Variation in fracture morphology as a function of test temperature for HAZ Region #1 samples in the transverse orientation.

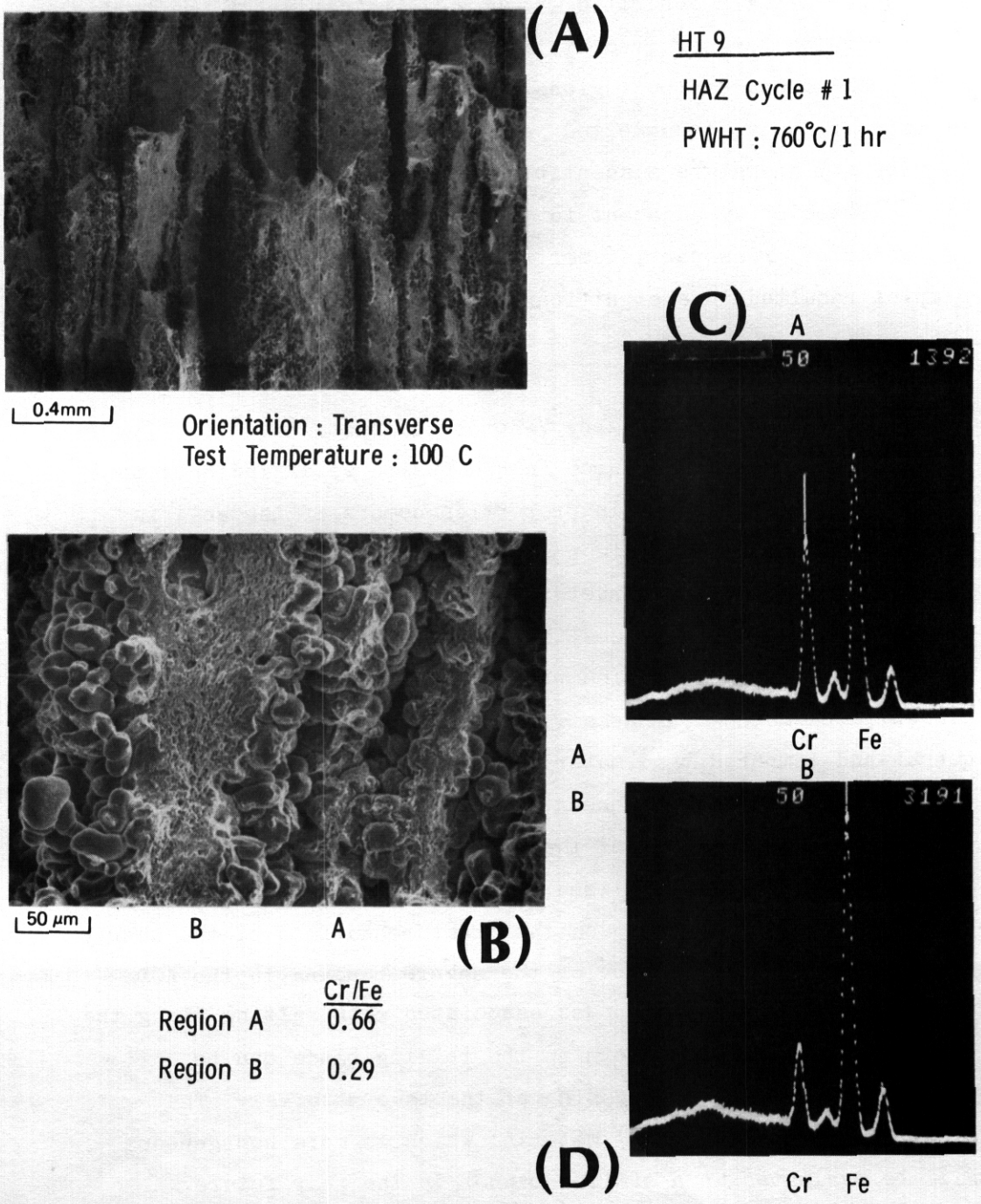

Figure 10. Partial melting on the fracture surface of HAZ Region #1 sample, a) SEM macrograph of fracture surface, b) Fractograph showing partial melting along ferrite stringers (A-A), c) EDS spectrum at partially melted region, d) EDS spectrum in unmelted region.

fracture exhibit a dendritic morphology indicative of the partial melting which has occurred at these sites. EDS analysis of the melted and resolidified regions revealed a significant increase in chromium relative to unmelted region. This suggests that the ferrite stringers are susceptible to preferential melting in the region immediately adjacent to the fusion line. In general, the incidence of gross partial melting along ferrite sringers in HAZ #1 samples resulted in a significant decrease in toughness.

7.6.4.6 Discussion

The results of Charpy V-notch toughness tests of simulated HAZ microstructures in HT9 fusion welds indicate that little or no degradation in properties occurs if the weld is subjected to an appropriate postweld heat treatment. Despite the wide variation in microstructure which exists across the HAZ, the PWHT essentially homogenizes the entire structure. In microstructures where a fine prior austenite grain size is present, the notch toughness is actually higher than the quench-and-tempered base material. The implication of these results are that the toughness of the weld region can be expected to be comparable to that of the base metal in a welded structure if the proper PWHT is utilized.

Secondary cracking on the fracture surface of the Charpy specimens was a consequence of the severe banding in the AOD material. A drop in toughness associated with melting along the ferrite stringers which form in the rolling bands can be eliminated by proper processing of the base material. The electroslag remelted (ESR) material which is more homogeneous will be evaluated in a similar manner in the near future.

7.6.5 Conclusions

1. A postweld heat treatment of 760 °C for one hour homogenizes the heat-affected zone microstructure and equilibrates the toughness relative to the quench-and-tempered base material.

2. The refinement of the prior austenite grain size in the region of the HAZ heated just above the upper critical temperature results in an improvement in toughness relative to the base material.

3. Notch orientation in relation to the rolling direction of the plate had only a minor effect on the toughness of individual HAZ microstructures.

4. Ferrite stringers in the as-received AOD plate promoted secondary cracking in the Charpy samples. Preferential melting was also observed along these stringers when the samples were heated to temperatures slightly below the bulk solidus.

5. Samples tested at temperatures below approximately -20 °C exhibited an interlath cleavage failure mode. In the transition region fracture occurred by means of a cleavage/ductile dimple mixed mode. Fracture on the upper shelf occurred completely by ductile dimple rupture.

7.6.6 References

1. J. C. Lippold, "Weldability of HT-9: The Autogenous GTA Process", ADIP Quarterly Progress Report, DOE/ER-0045-2, March 1980.
2. J. C. Lippold, "Tempering and Transformation Behavior of HT9 Weldments", ADIP Quarterly Progress Report, DOE/ER-0045-3, June 1980.
3. J. R. Hawthorne, "Fracture Toughness Testing of Alloy HT9 and Alloy 9Cr-1Mo (Modified)", ADIP Program Review Meeting, Germantown, MD, May 1981.

7.7 THE EFFECT OF POSTWELD HEAT TREATMENT ON THE TOUGHNESS OF THE HEAT-AFFECTED ZONE IN A 12Cr-1Mo-0.3V STEEL (HT9) -

J. C. Lippold (Sandia National Laboratories, Livermore, CA)

7.7.1 ADIP Task

The Department of Energy (DOE)/Office of Fusion Energy (OFE) cited the need for these data under the ADIP Task, Ferritic Alloy Development (Path E).

7.7.2 Objective

During the welding process, the fusion zone and portions of the heat-affected zone (HAZ) which are heated above approximately 900 C transform to a brittle, untempered martensite upon cooling to room temperature. A postweld heat treatment (PWHT) at 760°C for periods ranging from 0.5 to 2.5 hours are normally recommended in order to reduce the hardness and increase the toughness of the as-welded microstructure. Unfortunately, relatively high temperature PWHT's are difficult to perform on large sections, particularly in the field. The purpose of this investigation was to determine if a less stringent PWHT could be employed which would both minimize fabrication problems and ensure adequate properties in the weld region.

7.7.3 Summary

Samples both transverse and longitudinal to the rolling direction (R.D.) of the plate were subjected to thermal cycles in the Gleeble which simulated four distinct microstructures in the HAZ. Following the Gleeble heat treatment, the samples were tempered at either 760°C or 600°C for one hour and subsequently tested over a range of temperatures in the Charpy apparatus. Charpy test results revealed that the higher PWHT decreased the ductile-to-brittle transition temperature (DBTT) and increased the upper shelf energy of three of the microstructures. A fourth microstructure was relatively unaffected by the PWHT since the peak

temperature experienced by this HAZ region is not sufficient to reaustenitize the structure during welding. The region of the microstructure heated just slightly above the austenitization temperature during welding exhibits the best toughness properties due to the refinement of the austenite grain size.

The Charpy results indicate that a 600°C postweld heat treatment is not sufficient to increase the toughness of the weld region to a level which would guarantee the structural integrity of a large component. It is imperative that the ambient temperature toughness should be sufficient to ensure extended life during cyclic loading and periodic shutdown of the reactor.

7.7.4 Progress and Status

Four distinct HAZ microstructures which develop in GTA welds in HT9 have been identified and characterized in two previous reports (Ref. 1 and 2). In the majority of martensitic steels the most significant degradation of properties occurs in the HAZ rather than the fusion zone, particularly since weld filler metals can be selected which resist mechanical property degradation or respond more favorably to PWHT. As a result, this investigation will concentrate on the microstructural evolution of the HAZ during PWHT and the effect of the microstructural change on the toughness of the HAZ.

7.7.4.1 Experimental Approach

The National Fusion Heat (AOD melt practice) was supplied in the form of 15 mm (~ 5/8 in.) plate by General Atomic Co. for use in . The composition of this heat is listed in Table 40°C, air produce a , 20–22. itudinal and hen thermally cycled in the Gleeble to simulate the four distinct HAZ

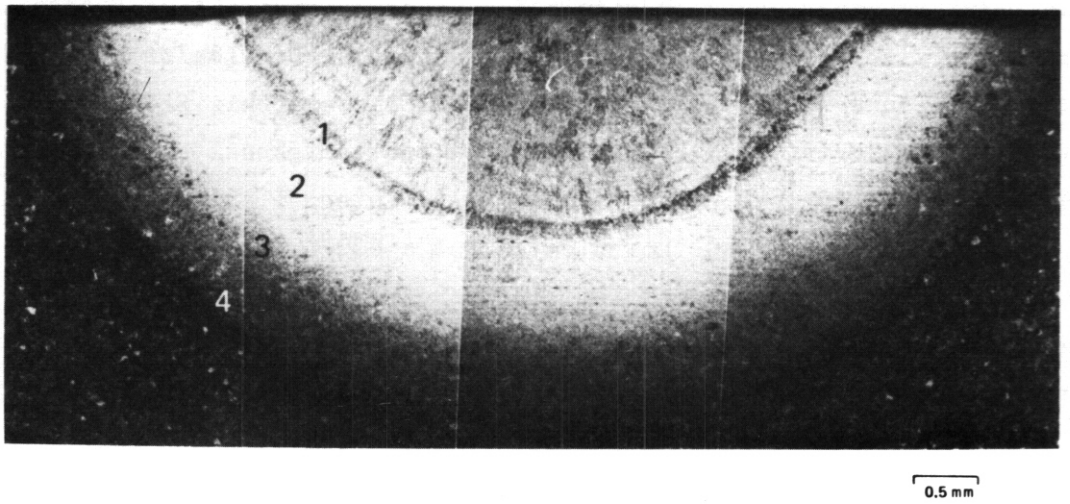

Autogenous GTA Weld

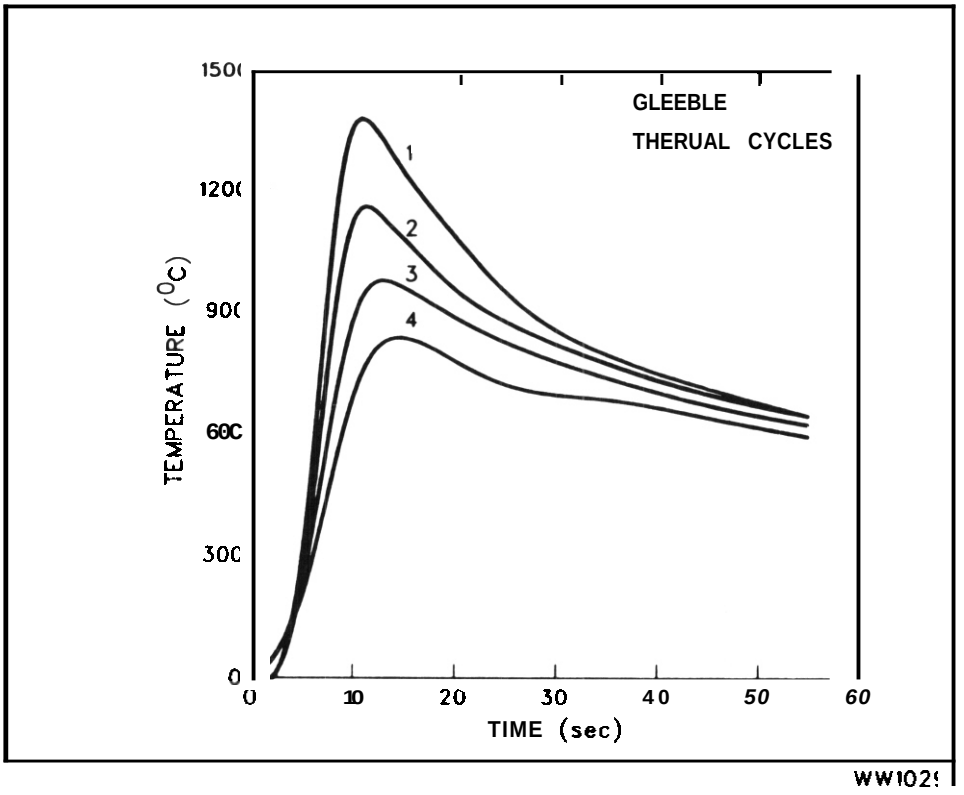

Figure 1. Simulated HAZ Thermal Cycles and their Relation to an Autogenous Gas Tungsten Arc Weld.

microstructures. The temperature-time history of the four cycles is shown in Figure 1. Following Gleeble cycling, the samples were subjected to a PWHT of either 760 or 600°C for 1 hour. Charpy V-notch samples were then machined from the tempered blanks insuring that the notch was located within the simulated HAZ microstructural region of the sample.

Table 1

Chemical Composition (wt%)

Cr	Ni	Mo	W	V	Si	Mn	C	P	S
12.14	0.53	0.64	0.50	0.24	0.25	0.63	0.15	.015	.010

The Charpy V-notch toughness of the samples was determined in the temperature range from -60 to 200°C. Following testing the samples were cleaned in alcohol and dessicated in preparation for SEM analysis.

7.7.4.2 Charpy V-notch Test Results

Charpy results plotted as energy absorbed (ft-lbs.) versus temperature for each of the four HAZ microstructures are presented in Fig. 2. The data for the individual microstructures include the different PWHT's and the variation in orientation relative to the rolling direction of the plate. Note that for HAZ regions #1-3 the DBTT is lower and the upper shelf energy higher for samples subjected to the high temperature PWHT (760°C). The largest variation in properties is observed for the HAZ #3 microstructure; the upper shelf energy for the 760°C PWHT is nearly the 600°C tempering treatment. Orientation effects appear to be minor, with both transverse and longitudinal samples falling within a scatterband.

Samples which were Gleeble cycled to simulate HAZ region #4 exhibited little variation in toughness, irrespective of PWHT.

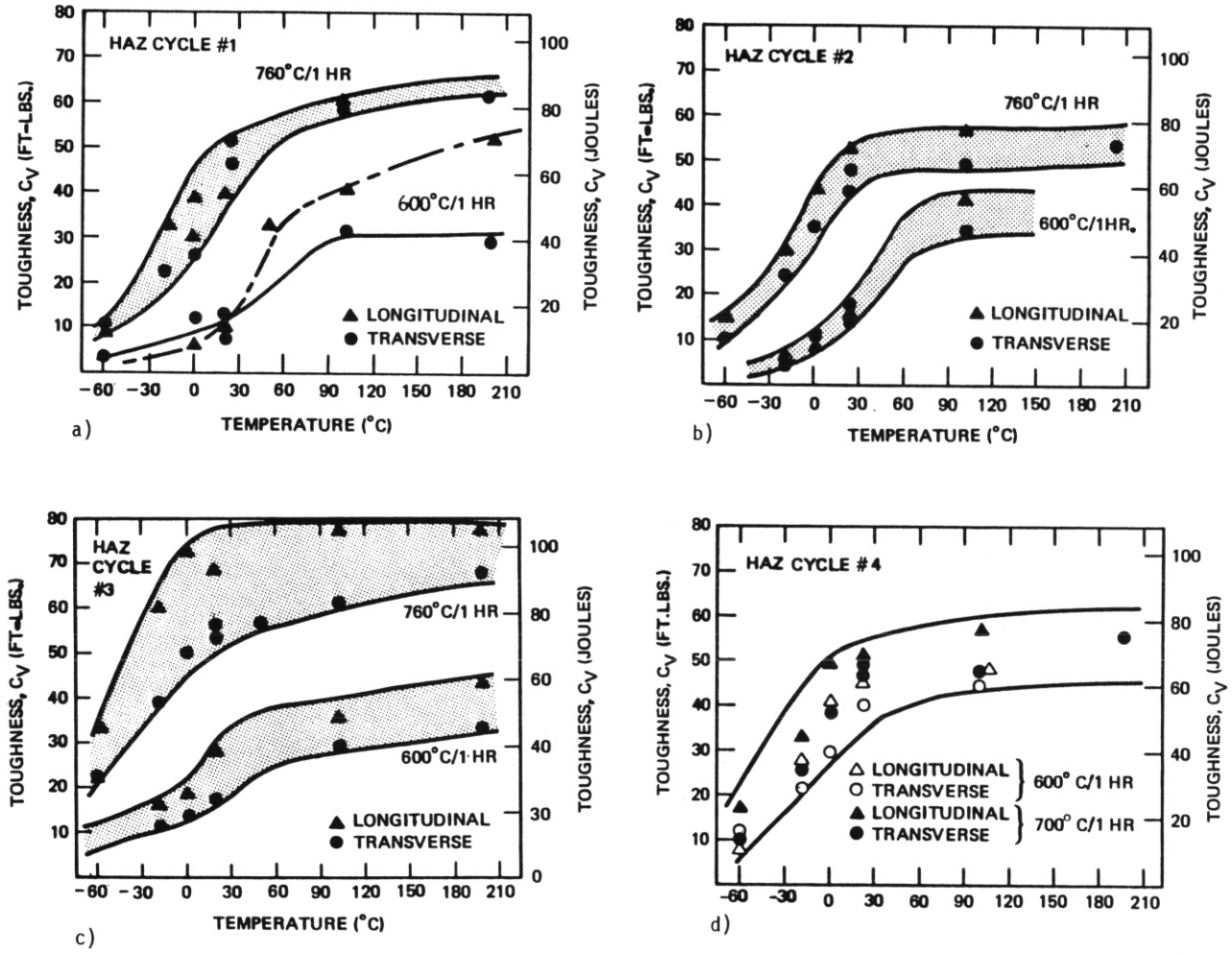

Figure 2. The Effect of Orientation and PWHT on the Toughness of Simulated HAZ Microstructures. a) Cycle #1, b) Cycle #2, c) Cycle #3, d) Cycle #4.

Since the peak temperature experienced by region #4 is not sufficient to reaustenitize the base metal microstructure the PWHT only serves to overtemper the preexisting quench-and-tempered microstructure.

7.7.4.3 Fracture Mode Transition

Photomacrographs of the Charpy V-notch fracture surfaces of samples tested at -60 and 0°C are shown in Fig. 3. All samples were tested in the transverse orientation and subjected to a PWHT of either 600 or 760°C. At -60°C all the fracture surfaces exhibit a large degree of faceted cleavage fracture. Despite the fracture appearance, the sample which simulated the HAZ region #3 microstructure showed surprising toughness (23 ft-lbs.) after a PWHT at 760°C. As the test temperature was increased to 0°C a change in fracture appearance accompanied an improvement in toughness for samples given the 760°C PWHT. Note the fibrous appearance of the fracture surfaces which were subjected to the higher temperature PWHT, in contrast to corresponding samples from regions 1, 2, and 3 which were heat treated at 600°C. The toughness values and fracture appearance shown in Fig. 3 indicate that at 0°C the HAZ of HT9 weldments would exhibit low toughness behavior (brittle, cleavage failure) after a PWHT at 600°C. However, if the same microstructure is heat treated at 760°C the notch toughness increases dramatically as fracture shifts to a more ductile failure mode.

The effect of PWHT on failure mode is illustrated by the fractographs in Fig. 4. At 25°C the HAZ region #1 microstructure exhibits upper shelf behavior when it is given a PWHT at 760°C as evidenced by both the ductile dimple fracture mode in Fig. 4 and the relatively high toughness on the energy absorbed versus temperature curve in Fig. 2a. When the same HAZ microstructure is given a PWHT at 600°C the failure occurs by cleavage along martensite lath boundaries (Fig. 4). The corresponding toughness is relatively low (-10 ft-lbs.) and lies on the lower shelf of the curve in Fig. 2a.

Effect of HAZ Cycle, Transverse Orientation

Test Temperature: -60°C

PWHT

(10.8) (9.0) (23.0) (10.5)

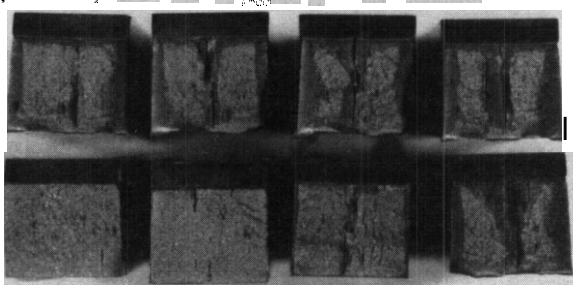

760°C/1 hr

600°C/1 hr

(3.5) (4.6) (10.5) (11.0)

Cycle # 1 **# 2** t 3 **t 4**

Test Temperature: 0°C

(26.0) (33.9) (51.5) (43.9)

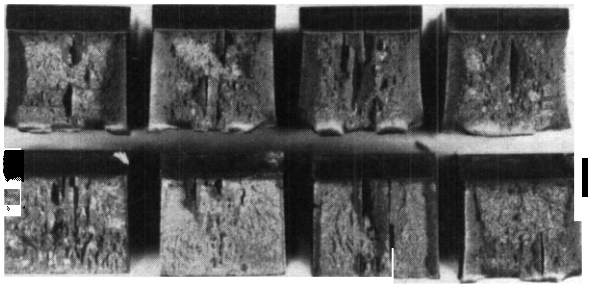

760°C/ 1 hr

600°C/ 1 hr

(12.9) (10.3) (13.7) (30.2)

Figure 3. Macrograph of Charpy Samples Tested at -60 and 0°C.

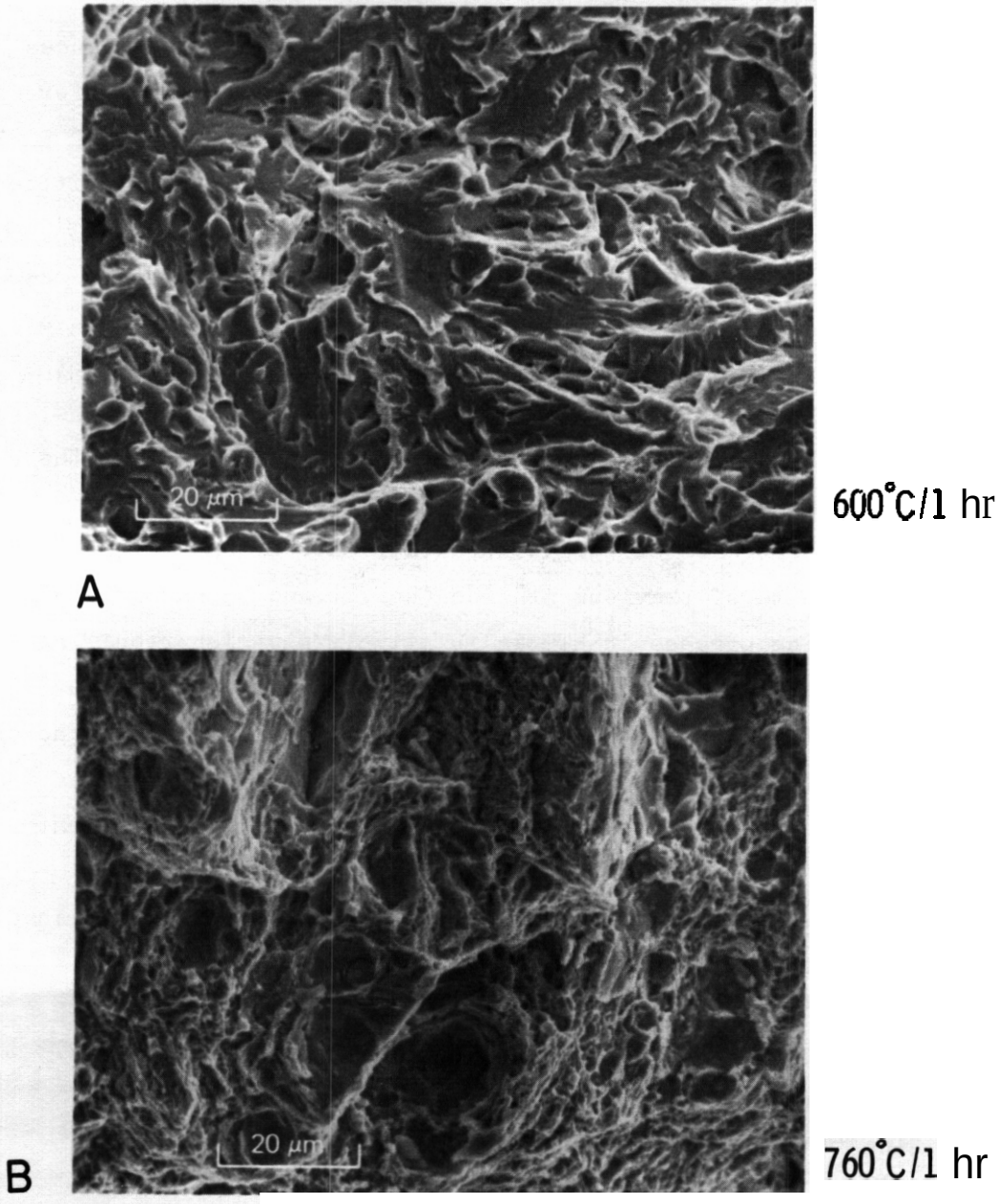

Figure 4. Fractographs of HAZ Cycle #1 Samples Tested at 25°C, a) 600°C PWHT, b) 760°C PWHT.

7.7.4.4 Discussion

The weld thermal cycle in the HAZ of HT9 weldments produces at least four distinct microstructures whose properties may differ considerably. The peak temperature experienced by the microstructures in regions 1-3 is sufficiently high to reaustenitise the martensitic base metal structure and at least partially resolutioniae the alloy carbides. Upon cooling below the M_S (~ 240° C) the reverted austenite transforms to martensite, the hardness of which is dictated by the amount of carbon which is dissolved in the austenite prior to transformation. The PWHT serves to temper the martensite by the diffusion of carbon out of the structure and the subsequent precipitation of alloy carbides along martensite lath boundaries and prior austenite grain boundaries.

The results of previous studies (Ref. 1 and 3) have revealed that the tempering process in HT9 is relatively sluggish requiring extended times at elevated temperatures to soften the martensite. The results of this investigation have shown that the change in notch toughness more or less parallels the softening reaction. The tempering curve shown in Fig. 5 illustrates this point. Note that tempering for 1 hr. at 600° C results in a significant drop in hardness relative to the peak as-welded hardness but that tempering at 760° C drops the hardness to the lower shelf in the righthand portion of the diagram. The additional drop in hardness reflects the substantial increase in toughness due to the increase in PWHT temperature from 600 to 760° C.

Since the peak temperature of the HAZ #4 cycle does not exceed the lower critical temperature the microstructure in this region is not hardened by formation of untempered martensite. As a result, the PWHT does not serve to soften the material but rather tends to overtemper the preexisting base metal structure. In the absence of untempered martensite the difference in PWHT temperature is not significant and thus the toughness data in this region can be plotted in a band, as shown in Fig. 2d.

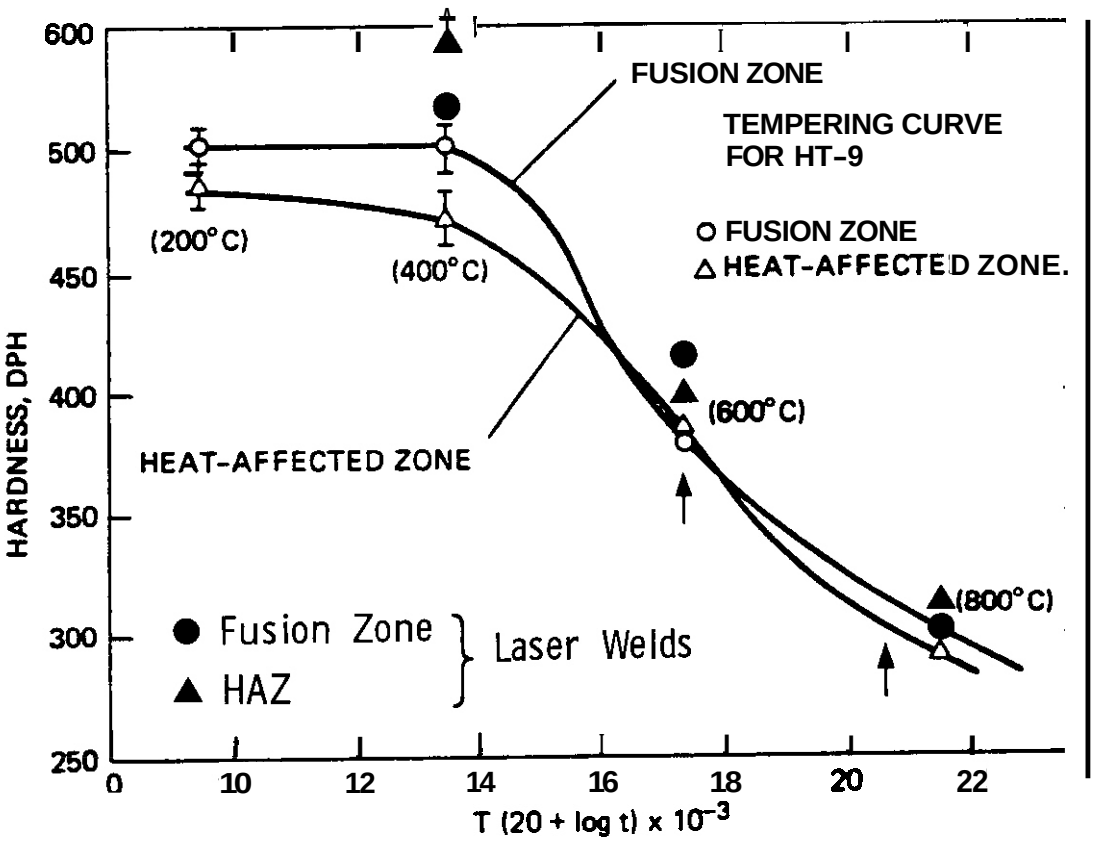

Figure 5. Tempering Curve for the Fusion Zone and HAZ of HT9. The arrows indicate the PWHT's used in this investigation.

7.7.5 Conclusions

1. Charpy V-notch results from Gleeble-simulated HAZ microstructures reveal that a postweld heat treatment (PWHT) at 600°C for 1 hr. results in lower relative notch toughness properties than for a PWHT at 760°C.

2. The variation in the PWHT was manifested by a 40-50°C increase in DBTT and a 20-40 ft-lb. decrease in upper shelf energy for three distinct HAZ microstructures which were reaustenitized during the Gleeble thermal cycle.

3. Lower shelf fracture behavior was associated with a cleavage-type failure mode, primarily along martensite lath boundaries. Upper shelf fracture occurred primarily by ductile rupture.

7.7.6 References

1. J. C. Lippold, "Weldability of HT-9: The Autogenous GTA Process", ADIP Quarterly Progress Report, DOE/ER-0045-2. March, 1980.
2. J. C. Lippold, "Tempering and Transformation Behavior of HT9 Weldments", ADIP Quarterly Progress Report, DOE/ER-0045-3, June 1980.
3. J. C. Lippold, "Tempering Behavior of Laser Welds in HT9", ADIP Quarterly Progress Report, DOE/ER-0045-6, March 1981.

7.8 INTERPRETIVE REPORT ON THE WELDABILITY OF 12Cr-1Mo-0.3V (HT9) MARTENSITIC STAINLESS STEEL, PART 2: SUITABILITY FOR FUSION REACTOR FIRST WALLS AND BLANKET STRUCTURES - J. C. Lippold (Sandia National Laboratories, Livermore, CA)

7.8.1 ADIP Task

The Department of Energy (DOE)/Office of Fusion Energy (OFE) has cited the need for this information under the ADIP Program Task, Ferritic Alloy Development (Path E).

7.8.2 Objective

Candidate alloys for fusion reactor first walls and blanket structures must meet stringent performance criteria in order to survive the aggressive environments during reactor operation. However, the "go or no go" issue of fabricability is perhaps of greater importance because it may, a priori, preclude the use of the alloy in large engineering devices. The objective of this review is to assess the suitability of the HT9 candidate alloy for fusion reactor service from the standpoint of both weldability and in-service performance.

7.8.3 Summary

A previous report[1] summarized the results of both commercial experience and ADIP-sponsored research concerned with the weldability of the HT9 candidate alloy. The general conclusion of this report was that HT9 exhibits adequate weldability and is suitable from a fabrication standpoint; however, the question of in-service behavior and survivability in an operating reactor have not been addressed. To date, the data to make such judgments are not available. Continuing research in the areas of irradiation damage, fatigue behavior, hydrogen embrittlement, and the synergism among these issues and others must be pursued before the suitability of HT9 weld microstructures in fusion reactor environments can be properly assessed.

7.8.4 References

1. J. C. Lippold and T. A. Lechtenberg, "Interpretive Report on the Weldability of 12Cr-1Mo-0.3V-0.5W (HT9) Martensitic Steel For Use in First Wall/Blanket Structures in Fusion Reactors, Part 1, A Review of Current Technology", ADIP Report for period ending September, 1981.

7.9 HYDROGEN EMBRITTLEMENT OF ESR PROCESSED 12Cr-1Mo STEEL - J. M. Hyzak and W. M. Garrison (Sandia National Laboratories, Livermore, CA)

7.9.1 ADIP Task

The Department of Energy (DOE) Office of Fusion Energy (OFE) has cited the need for these data under the ADIP Program Task, Ferritic Alloy Development (Path E).

7.9.2 Objective

The goal of this study is to evaluate the hydrogen compatibility of 12Cr-1Mo ferritic/martensitic steel for use in first wall and blanket structures. This report summarizes data on the effect of internal hydrogen on the room temperature tensile properties of ESR processed 12Cr-1Mo steel.

7.9.3 Summary

Tensile tests were performed to determine the effect of hydrogen on the ductility of a quenched-and-tempered 12Cr-1Mo alloy from the National Fusion Heat-ESR processed. Specimens were cathodically charged with hydrogen at 0.003 A/cm^2 and 0.006 A/cm^2 for 15 to 150 minutes. In the uncharged condition, the ESR specimens failed by intergranular rupture with prominent secondary cracking along prior austenite grain boundaries. For the least severe cathodic charge (0.003 A/cm^2 - 15 minutes), the tensile ductility (R_A) decreased 33% and the degree of secondary cracking increased. At 0.003 A/cm^2 for 150 minutes, the ductility decreased further and the fracture mode changed to classical intergranular fracture. These results generally matched those for the AOD processed 12Cr-1Mo alloy that had been tested previously.[1]

Auger analysis indicates that there is segregation of phosphorous and the carbide-forming elements Cr, Mo, W to the prior austenite grain boundaries. In the literature, phosphorous has been shown to embrittle these boundaries, especially in the presence of hydrogen.[2-5]

The combination of tensile data on hydrogen charged ESR and AOD 12Cr-1Mo steel present several reasons for concern regarding the susceptibility of this alloy to hydrogen embrittlement. Earlier results on hydrogen charged Sandvik HT-9[6] are addresssed in terms of these more recent findings.

7.9.4 Progress and Status

7.9.4.1 Experimental Procedure

Tensile tests were performed on hydrogen charged base metal samples from the National Fusion Heat of 12Cr-1Mo steel which had been electroslag remelted (ESR). The specimens were tested in the quenched-and-tempered condition. The material was taken from plate stock of the ESR processed alloy that had been supplied and characterized by General Atomic Co. The plate stock was austenitized at 1040°C/30 min. and air cooled, then tempered at 750°C for 1 hr. followed by air cooling. Test specimens were machined after heat treatment. Tensile bars had a nominal 0.287 cm (0.113 in.) gage diameter and a 2.03 cm (0.80 in.) uniform section. The tensile axis of each specimen was perpendicular to the rolling direction of the plate.

Test specimens were cathodically charged with hydrogen at current densities of 0.003 A/cm^2 (0.02 A/in^2) and 0.006A/cm^2 (0.04A/in^2) for times up to 150 minutes (Table I). Charging was done in a four percent sulfuric acid solution containing 5 mg/liter of sodium arsenate. Specimens were copper-plated in an acid copper bath immediately after charging to retain the hydrogen, and aged at room temperature for 24 hours before testing to allow distribution of the hydrogen. All tensile tests were conducted at 0.51 cm/min (0.02 in./min.) extension rate. Following completion of the tests, the fracture surfaces were examined by optical microscopy and SEM.

The first two of several planned Auger analyses were performed to identify chemical segregation that may be responsible for fracture at prior austenite grain boundaries. The material for

Auger analysis had the same quenched-and-tempered heat treatment as described above; however, the specimens were taken from the previously tested argon-oxygen decarburized (AOD) National Fusion Heat[1] and a piece of HT-9 Sandvik pipe.[6] The specimens were cathodically charged at 0.006 A/cm^2 for 24 hours to ensure brittle behavior, copper-plated to retain the hydrogen, and fractured in-situ at 10^{-9} torr.

7.9.4.2 Tensile Test Results - ESR Base Metal

The results of the 12Cr-1Mo ESR tensile tests are presented in Table I and are graphically compared in Fig. 1 to the previously published results on the 12Cr-1Mo AOD stock.' The uncharged ESR material had a 0.2% yield strength of approximately 718 MPa(104 ksi) and a reduction in area of 54%. Hydrogen charging at all three levels resulted in a loss of ductility; at 0.003 A/cm^2 for 15 minutes, the reduction in area decreased a maximum of 33% from the uncharged condition while for the most severe charge (0.006 A/cm^2 for 150 minutes) the ductility decreased over 90% to a value of only 4% R_A.

Examination of the fracture surfaces of the uncharged ESR specimens revealed a cup-cone type of fracture (Fig. 2a) with a dimpled rupture microscopic fracture mode. These are the same characteristics that were observed for the uncharged AOD tensile fractures.[1] There were also a large number of secondary cracks intersecting the fracture surface which appeared to follow some type of boundary (Fig. 2b and c). Metallographic cross-sections of these fractures confirmed that the secondary cracking was along prior austenite grain boundaries (Fig. 2d). This type of cracking will be termed "intergranular rupture",[7] and is significantly different from the classical faceted intergranular fracture. The fracture morphology changed with the addition of hydrogen charging, as shown in Fig. 3. For the least severe cathodic charge (0.003 A/cm^2 - 15 minutes), the shear lip around the perimeter of the fracture surface was reduced and the amount of secondary cracking was significantly

TABLE I
Tensile Properties of 12Cr-1Mo Steel - National Fusion Heat (ESR) Subject to Cathodic Charging

Spec #	Charging Cond.*	Yield Strength MPa (ksi)**	Ultimate Strength MPa (ksi)	Reduction in Area(%)
2	Uncharged	752.8 (109.2)	878.3 (127.4)	53.6
8	Uncharged	714.9 (103.7)+	879.7 (127.6)	54.8
5	0.003 A/cm -15 min.	751.1 (108.8)	934.8 (135.6)	35.9
7	0.003 A/cm -15 min.	726.6 (105.4)	911.4 (132.2)	49.7
4	0.003 A/cm -150 min.	766.6 (111.2)	820.4 (119.0)++	9.4
6	0.003 A/cm -150 min.	725.9 (105.3)	788.0 (114.3)++	17.3
1	0.006 A/cm -150 min.	782.5 (113.5)	858.7 (124.5)	15.7
3	0.006 A/cm -150 min.	717.0 (104.0)	720.4 (104.5)++	14.0

* Current density and charging time
** 0.2% approximated from load vs time output of plated specimens
\+ 0.2% yield strength using extensometer on unplated specimen
++ fracture stress

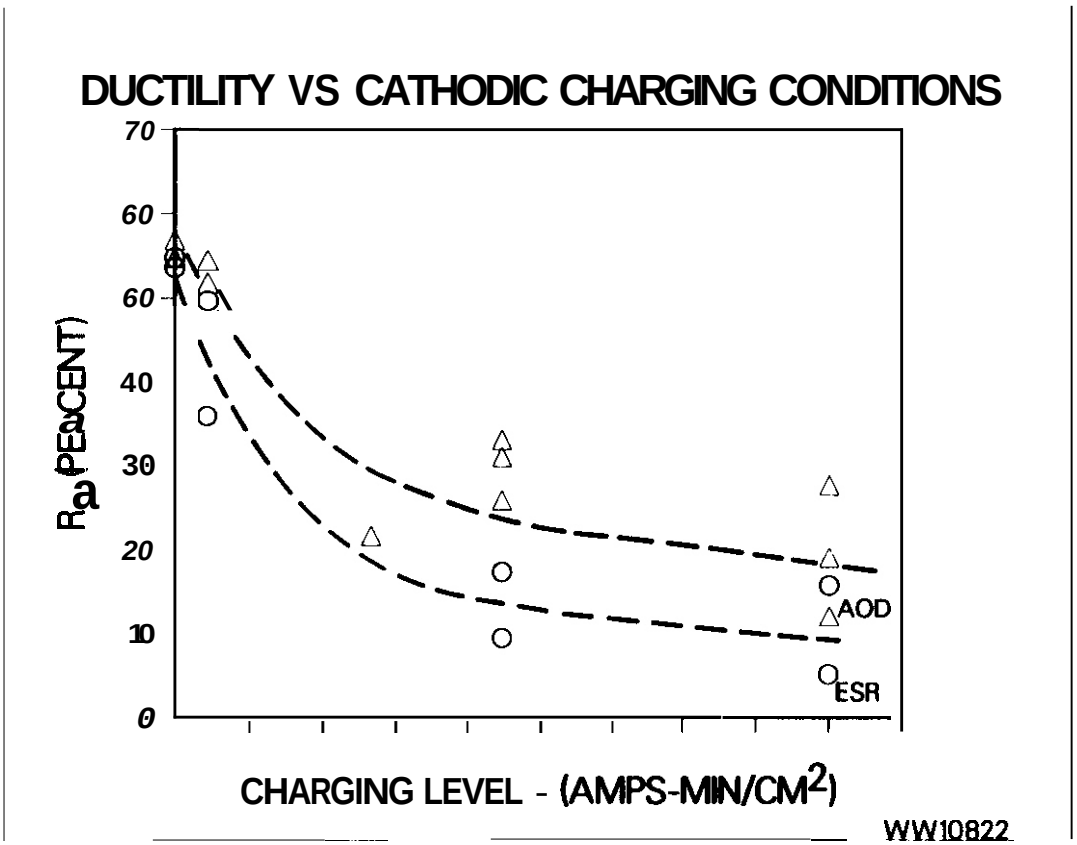

Figure 1. Reduction in Area (R_A) versus hydrogen charging level (current density x time) for ESR and AOD processed 12Cr-1Mo steel.

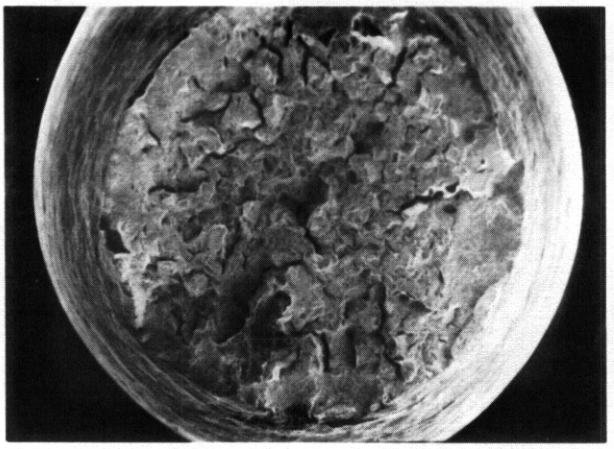

(a)

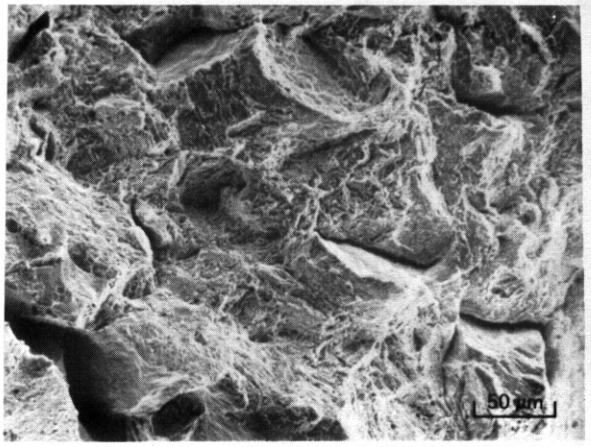

(b)

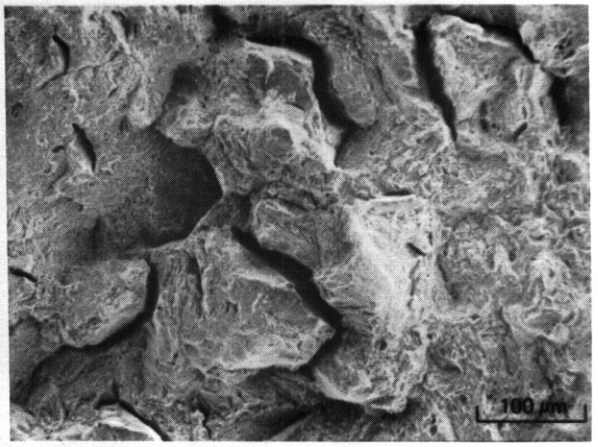

(c)

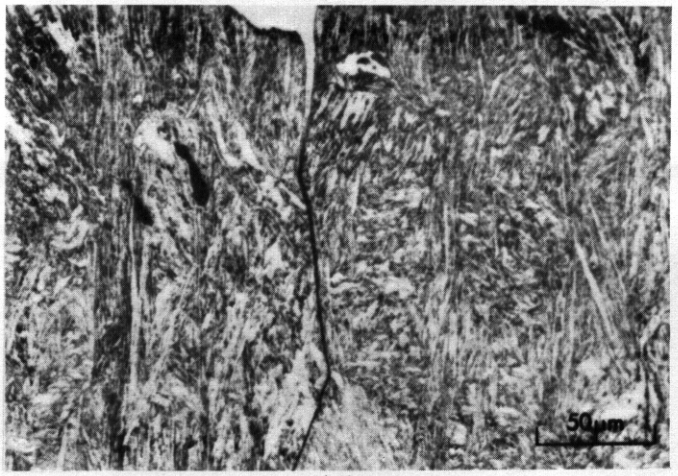

(d)

Figure 2. 12Cr-1Mo steel (ESR) uncharged tensile fracture: (a) low magnification of fracture surface; (b and c) higher magnification showing intergranular character of secondary cracks; (d) metallographic cross-section showing secondary cracking along prior austenite grain boundary.

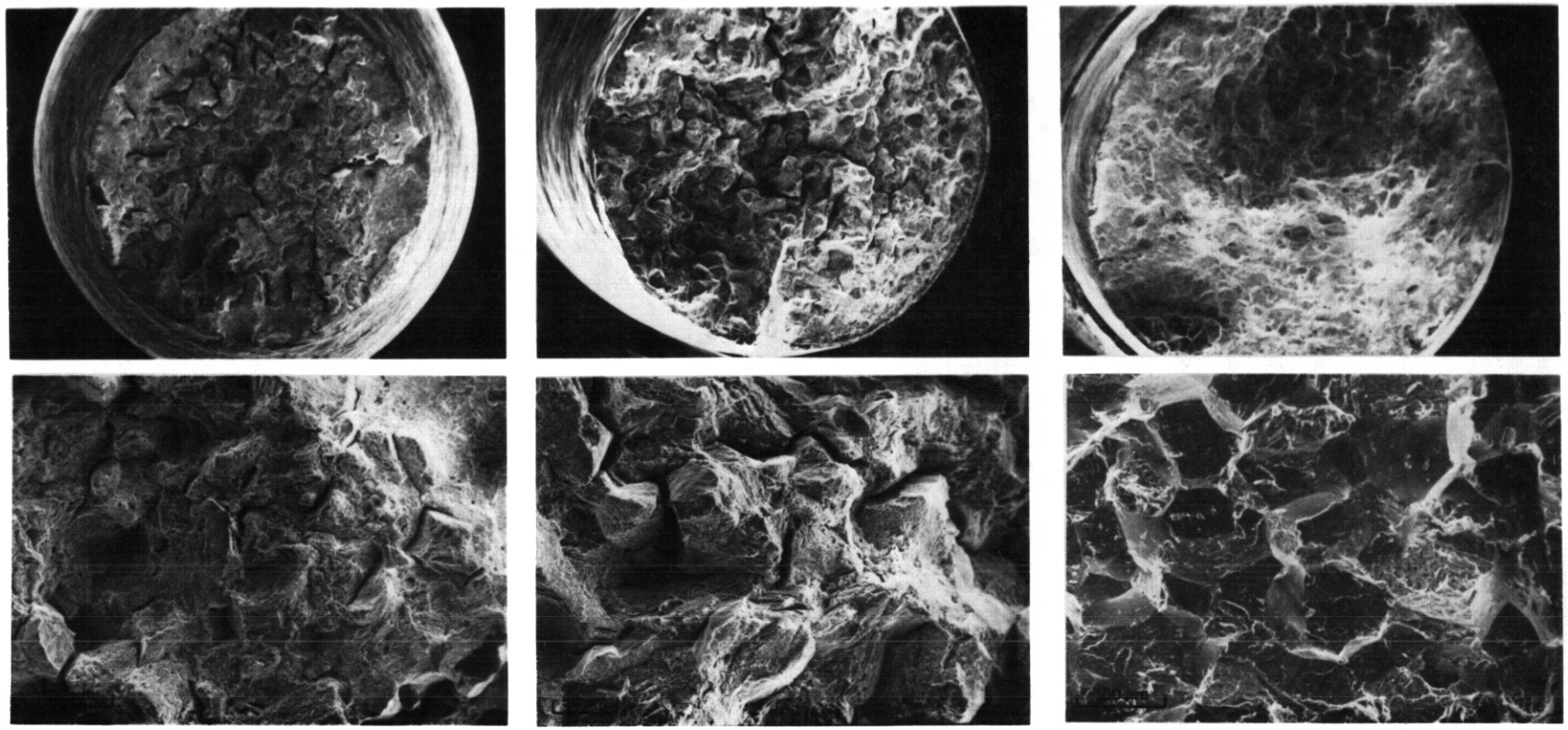

UNCHARGED | 0.003 A/cm^2 15 minutes | 0.003 A/cm^2 150 minutes

Figure 3. Change in tensile fracture mode with hydrogen charging level (current density and time) for ESR processed 12Cr-1Mo steel.

increased. The intergranular character of the secondary cracking was even more pronounced than for the uncharged specimens. At a charging level of 0.003 A/cm^2 for 150 minutes, the fracture changed to classical intergranular cracking which initiated at or very near the outer surface. This intergranular morphology is typical of hydrogen embrittled specimens.[7] At 0.006 A/cm^2 for 150 minutes, the specimens exhibited the same classical intergranular fracture mode. This transition to classical intergranular fracture with increasing hydrogen content was also observed for the AOD processed 12Cr-1Mo steel.[1]

7.9.4.3 Auger Analysis Results

Auger analyses were initiated to identify chemical segregation that may be associated with either the intergranular rupture or classical hydrogen assisted intergranular fracture. The results are shown in Table II for selected elements. The analyses compare the concentration of a given element on an intergranular facet (prior austenite grain boundary) with the concentration of the same element on a ductile fracture area (matrix). The data are intended for qualitative comparison rather than quantitative evaluation.

The results show that the concentration of the carbide forming elements (Cr, Mo, W) and phosphorous is significantly greater at the prior austenite grain boundaries than in the matrix. Segregation of these elements to the boundary is balanced by a decrease in iron concentration.

7.9.4.4 Discussion

The results of these tensile tests show that the ESR processed 12Cr-1Mo steel in the quenched-and-tempered condition is susceptible to hydrogen induced ductility losses at cathodic charging levels of only 0.003 A/cm^2 for 15 minutes. For more severe charging levels, the ductility loss is greater and the fracture mode changes from intergranular rupture to classical intergranular

Table II

Auger Analysis*

HT-9 Sandvik Pipe	Fe	Cr	Si	Mo	Ni	V	S	P	W
I. G. Facet **	44.0	21.0	1.2	1.0	0.5	9.0	0.1	2.0	0.3
Matrix	57.0	11.0	1.4	0.3	0.4	N/A	0.2	0.6	0.2
12Cr-1Mo AOD Heat									
I.G. Facet **	51.0	24.0	0.8	1.3	0.1	8.2	0.4	1.1	0.3
Matrix	62.0	13.0	0.7	0.3	0.6	5.3	0.3	0.3	0.1

* Atomic %

** Prior Austenite grain boundary

N/A Not Available

fracture. These results are qualitatively the same as for the 12Cr-1Mo AOD processed material evaluated previously. Together, these findings present some concern as to the susceptibility of 12Cr-1Mo steel to hydrogen embrittlement.

It would be premature to make conclusive statements concerning the hydrogen compatibility of the 12Cr-1Mo steel as a first wall material based on the tensile tests results accumulated to date. It is clear that these experiments do not simulate the conditions of a first wall; indeed, many of the actual MFE machine operating parameters are still subject to speculation. However, these tensile test results do provide reasons to question the hydrogen compatibility of the alloy. Foremost among the reasons is that in the uncharged condition both ESR and AOD material exhibit an intergranular rupture type of tensile fracture. Large secondary cracks which follow prior austenite grain boundaries are prominent on the fracture surface. Although additional study is required to confirm the failure mechanism, it is believed to result from the preferential initiation of voids at coarse $M_{23}C_6$ carbides which decorate the prior austenite boundaries. The fact that this alloy with a 750°C temper exhibits a preference for grain bondary cracking in the uncharged condition correlates with the observed increased susceptibility to grain boundary embrittlement when charged with hydrogen.

In addition, phosphorous segregation at the prior austenite boundaries may further sensitize these boundaries. Phosphorous segregation at grain boundaries has been shown to cause temper embrittlement[4,5] and increased susceptibility to hydrogen embrittlement' in many iron base alloys. Specifically, Lemble et al.[3] concluded that phosphorous segregation was responsible for temper embrittlement in a low alloy 12Cr steel. These studies have also shown the tendency for chromium and phosphorous to co-segregate as they did in the Auger analyses reported here. Additional Auger tests are planned to determine if the high phosphorous concentration at the prior austenite boundaries in the

present alloy is tied-up with the $M_{23}C_6$ carbides or occurs as a free contaminant. At present, however, the high phosphorous content at. the prior austenite boundaries provides another reason for concern regarding the hydrogen compatibility of the alloy.

The tensile tests results have been presented and evaluated in terms of cathodic charging levels (current density X time). Experiments are underway to determine an average hydrogen concentration for each charging condition. A new Leco hydrogen determinator has recently been installed at Sandia and the necessary tests are proceeding. Earlier in this program, the hydrogen contents were estimated using a vacuum extraction method which is considerably less accurate. Based upon vacuum extraction, the hydrogen levels for the three cathodic charging levels were estimated to range from 50-1500 appm. These values are significantly greater than the maximum anticipated hydrogen concentration in a first wall of 0.5 appm as predicted by Stoltz et al.[8]

This comparison has led some to discount the loss of ductility observed in the present tensile test results as only the product of a gross overtest. This, however, may not be the case. The hydrogen calculations reported[8] were for temperatures of 200-365°C where hydrogen trapping can be discounted and the concentration is dependent only upon the lattice solubility. However, at room temperature where the cathodic charging experiments are carried out, trapping is of paramount importance and can account for total hydrogen concentrations several orders of magnitude above those predicted by lattice solubility considerations alone.[9] As a result of the contribution of trapping, lattice concentrations of 0.5 appm at room temperature (as predicted by Stoltz et al) can be attained only in the presence of an overall concentration orders of magnitude greater than 0.5 appm. It is difficult to estimate trap densities in a complex alloy like a martensitic steel, especially in the presence of radiation damage and helium. Therefore, calculations of the associated room temperature hydrogen concentration for a first

wall structure cannot be made at present. However, values of 50-1000 appm may not be as much an overtest as one might conclude from lattice solubility calculations alone.

Finally, the hydrogen charged tensile results for the AOD and ESR processed National Fusion Heat do not agree with the original tests performed on the quenched-and-tempered Sandvik pipe material.[6] These earlier tests had shown no reduction in ductility or change in fracture mode after charging at 0.006 A/cm^2 for 150 minutes. Re-testing of the same material has shown that the original results were caused by the effects of re-heat treating the specimens after they had been machined. In more recent tests on the same material where specimens were machined from fully heat treated stock, the results were similar to those of the ESR and AOD tests. The fundamental cause of the history-dependent behavior of the Sandvik HT-9 is not known unequivocally, but those tests were not representative of the behavior of cathodically charged 12Cr-1Mo steel.

7.9.5 Conclusions

1. In the uncharged condition, ESR processed 12CR-1Mo steel tensile specimens in the quenched-and-tempered condition failed by an intergranular rupture fracture mode. Large secondary cracks intersecting the fracture surfaces followed prior austenite grain boundaries indicating a sensitization of these boundaries even before hydrogen charging.

2. Cathodic charging at 0.003 A/cm^2 for 15 minutes reduced the tensile ductility by 33% and increased the amount of secondary cracking. Charging at 0.003 A/cm^2 for 150 minutes further reduced the ductility and caused a fracture mode change to classical intergranular fracture.

3. Auger analyses of quenched-and-tempered 12Cr-1Mo steels showed segregation of the carbide formers (Cr, Mo, W) and phosphorous at the prior austenite grain boundaries.

4. The tensile results on cathodically charged 12Cr-1Mo ESR steel is qualitatively the same as observed previously for 12Cr-1Mo AOD processed material. These results present some concern as to the susceptibility of this alloy to hydrogen embrittlement.

7.9.6 References

1. J. M. Hyzak and W. M. Garrison, "The Effect of Hydrogen Charging on the Tensile Properties of HT-9 Base Metal", ADIP Semiannual Progress Report, Sept. 30, 1981, DOE/ER-0045-7, pp. 186-203.
2. N. Bandyopadhyay and C. J. McMahon, "Effect of Residual Impurities on Hydrogen Assisted Cracking in High-Strength Steels", Final Report, Naval Air Systems Command, Contract N 0019-77-C-0158, Dec. 1977.
3. Ph. Lemble, A. Pineau, J. L. Castagne, Ph. Dumoulin, and M. Guttmann, "Temper Embrittlement of 12% Cr Martensitic Steel", Metal Science, Aug. 1979, pp. 496-502.
4. I. Olefjord, "Temper Embrittlement", Int'l Metals Rev., 1978, (4), pp. 149-163.
5. J. Q. Clayton and J. F. Knott, "Phosphorous Segregation in Austenite in Ni-Cr and Ni-Cr-Mn Steels", Metal Science, 16, Mar. 1982, pp. 145-152.
6. J. M. Hyzak and R. E. Stoltz, "The Effect of Internal Hydrogen on the Mechanical Properties of HT-9: Room Temperature", ADIP Quarterly Progress Report, Mrach 31, 1981, DOE/ER-0045/6, pp. 180-190.
7. C. J. McMahon, V. Vitek, and J. Kameda, "Mechanics and Mechanisms of Intergranular Fracture", Developments in Fracture Mechanics-2, edited by G. G. Chell, Applied Science Publishers, New Jersey, p. 193.
8. R. E. Stoltz, M. I. Baskes, and G. W. Look, "Calculations of Hydrogen Isotope Loading in HT-9 First Wall Structures", ADIP Quarterly Progress Report, September 30, 1980, DOE/ER-0045, pp. 151-159.

9. J. P. Hirth, "Effects of Hydrogen on the Properties of Iron and Steels", Metall. Trans., 11A, June 1980, pp. 861–889.

7.10 TENSILE PROPERTIES OF FERRITIC (MARTENSITIC) STEELS AFTER LOW-TEMPERATURE HFIR IRRADIATION — R. L. Klueh and J. M. Vitek (Oak Ridge National Laboratory)

7.10.1 ADIP Task

ADIP Tasks are not defined for Path E, Ferritic Steels, in the 1978 program plan.

7.10.2 Objective

The goal of this project is to evaluate the properties of irradiated ferritic steels. Irradiation at reactor coolant temperature, near 55°C, in the High Flux Isotope Reactor (HFIR) is used to produce both displacement damage and transmutation helium at levels relevant to fusion reactor service.

7.10.3 Summary

In addition to the ferritic steels previously tested, experiment HFIR-CTR-33 also contained tensile specimens of 20%-cold-worked type 316 stainless steel for irradiation at about 55°C. The tensile behavior of the type 316 stainless steel was determined at room temperature and 300°C, and the results showed the irradiated properties of the two classes of steels to be quite similar.

7.10.4 Progress and Status

The HFIR-CTR-33 irradiation experiment was designed to determine the effect of transmutation helium on the tensile properties of 12 Cr-1 MoW and 9 Cr-1 MoVNb ferritic (martensitic) steels. Nickel was added to the base compositions to produce helium during HFIR irradiation. Specimens of 2 1/4 Cr-1 Mo steel (no nickel added) in two heat-treated conditions were also irradiated. These steels have been tested at room temperature and 300°C; the results have been reported.[1-3]

In addition to the ferritic steels, HFIR-CTR-33 also contained several 20%-cold-worked type 316 stainless steel (CW 316) tensile specimens. Because an extensive data base on irradiation effects exists for this alloy, it forms a basis for comparison with other alloys. This

report presents a comparison of the effects of irradiation on the ferritic steels with those on the type 316 stainless steel irradiated and tested under similar conditions.

7.10.4.1 Alloys Irradiated

Details on the chemical composition and tensile behavior of the 12 Cr-1 MoVW, 9 Cr-1 MoVNb, and 2 1/4 Cr-1 Mo steels were previously given.[1-3] The chemical composition of the type 316 stainless steel reference heat (X15893) is given in Table 7.10.1. Prior to the final 20% cold work (by rolling), the sheet was annealed for 1 h at 1050°C.

Table 7.10.1. Chemical Composition of Type 316 Stainless Steel Reference Heat X15893

Element	wt %	Element	Wt
Cr	17.28	Nb	<0.05
Mn	1.70	Ta	<0.05
Ni	12.44	Ti	<0.05
Mo	2.10	B	0.0004
co	0.3	C	0.0613
cu	0.3	S	0.0179
Si	0.67	P	0.037

7.10.4.2 Experimental Procedure

Sheet tensile specimens (SS-1 type) with a reduced gage section 20.3 mm long by 1.52 mm wide by 0.76 mm thick were irradiated[4] near 55°C to a maximum total fluence of 5×10^{26} neutrons/m^2. After immersion density measurements, specimens were tested at room temperature and 300°C in a vacuum chamber at a strain rate of 4.2×10^{-5}/s.

7.10.4.3 Results

As was true for the ferritic steels,[1] there was no detectable density change in type 316 stainless steel that could be attributed to the irradiation.

Room temperature and 300°C tensile tests were made on irradiated and unirradiated (control) specimens from the CW 316. Irradiation parameters, test conditions, and the measured tensile properties are given in Table 7.10.2. In Figs. 7.10.1 through 7.10.3 the CW 316 results are compared with the base compositions (without nickel additions) for 9 Cr-1 MoVNb, 12 Cr-1 MoVW, and 2 1/4 Cr-1 Mo steel.

Table 7.10.2. Tensile Properties of Unirradiated and Irradiated[a] Heat X15893 20%-Cold-Worked Type 316 Stainless Steel

Fluence, >0.1 MeV (neutrons/m^2)	Displacement Level (dpa)	Helium Concentration[b] (at. ppm)	Test Temperature (°C)	Strength (MPa)		Elongation (%)	
				Yield	Ultimate	Uniform	Total
0			25	665	743	11.1	14.9
0.63×10^{26}	5.2	159	25	854	867	0.8	8.6
1.3×10^{26}	9.5	416	25	892	905	0.8	7.7
0			300	595	645	1.8	4.4
1.1×10^{26}	7.8	305	300	723	731	0.6	3.3

[a]Irradiation was in HFIR at about 55°C.

[b]Calculated level of helium from transmutation of ^{58}Ni and ^{10}B.

The 9 Cr and 12 Cr steels were irradiated in the normalized-and-tempered conditions;[1,2] the microstructures were entirely tempered martensite (>99%). The 2 1/4 Cr-1 Mo steel was irradiated in two heat-treated conditions: normalized and tempered, where a tempered bainite microstructure was developed, and isothermally annealed, where the microstructure developed was 75 to 80% polygonal ferrite, the balance primarily bainite.

The yield strength of the unirradiated CW 316 is greater than that of the other four materials (Fig. 7.10.1); the ultimate tensile strength of the unirradiated CW 316 exceeds all but those for the 12 Cr-1 MoVW steel (Fig. 7.10.2). Irradiation produces a much larger increase in strength in the ferritic steels than in the CW 316. The highest strengths were observed for the normalized-and-tempered 2 1/4 Crl Mo steel and the 12 Cr-1 MoVW. The yield strength and ultimate tensile strength of the

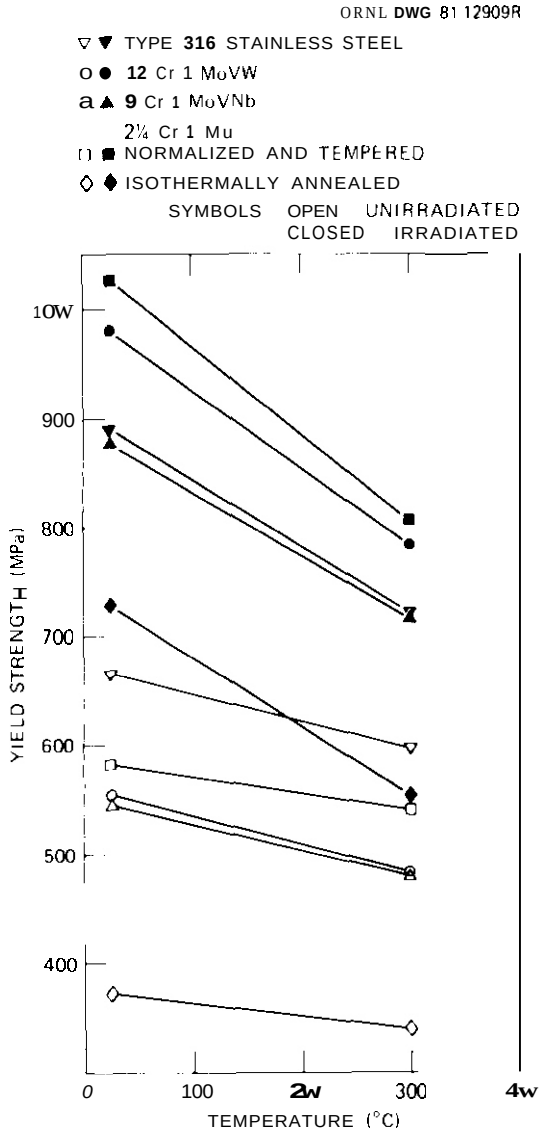

Fig. 7.10.1. The 0.2% Yield Strength Plotted Against Test Temperature for 20%-Cold-Worked Type 316 Stainless Steel, 12 Cr-1 MoVW, 9 Cr-1 MoVNb, and 2 1/4 Cr-1 Mo Steel Unirradiated and After HFIR Irradiation at about 55°C.

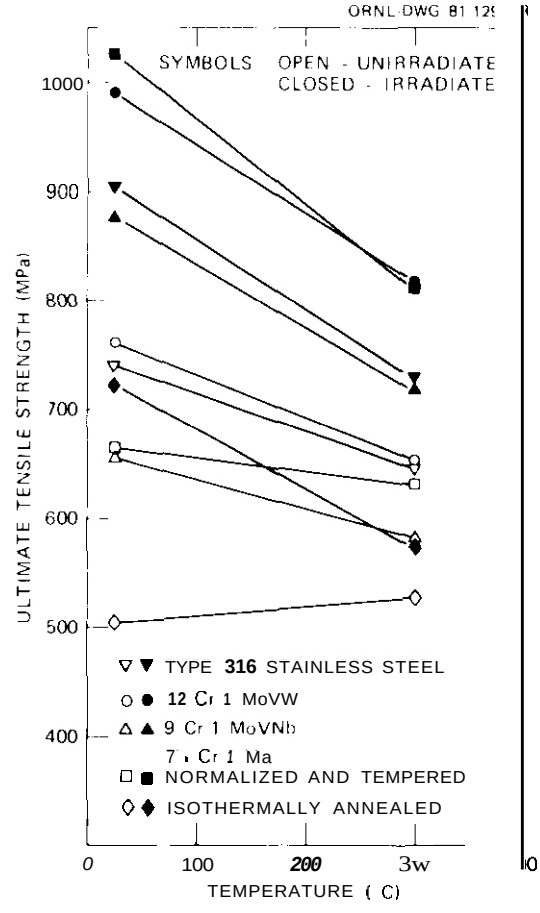

Fig. 7.10.2. The Ultimate Tensile Strength Plotted Against Test Temperature for 20%-Cold-Worked Type 316 Stainless Steel, 12 Cr-1 MoVW, 9 Cr-1 MoVNb, and 2 1/4 Cr-1 Mo Steel Unirradiated and After HFIR Irradiation at about 55°C.

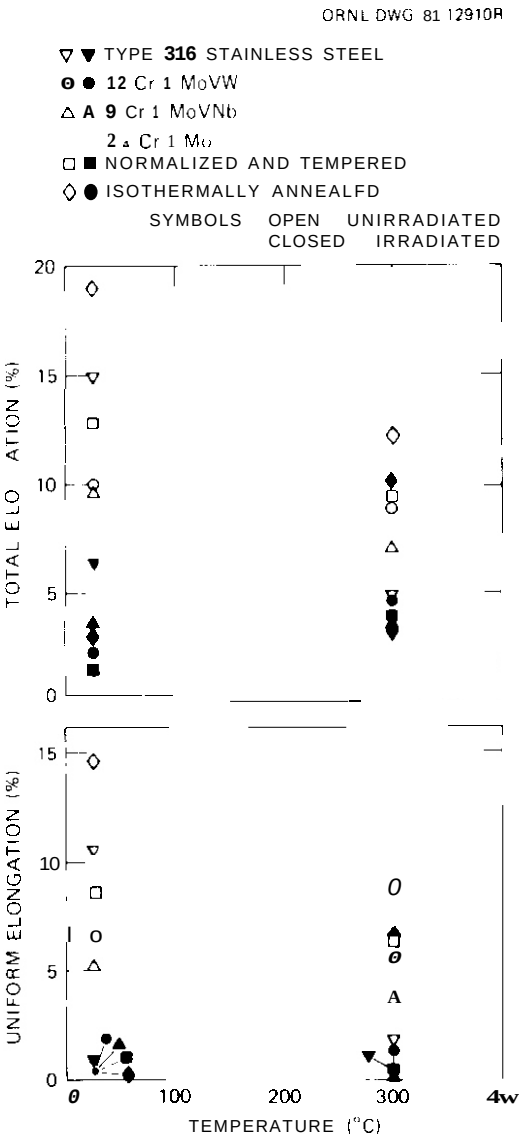

Fig. 7.10.3. The Uniform and Total Elongation Plotted Against Test Temperature for 20%-Cold-Worked Type 316 Stainless Steel, 12 Cr-1 MoVW, 9 Cr-1 MoVNb, and 2 1/4 Cr-1 Mo Steel Unirradiated and After HFIR Irradiation at about 55°C.

irradiated 9 Cr-1 MoVNb are similar to those of the CW 316, while the values for the irradiated, isothermally annealed 2 1/4 Cr-1 Mo steel are considerably below the respective values for the stainless steel.

To compare the relative hardening effects, we have calculated the ratio of irradiated to unirradiated strength properties, namely,

$$R_Y = Y_i / Y_u \text{ and } R_u = U_i / U_u \ ,$$

where Y_i and Y_u are the irradiated and unirradiated yield strengths and U_i and U_u the irradiated and unirradiated ultimate tensile strengths

(Table 7.10.3). Although it is risky to draw definitive conclusions from single values for each alloy, the data at both room temperature and 300°C show the relative increase in yield strength (R_y) due to irradiation is greater for the ferritic steels than for the CW 316. Although the isothermally annealed 2 1/4 Cr-1 Mo steel has the lowest yield strength, it shows the greatest relative increase at room temperature. There are only minor differences in most of the R, values; the only exceptions are the room-temperature values for the 2 1/4 Cr-1 Mo, which are larger than those for the high-chromium ferritics and the CW 316. Note the smaller R_u for the isothermally annealed 2 1/4 Cr-1 Mo steel at 300°C.

Table 7.10.3. Relative Hardening of Several Steels by Irradiation at about 55°C in HFIR

Alloy	Relative Hardening at Each Test Temperature			
	Room Temperature		300°C	
	R_y	R_u	R_y	R_u
CW 316	1.3	1.2	1.2	1.1
9 Cr-1 MoVNb	1.6	1.3	1.5	1.2
12 Cr-1 MoVW	1.8	1.3	1.6	1.3
2 1/4 Cr-1 Mo (normalized and tempered)	1.8	1.6	1.6	1.3
2 1/4 Cr-1 Mo (isothermally annealed)	2.1	1.5	1.6	1.1

In general, there is little difference in ductility between the irradiated CW 316 and the ferritic steels (Fig. 7.10.3) (the only exception is the isothermally annealed 2 1/4 Cr-1 Mo steel, which will be discussed below). We previously pointed out the low uniform elongation for the ferritic steels after irradiation and concluded that this was the result of the irradiation and test conditions.[1-3] Similar quite low uniform elongation values are also noted for the type 316 stainless steel (Fig. 7.10.3). However, there is a difference in stress-strain curves for the CW 316 and the ferritic steels, as seen by comparing the CW 316 curves (Fig. 7.10.4) and the curves for 12 Cr-1 MoVW steel (Fig. 7.10.5). Once the early uniform elongation is reached, the decrease in strength is much more gradual in the case of the CW 316 than the ferritic steel. At

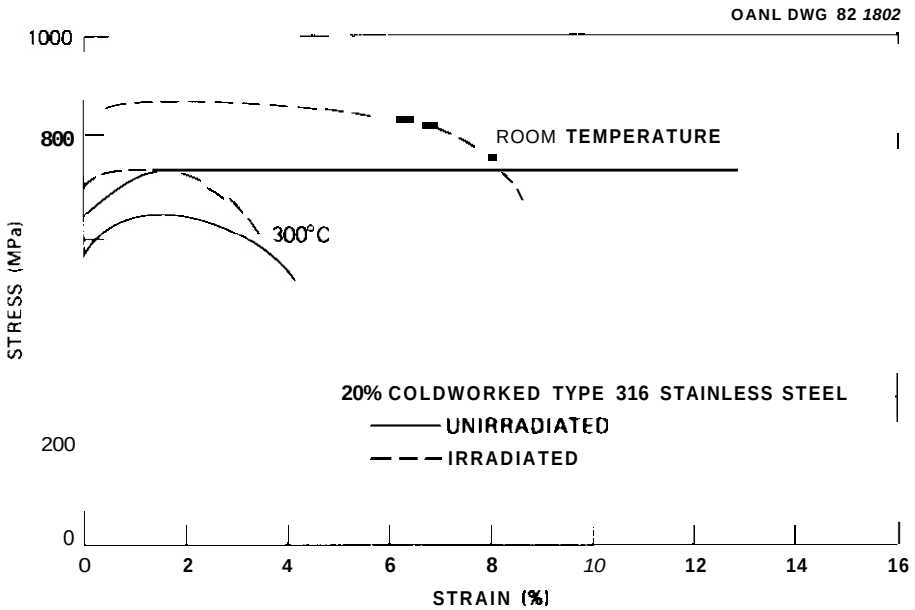

Fig. 7.10.4. Engineering Stress-Strain Curves at Room Temperature and 300°C for Unirradiated and HFIR-Irradiated 20%-Cold-Worked Type 316 Stainless Steel. Irradiation was in HFIR at about 55°C.

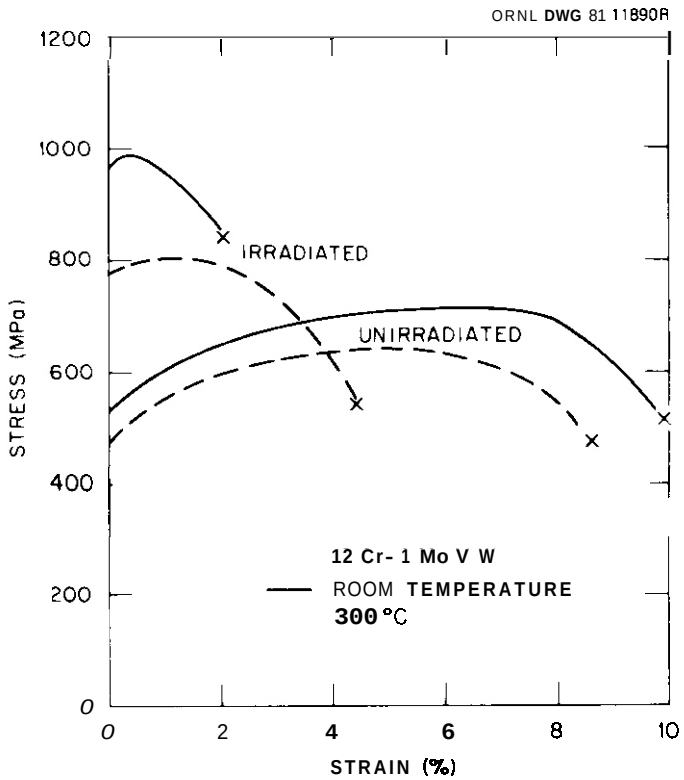

Fig. 7.10.5. Engineering Stress-Strain Curves at Room Temperature and 300°C for 12 Cr-1 MoVW Unirradiated and After Irradiation in HFIR at about 55°C.

300°C, the total elongations are similar for both materials. Thus, the difference in shape will probably be of minor consequence. Both types of curves may be indicative of channel deformation.

The stress–strain curves of the type observed for the ferritic steels (i.e., low uniform elongation followed by a rapid decrease in stress beyond the ultimate tensile strength) have been found in the bcc refractory metals molybdenum, tantalum, and niobium and their alloys.[5] The decreased uniform elongation has been attributed to the highly localized form of deformation termed channel deformation, because of its microscopic appearance [dislocation–free channels are observed by transmission electron microscopy (TEM)]. Fish et al.[6] observed channel deformation in the austenitic stainless steel type 304 after it was irradiated at 400°C to very high neutron fluences in EBR–II (up to 10.7×10^{26} neutrons/m^2, $E > 0.1$ MeV). For 370°C tensile tests, scanning electron microscopy (SEM) examination of the fracture surfaces revealed that ductile–type failure occurred after exposure to a low fluence, but as the fluence increased, slip was progressively confined to very narrow bands of planes. At the highest fluences, it was found that "shear on the active slip planes has become so extensive that the crystals have literally slipped apart."[6]

Wiffen and Maziasz irradiated CW 316 in HFIR at 55°C to somewhat similar dpa values to those achieved in the present experiment.[7] Tensile tests over the range 35 to 700°C produced results that were in general agreement with those reported here. Very low uniform elongations (0.2–0.6%) were found between 35 and 300°C; between 300 and 600°C, there was a significant improvement to 2.2 to 6.8% uniform elongation.

There is a significant improvement in ductility (both in uniform and total elongation) at 300°C for the isothermally annealed 2 1/4 Cr–1 Mo steel over that of all other steels tested, including the CW 316 (Fig. 7.10.3). The isothermally annealed steel had uniform and total elongations of 6.7 and 10.1%, respectively, compared with less than 1 and less than 4% for 9 Cr–1 MoVNb steel, normalized–and–tempered 2 1/4 Cr–1 Mo steel, and CW 316 and 1.8 and 5.1% for 12 Cr–1 MoVW steel.[1–3] This difference may be an important clue to the effect of microstructure on the irradiation behavior of these materials. The isothermally annealed steel

was primarily polygonal ferrite, while the other ferritic steels were either tempered bainite OK tempered martensite. More information will be required before this observation can be fully understood. It is also interesting to note that the CW 316 was the only steel for which the uniform and total elongation at 300°C was less than it was at room temperature (Fig. 7.10.3). Higher elongation at 300°C was noted for 12 Cr-1 MoVW steel' and 2 1/4 Cr-1 Mo steel,[3] and the values for the 9 Cr-1 MoVNb steel were essentially the same at the two temperatures.

In the tensile studies reported for the 9 Cr-1 MoVNb and 12 Cr-1 MoVW steels, data were obtained for steels to which nickel had been added.[1,2] When these steels contained 2% Ni, they were considerably stronger than the alloys without nickel. For the nickel-containing steels, the R_y and R_u values were similar to those without nickel, indicating similar relative amounts of irradiation hardening. Although the strength of these nickel-doped steels was considerably above that for the stainless steel — both before and after irradiation — the uniform and total elongation values were similar to those of the steels without nickel and thus compared favorably with the CW 316. In fact, at 300°C, the uniform and total elongation of these stronger steels were comparable to those for CW 316.

7.10.5 References

1. R. L. Klueh and J. M. Vitek, "Tensile Properties of Ferritic Steels After Low-Temperature HFIR Irradiation," *ADIP Quart. Prog. Rep. Dec. 31, 1980,* DOE/ER-0045/5, pp. 218–25.
2. R. L. Klueh and J. M. Vitek, "Tensile Properties of Ferritic Steels After Low-Temperature HFIR Irradiation," *ADIP Quart. Prog. Rep. Mar. 31, 1981,* DOE/ER-0045/6, pp. 139–47.
3. R. L. Klueh and J. M. Vitek, "Tensile Properties of Ferritic Steels After Low-Temperature HFIR Irradiation," *ADIP Semiannu. Prog. Rep. Sept. 30, 1981,* DOE/ER-0045/7, pp. 275–83.
4. M. L. Grossbeck and J. W. Woods, "An Irradiation Experiment to Scope the Tensile Properties of Ferritic Alloys — HFIR-CTR-33," *ADIP Quart. Prog. Rep. June 30, 1980,* DOE/ER-0045/3, pp. 30–34.

5. F. W. Wiffen, "The Tensile Properties of Fast Reactor Neutron Irradiated BCC Metals and Alloys," pp. 176–97 in *Defects and Defect Clusters in B.C.C. Metals and Their Alloys, Nucl. Met.* 18, ed. by R. J. Arsenault (Proc. 1973 Int. Conf. Aug. 14–16, 1973), National Bureau of Standards, Gaithersburg, Maryland.

6. R. L. Fish et al., "Swelling and Tensile Property Evaluation of High-Fluence EBR-II Thimbles," pp. 149–64 in *Effects of Radiation on Substructure and Mechanical Properties of Metals and Alloys,* ASTM STP 529, American Society for Testing and Materials, Philadelphia, 1973.

7. F. W. Wiffen and P. J. Maziasz, "The Influence of Neutron Irradiation at 55°C on the Properties of Austenitic Stainless Steels," *J. Nucl. Mater.* 103&104(1–3): 821–26 (1981).

7.11 HELIUM EMBRITTLEMENT TESTS ON FERRITIC STEELS — R. L. Klueh and J. M. Vitek (Oak Ridge National Laboratory)

7.11.1 ADIP Task

ADIP Tasks are not defined for Path E, Ferritic Steels, in the 1978 program plan.

7.11.2 Objective

The goal of this project is to evaluate the properties of irradiated ferritic steels. Irradiation in the High Flux Isotope Reactor (HFIR) is used to produce both displacement damage and transmutation helium at levels relevant to fusion reactor service.

7.11.3 Summary

Tensile tests at 700°C on nickel-doped 9 Cr-1 MoVNb and 12 Cr-1 MoVW steels that were irradiated at 55°C in HFIR to produce up to about 50 at. ppm He indicated that there was no helium embrittlement. These results contrast with literature data showing that very small amounts of helium can cause a large decrease in ductility for many alloys when tested under equivalent conditions.

7.11.4 Progress and Status

The HFIR-CTR-33 experiment was primarily designed to determine the effect of transmutation helium produced during irradiation at about 55°C on the tensile properties of 12 Cr-1 MoVW and 9 Cr-1 MoVNb ferritic (martensitic) steels. Nickel was added to the base composition to produce helium during HFIR irradiation.[1] We previously reported on the tensile behavior of the nickel-doped steels after irradiation.[1,2] No helium effects were detected in tensile tests at room temperature and 300°C. In this report we will present data for tensile tests at 700°C, where small amounts of helium are known to affect the ductility of several alloys.

7.11.4.1 Alloys Irradiated and Tested

The four heats of 12 Cr-1 MoVW and three of 9 Cr-1 MoVNb were prepared by combustion Engineering by electroslag remelting.[3] Heats of

12 Cr-1 MoVW with 0.5, 1, and 2% Ni and 9 Cr-1 MoVNb with 0.1 and 2% Ni were prepared. Also, for each steel a heat was prepared with 2% Ni but with additional chromium, molybdenum, and tungsten that was added to "adjust" the chromium equivalent to a value similar to the base steels with no nickel additions. (These alloys will be referred to as adjusted steels.) Details on the net chromium equivalent calculations were previously given.[1-3] The chemical composition of the seven heats are given in Table 7.11.1.

All seven alloys were prepared in 25-kg heats, and a sample of each was rolled into 3.2-mm plate. This plate was further rolled into 0.76-mm sheet for specimen fabrication.

All of the steels were tested in the normalized and tempered condition. Details on these heat treatments were previously given.[1,2] As normalized and tempered, all but the adjusted alloys were essentially 100% tempered martensite. The adjusted alloys contained 15 to 20% δ-ferrite.

In addition to the ferritic steels, the HFIR-CTR-33 capsule also contained some 20%-cold-worked type 316 stainless steel (CW 316) specimens, which were tested for comparison. Details on this material, taken from the fusion reference heat (X15893), were given in another section of this report.[4]

7.11.4.2 Experimental Procedure

Sheet tensile specimens in this experiment were of an SS-1 type with a reduced gage section 20.3 mm long by 1.52 mm wide by 0.76 mm thick.[1,2] The maximum total fluence for HFIR-CTR-33 was 5×10^{26} neutrons/m^2 and the maximum fast fluence 1.3×10^{26} neutrons/m^2 (>0.1 MeV).[5] However, the specimens being discussed in this report received less than the maximum, since they were near the end of the capsule. Tests were conducted in a vacuum chamber on a 44-kN-capacity Instron universal testing machine at a strain rate of 4.2×10^{-5}/s.

7.11.4.3 Results

Tests at 700°C were made on the 12 Cr-1 MoVW steel with 0.5, 1, and 2% Ni and 9 Cr-1 MoVNb with 0.1 and 2% Ni. The two nickel-adjusted steels

Table 7.11.1. Chemical Composition of Heats of Nickel-Doped and Undoped Ferritic Steels

Element	Composition, wt %[a]						
	12 Cr-1 MoVW (XAA-3587)	12 Cr-1 MoVW-1 Ni (XAA-3588)	12 Cr-1 MoVW-2 Ni (XAA-3589)	12 Cr-1 MoVW-2 Ni Adjusted (XAA-3592)	9 Cr-1 MoVNb (XA-3590)	9 Cr-1 MoVNb-2 Ni (XA-3591)	9 Cr-1 MoVNb-2 Ni Adjusted (XA-3593)
C	0.21	0.20	0.20	0.15	0.09	0.064	0.067
Mn	0.50	0.47	0.49	0.32	0.36	0.36	0.36
P	0.011	0.010	0.011	0.008	0.008	0.008	0.008
S	0.004	0.004	0.004	0.004	0.004	0.004	0.004
Si	0.18	0.13	0.14	0.07	0.08	0.08	0.10
Ni	0.43	1.14	2.27	2.30	0.11	2.17	2.24
Cr	11.99	11.97	11.71	13.60	8.62	8.57	12.30
Mo	0.93	1.04	1.02	1.59	0.98	0.98	1.70
V	0.27	0.31	0.31	0.30	0.209	0.222	0.29
Nb	0.018	0.015	0.015	0.016	0.063	0.066	0.074
Ti	0.003	0.003	0.003	0.002	0.002	0.002	0.002
Co	0.017	0.015	0.021	0.018	0.013	0.015	0.017
Cu	0.05	0.05	0.05	0.05	0.03	0.04	0.03
Al	0.030	0.017	0.028	0.018	0.013	0.015	0.016
B	<0.001	<0.001	<0.001	<0.001	<0.001	<0.001	<0.001
W	0.54	0.53	0.54	0.64	0.01	0.01	0.01
As	<0.001	0.002	<0.002	<0.002	<0.001	<0.001	<0.001
Sn	0.002	0.001	0.002	0.002	0.003	0.003	0.003
Zr	<0.001	<0.001	<0.001	<0.001	<0.001	<0.001	<0.001
N	0.020	0.016	0.017	0.014	0.050	0.053	0.059
O	0.005	0.007	0.007	0.007	0.007	0.006	0.007

[a]Balance iron.

were also tested. Unirradiated control specimens were tested for each steel, along with an irradiated and unirradiated specimen of CW 316. The irradiation parameters, test conditions, and measured tensile properties are given in Table 7.11.2.

Table 7.11.2. Tensile Properties at 700°C of Unirradiated and Irradiated Chromium–Molybdenum Steels and 20%–Cold–Worked Type 316 Stainless Steel. Irradiated samples were all irradiated in HFIR at about 55°C

Fluence >0.1 MeV (neutrons/m^2)	Displacement Level (dpa)	Helium Concentration (at. ppm)	Strength (MPa)		Elongation (%)	
			Yield	Ultimate	Uniform	Total
		12 Cr–1 MoVW				
0			110	142	3.1	19.6
0.63×10^{26}	5.2	13	103	123	2.2	20.5
		12 Cr–1 MoW–1 Ni				
0			93	121	2.5	19.0
0.89×10^{26}	6.4	28	95	105	1.2	22.9
		12 Cr–1 MoW–2 Ni				
0			139	163	2.1	34a
0.89×10^{26}	6.5	49	128	140	1.9	25.5
		12 Cr–1 MoW–2 Ni (adjusted)				
0			181	212	1.7	17.3
0.63×10^{26}	5.1	36	123	153	1.3	21.0
		9 Cr–1 MoVNb				
0			105	131	2.5	16.8
0.63×10^{26}	5.1	8				>10[b]
		9 Cr–1 MoVNb–2 Ni				
0			148	171	1.8	19.1
0.89×10^{26}	6.4	47	119	131	1.2	29.8
		9 Cr–1 MoVNb–2 Ni (adjusted)				
0			181	192	0.6	14.4
0.63×10^{26}	5.2	36	194	203	0.6	11.5
		20%–Cold–Worked Type 316 Stainless Steel				
0			368	400	1.5	8.5
0.89×10^{26}	6.6	234	330	341	0.3	0.3

[a]Crosshead stopped during test. Therefore, this value is probably too large by several percent.

[b]Data for this test was accidently not recorded; an attempt was made to estimate the elongation by fitting the fractured sample together and measuring the length (in a hot cell).

The helium concentrations in the 9 Cr-1 MoVNb and 12 Cr-1 MoVW steels ranged from about 8 and 13 at. ppm He (no nickel additions) to about 47 and 49 at. ppm He (2% Ni additions), respectively. The two 2% Ni-adjusted steel specimens contained about 36 at. ppm He. In almost all cases the yield strength and the ultimate tensile strength of the irradiated specimens were less than for the unirradiated condition. The only exceptions were the yield strength of 12 Cr-1 MoVW-1 Ni and the yield strength and ultimate tensile strength of the 9 Cr-1 MoVNb-2 Ni (adjusted) steel. For these exceptions, there was little difference in the irradiated and unirradiated values. The CW 316 (234 at. ppm He) also had a lower yield strength and lower ultimate tensile strength after irradiation.

The ductility of the ferritic steels at 700°C was only slightly affected by irradiation. There was no apparent decrease in total elongation of either the 9 Cr or 12 Cr steels with up to 47 at. ppm He. In fact, for most of the tests, the total elongation increased. A slight decrease in uniform elongation was noted for most of the tests. However, even after the decrease, the uniform elongation was generally greater than 1%. These minor changes in ductility for the martensitic steels are to be contrasted with the large change for the CW 316, where both the uniform and total elongations were only 0.3% after irradiation.

Kramer et al.[6] used cyclotron bombardment to inject a large number of alloys with a-particles to helium concentrations of 15 to 40 at. ppm. Injection temperatures were maintained below 150°C. Austenitic stainless steels (including type 316) in a solution annealed plus aged condition were injected, as were two ferritic (nontransformable) stainless steels (types 405 and 430, which contained 15–16% Cr). Only the uniform and total elongations at 700°C were reported.[6]

For the type 316 stainless steel injected with 40 at. ppm He, both the uniform and total elongations decreased by more than 50%, the uniform from 22 to 13% and the total from 46 to 15%. Decreases in ductility of varying amounts were also noted for the austenitic stainless steels type 304, 304L, 316L, and 316H that were injected with 15 to 31 at. ppm He.

The ferritic stainless steels injected with 40 at. ppm He showed the unusual behavior of a slight increase in uniform elongation while the

total elongation decreased. The proportionate decrease in total elongation was less than that for the austenitic stainless steels. The uniform elongation of the type 405 stainless steel increased from 4 to 6% and that of the 430 steel from 8 to 10%; elongation the type 405 decreased from 52 to 33% and that for the type 430 from 89 to 48%. From a comparison of these results with those of the present experiments, it is evident that the 9 Cr and 12 Cr martensitic steels exhibited a different behavior from that of the solution-annealed stainless steels and the ferritic stainless steels.

Because of the much larger amount of helium in the CW 316 irradiated in this experiment, it is not possible to draw firm conclusions from a comparison of the helium effects on the two types of alloys. Nevertheless, it appears that the effect of helium on the 9 Cr and 12 Cr martensitic steels is much less than for the CW 316. This also agrees with previous results[7] on the cold-worked material, where it was found that even for a low helium-to-dpa ratio, the total elongation decreased rapidly above 650°C.

7.11.4 References

1. R. L. Klueh and J. M. Vitek, "Tensile Properties of Ferritic Steels After Low-Temperature HFIR Irradiation," *ADIP* ***Quart.*** *Prog. Rep. Dec. 31, 1980,* DOE/ER-0045/5, pp. 218–25.
2. R. L. Klueh and J. M. Vitek, "Tensile Properties of Ferritic Steels After Low-Temperature HFIR Irradiation," *ADIP* ***Quart. Prog. Rep.*** *Mar. 31, 1981,* DOE/ER-0045/6, pp. 139–47.
3. M. L. Grossbeck, V. K. Sikka, T. K. Roche, and R. L. Klueh, "Preparation of Nickel-Doped Ferritic Alloys for HFIR Irradiation to Produce Helium," *ADP* ***Quart.*** *Prog. Rep. Dec. 31, 1979,* DOE/ER-0045/1, pp. 100–04.
4. R. L. Klueh and J. M. Vitek, "Tensile Properties of Ferritic (Martensitic) Steels After Low-Temperature HFIR Irradiation," Sect. 7.10, this report.
5. M. L. Grossbeck and J. W. Woods, "An Irradiation Experiment to Scope the Tensile Properties of Ferritic Alloys — HFIR-CTR-33," *ADIP* ***Quart.*** *Prog. Rep.* June *30, 1980,* DOE/ER-0045/3, pp. 30–34.

6. D. Kramer et al., "A Survey of Helium Embrittlement of Various Alloy Types," pp. 109–15 in *Irradiation Embrittlement and Creep in Fuel Cladding and Core Components*, British Nuclear Energy Society, London, 1972.

7. E. E. Bloom, "Mechanical Properties of Materials in Fusion Reactor First-Wall and Blanket Systems," *J. Nucl. Mater.* 85&86: 795–804 (1979).

7.12 RECONSTITUTION OF THE AD-2 FERRITICS EXPERIMENT - A.M. Ermi (Westinghouse Hanford Company)

7.12.1 ADIP Task

ADIP Program Task: Ferritic Steels Development (Path E)

7.12.2 Objectives

The objective of the AD-2 experiment is to provide baseline, high fluence data at several temperatures for the ferritic alloys HT-9 and 9Cr-1Mo. Developmental 2 1/4 Cr-1Mo is also being scoped in this experiment. The AD-2 experiment is designed to yield data concerning the irradiation effects on the mechanical properties of these alloys with emphasis on their fatigue, fracture toughness and weld properties. Characterization of the irradiation effects on the microstructure of these alloys will also be performed.

7.12.3 Summary

Six uninstrumented B-7c capsules were removed from the EBR-II after undergoing irradiation during Cycles 109-113. Several specimens were removed and distributed for interim examination, while the remaining specimens were re-encapsulated into four new B-7c capsules. In addition, some unirradiated specimens were included in the new capsules. Irradiation continued with Cycle 118 and will end after Cycle 123.

7.12.4 Progress and Status

7.12.4.1 Introduction

The AD-2 experiment has been designed to provide mechanical properties data on selected ferritic alloys for application in fusion reactor first walls and blankets. Of particular concern are the irradiation effects on the fracture and weld properties of the materials. Alloy selection and irradiation temperatures have been specified by the Alloy Development for Near Term Applications Working Group. This is the second report on the AD-2 experiment, which documents the events since the first report including specimen discharge after cycle 113 and the AD-2 reconstitution test matrix.

7.12.4.2 First Specimen Discharge

Details regarding the specimen preparation, heat treatments, test matrix and capsule loading have been previously reported. (1) The six B-7c capsules were inserted into the EBR-II in August, 1980 for Cycle 109, and were removed in June, 1981 after Cycle 113. Specimens in the peak flux position accumulated a fluence of 13 dpa.

Specimens to be examined from this first discharge were distributed as follows: ORNL received all tensile, Grodzinski fatigue and fatigue initiation specimens; HEDL received all Charpy, fracture toughness and fatigue crack growth specimens; and the TEM disk specimens were distributed to various participants in the ADIP and DAFS programs.

7.12.4.3 Reconstitution Text Matrix

Specimens irradiated in Cycles 109-113 but not examined were combined with new samples to form the AD-2 resonstitution (AD-2 RECON) test matrix. The same four test temperatures were used (390, 450, 500 and 550°C), although only four rather than six B-7c capsules were utilized. The complete AD-2 test matrix encompassing both irradiations is detailed in Table 7.12.1. The material code refers to the first digit(s) used to identify specific specimens.

Specimens added to the matrix but not initially irradiated include: (1) nickel-doped HT-9 (XAA-Series) and 9Cr-1Mo (XA-Series) tensile and Charpy; (2) HT-9 (Heat Treatment #1), 9Cr-1Mo (30176) and 9Cr-1Mo (Weld) Charpy; and (3) a few Path D long-range-ordered (LRO) tensile. Alloy compositions for all of the alloys are listed in Table 7.12.2, while the heat treatments are summarized in Table 7.12.3. Materials from TEM disk packets are not included in these tables, but are detailed elsewhere in this semi-annual report. (2)

7.12.4.4 Specimen Loading

The specimens were loaded into the four B-7c capsules, one weeper (390°C) and three designed to maintain temperatures of 450, 500 and 550°C. The specific level loadings for the four capsules are given in Tables 7.12.4 through 7.12.7. The fracture toughness specimens were

TABLE 7.12.1 AD-2 TEST MATRIX

MATERIAL [CODE]	TEST MATRIX				EXAMINATION				IRRADIATED SPEC.				UNIRRADIATED SPEC.				TEST MATRIX			
	390C	450C	500C	550C	390C	450C	500C	550C	390C	450C	500C	550C	390C	450C	500C	550C	390C	450C	500C	550C
T																				
HT-9 (#1) [UH]	20	10	20	10	10	5	10	5	10	5	10	5	-	-	-	-	10	5	10	5
HT-9 (#2) [TW]	10	5	10	5	10	2	10	2	-	3	-	3	-	-	-	-	-	3	-	3
HT-9 (XAA-3587)[SB]	-	-	-	-	-	-	-	-	-	-	-	-	4	4	1	4	4	4	1	4
HT-9, 1Ni [SC]	-	-	-	-	-	-	-	-	-	-	-	-	4	4	-	2	4	4	-	2
HT-9, 2Ni [SD]	-	-	-	-	-	-	-	-	-	-	-	-	4	4	1	4	4	4	-	4
HT-9, 2Ni Adj [SE]	-	-	-	-	-	-	-	-	-	-	-	-	4	-	-	-	4	-	-	-
9Cr-1Mo (30182) [XT]	9	3	9	6	4	1	4	3	5	2	5	3	-	-	-	-	5	2	5	3
9Cr-1Mo (XA-3590)[TA]	-	-	-	-	-	-	-	-	-	-	-	-	4	4	-	4	4	4	-	4
9Cr-1Mo-2Ni [TB]	-	-	-	-	-	-	-	-	-	-	-	-	4	4	1	4	4	4	1	4
9Cr-1Mo-2Ni Adj [TC]	-	-	-	-	-	-	-	-	-	-	-	-	-	4	-	-	-	4	-	-
2-1/4 Cr-1Mo [ZT]	6	3	6	3	3	1	3	1	3	2	3	2	-	-	-	-	3	2	3	2
LRO-16D [6]	-	-	-	-	-	-	-	-	-	-	-	-	-	-	-	2	-	-	-	2
LRO-42 [VH]	-	-	-	-	-	-	-	-	-	-	-	-	2	2	-	2	2	2	-	2
CRACK GROWTH [CG]																				
HT-9 (#1) [HT]	22	11	22	11	10	4	13	4	12	7	9	7	-	-	-	-	12	7	9	7
HT-9 (#2) [MR]	10	5	10	5	10	2	10	2	-	3	-	3	-	-	-	-	-	3	-	3
9Cr-1Mo (30182) [AS]	10	5	10	5	4	2	4	2	6	3	6	3	-	-	-	-	6	3	6	3
2-1/4 Cr-1Mo [ZC]	10	5	10	5	4	2	10	2	6	3	0	3	-	-	-	-	6	3	0	3
HT-9 (W) [RW]	10	-	10	10	4	-	5	4	6	-	5	6	-	-	-	-	6	-	5	6
HT-9 (HAZ) [WR]	5	-	5	5	2	-	2	2	3	-	3	3	-	-	-	-	3	-	3	3
HT-9 (W/HAZ)[RW]	2	-	2	2	2	-	2	2	-	-	-	-	-	-	-	-	-	-	-	-
9Cr-1Mo (W) [WM]	6	-	6	6	2	-	2	2	4	-	4	4	-	-	-	-	4	-	4	4
FATIGUE INITIATION [FI]																				
HT-9 (#4) [SF]	6	3	6	3	4	3	4	3	2	-	2	-	-	-	-	-	2	-	2	-
9Cr-1Mo (30182) [SI]	6	3	6	3	4	3	4	3	2	-	2	-	-	-	-	-	2	-	2	-
GRODZINSKI FATIGUE [GF]																				
HT-9 (#1) [SG]	10	5	10	5	10	3	10	3	-	2	-	2	-	-	-	-	-	2	-	2
9Cr-1Mo(30182)[SH]	2	0	2	2	2	0	2	2	-	-	-	-	-	-	-	-	-	-	-	-

continued next page →

TABLE 7 12 1 AD-2 TEST MATRIX (CONT)

MATERIAL [CODE]	INITIAL TEST MATRIX				INTERIM EXAMINATION				RECON OF IRRADIATED SPEC.				RECON OF UNIRRADIATED SPEC.				TOTAL RECON TEST MATRIX			
	390C	450C	500C	550C	390C	450C	500C	550C	390C	450C	500C	550C	390C	450C	500C	550C	390C	450C	500C	550C
FRACTURE TOUGHNESS [FT]																				
HT-9 (#3) [T4]	10	6	10	6	6	6	6	6	4	-	4	-	-	-	-	-	4	-	4	-
HT-9 (#4) [T5]	6	-	6	-	4	-	4	-	2	-	2	-	-	-	-	-	2	-	2	-
9Cr-1Mo (30182) [T6]	6	6	6	-	6	6	6	-	-	-	-	-	-	-	-	-	-	-	-	-
HT-9 (W) [T7]	7	6	7	3	6	6	6	3	1	-	1	-	-	-	-	-	1	-	1	-
HT-9 (W/HAZ) [HT]	7	6	7	3	6	6	6	3	1	-	1	-	5	7	5	5	6	7	6	5
CHARPY [C]																				
HT-9 (#1) [KT]	-	-	-	-	-	-	-	-	-	-	-	-	8	8	-	8	8	8	-	8
HT-9 (#3) [TT]	10	8	10	8	6	4	6	4	4	4	4	4	-	-	-	-	4	4	4	4
HT-9 (XAA-3587) [SB]	-	-	-	-	-	-	-	-	-	-	-	-	5	-	-	-	5	-	-	-
HT-9, 1Ni [SC]	-	-	-	-	-	-	-	-	-	-	-	-	-	-	3	-	-	-	3	-
HT-9, 2Ni [SD]	-	-	-	-	-	-	-	-	-	-	-	-	3	-	3	-	3	-	3	-
9Cr-1Mo (30176) [AF]	-	-	-	-	-	-	-	-	-	-	-	-	8	8	6	8	8	8	6	8
9Cr-1Mo (30182) [TV]	8	4	8	4	4	4	4	4	4	-	4	-	-	-	-	-	4	-	4	-
9Cr-1Mo (XA-3590) [TA]	-	-	-	-	-	-	-	-	-	-	-	-	-	5	-	5	-	5	-	5
9Cr-1Mo-2Ni [TB]	-	-	-	-	-	-	-	-	-	-	-	-	-	3	-	3	-	3	-	3
HT-9 (W) [T1]	7	4	7	4	7	4	7	4	-	-	-	-	-	-	-	-	-	-	-	-
HT-9 (W/HAZ) [TX]	7	-	7	-	7	-	7	-	-	-	-	-	-	-	-	-	-	-	-	-
9Cr-1Mo (W) [NL]	-	-	-	-	-	-	-	-	-	-	-	-	8	8	8	8	8	8	8	8
DISK PACKETS [D]																				
Various Alloys	8	4	8	4	4	2	4	2	4	2	4	2	2	2	2	2	6	4	6	4

TABLE Z ALLOY COMPOSITIONS FOR THE AD-Z TEST MATRIX[a]

ALLOY CONTENT,[b] wt %

Element	HT-9 (91353)	HT-9 (91354)	HT-9 (XAA-3587)	HT-9,1Ni (XAA-3588)	HT-9,2Ni (XAA-3589)	HT-9,2Ni Adj (XAA-3592)	9Cr-1Mo (30176)	9Cr-1Mo (30182)	9Cr-1Mo (XA-3590)	9Cr-1Mo-2Ni (XA-3591)	9Cr-1Mo-2Ni Adj (XA-3593)	2¼Cr-1Mo (38649)	LRO-16D	LRO-42
C	0.23	0.20	0.21	0.20	0.20	0.15	0.092	0.088	0.09	0.064	0.067	0.083	--	--
Mn	0.39	0.39	0.50	0.47	0.49	0.32	0.48	0.37	0.36	0.36	0.36	0.49	--	--
P	--	--	0.011	0.010	0.011	0.008	0.012	0.011	0.008	0.008	0.008	0.011	--	--
S	--	--	0.004	0.004	0.004	0.004	0.004	0.004	0.004	0.004	0.004	0.016	--	--
Si	0.23	0.14	0.18	0.13	0.14	0.07	0.15	0.19	0.08	0.08	0.10	0.19	--	--
Ni	0.46	0.49	0.43	1.14	2.27	2.30	0.09	0.09	0.11	2.17	2.24	--	30.965	39.5
Cr	12.34	12.39	11.99	11.97	11.71	13.60	8.32	8.47	8.62	8.57	12.30	2.17	--	--
Mo	0.99	0.99	0.93	1.04	1.02	1.59	0.86	0.88	0.98	0.98	1.70	0.99	--	--
V	0.45	0.45	0.27	0.31	0.31	0.30	0.20	0.21	0.209	0.222	0.29	--	22.964	22.4
Nb	--	--	0.018	0.015	0.015	0.016	0.06	0.07	0.063	0.066	0.074	--	--	--
Ti	--	--	0.003	0.003	0.003	0.002	0.001	0.001	0.002	0.002	0.002	--	--	0.4
Co	--	--	0.017	0.015	0.021	0.018	0.017	0.017	0.013	0.015	0.017	--	--	--
Cu	0.07	0.07	0.05	0.05	0.05	0.05	0.03	0.03	0.03	0.04	0.03	--	--	--
Al	--	--	0.030	0.017	0.028	0.018	0.011	0.009	0.013	0.015	0.016	--	--	--
B	--	--	<0.001	<0.001	<0.001	<0.001	<0.001	<0.001	<0.001	<0.001	<0.001	--	--	--
W	--	--	0.54	0.53	0.54	0.64	<0.01	<0.01	0.01	0.01	0.01	--	--	--
As	--	--	<0.001	0.002	<0.002	<0.002	<0.001	<0.001	<0.001	<0.001	<0.001	0.017	--	--
Sn	--	--	0.002	0.001	0.002	0.002	0.002	0.002	0.003	0.003	0.003	0.0088	--	--
Zr	--	--	<0.001	<0.001	<0.001	<0.001	<0.001	<0.001	<0.001	<0.001	<0.001	--	--	--
N	--	--	0.020	0.016	0.017	0.014	0.055	0.054	0.050	0.053	0.059	0.010	--	--
O	--	--	0.005	0.007	0.007	0.007	0.010	0.008	0.007	0.006	0.007	--	--	--
Pb	--	--	--	--	--	--	<0.001	<0.001	--	--	--	--	--	--
Sb	--	--	--	--	--	--	<0.001	<0.001	--	--	--	0.0024	--	--
Ce	--	--	--	--	--	--	--	--	--	--	--	--	--	0.1

[a] All materials from TEM disk packets not included.
[b] Balance Fe

TABLE 7.12.3 HEAT TREATMENTS FOR THE AD-2 TEST MATERIALS~

MATERIAL DESIGNATION	HEAT #	HEAT TREATMENT
HT-9(#1)	91353 91354	1038°C/10 min[b]/AC + 760°C/30 min/AC
HT-9(#2)	91353 91354	1038°C/30 min/AC + 760°C/2.5 hr/AC
HT-9(#3)	91354	Mill Annealed'
HT-9(64)	91353 91354	Mill Annealed[c]+ 1050°C/30 min/AC t 780°C/2.5 hr/AC
HT-9(W) HT-9(HAZ) HT-9(W/HAZ)	91353	Post-Weld Treatment: 780°C/1 hr/AC
HT-9	XAA-3587	1050°C/30 min/AC + 780°C/2.5 hr/AC
HT-9 + 1 Ni	XAA-3588	1050°C/30 min/AC + 780°C/2.5 hr/AC
HT-9 t 2 Ni	XAA-3589	1050°C/30 min/AC + 700°C/5 hr/AC
HT-9 t 2 Ni Adjusted	XAA-3592	1050°C/30 min/AC + 700°C/8 hr/AC
9Cr-1Mo	30182	1038°C/1 hr/AC + 760°C/1 hr/AC
9Cr-1Mo	30176	1038°C/30 min/AC + 760°C/30 min/AC
9Cr-1Mo(W)	30176 30182	Post-Weld Treatment: 780°C/1 hr/AC
9Cr-1Mo	XA-3590	1040°C/30 min/AC + 760°C/1 hr/AC
9Cr-1Mo-2Ni	XA-3591	1040°C/30 min/AC + 760°C/5 hr/AC
9Cr-1Mo-2Ni Adjusted	XA-3593	1050°C/30 min/AC + 700°C/8 hr/AC
2 1/4 Cr-1Mo	38649	900°C/30 min/AC + 700°C/1 hr/AC
LRO-16D	-	1050°C/10 min/WQ + 700°C/7 hr/AC t 650°C/24 hr/AC + 600°C/67 hr/AC
LRO-42	-	1100°C/15 min/WQ + 600°C/30.5 hr/AC + 540°C/21 hr/AC

[a] All materials from TEN Disk Packets not included.

[b] For material thickness < 0.100 inches, the 10 min is reduced to 4 min.

[c] Mill annealed condition: The bar stock was hot worked after soaking at 1149°C for a minimum of one hour, then 750°C/1 hr/AC.

TABLE 7.12.4 **SPECIMEN LOADING ARRANGEMENT FOR CAPSULE B-317a AT 390°C**

	LEVEL #	BASKET LENGTH (mm)	DISTANCE FROM MID-PLANE (mm)	SPECIFIC ALLOY LOADING [a]	
4 FI 1 TED	1	49.5	159	2 FI 2 FI	HT-9 (#4) 9 Cr-1Mo (30182)
13 FT	2	50.8	109	4 FT 2 FT 1 FT 6 FT	HT-9 (#3) HT-9 (#4) HT-9 (W) HT-9 (W/HAZ)
4 c 13 CG 16 T	3	55.7	56	4 c 4 T 4 T 4 T 4 T 6 CG 3 CG 4 CG	HT-9 (#3) HT-9 (3587) HT-9, 1 Ni HT-9, 2 Ni HT-9, 2 Ni Adj. 2 1/4 Cr-1Mo (38649) HT-9 (HAZ) 9 Cr-1Mo (W)
24 CG 8 T 1 TED	4	55.7	0	12 CG 6 CG 6 CG 4 T 4 T	HT-9 (#1) 9 Cr-1Mo (30182) HT-9 (W) 9 Cr-1Mo (3590) 9 Cr-1Mo-2Ni
12 C 5 T 4 D	5	49.5	-53	4 c 8 C 5 T 4 D	9 Cr-1Mo (30182) 9 Cr-1Mo (30176) HT-9 (#1) Disk Packets
12 C 10 T 2 D	6	49.5	-102	8 C 4 C 5 T 3 T 2 T 2 0	9 Cr-1Mo (W) HT-9 (#1) HT-9 (#1) 2 1/4 Cr-1Mo (38649) LRO-42 Disk Packets
12 C 5 T 1 TED	7	55.7	-155	5 C 3 C 4 C 5 T	HT-9 (3587) HT-9, 2 Ni HT-9 (#1) 9 Cr-1Mo (30182)

[a] See Table 7.12.1 for specimen name abbreviations; see Table 7.12.3 for specific thermomechanical treatments.

TABLE 7.12.5 SPECIMEN LOADING ARRANGEMENT FOR CAPSULE B-318a AT 450°C

	LEVEL #	BASKET LENGTH (mm)	DISTANCE FROM MID-PLANE (mm)	SPECIFIC ALLOY LOADING [a]
6 C 1 TED	1	49.5	159	6 C HT-9 (#1)
7 FT 2 C	2	50.8	109	7 FT HT-9 (W/HAZ) 2 C HT-9 (#1)
4 c 2 GF 19 T	3	55.7	56	4 C HT-9 (#3) 2 GF HT-9 (#1) 3 T HT-9 (#2) 4 T HT-9 (3587) 4 T HT-9, 1Ni 4 T HT-9, 2Ni 4 T 9 Cr-1Mo-2Ni Adj.
16 CG 8 T 1 TED	4	55.7	0	7 CG HT-9 (#1) 3 CG HT-9 (#2) 3 CG 9 Cr-1Mo (30182) 3 CG 2 1/4 Cr-1Mo (38649) 4 T 9 Cr-1Mo (3590) 4 T 9 Cr-1Mo-2Ni
8 C 5 T 2 D	5	49.5	-53	8 C 9 Cr-1Mo (30176) 5 T HT-9 (#1) 2 D Disk Packets
8 C 4 T 2 D	6	49.5	-102	8 C 9 Cr-1Mo (W) 2 T 2 1/4 Cr-1Mo (38649) 2 T LRO-42 2 D Disk Packets
8 C 2 T 1 TED	7	55.7	-155	5 C 9 Cr-1Mo (3590) 3 C 9 Cr-1Mo-2Ni 2 T 9 Cr-1Mo (30182)

[a] See Table 7.12.1 for specimen name abbreviations; see Table 7.12.3 for specific thennomechanical treatments.

TABLE 7.12.6 SPECIMEN LOADING ARRANGEMENT FOR CAPSULE B-319a AT 500°C

	LEVEL #	BASKET LENGTH (mm)	DISTANCE FROM MID-PLANE (mm)	SPECIFIC ALLOY LOADING [a]
3 FI 1 TED	1	49.5	159	2 FI HT-9 (#4) 1 FI 9 Cr-1Mo (30182)
13 FT	2	50.8	109	4 FT HT-9 (#3) 2 FT HT-9 (#4) 1 FT HT-9 (W) 6 FT HT-9 (W/HAZ)
6 C 7 CG	3	55.7	56	4 c HT-9 (#3) 2 C 9 Cr-1Mo (30176) 3 CG HT-9 (HAZ) 4 CG 9 Cr-1Mo (W)
20 CG 3 T 1 TED	4	55.7	0	9 CG HT-9 (#1) 6 CG 9 Cr-1Mo (30182) 5 CG HT-9 (W) 1 T HT-9 (3587) 1 T HT-9, 2Ni 1 T 9 Cr-1Mo-2Ni
a C 5 T 4 D	5	49.5	-53	4 c 9 Cr-1Mo (30182) 4 c 9 Cr-1Mo (30176) 5 T HT-9 (#1) 4 0 Disk Packets
8 C 8 T 2 D	6	49.5	-102	8 C 9 Cr-1Mo (W) 5 T HT-9 (#1) 3 T 2 1/4 Cr-1Mo (38649) 2 0 Disk Packets
6 C 5 T 1 FI 1 TED	7	55.7	-155	3 c HT-9, 1 Ni 3 c HT-9, 2 Ni 5 T 9 Cr-1Mo (30182) 1 FI 9 Cr-1Mo (30182)

[a] See Table 7.12.1 for specimen name abbreviations; see Table 7.12.3 for specific thennomechanical treatments,

TABLE 7.12.7 SPECIMEN LOADING ARRANGEMENT FOR CAPSULE B-321a AT 550°C

	LEVEL #	BASKET LENGTH (mm)	DISTANCE FROM MID-PLANE (mm)	SPECIFIC ALLOY LOADING [a]
3 FI 1 TED	1	49.5	159	2 FI HT-9 (#4) 1 FI 9 Cr-1Mo (30182)
13 FT	2	50.8	109	4 FT HT-9 (#3) 2 FT HT-9 (#4) 1 FT HT-9 (W) 6 FT HT-9 (W/HAZ)
6 C 7 CG	3	55.7	56	4 c HT-9 (#3) 2 C 9 Cr-1Mo (30176) 3 CG HT-9 (HAZ) 4 CG 9 Cr-1Mo (W)
20 CG 3 T 1 TED	4	55.7	0	9 CG HT-9 (#1) 6 CG 9 Cr-1Mo (30182) 5 CG HT-9 (W) 1 T HT-9 (3587) 1 T HT-9, 2Ni 1 T 9 Cr-1Mo-2Ni
8 C 5 T 4 D	5	49.5	-53	4 c 9 Cr-1Mo (30182) 4 c 9 Cr-1Mo (30176) 5 T HT-9 (#1) 4 D Disk Packets
8 C 8 T 2 D	6	49.5	-102	8 C 9 Cr-1Mo (W) 5 T HT-9 (#1) 3 T 2 1/4 Cr-1Mo (38649) 2 D Disk Packets
6 C 5 T 1 FI 1 TED	7	55.7	-155	3 c HT-9, 1 Ni 3 c HT-9, 2 Ni 5 T 9 Cr-1Mo (30182) 1 FI 9 Cr-1Mo (30182)

[a] *See* Table 7.12.1 for specimen name abbreviations; see Table 7.12.3 for specific thermomechanical treatments.

once again stacked vertically within the levels with spacers separating each specimen.

7.12.5 Future Work

Irradiation of specimens reconstituted in the AD-2 experiment began during EBR-II Cycle 118 in February 1982. Irradiation will continue through Cycle 123, making specimens available in February 1983. Specimens irradiated in both parts of the AD-2 experiment will accumulate ∿ 30 dpa.

7.12.6 References

1. R.J. Puigh and N.F. Panayotou, "Specimen Preparation and Loading for the AD-2 Ferritics Experiment," ADIP Quarterly Progress Report, DOE/ER-0045/3. June 1980, pp 260.
2. D.T. Peterson, "TEM Specimen Matrix for the AD-2 Reconstitution," ADIP Progress Report ER-0045/8, March 1982.

7.13 FRACTOGRAPHIC EXAMINATION OF COMPACT TENSION SPECIMENS OF UNIRRADIATED HT-9 AND MODIFIED 9Cr-1Mo WELDS - D. S. Gelles, F. H. Huang and N. F. Panayotou (Westinghouse Hanford Company)

7.13.1 ADIP Task

The Department of Energy (DOE)/Office of Fusion Energy (OFE) has cited the need to investigate ferritic alloys under the ADIP program task. Ferritic Steels Development (Path E). The tasks involved are akin to Task Number 1.B.13, Tensile Properties of Austenitic Alloys, and Task Number 1.C.2, Microstructure and Swelling in Austenitic Alloys

7.13.2 Objective

The objective of this effort is to provide baseline (preirradiation) fractographic data for comparison with irradiated specimens to be examined at a later date.

7.13.3 Summary

Miniature compact tension specimens of HT-9 and modified 9Cr-1Mo weld metal and HT-9 HAZ material have been tested and examined by scanning electron microscopy in order to provide baseline data for comparison with irradiated specimens, to provide understanding of the fracture process in these materials, and to assess the usefulness of crack opening displacement measurements based on fractographic analysis. For specimens tested at 205°C, crack propagation is found to be due to microvoid coalescence.

7.13.4 Progress and Status

7.13.4.1 Introduction

Procedures have been developed at Hanford Engineering Development Laboratory (HEDL) to allow fractographic examination of irradiated miniature compact tension specimens. Fractographic examination of such specimens can be expected to provide both improved understanding of the fracture toughness limits of the ferritic alloy class and understanding of the effects of microstructure on the fracture process. Furthermore, it appears possible to provide at least qualitative information on crack

opening displacement (COD) based on fractographic analysis which should be directly relatable to fracture toughness.

Therefore, the purpose of the present effort is twofold. 1) To provide baseline data on unirradiated HT-9 and modified 9Cr-1Mo miniature compact tension weld specimens, for future comparison with irradiated specimens, and 2) to present the concept of COD measurement based on fractographic analysis.

7.13.4.2 Theoretical Basis for COD Measurements

In the course of this effort, it has become apparent that quantitative stereographic analysis of fractographic information might provide measurements of the crack opening displacement for each specimen examined. Such COD measurements can provide an effective fracture criterion. Measurements of COD have been widely used in the U.K. and elsewhere as a tool to assess for example the significance of weld defects.'" The basis for the approach is as follows. Given a sharp crack in a plastic material, under stress the material will plastically deform at the crack tip until a local stress, σ_c, is reached at which point crack propagation will ensue. In Fig. 7.13.1, this sequence of events is depicted (I-IV) and comparison is made with the fracture toughness (J-R) curve for such a sequence using the same Aa calibration for crack extension. A measure of that critical local stress can be obtained by measurement of the crack opening displacement, δ_c. Therefore, for a given internal crack of detectable size, it can be shown that if the stress in a component of interest results in a crack opening displacement in excess of 6_c, fracture will occur. An effective fracture criterion based on COD then requires that the material be free of flaws of that detectable size and that stresses always be below σ_c.

Wells[3] has proposed the following relationship between critical crack extension force (G_c) and critical COD (6_c) involving the yield strength (a_Y)

$$G_c = n\ \sigma_y\ \delta_c \qquad (1)$$

where n is a plastic stress intensity factor which can be expected to

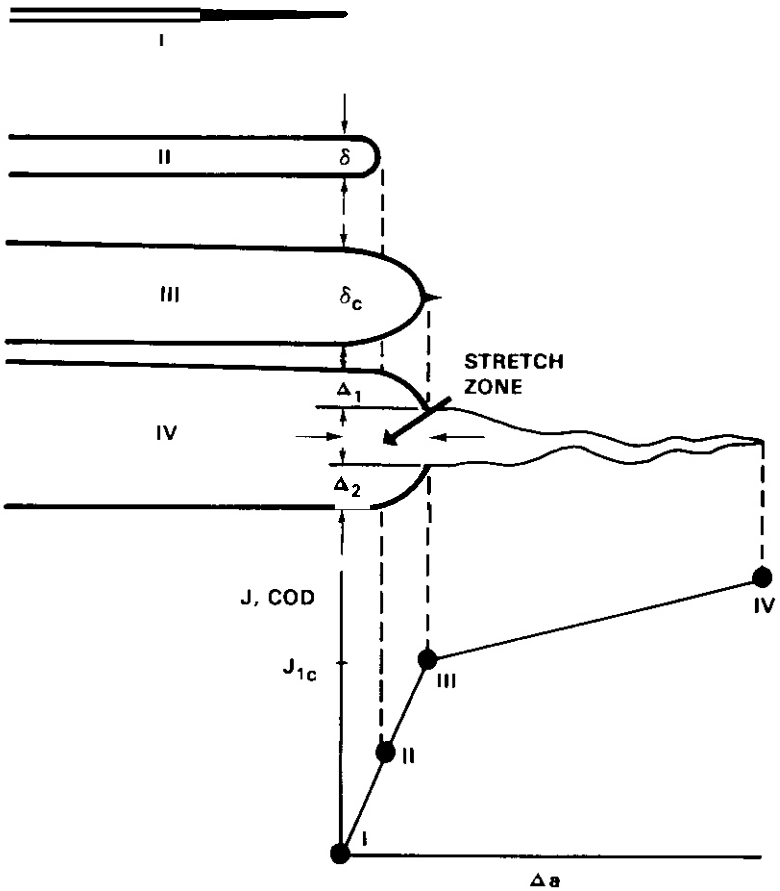

Fig. 7.13.1. Schematic diagram of the sequence of events which occur at a sharp crack tip in comparison with behavior on a corresponding J–R curve.

vary between 1 for plane stress and 2 for plane strain conditions. Comparison between J_{1c} and COD therefore provides the relationship

$$J_{1c} = m\,\sigma_y\,\delta_c \tag{2}$$

where again m varies between 1 and 2.

Several efforts to demonstrate the applicability of equations (1) and (2) have been made.[4–15] This has required development of procedures for measuring the critical crack opening displacement, δ_c, and several procedures have now been identified. In general, COD measurements either involve direct measurement,[4–7] external measurement of the notch mouth

opening,"[6-8] replication techniques (wherein a casting is made in mid test using for example rubber compounds injected into the crack),[9-11] Moiré measurements[12,13] or stereoscopic measurement of the fracture surface.[14,15] The results of these studies support the validity of equations (1) and (2) but the exact value or dependences of the plastic stress intensity factor (n or m) are not well understood. Of further note is work by Mills which concludes that m should be a function of the strain hardening coefficient; m equals 1 for low strain hardening alloys but 2 for high strain hardening, low strength materials (with strain hardening exponent > 0.2).

7.13.4.3 Experimental Procedure

Specimens were selected for examination to include all three weld conditions being investigated in Path E experiments: HT-9 weld metal, HT-9 heat affected zone (HAZ) metal and modified 9Cr-1Mo weld metal. All specimens had been tested at *205°C* which corresponds to the minimum in the J_{1c} versus temperature behavior for base metal.[17,18] In each case, the specimen selected for examination was the specimen tested to the highest Δa prior to heat tinting and subsequent deformation to failure at room temperature,

Fractograpic examinations were performed on a scanning electron microscope model ***JSM-35C*** operating at 25KV. Specimen tilts of 8" were found to be optimum for stereoscopic examination, and quantitative analysis employed a minicomputer coupled parallax measurement system designed by L. E. Thomas at HEDL.

Both halves of each specimen condition were analyzed in order both to obtain a better understanding of crack propagation behavior and to reduce uncertainties in COD measurement by avoiding the necessity for the assumption that crack initiation had occurred in the center of the stretch zone region. COD measurements were referenced to the termination of the fatigue crack surface as shown in Fig. 7.13.1 so that δ_c is defined by the sum of the parameters Δ_1 and Δ_2.

7.13.4.4 Results

7.13.4.4.1 Fracture toughness measurements. It is not the intent of the present report to fully describe the fracture toughness measurements on HT-9 and modified 9Cr-1Mo weld specimens. That will be done in a subsequent report. Rather the results are presented graphically and compared with results obtained previously on base metal specimens.[17,18] Fig. 7.13.2a provides comparison of J_{1c} measurements as a function of

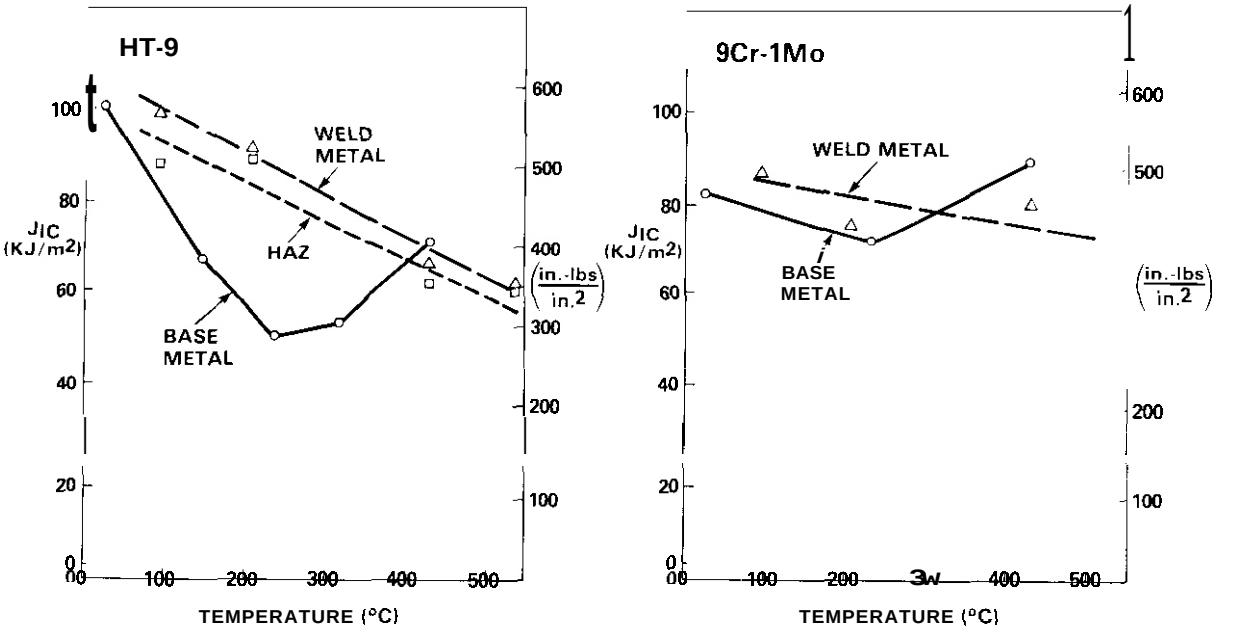

Fig. 7.13.2. Results of J_{1c} as a function of temperature for unirradiated HT-9 (a) and 9Cr-1Mo (b) based on miniature compact tension specimens.

test temperature for HT-9 base metal, weld metal and HAZ metal and Fig. 7.13.2b provides similar comparison for modified 9Cr-1Mo base metal and weld metal. Fracture toughness values of weld specimens of HT-9 and modified 9Cr-1Mo are not very different from those of the base metal. The temperature dependence is altered but the magnitude of J_{1c} is not significantly affected. Perhaps most surprisingly, the HT-9 weld metal and HAZ specimen were found to be significantly tougher than the base

metal at 205°C. These results therefore demonstrate that the toughness of martensitic stainless steels as measured by miniature compact tension tests is not significantly reduced due to welding providing that the welds are subsequently tempered.

7.13.4.4.2 Fractography. The fracture surfaces of miniature compact tension specimens display three general features. The region which was formed during fatigue precracking is generally flat and contains many river pattern steps which define the direction of crack propagation. The limits of this region define an arc or thumbnail shape which identifies the position of the crack prior to toughness testing. Adjacent to this region is a triangular region which is fairly flat and locates the material through which the crack propagates during J–R testing. That this is the area of greatest interest is demonstrated by heat tinting the freshly cracked region following J–R testing and prior to complete failure. The third region includes the remainder of the fracture surface; it is generally steeply sloped (at an angle of 45° to 60° to the fatigue surface) and often defines a trough on the fracture surface running from the triangular region to the ligament which last joins the specimen. From the above description, it is possible to understand why a miniature compact tension specimen may successfully provide J_{Ic} data despite the tendency for plane stress controlled fracture. Test data is only obtained during the early stages of crack propagation, and early propagation occurs in the center of the specimen well away from the specimen surfaces. Furthermore, because planar symmetry exists along the center plane of the specimen parallel to the flat specimen surfaces, plane strain must theoretically occur precisely at the center of the crack tip.

Therefore, fractographic analysis is centered on the triangular region bordering the fatigue precracked surface. This triangular region is shown in part (a) of Figs. *7.13.3*, *7.13.4* and *7.13.5* for CIT-9 HAZ and weld metal and modified 9Cr-1Mo weld metal respectively. Each of these figures provide four views of each specimen condition and is arranged to show in three dimensions the edge of the fatigue surface and the adjacent triangular region for both fracture surfaces. In stereo, (using a stereoscope) one should see a central line separating the two halves of the

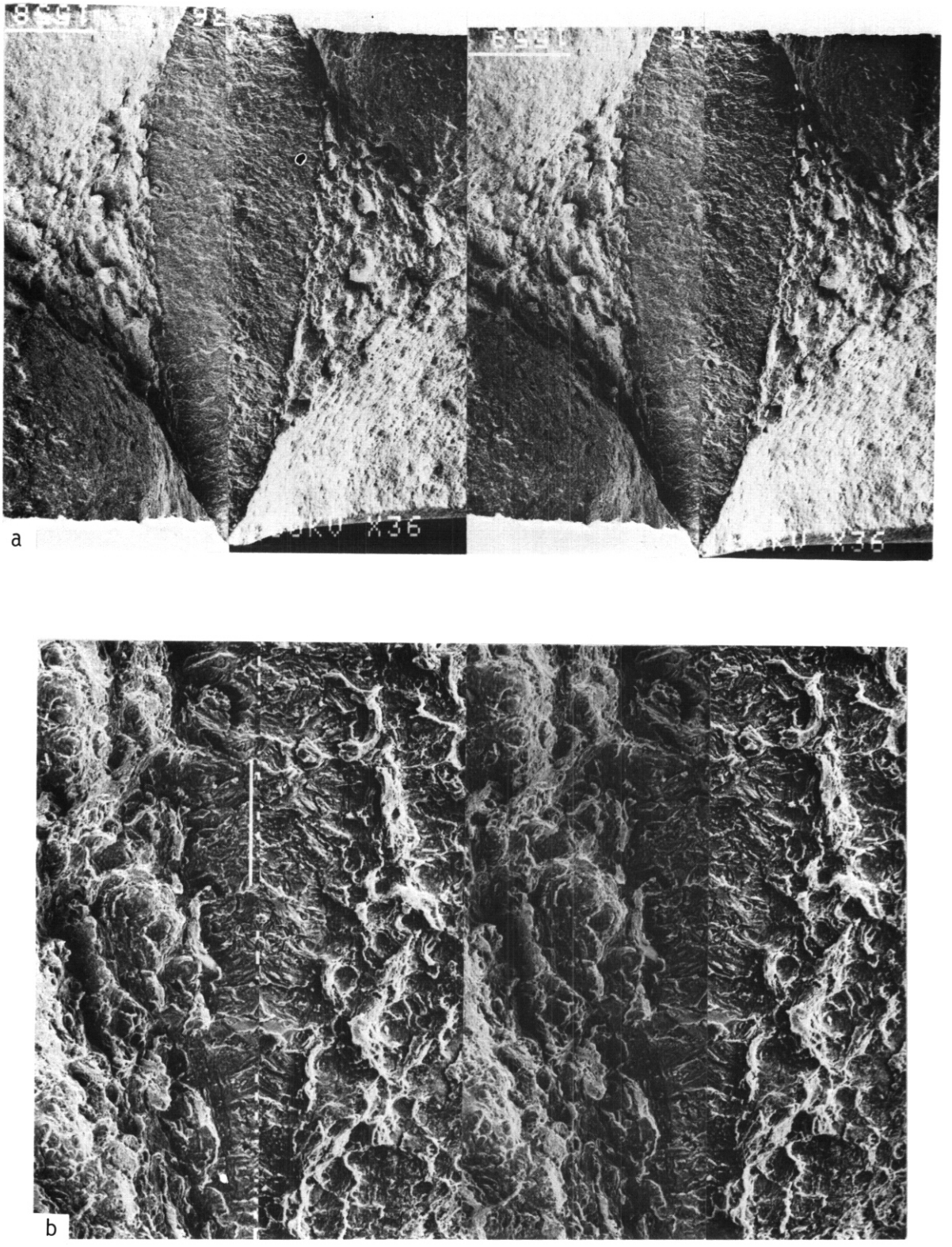

Fig. 7.13.3. Fractographs of an HT-9 HAZ miniature compact tension specimen tested at 205°C displayed as stereo pairs to show both halves of the fracture surface at **(a)** X36 and (b) X200.

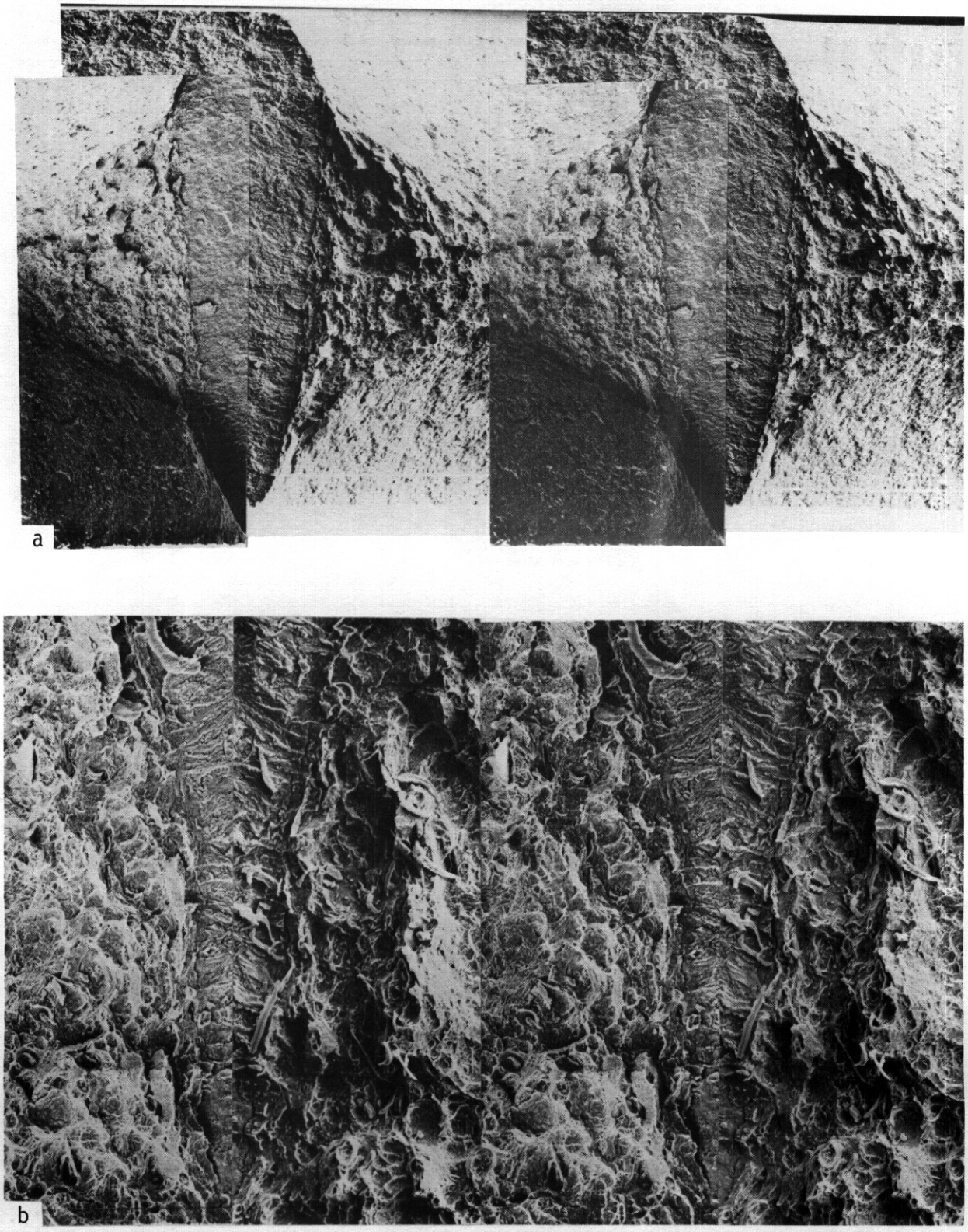

Fig. 7.13.4. Fractographs of an HT-9 weld metal miniature compact tension specimen tested at 205°C displayed as stereo pairs to show both halves of the fracture surface at (a) X36 and (b) X200.

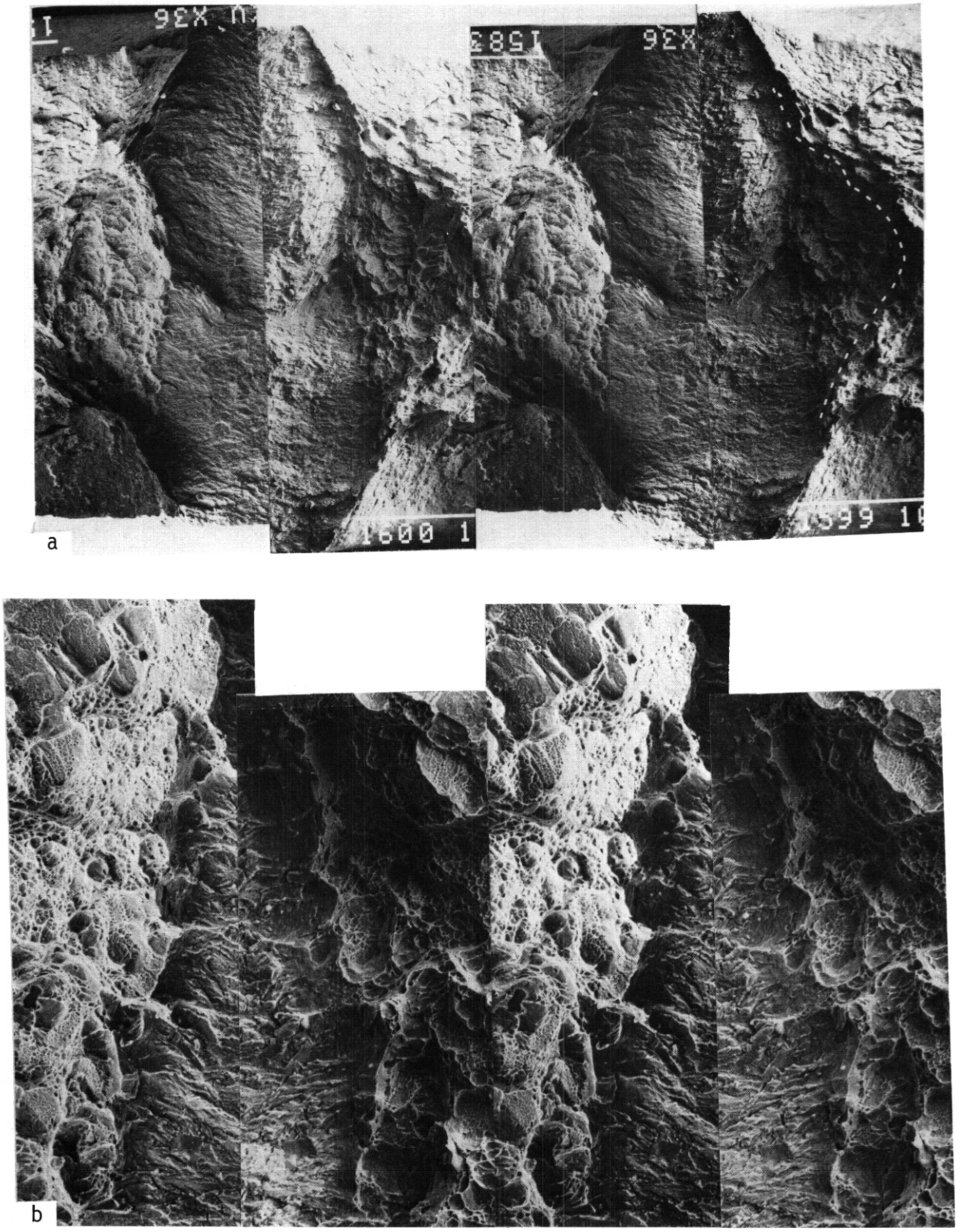

Fig. 7.13.5. Fractographs of a 9Cr-1Mo weld metal miniature compact tension specimen tested at 205°C displayed as stereo pairs to show both halves of the fracture surface at (a) X36 and (b) X200.

fatigue surface with the fracture surface to the right of that line exactly matching the fracture surface to the left. The micrograph to the right in each of these series also contains a dashed line which records the extent of the heat tinted region. For each of these figures the viewer should be able to envision the path which the crack took as the specimen was pulled apart (as if the fracture surface were folded open at the central line).

From parts (a) of Figs. 7.13.3, 7.13.4 and 7.13.5 the following observations can be made. The fatigue surfaces are relatively flat for the HT-9 specimens but the 9Cr-1Mo specimen contains a large bump in the fatigue surface and the remainder of the fatigue surface contains large undulations. The stretch zone separating the fatigue surface from the triangular region in all cases is difficult to see at X36 magnification and is on the order of 1 mm in width on the micrographs. The fracture surfaces created during the J-R test are very different from the fatigue surfaces. The features are more equiaxed and in many cases evidence for dimple rupture (cup-shaped features) can be seen. However, in every case, the larger undulations match up on both halves of the fatigue surface (one half containing a protrusion and the other containing a depression). Therefore, the cracks must be following weaknesses in the microstructure and the fracture process is very microstructure sensitive. Two further observations are of particular note. First, both weld metal fracture surfaces appear to contain two structure morphologies whereas the HAZ is more uniform. The best example of the two morphologies is shown in Fig. 7.13.5, the 9Cr-1Mo specimen, where a central rib extends from the fatigue surface bump, The texture of that rib appears much finer than that on adjacent regions. This appears to be a demonstration of a two phase microstructure in the weld metal specimens. Second, these adjacent regions in the 9Cr-1Mo specimen appear to be quite planar, and further comment about these features will be forthcoming.

Parts (b) of Figs, 7.13.3, 7.13.4 and 7.13.5 provide the same information using the same format at higher magnification. However, only the central portion of the triangular region immediately adjacent to the fatigue surface is shown. In each case, the stretch zone can be seen at higher magnification and is defined by the relatively featureless region

adjacent to the fatigue zone. The stretch regions contain steeply inclined surfaces and many examples of cracks or tears in the stretch zones can be identified. Adjacent to the stretch zone, are regions containing examples of dimple rupture. The modified 9Cr-1Mo specimen contains a finer distribution of smaller cups but good examples of matching cups can be found in the opposite halves of the HT-9 fracture surfaces as well.

From Figs. 7.13.3, 7.13.4 and 7.13.5, it is possible to demonstrate that the sequence of events depicted in Fig. 7.13.1 has occurred in each of the miniature compact tension specimens. However, crack propagation occurs by formation and coalescence of cavities ahead of the crack tip. Often, coalescence requires large shear strains because the cavities do not form in a planar array ahead of the crack tip. Also, stretch zone formation is not precisely as shown in Fig. 7.13.1 because significant amounts of tearing occur during stretch zone formation, and often these tears provide a preferred path for further stretch zone formation. (Several good examples can be found in Fig. 7.13.3b.)

Higher magnification fractographs confirm that crack propagation occurs by nucleation and coalescence of cavities. Examples shown in Fig. 7.13.6 are: a) HT-9 HAZ, b) HT-9 weld metal and c) and d) modified 9Cr-1Mo weld metal at low and high magnification. Examples of particles which provided nucleation sites can be identified for each material. The particle sizes range from 200 nm to 1500 nm. This indicates that the large $M_{23}C_6$ particles formed during tempering provide the nucleation sites for crack propagation.

Several regions in the modified 9Cr-1Mo weld metal fracture surface contained planar arrays of well defined cavities. The origin of these planar arrays appears to be martensite lath boundaries. This can be demonstrated by metallographic sections of the modified 9Cr-1Mo weld metal shown in Fig. 7.13.7a and b. Delta ferrite is not a significant component of the structure whereas well defined straight lath martensite boundaries are present as a result of the large prior austenite grain size in the weld metal. Fig. 7.13.7c is provided to demonstrate this point more clearly. Fig. 7.13.7c shows a stereo pair of the 9Cr-1Mo weld metal fracture surface after it has been partially masked, polished and etched with Villela's etch. In stereo, one should see a region in

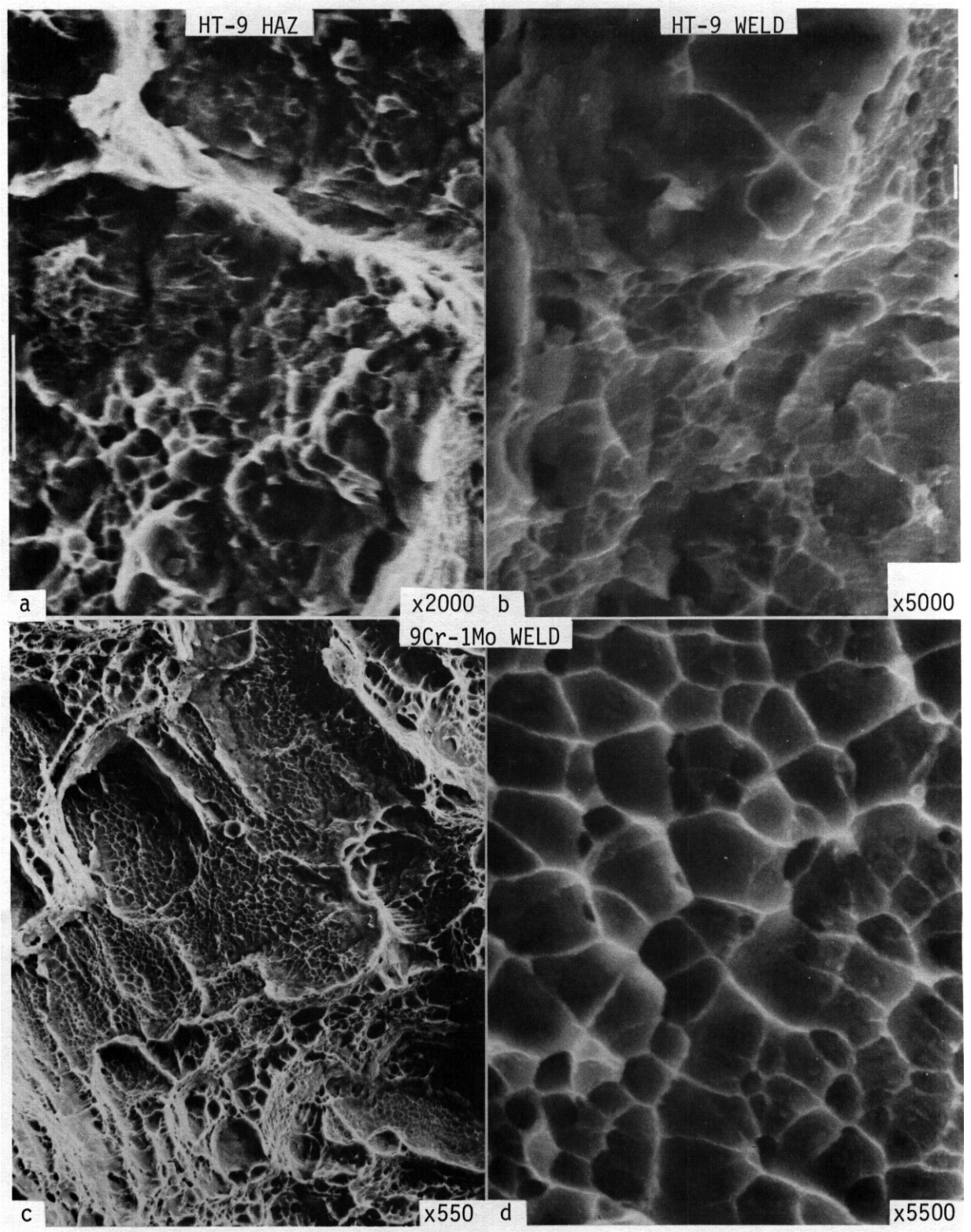

Fig. 7.13.6. Higher magnification fractographs showing dimple rupture due to microvoid coalescence.

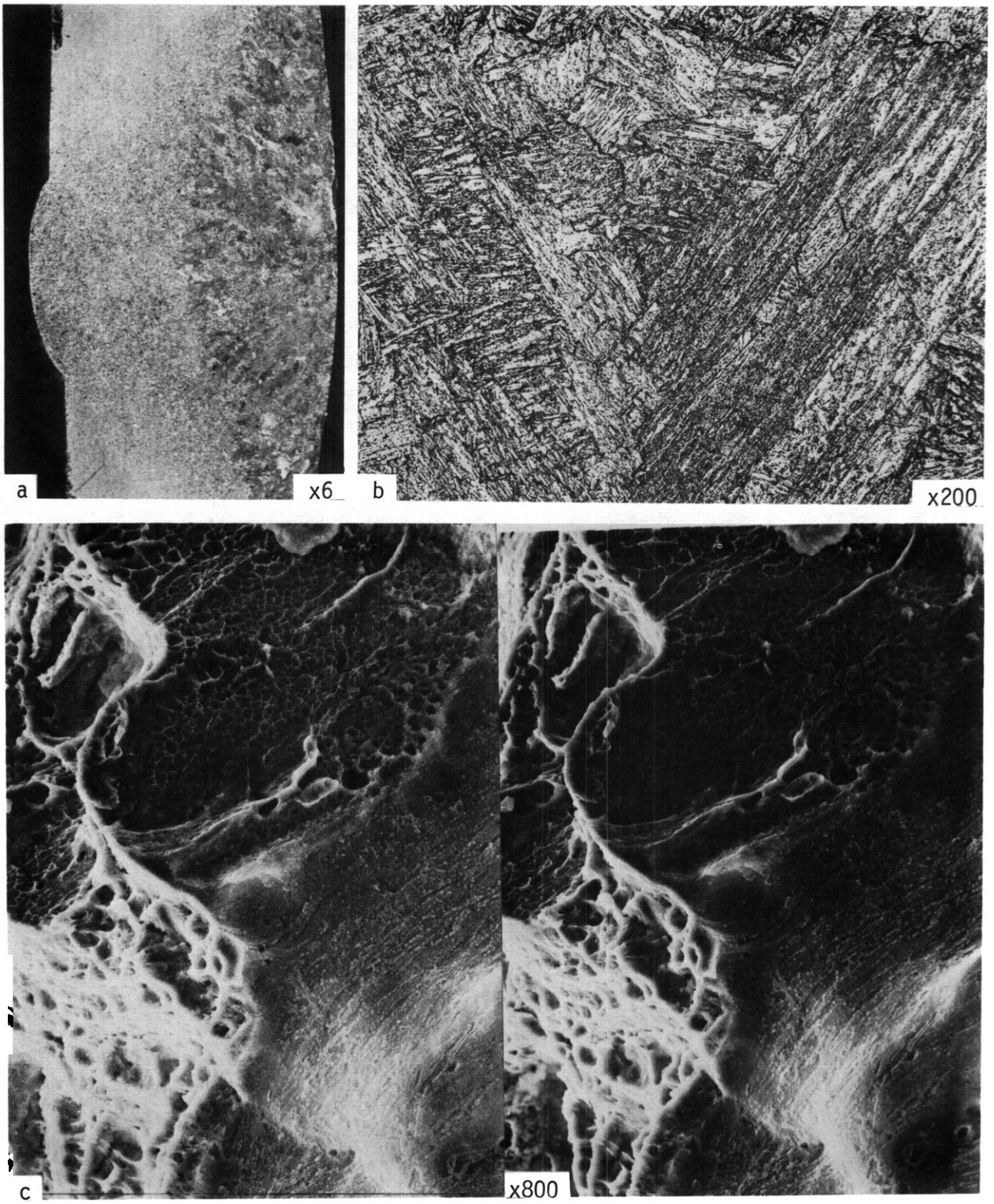

Fig. 7.13.7. Microstructure of the 9Cr-1Mo weld metal showing large martensite needles using optical metallography (a) and (b) and showing the relationship between martensite lath configuration and fracture surface topology as a stereo pair (c).

the upper part of the micrographs which shows the original fracture surface containing a planar array of well defined cavities. At the lower left of the micrographs, a different morphology exists consisting of a rough surface comprised of larger cavities. The region at the lower right has been polished and etched to show the martensite laths. The stereo pair was taken so the features on the polished surface are horizontal in the stereo model and the fracture surface is steeply inclined. By comparison of the etched martensite lath configurations with the fracture surface, it can be shown that the planar arrays of cavities correspond to martensite laths parallel to the fracture surface whereas the rough surface corresponds to martensite laths normal to the fracture surface. Therefore, the nucleation sites for crack propagation are again identified as $M_{23}C_6$ particles which developed at martensite lath boundaries.

7.13.4.4.3 COD Measurement. The concept of COD measurement from fractographic information has been examined for each of the micrograph series shown in Figs. 7.13.3, 7.13.4 and 7.13.5. Parallax measurements were made only at points on the fracture surface where opposing locations on the two matching surfaces could be unambiguously identified and these were referenced to the fatigue surface. Measurement locations were between 0.1 and 0.2 mm from the fatigue surface and therefore based on J-R curve information for the base metal,[17,18] these COD measurements should be overestimates of δ_c. (COD measurement was not possible based on stretch zone height[15] because the stretch zone was so poorly defined.) COD was then determined using the standard relationship

$$t = \frac{AH}{2M \sin(\theta/2)} \qquad (3)$$

where t is the steroscopically measured height, AH is the parallax, M is the fractograph magnification and θ is the tilt angle.

The COD measurements obtained were as follows: HT-9 HAZ specimen TA70, 0.093 ± 0.030 mm (standard deviation); HT-9 weld metal specimen T761, 0.084 ± 0.019 mm; and 9Cr-1Mo weld metal specimen T301, 0.052 ± 0.008 mm. Based on an estimate for yield strength at 205°C of 500 MPa[19,20]

and using equation (2) values for m are found to be 1.7, 1.9 and 2.7 respectively. Such values for m do not appear unreasonable. However, the area-to-area variations are unacceptably large and therefore, this technique cannot be recommended to provide engineering data. However, such measurements do provide improved understanding of the fracture process. For example, in the case of the 9Cr-1Mo specimen where two fracture surface structures could be identified, COD measurement on the two structures in adjacent areas give very similar results. These COD measurements therefore demonstrate that the two morphologies have similar toughness and so toughness is controlled by coalescence of cavities and not by nucleation events.

7.13.4.5 Discussion

The results of this effort provide two topics for discussion 1) effects of microstructure on crack propagation and 2) applicability of COD measurements from fractographic analysis.

7.13.4.5.1 Effects of microstructure on crack propagation. As is often the case, this study of miniature compact tension specimens of martensitic alloys tested at 205°C has shown that crack propagation occurs primarily by nucleation, growth and coalescence of cavities ahead of the propagating crack. Cavity nucleation is associated with precipitate particles in a size range typical of $M_{23}C_6$ and therefore it is proposed that carbide precipitates provide cavity nucleation sites. However, cracks can extend by two other related mechanisms. The crack initially extends by stretching in much the same manner as cavities grow: local plastic deformation increases the surface area of the crack probably by a surface step nucleation process associated with dislocation generation or annihilation at the surface. Also, tearing can occur during the stretching process, Tearing is probably the result of local plastic instability below the critical stress σ_C and may be a consequence of microstructural inhomogeneities. Therefore, we find that microstructure plays a strong role in determining the path of the crack.

However, the microstructure does not necessarily control the toughness of the material. Unless, the microstructure provides a weak path

for crack propagation (such as a continuous grain boundary precipitate) there will probably be sufficient plastic stretching and cavity growth so that the stresses required for crack propagation are in fact a measure of the strength of the matrix and not the precipitate. Therefore, one must be cautious when interpreting fractographic information in order to explain toughness response.

7.13.4.5.2 Applicability of COD measurements. On the other hand, COD measurements based on fractographic analysis can be expected to provide a direct measure of specimen toughness. The COD measurements made in this study do provide a qualitative estimate of toughness in the martensitic steels studied (based on the nominal value of m of 2). Also, the technique provides the unique opportunity to assess the difference in toughness between different components in a complex microstructure.

However, the technique has definite drawbacks. Large area-to-area variations are found. This is believed to be a real effect arising from non-uniform crack propagation which becomes masked during the bulk measurement. Such an effect provides an explanation for the curvature found in J-R curves. A second problem is to precisely determine the end of the stretch zone. The stretch zone is not well defined when tearing occurs, Yet the end of the stretch zone must be precisely defined to obtain critical COD measurements. (It can be suggested that Provenzano, et. al.[15] have overestimated m because they have misunderstood the consequences of tearing in the stretch zone and have therefore underestimated COD.) Because the scatter is *so* large for COD measurements based on fractographic analysis, it is not recommended that this technique be used to provide engineering data. However, the technique does provide a unique investigative tool for fracture toughness. Consequences of microstructure on toughness can be studied and it may be possible to study the effect of stress state on toughness by making COD measurements across the complete width of a specimen.

7.13.5 Conclusions

Fractographic examinations of compact tension specimens of HT-9 HAZ metal and weld metal and modified 9Cr-1Mo weld metal tested at 205°C have demonstrated:

1) Crack propagation is a result of microvoid formation at carbide particles and microvoid coalescence ahead of the propagating crack,

2) COD measurements based on stereoscopic fractographic analysis can provide a qualitive tool for fracture toughness determination. However, the primary use for the technique is expected to be in relating effects of microstructure on toughness, for which the technique is uniquely suited.

7.13.6 Future Work

Fractographic examination on Path E alloys will shift to miniature Charpy specimens irradiated in the AD-I1 test.

7.13.7 References

1. British Standard Methods for Crack Opening Displacement (COD) Testing, BS5762:1979.
2. J. D. Harrison, "The 'State-of-the-Art' in Crack Tip Opening Displacement (CTOD) Testing and Analysis," Report 7302.10/80/210.2 of the Welding Institute, Abington, Cambridgeshire, CB16A1, U.K.
3. A. A. Wells, "Crack Opening Displacements from Elastic-Plastic Analysis of Externally Notched Tension Bars," *Eng. Fract. Mech.*, I, (1969), p. 399.
4. F. M. Burdekin and D. E. W. Stone, "Crack Opening Displacement Approach to Fracture Mechanics in Yielding Materials," *J. Strain Anal.*, I, (1966), p. 145.
5. J. F. Knott, "Application of Fracture Mechanics to an Alloy Steel Used in Turbogenerator Low-Pressure Disks," *JISI*, *204*, (1966), p. 1014.
6. D. Elliott, E. F. Walker, M. J. May, "The Determination and Applicability of COD Test Data," *Inst. Mech. Eng.*, *77*, (1971), p. 217.
7. T. Ingham, G. R. Egan, D. Elliott and T. C. Harrison, "The Effect of Geometry on the Interpretation of COD Test Data," IBID, p. 200.
8. J. D. G. Sumpter and C. E. Turner, "Method for Laboratory Determination of J_{1c}," *Cracks and Fracture*, ASTM-STP-601, (ASTM 1976), p. 3.
9. J. N. Robinson and A. S. Tetelman, "Measurement of K_{1c} on Small Specimens Using Critical Crack Opening Displacement," *Fracture Toughness and Slow-Stable Cracking*, ASTM-STP-559, (ASTM 1974), p. 139.

10. B. A. Fields and K. J. Miller, "A Study of COD and Crack Initiation by a Replication Technique," *Eng. Fract. Mech.*, 9, (1977), p. 137.

11. C. F. Shih, H. G. deLorenzi and W. R. Andrews, "Studies on Crack Initiation and Stable Crack Growth," *Elastic-Plastic Fracture*, ASTM-STP-668, (ASTM 1979), p. 65.

12. P. F. Packman, "The Role of Interferometry in Fracture Studies," *Experimental Techniques* in *Fracture Mechanics*, 2, A. S. Kobayash, Ed., (Iowa State University Press, 1975), p. 59.

13. W. L. Hu and H. W. Liu, "Crack Tip Strain - A Comparison of Finite Element Method Calculations and Moiré Measurements," *Cracks and Fracture*, ASTM-STP-601, (ASTM 1976), p. 522.

14. D. Brock, "Correlation Between Stretch Zone Size and Fracture Toughness," *Eng. Fract. Mech.*, 6, (1974), p. 173.

15. V. Provenzano, C. M. Gilmore, F. A. Smidt, Jr. and J. R. Hawthorne, "Thickness and Temperature Effects on the J-Integral COD Realtionship," NRL Memorandum Report 4696, December 1981.

16. W. J. Mills, "On the Relationship Between Stretch Zone Formation and the J-Integral for High Strain-Hardening Materials," *J. Test & Eval.*, (1981), p. 56.

17. F. H. Huang and G. L. Wire, "Analysis of Single Specimen Tests on HT-9 for J_{1c} Determination," DOE/ER-0045/3, (September 1980), p. 236.

18. F. H. Huang and G. L. Wire, "Fracture Toughness Measurements for Unirradiated 9Cr-1Mo Using Electropotential Techniques," DOE/ER-0045/7, (September 1981), p. 220.

19. R. L. Klueh and J. M. Vitek, "Tensile Properties of Ferritic Steels After Low Temperature HFIR Irradiation," DOE/ER-0045/5, (October-December 1980), p. 218.

20. R. L. Klueh and J. M. Vitek, "Tensile Properties of Ferritic Steels After Low Temperature HFIR Irradiation," DOE/ER-0045/6, (January-March 1981), p. 139.

7.14 POSTIRRADIATION NOTCH DUCTILITY OF THE WELD HEAT AFFECTED ZONE (HAZ) OF ALLOY HT-9 PLATE (AOD HEAT) - J. R. Hawthorne (Naval Research Laboratory) and J. C. Lippold (Sandia National Laboratories, Livermore).

7.14.1 ADIP Task

The Department of Energy (DOE)/Office of Fusion Energy (OFE) has stated the need to investigate ferritic alloys under the ADIP program task. Ferritic Steel Development (Path E).

7.14.2 Objectives

Objectives of the present research task were to prepare and irradiate simulated weld heat affected zone (HAZ) specimens of Alloy HT-9 plate (Fusion Ferritic Program reference heat) for assessment of 288°C radiation embrittlement sensitivity as a function of location in the HAZ and 288°C radiation embrittlement sensitivity of the HAZ relative to parent material.

7.14.3 Summary

Alloy HT-9 is being evaluated for potential application as a first wall material in magnetic fusion reactors. The size and complexity of projected components may necessitate the use of welding for component fabrication; accordingly, studies of Alloy HT-9 radiation resistance capabilities are including assessments of weld deposits and weld HAZ materials. The present investigation represents a joint effort by the Naval Research Laboratory (NRL) and the Sandia National Laboratories at Livermore (SNLL).

Charpy-V (C_v) specimens simulating four positions across a weld HAZ and specimens of the parent plate material were irradiated at 288°C to $\sim 8 \times 10^{19}$ n/cm^2, E > 0.1 MeV. The HAZ specimens were thermally cycled on a Gleeble apparatus; individual thermal cycles provided peak temperatures of 1380, 1152, 974 or 828°C. Postirradiation notch ductility determinations revealed the HAZ to have essentially uniform radiation embrittlement sensitivity across its width. In addition,

the data showed the radiation resistance level of the HAZ to be comparable to that of the parent plate. The results in turn suggest that, for the 288°C service condition, the fracture resistance of irradiated HT-9 weldments will not be governed primarily by the weld HAZ.

7.14.4 Progress and Status

7.14.4.1 Introduction

The ferritic stainless steel composition, Alloy HT-9, is being assessed for possible first wall applications in magnetic fusion reactors by the Magnetic Fusion Materials Program of the Department of Energy. The investigations are exploring the fracture resistance capabilities of the alloy before and after elevated temperature irradiation. Initial evaluations of the alloy in rod product form revealed a promise for high temperature, high fluence applications. The studies have since been extended to include plate and weldment products and lower irradiation temperatures and typically are evaluating fracture resistance by means of notch ductility, dynamic fracture toughness and static fracture toughness determinations.

This study builds on recent investigations of plate performance in unirradiated and irradiated conditions (see Report Section 7.1 above) and HAZ performance in the unirradiated condition (see Report Section 7.6 above) by NRL and SNLL. Current objectives were to explore the potential for variable radiation embrittlement sensitivity through the thickness *of* a weld HAZ to identify that position within the HAZ having the poorest notch ductility and, finally, to determine whether the weld HAZ or the parent (base) material would be the weakest link, in terms of postirradiation fracture resistance, in service.

The experimental approach involved the irradiation of C_v specimens representing both simulated weld HAZ materials and base plate material for determinations of relative postirradiation performance. The irradiation temperature of 288°C was chosen on the basis of discussions with the sponsor.

The material stock for this study was a 1.7 cm thick plate from the Alloy HT-9 reference heat (Electralloy No. 9067) prepared by the AOD process. The specimens were taken in the transverse (TL-weak) and longitudinal (LT-strong) orientations; emphasis was given to the TL orientation. The HAZ specimens were thermally cycled using a Gleeble apparatus and procedures described by Lippold (see Section 7.6 above). Four thermal cycles were selected for study: Cycle no. 1 gave a peak temperature of 1380°C, Cycle no. 2 gave a peak temperature of 1152°C, Cycle no. 3 gave a peak temperature of 974°C, and Cycle no. 4 gave a peak temperature of 828°C. All HAZ specimens received a heat treatment of 760°C for 2 hours after welding simulation. The heat treatment of the parent plate consisted of 1040°C for 0.5 hours with air cooling followed by temper at 760°C for 2 hours. Specimen notches were cut perpendicular to the parent plate surface.

7.14.4.3 Material Irradiation

The materials were irradiated at 288°C for 742 hours in a fuel lattice position of the water cooled reactor at the State University of New York at Buffalo (USR). The HAZ and plate specimens were commingled in the irradiation assembly to permit direct comparisons. Specimen temperatures during irradiation were monitored continuously by means of thermocouples welded to the specimens. Iron neutron dosimeter wires were placed within the specimen array for neutron fluence determinations but have not yet been analyzed. From the dosimetry of the preceding experiment, a fluence ($E > 0.1$ MeV) of 8×10^{19} n/cm^2 is estimated.

7.14.4.4 Results

Results of pre- and postirradiation tests of the simulated HAZ materials are shown in Fig. 7.14.1 (SNLL determinations) and Fig. 7.14.2 (NRL determinations), respectively. Observations which can be made from the data are enumerated.

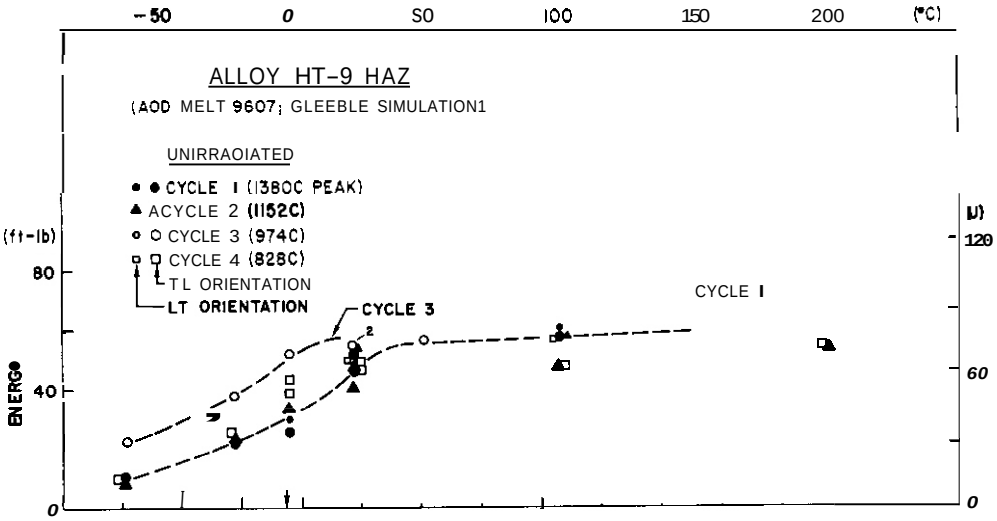

Fig. 7.14.1. Preirradiation Notch Ductility of Simulated Weld Heat Affected Zone (HAZ) Material Prepared by Gleeble Thermal Cycling (4 Peak Temperature Conditions).

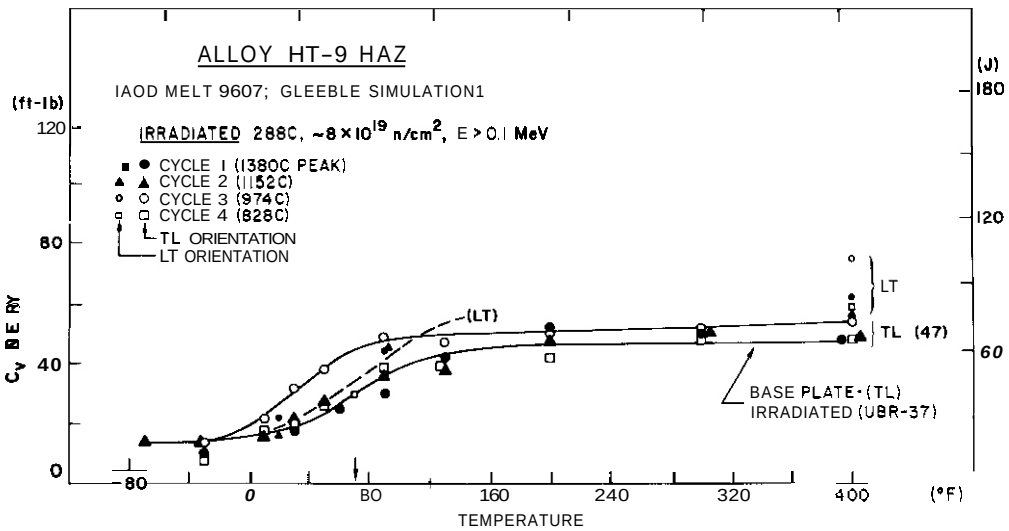

Fig. 7.14.2. Postirradiation Notch Ductility of the Simulated Weld Heat Affected Zone (HAZ) Materials.

(1) Postirradiation transition temperatures typically are below 25°C; upper shelf energy levels are above 605.

(2) Data for preirradiation condition of Cycles 1, 2, and 4 essentially overlap; likewise, data for the postirradiation condition of Cycles 1, 2, and 4 form a common data scatterband.

(3) The data trend for Cycle 3 is displaced to the left of that for Cycles 1, 2, and 4 for both the unirradiated and the irradiated condition; the magnitude of the displacements, however, are about the same. Accordingly, the radiation sensitivity of the Cycle 1 material appears to be comparable to that exhibited by Cycles 1, 2, and 4.

(4) The LT test orientation has a somewhat higher postirradiation upper shelf energy level than the TL test orientation; however, transition temperatures (41J index) are nearly the same.

(5) The superior notch ductility of Cycle 3 material (LT and TL orientations) can be attributed to its refined prior austenite grain size.

Figure 7.14.3 illustrates the postirradiation results for the plate specimens included in the present irradiation experiment (UBR-37) and for the specimens (LT orientation) included in a prior irradiation experiment (UBR-35) receiving approximately the same fluence. Transition temperature elevations and upper shelf reductions for the two orientations are about equal. Note that the LT orientation heat treatment: 1050°C for 0.5 hours, air cooling, and 780°C for 2.5 hours, differs somewhat from the TL orientation heat treatment. The results of Figs. 7.14.2 and 7.14.3 suggest that the HAZ and the base plate have similar radiation embrittlement sensitivities at 288°C and, more importantly, that weldment properties will not be governed primarily by the HAZ.

7.14.5 Conclusions

Two conclusions were drawn from this Alloy HT-9 investigation. First, the variation in radiation embrittlement sensitivity through the thickness of a weld HAZ is small or negligible for 288°C service conditions. Equally important, the weld HAZ does not offer inferior

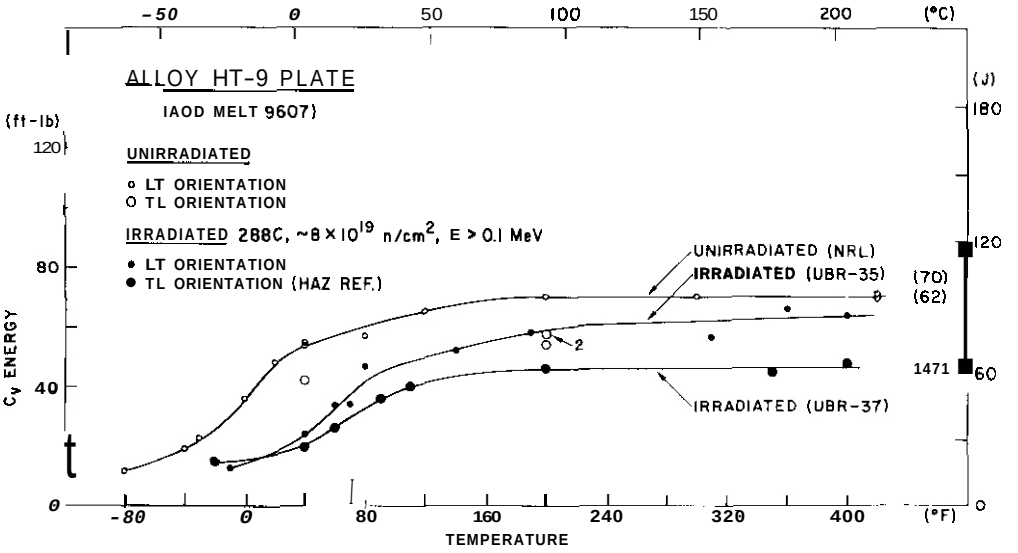

Fig. 7.14.3. Pre- and Postirradiation Notch Ductility of Parent Plate Material Used for the Simulated Weld Heat Affected Zone Materials. The Irradiation Experiment UBR-35 (LT Orientation) refers to Another Study, see Section 7.1 above.

postirradiation notch ductility compared to its parent plate for the fluence condition studied. Confirmation of these conclusions for the high fluence case will be beneficial to future design applications.

7.14.6 References

1. J. R. Hawthorne and F. A. Smidt, Jr., "Evaluation of Fracture Resistance of Ferritic Stainless Steels for First Wall and Blanket Applications," J. Nucl. Matls. 103 & 104:883-886 (1981).
2. F. A. Smidt, Jr., J. R. Hawthorne, and V. Provenzano, "Fracture Resistance of HT-9 After Irradiation at Elevated Temperature." pp. 269-284 in Effects of Radiation on Materials, Tenth Conference, ASTM STP 725, D. Kramer, H. R. Brager, and J. S. Perrin, Eds., American Society for Testing and Materials, 981.

8. STATUS OF IRRADIATION EXPERIMENTS AND MATERIALS INVENTORY

8.1 IRRADIATION EXPERIMENT STATUS AND SCHEDULE — M. L. Grossbeck (Oak Ridge National Laboratory)

There are a large number of planned, in-progress, or completed reactor irradiation experiments that support the ADIP program. Table 8.1.1 presents a summary of the parameters that describe experiments that have been completed. Experiments that have been removed from the reactor only recently, are currently undergoing irradiation, or are planned for future irradiation are included in the schedule bar charts of Table 8.1.2.

Experiments are now under way in the Oak Ridge Research Reactor (ORR) and the High Flux Isotope Reactor (HFIR), which are mixed spectrum reactors, and in the Experimental Breeder Reactor (EBR-II), which is a fast reactor.

During the reporting period experiments HFIR-MFE-RB1 and -RB2, the first program experiments to be irradiated in reflector positions of the HFIR, were installed. Although the flux is lower at this position than in the flux-trap region of the reactor, additional space permits larger spceimens to be irradiated. In addition, HFIR-CTR-34 and -35, the first elevated-temperature irradiation experiments for determination of impact properties of Path E alloys, were installed in the HFIR in peripheral target positions (PTP). The last of the series of transmission electron microscopy (TEM) disk irradiation experiments, HFIR-CTR-30, completed its irradition in the HFIR.

Table 8.1.1 Description Parameters for Completed ADIP Program Fission Reactor Irradiation Experiments

Experiment	Major Objective	Alloy	Reactor	Temperature (°C)	Displacement Damage (dpa)	Helium (at. ppm)	Duration (months)	Date Completed
ORR-MFE-1	Scope the effects of composition and microstructure on tensile, fatigue, and irradiation creep	Paths A, B, C	ORR	250–600	2	≤10	4	6/78
ORR-MFE-2	Scope the effects of composition and microstructure on tensile, fatigue, and irradiation creep	Paths A, B, C	ORR	300–600	6	≤60	15	4/80
Subassembly X-264	Effect of preinjected helium on microstructure, tensile properties, and irradiation creep	316, PE-16, V–20% Ti, V–15% Cr–5% Ta, Nb–1% Zr	EBR-I	500–825	[illegible]	≈–200	4	1[illegible]77
AA-X Subassembly X-287	Effect of preinjected helium on microstructure, tensile properties, and irradiation creep	316, PE-16, V–20% Ti, V–15% Cr–5% T[illegible], Nb–1% Zr	EBR-II	400–700	≈0	2–200	23	12[illegible]7[illegible]
Subassembly X-217D	Stress relaxation	Titanium alloys	EBR-II		2		1	1[illegible]78
Pins B285, B286, and B284	Swelling, fatigue, crack growth, and tensile properties	Titanium alloys	EBR-II	3[illegible] [illegible]0	2[illegible]		14	9[illegible]79
HFIR-CTR-3	Swelling and tensile properties	PE-16, Inconel 600	HFIR	300–700	4 3–9	3[illegible]0–1800	3	2/75
HFIR-CTR-4	Swelling and tensile properties	PE-16	HFIR	300–700	2 2–4.[illegible]	1[illegible]0–350	2	3/77
HFIR-CTR-5	Swelling and tensile properties	PE-16, Inconel 600	HFIR	300–700	4 3–9	3 0–1800	3	4/75
HFIR-CTR-6	Swelling and tensile properties	PE-16, Inconel 600	HFIR	300–700	4 3–9	3.0–1800	3	4/75

Table 8.1.1. (Continued)

Experiment	Major Objective	Alloy	Reactor	Temperature (°C)	Displacement Damage (dpa)	Helium (at. ppm)	Duration (months)	Date Completed
HFIR-CTR-7	Swelling and tensile properties	PE-16	HFIR	300–700	9–18	1250–3000	7	8/77
HFIR-CTR-8	Swelling and tensile properties	PE-16	HFIR	300–700	9–18	1250–3000	7	8/77
HFIR-CTR-9	Swelling and tensile properties	316, 316 + Ti	HFIR	280–680	10–16	400–1000	6	5/77
HFIR-CTR-10	Swelling and tensile properties	316, 316 + Ti	HFIR	280–680	10–16	400–1000	6	5/77
HFIR-CTR-11	Swelling and tensile properties	316, 316 + Ti	HFIR	280–680	10–16	400–1000	6	5/77
HFIR-CTR-12	Swelling and tensile properties	316, 316 + Ti	HFIR	280–680	7–10	200–500	4	2/77
HFIR-CTR-13	Swelling and tensile properties	316, 316 + Ti	HFIR	280–680	7–10	200–500	4	2/77
HFIR-CTR-14	Fatigue	316	HFIR	430	9–15	400–1000	7	12/77
HFIR-CTR-15	Fatigue	316	HFIR	550	6–9	200–400	4	10/78
HFIR-CTR-16	Weld characterization, swelling and tensile properties	316, PE-16, Inconel 600	HFIR	55	6–9	150–2700	4	8/77
HFIR-CTR-17	Weld characterization	316	HFIR	280–620	7–13	180–460	5.5	10/77
HFIR-CTR-18	Swelling and tensile properties	316, PE-16	HFIR	280–700	17–27	1600–5600	12	6/78
HFIR-CTR-19	Weld characterization	316	HFIR	280–620	7–10	200–500	4	12/77
HFIR-CTR-20	Fatigue	316	HFIR	430	6–9	200–400	4	1/78
HFIR-CTR-21	Fatigue	316	HFIR	550	9–15	400–1000	7	7/78
HFIR-CTR-22	Fatigue	316	HFIR	430	6–9	200–400	4	3/78
HFIR-CTR-23	Fatigue	PE-16	HFIR	430	6–9	370–1000	3.5	2/79
HFIR-CTR-24	Temperature calibration, and tensile properties	316	HFIR	300–620	2.2	30	1	12/78

Table 8.1.2. Objectives and Schedule for Current and Planned ADIP Program Reactor Irradiation Experiments

Experiment Designation	Major Objective
A. Oak Ridge Research Reactor	
ORR-MFE-3	[1] Effect of irradiation on postirradiation fatigue crack growth in representative path A, B, and C alloys.
ORR-MFE-4	[2] Effect of irradiation on tensile, fatigue, and irradiation creep of path A PCA (Prime Candidate Alloy) and path B base research alloys. Spectral tailoring to maintain correct He/dpa ratio. Irradiation on continuing basis. 330–600°C
ORR-MFE-5	In-reactor fatigue crack growth experiment. 325–460°C

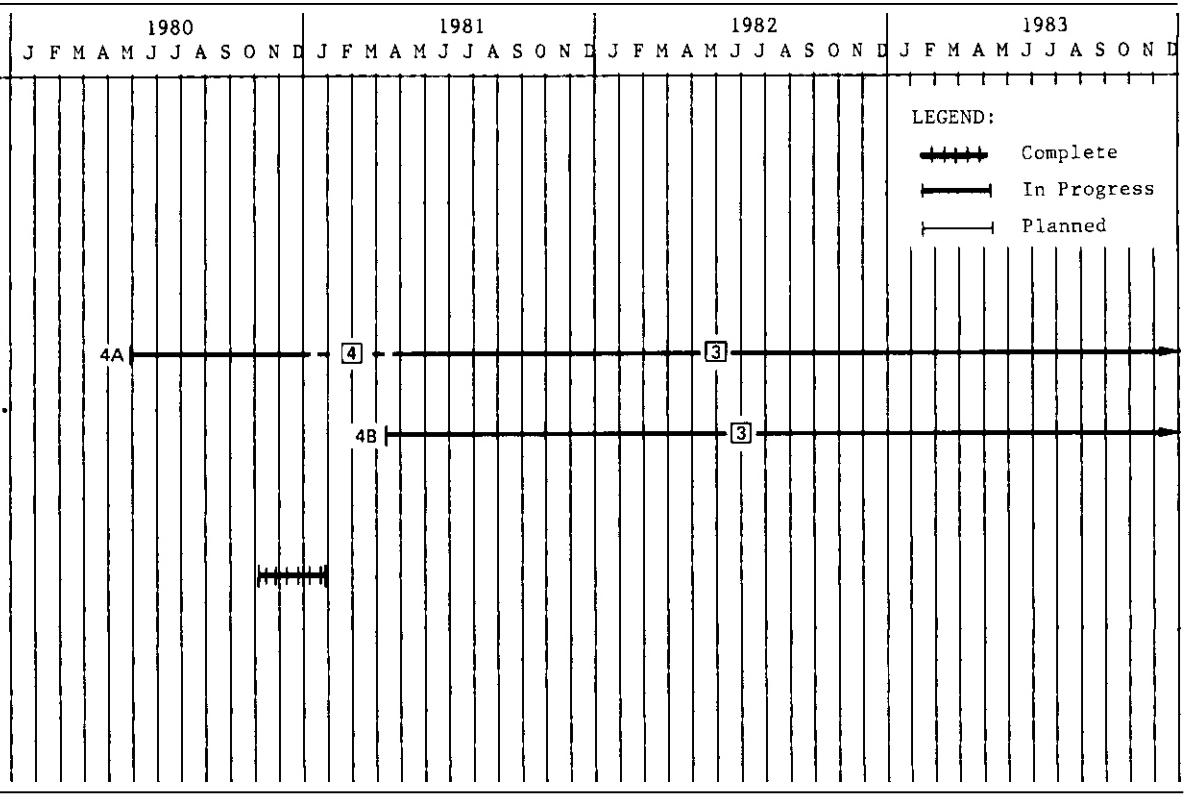

[1] Experiment cancelled.

[2] MFE-4A operates at 330 and 400°C. MFE-4B operates at 500 and 600°C.

[3] Approximate schedule for specimen charge out.

[4] Removed from reactor for thermocouple repairs.

Table B 1 2 (Continued)

Experiment Designation	Major Objective	1980 J F M A M J J A S O N D	1981 J F M A M J J A S O N D	1982 J F M A M J J A S O N D	1983 J F M A M J J A S O N D
B. Experimental Breeder Reactor (EBR-II)					
Experiment plan depends on alloy availability. EBR-II space not yet identified.	Effect of irradiation on swelling, tensile, fatigue, and crack growth properties of V and Nb scoping alloys. 370, 450, 550, and 650°C. Position in reactor not finalized, therefore no fluence estimate. [1]				
AD-2 (6 pins in separate subassemblies of row 4)	To supplement present EBR-II data on ferritic alloys with data on crack growth, fatigue, and fracture toughness. Temperature 390, 450, 500, and 550°C. 19 and 38 dpa.		[2]		

[1] Del y d for undetermined period.

[2] Int rim e ami ati n. Experiment out o reactor

Table 8.1.2. (Continued)

Experiment Designation	Major Objective
C. High Flux Isotope Reactor (HFIR)	
HFIR-CTR-25	Temperature calibration, tensile properties of MFE ref. 316, 2.25 dpa, 30 at. ppm He [1]
HFIR-CTR-26	Swelling and tensile properties of MFE ref. 316, 32 dpa, 1900 at. ppm He
HFIR-CTR-27	Swelling and tensile properties of MFE ref. 316, 56 dpa, 3450 at. ppm He
HFIR-CTR-28	Swelling and tensile properties of MFE ref. 316, 32 dpa, 1900 at. ppm He
HFIR-CTR-29	Swelling and tensile properties of MFE ref. 316, 56 dpa, 3450 at. ppm He
HFIR-CTR-30	Swelling and tensile properties, Paths A, B, and D micro-structural variations, 40 dpa, 2500 at. ppm He (Path A)
HFIR-CTR-31	Swelling and tensile properties, Paths A, B and D micro-structural variations, 20 dpa, 1200 ppm He (Path A)
HFIR CTR-32	Swelling and tensile properties, Paths A, B and D micro-structural variations, 10 dpa, 500 ppm He (Path A)
HFIR-CTR-33	Swelling and tensile properties, Path E alloys, 10 dpa, 50°C

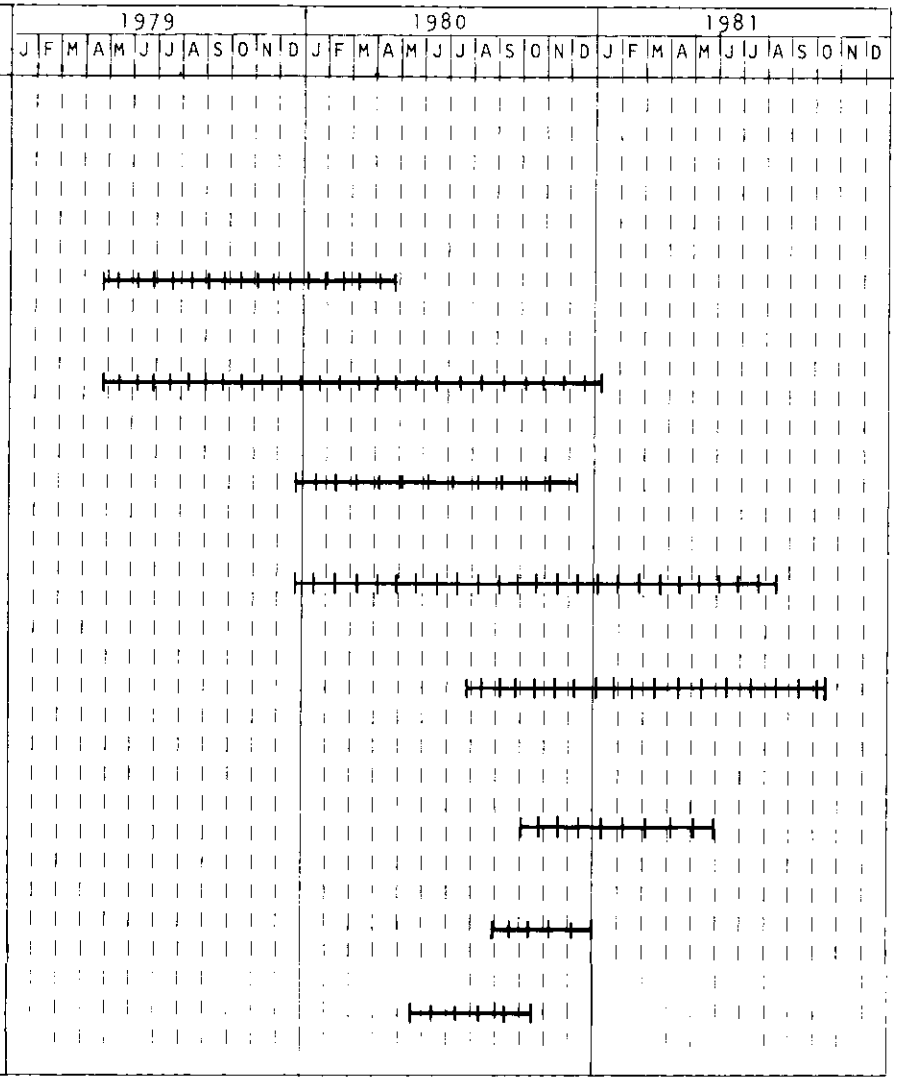

[1] Delayed for undetermined period.

Table 8.1.2. (Continued)

Experiment Designation	Major Objective
HFIR-MFE-T1	Swelling, tensile properties, and fatigue of path E alloys. 30 dpa, up to 250 ppm He depending upon alloy, 55°C.
HFIR-MFE-T2	Swelling, tensile properties, and fatigue of path E alloys. 7 dpa, up to 40 ppm He depending upon alloy, 55°C.
HFIR-MFE-T3	Impact properties of path E alloys. 10 dpa, up to 75 ppm He depending upon alloy, 55°C.
HFIR-MFE-RB1	Swelling, microstructure, crack growth, fracture toughness, impact, tensile, and fatigue properties of path E alloys, 55°C.
HFIR-MFE-RB2	Similar to HFIR-MFE-RB1.

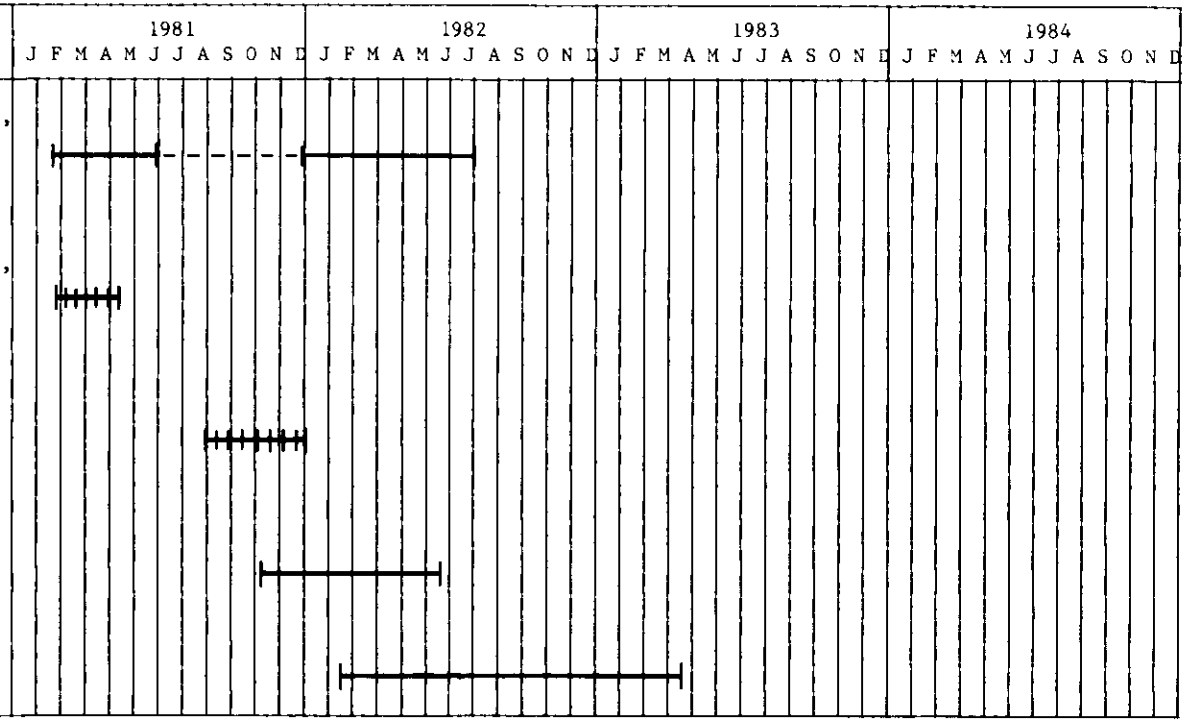

Table 8.1.2. (Continued)

Experiment Designation	Major Objective
HFIR-CTR-34	Impact properties of path E alloys. 10 dpa, 0 to 75 ppm He, 300, 400°C.
HFIR-CTR-35	Impact properties of path E alloys. 10 dpa, 0 to 75 ppm He, 300, 400°C.
HFIR-CTR-39	Swelling, tensile properties of path E alloys. 12 dpa, up to 90 ppm He, 300 to 500°C.
HFIR-CTR-40	Swelling, tensile properties of path E alloys. 12 dpa, up to 90 ppm He, 300 to 500°C.
HFIR-CTR-41	Swelling, tensile properties of path E alloys. 12 dpa, up to 90 ppm He, 300 to 500°C.
HFIR-CTR-42	Swelling, tensile properties of path A alloys. 10 dpa, 500 ppm He, 300 to 600°C.
HFIR-CTR-43	Swelling, tensile properties of path A alloys. 10 dpa, 500 ppm He, 300 to 600°C.

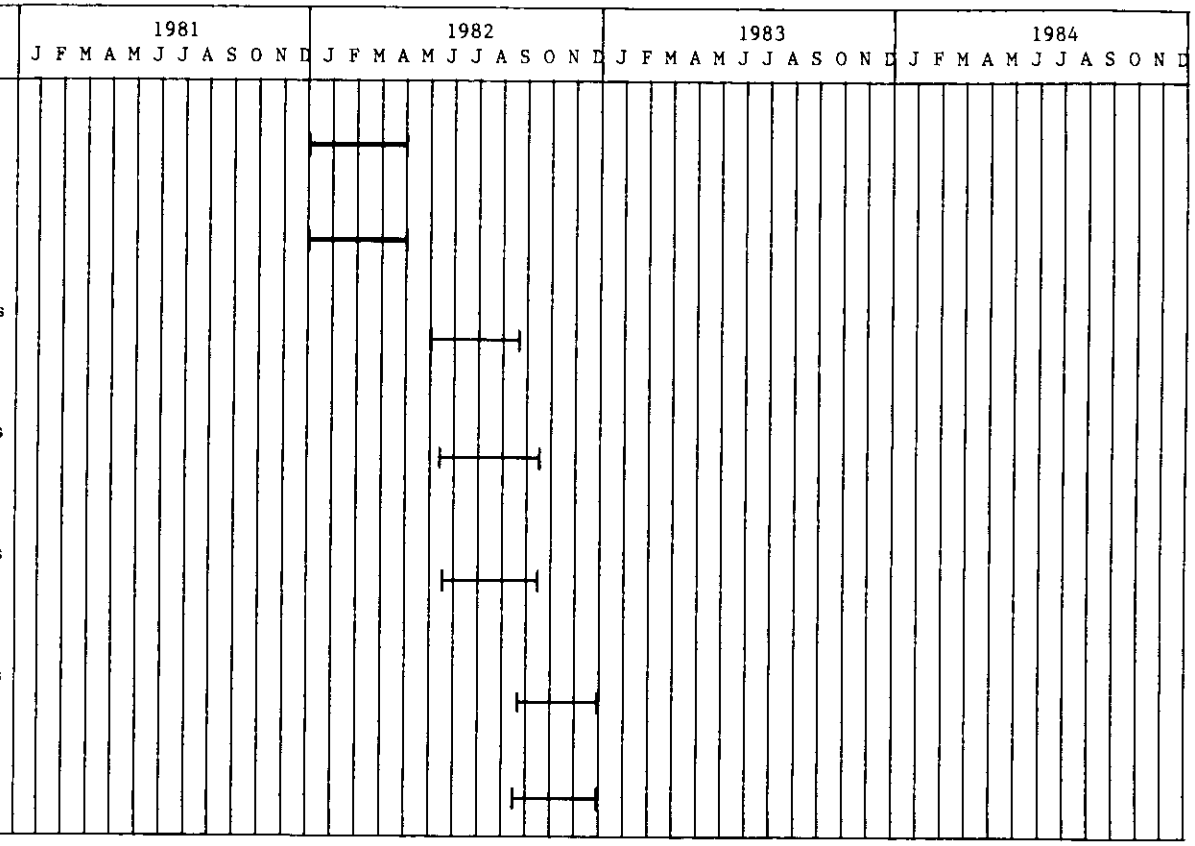

8.2 FUSION PROGRAM RESEARCH MATERIALS INVENTORY — F. W. Wiffen, T. K. Roche (Oak Ridge National Laboratory), J. W. Davis (McDonnell Douglas Company), and T. A. Lechtenberg (General Atomic Company)

8.2.1 ADIP Tasks

ADIP Task I.D.l, Materials Stockpile for MFE Programs.

8.2.2 Objective

Oak Ridge National Laboratory maintains a central inventory of research materials to provide a common supply of materials for the Fusion Reactor Materials Program. This will minimize unintended material variations and provide for economy in procurement and for centralized record keeping. Initially this inventory is to focus on materials related to first-wall and structural applications and related research, but various special purpose materials may be added in the future.

The use of materials from this inventory for research that is coordinated with or otherwise related technically to the Fusion Reactor Materials Program of DOE is encouraged.

8.2.3 Materials Requests and Release

Materials requests shall be directed to the Fusion Program Research Materials Inventory at ORNL (Attention: F. W. Wiffen). Materials will be released directly if:

(a) The material is to be used for programs funded by the Office of Fusion Energy, with goals consistent with the approved Materials Program Plans of the Materials and Radiation Effects Branch.

(b) The requested amount of material is available, without compromising other intended uses.

Materials requests that do not satisfy both (a) and (b) will be discussed with the staff of the Materials and Radiation Effects Branch, Office of Fusion Energy, for agreement on action.

8.2.4 Records

Chemistry and materials preparation records are maintained for all inventory material. All materials supplied to program users will be accompanied by summary characterization information.

8.2.5 Summary of Current Inventory and Material Movement During Period October 1, 1981 to March 31, 1982

A 15 Mg heat of 12 Cr-1 MoW ferritic steel (HT9) was procured by General Atomic Company from the Electralloy Corporation. It was melted by the argon-oxygen decarburization method (AOD). The description of the conversion was reported in a previous ADIP quarterly.[1] Half of the heat was remelted by the electroslag remelting process (ESR) and converted to final product form by Universal Cyclops. The conversion and chemical analyses are discussed in Sect. 7.4 of this progress report.

A condensed, qualitative description of the content of materials in the Fusion Program Research Materials Inventory is given in Table 8.2.1. This table indicates the nominal diameter of rod or thickness of sheet for product forms of each alloy and also indicates by weight the amount of each alloy in larger sizes available for fabrication to produce other product forms as needed by the program. Table 8.2.2 lists materials received into the inventory during this reporting period. Table 8.2.3 gives the materials distributed from the inventory.

Alloy compositions and more detail on the alloys and their procurement and/or fabrication are given in earlier ADIP quarterly progress reports.

8.2.6 Reference

1. T. A. Lechtenberg, R. D. Stevenson, S. N. Rosenwasser, B. E. Thurgood, and L. D. Thompson, "Procurement of National 12 Cr Heat and Evaluation of Welding Procedures for Irradiation Specimens," *ADIP Quart. Prog. Rep. March 31*, 1980, DOE/ER-0045/2, pp. 109—31.

Table 8.2.1. Summary Status of Materials Available in the Fusion Program Research Materials Inventory

Alloy	Product Form			
	Ingot or Bar,[a] Weight (kg)	Rod Diameter (mm)	Sheet Thickness (mm)	Thin-Wall Tubing. Wall Thickness (mm)
		Path A Alloys		
Type 316 SS	900	16 and 7.2	13 and 7.9	0.25
Path A PCA[b]	490	12	13	0.25
USSR – Cr-Mn Steel'	-	10.5	2.6	-
NONMAGNE 30[d]	-	18.5	10	-
		Path B Alloys		
PE-16	140	16 and 7.1	13 and 1.6	0.25
B-1	180	-		-
8-2	180	-		-
8-3	180	-		-
8-4	180	-		-
8-6	180	-		-
		Path C Alloys		
Ti-64	-		2.5 and 0.76	-
Ti-6242s	-	63	6.3, 3.2, and 0.76	-
Ti-5621S	-	-	2.5 and 0.16	-
Ti-38644	-	-	0.76 and 0.25	-
Nb-1% Zr	-	6.3	2.5, 1.5, and 0.76	-
Nb-5% Mo-1% Zr	-	6.3	2.5, 1.5. and 0.76	-
V-20% Ti	-	6.3	2.5, 1.5, and 0.76	-
V-15% Cr-5% Ti	-	6.3	2.5, 1.5. and 0.76	-
VANSTAR-7	-	6.3	2.5. 1.5, end 0.76	-
		Path D Alloys – No Material in Inventory		
		Path E Alloys		
HT9[e] (AOD fusion heat)	3400	-	28.5. 15.8, 9.5, and 3.1	-
HT9 (AOD/ESR fusion heat)	-	25, 50, end 75	28.5, 15.8, 9.5. and 3.1	-
HT9	-	-	4.5 and 18	-
HT9 + 1% Ni	-	-	4.5 and 18	-
HT9 + 2% Ni	-	-	4.5 and 18	-
HT9 + 2% Ni + Cr adjusted	-	-	4.5 and 18	-
T-9f modified	-	-	4.5 and 18	-
T-9 modified + 2% Ni	-	-	4.5 and 18	-
T-9 modified + 2% Ni + Cr adjusted	-	-	4.5 and 18	-
2 1/4 Cr-1 Mo	-	-	g	-

[a]Greater than 25 mm, minimum dimension.

[b]Prime Candidate Alloy.

[c]Rod and sheet of a USSR stainless steel supplied under the U.S.-USSR Fusion Reactor Materials Exchange Program.

[d]NONMAGNE 30 is an austenitic steel with base composition Fe-14% &-2% Ni-2% Cr. It was supplied to the inventory by the Japanese Atomic Energy Research Institute.

'Alloy 12 Cr-1 MoVW, with composition equivalent to Sandvik alloy HT9.

[f]T-9 is the alloy 9 Cr-1 MoVNb.

[g]Material is thick-wall pipe, rerolled as necessary to produce sheet or rod.

Table 8.2.2. Fusion Program Research Materials Inventory, Receipts 10-1-81 to 3-31-82

Alloy	Heat Fusion Identification	Product Form	Product Sizes	Source
12 Cr-1 MoVW[a]	AOD Fusion Heat 9607	Ingot	3.4 Mg	Electralloy Corporation
		Sheet	3.1, 9.5, 15.8, and 28.5 mm thick	Electralloy Corporation and Universal Cyclops
12 Cr-1 MoVW	AOD/ESR Fusion Heat 9607R	Sheet	3.1, 9.5, 15.8, and 28.5 mm thick	Electralloy Corporation and Universal Cyclops
		Rod	25, 50, and 75 mm diam	Electralloy Corporation and Universal Cyclops

[a]Equivalent to Sandvik alloy HT9.

Table 8.2.3. Fusion Program Research Materials Inventory, Disbursements 10–1–81 to 3-31-82

Alloy	Heat	Product Form	Dimensions[a] (mm)	Quantity (m)	Quantity (m^2)	sent to
Path A Alloys — Austenitic Stainless Steels						
Type 316 stainless steel reference heat	X–15893	Plate	12.7		0.186	Battelle Pacific Northwest Laboratories
		Rod	13.7	2.9		Metals processing croup, OWL
Path A–PCA	K–280	Sheet	0.41		0.043	Radiation Effects Group, OWL
		Sheet	0.76		0.73	Radiation Effects Group, ORNL
		Rod	4.19	1.57		Radiation Effects Group, OWL
		Rod	6.9	13.2		Radiation Effects Group, ORNL
		Rod	7.87	2.1		Radiation Effects Group. ORNL
		Sheet	0.51		0.12	University of Wisconsin, Madison
		Tubing	4.57 OD x 0.254 wall	2.3		HEUL
		Bar	102	1.83		Metals Processing Group. ORNL
		Bar	102	0.15		EG&G Idaho. Inc.
Path C Alloys — Reactive and Refractory Alloys						
V–15 Cr–5 Ti	834–6	Sheet	0.81		0.033	Westinghouse
Path E Attoys — Ferritic Steels						
12 Cr-1 MoVW	AOD, 9607	Sheet	28.5		0.30	Mechanical Properties Group, ORNL
		Sheet	28.5		0.28	Sandia Livermore Laboratory
		Sheet	28.5		0.25	Battelle Pacific Northwest Laboratories
		Sheet	15.8		0.73	Sandia Livermore Laboratory
		Sheet	15.8		0.04	Argonne National Laboratory
		Sheet	15.8		0.30	Battelle Pacific Northwest Laboratories
		Sheet	15.8		0.05	Mechanical Properties Group, ORNL
		Sheet	15.8		0.07	Naval Research Laboratory
		Sheet	9.5		0.32	Radiation Effects Group, ORNL
		Sheet	9.5		0.67	Mechanical Properties croup, ORNL
		Sheet	9.5		3.2	Sandia Livermore Laboratory
12 Cr-1 MoVW	AOD/ESR-9607R	Sheet	28.5		1.0	Sandia Livermore Laboratory
12 Cr-1 MoVW	ESR-XAA-3587	Sheet	0.76		0.0064	University of Wisconsin, Madison
2 1/4 Cr-1 Mo	72768	Sheet	0.76		0.013	University of Wisconsin. Madison

[a]Characteristic dimension — thickness for plate and sheet. diameter for rod and tubing.

9. MATERIALS COMPATIBILITY AND HYDROGEN PERMEATION STUDIES

9.1 CORROSION OF AUSTENITIC, FERRITIC, AND LONG-RANGE-ORDERED ALLOYS IN FLOWING LITHIUM — P. F. Tortorelli, J. H. DeVan, and C. T. Liu — (Oak Ridge National Laboratory)

9.1.1 ADIP Task

ADIP Task I.A.3, Perform Chemical and Metallurgical Compatibility Analyses.

9.1.2 Objective

The purpose of this task is to evaluate the corrosion resistance of candidate first-wall materials to flowing lithium in the presence of a temperature gradient. Corrosion rates (in both dissolution and deposition) are measured as functions of time, temperature, additions to the lithium, and flow conditions. These measurements are combined with chemical and metallographic examinations of specimen surfaces to establish the mechanisms and rate-controlling processes for dissolution and deposition reactions.

9.1.3 Summary

Results from lithium thermal-convection loop (TCL) tests of type 316 stainless steel, Sandvik HT9, and a long-range-ordered (LRO) alloy composed of Fe–31.8 Ni–22.5 V–0.4 Ti (wt %) are reported. Type 316 stainless steel and HT9 had similar steady-state dissolution rates at 500°C. The LRO alloy was rapidly corroded in type 316 stainless steel TCLs. However, results from isothermal tests in lithium showed that dissimilar-metal transfer probably made a very significant contribution to the overall LRO alloy corrosion rate measured in the above experiments.

9.1.4 Progress and Status

We have continued our mass transfer studies in flowing lithium using previously described' TCLs with accessible specimens. These loops are designed so that lithium samples can be taken and corrosion coupons can be withdrawn and inserted without interrupting the lithium flow. In the preceding progress report,[2] dissolution rate data from one such loop of type 316 stainless steel was reported as a function of the maximum loop

temperature, T_{max}. The dissolution rate was first established as a function of time at 600°C and then T_{max} was varied while a constant temperature differential of 150°C was maintained across the loop. The steady-state dissolution rate at each temperature, R_s, was obtained from the slope of the least squares fit line on a weight loss versus exposure time plot. In the preceding progress report,[2] such dissolution rates were reported for maximum temperatures of 500, 550, and 600°C. Since then, we have operated the loop at a T_{max} of 500°C for an additional 3500 h in order to obtain a better value for the steady-state dissolution rate at that temperature (see Fig. 9.1.1). The new data resulted in a lower

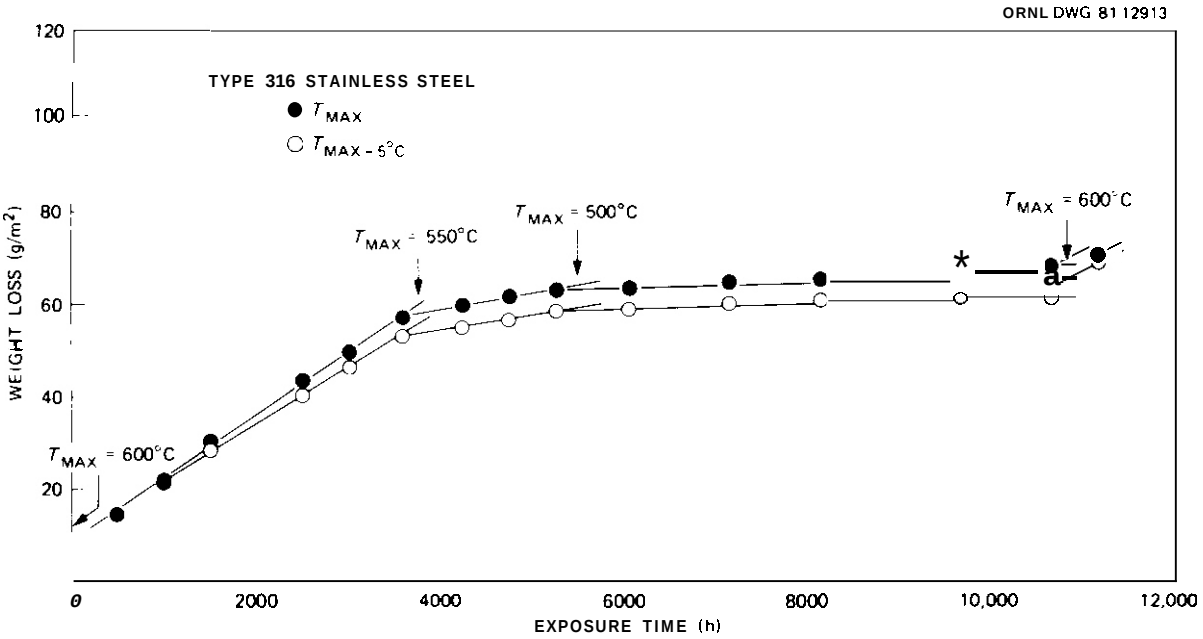

Fig. 9.1.1. Weight Loss Versus Exposure Time for Type 316 Stainless Steel at Various Maximum Loop Temperatures.

dissolution rate (0.4 mg/m^2·h) than reported previously' but does not significantly affect the apparent activation energy (see ref. 2). The steady-state dissolution rates measured in this TCL for type 316 stainless steel are therefore

T_{max} (°C)	R_s (mg/m^2·h)
500	0.4
550	3.6
600	13.6

After operating at a T_{max} of 500°C, we then increased the maximum temperature to 600°C and, as shown in Fig. 9.1.1, observed a return to a corrosion rate that is approximately the same as that measured earlier.

We have recently started operation of a lithium–type 316 stainless steel loop in which path A PCA specimens with different thermomechanical treatments are being exposed. In addition to yielding information on the dissolution rate of PCA relative to that of standard type 316 stainless steel, this series of experiments will allow an initial determination of the effects of microstructure on corrosion of austenitic stainless steel by lithium.

During the period since the preceding progress report,[2] a lithium–Sandvik HT9 TCL of the type described above began operation with a T_{max} of 500°C and a AT of 150°C. The weight loss versus exposure time data for the HT9 specimen at 500°C **are** shown in Fig. 9.1.2. Note that the dissolution rate rapidly decreased and that an approximate dissolution rate can be gotten from the slope of the least squares fit line between 1000 and 5060 h. This rate for HT9 in thermally convective lithium is *0.4* $mg/m^2 \cdot h$, which is the same value as that measured for type 316 stainless steel at

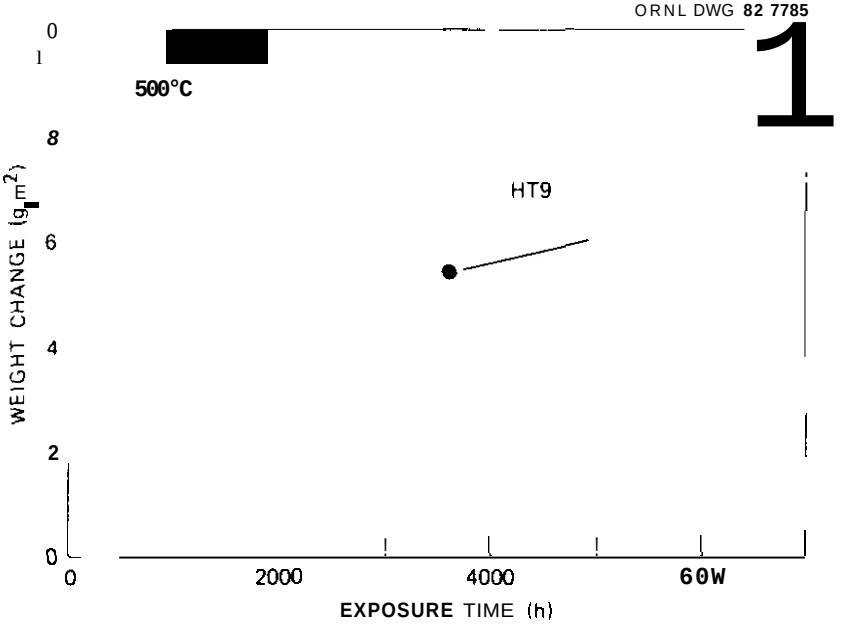

Fig. 9.1.2. Weight Loss Versus Exposure Time for HT9 Exposed to Flowing Lithium at 500°C.

500°C (*see* above). This is not unexpected, however, since at steady state the surface compositions of exposed type 316 stainless steel and HT9 probably do not differ greatly. Initially, the type 316 stainless steel is preferentially depleted of nickel and a ferritic surface is formed.[3] Its chromium concentration is also reduced so that, when a steady-state condition is reached, the surface compositions of the type 316 stainless steel and HT9 would be similar. This does not necessarily mean that the steady-state dissolution rates of the two alloys should be exactly the same because of possible solid-state-diffusion effects, but, as shown here, they do not differ significantly at 500°C. Because of the low weight losses at 500°C, we will continue to operate the HT9 TCL at T_{max} = 500°C in order to obtain a statistically better dissolution rate. We then plan to raise T_{max} in order to (1) compare dissolution rates of type 316 stainless steel and HT9 at higher temperatures and (2) ultimately obtain an activation energy for HT9 dissolution by flowing lithium.

In preceding progress reports,[2,4] we presented results from experiments conducted to assess the corrosion resistance of an Fe-3.18 Ni-22.5 W.4 Ti (wt %) LRO-35 alloy to flowing lithium. Because of a lack of sufficient LRO material, the tests are being conducted in type 316 stainless steel TCLs of the kind described above. The use of the stainless steel loop material imposes a severe chemical gradient between the LRO specimens and the loop wall, especially considering that surfaces of the loops' hot legs have been preferentially leached of nickel from prior exposures to lithium. Such an arrangement provides a worse case for the dissolution of the LRO alloy in flowing lithium. The LRO-35 coupons were placed in the two hottest positions (600 and 570°C) of two type 316 stainless steel TCLs.

We had previously reported[2] that the LRO specimens corroded very rapidly when exposed to flowing lithium at 600°C in type 316 stainless steel TCLs. The resulting LRO surfaces were depleted in nickel and correspondingly enriched in iron and vanadium. Corrosion rates of the LRO were much greater than those of type 316 stainless steel previously exposed in these loops. We continued to expose the LRO coupons after 5000 h in one of the two loops, and the updated 600°C data for this TCL

are shown in Fig. 9.1.3. Note that the dissolution rate (the slope of the weight loss versus time curve) markedly decreased after about 4000 h such that two straight lines of different slopes can closely approximate the data. If this is done, one can ascribe a different dissolution rate to each time interval from the respective slopes. These rates are 135 $mg/m^2 \cdot h$ for 500 h $< t <$ 4000 h and 50 $mg/m^2 \cdot h$ for 4000 h $< t <$ 8000 h, where t is the exposure time. These rates are much higher than that for the steady-state dissolution of type 316 stainless steel in thermally convective lithium (~14 $mg/m^2 \cdot h$, see above).

After 7500 h of exposure, metallographic examination of polished cross sections revealed a corrosion-induced microstructure similar to that observed after 2500 h (ref. 2) (see Fig. 9.1.4). However, the depths of the corroded layers are correspondingly greater for the longer exposures.

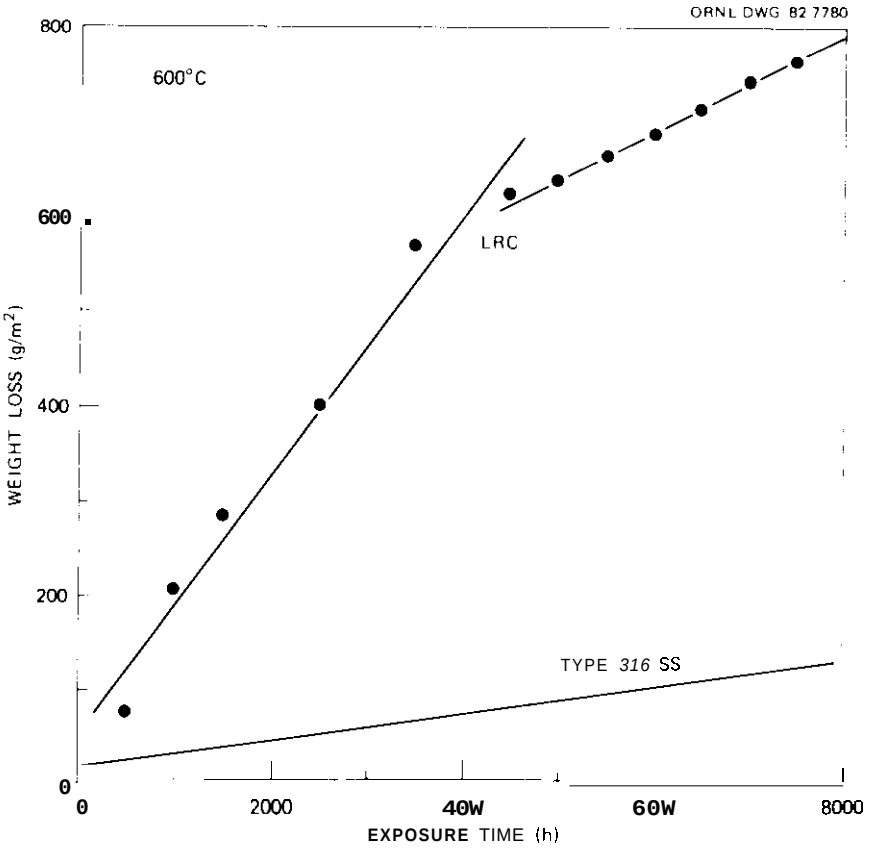

Fig. 9.1.3. Weight Loss Versus Exposure Time for LRO-35 Exposed to Flowing Lithium at 600°C in a Type 316 Stainless Steel Thermal-Convection Loop.

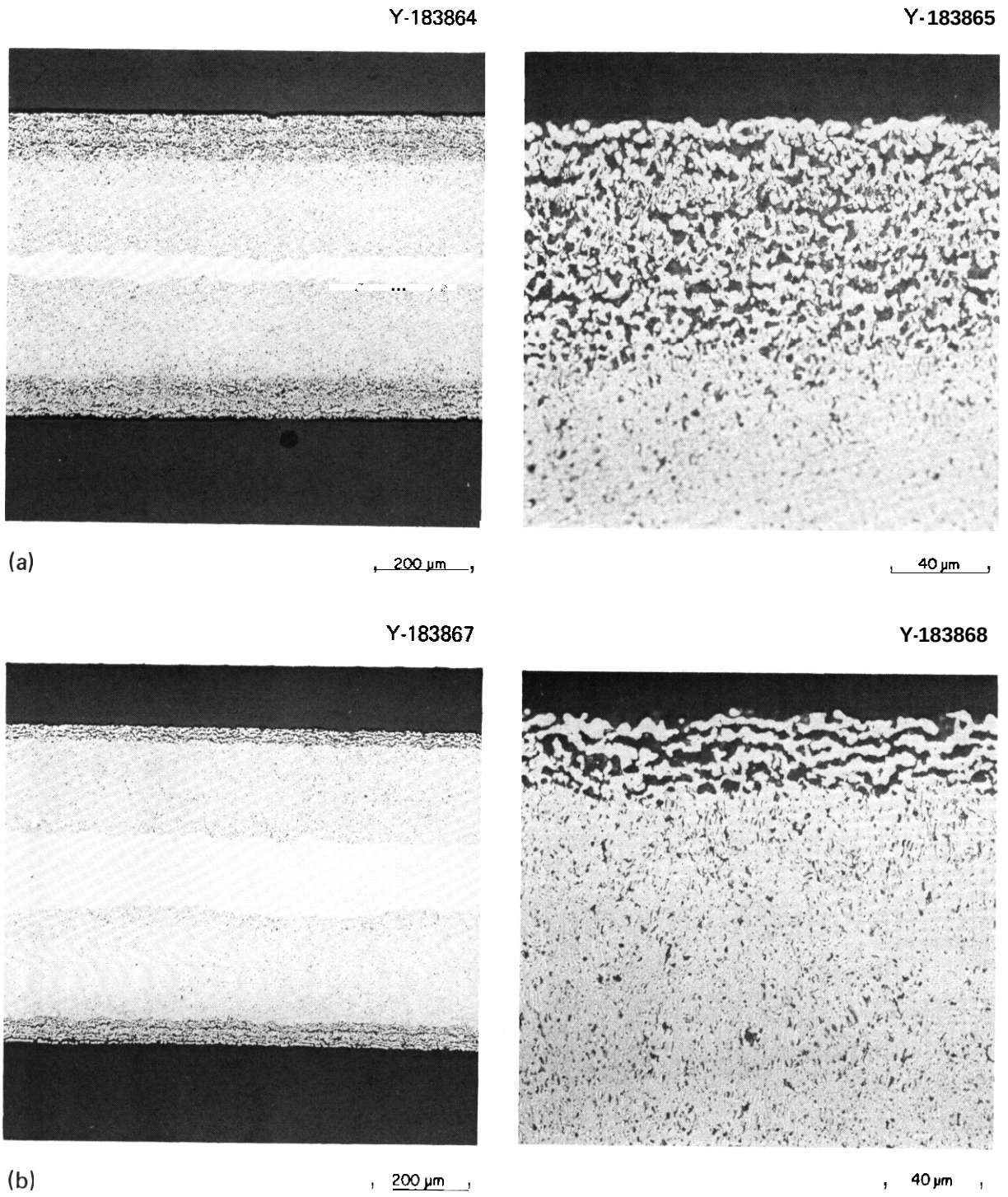

Fig. 9.1.4. Polished Cross Sections of LRO-35 Exposed to Flowing Lithium for 7500 h at (a) 600°C and (b) 570°C.

We have not yet analyzed these layers, but we may assume that, as found earlier,[2] they are almost totally depleted of nickel. This may help explain the break in the weight loss versus exposure time curve shown in Fig. 9.1.3. While we are not sure about the reason for such behavior, it probably is related to a reduction in the nickel available for the depletion process since much of the starting material has been consumed and a similar break in the curve occurred when the 570°C LRO specimen reached about the same total weight loss (-600 g/m^2) at about 5500 h (see Fig. 9.1.5). It is also interesting to note that the LRO specimens in the other TCL did not lose more than about 430 g/m^2 before their exposures were terminated, and their dissolution rates therefore did not show any changes with time. It thus appears that the onset of a reduced corrosion rate can be correlated with a definite amount of material (nickel) removed.

As mentioned above, the positioning of LRO-35 coupons in the ferritic hot leg of a type 316 stainless steel TCL imposes a severe chemical

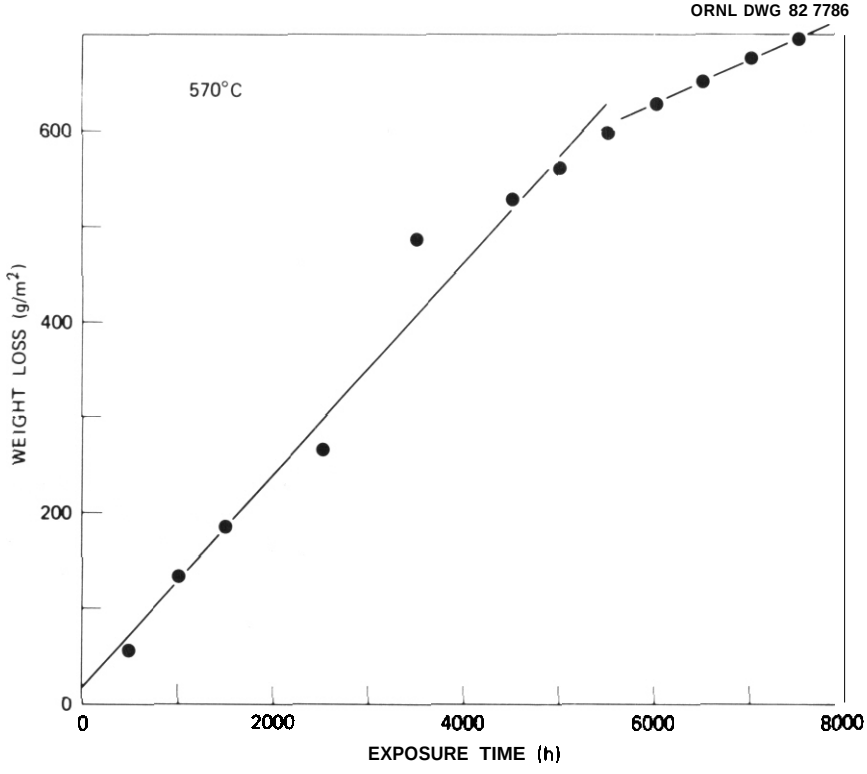

Fig. 9.1.5. Weight Loss Versus Exposure Time for LRO-35 Exposed to Flowing Lithium at 570°C in a Type 316 Stainless Steel Thermal-Convection LOOP.

gradient and therefore should represent a worse case for dissolution of the LRO alloy. In order to qualitatively determine the magnitude of the contribution from dissimilar-metal transfer, we conducted capsule tests in which LRO alloys were exposed to lithium in capsules of the same LRO alloy and 9 Cr-1 Mo steel. In this way, weight changes could be measured under isothermal conditions both in the presence and absence of a chemical gradient similar to that existing in the TCL experiments. The results are listed in Table 9.1.1 and show that, while minimal weight losses were measured when the capsule and specimen materials were of the same composition, significant weight losses of LRO alloy occurred when the capsule material was 9 Cr-1 Mo steel. Although the specimens have not yet been metallographically examined or analyzed for concentration gradients, we can assume that most of the weight loss can be attributed to nickel transfer and that part of the dissolution weight loss may be offset by transfer of chromium in the opposite direction. We can thus conclude from the present results that dissimilar metal transfer of nickel makes a significant contribution to the large weight losses of LRO-35 reported above for the TCL experiments.

Table 9.1.1. Weight Losses of LRO Specimens Exposed to Static Lithium in Capsules of Similar and Dissimilar Compositions

Specimen Material[a]	Capsule Material	Exposure Temperature (°C)	Weight Loss[b] (g/m^2)
LRO-35	LRO-35	650	0.1[c]
LRO-35	9 Cr-1 Mo	600	14.1
LRO-37	LRO-37	600	0.6
LRO-37	9 Cr-1 Mo	600	18.0

[a]LRO-35: Fe–31.8 Ni–22.5 V–0.4 Ti (wt %).
LRO-37: Fe–39.5 Ni–22.4 V–0.4 Ti (wt %).

[b]Average of two specimens unless otherwise noted.

[c]Average of three specimens.

9.1.5 Conclusions

1. Initial data from a lithium-HT9 TCL experiment indicated that HT9 and type 316 stainless steel had similar, low steady-state dissolution rates at 500°C (<0.5 $mg/m^2 \cdot h$).

2. *An* Fe-31.8 Ni-22.5 V-0.4 Ti (wt %) LRO-35 alloy was rapidly corroded when placed in type 316 stainless steel TCLs. Exposure to the flowing lithium in these loops resulted in severe depletion of nickel from LRO-35. Measurements from capsule tests showed that dissimilar-metal transfer of the nickel from the LRO coupons to the loop wall probably made a very significant contribution to the overall corrosion rate. Rates in an all-LRO system should therefore be less than those measured in the present tests.

9.1.6 References

1. J. H. DeVan and J. R. DiStefano, "Thermal-Convection Loop Tests of Type 316 Stainless Steel in Lithium,'' *ADIP Quart. Prog. Rep. March 31, 1978*, DOE/ET-0058/1, pp. 200-08.
2. P. F. Tortorelli, J. H. DeVan, and C. T. Liu, "Corrosion of Iron-Base Alloys in Flowing Lithium," *ADIP Quart. Prog. Rep. Sept. 30, 1981*, DOE/ER-0045/7, pp. 312-20.
3. P. F. Tortorelli, J. H. DeVan, and J. E. Selle, "Corrosion in Lithium Stainless Steel Thermal-Convection Systems," pp. 13-55-13-63 in *Proc. 2d Int. Conf. Liquid Metal Technology in Energy Production*, CONF-800401-P2, U.S. Department of Energy, 1980.
4. P. F. Tortorelli and J. H. DeVan, "Corrosion of an Iron-Base Long-Range-Ordered Alloy in Flowing Lithium," *ADIP Quart. Prog. Rep. March 31, 1981*, DOE/ER-0045/6, pp. 229-34.

9.2 ENVIRONMENTAL EFFECTS ON PROPERTIES OF STRUCTURAL ALLOYS - O. K. Chopra, D. L. Smith, and W. E. Ruther (Argonne National Laboratory)

9.2.1 ADIP Task

ADIP tasks are not defined in the 1978 program plan.

9.2.2 Objective

The objective of this program is to investigate the influence of chemical environment on the compatibility, corrosion, and mechanical properties of structural alloys under conditions of interest for fusion reactors. Test environments to be investigated include lithium, lead-lithium, helium, and water. Emphasis will be placed on the combined effect of stress and chemical environment on corrosion and mechanical behavior of materials. Initial investigations are focused on the influence of flowing lithium and lead-lithium environments on compatibility and mechanical properties of structural materials.

9.2.3 Summary

Compatibility tests were conducted with several candidate structural materials to study the corrosion behavior in flowing lithium, and fatigue tests were performed with HT-9 alloy specimens that were preexposed to lithium. The results indicate that the corrosion rate of ferritic steels is an order of magnitude lower than for the austenitic stainless steel. The corrosion rate for cold-worked Type 316 stainless steel is a factor of 3 greater than that for the annealed steel. Preexposure (1100 h) of the HT-9 alloy to low-nitrogen lithium has no effect on fatigue life. Preliminary scoping studies indicate that V-15Cr and V-15Cr-5Ti alloys are highly corrosion resistant in 523 K (250°C) deoxygenated water.

9.2.4 Progress and Status

9.2.4.1 Lithium Environment

The effects of a flowing lithium environment on the corrosion behavior and low-cycle fatigue properties of ferritic and austenitic steels are being investigated. Tests are conducted in a forced-circulation lithium loop equipped with a cold-trap purification system to control the concentration of nonmetallic elements, e.g., N, C, and H. The cold-trap temperature is maintained at 498 K (225°C). Hot trapping with Ti or Zr foils (or use of dissolved getters) was used to reduce the nitrogen level to ~50 wppm in lithium, which is considerably below that attainable by cold trapping. Data obtained from constant-stress compatibility tests and continuous-cycle fatigue tests in lithium at 755 K (482°C) were presented in earlier reports.[1,2] The results indicate that for applied stresses below the yield stress of the material, the corrosion behavior of the HT-9 alloy and Type 304 stainless steel is independent of stress. The fatigue properties of these materials are strongly influenced by the concentration of nitrogen in lithium. For example, the fatigue life of the HT-9 alloy in lithium containing 100-200 ppm nitrogen is a factor of 2 to 10 greater, depending on the value of total strain range, than in lithium with 1000-1500 ppm nitrogen. Furthermore, the fatigue life of the HT-9 alloy in low-nitrogen lithium is independent of strain rate. During the current reporting period, compatibility tests were conducted with several candidate structural materials to study the corrosion behavior in flowing lithium, and fatigue tests were performed with HT-9 alloy specimens preexposed for 4.0 Ms (1100 h) in lithium at 755 K.

Flat corrosion coupons that were ~72 x 13 mm in size and 0.2 to 0.5 mm thick were exposed to lithium for 4.7 and 10.8 Ms (1300 and 3000 h) at 755 K. The ferritic steels (i.e., HT-9 alloy and Fe-9Cr-1Mo steel) were in the normalized and tempered condition while Types 304 and 316 stainless steel were solution annealed. A 20% cold-worked Type 316 stainless steel specimen was also exposed. During exposure, the

concentration of nitrogen in lithium was maintained at 50-100 ppm. The corrosion behavior was evaluated from measurements of weight loss and depth of internal corrosive penetration. The results are given in Table 9.2.1. The dissolution rate (expressed as weight loss per unit area of the specimen) for the ferritic steels is an order of magnitude lower than that for the austenitic stainless steels and the rate for the cold-worked Type 316 stainless steel is a factor of 3 greater than for the annealed material. The depth of internal corrosive penetration also shows the same behavior. The weight loss for all alloys shows a linear dependence with time, i.e., the dissolution rates after 4.7 and 10.8 Ms are approximately the same. For the HT-9 alloy and Type 316 stainless steel, the dissolution rates are a factor of 6 greater than those observed in static lithium or thermal convection loops with small temperature gradients (i.e., $\Delta T \simeq 150$ K).[3,4] Such behavior is expected in lithium loops with large temperature gradients because of greater mass transfer and deposition of metal elements.

Table 9.2.1. Dissolution Rate and Depth of Internal Penetration for Alloys Exposed at 755 K to Flowing Lithium Containing 50-100 ppm Nitrogen

Alloy	Dissolution Rate, $mg/m^2 \cdot h$		Maximum Penetration, μm, after 10.8 Ms (3000 h)
	4.68 Ms (1300 h)	10.8 Ms (3000 h)	
HT-9	0.23	0.45	3
Fe-9Cr-1Mo	0.25	0.33	4
304L SS	2.41	1.50	30
316 ss	5.13	5.40	60
316 CW	18.39	-	-

Micrographs of the surface of the specimens exposed to lithium for 4.7 and 10.8 Ms are shown in Figs. 9.2.1 and 9.2.2, respectively. For all alloys, the surfaces have a pebbled or granular structure. The size of the grains is larger after a 10.8-Ms exposure than for a 4.7-Ms exposure to lithium. In addition, the austenitic stainless steels,

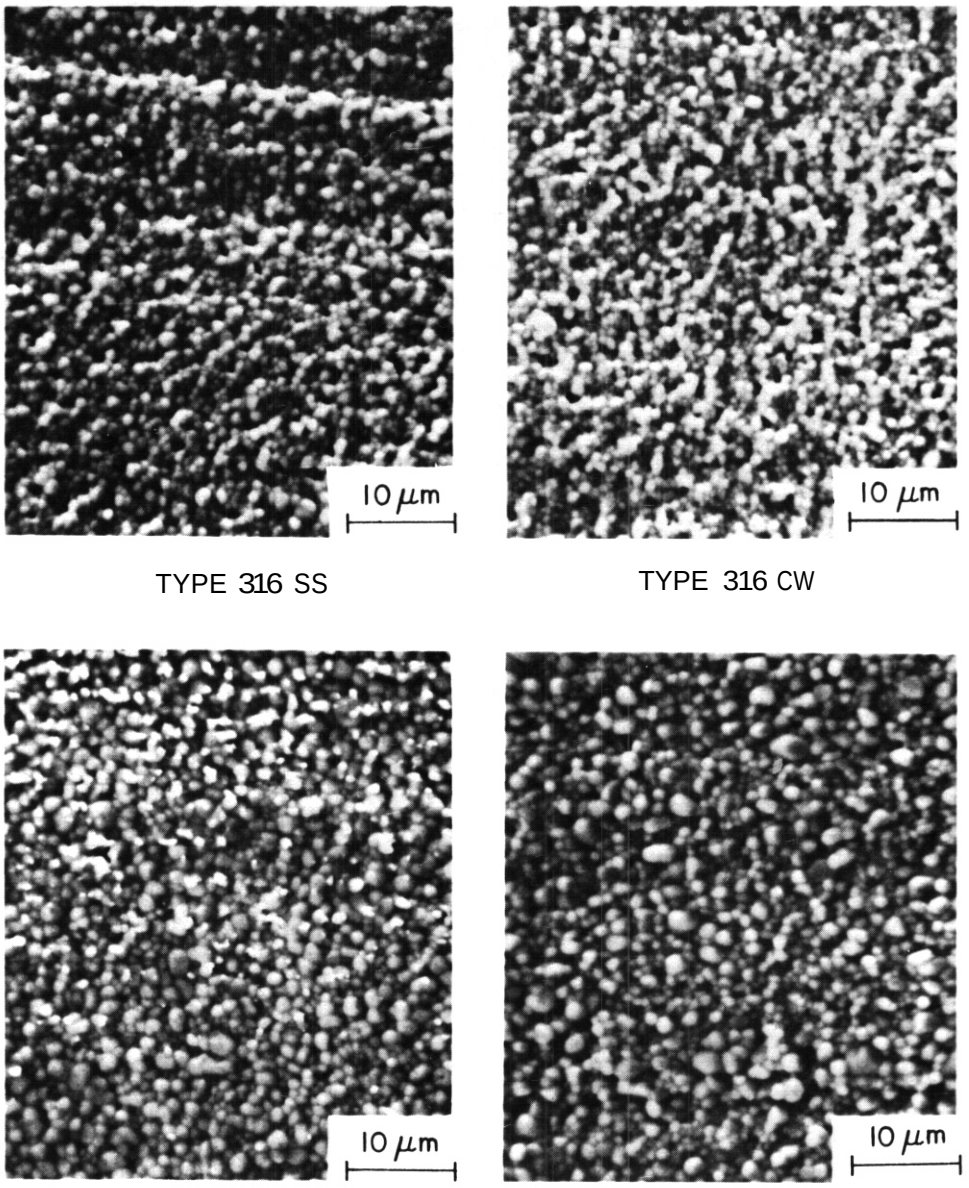

Fig. 9.2.1. Micrographs of the Surfaces of the Corrosion Coupons Exposed to Lithium for 4.7 Ms (1300 h) at 755 K.

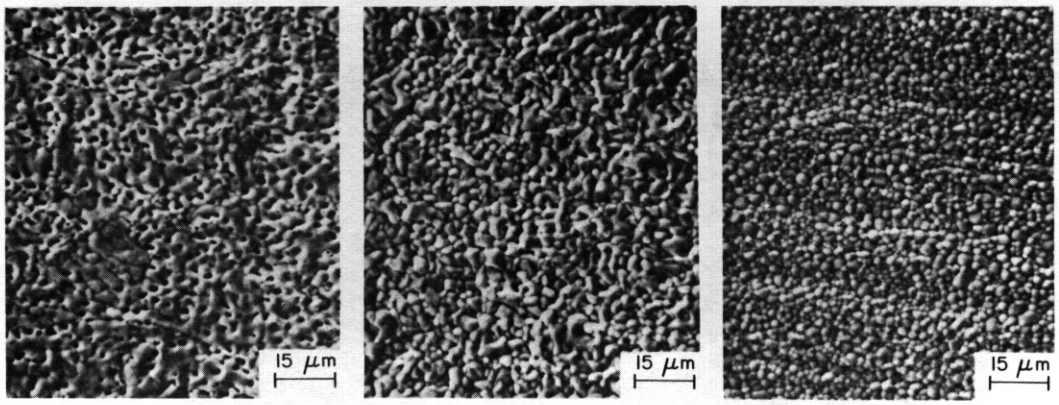

TYPE 316 SS TYPE 304 SS HT-9 ALLOY

Fig. 9.2.2. Micrographs of the Surfaces of the Corrosion Coupons Exposed to Lithium for 10.8 Ms (3000 h) at 755 K.

particularly Type 316 stainless steel, show many holes on the surface. A typical energy dispersive x-ray analysis of the surface of austenitic stainless steels yields <1% nickel and ~12% chromium. Micrographs of the cross section of Type 316 stainless steel and HT-9 alloy specimens and the distribution of major elements across the corrosion layer are shown in Fig. 9.2.3. A porous corrosion layer is observed for Type 316 stainless steel, whereas the HT-9 alloy shows little or no corrosion. Both steels have a 10-μm-thick layer depleted in chromium, and the Type 316 stainless steel shows depletion of nickel over the entire corrosion scale. The porosity in the corrosion layer is associated with nickel depletion.

The influence of lithium preexposure on the cyclic properties of the HT-9 alloy was investigated by conducting fatigue tests with specimens that were preexposed for 4.0 Ms (1100 h) to flowing lithium at 755 K. The concentration of nitrogen in lithium during the exposure was ~50 ppm. Figure 9.2.4 shows the strain-life behavior of the HT-9 alloy, with and without preexposure, tested in low-nitrogen lithium at 755 K. The results show that preexposure of the material to lithium has no effect on fatigue life. In fact, for a given plastic strain range, the fatigue life of lithium-exposed steel is greater than that for the unexposed material. Micrographs of the surface and the cross section of

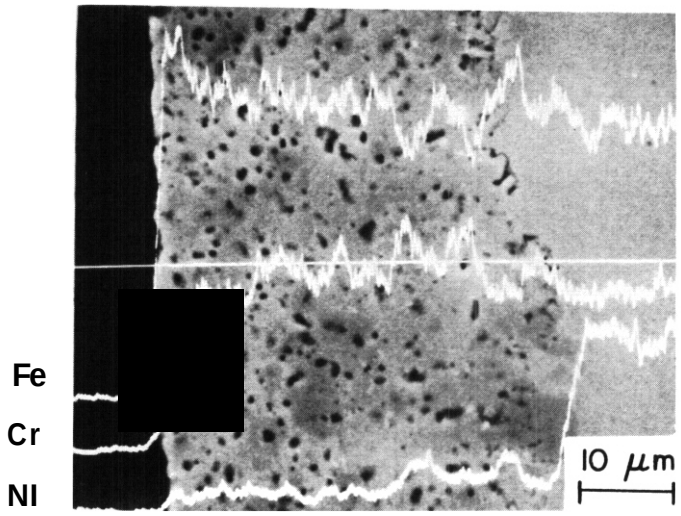

TYPE 316 SS

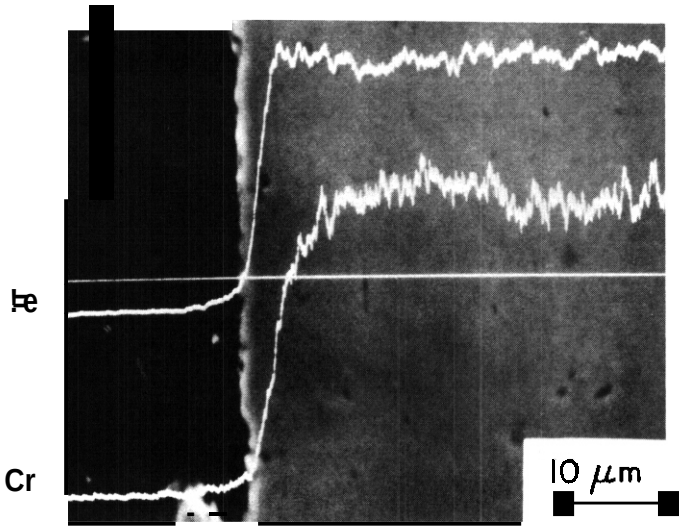

HT-9 ALLOY

Fig. 9.2.3. Micrographs and Concentration Profiles for Major Elements Across the Corrosion Layer of Type 316 Stainless Steel and HT-9 Alloy Exposed to Lithium for 10.8 Ms (3000 h) at 755 K.

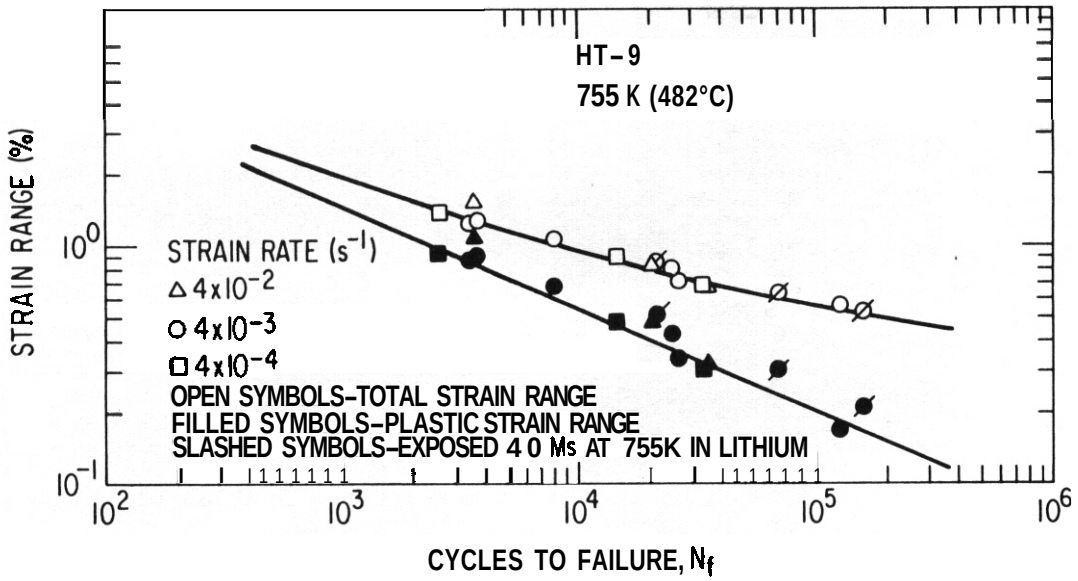

Fig. 9.2.4. Effect of Strain Fate and Lithium Exposure on the Fatigue Life of HT-9 Alloy Tested at 482°C in Lithium Containing 50-200 ppm Nitrogen.

the lithium-exposed specimens are shown in Fig. 9.2.5. The surface has an etched and granular appearance; however, internal corrosive penetration is not observed in the specimens.

9.2.4.2 Water Environment

A preliminary scoping experiment was conducted to evaluate the corrosion resistance of two vanadium alloys (V-15Cr-5Ti and V-15Cr) to high-temperature (-523 K) water. Sheet specimens of the two vanadium alloys were electropolished, rinsed, and weighed before testing in a refreshed autoclave. The water was degassed and pressurized with nitrogen. The water was characterized as follows: dissolved oxygen was 0.04 ppm, specific conductance was 0.9 μmho, and refreshment flow was 0.15 mℓ/s for the 8-52 autoclave. The test temperature was maintained at 523 K for the 0.31-Ms (85.3-h) test (a short-term excursion to 551 K occurred early in the test). Weight gains for the specimens (5.5 cm^2 in area) are summarized in Table 9.2.2. Post-exposure examination revealed

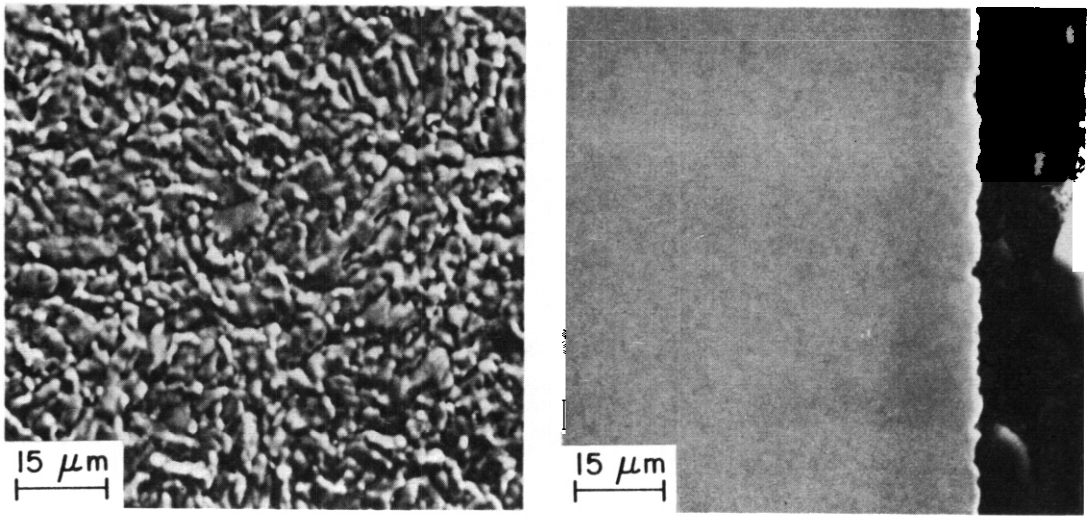

Fig. 9.2.5. Micrographs of the Surface and Cross Section of Lithium-exposed Fatigue Specimen of HT-9 Alloy.

Table 9.2.2. Corrosion Weight Gains of Vanadium Alloy Specimens

Material	Specimen	Weight Gain, g	$\Delta W/cm^2$, $\mu g/cm^2$
V-15Cr	C-1	4×10^{-6}	0.7
	c-2	5×10^{-6}	0.9
V-15Cr-5Ti	T-2	1.31×10^{-4}	23.0
	T-2	1.30×10^{-4}	23.0

no observable change in appearance. The V-15Cr alloy exhibited better corrosion resistance than the V-15Cr-5Ti alloy; however, both alloys appear to be highly corrosion resistant in 523 K deoxygenated water. For comparison, the corrosion rates for austenitic stainless steels in high-purity water are of the order of 6 $\mu g/cm^2$ under similar conditions.

9.2.5 Conclusions

The corrosion rate of ferritic steels in cold-trapped and flowing lithium at 755 K is a factor of ~10 lower than for the austenitic stainless steels, and the rate for cold-worked Type 316 stainless steel is a factor of 3 greater than for the annealed material. The higher

corrosion rates for austenitic stainless steels are primarily due to selective dissolution of nickel from the steel. For both ferritic and austenitic steels, the corrosion rates in cold-trapped lithium are a factor of ~6 greater than that in static lithium or circulating lithium loops with small AT.

Preexposure of the HT-9 alloy to low-nitrogen lithium has no effect on the fatigue life. Although the surfaces of the lithium-exposed specimens have an etched appearance, preexposure of the HT-9 alloy to low-nitrogen lithium does not cause internal corrosive attack.

Preliminary scoping tests indicate that V-15Cr and V-15Cr-5Ti exhibit excellent corrosion resistance in 523 K deoxygenated water.

9.2.6 References

1. O. K. Chopra and D. L. Smith, "Environmental Effects on Properties of Ferritic Steels," ADIP Quarterly Progress Report, December 31, 1980, DOE/ER-0045/5, pp. 156-169.
2. O. K. Chopra and D. L. Smith, "Environmental Effects on Properties of Structural Alloys," ADIP Semiannual Progress Report, September 30, 1981, DOE/ER-0045/7, pp. 321-347.
3. P. F. Tortorelli, J. H. Devan, and C. T. Liu, "Corrosion of Iron-Base Alloys in Flowing Lithium," ibid., pp. 312-320.
4. P. F. Tortorelli, J. H. Devan, and R. M. Yonco, "Compatibility of Fe-Cr-Mo Alloys with Static Lithium," presented at Corrosion/81 T-2-1 Meeting, Toronto, Canada, 1981.

9.3 CORROSION OF AUSTENITIC AND FERRITIC STEELS IN STATIC Pb–17 at. % Li —

P. F. Tortorelli and J. H. DeVan (Oak Ridge National Laboratory)

9.3.1 ADIP Task

ADIP Task I.A.3, Perform Chemical and Metallurgical Compatibility Analyses.

9.3.2 Objective

The purpose of this program is to determine the chemical compatibility of fusion reactor candidate material with possible coolants and tritium breeding materials. Specimens are exposed to static lithium and lithium-lead melts to identify the kinetics and mechanisms that govern corrosion. Other program objectives include (1) to determine the effects of N, C, H, and O on apparent solubilities of metals in lithium and lithium-lead; (2) to determine the carbon and nitrogen partitioning coefficients between alloys and these melts; (3) to determine the effects of soluble (Ca, Al) and solid (Y, Zr, Ti) active metal additions on corrosion by lithium; and (4) to determine the tendencies for mass transfer between dissimilar metals.

9.3.3 Summary

Specimens of type 316 stainless steel and Sandvik HT9 were exposed to static, molten Pb–17 at. % Li. Weight losses of these alloys exposed to Pb–17 at. % Li were much greater than those measured in static, pure lithium. Decreased weight losses at longer exposure times were thought to be a result of possible corrosion product formation on the specimen surfaces due to impurities in the melt.

9.3.4 Progress and Status

Molten lead-lithium provides one possible alternative to molten lithium for tritium breeding in fusion reactors.' We are therefore studying the compatibility of candidate structural alloys with molten lead-lithium by exposing tensile specimens of type 316 stainless steel and Sandvik HT9 to the low-melting-point (235°C) eutectic composition of Pb–17 at. % Li. The experimental conditions were similar to those used

for pure lithium static tests,' and the specific procedures for Pb–17 at. % Li were fully described in the preceding progress report.[3] Following exposure of tensile specimens in capsules of similar composition containing Pb–17 at. % Li, the specimens were cleaned by immersion in liquid mercury and/or pure lithium followed by a water rinse. Use of lithium for this purpose was found to be more efficient and did not affect the specimens at temperatures near the melting point of lithium. The cleaning procedure was repeated until specimen weights became constant, which then indicated that most of the residual lead had been removed. The lead used in the present experiments was as-received high purity (99.99%) metal while the lithium was previously purified by cold trapping and gettering. Post-test melting point analysis of the lead-lithium extracted from selected capsules indicated that the composition of these samples was indeed Pb–17 at. % Li.

In the preceding progress report,[3] specimen weight changes were reported for type 316 stainless steel and Sandvik HT9 [Fe–11.3 Cr–1 Mo (wt %)] exposed to static Pb–17 at. % Li at 300 to 500°C for 1000, 3000, and 5000 h and 1000 and 3000 h, respectively. More recent results have now been gotten for HT9 exposed at 300, 400, and 500°C for 5000 h and for type 316 stainless steel at 600 and 700°C for 1000, 3000, and 5000 h. These new data are listed in Tables 9.3.1 and 9.3.2, which also contain

Table 9.3.1. Weight Losses of Type 316 Stainless Steel Exposed to Static Pb–17 at. % Li

Exposure Temperature (°C)	Weight Loss[a] (g/m^2)		
	1000 h	3000 h	5000 h
300	0.4	0.4	1.0
400	0.9	1.2	3.2
500	7.6	14.6	12.2
600	12.1	25.9	13.0
700	6.0	12.0	5.5

[a]Average of measurements from two specimens.

Table 9.3.2. Weight Losses of HT9[a] Exposed to Static Pb–17 at. % Li

Exposure Temperature (°C)	Weight Loss[b] (g/m^2)		
	1000 h	3000 h	5000 h
300	2.3	6.6	6.0
400	3.2	5.6	5.0
500	6.5	7.6	7.6

[a]Normalized and tempered.

[b]Average of measurements from two specimens.

the previously reported[3] results. All of these weight changes are much greater than those measured for specimens exposed in argon under otherwise identical conditions. However, the room temperature tensile properties of the specimens exposed to Pb–17 at. % Li were not significantly different relative to the argon-exposed control specimens.

Consideration of the data in Table 9.3.1 reveals that there is a consistent decrease in the total weight loss of type 316 stainless steel between 3000 and 5000 h at 500, 600, and 700°C (see Figs. 9.3.1–9.3.3). Additionally, the weight losses at 700°C were smaller than those at 600°C. These observations indicate a change in corrosion mechanism at longer times and/or higher temperatures. Since the weight changes of the specimens at 500, 600, and 700°C were first negative, then became positive between 3000 and 5000 h, it appears that some corrosion product formation on the specimen occurred at a rate greater than that for dissolution. While we would not expect oxidation of the steel with the initial lithium activity of the Pb-17 at. % Li melt, such a process could occur at longer times and higher temperatures if (1) the oxygen concentration of the melt was sufficiently high to decrease the lithium activity substantially and oxidize the corroded steel surface or (2) the melt composition changed in some other way (at least locally) during the test. In pure lead, oxide films have been shown to inhibit dissolution of steel.[4] Alternatively, another impurity may be involved in corrosion product formation at the

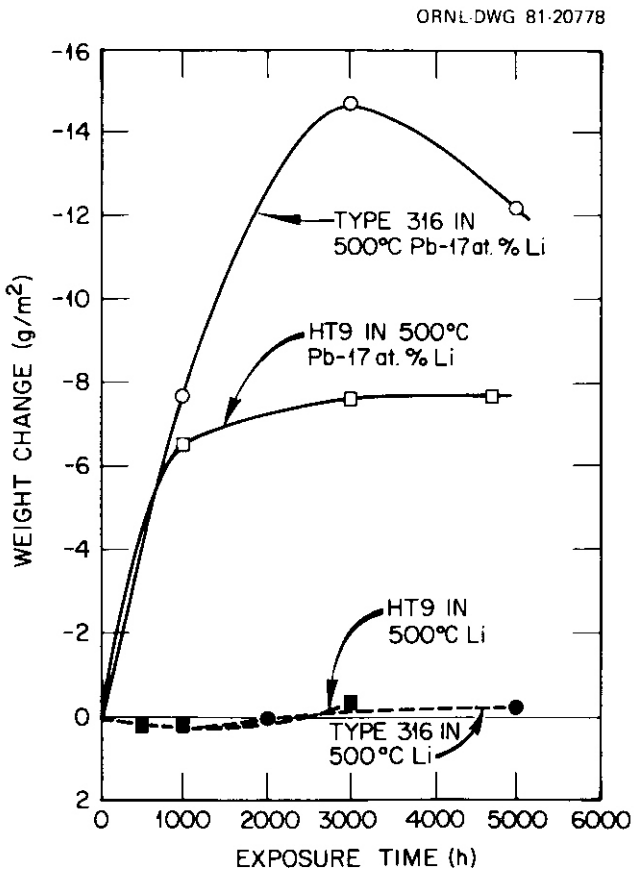

Fig. 9.3.1. Weight Change Versus Exposure Time for Type 316 Stainless Steel and HT9 Exposed to Static Lithium and Pb–17 at. % Li at 500°C.

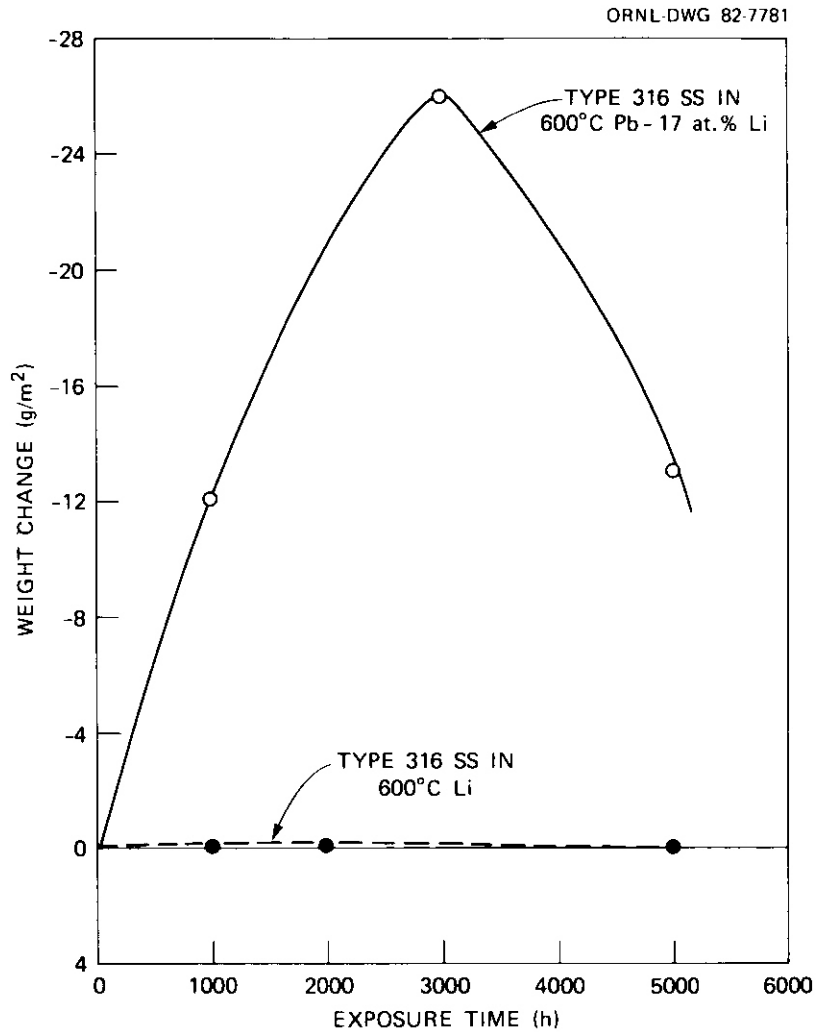

Fig. 9.3.2. Weight Change Versus Exposure Time for Type 316 Stainless Steel Exposed to Static Lithium and Pb–17 at. % Li at 600°C.

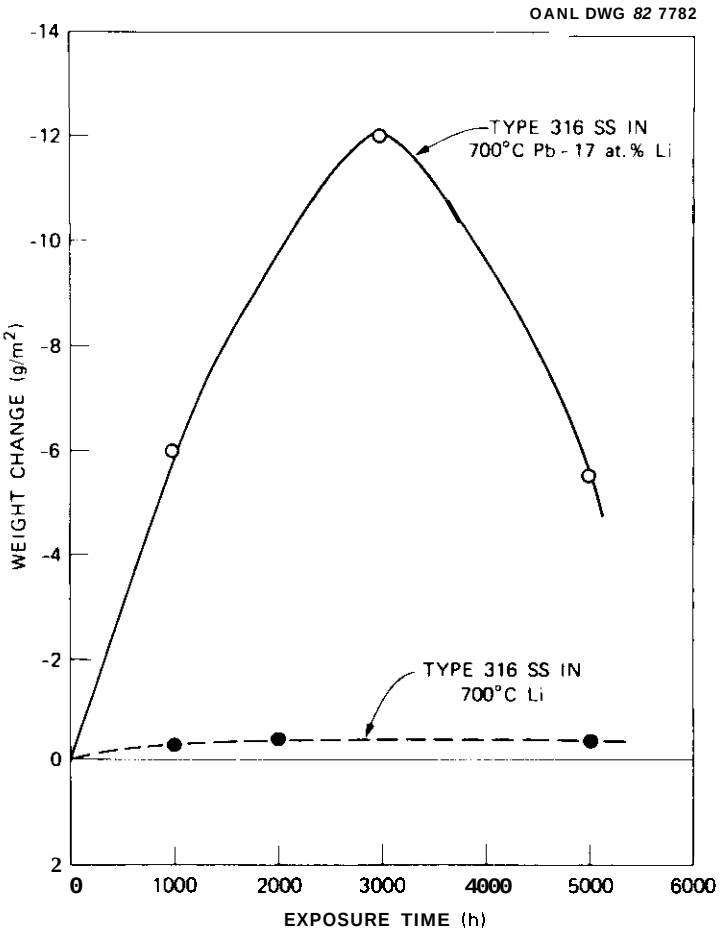

Fig. 9.3.3. Weight Change Versus Exposure Time for Type 316 Stainless Steel Exposed to Static Lithium and Pb–17 at. % Li at 700°C.

specimen surface. We are currently using x-ray diffraction to determine if such layers exist and, if so, their composition. Metallographic examination of polished cross sections did not reveal much evidence of such layers (Fig. 9.3.4), but they may be too thin to definitively identify in that manner. An alternative explanation for the increasing specimen weights at longer times and higher temperatures may be an inability to remove all the lead that has penetrated these particular specimens. However, comparison of the microstructures of the different specimens did not reveal any evidence of such residual lead or extended attack at longer times or at 700°C (Fig. 9.3.4). We are continuing our work in this area in order to better understand and characterize the corrosion in Pb–17 at. % Li. In addition to the x-ray diffraction analysis, detailed

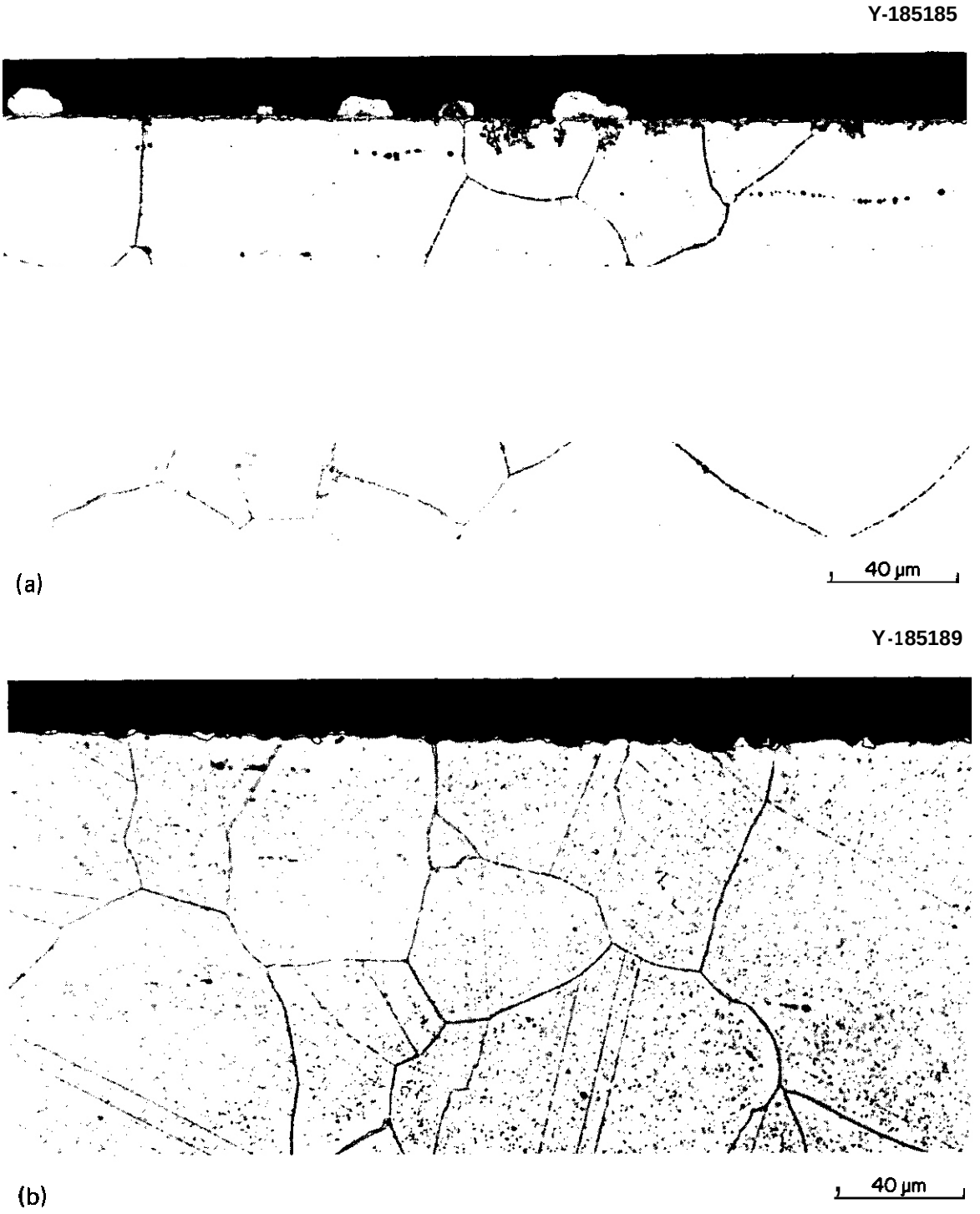

Fig. 9.3.4. Polished and Etched Cross Sections of Type 316 Stainless Steel Exposed to Pb—17 at. % Li for 5000 h at (a) 600°C. (b) 700°C.

chemical analyses of the lead-lithium and the surface regions of selected specimens and similar type 316 stainless steel capsule tests with pure lead are being undertaken.

It was reported previously[3] that lead alloyed with 17 at. % Li was more aggressive toward type 316 stainless steel and HT9 than pure lithium. The present data are consistent with this finding. Weight changes in pure, static lithium and in static Pb-17 at. % Li are plotted versus exposure time at 500, 600, and 700°C in Figs. 9.3.1 through 9.3.3, respectively. In each case (type 316 stainless steel at 500, 600, and 700°C and HT9 at 500°C), the corrosion of the specimens exposed to Pb-17 at. % Li was much greater than the negligible corrosion of the specimens exposed to pure lithium. However, the influence of impurities in the lead-lithium melt is not definitely known at this time and, as mentioned above, further work is being done to understand their role.

9.3.5 Conclusions

1. Weight losses of type 316 stainless steel and HT9 exposed to static Pb-17 at. % Li were much greater than those measured in static pure lithium.

2. Decreased weight losses at longer exposure times were observed for type 316 stainless steel exposed at 500, 600, and 700°C. This behavior is thought to be caused by possible corrosion product formation on the specimen surfaces due to impurities in the melt.

9.3.6 References

1. D. K. Sze, R. Clemmer, and E. T. Cheng, *LiPb, A Novel Material for Fusion Applications*, UWFDM-378, University of Wisconsin, Madison, October 1980.
2. P. F. Tortorelli, J. H DeVan, and R. M. Yonco, "Compatibility of Fe-Cr-Mo Alloys with Static Lithium," *J. Muter. Energy Syst.* 2: 5-15 (1981).
3. P. F. Tortorelli and J. H. DeVan, "Compatibility of Austenitic and Ferritic Steels with Pb-17 at. % Li," *ADIP Semiannu. Prog. Rep. Sept. 30, 1981*, DOE/ER-0045/7, pp. 300-11.
4. R. C. Asher, D. Davies, and S. A. Reetham, "Some Observations on the Compatibility of Structural Materials with Molten Lead," *Corros. Sci.* 17: 545-57 (1977).

9.4 COMPATIBILITY STUDIES OF STRUCTURAL ALLOYS WITH SOLID BREEDER MATERIALS – O. K. Chopra and D. L. Smith (Argonne National Laboratory)

9.4.1 ADIP Task

ADIP tasks are not defined in the 1978 program plan.

9.4.2 Objective

The objective of this task is to evaluate the compatibility of candidate solid breeder materials with structural alloys. The interactions between breeder materials and alloys are investigated as a function of temperature, time, and environmental parameters (i.e., sealed systems or flowing helium environment with different moisture content). Reaction rates are determined by measuring the thickness of corrosion scales and the depth of internal penetration. These measurements, coupled with metallographic evaluation of the alloy surfaces, are used to establish the mechanisms and rate-controlling processes for the corrosion reactions. Breeder materials to be investigated include Li_2O, $LiAlO_2$, Li_2SiO_3, Li_2TiO_3, and Li_2ZrO_3.

9.4.3 Summary

The compatibility of solid Li_2O, $LiAlO_2$, and Li_2SiO_3 breeder materials with Type 316 stainless steel and HT-9 alloy has been investigated at 773 K (500°C). The results show that for Li_2O, the alloy-ceramic interactions at 773 K are similar to that observed at 973 K (700°C). Both steels show a uniform layer of internal penetration and a thick outer scale that consists of the ceramic material embedded with iron-rich corrosion products. Specimens exposed with $LiAlO_2$ or Li_2SiO_3 show no measurable interaction. A compatibility test with Li_2O has been initiated at 823 K (550°C) in a flowing helium environment containing controlled amounts of moisture and hydrogen.

9.4.4 Progress and Status

A comparative evaluation of the reactivity of the HT-9 alloy and Type 316 stainless steel with solid Li_2O, $LiAlO_2$, Li_2SiO_3 at 973 K (700°C) was presented in an earlier report.' For these tests, tube specimens packed with the ceramic material were sealed under vacuum, enclosed in a quartz tube, and annealed for 3.6 and 7.2 Ms (1000 and 2000 h). The results indicate that Li_2O is the most reactive of the three breeding materials. Reactivity of the HT-9 alloy is comparable to that of Type 316 stainless steel. Specimens exposed with Li_2O developed a thick reaction scale that consisted of internal corrosive penetration and an outer adherent layer of ceramic material embedded with reaction products. Two reaction products, Li_5FeO_4 and $LiCrO_2$, were detected in the reaction scales on the HT-9 and Type 316 stainless steel specimens. Li_5FeO_4 was predominant in the outer scale whereas $LiCrO_2$ was observed at the alloy-ceramic interface. The results showed that the thickness of the reaction scale was the same after 3.6 or 7.2 Ms.

During the current reporting period, compatibility tests were conducted at 773 K (500°C) using the capsule-test specimens. After annealing for 3.6 and 7.2 Ms, the various specimens were sectioned and examined metallographically to determine the thickness of the reaction scale and distribution of the constituents in the scale. The Li_2O powder in both HT-9 and Type 316 stainless steel capsules was firm and compacted, whereas $LiAlO_2$ and Li_2SiO_3 retained a loose and powdery appearance after the test. Furthermore, specimens exposed with Li_2O had an adherent and brownish layer of reaction scale; consequently, the thickness of the specimens after the test was greater than the initial thickness.

The total thickness of the reaction scale was obtained from the difference between the sound metal remaining (i.e., the unreacted material) and the specimen thickness after the test. The depth of internal penetration was determined from the difference between the initial thickness of the specimen and the sound metal remaining. The

average values of total scale thickness and depth of internal penetration for the HT-9 alloy and Type 316 stainless steel exposed with Li_2O at 773 K for 3.6 and 7.2 Ms are given in Table 9.4.1. Data from the test at 973 K are included for comparison. The results at 773 K are similar to those observed at 973 K, i.e., the specimens show some internal penetration and an outer reaction scale. The values of total scale thickness and penetration are the same after 3.6 and 7.2 Ms. Also, the reactivity of the HT-9 ferritic steel is not significantly different from that of Type 316 stainless steel. For both steels, values of the total scale thickness and internal penetration at 773 K, respectively, are a factor of ~3 and 4 lower than those at 973 K.

Micrographs and concentration profiles for the major constituents across the reaction scale on Type 316 stainless steel and the HT-9 alloy exposed with Li_2O for 7.2 Ms are shown in Figs. 9.4.1a and b, respectively. The black region in the micrographs is the ceramic material.

Table 9.4.1. Average Values of Total Scale Thickness and Penetration for Alloys Exposed with Li_2O at 773 and 973 K

		HT-9 Alloy		Type 316 SS	
Temp., K	Time, Ms (h)	Total Scale, µm	Penetration, µm	Total Scale, µm	Penetration, µm
773	3.6 (1000)	29	9	19	5
	7.2 (2000)	19	5	16	4
973	3.6 (1000)	74	26	51	16
	7.2 (1000)	63	20	59	18

Both steels show an ~4-µm-thick uniform layer of internal penetration and an ~12-pm-thick outer layer of reaction scale that consists of ceramic material embedded with iron-rich reaction products. Chromium is not observed in the outer reaction scale. For Type 316 stainless steel, enrichment of chromium is observed at the interface between internal

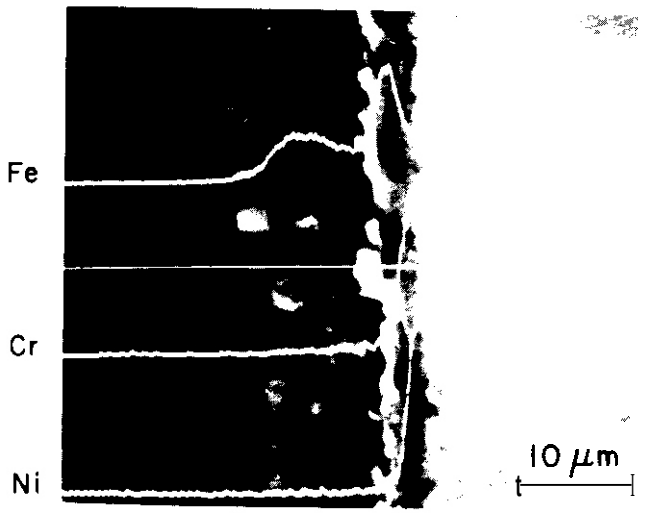

TYPE 316 SS

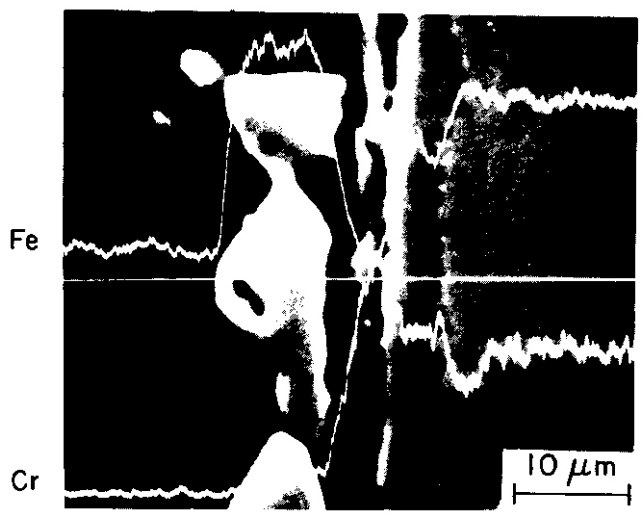

HT-9 ALLOY

Fig. 9.4.1. Micrographs and Concentration Profiles for Major Constituents of Type 316 Stainless Steel and HT-9 Alloy Exposed to Li_2O for 7.2 Ms at 773 K.

penetration and the matrix, whereas for the HT-9 alloy, the ceramic-steel interface shows chromium enrichment. Similar behavior is observed for the specimens exposed for 3.6 Ms.

The corrosion behavior of Type 316 stainless steel exposed with Li_2O at 773 K is similar to that observed at 973 K. However, the interaction between the HT-9 alloy and Li_2O is different at 773 and 973 K. A very selective attack is observed at 973 K, i.e., specimens show a network of chromium-rich oxide separated by regions of ~98% iron matrix. At 773 K, the specimens exhibit a uniform attack.

A very weak interaction was observed for the capsules exposed with $LiAlO_2$ or Li_2SiO_3 breeder material. The alloy specimens showed some reaction products at the surfaces, but no measurable internal corrosive attack. X-ray diffraction analyses of the specimens are in progress to identify the various reaction products.

A significant result from the capsule-compatibility tests is that the thickness of the reaction scale is the same after 3.6 and 7.2 Ms. This behavior suggests that the interactions between alloy and ceramic stop after a short time. It is probable that in a closed system, such as sealed capsules, the chemical activity of the reactive species decreases with time. A better understanding of the nature of the corrosive interactions can be gained by conducting compatibility tests in an open system, i.e., a flowing helium environment with controlled partial pressure of oxygen.

Figure 9.4.2 shows a schematic of the compatibility test facility to study the alloy-ceramic interactions in a flowing helium environment. The facility consists of two separate corrosion retort systems, each consisting of three specimen exposure tubes located inside a furnace. A schematic of the specimen exposure tube is shown in Fig. 9.4.3. The gas environment is provided by premixed gas mixtures of He, H_2O, and H_2. The exact composition of the environment is established by monitoring the flow of individual gas mixtures. The gases enter the specimen exposure tube at the back via an inlet tube that extends to the front of the exposure chamber to preheat the gases. The gases flow past

SOLID BREEDER **CORROSION** RETORT SYSTEMS

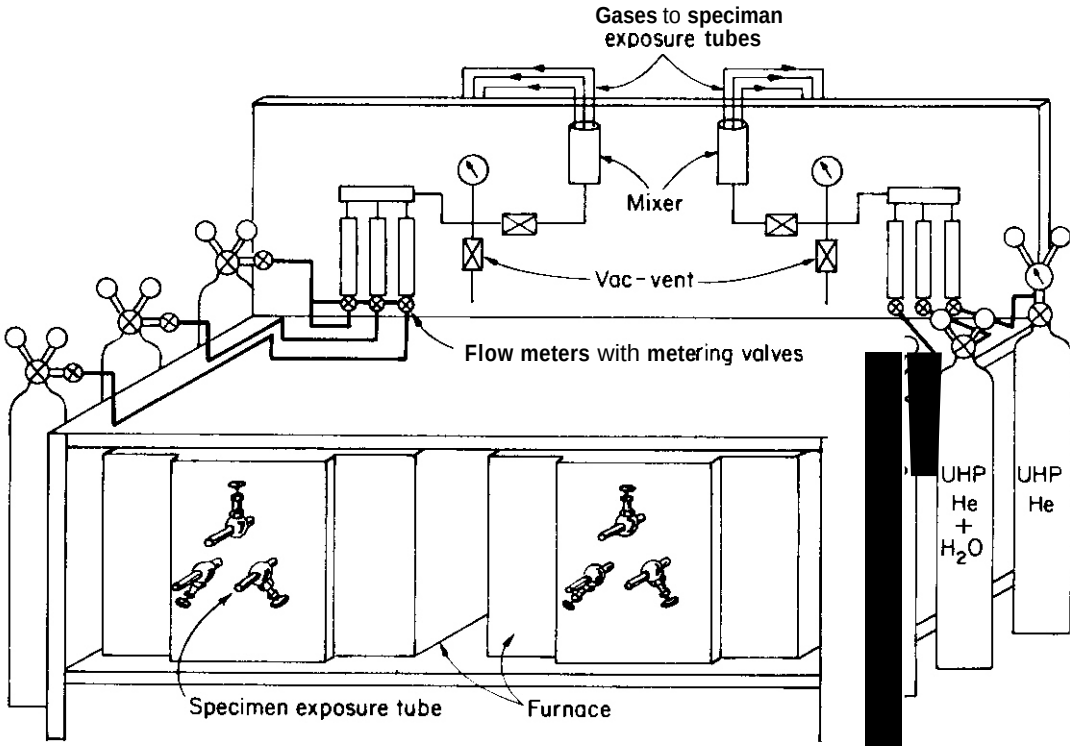

Fig. *9.4.2.* **Schematic of the Compatibility Test Facility to Study Alloy-Ceramic Interactions in a Flowing Gas Environment.**

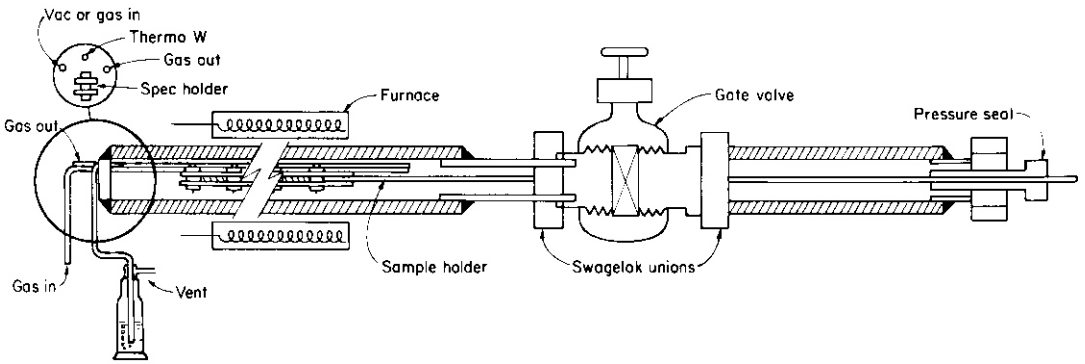

Fig. *9.4.3.* **Schematic of the Specimen Exposure Tube.**

the specimen bundle and exit at the back. The alloy specimens, 10 x 10 x 0.4 mm in size, are sandwiched between two 10 x 10 x 1.5 mm specimens of the ceramic material and mounted in a specimen holder such that the surface of the ceramic specimens is exposed to the flowing gas environment. The alloy-ceramic couples are assembled inside a glove box and transferred to the furnace in a specimen transfer tube fitted with a vacuum-tight gate valve. The specimen exposure tubes are evacuated and flushed with pure helium before introducing the specimens into the furnace.

A compatibility test with Li_2O has been initiated at 823 K in flowing helium containing ~90 ppm H_2O and ~1 ppm H_2. The alloy specimens include 20% cold-worked Type 316 stainless steel, HT-9 alloy, Fe-9Cr-1Mo steel, and pure nickel. The alloy-ceramic couples will be exposed for 1.8, 3.6, and 7.2 Ms (500, 1000, and 2000 h). This test is being conducted as part of the cooperative US/Japanese exchange with Dr. Kurasawa of the Japan Atomic Energy Research Institute.

9.4.5 Conclusions

Data from the capsule compatibility tests indicate that the interactions at 773 K between Type 316 stainless steel or HT-9 alloy and Li_2O are similar to those observed at 973 K. However, the thickness of the reaction scale and internal penetration is lower at 773 K than at 973 K. At 773 K, both steels show an ~4-μm-thick uniform layer of penetration and an ~12-μm-thick outer reaction scale. The thickness of the reaction scale is the same after 3.6 and 7.2 Ms. Specimens exposed with $LiAlO_2$ or Li_2SiO_3 show no measurable interactions. A compatibility test with Li_2O has been initiated at 823 K in a flowing helium environment containing ~90 ppm H_2O and ~1 ppm H_2.

9.4.6 References

1. O. K. Chopra and D. L. Smith, "Environmental Effects on Properties of Structural Alloys," ADIP Semiannual Progress Report, September 30, 1981, DOE/ER-0045/7, pp. 321-327.

DOE/ER-0045/8
Distribution
Category
UC-20, 20c

DISTRIBUTION

1. Ames Laboratory, Ames, IA 50011

   F. V. Nolfi

2–7. Argonne National Laboratory, 9700 South Cass Avenue, Argonne, IL 60439

   L. Greenwood
   V. Maroni
   R. F. Mattas
   R. E. Nygren
   D. L. Smith
   H. Wiedersich

8–9. Battelle-Pacific Northwest Laboratory, P.O. Box 999, Richland, WA 99352

   J. L. Brimhall
   D. Dingee

10. Brookhaven National Laboratory, Upton, NY 11973

   C. L. Snead, Jr.

11. Carnegie-Mellon University, Schenley Park, Pittsburgh, PA 15213

   J. C. Williams

12–195. Department of Energy, Technical Information Center, Office of Information Services, P.O. Box 62, Oak Ridge, TN 37830

   For distribution as shown in TID-4500 Distribution Category, UC-20 (Magnetic Fusion Energy), and UC-20c (Reactor Materials)

196–202. Department of Energy, Office of Fusion Energy, Washington, DC 20545

   M. M. Cohen
   G. M. Haas
   T. C. Reuther, Jr. (5 copies)

203. Department of Energy, Oak Ridge Operations Office, P.O. Box E, Oak Ridge, TN 37830

   Office of Assistant Manager for Energy Research and Development

204. Energy Technology Engineering Center, P.O. Box 1449, Canoga Park, CA 91304

ETEC Library

205. General Atomic Company, P.O. Box 81608, San Diego, GA 92138

D. I. Roberts

206–208. Lawrence Livermore Laboratory, P.O. Box 808, Livermore, CA 94550

E.N.C. Dalder
M. Guinan
C. M. Logan

209. Massachusetts Institute of Technology, 138 Albany Street, Cambridge, MA 02139

Θ. K. Harling

210–211. Massachusetts Institute of Technology, 77 Massachusetts Ave., Cambridge, MA 02139

N. J. Grant
V. B. Vander Sande

212–213. McDonnell Douglas Astronautics Company, East, P.O. Box 516, St. Louis, MO 63166

J. W. Davis
D. L. Kummer

214. National Materials Advisory Board, 2101 Constitution Ave., Washington, DC 20418

K. M. Zwilsky

215–217. Naval Research Laboratory, Washington, DC 20375

Superintendent, Materials Science and Technology Division
J. A. Sprague
H. Watson

218–254. Oak Ridge National Laboratory, P.O. Box X, Oak Ridge, TN 37830

Central Research Library (2 copies)
Document Reference Section
Laboratory Records Department (2 copies)
Laboratory Records Department, RC
ORNL Patent Section
E. E. Bloom (10 copies)
D. N. Braski
J. H. DeVan
I. T. Dudley
M. L. Grossbeck
M. R. Hill (3 copies)

R. L. Klueh
R. A. Lillie
C. T. Liu
K. C. Liu
L. K. Mansur
P. J. Maziasz
C. J. McHargue
T. K. Roche
A. F. Rowcliffe
J. L. Scott
P. F. Tortorelli
J. M. Vitek
F. W. Wiffen

255—256. Rensselaer Polytechnic Institute, Materials Engineering Department, Troy, NY 12181

D. Steiner
N. Stoloff

257—258. Sandia National Laboratories, Livermore Division 8316, Livermore, CA 94550

W. Bauer
J. Swearengen

259. Science Applications, Inc., 1200 Prospect, La Jolla, CA 92037

H. Gurol

260—261. University of California, Department of Chemical, Nuclear, and Thermal Engineering, Los Angeles, CA 90024

R. W. Conn
N. M. Ghoniem

262. University of California, Santa Barbara, CA 93106

G. R. Odette

263. University of Missouri, Department of Mechanical and Aerospace Engineering, Columbia, MO 65211

M. Jolles

264. University of Virginia, Department of Materials Science, Charlottesville, VA 22901

W. A. Jesser

265. University of Wisconsin, 1500 Johnson Drive, Madison, WI 53706

W. G. Wolfer

266. Westinghouse Electric Company, Fusion Power Systems Department, P.O. Box 10864, Pittsburgh, PA 15236

R. E. Gold

267. Westinghouse Electric Company, Advanced Reactors Division, P.O. Box 158, Madison, PA 15663

W. A. Boltax

268–275. Westinghouse Hanford Company, P.O. Box 1970, Richland, WA 99352

H. R. Brager
D. G. Doran
A. M. Ermi
F. A. Garner
D. S. Gelles
E. C. Opperman
R. W. Powell
J. L. Straalsund

U.S GOVERNMENT PRINTING OFFICE 1982 546-067/149